Springer Proceedings in Physics 248

Anjan Giri
Rukmani Mohanta *Editors*

Workshop on Frontiers in High Energy Physics 2019

FHEP 2019

Springer

Springer Proceedings in Physics

Volume 248

Indexed by Scopus

The series Springer Proceedings in Physics, founded in 1984, is devoted to timely reports of state-of-the-art developments in physics and related sciences. Typically based on material presented at conferences, workshops and similar scientific meetings, volumes published in this series will constitute a comprehensive up-to-date source of reference on a field or subfield of relevance in contemporary physics. Proposals must include the following:

- name, place and date of the scientific meeting
- a link to the committees (local organization, international advisors etc.)
- scientific description of the meeting
- list of invited/plenary speakers
- an estimate of the planned proceedings book parameters (number of pages/articles, requested number of bulk copies, submission deadline).

More information about this series at http://www.springer.com/series/361

Anjan Giri · Rukmani Mohanta
Editors

Workshop on Frontiers in High Energy Physics 2019

FHEP 2019

Springer

Editors
Anjan Giri
Physics Department
IIT Hyderabad
Hyderabad, Telangana, India

Rukmani Mohanta
School of Physics
University of Hyderabad
Hyderabad, Telangana, India

ISSN 0930-8989 ISSN 1867-4941 (electronic)
Springer Proceedings in Physics
ISBN 978-981-15-6291-4 ISBN 978-981-15-6292-1 (eBook)
https://doi.org/10.1007/978-981-15-6292-1

This Springer imprint is published by the registered company Springer Nature Singapore Pte Ltd.
The registered company address is: 152 Beach Road, #21-01/04 Gateway East, Singapore 189721, Singapore

Dedicated to our parents.

Organization

The Conference on Frontiers in High Energy Physics 2019 (FHEP 2019) was jointly organized by the University of Hyderabad and IIT Hyderabad, Hyderabad, India.

International Advisory Committee

B. Ananthanarayan	IISc, Bengaluru
Sukanta Bose	IUCAA, Pune
Mu-Chun Chen	UC, Irvine
Sridhara Dasu	University of Wisconsin
Amol Dighe	TIFR, Mumbai
Anjan Giri	IIT Hyderabad
Shaaban Khalil	ZCST, Giza
Anupam Mazumdar	University of Groningen
Rukmani Mohanta	University of Hyderabad
Raghavan Rangarajan	Ahmedabad University
S. Uma Sankar	IIT Bombay
Louis Strigari	Texas A&M University
L. Sriramkumar	IIT Madras
Karim Trabelsi	LAL, Paris
Urjit Yajnik	IIT Bombay

Local Organizing Committee

Shantanu Desai	IIT Hyderabad
Anjan Giri	IIT Hyderabad Convener
E. Harikumar	University of Hyderabad
Rukmani Mohanta	University of Hyderabad- Co-Convener
Narendra Sahu	IIT Hyderabad
Soma Sanyal	University of Hyderabad

Preface

In continuation of the practice of publishing the proceedings for conferences covering the latest development, we decided to publish the proceedings for the Frontiers in High Energy Physics 2019 (FHEP 2019). Apart from the excellent talks by the invited speakers, and presentation of new results and discussions, publication of the proceedings constitutes an important aspect of any conference, and the conference under consideration (FHEP 2019) is in no way different. It is very important that we spread the scientific ideas, invited talks, new results, contributed talks, and presentations during the meeting through the proceedings of the conference which will be available to all, not just the conference participants. Beginning researchers and scientists who are working in other related areas will find the present volume very interesting and useful in the sense that most aspects of High Energy Physics currently discussed are nicely covered with interesting articles by experts in the field.

Frontiers in High Energy Physics (FHEP 2019) conference is an outcome of many similar conferences held in the last few years, and from now onward it is going to be held every year at different places. Around 130 physicists and researchers, including many from outside India, participated in FHEP 2019 to discuss the latest advancements in the fields of interest. The area of High Energy Physics is going through an important and crucial phase in the sense that we have understood well the electroweak sector and discovered the last elusive particle, the Higgs boson, but there is no future direction. It actually opens up an ocean of opportunities to hypothesize and test new ideas. Interestingly, observations in the last few decades in this sector not only confirmed to the predictions of the framework of the standard model but also showed there is no evidence against it. Experimental results in the neutrino sector provide us the clue that there is much more unexplored which may give us the clue to many aspects of the Universe we live in. Experiments in the domain of Astroparticle Physics educated us with the hint that most of the total energy budget of the Universe is believed to be Dark Matter or Dark Energy. Accelerator-based Collider experiments allowed us to recreate the Universe at very early stages of evolution (we get to know about the Physics in the very hot and dense state supposed to be prevailing in the very early

Universe, the Quark Gluon Plasma, and the Physics of Heavy Ions). The High Energy experiments are providing us inputs about the Physics related to the standard model and possibly some information/hint beyond it (also known as Energy frontier). Similarly, experiments in Flavor Physics and Neutrino Physics (termed as Intensity frontier) are believed to be very helpful to obtain precision results in this sector and hopefully decipher indirectly the Physics beyond the standard model. Moreover, the observation of Gravitational waves by the LIGO and then also by the Virgo Collaborations confirm to the Century-old prediction by Einstein, where two super-massive Black Holes collide, and as a result the Gravitational waves are produced which eventually are detected by earth-based experiments, as mentioned above. In addition, there are many space-based experiments in Astrophysics and Cosmology which started providing us important information regarding the Universe at large scales (this area is also known as Cosmic Frontier). Needless to mention, there are many ongoing experiments and many future experiments planned in all the three frontiers which cover Physics from the smallest scale to the largest scale possible. Eventually, the development in these frontiers will lead us to the future in Science, Technology, and societal applications. The most important aspect of this conference is that it covered Physics topics associated with the Cosmic, Energy, and Intensity frontiers in one single platform. It is very important that Scientists working in one area should know the development and new ideas discussed and being developed in different related areas for the advancement in the right direction. We truly believe that the topic discussed during the conference and the articles published in these proceedings will be very useful to many in the fields across disciplines and will give impetus to new ideas and interesting developments.

The conference FHEP 2019 was held at the University of Hyderabad, Hyderabad, India, during 14–17 October, 2019, which was jointly organized by the University of Hyderabad and IIT Hyderabad. This volume includes manuscripts from both invited and contributed talks and poster contributions from Gravitation and Cosmology, Neutrino and Dark Matter, Beyond the Standard Model and Collider Physics, QCD and Heavy Ion Physics, and Flavor Physics. Some new results are also presented, including the review talks on the new developments during the past year covering almost all areas of High Energy Physics. The articles in this volume are very nicely written which gives a reader in this area regarding the status, latest results and possible new directions. The book is intended for both young as well as advanced researchers of the field who are actively following the exciting time that we are going through when we are expecting something new to show up either at the energy frontier or maybe at the intensity and cosmic frontiers.

Hyderabad, India

Anjan Giri
Rukmani Mohanta

Acknowledgements

Organizing a conference like FHEP 2019 (Conference on Frontiers in High Energy Physics 2019) and bringing out the proceedings of the conference is undoubtedly a difficult job, and it would not have been possible to do so without the support and active participation of our colleagues and many students in both the organizing Institutes. The cooperation we received from the Advisory Committee members during the organization of the conference was truly exemplary. We thank all the members of the Advisory Committee from the bottom of our heart for their help in making FHEP 2019 a grand success. We take this opportunity to specially thank Urjit Yajnik, Sukanta Bose, Raghavan Rangarajan, S. Uma Sankar, L. Sriram Kumar, Sridhar Dasu, Karim Trabelsi, and other members in the Advisory committee regarding various organizational aspects including their help in suggesting possible invited speakers and the perfect balance between various topics discussed during the conference which made FHEP 2019 an enjoyable and fruitful meeting. We thank all the members of the Local Organizing Committee for their constant support and encouragement for organizing the conference smoothly. We would also like to thank the members of our Editorial board for their constant support in reviewing the abstracts, finalizing the programs, and finally reviewing the proceedings' drafts. Our special thanks to Narendra Sahu and E. Hari Kumar for innumerable discussions and suggestions during the process for all the support extended to us at critical times. We must also take this opportunity to thank our colleagues in School of Physics, University of Hyderabad, and Department of Physics, IIT Hyderabad. It was indeed a pleasure to work with you all!

The success of a conference depends largely on the exciting discussion, the mesmerizing lectures from the experts, and the fruitful discussions. We would like to express our sincere thanks to all our renowned invited speakers, presenters, and the rest of the enthusiastic participants for making FHEP 2019 a very successful conference. We were lucky to have a large pool of research scholar volunteers who worked relentlessly during the conference. It would have been a Herculean task to organize this event without the active support of our students, in particular, Suchismita Sahoo, Mitesh Behera, Rudra Majhi, Atasi Ray, Aishwarya Bhatt, Dinesh Singha, Akshay Chatla, Manas Mohapatra, Subhasmita Mishra, Seema

Choudhury, Lopamudra Nayak, Rashmi Dhamija, Vishnu Rajagopal, Haritha CP, Sovan Sau, Abhishek Saha, and Karthik Jain M. Thank you all very much for providing the helping hand during the entire duration of preparation till the conclusion. We would also thank the Vice-Chancellor, University of Hyderabad, and the Director, IIT Hyderabad, for their constant support and encouragement and the staff members both at the School of Physics, University of Hyderabad, and Department of Physics, IIT Hyderabad for providing the assistance whenever needed. Needless to say, the conference would not have been possible without the active and financial support from University of Hyderabad and IIT Hyderabad.

We would like to express our sincere thanks to Dr. Loyola D'Silva, Publishing Editor (Springer Nature, Singapore) and Ms. Shalini Monica C., Project Coordinator (Springer Nature, India) for constantly working with us from the beginning to bring out this volume.

Hyderabad, India

Anjan Giri
Rukmani Mohanta

Contributions

Abhisek Saha	University of Hyderabad
Abhishek Mathur	Raman Research Institute
Abhishek Naskar	Indian Statistical Institute, Kolkata
Agnivo Sarkar	IIT Gandhinagar
Ahmed Rizwan	NIT Surathkal
Aishwarya Bhatta	University of Hyderabad
Ajit Srivastava	Institute of Physics, Bhubaneswar
Akshay Chatla	University of Hyderabad
Aman Awasthi	IIT Bombay
Ananya Mukherjee	Physical Research Laboratory, Ahmedabad
Anjan Giri	IIT Hyderabad
Anju Dahiya	University of Delhi
Antonio De Felice	YITP, Kyoto University
Archita Bhattacharyya	Indian Statistical Institute, Kolkata
Arvind Kumar Mishra	Physical Research Laboratory, Ahmedabad
Atasi Ray	University of Hyderabad
Barilang Mawlong	University of Hyderabad
Bhawna Gomber	University of Hyderabad
Bipin Sonawane	Amity University, Mumbai
Chayan Majumdar	IIT Bombay
Christopher Hearty	University of British Columbia/IPP
Debabrata Chandra	Indian Statistical Institute, Kolkata
Debasis Sahu	F.M. University, Balasore
Debasish Majumdar	SINP, Kolkata
Debika Kangsha Banik	Dibrugarh University
Dibyendu Nanda	IIT Guwahati
Dinesh Kumar Singha	University of Hyderabad
Diptimoy Ghosh	IISER Pune
Harikumar E.	University of Hyderabad
Gagan Mohanty	TIFR, Mumbai
Haritha C. P.	University of Hyderabad

Harleen Dahiya	NIT Jalandhar
Himanshu Verma	IIT Bombay
Itishree Sethi	IIT Hyderabad
Jyotirmoi Borah	IIT Guwahati
Kajal Samanta	IIT Guwahati
Kalpana Bora	Gauhati University
Karthik Jain M.	University of Hyderabad
Kartik Joshi	IISER Mohali
Khusboo Dixit	IIT Jodhpur
L. Sriramkumar	IIT Madras
Lopamudra Nayak	IIT Hyderabad
Madhurima Pandey	SINP, Kolkata
Manas Mohapatra	IIT Hyderabad
Michael Ratz	University of California, Irvine
Mitesh Kumar Behera	University of Hyderabad
Mu-Chun Chen	University of California, Irvine
M. Sivakumar	University of Hyderabad
N. Sushree Ipsita	IIT Hyderabad
N. Nimai Singh	Manipur University
Narendra Sahu	IIT Hyderabad
Navdeep Kaur	NIT Jalandhar
A. Naveena Kumar	NIT Surathkal
Neelu Mahajan	GGDSD College, Chandigarh
Nilakshi Das	NIT Silchar
Nimmala Narendra	IIT Hyderabad
Nishita Desai	TIFR, Mumbai
Nitin Joshi	IIT Ropar
Nur Jaman	CTP, Jamia Millia Islamia
Prabhat Ranjan Pujahari	IIT Madras
Pravata Mohanty	TIFR, Mumbai
P. K. Suresh	University of Hyderabad
Priyanka Kumar	Gauhati University
Priyanka Sarmah	IIT Bombay
Raghavan Rangarajan	Ahmedabad University
Raghunath Sahoo	IIT Indore
Rajeev N.	NIT Silchar
Rashmi Dhamija	IIT Hyderabad
Rathin Adhikari	CTP, Jamia Millia Islamia
Richa Arya	Physical Research Laboratory, Ahmedabad
Rijeesh Keloth	IIT Hyderabad
Rishav Roshan	IIT Guwahati
Ritu Aggarwal	Savitribai Phule Pune University
Rudra Majhi	University of Hyderabad
Rukmani Mohanta	University of Hyderabad
Salil Joshi	University of Hyderabad

Sarath N.	Cochin University of Science & Technology
Satvir Kaur	NIT Jalandhar
Seema Choudhury	IIT Hyderabad
Shantanu Desai	IIT Hyderabad
Shibasis Roy	IMSc Chennai
Shrihari Gopalakrishna	IMSc Chennai
Shriniketan Acharya	University of Hyderabad
Shivaramakrishna Singirala	IIT Indore
Siddhartha Karmakar	IIT Indore
Soma Sanyal	University of Hyderabad
Soumen Nayak	University of Hyderabad
Sourav Dey	Tel Aviv University, Israel
Sourov Roy	IACS, Kolkata
Sovan Saul	University of Hyderabad
Sruthilaya M.	University of Hyderabad
Subhasmita Mishra	IIT Hyderabad
Subhendra Mohanty	Physical Research Laboratory, Ahmedabad
Subhendu Rakshit	IIT Indore
Suchismita Sahoo	Physical Research Laboratory, Ahmedabad
Sudhanwa Patra	IIT Bhilai
Sudhir Vempati	IISc, Bengaluru
Suhail Khan	CTP, Jamia Millia Islamia
Sukanya Bhattacharya	Physical Research Laboratory, Ahmedabad
Sukanta Bose	IUCAA, WSU
Suman Kumbhakar	IIT Bombay
Supriya Senapati	IIT Bombay
Swayamshree Senapatil	University of Hyderabad
Takaaki Nomura	KIAS
Tanmay Kumar Poddar	Physical Research Laboratory, Ahmedabad
Tony Pinhero	Indian Statistical Institute, Kolkata
Urjit Yajnik	IIT Bombay
Varun Sharma	University of Wisconsin Madison (US)
Vishnu Rajagopal	University of Hyderabad
Wolfgang Altmannshofer	UC Santa Cruz

Contents

Contributors

Rathin Adhikari Centre for Theoretical Physics, Jamia Millia Islamia (Central University), New Delhi, India

Ritu Aggarwal Savitribai Phule Pune University, Pune, India

C. L. Ahmed Rizwan Department of Physics, National Institute of Technology Karnataka (NITK), Mangaluru, India

K. M. Ajith Department of Physics, National Institute of Technology Karnataka (NITK), Mangaluru, India

Wolfgang Altmannshofer Santa Cruz Institute for Particle Physics, University of California, Santa Cruz, CA, USA

K. S. Ananthram Department of Physics, National Institute of Technology Karnataka (NITK), Mangaluru, India

Richa Arya Physical Research Laboratory, Ahmedabad, India;
Indian Institute of Technology Gandhinagar, Gandhinagar, India

Biswajit Banerjee Astroparticle Physics and Cosmology Division, Saha Institute of Nuclear Physics, HBNI, Kolkata, India

Shibaji Banerjee Department of Physics, Kolkata, India

Mitesh Behera University of Hyderabad, Hyderabad, India

Imtiyaz Ahmad Bhat Centre for Theoretical Physics, Jamia Millia Islamia (Central University), New Delhi, India

Aishwarya Bhatta School of Physics, University of Hyderabad, Hyderabad, India

Biplob Bhattacherjee Centre for High Energy Physics, Indian Institute of Science, Bangalore, India

Bipul Bhuyan Indian Institute of Technology Guwahati, Assam, India

Anirban Biswas School of Physical Sciences, Indian Association for the Cultivation of Science, Kolkata, India

Kalpana Bora Gauhati University, Guwahati, Assam, India

Debasish Borah Department of Physics, Indian Institute of Technology, Guwahati, Assam, India

Jyotirmoi Borah Indian Institute of Technology Guwahati, Assam, India

Pritibhajan Byakti Centre for High Energy Physics, Indian Institute of Science, Bangalore, India;
Department of Physics, Pandit Deendayal Upadhyaya Adarsha Mahavidyalaya (PDUAM) Eraligool, Karimganj, Assam, India

Mu-Chun Chen Department of Physics and Astronomy, University of California, Irvine, CA, USA

S. Choudhury Indian Institute of Technology Hyderabad, Telangana, India

Debika Chowdhury Department of Theoretical Physics, Tata Institute of Fundamental Research, Mumbai, India

Baradhwaj Coleppa Physics Discipline, Indian Institute of Technology Gandhinagar, Gandhinagar, Gujarat, India

Harleen Dahiya Department of Physics, Dr. B.R. Ambedkar National Institute of Technology, Jalandhar, India

Nilakshi Das National Institute of Technology Silchar, Silchar, India

Antonio De Felice Yukawa Institute for Theoretical Physics, Kyoto University, Kitashirakawa Oiwakecho, Sakyo Ward, Kyoto, Japan

Nishita Desai Department of Theoretical Physics, Tata Institute of Fundamental Research, Mumbai, India

S. Dey Tel Aviv University, Tel Aviv, Israel

Khushboo Dixit Indian Institute of Technology Jodhpur, Jodhpur, India

Rupak Dutta National Institute of Technology Silchar, Silchar, India

Sougata Ganguly School of Physical Sciences, Indian Association for the Cultivation of Science, Kolkata, India

Bhawna Gomber University of Hyderabad, Hyderabad, India

Shrihari Gopalakrishna Institute of Mathematical Sciences (IMSc), Chennai, India;
Homi Bhabha National Institute (HBNI), Anushaktinagar, Mumbai, India

Ashadul Halder Department of Physics, Kolkata, India

E. Harikumar School of Physics, University of Hyderabad, Hyderabad, Telangana, India

Nur Jaman Centre for Theoretical Physics, Jamia Millia Islamia, New Delhi, India

Soumya Jana Département de Physique Théorique, Université de Genève, 1211 Gen ève 4, Switzerland

Siddhartha Karmakar Discipline of Physics, Indian Institute of Technology Indore, Simrol, Indore, India

Manjit Kaur Panjab University, Chandigarh, India

Navdeep Kaur Department of Physics, Dr. B.R. Ambedkar National Institute of Technology, Jalandhar, India

Satvir Kaur Department of Physics, Dr. B.R. Ambedkar National Institute of Technology, Jalandhar, India

Dinesh Kumar University of Rajasthan, Jaipur, India;
National Centre for Nuclear Research, Warsaw, Poland

Priyanka Kumar Cotton University, Guwahati, Assam, India

Ashutosh Kumar Alok Indian Institute of Technology Jodhpur, Jodhpur, India

Arvind Kumar Mishra Theoretical Physics Division, Physical Research Laboratory, Navrangpura, Ahmedabad, India;
Indian Institute of Technology Gandhinagar, Gandhinagar, Gujarat, India

Santosh Kumar Rai Regional Center for Accelerator-based Particle Physics, Harish-Chandra Research Institute, HBNI, Prayagraj, Allahabad, India

Suman Kumbhakar Indian Institute of Technology Bombay, Mumbai, India

Ashwani Kushwaha Centre for High Energy Physics, Indian Institute of Science, Bangalore, India;
INFN-Sezione di Napoli, Complesso Universitario di Monte S. Angelo, Napoli, Italy

R. B. MacKenzie Groupe de physique des particules, Département de physique, Université de Montréal, Montréal, QC, Canada

Neelu Mahajan Department of Physics, G.G.D.S.D College, Chandigarh, India

Rudra Majhi University of Hyderabad, Hyderabad, India

Chayan Majumdar Indian Institute of Technology Bombay, Mumbai, India

Debasish Majumdar Astroparticle Physics and Cosmology Division, Saha Institute of Nuclear Physics, HBNI, Kolkata, India

Subhasmita Mishra IIT Hyderabad, Hyderabad, India

Anuradha Misra Department of Physics, University of Mumbai, Mumbai, India

Rukmani Mohanta School of Physics, University of Hyderabad, Hyderabad, India

P. K. Mohanty Tata Institute of Fundamental Research, Mumbai, India

Subhendra Mohanty Theoretical Physics Division, Physical Research Laboratory, Ahmedabad, India

Manas K. Mohapatra Indian Institute of Technology, Kandi, Hyderabad, India

Ananya Mukherjee Theoretical Physics Division, Physical Research Laboratory, Ahmedabad, Gujarat, India

Dibyendu Nanda Department of Physics, Indian Institute of Technology, Guwahati, Assam, India

A. Naveena Kumara Department of Physics, National Institute of Technology Karnataka (NITK), Mangaluru, India

Bibekananda Nayak P. G. Department of Applied Physics and Ballistics, Fakir Mohan University, Balasore, Odisha, India

Takaaki Nomura School of Physics, Korea Institute for Advanced Studay (KIAS), Seoul, Republic of Korea

Madhurima Pandey Astroparticle Physics and Cosmology Division, Saha Institute of Nuclear Physics, HBNI, Kolkata, India

Sujata Pandey Discipline of Physics, Indian Institute of Technology Indore, Simrol, Indore, India

M. B. Paranjape Groupe de physique des particules, Département de physique, Université de Montréal, Montréal, QC, Canada

Mahadev Patgiri Cotton University, Guwahati, Assam, India

Sudhanwa Patra Department of Physics, IIT Bhilai, GEC Campus, Raipur, India

Avik Paul Astroparticle Physics and Cosmology Division, Saha Institute of Nuclear Physics, HBNI, Kolkata, India

Tanmay Kumar Poddar Theoretical Physics Division, Physical Research Laboratory, Ahmedabad, India

Prabhat R. Pujahari Physics Department, Indian Institute of Technology Madras, Chennai, TN, India

H. V. Ragavendra Department of Physics, Indian Institute of Technology Madras, Chennai, India

Vishnu Rajagopal School of Physics, University of Hyderabad, Hyderabad, Telangana, India

N. Rajeev National Institute of Technology Silchar, Silchar, India

Subhendu Rakshit FHEP 2019, Hyderabad, India;
Discipline of Physics, Indian Institute of Technology Indore, Simrol, Indore, India

Raghavan Rangarajan School of Arts and Sciences, Ahmedabad University, Ahmedabad, India

Kumar Rao Indian Institute of Technology Bombay, Mumbai, India

Michael Ratz Department of Physics and Astronomy, University of California, Irvine, CA, USA

Vaibhav Rawoot Amity School of Applied Sciences, Amity University Mumbai, Mumbai, India

Atasi Ray School of Physics, University of Hyderabad, Hyderabad, India

Saurabh D. Rindani Theoretical Physics Division, Physical Research Laboratory, Navrangpura, Ahmedabad, India

Sourov Roy School of Physical Sciences, Indian Association for the Cultivation of Science, Kolkata, India

Abhisek Saha University of Hyderabad, Hyderabad, India

Raghunath Sahoo Discipline of Physics, School of Basic Sciences, Indian Institute of Technology Indore, Indore, India

Suchismita Sahoo Department of Physics, Central University of Karnataka, Kalaburagi, India

Debasis Sahu P. G. Department of Applied Physics and Ballistics, Fakir Mohan University, Balasore, Odisha, India

S. Uma Sankar Indian Institute of Technology Bombay, Mumbai, India

Soma Sanyal University of Hyderabad, Hyderabad, India

Agnivo Sarkar Physics Discipline, Indian Institute of Technology Gandhinagar, Gandhinagar, Gujarat, India

Neelakshi Sarma Gauhati University, Guwahati, Assam, India

Priyanka Sarmah Indian Institute of Technology Bombay, Mumbai, India

Sovan Sau University of Hyderabad, Hyderabad, India

Supriya Senapati Indian Institute of Technology Bombay, Mumbai, India

Swayamshree Senapati University of Hyderabad, Hyderabad, India

Itishree Sethi Department of Physics, IIT Hyderabad, Kandi, India

Varun Sharma University of Wisconsin, Madison, WI, USA

Shivaramakrishna Singirala IIT Indore, Indore, India

A. Soffer Tel Aviv University, Tel Aviv, Israel

Bipin Sonawane Amity School of Applied Sciences, Amity University Mumbai, Mumbai, India

C. Soumya Institute of Physics, Bhubaneswar, India

L. Sriramkumar Department of Physics, Indian Institute of Technology Madras, Chennai, India

Ajit M. Srivastava Institute of Physics Sachivalaya Marg, Bhubaneswar, India

Sudhir K. Vempati Centre for High Energy Physics, Indian Institute of Science, Bangalore, India

U. A. Yajnik Physics Department, Indian Institute of Technology Bombay, Mumbai, India

Part I
Gravitation and Cosmology

Chapter 1
Re-visiting Gravitational Wave Events with Pulsars as Weber Detectors

Ajit M. Srivastava

Abstract Many gravitational wave (GW) signals have been detected by LIGO and Virgo. These waves reached earth directly from their respective sources. We consider the possibility that, when these waves travel to different pulsars causing (tiny) transient deformations in the pulsar shape, then the resultant transient change in the pulsar moment of inertia may be detectable by the extremely precisely measured pulsar signals. This is especially likely when the signal frequency is in resonance with some neutron star oscillation mode. In this situation, the pulsars will act as a remotely stationed Weber gravitational wave detector. This technique also allows us to detect past GW events where the direct signals were missed. We have considered various GW events, for example different supernova events as recorded in astronomical records, and have determined specific pulsars whose signals should carry the imprints of these GW events reaching earth in near future.

PACS 97.60.Gb · 95.55.Ym · 04.80.Nn · 26.60.+c

1.1 Introduction

Detection of gravitational waves (GW) by LIGO and Virgo has allowed us to observe remarkable events of coalescing black holes (BH) as well as neutron stars. We discuss a new class of GW detectors [1]. We consider the deformations caused by the gravitational wave (GW) passing through a pulsar. This leads to variation in its moment of inertia affecting spin rate of the pulsar as well as its pulse profile. Careful monitoring of extremely precisely measured pulses from the pulsars can reveal the arrival of GW signals on those pulsars. The effect will be most pronounced at resonance. The pulsars thus act as remotely stationed Weber detectors of gravitational waves with their signals being monitored on earth [1]. A very important use of this technique will be in detection of those GW events whose direct GW signal reached earth in

A. M. Srivastava (✉)
Institute of Physics Sachivalaya Marg, Bhubaneswar 751005, India
e-mail: ajit@iopb.res.in

A. Giri and R. Mohanta (eds.), *Workshop on Frontiers in High Energy Physics 2019*, Springer Proceedings in Physics 248,
https://doi.org/10.1007/978-981-15-6292-1_1

past. Knowing the GW source, and the locations of different pulsars allows us to predict when the imprints of that particular GW event can be seen on the specific pulsar signal in future. This allows for re-visiting the same source again and again via different pulsars giving us opportunity to make detailed investigations of that GW source, along with the properties of the relevant pulsar interiors. It is known that a typical supernova event can be a powerful source of GW emission [5]. With the location and date of these events known, our technique allows us to directly observe that specific supernova event, in some sense allowing us to visit past events. Clearly there will be numerous GW events (supernova events, merger events etc.) which are not even identified by any known records. Continuous monitoring of pulsar signals for such transient perturbations can reveal existence of such GW sources.

The most crucial element underlying this proposal is extreme accuracy with which pulsar signals are monitored on earth. We will start by discussing the basic features of the pulsar signals in the next section. We will also briefly recall our earlier work [2] where it was proposed that this extreme precision of pulsar observations can be used to monitor density fluctuations occurring inside pulsar cores, e.g. those occurring during a phase transition. We will also discuss that these density fluctuations can lead to rapidly changing quadrupole moment of the pulsar leading to GW emission. In subsequent section we will then discuss the response of the neutron star (NS) to external GWs and show that it can act as a Weber detector at resonance. We will then discuss specific past GW events and make predictions of specific dates on which such past GW events can be seen imprinted on different pulsar signals.

1.2 Pulsars and Phase Transitions

We start by recalling basic properties of a pulsar which is a rapidly rotating neutron star. Neutron stars typically form in supernova explosions. Their masses are typically in the range of 1–2 solar mass, and radius about 10–15 km. Central density of NS can be as high as 5–10 times the nuclear equilibrium density of $0.16/\text{fm}^3 \simeq 10^{14}$ grams/cm^3. It is believed that there is a superfluid phase of nucleons in the interior of neutron stars. Observational evidence for this superfluid nucleonic phase arises from pulsar observations. Pulsars are rapidly rotating neutron stars, detected by their periodic pulses (electromagnetic waves), which are beamed emission from the magnetic poles of the neutron star. Superfluid phase in the pulsar interior allows for vortex lattice to form. These vortices are pinned at the interface with the pulsar crust. Many pulsars show the phenomenon of glitches which is a rapid increase in the rotation speed of the pulsar, followed by a slow relaxation. The most consistent explanation for these glitches is in terms of vortex depinning from crust. We mention here that there have been observations of anti-glitches (sudden slowing down of pulsar) which cannot be accounted for by this vortex-depinning mechanism.

Pulsar timings are extremely precisely measured, indeed they are the best clocks available in space. For example, the pulsar J0437-4715 has a pulse time period P = 0.005757451936712637 sec. This is known with the error of 1.7×10^{-17} sec. We

use this incredible precision for detecting changes occurring in the configuration of a neutron star. We have argued that this extreme accuracy of pulsar timings can be used to probe various phase transitions occurring inside the pulsar core, for example transitions to exotic phases of QCD, or nucleonic superfluidity [2]. We used association of phase transitions with density fluctuations which inevitably arise during phase transitions. Importantly, the statistical properties of the density fluctuations crucially depend on the nature of the phase transition. Any density fluctuations in the neutron star will have observational effects. It will affect its moment of inertia (MI) and quadrupole moment Q which can be detected by precision measurements of pulse shape/timing. Note that these changes in MI and Q can have both signs, + and −. Random density fluctuations will lead to changes in all components of MI tensor. Changes in the diagonal components of MI will result in rapid changes in the rotation of pulsar. As density fluctuations dissipate away, leading to a uniform new phase in the core, some part of change in MI will be restored, but not fully. This is exactly the pattern of glitches and anti-glitches where often only few percent of the change in rotation is recovered. Also, as we find changes of both + and − sign in MI, glitches and anti-glitches are both naturally accommodated in this picture. Importantly, there has to be also transient change in the off-diagonal components of MI and Q. These are distinctive predictions of our model. Changes in off-diagonal components will lead to wobbling of star (on top of any present initially). This will lead to modulation of pulse intensity as the direction of radiation emission wobbles. We have made estimates of the changes in MI and Q for specific models, e.g. first order phase transition with specific bubble sizes, formation of QCD Z(3) strings/domain walls, as well as formation of superfluid vortices in a nucleon superfluid phase transition. We estimate fractional changes of various components of MI and Q caused by density fluctuations in these cases. Due to large range of distance scales involved (from relevant correlation lengths to pulsar core size), one needs to extrapolate the results. With these limitations we expect fractional changes in various moment components of order ranging from 10^{-14} to 10^{-10}.

An important implication of these density fluctuation is that rapid changes in quadrupole moment Q will lead to gravitational waves. We get a small value of Q/I arising from density fluctuations of order 10^{-10} which is much smaller than the value of 10^{-6} typically invoked from structural deformation in a neutron star. However, it is more than compensated by the very short time scale of microseconds when gravitational wave (GW) power is calculated as GW power is proportional to the square of third time derivative of the quadrupole moment. Fastest time scale for conventional mechanism of gravitational wave emission is milliseconds (from pulsar rotation), with the largest values of Q/I of order 10^{-3}. In our case, for phase transitions, Q/I is very tiny, of order 10^{-10}. However, here the time scale is at most microseconds. In fact, for topological defect induced density fluctuations, the time scale can be much shorter as initial defect network coarsens very fast. This very short time scale can lead to powerful GW bursts even for such tiny changes in Q/I thereby providing a new source of gravitational radiation.

1.3 Pulsars as Weber Detectors

Now we discuss changes in pulsar due to external influence. A gravitational wave passing through a pulsar will cause (very) tiny deformations in the pulsar shape, affecting its rotation. The effect will be most pronounced at resonance and may be detectable by accurate observations of the pulsar signal. We will argue below that resonance is likely with pulsar equation of state and tidal deformability constrained by recent BNS merger event. The pulsar, thus, acts as a remotely stationed Weber detector of gravitational waves whose signal can be monitored on earth [1].

Consider a pulsar under influence of external gravitational waves (GW), coming, say, from a merger event far away. For simplicity, we take the equilibrium configuration of the pulsar to be spherical. Under the influence of external gravitational wave, the pulsar will undergo quadrupolar deformations. Deformation of neutron star in the Tidal field E_{ij} of the gravitational wave is given by

$$Q_{ij} = -\lambda_d E_{ij} \ . \tag{1.1}$$

E_{ij} is the tidal field of the external GW and λ_d is the tidal deformability given by $\lambda_d = \frac{2}{3} k_2 \frac{R^5}{G}$. k_2 is known as the second Love number. Recent BNS mergers have put constraints on the value of k_2 to be in the range $k_2 \simeq 0.05 - 0.15$ [3]. $E_{ij} = R_{i0j0}$ ($R_{\mu\nu\lambda\rho}$ being the Riemann curvature tensor) can be written in terms of GW strain amplitude for a specific polarization in the transverse traceless (TT) gauge. For a GW with wavelength λ, denoting the strain h_+ for the + polarization by h, the amplitude of resulting E_{ij} is given by

$$E_{xx} = -E_{yy} = \frac{2\pi^2 h c^2}{\lambda^2}, \tag{1.2}$$

For simplicity, we take the initial NS configuration to be spherically symmetric, and the deformation to be ellipsoidal, with the dimension in the direction of GW propagation remaining unchanged. Then using (1.1) and (1.2), we get the change in the moment of inertia of the NS to be [1]

$$\frac{\Delta I_{xx}}{I} = -\frac{\Delta I_{yy}}{I} \simeq \frac{k_2}{3} \frac{R^3 c^2}{GM\lambda^2} 20h \tag{1.3}$$

Here M is the mass of NS and R is its equilibrium radius. We will use sample values $M = M_{Sun}$ and R = 10 km. Highest sensitivity will be reached for smallest values of λ (we mention that the above equations are valid for static case, this requires λ to be much larger than NS radius. Range of frequencies we consider are below kHz, so this approximation holds).

As a typical astrophysical source of GW, we take binary neutron Star (BNS) merger, such as the one detected by LIGO/Virgo The highest value of GW frequency being about 1 kHz, and we use k2 = 0.1 as a sample value. This gives $\frac{\Delta I_{xx}}{I} = 10^{-2} h$.

Peak strength of the GW signal for the LIGO-Virgo detected BNS merger event had $h \sim 10^{-19}$, with the earth-Source distance of about 130 million light years. The main advantage of the pulsar Weber detector is that it could be very close to the GW source (BNS merger in this case). Suppose it was at 100 light year distance from the BNS merger. (Note, most neutron stars/pulsars are in globular clusters with very dense cores, so this situation may not be very unlikely). Then the GW strength at the pulsar will be $h \sim 10^{-13}$. Resulting fractional change in moment of inertia (for the Relevant component), hence change in spin rate, will be

$$\frac{\Delta\nu}{\nu} = -\frac{\Delta I}{I} \simeq 10^{-15} \tag{1.4}$$

If the detector pulsar was 10,000 light years away from BNS merger, this number will be $\sim 10^{-17}$. Such fractional changes in the spin rate of pulsars should be detectable by precision measurements of the pulses. For millisecond pulsars, accuracy of pulse timings have been measured to an accuracy better than $10^{-15} - 10^{-17}$ seconds. Note that such remarkable accuracy for pulse timings typically requires folding over large number of pulses. For this it is important to realize that a neutron star acting as a Weber detector at resonance will exhibit the *Ringing effect*. Indeed, this is how Weber detector achieves very high accuracy. Above estimates for pulsar spin rate changes did not account for resonance, which can dramatically increase the effects of GW. For example, resonant tidal deformations from orbiting binaries can lead to rupture of NS crust. It has been argued that viscous effects may not be very dominant for the relevant time scales. More precisely, one needs to know the quality factor Q for NS interior For specific modes, the resonant frequencies of NS can be in the Range of 100 Hz–1 kHz. Note that this is precisely the range relevant for a typical BNS merger GW source, also for BH mergers of suitable masses. Thus the possibility remains that resonance effects may lead to significant enhancement of the effect of GW on NS spin rate change.

Although, significant amplitude enhancement due to resonance generally requires sustained periodic signal, which is unlikely for the case of a burst of GW, we recall that for Weber detector, use of material of very high quality factor (with Q factor of order 10^6) was important. This is because with high Q material, even for a short GW pulse, there is strong ringing effect for a Weber detector operating at resonance which helps in enhancing signal to noise ratio. Due to this ringing effect, the detector continues to vibrate in the resonant mode for significant time even after the passing of the GW pulse through the detector due to energy absorbed from the pulse in the resonant mode. For example, for a GW pulse lasting a few ms, the resonant bar can continue to ring for time of order 10 min with same frequency, thereby allowing separation between noise and signal. Thus, if the pulsar continues to ring for significant time after the GW pulse has passed through it, then the radio pulses will continue to retain this "definite frequency signal" hidden within. We then reach an important conclusion that one needs to know the Q factor for NS interior. This information has to come from QCD calculations. Normally one focuses on properties of QCD matter

like the equation of state, viscosity etc. We realize that the quality factor Q is also a very important property for the NS interior.

We thus conclude that the pulsars spread out in space may act as GW detectors giving us a family of remotely stationed resonant Weber detectors. They detect GW, then communicate this detection to earth based "Pulsar Observatories" by their pulses carrying the imprints of GW (arising from tiny deformations in NS configuration from GW). These imprints have extremely high degree of fidelity. So, signal transmission from pulsar detector to earth has high quality. Of course, if one is lucky then some GW source may be close to the pulsar being observed. The GW signal may be very strong on the pulsar, hence strongly affecting its pulses which can be observed on earth. However, most observed pulsars, especially millisecond pulsars, are within our galaxy, so chances of this is very small, may be 1 in 3000 years. What is needed is to have very accurate measurements of pulsar timings of far away pulsars. Reaching out for extra galactic pulsars will be very important. Possibility of some GW source close to the pulsar, while being very far away from us, will show the real strength of this technique.

1.4 Re-visiting Past GW Events

Now we consider cases when gravitational waves have already reached earth in past, either detected, or missed. For past GW events, pulsar mediated signals will reach us in future at precisely determined times. This provides us the opportunity to revisit those events in future, possibly several times. Gravitational waves from GW events which have already been detected on earth, or the GW signal has passed earth in past, without detection, will also reach pulsars, say in our galaxy, and will modify their pulses. The modified pulse of the pulsar will carry the imprints of the original GW signal, which will reach us much later. Total path length for this GW being distance between GW source to the pulsar detector + distance between the pulsar detector and the Earth. This will clearly reach us much after the arrival of the original GW signal which was directly along the path from the GW source to the Earth. Knowing the GW source, and the date of detection of GW on earth, one can determine for each specific pulsars, when its GW-perturbed signals will reach us on earth. This gives us the remarkable possibility of re-visiting the past GW events. If it works, it will be important giving us ability to look at events which occurred in far past. It will also allow repeated source of information about the GW source with same signal coming again and again from different pulsars as well as properties of NS and its interiors (specific to the pulsar whose signal is being observed). Further, it will allow multiple detectors, located at astrophysical distance scales, which can be used for accurate localization of GW source. This will be of crucial importance for events like BH mergers where no other signals are emitted except GW as localization of such events is not very accurate with only GW detectors on the Earth. An important feature of pulsar detectors will be that depending on source direction w.r.t pulsar spin, the pulse Profile will be modified. Thus, in principle, single pulsar observation

will have detailed information about source direction. It may also enable detection of any circularly polarized components in the incoming gravitational wave (which could arise, e.g. from fluid circulation in core collapsed supernova).

We have analyzed specific GW events detected by LIGO/Virgo and have identified specific pulsars whose perturbed signals will reach us, say, within next 50 years. We give here few examples. For detailed set, we refer to [4]. GWs from the bh-bh merger event GW170814 will reach the pulsar J0437-4715 affecting its pulses. The perturbed pulses will reach us on the date 1/14/2035. However, the error in the date is years 2035–2043. The central year is 2038 corresponding to the mean values of the coordinates. We quote here the exact date (even though error is in tens of years) only to illustrate the fact that the error is arising from error in astronomical coordinates of the GW source and the pulsar. If these observations are improved, the uncertainty in the signal arrival date on the earth will also decrease.

Among the known sources of GW events there is an important class of known supernova events. It is known that a typical supernova (type-II, or even type I) can lead to GW emission (due to anisotropic explosion) with GW strain being as high as 10^{-20} at a distance of 10 kpc [5]. We have analyzed recorded supernova events. GWs from these will leave imprints on the pulsars. We quote some examples below. For example GWs from the supernova SN1604 will reach earth via pulsar J1759-1956 on 3/1/2020 (error in year being 2020–2060, mean year being 2039). In [4] we have also given events whose pulsar mediated signals are expected to have reached earth within past 50 years in view of recorded pulsar data. For example, SN185 supernova signal, while expected to come in future during year 2033–2066 via pulsar J0900-3144, is also expected to have reached earth during 1985–2004 via pulsar J2241-5236. Careful checking of recorded pulsar data can reveal many unrecorded GW events. One can ask how far back in past we can go with this technique? Just from the size of the Milky Way, we note that the oldest GW signals one can detect at present using galactic pulsars are those which passed by earth about 200,000 years ago.

1.5 Conclusions

We have argued that pulsars far away can act as remotely stationed Weber detectors of gravitational waves, especially at resonance which is likely for known resonant bands of neutron stars and typical frequencies of GW merger events. We have emphasized that it is important to accurately measure signals of pulsars in other galaxies. Possibility of some GW source close to the pulsar, while being very far away from us, will show the real strength of this technique. (We mention that for very distant pulsars, timing errors are large due to inter-galactic medium changes. This is important for long time stability of signal. But for a GW pulse, it may not be important.) For past GW events, Pulsar mediated signals will reach us in future at precisely determined times providing us the opportunity to revisit those events. We acknowledge that various estimates we have made are crude, it is not very clear if the effects are observable with present level of accuracy of pulsar measurements. However, at the same time,

we emphasize that for past GW events recorded on earth, the prediction of dates on which "perturbed-signals" from pulsars will reach earth is beyond question (apart from error estimates in timing). It is just trigonometry. It is then worth the effort that we focus on improving accuracy of predicted dates and attempt to make best possible measurements of pulses at those times. After all, we do not know neutron stars interiors so well, they just might surprise us pleasantly. At the end we give a quotation about resonant bar detectors from the review article on GW detectors [6]. For the GW antenna material for the resonant bar detector, it says:

> An ideal resonant bar would consist of a piece of nuclear matter, with high density and a velocity of sound comparable to the velocity of light! Since this is not available except in neutron stars, we must find a form of molecular matter which, to maximize coupling to gravitational waves, combines high velocity of sound v_s, and high density. To reduce the thermal noise we require a low acoustic loss Q^{-1}.

Our proposal in this work shows that, indeed, neutron star can be realized as a resonant bar GW detector.

Acknowledgements Thanks to the organizers for a great conference. Helpful comments from participants are gratefully acknowledged.

References

1. A. Das, S.S. Dave, O. Ganguly, A.M. Srivastava, Phys. Lett. B **791**, 167 (2019)
2. P. Bagchi, A. Das, B. Layek, A.M. Srivastava, Phys. Lett. B **747**, 120 (2015)
3. B.P. Abbott et al., LIGO scientific collaboration and virgo collaboration. Phys. Rev. Lett. **119**, 161101 (2017)
4. M. Biswal, S.S. Dave, A.M. Srivastava, arXiv:1909.04476
5. C.D. Ott, Class. Quant. Grav. **26**, 063001 (2009); D. Falta, R. Fisher, G. Khanna, Phys. Rev. Lett. **106**, 201103 (2011)
6. L. Ju, D.G. Blair, C. Zhao, Rep. Prog. Phys. **63**, 13117 (2000)

Chapter 2
Effective Chemical Potential in Spontaneous Baryogenesis

Raghavan Rangarajan

Abstract Models of spontaneous baryogenesis have an interaction term $\partial_\mu \theta j_B^\mu$ in the Lagrangian, where j_B^μ is the baryonic current and θ can be a pseudo-Nambu-Goldstone boson. Since the time component of this term, $\dot{\theta} j_B^0$, equals $\dot{\theta} n_B$ for a spatially homogeneous current, it is usually argued that this term implies a splitting in the energy of baryons and antibaryons thereby providing an effective chemical potential for baryon number. In thermal equilibrium, one then obtains $n_B \sim \dot{\theta} T^2$. We however argue that a term of this form in the Lagrangian does not contribute to the single particle energies of baryons and antibaryons. We show this for both fermionic and scalar baryons. But we find that despite the above result the baryon number density obtained from a Boltzmann equation analysis can be proportional to $\dot{\theta} T^2$. Our arguments are very different from that in the standard literature on spontaneous baryogenesis. This presentation is based on Phys. Rev. D98 (2018) no.8, 083527 with A. Dasgupta and R.K. Jain.

2.1 Introduction

Understanding the matter-antimatter asymmetry of the Universe is one of the most interesting issues at the interface of particle physics and cosmology. We believe that at very early times there was an equal amount of matter and antimatter in the Universe. However if you look around us today there is not much evidence of that. Probes sent to various planets and the interaction of the solar winds with planets indicates that the solar system is made up only of matter. Furthermore, the antimatter seen in cosmic rays is well explained by secondary interactions with the interstellar medium indicating that our galaxy too is made up of only matter. If one goes to larger scales and considers a matter symmetric Universe with clusters containing both matter and antimatter then one would expect to see signals from collisions of

R. Rangarajan (✉)
School of Arts and Sciences, Ahmedabad University, Navrangpura, Ahmedabad 380009, India
e-mail: raghavan@ahduni.edu.in
URL: https://ahduni.edu.in/raghavan-rangarajan

A. Giri and R. Mohanta (eds.), *Workshop on Frontiers in High Energy Physics 2019*, Springer Proceedings in Physics 248,
https://doi.org/10.1007/978-981-15-6292-1_2

galaxies and antigalaxies, and a gamma ray excess coming from the intracluster gas of X-ray emitting clusters. On still larger scales, it has been argued that unless matter and antimatter domains are separated on a scale of at least about 1000 Mpc (the size of the observable Universe today is 14,000 Mpc) the photons from annihilations taking place between redshifts of 1000 and 20 (380,000 yr to 100 million yr after the Big Bang) would have shown up in the diffuse cosmic gamma ray spectrum [1]. There have been attempts to create a Universe with large matter and antimatter domains. However we shall implicitly consider below that in the entire observable Universe the baryon asymmetry is uniform and has the value compatible with primordial nucleosynthesis.

The conventional approach to baryogenesis in cosmology is based on the three well known (and necessary) Sakharov's conditions [2]: (i) violation of baryon number (ii) violation of C- and CP-symmetries and (iii) being out of thermal equilibrium. However, there exist some interesting scenarios wherein one or more of these conditions are not satisfied. The spontaneous baryogenesis scenario is one such novel scenario in which the baryon asymmetry is generated in thermal equilibrium.

Models of spontaneous baryogenesis [3, 4] have an interaction of the form $\partial_\mu \theta j^\mu$ in the Lagrangian density, where j^μ is related to the baryonic current and θ may be a pseudo-Nambu-Goldstone boson. Now, $\int d^3x j^0 = Q$, where Q is the charge associated with j^μ, and ignoring spatial variations in j^0, $j^0 = Q/V = n$, where n is the net number density of the quanta associated with scalars or fermions ϕ or ψ. The coefficient of n in the Lagrangian density, i.e. $\dot{\theta}$, has been interpreted to be equivalent to an energy splitting in particle and antiparticle energies and thus an effective chemical potential for ϕ or ψ, provided the rate of change of $\dot{\theta}$ is sufficiently slow. This can then give rise to a particle-antiparticle asymmetry in thermal equilibrium. This interpretation has been invoked in spontaneous baryogenesis, including at the electroweak phase transition, and in flat direction baryogenesis, radion baryogenesis, quintessential baryogenesis, etc.

In this article we question the arguments underlying the above interpretation. We argue that a $\dot{\theta} n$ term in the Lagrangian density does not necessarily imply a split in the energies of particles and antiparticles and hence does not automatically lead to an interpretation of $\dot{\theta}$ being an effective chemical potential. We also argue that dispersion relations $k^0(\mathbf{k})$ do not necessarily give particle and antiparticle energies. For the latter one must obtain the Hamiltonian and take its expectation value in single particle and antiparticle states. The energies one obtains do not always agree with the expressions for k^0. In particular, while k^0 may contain $\dot{\theta}$ the single particle and antiparticle energies may not.

For the models under discussion we include a baryon number violating interaction and further study the Boltzmann equation, similar to the approach of [5]. For scenarios with a $\dot{\theta} j^0$ term in the Lagrangian density, the dispersion relations are modified, but, interestingly, even for cases where single particle and antiparticle energies are the same one does get a net baryon asymmetry due to the modified dispersion relations. Depending on the baryon number violating term, one gets different expressions for the asymmetry. This mechanism of generation of asymmetry from a $\dot{\theta} j^0$ term is

very different from that originally proposed in spontaneous baryogenesis and similar scenarios.

The outline of our article is as follows. In Sects. 2.2 and 2.3 we discuss the case of a fermion current coupled to the derivative of a field θ. We obtain the dispersion relation and the single particle and antiparticle energies. We then perform an analysis using the Boltzmann equation. In Sect. 2.4 we consider the case of a scalar field with an interaction similar to that in Sect. II, i.e., a coupling of the scalar field current with $\partial_\mu\theta$. As in the fermionic case, we obtain the dispersion relations and single particle and antiparticle energies and then perform an analysis using the Boltzmann equation. We summarize our conclusions in Sect. 2.5. More details can be found in [6].

2.2 Fermions and $\partial_\mu\theta J^\mu_\psi$

Let us first consider fermions ψ coupled to a field θ as

$$\mathcal{L} = i\bar{\psi}\gamma^\mu\partial_\mu\psi - m\bar{\psi}\psi + \frac{1}{2}v^2\partial_\mu\theta\partial^\mu\theta - \partial_\mu\theta j^\mu_\psi - V(\theta,\psi) \tag{2.1}$$

Here θ may be a pseudo-Nambu-Goldstone boson associated with the spontaneous breaking of some symmetry at a scale v, and the fermionic current is $j^\mu_\psi = \bar{\psi}\gamma^\mu\psi$. In the literature, it has been argued that the time component of the interaction term $\partial_\mu\theta j^\mu_\psi$ in the Lagrangian density is $\dot{\theta}(n_\psi - n_{\bar{\psi}})$, if spatial variations in j^0 can be ignored, and so $\dot{\theta}$ acts like an effective chemical potential for ψ, in that it gives contributions with different signs to the single particle energies of particles and antiparticles which would enter in a Fermi-Dirac distribution. This would lead to a net asymmetry in ψ if the interactions of ψ that change ψ number are in thermal equilibrium. Let us investigate this proposition.

We first obtain the Hamiltonian density from the Lagrangian density as $\mathcal{H} = \sum_\varphi p_\varphi\dot{\varphi} - \mathcal{L}$, where φ represents the fermionic and the θ fields. $\Pi_\psi = i\bar{\psi}\gamma^0$. Assuming θ has no other time derivative couplings $\Pi_\theta = v^2\dot{\theta} - \bar{\psi}\gamma^0\psi$. Then the Hamiltonian density is

$$\begin{aligned}\mathcal{H} &= \Pi_\psi\dot{\psi} + \Pi_\theta\dot{\theta} - \mathcal{L}\\ &= -i\bar{\psi}\gamma^i\partial_i\psi + m\bar{\psi}\psi + \frac{1}{2}v^2\dot{\theta}^2 + \frac{1}{2}v^2(\nabla\theta)^2 + \partial_i\theta\bar{\psi}\gamma^i\psi + V(\theta,\psi)\end{aligned} \tag{2.2}$$

One might now conclude, from the form of the Hamiltonian density in (2.2), that particles and antiparticles have the same energy and that the $\dot{\theta}$ term does not lead to energy splitting.[1] But then one could argue that one should write the Hamiltonian in terms of Π_θ and not $\dot{\theta}$ and that gives a $(\Pi_\theta/v^2)j^0$ term in the Hamiltonian. This

[1] A similar argument was made in the arXiv version of [7].

might suggest that energies of particles and antiparticles may also depend on Π_θ. To resolve the matter of the energy of particles and antiparticles in the presence of the θ field we shall obtain the expectation value of the Hamiltonian operator in single fermion and antifermion particle states to see the effect of the $\dot{\theta}$ term on single particle/antiparticle energies.

In standard free fermion field theory one writes down a Lagrangian density for a free field ψ. One can then expand

$$\psi(\mathbf{x}, t) = \sum_s \int d^3k \left[b_s(\mathbf{k}) u_s(\mathbf{k}) f(t) \exp(+i\mathbf{k}.\mathbf{x}) + d_s^\dagger(\mathbf{k}) v_s(\mathbf{k}) g(t) \exp(-i\mathbf{k}.\mathbf{x}) \right] . \tag{2.3}$$

One then substitutes this in the Euler-Lagrange equation, i.e., the Dirac equation, and obtains $f(t) = \exp(-ik^0 t)$ and $g(t) = \exp(+ik^0 t)$, where $k^0 = \sqrt{\mathbf{k}^2 + m^2}$, after associating positive and negative 'energy' solutions with spinors u and v respectively. One subsequently obtains solutions for u and v. One then writes the Hamiltonian density $\mathcal{H} = p_\psi \dot{\psi} - \mathcal{L}$ and substituting the above expression for ψ in $\mathcal{H}$, one finds that the eigenvalue, and expectation value, of the Hamiltonian for a one particle state is k^0. It is at this stage that one makes the identification that $k^0 = \sqrt{\mathbf{k}^2 + m^2}$ is the energy E of the one particle state.

We follow the same logic for our study. We start with a general expansion for the fermion field as in (2.3). Then we obtain the functions $f(t)$ and $g(t)$ from the Euler-Lagrange equation for the Lagrangian density in (2.1). Spontaneous baryogenesis scenarios must include baryon (ψ) number violating interactions (such as the last term of (2.5) of [4]) to generate a difference in particle-antiparticle number densities from a difference in particle-antiparticle energies. Such interactions are not relevant for the discussion below and we ignore $V(\theta, \psi)$ in the equation of motion for the fermionic field/spinors. The equation for u is

$$[i\gamma^0 \dot{f}/f - \gamma^i k^i - m - \dot{\theta}\gamma^0] u = 0 , \tag{2.4}$$

where we have ignored spatial variations in θ. Multiplying from the left by $[i\gamma^0 \dot{f}/f - \gamma^i k^i - \dot{\theta}\gamma^0 + m]$, we get

$$(i\dot{f}/f - \dot{\theta})^2 = k_i^2 + m^2 \equiv E_*^2 . \tag{2.5}$$

Keeping the positive square root on the r.h.s. above, i.e. the positive 'energy' solution, $\dot{f}/f = -i(E_* + \dot{\theta})$ and so

$$f = e^{-i\int (E_* + \dot{\theta}) dt} \equiv e^{-i\int k_u^0 dt} , \tag{2.6}$$

where $k_u^0 = E_* + \dot{\theta}$. Similarly we get

$$[i\gamma^0 \dot{g}/g + \gamma^i k^i - m - \dot{\theta}\gamma^0] v = 0 , \tag{2.7}$$

and multiplying from the left by $[i\gamma^0 \dot{g}/g + \gamma^i k^i - \dot{\theta}\gamma^0 + m]$ we get

$$(i\dot{g}/g - \dot{\theta})^2 = k_i^2 + m^2 \equiv E_*^2. \tag{2.8}$$

Now, keeping the negative 'energy' solution, $\dot{g}/g = i(E_* - \dot{\theta})$ and so we get

$$g = e^{+i\int(E_* - \dot{\theta})dt} \equiv e^{+i\int k_v^0 dt}\,, \tag{2.9}$$

with $k_v^0 = E_* - \dot{\theta}$. Now let us solve for u and v. If one puts the above expression for f in (2.4) then the $\dot{\theta}$ cancels out and the equation for u is

$$[E_*\gamma^0 - \gamma^i k^i - m]u = 0\,. \tag{2.10}$$

Similarly for v we get

$$[E_*\gamma^0 - \gamma^i k^i + m]v = 0\,. \tag{2.11}$$

These are the standard equations for the spinors with solutions in the Dirac-Pauli representation as

$$\begin{aligned} u_s(k) &= \alpha \begin{pmatrix} \widetilde{u}_s \\ \frac{\boldsymbol{\sigma}.\mathbf{k}}{(E_*+m)}\widetilde{u}_s \end{pmatrix} \\ v_s(k) &= \beta \begin{pmatrix} \frac{\boldsymbol{\sigma}.\mathbf{k}}{(E_*+m)}\widetilde{v}_s \\ \widetilde{v}_s \end{pmatrix}, \end{aligned} \tag{2.12}$$

where $\widetilde{u}_1 = \widetilde{v}_2 = \begin{pmatrix} 1 \\ 0 \end{pmatrix}$ and $\widetilde{u}_2 = \widetilde{v}_1 = \begin{pmatrix} 0 \\ 1 \end{pmatrix}$. $\widetilde{u}_{s'}^\dagger \widetilde{u}_s = \widetilde{v}_{s'}^\dagger \widetilde{v}_s = \delta_{ss'}$. σ_i are the Pauli matrices. We will first determine the normalisation constants α and β using commutation relations.

Using the equal time commutation relation

$$\left\{\psi(\mathbf{x}, t), \Pi_\psi(\mathbf{y}, t)\right\} = i\delta(\mathbf{x} - \mathbf{y})\,, \tag{2.13}$$

where $\Pi_\psi = i\bar{\psi}\gamma^0$, and which implies

$$\{d_s(\mathbf{k}), d_{s'}^\dagger(\mathbf{k}')\} = \frac{(E_* + m)}{2(2\pi)^6|\beta|^2 E_*}(2\pi)^3\delta(\mathbf{k} - \mathbf{k}')\delta_{ss'}\,, \tag{2.14}$$

and demanding the commutation relations

$$\begin{aligned} \{b_s(\mathbf{k}), b_{s'}^\dagger(\mathbf{k}')\} &= (2\pi)^3\delta(\mathbf{k} - \mathbf{k}')\delta_{ss'} \\ \{d_s(\mathbf{k}), d_{s'}^\dagger(\mathbf{k}')\} &= (2\pi)^3\delta(\mathbf{k} - \mathbf{k}')\delta_{ss'} \end{aligned} \tag{2.15}$$

we get

$$|\alpha|^2 = \frac{E_* + m}{2(2\pi)^6 E_*}, \qquad |\beta|^2 = \frac{E_* + m}{2(2\pi)^6 E_*}\,. \tag{2.16}$$

One can also show that $\{b_s(\mathbf{k}), d_{s'}(\mathbf{k}')\}$ and $\{b_s^\dagger(\mathbf{k}), d_{s'}^\dagger(\mathbf{k}')\}$ are 0. Further imposing

$$\left\{\psi(\mathbf{x},t), \psi(\mathbf{y},t)\right\} = \left\{\psi^\dagger(\mathbf{x},t), \psi^\dagger(\mathbf{y},t)\right\} = 0 \tag{2.17}$$

allows us to show that all other commutation relations involving the annihilation and creation operators, such as $\{b_s(\mathbf{k}), d_{s'}^\dagger(\mathbf{k}')\}$, etc., are 0.

Then the fermionic Hamiltonian (ignoring spatial variation in θ) is

$$\begin{aligned} H &= \sum_{s,s'} \int d^3k\, (2\pi)^3 \left[\overline{u}_s(\mathbf{k})(\gamma^i k_i + m) u_{s'}(\mathbf{k}) b_s^\dagger(\mathbf{k}) b_{s'}(\mathbf{k}) \right. \\ &\quad \left. + \overline{v}_s(\mathbf{k})(-\gamma^i k_i + m) v_{s'}(\mathbf{k}) d_s(\mathbf{k}) d_{s'}^\dagger(\mathbf{k})\right] \\ &= \sum_s \int d^3k\, (2\pi)^3 \frac{2E_*^2}{(E_* + m)} \Big(|\alpha|^2 b_s^\dagger(\mathbf{k}) b_s(\mathbf{k}) \\ &\quad - |\beta|^2 d_s(\mathbf{k}) d_s^\dagger(\mathbf{k}) \Big). \end{aligned} \tag{2.18}$$

Now, using (2.14), the normal ordered fermionic Hamiltonian becomes

$$: H := \sum_s \int \frac{d^3k}{(2\pi)^3} \left[b_s^\dagger(\mathbf{k}) b_s(\mathbf{k}) + d_s^\dagger(\mathbf{k}) d_s(\mathbf{k})\right] \sqrt{\mathbf{k}^2 + m^2}\,. \tag{2.19}$$

The only $\dot{\theta}$ dependence in the fermionic field is in f and g but, as in the standard case, the only terms above that survive go as $f^* f$ and $g^* g$ and so the $\dot{\theta}$ dependence drops out. Therefore the eigenvalue, and expectation value, of the Hamiltonian is $\sqrt{\mathbf{k}^2 + m^2}$ for a fermion or an antifermion state and does not contain $\dot{\theta}$. The above calculation also underscores the point that in this case the $k_{u,v}^0$ in the exponent of f, g, which do contain $\dot{\theta}$, are not to be identified with fermionic energies, that is, even if the dispersion relations $k^0(\mathbf{k})$ contain $\dot{\theta}$ the fermionic energies do not. We realize that it is inconsistent to keep the $\dot{\theta}$ term and ignore other interactions of ψ in the equation of motion for the fermionic field/spinors. However, here we are merely trying to point out that the naive identification of $\dot{\theta}$ with a difference in fermion-antifermion energies is not justified.

2.3 Boltzmann Equation

In [5] the authors have also discussed the identification of $\dot{\theta}$ with an effective chemical potential. They study the kinetic equation for baryons and find that while the naive interpretation of $\dot{\theta}$ as an effective chemical potential is not appropriate, surprisingly the kinetic equation indicates that the baryon number density is dependent on $\dot{\theta}$ in a

way that $c\dot{\theta}$ plays a role similar to that of an effective chemical potential, where c is a constant whose value may be different for different types of B-nonconserving reactions. Our analysis below is similar to that in [5] but the fermions in our Lagrangian density are transformed so that the Lagrangian density contains a term $(\partial_\mu\theta)J^\mu$, where J^μ is the baryonic current, as in models of spontaneous baryogenesis.

In [5] one considers the Lagrangian density of a complex scalar field Φ interacting with fermions Q_1 and L.

$$\begin{aligned}\mathcal{L}(\Phi, Q, L) = g^{\mu\nu}\partial_\mu\Phi^*\partial_\nu\Phi - V(\Phi^*\Phi) + \bar{Q}_1(i\gamma^\mu\partial_\mu - m_Q)\,Q_1 \\ +\bar{L}(i\gamma^\mu\partial_\mu - m_L)L + \mathcal{L}_{int}(\Phi, Q_1, L)\,,\end{aligned} \tag{2.20}$$

where Q_1 and Φ have nonzero baryonic numbers 1/3 and -1, while L does not carry baryonic charge.

$$\mathcal{L}_{int} = \frac{\sqrt{2}}{m_X^2}\frac{\Phi}{v}\,(\bar{L}\gamma_\mu Q_1)(\overline{Q_1^c}\gamma_\mu Q_1) + h.c.\,, \tag{2.21}$$

where Q_1^c is a charge conjugated quark spinor and m_X and f are parameters with dimensions of mass.

$$V(\Phi^*\Phi) = \lambda\left(\Phi^*\Phi - v^2/2\right)^2. \tag{2.22}$$

After spontaneous symmetry breaking in the Φ sector, and ignoring the heavy radial mode, $\Phi \to ve^{i\theta}/\sqrt{2}$, and introducing a rotated field Q_2 through $Q_1 = e^{-i\theta/3}Q_2$, one gets

$$\begin{aligned}\mathcal{L}_2(\theta, Q, L) = \frac{v^2}{2}\partial_\mu\theta\partial^\mu\theta + \bar{Q}_2(i\gamma^\mu\partial_\mu - m_Q)Q_2 + \bar{L}(i\gamma^\mu\partial_\mu - m_L)L \\ +\left(\frac{1}{m_X^2}\,(\bar{L}\gamma_\mu Q_2)(\overline{Q_2^c}\gamma_\mu Q_2) + h.c.\right) + (\partial_\mu\theta)J^\mu - U(\theta)\,,\end{aligned} \tag{2.23}$$

where the quark baryonic current is $J_\mu = (1/3)\bar{Q}_2\gamma_\mu Q_2$, and an explicit symmetry breaking term is included as $U(\theta)$.

We now consider the process $Q_2Q_2 \leftrightarrow L\bar{Q}_2$ ($12 \leftrightarrow 34$). Then

$$\begin{aligned}\dot{n}_Q + 3Hn_Q \sim \int dt \int d\tau_{L\bar{Q}}\,d\tau_{QQ}|A|^2\delta(\mathbf{k}_{in} - \mathbf{k}_{out})\exp[-it(k_1^0 + k_2^0 - k_3^0 - k_4^0)] \\ \times(f_3f_4 - f_1f_2)\end{aligned} \tag{2.24}$$

$$\begin{aligned}= \int d\tau_{L\bar{Q}}\,d\tau_{QQ}|A|^2\delta(\mathbf{k}_{in} - \mathbf{k}_{out})\delta(k_1^0 + k_2^0 - k_3^0 - k_4^0) \\ \times(f_3f_4 - f_1f_2)\end{aligned} \tag{2.25}$$

where A is the invariant amplitude, $\mathbf{k}_{in,out}$ refers to the total incoming and outgoing 3-momentum, and $d\tau_{ab} = d^3k_a d^3k_b/[4E_aE_b(2\pi)^6]$ is the phase space factor. $k_{1,2}^0 =$

$E_{1,2} - \dot{\theta}/3$, $k_3^0 = E_3$ and $k_4^0 = E_4 + \dot{\theta}/3$. The E_I's are physical energies and are $(\mathbf{k}_I^2 + m_I^2)^{\frac{1}{2}}$ while the k_I^0 appear in the expansion of the fermion field as in (2.3), (2.6) and (2.9). (Because of a difference in the signs of the $\partial_\mu \theta J^\mu$ term, and of a factor of 1/3 in J^μ, in (2.23) and (2.1) the expressions for $k_{1,2,4}^0$ and $k_{u,v}^0$ are a bit different.) Note that to get the k^0 delta function $\dot{\theta}$ has to be constant in time.[2] In the spontaneous baryogenesis scenario θ is slow moving compared to the time scale for particle interactions, and so one can take $\dot{\theta}$ to be nearly constant. This requirement agrees with comments in Sect. IV-C of [5].

The particle distribution functions are given by

$$f_I = \exp[-E_I/T + \xi_I] \tag{2.26}$$

where $\xi_I = \mu_I/T$ and μ_I is the chemical potential of species I, and the antiparticle chemical potential is the negative of that of the particle (presuming fast annihilation of particle-antiparticle pairs into, say, photons).

Then one gets

$$\begin{aligned} \dot{n}_Q + 3Hn_Q \sim & \int d\tau_{L\bar{Q}}\, d\tau_{QQ} |A|^2 \delta(\mathbf{k}_{in} - \mathbf{k}_{out}) \delta(E_1 + E_2 - E_3 - E_4 - \dot{\theta}) \\ & \times (f_3 f_4 - f_1 f_2) \qquad (2.27) \\ = & \int d\tau_{L\bar{Q}}\, d\tau_{QQ} |A|^2 \delta(\mathbf{k}_{in} - \mathbf{k}_{out}) \delta(E_1 + E_2 - E_3 - E_4 - \dot{\theta}) \\ & \times \exp[-E_{in}/T] \left(e^{\xi_3 + \xi_4 + \dot{\theta}/T} - e^{\xi_1 + \xi_2} \right), \qquad (2.28) \end{aligned}$$

where we have set $E_{in} \equiv E_1 + E_2 = E_3 + E_4 + \dot{\theta}$ in the factor with the distribution functions, using the energy delta function. Following the analysis below (4.15) of [5], if Q and L are in thermal equilibrium the collision integral on the r.h.s of (2.28) vanishes and $\xi_3 + \xi_4 + \dot{\theta}/T = \xi_1 + \xi_2$, or $\xi_L = 3\xi_Q - \dot{\theta}/T$, assuming $Q - \bar{Q}$ annihilation processes to photons are in thermal equilibrium giving $\xi_{\bar{Q}} = -\xi_Q$. Furthermore, let us assign a charge q of 1/3 to B, +1 to L and 0 to Φ. In our Lagrangian q is conserved (both before and after symmetry breaking). Assuming that q conserving processes are in thermal equilibrium and that initial q is 0, then $\xi_Q/3 + \xi_L = 0$.[3] Combining these relations we get $\xi_Q = 0.3\,\dot{\theta}/T$, and

$$n_B = B_Q n_Q = \frac{1}{6} g_Q B_Q \xi_Q T^3 = \frac{1}{20} g_Q B_Q \dot{\theta} T^2 = \frac{1}{30} \dot{\theta} T^2 \tag{2.29}$$

where g_Q is the number of spin states of Q, namely 2, and B_Q is the baryonic charge of Q.

---

[2] We would like to thank Prof. A. D. Dolgov for highlighting this to us.

[3] This is slightly different from the approach in [6], and we thank Prof. Michael Ratz for pointing out that one may not use $B + L$ conservation as that symmetry is broken by $U(\theta)$.

The above analysis shows that $\dot{\theta}$ can play the role of a chemical potential for quarks, *but with a multiplicative factor* (such as 3/10 for the above case). But this does not follow simply from the argument that a $\dot{\theta} j^0$ term in the Lagrangian density for fermions implies an energy splitting for fermions and antifermions. In fact, as we have shown above, there is no split in the single particle energies of quarks and antiquarks in the presence of a non-zero $\dot{\theta}$. The multiplicative factor depends on what is the baryon number violating process in thermal equilibrium, and which charge, $B + L$ in our case, is conserved. The former determines what are the *in* and *out* particles in the collision integral and the form of the last bracket in (2.28), which is then set to 0. The latter gives another relation between chemical potentials.

2.4 Scalars and $\partial_\mu \theta J^\mu$

Let us now consider scalars coupled to another field as

$$\mathcal{L} = \partial_\mu \phi^* \partial^\mu \phi - m^2 \phi^* \phi + \frac{1}{2} v^2 \partial_\mu \theta \partial^\mu \theta + \partial_\mu \theta j^\mu - V(\theta, \phi) \tag{2.30}$$

where $j^\mu = i(\phi^* \partial^\mu \phi - \partial^\mu \phi^* \phi)$ is the scalar current and its zeroth component is the scalar charge density, $n_\phi - n_{\phi^*}$, ignoring spatial variation in j^0. As in Sect. 2.2 we take the field expansion to be

$$\phi(\mathbf{x}, t) = \int d^3k \left[a(\mathbf{k}) f(t) e^{i\mathbf{k}.\mathbf{x}} + b^\dagger(\mathbf{k}) g(t) e^{-i\mathbf{k}.\mathbf{x}} \right] . \tag{2.31}$$

Then the equation of motion for ϕ, assuming θ is homogeneous, gives

$$\ddot{f} + \mathbf{k}^2 f - 2i\dot{\theta}\dot{f} + (m^2 - i\ddot{\theta}) f = 0 \tag{2.32}$$

Taking $\ddot{\theta} \approx 0$, if θ is assumed to be slowly rolling, we get

$$\ddot{f} - 2i\dot{\theta}\dot{f} + (\mathbf{k}^2 + m^2) f = 0 \tag{2.33}$$

Keeping the solutions that reduce to the standard positive and negative energy solutions in the absence of θ, we get

$$f(t) = \alpha e^{-it(\sqrt{\mathbf{k}^2 + m^2 + \dot{\theta}^2} - \dot{\theta})} \equiv \alpha e^{-ik_1^0 t} \tag{2.34}$$

and

$$g(t) = \beta e^{it(\sqrt{\mathbf{k}^2 + m^2 + \dot{\theta}^2} + \dot{\theta})} \equiv \beta e^{ik_2^0 t} , \tag{2.35}$$

where

$$k_1^0 = \sqrt{\mathbf{k}^2 + m^2 + \dot{\theta}^2} - \dot{\theta} = \sqrt{E_*^2 + \dot{\theta}^2} - \dot{\theta} \tag{2.36}$$

and

$$k_2^0 = \sqrt{\mathbf{k}^2 + m^2 + \dot{\theta}^2} + \dot{\theta} = \sqrt{E_*^2 + \dot{\theta}^2} + \dot{\theta}\,. \tag{2.37}$$

$E_* = (\mathbf{k}^2 + m^2)^{\frac{1}{2}}$, as before. Then

$$\phi(\mathbf{x}, t) = \int d^3k \left[\alpha\, a(\mathbf{k}) e^{i\mathbf{k}.\mathbf{x} - ik_1^0 t} + \beta\, b^\dagger(\mathbf{k}) e^{-i\mathbf{k}.\mathbf{x} + ik_2^0 t}\right]. \tag{2.38}$$

Following a procedure similar to that in Sect. 2.2 we get

$$|\alpha|^2 = |\beta|^2 = \frac{1}{(2\pi)^6} \frac{1}{2(E_*^2 + \dot{\theta}^2)^{\frac{1}{2}}}\,. \tag{2.39}$$

Assuming θ has no other derivative couplings, $\Pi_\theta = v^2\dot{\theta} + i(\phi^*\dot{\phi} - \dot{\phi}^*\phi)$ and the Hamiltonian density is [6]

$$\mathcal{H} = \Pi_\phi \dot{\phi} + \Pi_{\phi^*}\dot{\phi}^* + \Pi_\theta \dot{\theta} - \mathcal{L} \tag{2.40}$$

$$= \dot{\phi}^*\dot{\phi} + |\nabla\phi|^2 + m^2\phi^*\phi + \frac{1}{2}v^2\dot{\theta}^2 + i\dot{\theta}(\phi^*\dot{\phi} - \dot{\phi}^*\phi) + V(\theta, \psi) \tag{2.41}$$

Unlike in the fermionic case, here $\dot{\theta}$ appears in the Hamiltonian with j_0 and so looks like an effective chemical potential. Now one may believe that in this case one will get a $\dot{\theta}$ splitting in the energy. But the normal ordered Hamiltonian of the terms involving ϕ gives

$$:H: = \int \frac{d^3k}{(2\pi)^3} \left[a^\dagger(\mathbf{k})a(\mathbf{k}) + b^\dagger(\mathbf{k})b(\mathbf{k})\right] \frac{E_*^2}{(E_*^2 + \dot{\theta}^2)^{\frac{1}{2}}}$$
$$- \left[(a^\dagger(\mathbf{k})b^\dagger(-\mathbf{k}) + a(\mathbf{k})b(-\mathbf{k})\right] \frac{\dot{\theta}^2}{(E_*^2 + \dot{\theta}^2)^{\frac{1}{2}}}\,. \tag{2.42}$$

The particle and antiparticle energies E are defined as the expectation value of the Hamiltonian in single particle and antiparticle states (rather than eigenvalues of the Hamiltonian because of the terms in the second bracket above). They are the same and are given by

$$E = \frac{E_*^2}{(E_*^2 + \dot{\theta}^2)^{\frac{1}{2}}} = \frac{\mathbf{k}^2 + m^2}{(\mathbf{k}^2 + m^2 + \dot{\theta}^2)^{\frac{1}{2}}}\,. \tag{2.43}$$

It is not at all obvious that the Hamiltonian in (2.41) will give no energy splitting between particles and antiparticles. Naively, one would have concluded the opposite.

We now consider an interaction $g\phi^*\phi\chi^*\phi + h.c.$ and do a Boltzmann equation analysis as in Sect. 2.3 for the process $\phi^*\,\phi \leftrightarrow \chi\phi^*(12 \leftrightarrow 34)$. We assume ϕ has baryon number equal to 1 and χ has lepton number equal to 1. We start from

$$\dot{n}_B + 3Hn_B \sim \int dt \int d\tau_{\chi\phi^*}\, d\tau_{\phi^*\phi} |A|^2 \delta(\mathbf{k}_{in} - \mathbf{k}_{out}) \exp[-it(k_1^0 + k_2^0 - k_3^0 - k_4^0)] \times (f_3 f_4 - f_1 f_2)\,. \tag{2.44}$$

If we assume $\dot{\theta}$ is small compared to E_{*I} then we get

$$\begin{aligned} \dot{n}_B + 3Hn_B &\sim \int d\tau_{\chi\phi^*}\, d\tau_{\phi^*\phi} |A|^2 \delta(\mathbf{k}_{in} - \mathbf{k}_{out}) \delta(E_1 + E_2 - E_3 - E_4 - \dot{\theta}) \\ &\quad \times (f_3 f_4 - f_1 f_2) \\ &= \int d\tau_{\chi\phi^*}\, d\tau_{\phi^*\phi} |A|^2 \delta(\mathbf{k}_{in} - \mathbf{k}_{out}) \delta(E_1 + E_2 - E_3 - E_4 - \dot{\theta}) \\ &\quad \times \exp[-E_{in}/T] \left(e^{\xi_3 + \xi_4 + \dot{\theta}/T} - e^{\xi_1 + \xi_2} \right), \end{aligned} \tag{2.45}$$

In thermal equilibrium the collision integral vanishes and, assuming $\phi - \phi^*$ annihilation processes are in thermal equilibrium, $\xi_{\phi^*} = -\xi_\phi$. Then $\xi_\chi = \xi_\phi - \dot{\theta}/T$. Furthermore, let us assign a charge q of 1 to ϕ and to χ. In our Lagrangian q is conserved. Assuming that q conserving processes are in thermal equilibrium and that initial q is 0, $\xi_\chi = -\xi_\phi$. Then $\xi_\phi = (1/2)\dot{\theta}/T$ and

$$n_B = B_\phi(n_\phi - n_{\phi^*}) = \frac{1}{3}\xi_\phi T^3 = \frac{1}{6}\dot{\theta}T^2\,. \tag{2.46}$$

Again, $\dot{\theta}$ with a multiplicative factor has played the role of a chemical potential for ϕ. More precisely, for this particular case, $\dot{\theta}/2$ is the chemical potential for ϕ. But there is no split in the single particle energies of ϕ particles and antiparticles, though unlike in the fermionic case they are amended, equally, by the presence of $\dot{\theta}$.

2.5 Discussion and Conclusion

Spontaneous baryogenesis presumes that a term of the form $\dot{\theta} j^0 \sim \dot{\theta} n$ in the Lagrangian density, where j^0 is the zeroth component of the particle current and n is the net particle number density, translates into a splitting of energies of particles and antiparticles, and therefore acts as an effective chemical potential which then gives rise to a matter-antimatter asymmetry or baryon asymmetry in a system in thermal equilibrium. Our analysis above implies that there are two separate issues here. One is whether or not the term in the Lagrangian density gives rise to an energy splitting, and the second is whether or not one obtains a matter-antimatter asymmetry. For both fermions and scalars we find in Sects. 2.2 and 2.4 that $\dot{\theta} j^0$ modifies the

mode functions of the corresponding quantum fields, but it does not lead to a splitting of single particle and antiparticle energies. However, because of the modified mode functions, if baryon number violating interactions are in the thermal equilibrium then equating the collision integral on the r.h.s. of the Boltzmann equation to 0 gives a non-zero chemical potential for particle number. This then gives rise to a matter-antimatter asymmetry, or baryon asymmetry if the particles carry baryon number.

It may be noted that obtaining the Hamiltonian density in terms of the field and its time derivative and trying to relate the presence or absence of a $\dot{\theta} j^0$ in the Hamiltonian density with particle-antiparticle energy splitting is inappropriate and misleading. For the fermionic case there is no $\dot{\theta} j^0$ term in the Hamiltonian density while it does appear for the scalar case. But in both cases the single particle energies for particles and antiparticles are the same.

The presumption that a term of the form $\dot{\theta} j^0 \sim \dot{\theta} n$ in the Lagrangian density gives rise to a splitting in energies of particles and antiparticles has been widely used in the literature in models of spontaneous baryogenesis, including at the electroweak phase transition, flat direction baryogenesis, radion baryogenesis, quintessential baryogenesis, etc. Our analysis above indicates that this presumption may not hold even though such a term may ultimately give rise to a matter-antimatter asymmetry.

References

1. A.G. Cohen, A. De Rujula, S.L. Glashow, A Matter - antimatter universe? Astrophys. J. **495**, 539–549 (1998) [astro-ph/9707087]. https://doi.org/10.1086/305328
2. A.D. Sakharov, Violation of CP Invariance, C asymmetry, and baryon asymmetry of the universe. Pisma Zh. Eksp. Teor. Fiz. **5**, 32–35 (1967) [JETP Lett. **5**, 24 (1967)]
3. A.G. Cohen, D.B. Kaplan, Thermodynamic generation of the baryon asymmetry. Phys. Lett. B **199**, 251–258 (1987)
4. A.G. Cohen, D.B. Kaplan, Spontaneous baryogenesis. Nucl. Phys. **B308**, 913–928 (1988)
5. E.V. Arbuzova, A.D. Dolgov, V.A. Novikov, General properties and kinetics of spontaneous baryogenesis. Phys. Rev. **D94**(12), 123501 (2016). arXiv:1607.01247
6. A. Dasgupta, R.K. Jain, R. Rangarajan, Effective chemical potential in spontaneous baryogenesis. Phys. Rev. **D98**(8), 083527 (2018). arXiv:1808.04027 [hep-ph]. https://doi.org/10.1103/PhysRevD.98.083527
7. A. Dolgov, K. Freese, R. Rangarajan, M. Srednicki, Baryogenesis during reheating in natural inflation and comments on spontaneous baryogenesis. Phys. Rev. D **56**, 6155–6165 (1997). arxiv.org/abs/hep-ph/9610405 https://doi.org/10.1103/PhysRevD.56.6155

Chapter 3
PAAI in the Sky: Towards a Particulate Mechanism for Dark Energy and Concordant Dark Matter

R. B. MacKenzie, M. B. Paranjape, and U. A. Yajnik

Abstract We propose the origins of Dark Energy in a hidden sector with a pair of very light fermions, oppositely charged under an abelian gauge force $U(1)_X$ but of unequal mass. The system is dubbed PAAI, plasma which is abelian, asymmetric and idealised. For a range of the hidden fine structure constant values and the value of mass of the lightest fermion the PAAI is argued to simulate Dark Energy. Additional fermions from the same sector are shown to account for Dark Matter. Further, residual X-magnetic fields can mix with Maxwell electromagnetism to provides the seed for cosmic-scale magnetic fields. Thus the scenario can explain several cosmological puzzles from within the same hidden sector.

3.1 Introduction

There are several important unresolved issues in our current understanding of cosmology. Paramount among these are the problems of Dark Matter (DM) and Dark Energy (DE). Within the Λ-CDM model DM assists in galaxy formation and should be a gas of non-relativistic particles, while the issue of DE is closely tied to that of the cosmological constant [1], since data [2] suggests that its energy density is constant over the epochs scanned by the cosmic microwave background (CMB). If treated as a dynamical phenomenon, DE demands an explanation for the equation of state $p = -\rho$ in terms of relativistic phenomena. From the point of view of naturalness, explaining a value of a dynamically generated quantity which is many orders of magnitude away from any of the scales of elementary particle physics or gravity is a major challenge. There are explanations that obtain such a sector as directly related to and derived from more powerful principles applicable at high scales [3–5]. On the

R. B. MacKenzie · M. B. Paranjape
Groupe de physique des particules, Département de physique, Université de Montréal, Montréal, QC, Canada

U. A. Yajnik (✉)
Physics Department, Indian Institute of Technology Bombay, Mumbai, India
e-mail: yajnik@iitb.ac.in

A. Giri and R. Mohanta (eds.), *Workshop on Frontiers in High Energy Physics 2019*, Springer Proceedings in Physics 248,
https://doi.org/10.1007/978-981-15-6292-1_3

other hand, extended and space filling objects, specifically domain walls as possible solutions to understanding Dark Energy have been proposed earlier in a variety of scenarios [6–10]. In this paper we pursue the latter approach, of invoking new species of particles and their interactions at the new low mass scale, agnostic of their connection to the known physics other than gravity. A more extensive discussion of the results reported here can be found in [11].

We consider a new sector of particles with interaction mediated by an unbroken abelian gauge symmetry denoted $U(1)_X$. The core of our mechanism involves the existence of a fermionic species that enters into a ferromagnetic state. As we will show, it is required to have an extremely small mass and hence an extremely large magnetic moment; we dub this species the *magnino*,[1] denoted M. We assume that the medium remains neutral under the X-charge due to the presence of a significantly heavier species Y of opposite charge which does not enter the collective ferromagnetic state. The wall complex resulting from the formation of magnetic domains then remains mutually bound, and due to interaction strength much larger than cosmic gravity, remains frozen. The binding of the heavier species to this complex due to the requirement of X-electrical neutrality then ensures that these particles remain unevolving, and after averaging over the large scales of the cosmic horizon act like a homogeneous space filling medium of constant density.

It is possible to explain DM within the same sector, including possible dark atoms formed by such species [13–16]. This would also solve the *concordance problem*, that is, the comparable energy densities carried in the cosmological energy budget by the otherwise-unrelated components, DM and DE. Further, the X-electromagnetism is expected to mix kinetically with the standard electromagnetism. The existence of cosmic magnetic fields at galactic and intergalactic scales [17–19] is an outstanding puzzle of cosmology. Our mechanism relying as it does on spontaneous formation of domains of X-ferromagnetism has the potential to provide the seeds needed to generate the observed fields through such mixing.

In the following, in Sect. 3.2 we motivate the origin of negative pressure for extended objects in cosmology. In Sect. 3.3 we discuss the calculation of the exchange energy for a spin polarised PAAI. Thus we motivate the possibility of occurrence of an extended structure of domain walls, and their metastable yet long lived nature. In Sect. 3.4 we discuss the main results of our proposal, obtaining suggestive values for the masses and abundances for the scenario to successfully explain DE. In Sect. 3.5 we take up the possibility of concordant models with DM species arising compatible with this DE proposal. In Sect. 3.6 we discuss the possibility of obtaining an explanation of origin of cosmic magnetic fields from mixing of this $U(1)_X$ with standard electromagnetism. Section 3.7 contains the conclusion.

[1] The term *magnino* was earlier introduced in a different connotation in [32, 33].

3.2 Cosmic Relics and the Origin of Negative Pressure

A homogeneous, isotropic universe is described by the Friedmann equation for the scale factor $a(t)$ supplemented by an equation of state relation $p = w\rho$. Extended relativistic objects in gauge theories in the cosmological setting [20] are known to lead to negative values for w [21, 22]. A heuristic argument runs as follows. In the case of a frozen-out vortex line network, the average separation between string segments scales as $1/a^3$ but there is also an increment in the energy proportional to a due to an average length of vortex network proportional to a entering the physical volume. As such, the energy density of the network has to be taken to scale as $1/a^2$, and we get the effective value $w = -1/3$. Likewise, for a domain wall complex, the effective energy density scales as $1/a$ and $w = -2/3$. By extension, for a relativistic substance filling up space homogeneously, the energy density is independent of the scale factor, and has $w = -1$. In quantum theory this arises naturally as the vacuum expectation value of a relativistic scalar field. In the following, we consider a scenario that gives rise to a complex of domain walls whose separation scale is extremely small compared to the causal horizon and which remains fixed during expansion, and hence simulates an equation of state $p = -\rho$.

3.3 Ferromagnetic Instability of PAAI

A system of fermions can be treated as a gas of weakly interacting quasi-particles in the presence of oppositely charged much heavier ions or protons which are mostly spectators and serve to keep the medium neutral. The total energy of such a system can be treated as a functional of electron number density, according to the Hohenberg-Kohn theorem. In a relativistic setting, it becomes a functional of the covariant 4-current, and hence also of the electron spin density [23]. In the Landau fermi liquid formalism the quasi-particle energy receives a correction from an interaction strength f with other quasi-particles which can be determined from the forward scattering amplitude $\mathcal{M}$ [24]

$$f(\mathbf{p}s,\ \mathbf{p}'\mathbf{s}') = \frac{m}{\varepsilon^0(\mathbf{p})}\frac{m}{\varepsilon^0(\mathbf{p}')}\mathcal{M}(\mathbf{p}s,\ \mathbf{p}'s'), \tag{3.1}$$

where ε^0 is the free particle energy and $\mathcal{M}$ is the Lorentz-covariant $2 \to 2$ scattering amplitude in a specific limit not discussed here. The exchange energy can equivalently be seen to arise as a two-loop correction to the self-energy of the fermion [25]. Using f this one can compute the exchange energy $E_{\rm xc}$, as

$$E_{\rm xc} = \sum_{\pm\mathbf{s}}\sum_{\pm\mathbf{s}'}\int \frac{d^3p}{(2\pi)^3}\frac{d^3p'}{(2\pi)^3} f(\mathbf{p}s,\ \mathbf{p}'\mathbf{s}')n(\mathbf{p},\mathbf{s})n(\mathbf{p}',\mathbf{s}') \tag{3.2}$$

and the effective quasi-particle energy is the kinetic energy of the quasi-particles with renormalised mass parameter $E_{\rm kin}$ plus the spin-dependent exchange energy in a spin-polarised background. For this purpose it is necessary to calculate the self energy with a Feynman propagator in the presence of non-zero number density, and spin imbalance [26].

To set up a spin-asymmetric state, we introduce a parameter ζ such that the net density n splits up into densities of spin up and down fermions as

$$n_\uparrow = n(1+\zeta) \quad \text{and} \quad n_\downarrow = n(1-\zeta) \tag{3.3}$$

Correspondingly, we have Fermi momenta $p_{F\uparrow} = p_F(1+\zeta)^{1/3}$ and $p_{F\downarrow} = p_F(1-\zeta)^{1/3}$, with $p_F^3 = 3\pi^2 n$. The exchange energy was calculated in [26] and the final expression is too long to be quoted in this presentation. However the leading order expansions in $\beta = p_F/m$ for the fully polarised case $\zeta = 1$ is [11]

$$E_{\rm kin}(\zeta=1) = m^4\left\{\frac{\tilde{\beta}^5}{20\pi^2} - \frac{\tilde{\beta}^7}{112\pi^2} + O\left(\beta^9\right)\right\} \tag{3.4}$$

$$E_{\rm xc}(\zeta=1) = -\alpha_X m^4\left\{\frac{\tilde{\beta}^4}{2\pi^2} - \frac{7\tilde{\beta}^6}{27\pi^2} + O\left(\tilde{\beta}^8\right)\right\} \tag{3.5}$$

where $\tilde{\beta} = 2^{1/3}\beta$. The $\zeta = 0$ case has same leading power laws with different coefficients. Thus the exchange energy tends to lower the quasi-particle energy parametrically determined by α, with either $\zeta = 0$ or $\zeta = 1$ becoming the absolute minimum depending on β. For comparison, in this notation, the rest mass energy of the degenerate gas is $E_{\rm rest} = m^4\beta^3/(3\pi^2)$.

Exploring the energy expression presents three possibilities; $\zeta = 1$ is not a minimum at all, $\zeta = 1$ is a local minimum but $E(0) < E(1)$ i.e. a metastable vacuum and finally, $\zeta = 1$ is the absolute minimum with $\zeta = 0$ unstable vacuum. In Fig. 3.1 we have plotted the approximate regions of the three phases in the parameter space.

3.3.1 Evolution and Stability of Domain Walls

We expect domain walls to occur in this spin polarised medium just like in ferromagnets. However due to the $SU(2)$ of spin being simply connected, the defects are not topologically stable and can unwind. However these processes are suppressed by a competition between the gradient energy and the extra energy stored in the domain walls, and there is a Ginzberg temperature T_G [20] below which thermal fluctuations cannot destabilise the walls trivially. The mechanism for destabilisation is then the one studied in detail in [27]. The rate for such decay is governed by an exponential factor $\exp(-B/\lambda)$ [28] where the exponent is the Euclidean action of a suitable "bounce" solution connecting the false and the true vacua [29]. On phenomenologi-

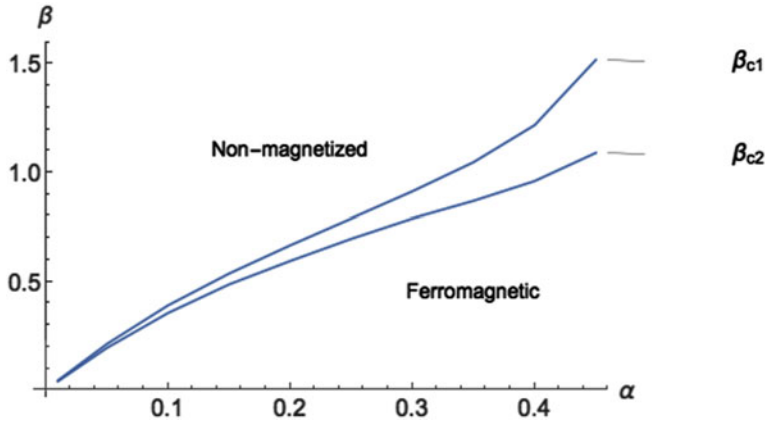

Fig. 3.1 Phase plot in the fine structure constant α versus $\beta = p_F/m$ plane showing the allowed region of spontaneous ferromagnetism

cal grounds we need this complex to be stable for $\approx 10^{17}$ s. The bounce B is typically $\propto 1/\lambda$ where λ is a generic dimensionless coupling constant. Then large suppression factors $\sim 10^{-30}$ are natural for $\lambda \sim 0.01$. The other mechanism for disintegration of the DW network resides in the magnino gas becoming non-degenerate.

3.4 A Minimal Model for Dark Energy

We consider a hitherto unobserved sector with particle species we generically call M and Y. They are assumed to be oppositely charged under a local abelian group $U(1)_X$ with fine structure constant α_X. The mass m_M of M is assumed in the sub-eV range while the Y mass m_Y is assumed to be much larger. Charge neutrality requires that the number densities of the two species have to be equal, in turn this means that the Fermi energies are also the same. The hypothesis of larger mass is to ensures that Y with Compton wavelength $M^{-1} \ll p_F^{-1}$ does not enter into a collective magnetic phase.

We start our considerations at time t_1 when the temperature is just below T_G so that the wall complex has materialised. The parameters of this wall complex are ω, the thickness of individual walls and L the average separation between walls. On the scale of the horizon, the wall complex behaves just like a space filling homogeneous substance. Further, due to the demand of neutrality, the heavier gas Y cannot expand either, although it has no condensation effects. Let us denote the number density of the magninos trapped in the walls to be n^X_{walls} and the remainder residing in the enclosed domains by n^X_{bulk}. Averaged (coarse grained) over a volume much larger than the L^3, this gives the average number density of the magninos to be

$$\langle n^X \rangle = \frac{\omega}{L} n^X_{\text{walls}} + \left(1 - \frac{\omega}{L}\right) n^X_{\text{bulk}} \tag{3.6}$$

And from the neutrality condition we have

$$\langle n^X \rangle = \langle n^Y \rangle \tag{3.7}$$

Then we can demand that PAAI in this phase acts as the DE, so that assuming Y to be non-relativistic, and ignoring other contributions,

$$\rho^Y \approx m_Y \langle n^Y \rangle = \rho_{\text{DE}} = 2.81 \times 10^{-11} (\text{eV})^4 \tag{3.8}$$

We can express the number density of Y as a ratio of the number density $n_\gamma = 3.12 \times 10^{-12} (\text{eV})^3$ of photons, and set $\eta^Y = \langle n^Y \rangle / n_\gamma$. Then we can obtain conditions that determine the ratio

$$\frac{m_M}{m_Y} = \frac{\beta^Y}{\beta} \approx (\eta^Y)^{4/3} \times 10^{-6} \ll 1 \tag{3.9}$$

These are the essential constraints determining the key parameters of our model. Then we find that m_M ranges over 10^{-4} to 10^{-6} eV corresponding to η^Y ranging from 10^{-5} to 10^{-8}; and m_Y respectively ranges from 1keV to 1GeV. The details can be found in [11].

3.5 Flavoured Models and Cosmic Concordance

It is now interesting to explore whether this hidden sector admitting X-ferromagnetic condensation mechanism also has possibilities for the DM. This requires the existence of additional number of stable species which become non-relativistic while the lightest particles continue to simulate Dark Energy. Let us denote the *general* requirements to be obeyed by such *flavoured* scenarios to be **GF**. The wish list of such requirements is

GF1 The charges of these species under $U(1)_X$ are opposite in sign for M-type versus Y-type. However we leave open the possibility that the magnitudes of these charges can be small integer multiples of each other.

GF2 The heavier species of M-types and Y-types should be stable against decay into the corresponding lighter ones even if their Q_X charges tally. This is analogous to flavour symmetry in the observed sector, where the purely electromagnetic conversion of heavier leptonic flavours into lighter ones is not observed.

GF3 The lightest pair M_1 and Y_1 (more generally at least one effective degree of freedom of species of each type) have equal and opposite charges, and satisfy the requirement of the DE scenario of Sect. 3.4.

GF4 The heavier species (more generally the remainder degrees of freedom) do not undergo condensation.

Within these general criteria the simplest scenario that can be thought of may be called **FI**. It has the following straightforward requirements

FI-1 The pair of species M_2 and Y_2 with $Q_X(M_2) = -Q_X(Y_2)$
FI-2 This pair of species accounts for the observed DM.

Thus we demand, with $n_{M2} = n_{Y2}$ designating the number densities, that

$$(m_{M2} + m_{Y2})n_{Y2} = \rho_{\rm DM} = 1.04 \times 10^{-11}(\text{eV})^4 \tag{3.10}$$

so that

$$m_{M2} + m_{Y2} = \left(\frac{1}{\eta^{Y2}}\right) 3.33\text{eV} \tag{3.11}$$

In order for either of X_2 or Y_2, or both together to act as DM, the right hand side of the above equation has to be at least a few keV to satisfy the generally accepted phenomenological requirement on Dark Matter. Thus we need

$$\eta^{Y2} \lesssim 10^{-3} \qquad \text{to ensure DM mass} \gtrsim \text{keV} \tag{3.12}$$

From Sect. 3.4, we have that η^Y can take on any value $\lesssim 10^3$ and account for DE adequately. The DM constraint on the second flavour restricts its abundance to $\lesssim 10^{-3}$. In this scenario η^Y and η^{Y2} need not be related, and a few orders of magnitude difference in abundance could be easily explained by dynamics occurring within that sector in an expanding universe. Further we shall see later that the large value of η^Y makes the scenario capable of explaining the origins of cosmic magnetic fields, while the small η^{Y2} value can separately solve the DM puzzle.

The scenario FI requires that at least one of M_2 and Y_2 is heavy enough to be the DM particle. But it leaves the mass of the other particle undetermined. A scenario that is more restrictive about the mass of M_2 could arise as follows, and we denote this scenario **FII**.

FII-1 There are two species M_1 and M_2, of the same charge $Q_X(M_2) = Q_X(M_1)$.
FII-2 $\eta^{M1} = \sigma\eta^{M2}$ where σ is a numerical factor
FII-3 Only M_1 is the magnino, capable of condensing.
FII-4 There is only one species of Y type, with $Q_X(Y) = -Q_X(M_1)$.

For neutrality of the medium we need $\eta^Y = \eta^{M1} + \eta^{M2}$. Then in this scenario, the fraction equivalent to η^{M1} of the Y particles will suffice to keep the condensed state of M_1 neutral, and thus the mass of Y will be determined as in Sect. 3.4 The remainder Y particles, in abundance η^{M2} scale like free matter particles. Then analogous to conditions (3.11) (3.12), we get

$$m_{M2} + m_Y = \left(\frac{1}{\eta^{Y2}}\right) 3.33\text{eV} \tag{3.13}$$

$$\eta^{M2} \lesssim 10^{-3} \tag{3.14}$$

The point is that m_Y is already determined by the value of η^{M1} from DE Condition, and if $\eta^{M1} \gtrsim 1$ then mass of Y would be determiend to be too small to be DM candidate. In this case, without proliferating unknown mass values, m_{M2} can be the DM candidate.

This Dark Matter sector is along the lines of [13], and through out its history could have been partially ionised and could be progressively becoming neutral. In particular it represents the class of self interacting Dark Matter including van der Waals forces that may result between such atoms due to very low binding energy. It has been argued for example in [30] that such a model potentially explains the diversity in the rotation curves of galaxies.

3.6 Origin of Cosmic Magnetic Fields

The origin and evolution of galactic scale magnetic fields is an open question [17, 31]. In particular the extent of seed magnetic field as against that generated by subsequent motion is probably experimentally distinguishable [18, 19]. In the present case, we can estimate the field strength of the X-magnetism in each domain, and since the domain structure is completely random we expect zero large scale magnetic field on the average. Residual departure from this average can be estimated by assuming that the deviation from the mean grows as $\sqrt{N}$ as we include N domains. Thus if the X-magnetic field in individual domains has the value B_{dom} then on the scale of galactic clusters L_{gal} it possesses a root mean square value $\overline{\Delta B} \equiv B_{\text{dom}}(L/L_{\text{gal}})^{3/2}$.

Assuming $U(1)_X$ field mixes kinetically with standard electromagnetism through term of the form $\xi F^{\mu\nu} F^X_{\mu\nu}$, we consider the possibility of a seed of 10^{-30}T with a coherence length of 0.1 kpc$\sim 3 \times 10^{18}$ meter obtained with $\xi = 10^{-8}$. With B_{dom} calculated from the formalism of Sect. 3.3 we can obtain

$$\overline{\Delta B}_{\text{seed}} = 10^{-30} T \sim 10^{-8} \times \left(\frac{m_M}{\text{eV}}\right)^2 \left(\frac{\alpha_X}{\alpha}\right)^{1/2} \beta^3 \left(\frac{L}{\text{meter}}\right)^{3/2} \times 10^{-40} T \tag{3.15}$$

From this, representative values for L for $\beta = 0.1$ are in the range 10^{14}-10^{15} meter which is a fraction of the Milky Way size. A detailed treatment to estimate the residual fluxes on large coherence length scales could trace the statistics of flux values in near neighbour domains and the rate at which the magnetic flux could undergo percolation, providing perhaps a smaller value for L, comparable to the above estimate.

3.7 Conclusions

We have proposed the possibility of a negative pressure medium as arising from nothing more radical than a peculiar ground state of a pair of asymmetric fermion species interacting through an unbroken abelian gauge force. In an attempt to highlight the potential utility of the PAAI to cosmology, specifically to DE and to cosmic ferromagnetism, we have been agnostic about the earlier history of this sector. A study of temperature dependence of this phenomenon as also phenomenological inputs from the cosmic dawn data would help to sharpen this scenario. Large scale magnetic fields could arise from the same scenario and Dark Matter can be accommodated within the same hidden sector.

Acknowledgements We thank NSERC, Canada for financial support and the Minist re des relations internationales et la francophonie of the Government of Québec for financing within the cadre of the Québec-Maharashtra exchange. RBM and MBP also thank IIT Bombay for financial support and hospitality.

References

1. S. Weinberg, Rev. Mod. Phys. **61**, 1 (1989)
2. N. Aghanim et al. (collaborationPlanck) (2018). arxiv:1807.06209
3. M. Li, X.-D. Li, S. Wang, Y. Wang, Commun. Theor. Phys. **56**, 525 (2011). arxiv:1103.5870
4. U.K. Dey, T.S. Ray, U. Sarkar, Nucl. Phys. **B928**, 258 (2018). arxiv:1705.08484
5. J.I. Kapusta, Phys. Rev. Lett. **93**, 251801 (2004), hep-th/0407164
6. R.A. Battye, M. Bucher, D. Spergel, Phys. Rev. **D60**, 043505 (1999). arxiv:astro-ph/9908047
7. R.A. Battye, A. Moss, Phys. Rev. **D76**, 023005 (2007). arxiv:astro-ph/0703744
8. L. Conversi, A. Melchiorri, L. Mersini-Houghton, J. Silk, Astropart. Phys. **21**, 443 (2004). arxiv:astro-ph/0402529
9. A. Friedland, H. Murayama, M. Perelstein, Phys. Rev. **D67**, 043519 (2003). arxiv:astro-ph/0205520
10. U.A. Yajnik, EPJ Web Conf. **70**, 00046 (2014)
11. R.B. MacKenzie, M.B. Paranjape, U.A. Yajnik (2019). arxiv:1901.00995
12. Note1, notethe term *magnino* was earlier introduced in a different connotation in [R.M. Kulsrud, Ann. Rev. Astron. Astrophys. **37**, 37 (1999)][S. Raby, G. West, Phys. Lett. **B194**, 557 (1987)]
13. J.L. Feng, M. Kaplinghat, H. Tu, H.-B. Yu, JCAP **0907**, 004 (2009). arxiv:0905.3039
14. K.K. Boddy, M. Kaplinghat, A. Kwa, A.H.G. Peter, Phys. Rev. **D94**, 123017 (2016). arxiv:1609.03592
15. J.M. Cline, Z. Liu, G. Moore, W. Xue, Phys. Rev. **D89**, 043514 (2014). arxiv:1311.6468
16. J.M. Cline, Z. Liu, W. Xue, Phys. Rev. **D85**, 101302 (2012). arxiv:1201.4858
17. R.M. Kulsrud, E.G. Zweibel, Rept. Prog. Phys. **71**, 0046091 (2008). arxiv:0707.2783
18. R. Durrer, A. Neronov, Astron. Astrophys. Rev. **21**, 62 (2013). arxiv:1303.7121
19. K. Subramanian, Rept. Prog. Phys. **79**, 076901 (2016). arxiv:1504.02311
20. T.W.B. Kibble, Phys. Rept. **67**, 183 (1980)
21. E.W. Kolb, M.S. Turner, *titleThe Early Universe* (Addison-Wesley Pub. Co., Boston, 1990; revised 2003)
22. S. Dodelson, *titleModern Cosmology* (Addison-Wesley Pub. Co., Boston, 2003)
23. A.K. Rajagopal, J. Callaway, Phys. Rev. B **7**, 1912 (1973)
24. G. Baym, S.A. Chin, Nucl. Phys. **A262**, 527 (1976)

25. S.A. Chin, Annals Phys. **108**, 301 (1977)
26. B.X. Xu, A.K. Rajagopal, M.V. Ramana, J. Phys. C: Solid State Physics **17**, 1339 (1984)
27. J. Preskill, A. Vilenkin, Phys. Rev. **D47**, 2324 (1993). arxiv:hep-ph/9209210
28. I. Yu. Kobzarev, L.B. Okun, M.B. Voloshin, Sov. J. Nucl. Phys. **20**, 644 (1975), note[Yad. Fiz. 20, 1229 (1974)]
29. S.R. Coleman, Phys. Rev. **D15**, 2929 (1977), note[Erratum: Phys. Rev.D 16, 1248 (1977)]
30. A. Kamada, M. Kaplinghat, A.B. Pace, H.-B. Yu, Phys. Rev. Lett. **119**, 111102 (2017). arxiv:1611.02716
31. R.M. Kulsrud, Ann. Rev. Astron. Astrophys. **37**, 37 (1999)
32. S. Raby, G. West, Phys. Lett. **B200**, 547 (1988)
33. S. Raby, G. West, Phys. Lett. **B194**, 557 (1987)

Chapter 4
The Phenomenology of Modified Gravity Models

Antonio De Felice

We review here some modified gravity theories which have been introduced recently, in the light of most recent hints we get from data sets.

4.1 Introduction

In these last few years, cosmology has undergone tremendous changes, whose impact is changing our view of our universe and of the theory of physics which is supposed to determine the dynamics of large scales environment.

In particular, about thirty years ago, a revolution came after the discovery of cosmic acceleration, due for a large part, from the observations given by the Hubble telescope. We call it here a "revolution" because it was quite unexpected. At that time, and even now some few remain, several people would think that effect was something which was too drastic that could have been due not to the fact of the presence of a cosmological constant, but rather to some unknown sistematics or miserintepretation of the data themselves.

Now the fact that the universe is accelerating is widely accepted, and because of this, many people started trying to give an explanation of such a phenomenon.

The first model of such acceleration has been introduced in the form of a cosmological constant. Although there was no robust theoretical prediction about its presence and mostly its numerical value, most people thought that this new general relativity, namely GR + Lambda, was the ultimate theory of gravity, at least in the classical domain. Effectively, data converged quite well to the picture given by such a theory. A theory which has a tiny cosmological constant, whose value is different by several orders of magnitude from any prediction given in the realm of QFT.

A. De Felice (✉)
Yukawa Institute for Theoretical Physics, Kyoto University, Kitashirakawa Oiwakecho, Sakyo Ward, Kyoto 606-8502, Japan
e-mail: antonio.defelice@yukawa.kyoto-u.ac.jp

A. Giri and R. Mohanta (eds.), *Workshop on Frontiers in High Energy Physics 2019*, Springer Proceedings in Physics 248,
https://doi.org/10.1007/978-981-15-6292-1_4

Therefore, accepting the theory as exact, the problem of cosmology for several years was the "cosmological constant problem," that is, the only thing left to understand was not its presence but its value.

This nice picture might be indeed the picture of the universe, however, we feel this simple picture does not need to be real. Afterall, covariance theory allows an infinite possibilities to describe a model which makes the universe accelerate at late times. Sometimes, we hear the Occam razor as a way to falsify everything but ΛCDM. This logic is quite ununderstandable, as in fact, if that was true, then classical mechanics would be simpler that General Relativity, a $U(1)$ theory, QED, would have been the ultimate theory of particle physics. However, in the context of data analysis, Occam razor could be transformed into a different statement. Given two theories if the fit to the daya for both of them give the same value of χ^2, then the theory with less free parameters is more plausible. Therefore, as it should be, everything goes in the end to the ability of a certain model to fit the data. No matter what the model is built of.

Starting from this assumptions, we will study here some of the models introduced recently in the literature.

4.2 Minimal Theories of Gravity

In this section, we discuss several different theories of gravity all sharing the property that the degrees of freedom from the gravity sector are only two. These two gravity modes correspond to the gravitational waves. Therefore these theories represent minimal modifications, from the number of degrees of freedom point of view, with respect to GR.

Among these minimaly modified gravity (MMG) theories we will classify them as:

1. Type-I MMG. These theories are those theories, with only two gravity degrees of freedom, which admit an Einstein frame.
2. Type-II MMG. These theories are those theories, with two only gravity degrees of freedom, which do not admit insted an Einstein frame.

A similar classification can also be made in general theories of gravity, however here the difference is that the theory is minimal that is we need to make sure that the theory at hand has two degrees of freedom, non-linearly and on any background.

4.2.1 Type-I: MMG

In this context we propose here the theory of MMG [1, 2]. The idea is simple, we consider the Hamiltonian of General Relativity and we perform a canonical transformation. Namely, we start from

$$H_{\rm tot} = \int d^3x [\mathcal{N}\mathcal{H}_0(\Gamma,\Pi) + \mathcal{N}^i\mathcal{H}_i(\Gamma,\Pi) + \lambda\Pi_{\mathcal{N}} + \lambda^i\Pi_i]\,, \tag{4.1}$$

where

$$\mathcal{H}_0 = \frac{2}{M^2\sqrt{\Gamma}}\left(\Gamma_{ik}\Gamma_{jl} - \frac{1}{2}\,\Gamma_{ij}\Gamma_{kl}\right)\Pi^{ij}\Pi^{kl} - \frac{M^2\sqrt{\Gamma}}{2}\,R(\Gamma)\,,$$
$$\mathcal{H}_i = -2\sqrt{\Gamma}\Gamma_{ij}D_k\left(\frac{\Pi^{jk}}{\sqrt{\Gamma}}\right),$$

where Π_N is conjugate to $\mathcal{N}$, Π^i to $\mathcal{N}_i$ and Π^{ij} to Γ_{ij}, and $\Gamma_{ij}, \mathcal{N}, \mathcal{N}_i$ are the ADM variables of the Einstein frame metric:

$$ds^2_{\rm EF} = g^{\rm EF}_{\mu\nu}\,dx^\mu\,dx^\nu = -\mathcal{N}^2\,dt^2 + \Gamma_{ij}\,(dx^i + \mathcal{N}^i\,dt)\,(dx^j + \mathcal{N}^j\,dt)\,. \tag{4.2}$$

Instead matter will be coupled with the Jordan frame metric,

$$ds^2_{\rm JF} = g^{\rm JF}_{\mu\nu}\,dx^\mu\,dx^\nu = -N^2\,dt^2 + \gamma_{ij}\,(dx^i + N^i\,dt)\,(dx^j + N^j\,dt)\,. \tag{4.3}$$

Then we introduce the generating functional as

$$F = -\int d^3x (M^2\sqrt{\gamma}\,f(\tilde{\Pi},\tilde{\mathcal{H}}) + N^i\,\Pi_i)\,, \tag{4.4}$$

where

$$\tilde{\Pi} = \frac{1}{M^2\sqrt{\gamma}}\,\Pi^{ij}\,\gamma_{ij}\,, \qquad \tilde{\mathcal{H}} = \frac{1}{M^2\sqrt{\gamma}}\,\Pi_{\mathcal{N}}\,N\,. \tag{4.5}$$

We will then have a new Hamiltonian. After having gone to this new Hamiltonian we introduce matter field Hamiltonians coupled with the Jordan frame metric. In this case the theory will be essentially different from General Relativity.

When we introduce matter fields, we need also to introduce a gauge fixing term, as otherwise the Hamiltonian constraint would only be a second class constraint instead of first class.

4.2.2 Type-II: MTMG

This theory is known to be of Type-II. The aim for such a theory is to provide cosmological phenomenology to massive gravity. Unfortunately, the original model, on FLRW backgrounds, suffer from the presence of light modes whose kinetic term vanish as the metric becomes more and more isotropic and homogeneous.

A way out of this problem, is to introduce a theory which only possesses tensor degrees of freedom, that is we need a minimal theory of massive gravity (MTMG)

[3–7] (see also [8, 9] for extensions). In fact, in this case, any unwanted degree of freedom, which would be unstable in standard massive gravity, is bound to play no role other than a being a Lagrange multiplier. However, even then these modes do not propagate any longer on any background, still they set conditions since they are merely Lagrange multipliers. Some of these conditions end up changing the equation of motion for the perturbations, leading to signatures which can indentify these models from others and in particular from ΛCDM.

One of the equations of motion for such a model can be written as

$$(c_3 + c_2 X + c_1 X^2)\,(\dot{X} + N\,H\,X - M\,H) = 0\,, \tag{4.6}$$

where $c_{1,2,3}$ are constants, whereas $X = \tilde{a}/a$, where a is the scale factor, whereas $\tilde{a}$ is the scale factor for the fiducial metric, which on fixing unitary gauge corresponds on a given external field. We also have H which is the Hubble parameter, i.e. $H = \dot{a}/(aN)$. Finally $N$is the lapse function for the physical metric, and M is the lapse for the fiducial metric (intended to be an external given field in unitary gauge). It is evident that two branches of solutions exist, namely:

1. Self-accelerating brnach, for which $c_3 + c_2 X + c_1 X^2 = 0$, and leads to $X =$ constant.
2. Normal branch. For this latter branch we have

$$\frac{\dot{X}}{N} = \frac{1}{N}\frac{dX}{dt} = \frac{1}{N}\frac{da}{dt}\frac{dX}{da} = aH\frac{dX}{da} = H\left(\frac{M}{N} - 1\right), \tag{4.7}$$

or

$$\frac{dX}{d\bar{N}} = \frac{M}{N} - 1\,, \tag{4.8}$$

where $\bar{N} = \ln(a/a_0)$. Therefore, for a given M/N, we will have an evolution for X. It is still possible to have $\dot{X} = 0$, when $M = N$, but not necesserely.

For both branches, we can write down the Friedmann equation as

$$3M_{\rm P}^2 H^2 = \frac{m^2 M_{\rm P}^2}{2}\left[c_4 + 3c_3 X + 3c_2 X^2 + c_1 X^3\right] + \sum_i \rho_i\,, \tag{4.9}$$

so that it is evident that the first branch will lead to an effective cosmological constant on the background, whereas the second branch might have non-trivial dynamical effects on the background. On introducing $\rho_i = 3M_{\rm P}^2\varrho_i$, then we can write down once more the Friedmann equation as

$$H^2 = \varrho_X + \sum_i \varrho_i\,, \tag{4.10}$$

where

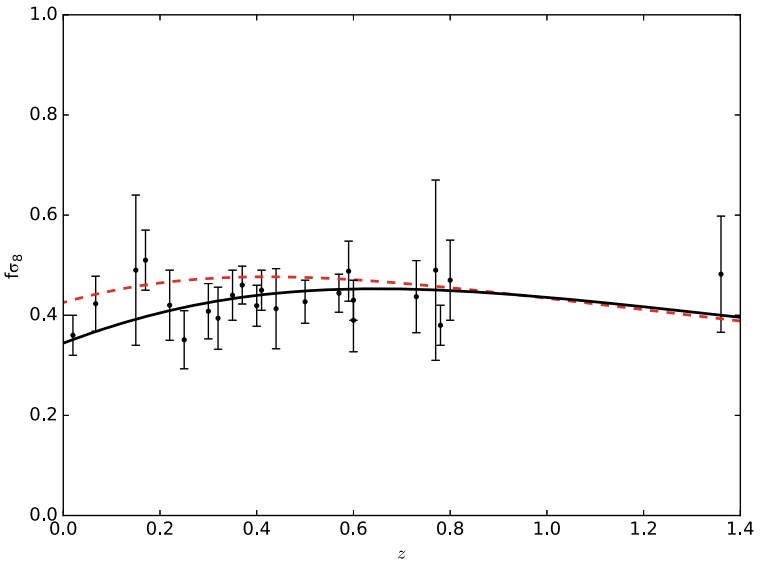

Fig. 4.1 Evolution of growth of perturbations for MTMG. It is indeed possible to fit the data better than ΛCDM, however, the error bars for the data are still too large. Future data sets should make clear whether a cosmological constant will be strongly constrained by the growth of structures

$$\varrho_X \equiv \frac{m^2}{6}\left(c_4 + 3c_3 X + 3c_2 X^2 + c_1 X^3\right). \tag{4.11}$$

As an application of such a theory, we have shown that we can get an effective gravitational constant which is less than the Newton gravitational constant at large scales (Fig. 4.1), i.e. any scale inside the limit of cosmological perturbation theory (see also [10, 11]). This effect is difficult to achieve in the context of Horndeski theories.

4.3 Conclusions

In this short review of minimal theories of gravity, we have seen that it is not impossible to find theories which, as General Relativity, only has two degrees of freedom. We can achieve this goal by either introducing a fiducial metric, and setting non-trivial constraints in order to remove unwanted degrees of freedom, or by performing a canonical transformation from the original theory to another one, introducing a gauge-fixing term and finally the wanted matter fields. In both cases, we will in general have a phenomenology at large scales which will differ substantially from Λ-CDM.

If already now, latest data seem to point towards a tension between early-time and late-time data, in the near future, we will see whether General Relativity will

keep its leading role as a gravitational theory, or it will need to be replaced by some other theory. What is that theory, if it exists, is still completely obscure. Maybe dark energy is more complicated than originally thought.

Acknowledgements The author wants to thank the organizers of the FHEP 2019 workshop, and in particular prof. Giri, for the kindness shown to me during my stay in Hyderabad.

References

1. K. Aoki, C. Lin, S. Mukohyama, Phys. Rev. **D98**, 044022 (2018). ArXiv:1804.03902
2. K. Aoki, A. De Felice, C. Lin, S. Mukohyama, M. Oliosi, JCAP **1901**, 017 (2019). ArXiv:1810.01047
3. A. De Felice, S. Mukohyama, Phys. Lett. **B752**, 302 (2016). ArXiv:1506.01594
4. A. De Felice, S. Mukohyama, JCAP **1604**, 028 (2016). ArXiv1512.04008
5. A. De Felice, S. Mukohyama, Phys. Rev. Lett. **118**, 091104 (2017). ArXiv:1607.03368
6. N. Bolis, A. De Felice, S. Mukohyama, Phys. Rev. **D98**, 024010 (2018). ArXiv:1804.01790
7. A. De Felice, F. Larrouturou, S. Mukohyama, M. Oliosi, Phys. Rev. **D98**, 104031 (2018). ArXiv:1808.01403
8. A. De Felice, S. Mukohyama, M. Oliosi, Phys. Rev. **D96**, 024032 (2017). ArXiv:1701.01581
9. A. De Felice, S. Mukohyama, M. Oliosi, Phys. Rev. **D96**, 104036 (2017). ArXiv:1709.03108
10. M.C. Pookkillath, A. De Felice, S. Mukohyama (2019). ArXiv:1906.06831
11. F. Giacomello, A. De Felice, S. Ansoldi, JCAP **1903**, 038 (2019). ArXiv:1811.10885

Chapter 5
Unique Contributions to the Scalar Bispectrum in 'Just Enough Inflation'

H. V. Ragavendra, Debika Chowdhury, and L. Sriramkumar

Abstract A scalar field rolling down a potential with a large initial velocity results in inflation of a finite duration. Such a scenario suppresses the scalar power on large scales improving the fit to the cosmological data. We find that the scenario leads to a hitherto unexplored situation wherein the boundary terms dominate the contributions to the scalar bispectrum over the bulk terms. We show that the consistency relation governing the scalar non-Gaussianity parameter $f_{\rm NL}$ is violated on large scales and that the contributions at the initial time can substantially enhance the value of $f_{\rm NL}$.

5.1 Suppressing the Power on Large Scales

It is well known that a featureless and nearly scale invariant primordial spectrum, as is generated in slow roll models of inflation, is remarkably consistent with the observations of the anisotropies in the Cosmic Microwave Background (CMB) (for the most recent constraints from Planck, see [1]). However, intriguingly, it has been repeatedly noticed that suppressing the primordial scalar power on large scales roughly corresponding to the Hubble radius today improves the fit to the CMB data at the lower multipoles [2–6]. There has been a constant effort to construct models of inflation that naturally result in lower power on the largest observable scales (see, for example, [7–14]).

In the standard slow roll models of inflation, the scalar fields are assumed to start on the inflationary attractor, and they evolve along the attractor until the end of inflation. A model that has drawn recent attention in the context of suppressing power on large scales involves a scalar field which begins its journey down the inflationary potential with the largest initial velocity possible (for the original discussion, see [8];

H. V. Ragavendra · L. Sriramkumar (✉)
Department of Physics, Indian Institute of Technology Madras, Chennai 600036, India
e-mail: sriram@physics.iitm.ac.in

D. Chowdhury
Department of Theoretical Physics, Tata Institute of Fundamental Research, Mumbai 400005, India

A. Giri and R. Mohanta (eds.), *Workshop on Frontiers in High Energy Physics 2019*, Springer Proceedings in Physics 248,
https://doi.org/10.1007/978-981-15-6292-1_5

for recent discussions, see [15–19]). In fact, in such a situation, inflation begins only after about an e-fold or two, when the friction arising due to the expansion of the universe has reduced the velocity of the field adequately. Thereafter, the field rolls slowly down the inflationary potential and, as usual, inflation is terminated as the field approaches the bottom of the potential. Clearly, it is the large initial velocity of the field that results in inflation of a finite duration.

In slow roll inflation, the standard Bunch–Davies initial conditions are imposed on the perturbations when the modes are well inside the Hubble radius. Based on the constraints on the tensor-to-scalar ratio, it is possible to arrive at lower bounds on the required duration of inflation (when counted backwards from its end) if the largest observable scale today is to have emerged from sufficiently inside the Hubble radius. These arguments suggest that (under certain general conditions) inflation has to last for *at least* 60–65 e-folds in order for all observable scales to begin their evolution in the sub-Hubble domain (in this context, see [20, 21]). In a scenario with kinetically dominated initial conditions, as we mentioned, inflation naturally lasts for a finite duration. If this duration is less than the above-mentioned number of e-folds, then a certain range of large scale modes of cosmological interest would never have been inside the Hubble radius. If we now choose to impose the Bunch–Davies initial conditions on the perturbations (irrespective of whether they are inside or outside the Hubble radius) when the scalar field rolls down with a large initial velocity, then one finds that the scalar power spectrum exhibits suppressed power on the largest scales. Interestingly, if the duration of inflation is chosen suitably, one finds that the power spectrum improves the fit to the CMB data at the lower multipoles [19].

Typically, features in the inflationary power spectra are generated due to deviations from slow roll and these departures also lead to larger levels of non-Gaussianities (see, for instance, [22–29]). In this work, we examine if the scalar bispectrum generated in the scenario with kinetically dominated initial conditions is consistent with the recent constraints from Planck on the scalar non-Gaussianity parameter $f_{\rm NL}$ [30]. We numerically evaluate the scalar bispectrum in such a situation and show that, since the initial conditions on the perturbations are imposed at a finite early time, the contributions due to the boundary terms in the third order action governing the scalar bispectrum dominate the contributions due to the bulk terms. This interesting situation does not seem to have been encountered earlier in the literature.

We shall set $\hbar = c = 1$ and $M_{\rm Pl} = (8\,\pi\,G)^{-1/2}$. As usual, a and H shall denote the scale factor and the Hubble parameter associated with the Friedmann universe. Moreover, an overdot and overprime shall denote derivatives with respect to the cosmic and the conformal time coordinates, respectively. Further, while N shall denote e-folds, k shall represent the wavenumber of the modes.

5.2 Scalar Power Spectrum in 'Just Enough Inflation'

To illustrate the suppression of power on large scales that can arise in scenarios with kinetically dominated initial conditions, we shall consider two models of inflation driven by the canonical scalar field ϕ, viz. the quadratic potential

$V(\phi) = m^2\,\phi^2/2$ and the Starobinsky model described by the potential $V(\phi) = (\Lambda/8)\,[1 - \mathrm{e}^{-\sqrt{2/3}\,(\phi/M_{_{\rm Pl}})}]^2$. We start the evolution of the background with a large initial velocity for the scalar field such that the first slow roll parameter $\epsilon_1 = \dot{\phi}^2/(2\,H^2 M_{_{\rm Pl}}^2)$ is initially close to its maximum value, i.e. $\epsilon_{1\rm i} \simeq 3$ [15–19]. The initial value of the scalar field is chosen such that inflation lasts for about 60 e-folds. The expansion of the universe rapidly slows down the field and inflation sets in (i.e. ϵ_1 becomes less than unity) after about an e-fold or so. As the velocity of the field reduces further, it soon settles down on the slow roll inflationary attractor with a small, nearly constant, velocity.

We shall numerically evolve the perturbations in such a background and calculate the resulting observable quantities of interest, viz. the scalar power and bispectra and the corresponding scalar non-Gaussianity parameter. Actually, for each model, we shall consider two situations wherein the perturbations are evolved from two different initial points in time, viz. from the onset of inflation (say, $N_{_{\rm I}}$, when $\epsilon_1 = 1$) and from the time (say, $N = 0$) when we begin the evolution of the background scalar field. Recall that the Bunch–Davies initial conditions are imposed on the perturbations when $k \gg \sqrt{z''/z}$, where $z = \sqrt{2\,\epsilon_1}\,M_{_{\rm Pl}}\,a$. During slow roll inflation, $\sqrt{z''/z} \simeq \sqrt{2}\,a\,H$, and hence the above condition essentially corresponds to the modes being well inside the Hubble radius. Interestingly, we find that the equivalence $\sqrt{z''/z} \simeq a\,H$ proves to be roughly true even when the scalar field is rolling down the potential with a large initial velocity. Since we begin the evolution of the perturbations at a specific time, there naturally arises a finite initial value of the quantity $\sqrt{z''/z}$ (evaluated at $N = 0$ or $N_{_{\rm I}}$), which we shall refer to as $k_{\rm i}$. This implies that, in the scenario of our interest, modes with $k < k_{\rm i}$ would never be inside the Hubble radius. Despite this, if we were to impose the Bunch–Davies initial conditions on *all* the modes at the beginning of their evolution (i.e. at $N = 0$ or $N_{_{\rm I}}$), then one arrives at a scalar power spectrum with a sharp drop in amplitude for modes with $k \lesssim k_{\rm i}$. In Fig. 5.1, we have plotted the scalar power spectra $\mathcal{P}_{_{\rm S}}(k)$ arising in these two cases for suitable values of the parameters involved. Clearly, the spectra exhibit a distinct suppression of power over the modes that were never inside the Hubble radius (i.e. for $k < k_{\rm i}$). The power spectra also contain oscillations (for modes with $k \simeq k_{\rm i}$) before they turn nearly scale invariant at smaller scales. The two sets of spectra presented in the figure differ only in the nature of the transient oscillations with a higher initial velocity leading to oscillations of stronger amplitude and wider range.

5.3 Evaluation of the Scalar Bispectrum

The scalar bispectrum $G(\boldsymbol{k}_1, \boldsymbol{k}_2, \boldsymbol{k}_3)$—where $\boldsymbol{k}_1$, $\boldsymbol{k}_2$ and $\boldsymbol{k}_3$ constitute a triangular configuration of wavevectors—is determined by the action describing the curvature perturbation at the third order (see, for example, [31, 32]). This action, in turn, is arrived at from the original action governing the system of the gravitational and scalar fields. The third order action that is often used to calculate the scalar bispectrum contains six terms, which are arrived at after repeated integration by parts (in this

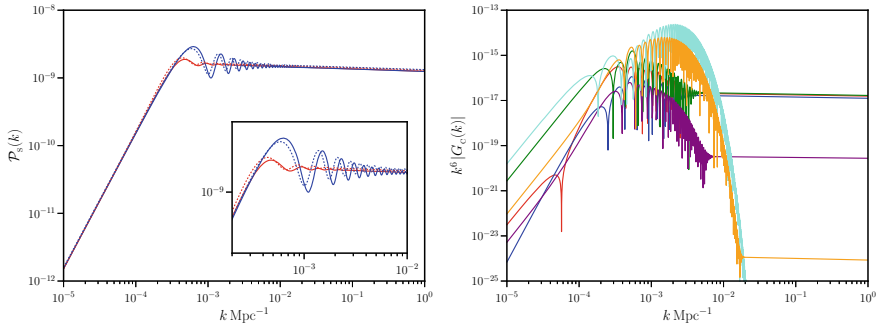

Fig. 5.1 **Left:** The scalar power spectra generated in the quadratic potential (as solid lines) and the Starobinsky model (as dotted lines) with kinetically dominated initial conditions have been plotted for the two cases wherein the perturbations are evolved from $N_{\rm i}$ (in red) and $N = 0$ (in blue). We have evolved the field from $\phi_{\rm i} = 18.85\,M_{\rm Pl}$ and $8.3752\,M_{\rm Pl}$ in the quadratic potential and the Starobinsky model respectively, and have set $\epsilon_{1{\rm i}} = 2.99$. The parameters m and Λ have been chosen suitably so that the spectra match over the range of modes which exhibit a suppression in power (for $k < k_{\rm i}$) and in the nearly scale invariant regime (which occurs for $k \gg k_{\rm i}$). We find that this is possible if we set $m/M_{\rm Pl} = (5.0 \times 10^{-6}, 4.9 \times 10^{-6})$ and $\Lambda/M_{\rm Pl}^4 = (5.8 \times 10^{-10}, 5.7 \times 10^{-10})$ in the cases evolved from $N_{\rm i}$ and $N = 0$, respectively. In these four instances, the pivot scale $k_* = 5 \times 10^{-2}\,\mathrm{Mpc}^{-1}$ leaves the Hubble radius at (57.48, 58.50) and (57.07, 58.08) e-folds *before the end of inflation*. Also, in these cases, we find that, $k_{\rm i}/\mathrm{Mpc}^{-1} = (2.38 \times 10^{-4}, 2.32 \times 10^{-3})$ and $(2.38 \times 10^{-4}, 1.92 \times 10^{-3})$. Note that the two sets of spectra differ only in the amplitude and range of the oscillations that arise near $k_{\rm i}$. **Right:** The different contributions to the scalar bispectrum in the equilateral limit—the bulk contributions $G_1(k) + G_3(k)$ (in red), $G_2(k)$ (in blue), $G_4(k) + G_7(k)$ (in green), $G_5(k) + G_6(k)$ (in purple), and the boundary contributions $G_8(k)$ (in cyan) and $G_9(k)$ (in orange)—have been plotted in the scenario wherein the perturbations are evolved from the onset of inflation in the quadratic potential. Evidently, the contributions due to the boundary terms dominate the contributions due to the bulk terms over a range of modes. Moreover, note that the contributions due to the boundary terms prove to be considerably more significant around $k_{\rm i}$, before they die down rapidly on smaller scales. We find that the scalar bispectrum has roughly the same shape in all the models and cases we have considered

context, see, for instance, [26, 33]). In the case of standard slow roll inflation, it can be shown that, barring one term, the *temporal* boundary terms arising due to integration by parts do not contribute to the scalar bispectrum [33]. (It can be easily shown that the spatial boundary terms do not contribute in any situation.) The boundary term that contributes (which we shall refer to as the seventh term) is often included as a term that arises due to a field redefinition [26, 31, 33]. The remaining terms do not contribute in slow roll inflation for two reasons: the contributions from the extreme sub-Hubble domain are regulated by the introduction of a cut-off (which is necessary to choose the correct perturbative vacuum) and the late time contributions prove to be insignificant since the amplitude of the curvature perturbation freezes on super-Hubble scales [33].

In the scenario of our interest, while modes with $k < k_{\rm i}$ always remain on super-Hubble scales, modes with $k > k_{\rm i}$ begin in the sub-Hubble regime and eventually reach super-Hubble scales. As the amplitude of all these modes freeze in the super-

Hubble regime, the contributions due to the boundary terms at late times turn out to be insignificant (apart from the seventh term usually taken into account through a field redefinition) as in the standard slow roll case. However, since the modes are evolved from a finite past, we find that we cannot ignore the contributions arising due to the boundary terms evaluated at the initial time (i.e. at $N_{\rm i}$ or at $N = 0$). We numerically evaluate the contributions due to the six standard bulk terms and the seventh term often absorbed through a field redefinition. We also calculate the contributions due to all the boundary terms [34]. In Fig. 5.1, we have illustrated the various contributions to the scalar bispectrum in the equilateral limit. Interestingly, we find that over a range of modes near $k_{\rm i}$, the boundary terms turn out to be comparable to and even larger than the bulk terms. This is a rather novel result that does not seem to have been encountered earlier in the literature.

We had mentioned that the contributions to the scalar bispectrum from the sub-Hubble regime are regulated by the introduction of a cut-off [22, 28]. As is usually done, we introduce a democratic (in the space of wavenumbers) cut-off of the form $\mathrm{e}^{-\kappa\,(k_1+k_2+k_3)/(3\,a\,H)}$, where κ is a suitable cut-off parameter, when calculating the contributions due to both the bulk and the boundary terms. In slow roll inflation or in situations involving brief periods of fast roll sandwiched between epochs of slow roll, the value of the cut-off parameter κ is chosen depending on the depth inside the Hubble radius from which the integrals characterizing the bulk terms are carried out (in this context, see [28]). But, in the scenario of our interest, a range of modes (with $k < k_{\rm i}$) are never inside the Hubble radius and another range (with $k > k_{\rm i}$) do not spend an adequate amount of time in the sub-Hubble regime. Since the large scale modes (i.e. $k < k_{\rm i}$) always remain on super-Hubble scales, the bispectrum evaluated over these range of modes is completely independent of the choice of the cut-off parameter κ. However, we find that the results depend on the choice of κ for modes around $k_{\rm i}$ which do not spend an adequate amount of time in the sub-Hubble regime. As there exists no definitive procedure that can be adopted to circumvent this ambiguity, we make a judicious choice of κ for the remaining set of modes (i.e. for $k > k_{\rm i}$) based on the natural demand that we are to recover the standard slow roll results at suitably small scales which emerge from sufficiently inside the Hubble radius (say, $k > 10^2\, k_{\rm i}$). We should mention here that we have set $\kappa = 0.3$ for *all* the modes in arriving at the results plotted in Fig. 5.1.

5.4 Amplitude and Shape of $f_{\rm NL}$

With the scalar power and bispectra at hand, we can now evaluate the resulting non-Gaussianity parameter $f_{\rm NL}$. In Fig. 5.2, we have plotted $f_{\rm NL}$ in the equilateral and the squeezed limits for the two cases in each of the two models we have considered. Let us first discuss the results in the equilateral limit. In the equilateral limit, while $f_{\rm NL}$ has a roughly constant value over wavenumbers $k < k_{\rm i}$, it exhibits oscillations around $k_{\rm i}$ before eventually settling down to the usual slow roll value for $k \gg k_{\rm i}$. Curiously, the constant value at large scales is higher in the case wherein the perturbations are

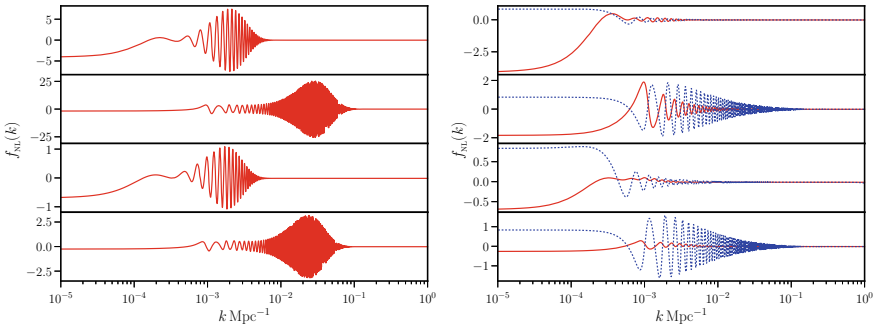

Fig. 5.2 **Left**: The behavior of the non-Gaussianity parameter $f_{\rm NL}(k)$ has been plotted in the equilateral limit for the quadratic potential (in the top two panels) and the Starobinsky model (in the bottom two panels) in the two cases evaluated from $N_{\rm I}$ (in panels one and three, counted from the top) and $N = 0$ (in panels two and four). As expected, the non-Gaussianity parameter exhibits a burst of oscillations around $k_{\rm i}$ before it settles down to the slow roll value at small scales. In a given model, $f_{\rm NL}$ is considerably larger in the case wherein the bispectrum is calculated from $N = 0$ (plotted in panels two and four) than in the case wherein it is computed from the onset of inflation (plotted in panels one and three). Interestingly, $f_{\rm NL}$ is significantly smaller in the Starobinsky model than in the quadratic potential. **Right:** The behavior of $f_{\rm NL}$ in the squeezed limit has been plotted (in red) in the same fashion (as on the left) for the two models and in the two situations of our interest. We have also plotted the quantity $f_{\rm NL}^{\rm CR}$ (in blue) for all the cases. It is clear that the consistency condition is violated at large and intermediate scales before it is restored at suitably small scales (roughly for $k \gtrsim 10^2\, k_{\rm i}$)

evolved from the onset of inflation. However, over the oscillatory regime, the value of $f_{\rm NL}$ is larger in the case wherein the perturbations are evolved from a higher initial velocity of the background scalar field. Importantly, we should clarify that even the largest value of $f_{\rm NL}$ we encounter lies within the constraints (viz. $f_{\rm NL} = -26 \pm 47$ for the equilateral shape) arrived at recently by Planck [30]. Interestingly, under the same conditions, the amplitude of $f_{\rm NL}$ turns out to be significantly smaller in the Starobinsky model than in the quadratic potential.

Let us now turn to the behavior of the scalar non-Gaussianity parameter in the squeezed limit. In Fig. 5.2, apart from $f_{\rm NL}$ in the squeezed limit, we have also plotted the consistency condition, viz. $f_{\rm NL}^{\rm CR} = (5/12)\,(n_{\rm s} - 1)$, where $n_{\rm s}$ is the scalar spectral index, again for both the models and in the two cases of our interest. Clearly, in the squeezed limit, the non-Gaussianity parameter has broadly the same shape as in the equilateral limit. It is roughly constant at small wavenumbers, which is followed by a burst of oscillations over the intermediate range, before its amplitude is restored to the standard slow roll value at larger wavenumbers. However, the strength of the oscillations in the squeezed limit proves to be considerably smaller than in the equilateral limit. Moreover, the consistency condition is violated for the large scale modes (for which the Bunch–Davies conditions are imposed in the super-Hubble domain), and it is eventually restored for small scale modes that emerge from sufficiently deep inside the Hubble radius.

5.5 Conclusions

The model of 'just enough inflation' is attractive for the reason that it leads to a suppression of power on large scales which provides a better fit to the CMB data than a nearly scale invariant spectrum produced in conventional slow roll inflation. It then becomes important to examine whether the non-Gaussianities generated in the model are consistent with the recent constraints from Planck [30].

In this work, we have numerically calculated the scalar bispectrum and the corresponding non-Gaussianity parameter $f_{\rm NL}$ arising in this scenario for two models, viz. the quadratic potential and the Starobinsky model. Due to the fact that the initial conditions on the perturbations are imposed in the finite past when the scalar field is rolling rapidly down the inflationary potential, the model presents a novel and hitherto unexplored situation as far as the calculation of the scalar bispectrum is concerned. We find that, apart from the standard contributions due to the bulk terms in the third order action governing the curvature perturbation, there also arise contributions to the scalar bispectrum from the temporal boundary terms which are usually ignored. In fact, over a range of modes, we find that the contributions due to the boundary terms evaluated at the initial time (when the Bunch–Davies conditions are imposed on the perturbations) prove to be dominant when compared to the contributions due to the bulk terms. Moreover, we notice that the extent of the scalar non-Gaussianity generated depends on the velocity of the scalar field when the initial conditions are imposed on the perturbations, with the maximum value of $f_{\rm NL}$ being larger when the velocity of the field is higher. Further, we find that, in the squeezed limit, the consistency condition governing the scalar bispectrum is violated for the large scale modes which are never inside the Hubble radius and exhibit a suppression in the power spectrum. Lastly and, importantly, the amplitude of $f_{\rm NL}$ generated in the quadratic potential and the Starobinsky model prove to be significantly different. These unique signatures of the scenario in the bispectrum can help in distinguishing it from other models that achieve similar suppression in scalar power and hence may seem degenerate in their performance against the existing CMB data at the level of the power spectrum [34].

Acknowledgements The authors thank Dhiraj Hazra for discussions and comments on the manuscript. HVR and DC thank the Indian Institute of Technology Madras (IITM), Chennai, India, and the Tata Institute of Fundamental Research, Mumbai, India, respectively, for financial support. HVR and LS acknowledge the use of the cluster computing facilities at IITM where the numerical computations were carried out. LS acknowledges support from the Science and Engineering Research Board, Department of Science and Technology, Government of India, through the Core Research Grant CRG/2018/002200.

References

1. Y. Akrami et al., arXiv:1807.06211 (2018)
2. S.L. Bridle, A.M. Lewis, J. Weller, G. Efstathiou, Mon. Not. Roy. Astron. Soc. **342**, L72 (2003). https://doi.org/10.1046/j.1365-8711.2003.06807.x
3. A. Shafieloo, T. Souradeep, Phys. Rev. D **70**, 043523 (2004). https://doi.org/10.1103/PhysRevD.70.043523
4. P. Hunt, S. Sarkar, Phys. Rev. D **70**, 103518 (2004). https://doi.org/10.1103/PhysRevD.70.103518
5. P. Hunt, S. Sarkar, Phys. Rev. D **76**, 123504 (2007). https://doi.org/10.1103/PhysRevD.76.123504
6. D.K. Hazra, A. Shafieloo, G.F. Smoot, JCAP **1312**, 035 (2013). https://doi.org/10.1088/1475-7516/2013/12/035
7. J.M. Cline, P. Crotty, J. Lesgourgues, JCAP **0309**, 010 (2003). https://doi.org/10.1088/1475-7516/2003/09/010
8. C.R. Contaldi, M. Peloso, L. Kofman, A.D. Linde, JCAP **0307**, 002 (2003). https://doi.org/10.1088/1475-7516/2003/07/002
9. B.A. Powell, W.H. Kinney, Phys. Rev. D **76**, 063512 (2007). https://doi.org/10.1103/PhysRevD.76.063512
10. G. Nicholson, C.R. Contaldi, JCAP **0801**, 002 (2008). https://doi.org/10.1088/1475-7516/2008/01/002
11. R.K. Jain, P. Chingangbam, J.O. Gong, L. Sriramkumar, T. Souradeep, JCAP **0901**, 009 (2009). https://doi.org/10.1088/1475-7516/2009/01/009
12. R.K. Jain, P. Chingangbam, L. Sriramkumar, T. Souradeep, Phys. Rev. D **82**, 023509 (2010). https://doi.org/10.1103/PhysRevD.82.023509
13. D.K. Hazra, A. Shafieloo, G.F. Smoot, A.A. Starobinsky, Phys. Rev. Lett. **113**(7), 071301 (2014). https://doi.org/10.1103/PhysRevLett.113.071301
14. D.K. Hazra, A. Shafieloo, G.F. Smoot, A.A. Starobinsky, JCAP **1408**, 048 (2014). https://doi.org/10.1088/1475-7516/2014/08/048
15. E. Ramirez, D.J. Schwarz, Phys. Rev. D **85**, 103516 (2012). https://doi.org/10.1103/PhysRevD.85.103516
16. E. Ramirez, Phys. Rev. D **85**, 103517 (2012). https://doi.org/10.1103/PhysRevD.85.103517
17. W.J. Handley, S.D. Brechet, A.N. Lasenby, M.P. Hobson, Phys. Rev. D **89**(6), 063505 (2014). https://doi.org/10.1103/PhysRevD.89.063505
18. L.T. Hergt, W.J. Handley, M.P. Hobson, A.N. Lasenby, Phys. Rev. D **100**(2), 023502 (2019). https://doi.org/10.1103/PhysRevD.100.023502
19. L.T. Hergt, W.J. Handley, M.P. Hobson, A.N. Lasenby, Phys. Rev. D **100**(2), 023501 (2019). https://doi.org/10.1103/PhysRevD.100.023501
20. S. Dodelson, L. Hui, Phys. Rev. Lett. **91**, 131301 (2003). https://doi.org/10.1103/PhysRevLett.91.131301
21. A.R. Liddle, S.M. Leach, Phys. Rev. D **68**, 103503 (2003). https://doi.org/10.1103/PhysRevD.68.103503
22. X. Chen, R. Easther, E.A. Lim, JCAP **0706**, 023 (2007). https://doi.org/10.1088/1475-7516/2007/06/023
23. R. Flauger, E. Pajer, JCAP **1101**, 017 (2011). https://doi.org/10.1088/1475-7516/2011/01/017
24. P. Adshead, W. Hu, C. Dvorkin, H.V. Peiris, Phys. Rev. D **84**, 043519 (2011). https://doi.org/10.1103/PhysRevD.84.043519
25. P. Adshead, C. Dvorkin, W. Hu, E.A. Lim, Phys. Rev. D **85**, 023531 (2012). https://doi.org/10.1103/PhysRevD.85.023531
26. J. Martin, L. Sriramkumar, JCAP **1201**, 008 (2012). https://doi.org/10.1088/1475-7516/2012/01/008
27. F. Arroja, M. Sasaki, JCAP **1208**, 012 (2012). https://doi.org/10.1088/1475-7516/2012/08/012

28. D.K. Hazra, L. Sriramkumar, J. Martin, JCAP **1305**, 026 (2013). https://doi.org/10.1088/1475-7516/2013/05/026
29. S. Basu, D.J. Brooker, N.C. Tsamis, R.P. Woodard, Phys. Rev. D **100**(6), 063525 (2019). https://doi.org/10.1103/PhysRevD.100.063525
30. Y. Akrami et al., arXiv:1905.05697 (2019)
31. J.M. Maldacena, JHEP **05**, 013 (2003). https://doi.org/10.1088/1126-6708/2003/05/013
32. D. Seery, J.E. Lidsey, JCAP **0506**, 003 (2005). https://doi.org/10.1088/1475-7516/2005/06/003
33. F. Arroja, T. Tanaka, JCAP **1105**, 005 (2011). https://doi.org/10.1088/1475-7516/2011/05/005
34. H.V. Ragavendra, D. Chowdhury, L. Sriramkumar, manuscript in preparation (2020) arXiv:2003.01099 [astro-ph.CO]

Chapter 6
Flavons and Baryogenesis

Mu-Chun Chen

Abstract In this talk, I first discuss a popular scenario of electroweak baryogenesis through varying Yukawa couplings and show that A. Braconi et al. (Phys Rev D100 (1), 015032) [1] the instability of the Higgs potential already is encountered at the TeV scale. I will next present a novel mechanism of baryogenesis through flavon decay M.-C. Chen et al. (Phys Rev D100 (1), 035011) [2]. These notes are based on an invited talk by the author at FHEP 2019 in Hyderabad, India.

6.1 Introduction

The origin of the observed cosmological matter-antimatter asymmetry of the Universe remains an outstanding question in both particle physics and cosmology. Sakharov pointed out [3] that in order for the matter-antimatter asymmetry to be generated dynamically, three conditions are required: (i) Baryon number violation, (ii) C and CP violations, and (iii) departure from thermal equilibrium. There are three possible ways to realize departure from thermal equilibrium that have been utilized in mechanisms for baryogenesis: (i) Out-of-equilibrium decay of heavy particles, (ii) electroweak phase transition, and (iii) dynamics of topological defects.

In this talk, I first discuss a popular scenario of electroweak baryogenesis through varying Yukawa couplings, and show that [1] it leads to an unstable Higgs potential at a very low scale. I will next present a novel mechanism of baryogenesis through flavon decay [2].

M.-C. Chen (✉)
Department of Physics and Astronomy, University of California,
Irvine, CA 92697-4575, USA
e-mail: muchunc@uci.edu

A. Giri and R. Mohanta (eds.), *Workshop on Frontiers in High Energy Physics 2019*, Springer Proceedings in Physics 248,
https://doi.org/10.1007/978-981-15-6292-1_6

6.2 Baryogenesis with Varying Yukawa

In electroweak baryogenesis (EWBG), the out-of-equilibrium condition is achieved if the electroweak phase transition (EWPT) is strongly first order. This in turn requires a light Higgs mass, $m_H \lesssim 72$ GeV in the Standard Model (SM). Clearly this constraint is in conflict with the observed Higgs mass of 125 GeV.

It was originally pointed out in [4, 5] that additional large Yukawa coupling constants in the early Universe can drive the electroweak phase transition to be strongly first order. The Frogatt-Nielsen mechanism is proposed for driving the variation in the Yukawa couplings, making them large before and during the EWPT.

6.2.1 Stability of the Higgs Potential

Large Yukawa couplings will also have a substantial effect on the running of the Higgs quartic coupling, given that the β function for the quartic coupling is sensitive to changes in the Yukawa couplings. In the Standard Model, the Higgs quartic coupling becomes negative around 10^{10} GeV, rendering the Higgs potential unstable. Increasing the number of Yukawa couplings that are of order one drastically lowers the scale at which the quartic coupling becomes negative. This can be seen analytically from the 1-loop β function. If additional quark Yukawa couplings of order one are present, the β function coefficient becomes

$$\beta_\lambda^{(1)} \approx 24\lambda^2 + 12\lambda n y^2 - 6 n y^4 \,, \tag{6.1}$$

where n is the number of order one Yukawa couplings. The addition of these large Yukawa couplings will make the negative term dominant, driving the Higgs quartic coupling negative at a lower scale.

In Fig. 6.1, the number of Yukawa couplings equal to 1.0 were successively increased at the electroweak scale. The top quark Yukawa coupling and all other parameters were kept at their Standard Model values. It is clear that this drastically

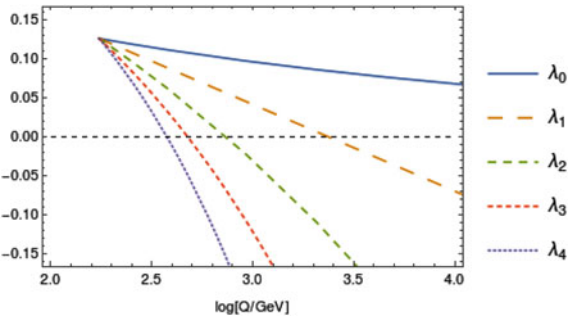

Fig. 6.1 RGE running of the Higgs quartic coupling with additional Yukawa couplings equal to 1.0, and Standard Model boundary conditions imposed at the electroweak scale. The number of additional Yukawa couplings is given by n, with $n = 0$ corresponding to the case of the Standard Model. Figure is taken from [1]

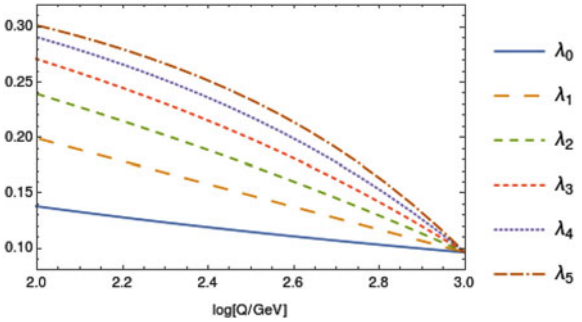

Fig. 6.2 RGE running of the Higgs quartic coupling with additional Yukawa couplings of order one and boundary conditions imposed at the TeV scale. The number of additional Yukawa couplings is given by n, $n = 0$ corresponds to the case of the Standard Model. Figure is taken from [1]

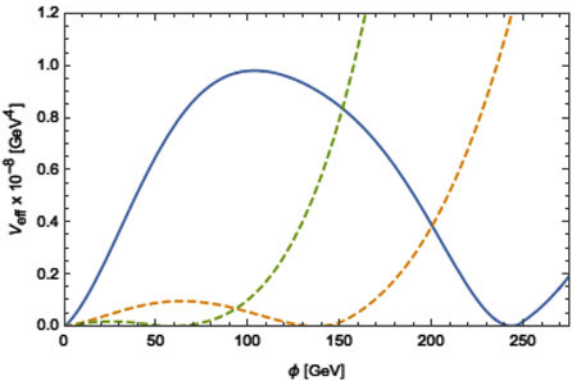

Fig. 6.3 The effective potential with varying Yukawa couplings. Solid blue line: The effective potential with $y_1 = 2.0$, and Standard Model values of the Higgs sector parameters. Dashed lines: The effective potential with RGE-improved values of the Higgs sector parameters. The orange curve uses $y_1 = 1.0$; the green curve uses $y_1 = 2.0$. Figure is taken from [1]

lowers the scale at which the Higgs quartic coupling becomes negative, pushing it very close to the electroweak scale. In Fig. 6.2, Yukawa couplings equal to 1.0 are imposed at 1 TeV. As it can be seen from the figure, this increases the Higgs quartic coupling at the electroweak scale, and in turn has the effect of lowering the Higgs mass.

At the electroweak scale, the parameters of the Higgs potential are $\mu = 89$ and $\lambda = 0.13$. This allows for a first order phase transition with varying Yukawa couplings at 115 GeV, and shown by the solid blue line in Fig. 6.3. However, this does not take into account the effects that additional large Yukawa couplings would have on the running of the RGEs and therefore on the values of the Higgs parameters at that scale. To account for these effects, the RGEs were run downwards from the TeV scale, with a successively increased number of large Yukawa couplings. The potential of the two

most extreme cases are shown, where the top Yukawa coupling retains its Standard Model value but the five additional quark Yukawa couplings are set equal to 1.0 and 2.0, corresponding to the orange and green curves in Fig. 6.3.

The large Yukawa couplings increase the value of the quartic coupling at the electroweak scale, which in turn lowers both the vev and the temperature at which a phase transition occurs. For a transition to be considered strongly first order, it must meet the condition that $\phi_c/T_c \gtrsim 1$. In the case of the additional five quark Yukawa couplings equal to 1.0, the quartic coupling increases to 0.27 which lowers the vev to 137 GeV, leading to a Higgs mass of 95 GeV. In this scenario the critical temperature decreases to 112 GeV, and ϕ_c/T_c decreases to 1.23. In the case of additional Yukawa couplings equal to 2.0, the quartic coupling increases to 0.97, the vev decreases to only 58 GeV, the critical temperature decreases to 52 GeV, with $\phi_c/T_c = 1.12$. The predicted Higgs mass in this case is also lowered, to 80 GeV.

All together, these limitations render this simplest setup with large varying Yukawa couplings not a viable mechanism for baryogenesis.

6.3 Baryogenesis Through Flavon Decay

6.3.1 The Mechanism

Consider the following couplings of the SM charged leptons to a SM singlet scalar, the flavon S, which is charged under the flavor symmetry $\mathrm{U}(1)_{\mathrm{FN}}$,

$$\mathscr{L} \supset y_0^{fg} \left(\frac{v_S + S}{\Lambda}\right)^{n_{fg}} \overline{e}_{\mathrm{R}}^{g} \cdot \phi^* \cdot \ell_{\mathrm{L}}^{f} + \mathrm{h.c.} \tag{6.2}$$

Here, ϕ denotes the electroweak Higgs doublet and v_S is the flavon VEV, while Λ being the cutoff scale of the flavor symmetry, y_0 an $\mathcal{O}(1)$ coupling constant and n_{fg} integers related to the Froggatt–Nielsen charges under $\mathrm{U}(1)_{\mathrm{FN}}$. These couplings lead to the following flavon decays,

$$S \to \overline{\ell}_{\mathrm{L}} + \phi + e_{\mathrm{R}} \,, \qquad S^* \to \ell_{\mathrm{L}} + \phi^* + \overline{e}_{\mathrm{R}}, \tag{6.3}$$

are left-right violating, while preserving total lepton number. Crucially, if there is an initial flavon asymmetry, say an excess of S over S^*, after the flavons decay, there will be more left-handed antileptons than left-handed leptons.

For our scenario scenario to work, the flavon is required to have a large primordial asymmetry when it decays. This means that an asymmetry must be created and that flavon number must be conserved during the flavon oscillations. A concrete example of a setting in which the large asymmetry is generated is the Affleck–Dine mechanism [6].

A reason for concern might be the origin of the U(1) symmetry that ensures flavon number conservation. For instance, in supersymmetric scenarios, the scalar fields are complex. In such models, one starts with more degrees of freedom and the flavon is a complex linear combination of these fields, whose mass term preserves a U(1) symmetry. We will assume that for energy scales far below Λ an approximate $\mathrm{U}(1)_S$ is preserved by the flavon potential, i.e.

$$\mathscr{V}_S = m^2|S|^2 + \begin{pmatrix} S - \text{number violating terms} \\ \text{suppressed by powers of } \Lambda \end{pmatrix}. \tag{6.4}$$

By assumption, the flavon we consider is a weakly coupled scalar field. Hence it can perform coherent oscillations around the $T = 0$ minimum of its potential. In fact, thermal corrections to the potential will push the flavon away from its expectation value at $T = 0$ [7]. The energy density stored in these oscillations, ρ_S, only drops as a^{-3} whereas the energy density of radiation, ρ_{rad}, drops as a^{-4}, where a is the scale factor. It is expected that at a time t_*, corresponding to a temperature T_*, the energy density stored in flavon oscillations starts dominating over the radiation contribution (Fig. 6.4).

The flavon decays to SM leptons with a decay rate

$$\Gamma_S \sim \frac{1}{\varepsilon} \frac{|n_\tau\, y_\tau|^2}{64\pi^3} \frac{m_S^3}{\Lambda^2}. \tag{6.5}$$

While most of the decay products thermalize with the radiation and contribute to the radiation density, the right-handed electrons might not come into chemical equilibrium before the sphalerons have switched off.

The evolution of the relevant energy densities is given by

$$\frac{\mathrm{d}\rho_S}{\mathrm{d}t} + 3H\,\rho_S = -\Gamma_S\,\rho_S, \tag{6.6a}$$

$$\frac{\mathrm{d}\rho_{\mathrm{rad}}}{\mathrm{d}t} + 4H\,\rho_{\mathrm{rad}} = \Gamma_S\,\rho_S, \tag{6.6b}$$

where the Hubble rate is determined by the Friedmann equation

$$H^2 = \frac{8\pi}{3M_{\mathrm{Pl}}^2}(\rho_S + \rho_{\mathrm{rad}}), \tag{6.7}$$

with $M_{\mathrm{Pl}} \simeq 1.2 \times 10^{19}$ GeV being the Planck mass.

Among other leptons, flavon decays into right-handed electrons with a branching fraction of $B_e \sim \left(\frac{n_e\, y_e}{n_\tau\, y_\tau}\right)^2 \sim 7.5 \times 10^{-7}$. Through its decays, the flavon asymmetry will get partially converted into an asymmetry in right-handed electrons. Like in leptogenesis [8], this asymmetry is turned into a baryon asymmetry by sphalerons. Similarly to Dirac leptogenesis [9], our scenario does not require $B-L$ violation. However, our scenario works both for Dirac and Majorana neutrinos.

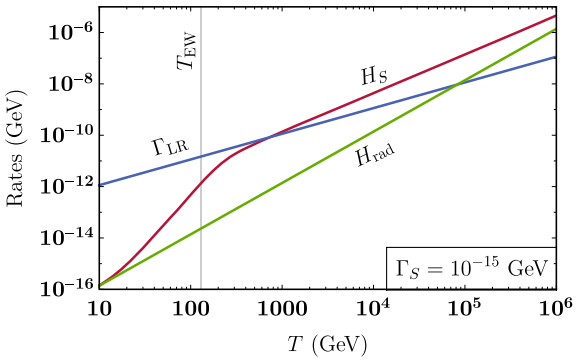

Fig. 6.4 Energy densities stored in flavon oscillations, ρ_S, and in radiation $\rho_{\rm rad}$, with respect to temperature. As a benchmark scenario, it is assumed that ρ_S starts dominating at $T_* = 100$ TeV and the flavon decay rate is $\Gamma_S = 10^{-15}$ GeV, which corresponds to a decay temperature $T_{\rm d} \simeq 10$ GeV. We also show the temperature when the EW sphalerons shut off, $T_{\rm EW} \sim 160$ GeV. Figure is taken from [2]

Right-handed electrons equilibrate with the SM plasma mainly through their interactions with the Higgs boson and $2 \to 2$ scatterings. This equilibration rate is [10]

$$\Gamma_{\rm LR} \simeq 10^{-2}\, y_e^2\, T, \tag{6.8}$$

Comparing this rate to the Hubble rate for a radiation-dominated universe, one finds that the right-handed electrons come into equilibrium at $T \sim 10^5$ GeV. Hence, in standard cosmology, any asymmetry in the right-handed electrons would be washed out long before the EW transition at $T \sim 160$ GeV. However, in a universe that is dominated by a flavon until temperatures around the electroweak scale, right-handed electrons may *not* equilibrate. This is demonstrated in the comparison of the Hubble rate and the left-right equilibration rate as shown in Fig. 6.5.

6.3.2 *Baryon Asymmetry*

In Fig. 6.6 he dimensionless quantity $\eta_{\rm R} = \frac{n_{\rm R}}{s}$ is shown, where s is the entropy density, for a benchmark scenario with

$$m_S = 1 \text{ TeV}\ ,\ \eta_S = 1\ ,\ T_* = 100 \text{ TeV}. \tag{6.9}$$

As the right-handed electron asymmetry is produced through flavon decays, it is proportional to the flavon number density. When the Hubble rate drops below the left-right equilibration rate, the asymmetry is washed out by SM interactions. Smaller Γ_S can delay the equilibration until after sphalerons shut off at $T_{\rm EW} \sim 160$ GeV. However, this also means that a smaller number of flavons decay before $T_{\rm EW}$. Thus

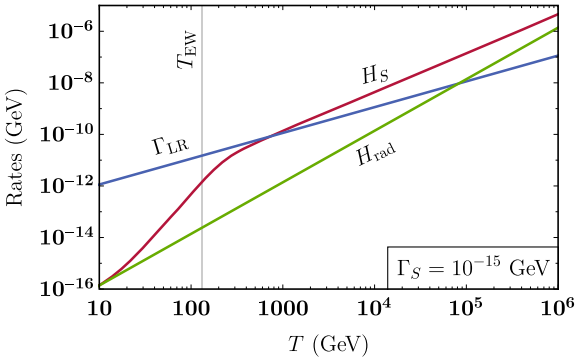

Fig. 6.5 Comparison of the equilibration rate of right-handed electrons, $\Gamma_{\rm LR}$, to the Hubble rates in a radiation dominated universe, $H_{\rm rad}$ and in a universe with intermediate flavon domination, H_S. For this benchmark case the flavon energy density starts dominating at $T_* = 10^7$ TeV and the flavon decays at $T_{\rm d} \simeq 10$ GeV. Figure is taken from [2]

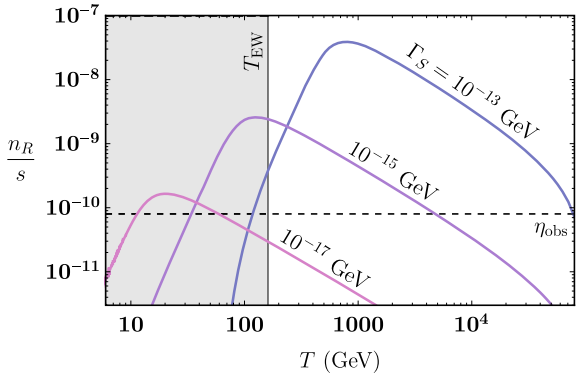

Fig. 6.6 Right-handed electron asymmetry generated through asymmetric flavon decays for different values of the flavon decay rate Γ_S. Observed baryon asymmetry $\eta_{\rm obs} \simeq 8 \times 10^{-11}$ is shown for reference. Figure is taken from [2]

there is generally a balancing between the flavon lifetime and $\Gamma_{\rm LR}$ that describes the region where the right amount of right-handed electron asymmetry is produced before the sphalerons shut off.

While sphalerons violate $B+L$, they conserve $B-L$. Hence a lepton asymmetry will be turned into a baryon asymmetry [8]. In our scenario, the baryon asymmetry is

$$\eta_B \equiv \frac{n_B}{s} \simeq \frac{198}{481} \frac{n_{\rm R}}{s}\Big|_{T_{\rm EW}}. \tag{6.10}$$

We numerically solve Fig. 6.6 to find the electron asymmetry and the entropy of the universe at $T_{\rm EW} \simeq 160$ GeV. The results are shown in Figs. 6.6 and 6.7. As can be seen in Fig. 6.7, there is a large parameter space where asymmetric flavon decays produce the observed BAU.

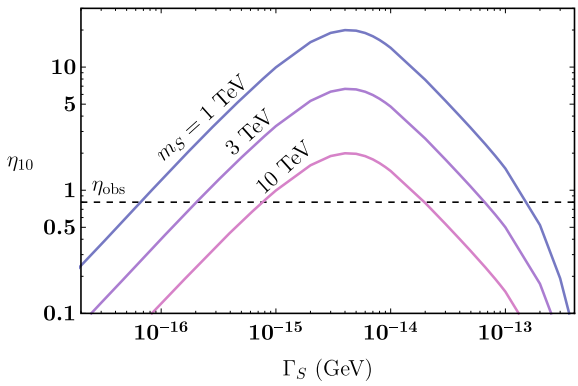

Fig. 6.7 Baryon asymmetry ($\eta_{10} \equiv \eta_B \times 10^{10}$) of the universe as a function of the flavon decay rate Γ_S for different values of the flavon mass m_S. As a benchmark scenario we take the initial flavon asymmetry $\eta_S = 1$. The observed baryon asymmetry $\eta_{\rm obs} \simeq 8 \times 10^{-11}$ is shown for reference. Figure is taken from [2]

Our scenario is rather sensititve to the flavon decay rate. If the flavon decays too early, $T_{\rm d} \gg T_{\rm EW}$, right-handed electrons equilibrate and (essentially) no baryon asymmetry is generated. If the flavon decays too late, $T_{\rm d} \ll T_{\rm EW}$, the right-handed electron asymmetry is produced when sphalerons are inoperative, and again no baryon asymmetry emerges. We find that the observed baryon asymmetry is produced for $10^{-16}\,{\rm GeV} \lesssim \Gamma_S \lesssim 10^{-13}\,{\rm GeV}$.

6.4 Summary

In this talk, I have discussed a popular scenario of electroweak baryogenesis through varying Yukawa couplings. It is demonstrated that [1] the instability of the Higgs potential already is encountered at the TeV scale. Thus the scenario in its simplest form does not work.

I then presented a novel mechanism of baryogenesis through flavon decay [2] in which the observed baryon asymmetry can be produced in flavon decays. This scenario requires the flavon to decay around the time of the electroweak transition and that the flavon carries an $\mathcal{O}(10^{-2} - 1)$ primordial asymmetry. The flavon mass is $\mathcal{O}(1 - 10\,{\rm TeV})$. The role of the flavon is twofold:

1. Its decays produce a left-right asymmetry in the lepton sector, the left-handed part of which is converted to a baryon asymmetry by sphalerons.
2. It dominates the universe before the EW scale, thus increasing the Hubble rate and preventing the right-handed electrons from equilibrating.

Acknowledgements I would like to thank Professors Anjan Giri and Rukmani Mohanta for organizing such a productive FHEP 2019. I would also like to thank Arianna Braconi, Jeffrey Gaswint, Seyda Ipek, and Michael Ratz, for their collaborations on the work presented in these notes. The work of M.–C.C. is supported, in part, by National Science Foundation under Grant No. PHY-1719438.

References

1. A. Braconi, M.-C. Chen, G. Gaswint, G. Gaswint, Phys. Rev. **D100** (1), (2019), 015032, arXiv:1810.02522 [hep-ph]
2. M.-C. Chen, S. Ipek, M. Ratz, Phys. Rev. **D100** (3), (2019), 035011, arXiv:1903.06211 [hep-ph]
3. A. D. Sakharov, Pisma Zh. Eksp. Teor. Fiz. **5** (1967), 32, [Usp. Fiz. Nauk161,no.5,61(1991)]
4. M. Berkooz, Y. Nir, T. Volansky, Phys. Rev. Lett. **93** (2004), 051301, arXiv:hep-ph/0401012 [hep-ph]
5. I. Baldes, T. Konstandin, G. Servant, JHEP **12** (2016), 073, arXiv:1608.03254 [hep-ph]
6. I. Affleck, M. Dine, Nucl. Phys. B **249**, 361 (1985)
7. B. Lillard, M. Ratz, M. P. Tait, Tim, S. Trojanowski, JCAP **1807** (7), (2018), 056, arXiv:1804.03662 [hep-ph]
8. M. Fukugita, T. Yanagida, Phys. Lett. B **174**, 45 (1986)
9. K. Dick, M. Lindner, M. Ratz, D. Wright, Phys. Rev. Lett. **84** (2000), 4039, arXiv:hep-ph/9907562 [hep-ph]
10. D. Bödeker, D. Schröder, arXiv:1902.07220 [hep-ph]

Chapter 7
Spontaneous Baryogenesis in Quintessential Inflation

Nur Jaman

Abstract We study the possibility of generating baryon asymmetry with an effective field theory with quintessential inflation. The same scalar field, inflaton, breaks some $U(1)$ global baryonic symmetry and gives rise to baryon asymmetry in thermal equilibrium, evading one of Sakharov conditions, *à la* Spontaneous baryogenesis. Here we explore this scenario in a model-independent way, where no specific potential for inflation is chosen and various aspects of baryon asymmetry are discussed.

7.1 Introduction

In quintessential inflation [1–3], the same scalar field is accounted for the early accelerated expansion with its slow-roll, dubbed, *inflation* and survives in the post inflationary era. The scalar field energy during its evolution should not disturb the structure formation, hence a specific steepness of the potential is required (see [4] and references there). In general, a runaway type of potential is suitable for this and demanding an alternative reheating mechanism(instant preheating for example). The scalar field energy density remains sub-dominant until recently taking over the background density and gives accelerated expansion, acting as source as dark energy. In models where the scalar field tracks the background density in the radiation and matter era, *scaling solution* [5], late time dynamics is independent of the initial condition, however since the scaling solution is non-accelerating a septate exit mechanism may be required for those kinds of models.

In this article, we discuss the possibility of the same scalar field to generate baryonic asymmetry in the Universe. The success of a model for cosmology needs a requirement that around the temperature of MeV, there should be baryon to anti-baryon asymmetry [6], $4 \times 10^{-10} \leq \eta \equiv \frac{n_b - n_{\bar{b}}}{s} \leq 7 \times 10^{-10}$, with the entropy density, s, $n_{b(\bar{b})}$ is the baryon(anti-baryon) density. The particle physics requirement tells us that to generate the asymmetry three conditions by Sakharov needed to be

N. Jaman (✉)
Centre for Theoretical Physics, Jamia Millia Islamia 110025, New Delhi, India
e-mail: nurjaman@ctp-jamia.res.in

A. Giri and R. Mohanta (eds.), *Workshop on Frontiers in High Energy Physics 2019*, Springer Proceedings in Physics 248,
https://doi.org/10.1007/978-981-15-6292-1_7

satisfied, (i) baryon non-conservation (ii) C violation and CP violation and (iii) out of the equilibrium process. The standard model of particle physics is unable to give a successful theory of baryon asymmetry, although all three requirements can be satisfied. In this article, we explore the possibility of generating baryon asymmetry by violating the third condition. The scalar field couples to a non-conserved baryonic current of the type $\partial_\mu j_B^\mu$ which is generated by the breaking some "$U(1)$ global symmetry" hence giving an effective theory framework. The interaction is CPT violating and the asymmetry can be generated even in thermal equilibrium after the inflation, namely spontaneous baryogenesis [7].

7.2 Perquisite Inputs and Inflationary Dynamics

Consider the action for scalar field

$$S = \int d^4x\sqrt{-g}\left[\frac{M_{Pl}^2}{2}R - \frac{1}{2}g^{\mu\nu}\partial_\mu\phi\partial_\nu\phi - V(\phi)\right], \tag{7.1}$$

The energy scale associated inflation can be found from the amplitude of scalar density perturbation when the cosmological scale exit the horizon

$$A_s^2 = \frac{V_{\text{inf}}}{150\pi^2 M_{Pl}^4\epsilon}, \tag{7.2}$$

where $\epsilon = \frac{M_{Pl}^2}{2}\left(\frac{V'}{V}\right)^2$, the slow-roll parameter. COBE normalization gives $A_s^2 = 4\times10^{-10}$ [8] from which one determines inflationary energy scale

$$V_{\text{inf}}^{1/4} = 0.014\times r^{1/4}M_{Pl}, \tag{7.3}$$

where r is the ratio of tensor to scalar perturbation. The Hubble parameter during inflation is given by

$$H_{\text{inf}} = \frac{V_{\text{inf}}^{1/2}}{\sqrt{3}M_{\text{Pl}}} = 2.7\times10^{14}r^{1/2}\,\text{GeV}. \tag{7.4}$$

The inflation ends when the acceleration stop or w_ϕ takes value $-\frac{1}{3}$, which implies

$$\dot{\phi}_{\text{end}} = V_{\text{end}}^{1/2}. \tag{7.5}$$

The Hubble parameter at the inflation end becomes

$$H_{\rm end} = \frac{V_{\rm end}^{1/2}}{\sqrt{2}M_{Pl}}. \tag{7.6}$$

The small values for the parameters r and ϵ suggest that we can take the approximation $H_{end} \approx H_{inf}$. In quintessential inflation scenario, the inflaton field runs into the kinetic regime where the energy density is given by kinetic energy of the field after the inflation end and it evolves as

$$\rho_\phi = \rho_{\phi,\rm end}\left(\frac{a_{\rm end}}{a}\right)^6. \tag{7.7}$$

where $\rho_{\phi,\rm end} = \frac{3}{2}V_{\rm end}$. If one consider that after inflation the universe is reheated by a mechanism of instant preheating [9, 10], the radiation energy density produced is given by

$$\rho_{\rm r} \approx \frac{g^2 V_{\rm end}}{8\pi^3}\left(\frac{a_{\rm end}}{a}\right)^4, \tag{7.8}$$

where, g is coupling constant. The universe continues to be kinetic regime till the dominant component become radiation at scale factor value $a(r)$ such that $\rho_\phi(a_{\rm r}) = \rho_{\rm r}(a_{\rm r})$ which gives

$$\frac{a_{\rm r}}{a_{\rm end}} = \frac{\sqrt{12\pi^3}}{g}. \tag{7.9}$$

The radiation particle density produced by instant preheating [3]

$$n = \frac{g^{3/2}V_{\rm end}^{3/4}}{8\pi^3}\left(\frac{a_{\rm end}}{a}\right)^3. \tag{7.10}$$

The radiation or relativistic degrees of freedom eventually will build up a thermal equilibrium in the Universe when the interaction rate will be grater the expansion rate, $\Gamma > H$. Where $\Gamma \sim n\sigma$, with σ is annihilation cross-section for the relativistic particles.

$$\sigma \sim \frac{\alpha^2}{T_{\rm end}^2}\left(\frac{a}{a_{\rm end}}\right)^2, \tag{7.11}$$

where T_{end} is the temperature at inflation end(assuming instant preheating). Under the assumption that when the thermal equilibrium is reached at $\Gamma \sim H$, the universe is in kinetic regime, we find the scale factor as

$$\frac{a_{\rm th}}{a_{\rm end}} \sim \frac{2^{9/8}\pi^{3/2}T_{\rm end}}{\alpha\, g^{3/4}M_{Pl}^{3/4}H_{\rm end}^{1/4}}. \tag{7.12}$$

Now radiation energy density for relativistic species are given by

$$\rho_{\rm r} = \frac{\pi^2}{30} g_* T^4. \tag{7.13}$$

Using (7.8) and (7.13) we find

$$T_{\rm end} \sim \frac{(15/2)^{1/4} g^{1/2} M_{Pl}^{1/2} H_{\rm end}^{1/2}}{\pi^{5/4} g_*^{1/4}}. \tag{7.14}$$

And using $H_{end} \approx H_{inf}$ we find

$$T_{\rm end} \simeq 1.3 \times 10^{-3} g^{1/2} r^{1/4} M_{Pl}. \tag{7.15}$$

Using (7.9), The temperature at the beginning of radiation era

$$T_r = T_{\rm end} \frac{a_{\rm end}}{a_r} \sim \left(\frac{15}{288\pi^{11} g_*} \right)^{1/4} g^{3/2} M_{\rm Pl}^{1/2} H_{\rm end}^{1/2}. \tag{7.16}$$

Since at high temperature(>100 GeV) g_* does not change and temperature varies as $T \propto a^{-1}$, using this fact and (7.12), we obtain the thermal equilibrium temperature,

$$T_{\rm th} \sim \frac{\alpha\, g^{3/4} M_{Pl}^{3/4} H_{\rm end}^{1/4}}{2^{9/8} \pi^{3/2}}. \tag{7.17}$$

Now the coupling constant, g of instant preheating is constraint by relic gravity wave [11] and have a value $g \geq 1.05 \times 10^{-3} \sqrt{r}$. Using the lower bound of g, $r = 0.05$, $H_{\rm end} \approx H_{\rm inf}$ and $\alpha = 0.1$, we found $T_{\rm end} \approx 2.3 \times 10^{13}$ GeV, $T_{\rm th} \approx 2.7 \times 10^{12}$ GeV and $T_r \approx 10^8$ GeV.

7.3 Baryogensis

For quintessential inflation, the scalar field ϕ survives after inflation and enter into the kinetic regime. In order to give baryon asymmetry, ϕ must couple to some other fields, let after breaking of some $U(1)$ global symmetry this happens to be a non-conserved baryon current [12] with a cut-off. The effective Lagrangian took the form

$$\mathcal{L}_{\rm eff} = \frac{\lambda'}{M} \partial_\mu \phi J^\mu, \tag{7.18}$$

with λ' is the coupling for the interaction, J^μ is the non-conserved baryonic current and M is the cut-off energy scale of the effective theory. In homogeneous the FRW background, we have

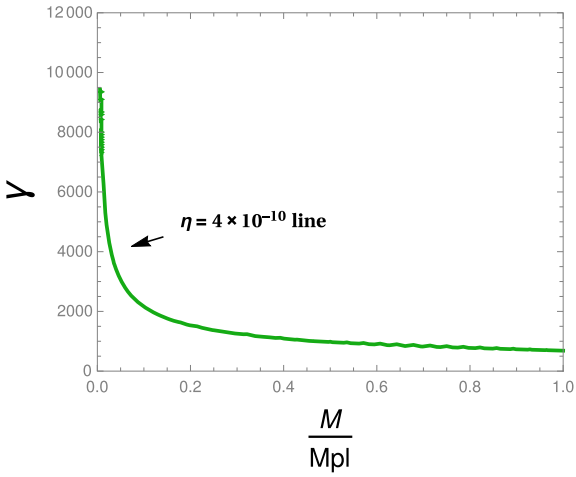

Fig. 7.1 allowed value of the cut-off scale with γ under the observational value of η_F [12]

$$\mathcal{L}_{\text{eff}} = \frac{\lambda'}{M}\dot{\phi}\Delta n \equiv \mu(t)\Delta n, \tag{7.19}$$

where $j^0 = \Delta n$, the baryon number density with $\mu(t) \equiv \lambda'\dot{\phi}/M$, the effective chemical potential. The interaction term is CPT violating. In thermal equilibrium we have the number density (Fig. 7.1)

$$\Delta n(t;\xi) = \bar{g}\int \frac{d^3\mathbf{p}}{(2\pi)^3}[f(E,\mu) - f(E,-\mu)], \tag{7.20}$$

with $\xi = \mu/T$ and $\bar{g}$ being baryonic degrees of freedom. In the limit $\xi < 1$, we have

$$\Delta n(T;\xi) \simeq \frac{\bar{g}T^3}{6}\xi + \mathcal{O}(\xi^2) \simeq \frac{\lambda'\bar{g}}{6M}T^2\dot{\phi}, \tag{7.21}$$

The freeze-out value for the baryon asymmetry is computed as the ratio of to entropy density, s at the freeze-out temperature

$$s = \frac{2\pi^2}{45}g_* T^3 \tag{7.22}$$

$$\eta_F \equiv \frac{\Delta n}{s}\bigg|_{T=T_F} \simeq 0.38\lambda'\left(\frac{\bar{g}}{g_*}\right)\frac{\dot{\phi}(T_F)}{MT_F}, \tag{7.23}$$

where g_* is the degrees of freedom at freeze-out temperature T_F. The baryogenesis is effective for $T_F < T < T_{th}$. Here two things are crucial to determine the freeze-out asymmetry value, $\dot{\phi}(T_F)$ which ask for particular inflation potential and T_F which require the specification of the baryon number violating interaction. However, we know that the scalar field continues to be in the kinetic regime at least up to the

radiation era. It is reasonable to assume that freeze out of the process takes place before the radiation era begins. In this case

$$\dot{\phi} \simeq \sqrt{V_{\rm end}} \left(\frac{a_{\rm end}}{a}\right)^3. \tag{7.24}$$

Under this consideration one can easily show, using (7.6), (7.23) and (7.24), $\bar{g} \approx 1$ and $g_* \approx 100$

$$\eta_F \approx 5.4 \times 10^{-3} \frac{\lambda' H_{\rm end} M_{Pl}}{M T_F} \left(\frac{a_{\rm end}}{a_F}\right)^3. \tag{7.25}$$

Let us define a quantity $\gamma \equiv \frac{a_F}{a_{\rm th}} = \frac{T_{\rm th}}{T_F}$, using this we obtain

$$\eta_F \approx 5.4 \times 10^{-3} \frac{\lambda' H_{\rm end} M_{Pl}}{M \gamma^2 T_{\rm th}} \left(\frac{a_{\rm end}}{a_{\rm th}}\right)^3. \tag{7.26}$$

Finally using (7.12), (7.14) and (7.17) we get

$$\eta_F = 1.86 \times 10^{-2} \lambda' \frac{\alpha^2 M_{Pl}}{M \gamma^2}. \tag{7.27}$$

We can always use $T_{\rm th} \lesssim T_F \lesssim T_{\rm r}$, without specifying the underlying actual process that gives $1400 < \gamma < 10^4$, putting a bound on the cut-off scale $10^{-2} M_{Pl} \lesssim M \lesssim M_{Pl}$ for $\alpha = 0.1$ and $\lambda' = 1$.

7.4 Summary and Outlook

The CPT violation discussed here is dynamical and much suppressed the cut-off scale compared to other similar type other interaction hence not detectable at TeV scale [11]. Also the generated asymmetry survives the sphaleron process upto electroweak sacle by considering an initial $B - L$ [11]. The prospects of relic gravitational wave with the kinetic regime seems hard to be under detectable range [11] for the type of model we discussed. The scalar field after giving the successful inflation and baryogenesis said have oscillation [13] before it emerges again in late time. This feature can be used to solve for H_0 tension problem [14] which may be an interesting investigation.

Acknowledgements The author is thankful to Safia Ahmad, Antonio De Felice, Sachiko Kuroyanagi and M. Sami for collaborating in this topic. He is also thankful to organizer of *International Workshop on frontiers in high energy physics, FHEP 2019* and University of Hyderabad where the work was orally presented.

References

1. A.D. Linde, Phys. Lett. **129B**, 177 (1983)
2. P. J. E. Peebles, A. Vilenkin, Phys. Rev. D **59**, no. 6, 063505 (1999) [astro-ph/9810509]
3. M.W. Hossain, R. Myrzakulov, M. Sami, E.N. Saridakis, Int. J. Mod. Phys. D **24**(05), 1530014 (2015)
4. M.A. Skugoreva, M. Sami, N. Jaman, Phys. Rev. D **100**(4), 043512 (2019)
5. E.J. Copeland, A.R. Liddle, D. Wands, Phys. Rev. D **57**, 4686 (1998)
6. A. De Felice, S. Nasri, M. Trodden, Phys. Rev. D **67**, 043509 (2003)
7. A.G. Cohen, D.B. Kaplan, Phys. Lett. B **199**, 251 (1987)
8. E.F. Bunn, A.R. Liddle, M.J. White, Phys. Rev. D **54**(10), R5917 (1996)
9. M. Sami, V. Sahni, Phys. Rev. D **70**(8), 083513 (2004)
10. M. Sami, N. Dadhich, TSPU Bulletin **44N7**, 25 (2004)
11. S. Ahmad, A. De Felice, N. Jaman, S. Kuroyanagi, M. Sami, Phys. Rev. D **100**(10), 103525 (2019)
12. A. D. Dolgov,[hep-ph/9707419]
13. A. De Simone, T. Kobayashi, JCAP **1608**(08), 052 (2016)
14. V. Poulin, T.L. Smith, T. Karwal, M. Kamionkowski, Phys. Rev. Lett. **122**(22), 221301 (2019)

Chapter 8
Primordial Black Holes from Warm Inflation

Richa Arya

Abstract Primordial Black Holes (PBHs) serve as a unique probe to the physics of the early Universe phenomenon, cosmic inflation. In light of this, we study the formation of PBHs by the collapse of overdense perturbations generated during a model of warm inflation. Warm inflation is a description in which the inflaton dissipates into the radiation fields both during and after the inflationary phase. In our study, we discuss the role of the inflaton dissipation to the enhancement in the primordial power spectrum at the PBH scales. Our analysis shows that for some range of model parameters, we can produce an interesting abundance of tiny mass PBHs ($\sim 10^3$ g) for our warm inflation model. Further, we also discuss the constraints on the initial mass fraction of the generated PBHs and the possibility of Planck mass PBH relics to constitute the dark matter.

8.1 Introduction

Primordial Black Holes (PBHs) are the black holes that could have produced in the very early Universe [1, 2]. They are interesting to study as they serve as probes to the physics of the early Universe. PBHs provide constraints on the amplitude of the primordial power spectrum and the inflationary models [3–5]. Also, they are the candidates for the dark matter. While the CMB or LSS observations probe the fluctuation k modes ranging from $10^{-4} - 1$ Mpc^{-1}, PBHs provide a probe to a huge range of modes from $10^{-2} - 10^{23}$ Mpc^{-1}. For a review on PBHs, see [6, 7].

In our work, we study an inflationary scenario known as Warm Inflation and discuss the primordial black hole generation by the collapse of large inhomogeneities generated during it [8]. Warm Inflation [9, 10] is a description of inflation in which the inflaton is coupled sufficiently enough to the other fields during the inflationary phase, such that it dissipates its energy into them even during inflation. As a result,

R. Arya (✉)
Physical Research Laboratory, Ahmedabad 380009, India

Indian Institute of Technology Gandhinagar, Palaj, Gandhinagar 382355, India
e-mail: richaarya@prl.res.in

A. Giri and R. Mohanta (eds.), *Workshop on Frontiers in High Energy Physics 2019*, Springer Proceedings in Physics 248,
https://doi.org/10.1007/978-981-15-6292-1_8

the Universe constitutes a thermal bath of particles and has a temperature throughout the inflation. Also, in warm inflation, the primordial power spectrum is sourced by the thermal fluctuations. We study the features in the primordial power spectrum for our warm inflation model at the small scales (PBH modes). In our analysis, we find that the primordial curvature power spectrum is red-tilted (spectral index, $n_s < 1$) for the CMB and LSS modes, whereas it is blue-tilted ($n_s > 1$) for the PBH modes. Also, for some parameter space, the amplitude of the power spectrum at small scales is many orders of magnitude higher than the amplitude for the CMB scales ($P_{\mathcal{R}}(k_P) = 2.1 \times 10^{-9}$ at the pivot scale $k_P = 0.05\ \mathrm{Mpc}^{-1}$), sufficient for the PBH generation.

8.2 Formation of Primordial Black Holes

PBHs can be generated through many mechanisms. Here we consider the PBH formation by the collapse of overdense perturbations generated during a model of warm inflation. These fluctuations leave the horizon during inflation and then re-enter at later epochs (we assume radiation dominated era), and collapse to form PBHs.

8.2.1 Mass of the Generated PBHs

The mass of the generated PBH, M_{PBH}, depends on the time of its formation and is nearly a fixed fraction of the horizon mass at that epoch [3]. Therefore, when any kth mode re-enters the horizon (i.e. comoving wavenumber $k = aH$) with an overdensity δ greater than a critical density δ_c, it collapses to form PBH with mass

$$M_{\mathrm{PBH}}(k) = \gamma \frac{4\pi}{3} \rho H^{-3}|_{k=aH}. \tag{8.1}$$

Here H is the Hubble expansion rate and ρ is the energy density of the Universe at the epoch of PBH formation, γ is the fraction of the horizon mass in the PBH. We express the r.h.s. of (8.1) explicitly as a function of k and obtain

$$M_{\mathrm{PBH}}(k) \approx\ 5 \times 10^{15} \mathrm{g} \left(\frac{g_{*0}}{g_{*i}}\right)^{1/6} \left(\frac{10^{15}\mathrm{Mpc}^{-1}}{k}\right)^2. \tag{8.2}$$

Here g_{*0}, and g_{*i} are the relativistic degrees of freedom today and at the time of formation of PBH, respectively. This relation shows that the heavy mass PBHs form later in time (as small k modes leave the horizon early and re-enter late) than the lighter PBHs.

8.2.2 Initial Mass Fraction of PBHs

The initial mass fraction of a PBH with mass $M_{\rm PBH}$ is defined as the ratio of the energy density in PBH to the total energy density of the Universe at the time of PBH formation.

$$\beta(M_{\rm PBH}) \equiv \frac{\rho^i_{\rm PBH}}{\rho^i_{\rm total}} = \frac{\Omega_{\rm PBH0}(M_{\rm PBH})}{\Omega_{r0}^{3/4}} \left(\frac{g_{*i}}{g_{*0}}\right)^{1/4} \left(\frac{M_{\rm PBH}}{M_0}\right)^{1/2} \gamma^{-1/2}\,, \tag{8.3}$$

where $\Omega_{\rm PBH0}(M_{\rm PBH}) = \frac{\rho_{\rm PBH0}}{\rho_{\rm crit}}$ is the present density parameter for PBH of mass $M_{\rm PBH}$, and $\Omega_{r0} = \frac{\rho_{r0}}{\rho_{\rm crit}} \approx 5.38 \times 10^{-5}$ is the present density parameter for radiation, with the critical energy density $\rho_{\rm crit} = 1.054 \times 10^{-5} h^2$ GeV cm^{-3} and $h = 0.7$, $M_0 = \frac{4\pi}{3}\rho_{cr} H_0^{-3} \approx 4.62 \times 10^{22} M_\odot$ is the mass corresponding to the present horizon size. From (8.3), we can obtain the upper bound on initial mass fraction for different masses of PBHs by putting the bounds on $\Omega_{\rm PBH0}$ from various observations.

8.2.3 Press-Schechter Theory for PBH Formation

Theoretically, we can estimate the initial mass fraction of PBHs using Press-Schechter formalism for the formation of collapse objects. We assume that the initial seeds of density perturbations are gaussian and are smoothened by a gaussian window function over a radius $R = (aH)^{-1}$.

The mass variance is then given as

$$\sigma^2(R) = \int_0^\infty \tilde{W}^2(kR) P_\delta(k) \frac{dk}{k} \tag{8.4}$$

where $P_\delta(k)$ is the matter power spectrum, and $\tilde{W}(kR)$ is the Fourier transform of the window function $\tilde{W}(kR) = \exp(-k^2R^2/2)$. The primordial curvature power spectrum $P_{\mathcal{R}}(k)$ can be related to the density power spectrum $P_\delta(k)$ as [11]

$$P_\delta(k) = \frac{4(1+w)^2}{(5+3w)^2} \left(\frac{k}{aH}\right)^4 P_{\mathcal{R}}(k), \tag{8.5}$$

where w is the equation of state and is equal to 1/3 for a radiation dominated era. For any parameterization of the primordial power spectrum, we substitute (8.5) into (8.4) and integrate it.

In Press-Schechter theory, the initial mass fraction of a PBH with mass $M_{\rm PBH}$ is given as [12]

$$\beta(M_{\rm PBH}) = \frac{2}{\sqrt{2\pi}\sigma(R)} \int_{\delta_c}^1 \exp\left(\frac{-\delta^2(R)}{2\sigma^2(R)}\right) d\delta(R) = \text{erfc}\left(\frac{\delta_c}{\sqrt{2}\sigma(R)}\right) \tag{8.6}$$

where erfc is the complimentary error function, and we take $\delta_c = 0.5$. We substitute the expression for $\sigma(R)$ calculated from (8.4) in this equation, and then using the observational bounds on $\beta(M_{\rm PBH})$, we obtain the upper limit on the amplitude of primordial power spectrum to form PBHs. For various mass of PBHs, the upper bound is obtained to be $P_{\mathcal{R}}(k_{\rm PBH}) < \mathcal{O}(10^{-2} - 10^{-1})$.

8.3 Primordial Power Spectrum for Warm Inflation

Now we discuss the form of the primordial power spectrum we study in the context of warm inflation. The basic idea of warm inflation is that the inflaton is sufficiently coupled to the other fields during inflation and dissipates its energy into them. Therefore, the equation of motion of the inflaton field ϕ during inflation is modified as

$$\ddot{\phi} + (3H + \Upsilon)\dot{\phi} + V'(\phi) = 0, \tag{8.7}$$

where $\Upsilon\dot{\phi}$ is the dissipative term due to inflaton dissipation into other fields. In our notation, overdot and $'$ represent the derivative w.r.t time and ϕ, respectively. Here we consider the inflaton potential $V(\phi) = \lambda\phi^4$. The dissipation coefficient $\Upsilon(\phi, T)$ can have various forms [13, 14]. In this study, we consider it to be cubicly dependent on the temperature of the thermal bath, $\Upsilon \propto T^3$. We define a dissipation parameter $Q \equiv \Upsilon/3H$ and rewrite (8.7) as

$$\ddot{\phi} + 3H(1 + Q)\dot{\phi} + V'(\phi) = 0. \tag{8.8}$$

$Q \gg 1$ is termed as the strong dissipative regime of warm inflation and $Q \ll 1$ as the weak dissipative regime of warm inflation.

In warm inflation, the primordial power spectrum is sourced by the thermal fluctuations and is given as [15, 16]

$$P_{\mathcal{R}}(k) = \left(\frac{H_k^2}{2\pi\dot{\phi}_k}\right)^2 \left[1 + 2n_k + \left(\frac{T_k}{H_k}\right)\frac{2\sqrt{3}\pi Q_k}{\sqrt{3 + 4\pi Q_k}}\right] G(Q_k), \tag{8.9}$$

where the subscript k refers to the epoch when the kth mode of cosmological perturbations leaves the horizon during inflation. Here n_k is the Bose-Einstein distribution of the inflaton particles. The growth factor $G(Q_k)$ arises because of the inhomogeneous perturbations in the radiation contributing to the inflaton perturbations and depends on the form of dissipation coefficient [17].

$$\text{For } \Upsilon \propto T^3 \qquad G(Q_k)_{\rm cubic} = 1 + 4.981\, Q_k^{1.946} + 0.127\, Q_k^{4.330}.$$

If $Q_k \ll 1$, the growth factor is almost 1. But for $Q_k \gg 1$, $G(Q_k)$ contributes significantly to the power spectrum.

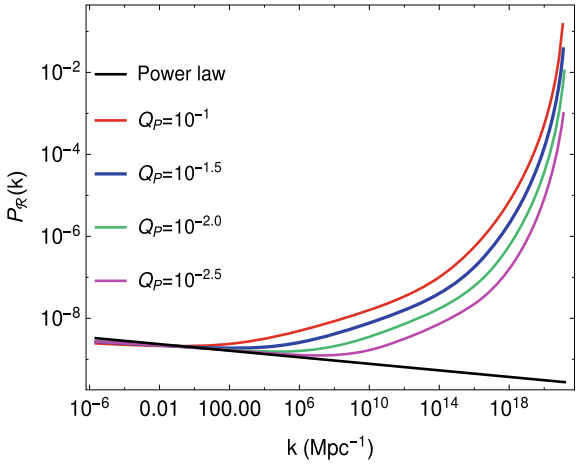

Fig. 8.1 Plot of the primordial power spectrum $P_{\mathcal{R}}(k)$ versus k for our warm inflation model with different values of Q_P [8]. Here Black line represents the standard power law parameterization considered in cold inflation

Now we plot the primordial power spectrum for our warm inflation model. We parameterize the power spectrum in terms of the dissipation parameter at the pivot scale, Q_P, and inflaton self coupling λ (For details, see our paper [18]). For each Q_P value, we choose λ such that the power spectrum is normalised at the pivot scale i.e. $P_{\mathcal{R}}(k_P) = 2.1 \times 10^{-9}$.

We consider various cases of inflation with different valued $Q_P = 10^{-1}, 10^{-1.5}$, 10^{-2}, and $10^{-2.5}$ (weak dissipation regime when the CMB scales exit the horizon) to plot Fig. 8.1. We find that the primordial curvature power spectrum for this warm inflationary model has a blue-tilt ($n_s > 1$) for the PBH scales (large k). As can be seen, for some Q_P values, a large amplitude of $P_{\mathcal{R}}(k)$ is achieved near the end of inflation at $k \sim 10^{21}$ Mpc^{-1}. For large dissipation, the amplitude of the primordial power spectrum is larger as compared to the smaller dissipation case.

8.4 Results and Discussion

Now we discuss the PBHs formed from our warm inflation model, $V(\phi) = \lambda\phi^4$ with dissipation coefficient $\Upsilon \propto T^3$.

8.4.1 Initial Mass Fraction and Mass of the PBHs Formed

We calculate and plot the inital mass fraction $\beta(M)$ of the generated PBH versus the mass of the PBH in Fig. 8.2 for the cases when $Q_P = 10^{-1.7}, 10^{-1.8}, 10^{-1.9}$, and 10^{-2}. We can see that the mass of PBHs generated from our warm inflation model

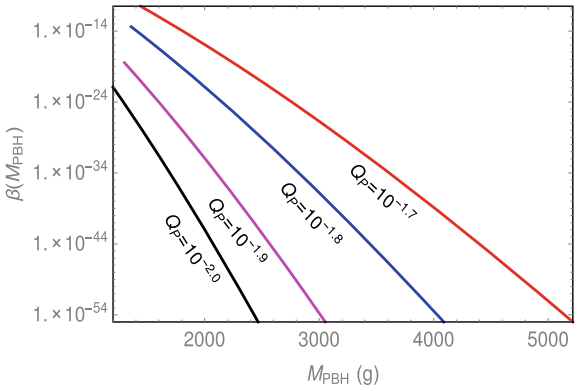

Fig. 8.2 Plot of the initial mass fraction of the generated PBH versus its mass [8]

is of the order $M_{\rm PBH} \sim 10^3$ g. Also, large dissipation leads to more massive PBH formation, whereas small dissipation produces small mass PBHs.

8.4.2 Constraints on the Abundance of PBHs Formed

The order of mass of the PBH formed from our warm inflation model, $M_{\rm PBH} \sim 10^3$ g. Such a tiny mass of PBH would have evaporated by now (lifetime $\sim 10^{-19}$ sec). We find that for the cases with $Q_P = 10^{-1.8}, 10^{-9}, 10^{-2}$, the obtained initial mass fraction is in accordance with the upper limit ($\beta(M_{\rm PBH}) < 10^{-14}$) obtained from the abundance of stable and long lived decaying particles produced by evaporating PBHs. The case with $Q_P = 10^{-1.7}$ overproduces PBHs, which is inconsistent with the upper bounds on β, and hence should be ruled out.

8.4.3 PBH Relics as Constituent of Dark Matter

It is also argued that PBH evaporation ceases when PBH mass gets close to the Planck mass, and such Planck mass relics can thus constitute the present dark matter. The present density of the Planck mass relics should be less than the cold dark matter density, so that it does not overclose the Universe today. For our warm inflation models with $Q_P = 10^{-1.9}$, and $Q_P = 10^{-2}$, we find that the calculated initial mass fraction lies within the limit ($\beta(10^3 g) < 10^{-16}$), and hence the possibility to form DM remains valid. However, Planck mass relics are extremely tiny and almost impossible to detect by non-gravitational measures.

8.5 Summary

PBHs are a remarkable probe to the physics of early Universe, particularly inflation. We discussed the PBH generation from a model of warm inflation. The primordial power spectrum has a blue-tilt at the small scales, with a large amplitude required for PBH generation. For various cases of dissipation, PBHs of mass $\mathcal{O}(10^3$ g) are formed. The initial mass fraction of PBHs is observationally constrained, and for one case of our model, the PBHs are overproduced, hence should be ruled out. There is also a possibility that the Planck mass remnants of the evaporating PBHs constitute the dark matter.

References

1. B.J. Carr, S.W. Hawking, Mon. Not. Roy. Astron. Soc. **168**, 399 (1974)
2. B.J. Carr, Astrophys. J. **201**, 1 (1975)
3. A.M. Green, A.R. Liddle, Phys. Rev. D **56**, 6166 (1997)
4. A.S. Josan, A.M. Green, K.A. Malik, Phys. Rev. D **79**, 103520 (2009)
5. A.M. Green, Fundam. Theor. Phys. **178**, 129 (2015)
6. M.Y. Khlopov, Res. Astron. Astrophys. **10**, 495 (2010)
7. M. Sasaki, T. Suyama, T. Tanaka, S. Yokoyama, Class. Quant. Grav. **35**(6), 063001 (2018)
8. R. Arya, arXiv:1910.05238 [astro-ph.CO]
9. A. Berera, L.Z. Fang, Phys. Rev. Lett. **74**, 1912 (1995)
10. A. Berera, Phys. Rev. Lett. **75**, 3218 (1995)
11. A.R. Liddle, D.H. Lyth, Phys. Rept. **231**, 1 (1993)
12. W.H. Press, P. Schechter, Astrophys. J. **187**, 425 (1974)
13. I. G. Moss and C. Xiong, hep-ph/0603266
14. M. Bastero-Gil, A. Berera, R.O. Ramos, JCAP **1109**, 033 (2011)
15. R.O. Ramos, L.A. da Silva, JCAP **1303**, 032 (2013)
16. S. Bartrum, M. Bastero-Gil, A. Berera, R. Cerezo, R.O. Ramos, J.G. Rosa, Phys. Lett. B **732**, 116 (2014)
17. M. Benetti, R.O. Ramos, Phys. Rev. D **95**(2), 023517 (2017)
18. R. Arya, A. Dasgupta, G. Goswami, J. Prasad, R. Rangarajan, JCAP **1802**, 043 (2018)

Chapter 9
Criticality of Charged AdS Black Hole with a Global Monopole

A. Naveena Kumar, C. L. Ahmed Rizwan, and K. M. Ajith

Abstract We discuss the phase transition of charged AdS black hole surrounded by a global monopole. The cosmological constant is taken as fluid pressure and the corresponding conjugate variable as volume. In this extended phase space, the criticality is investigated from P-V isotherms, Gibbs free energy behavior and coexistence curves. The critical behavior of the Black Hole is analogous to classical van der Waals gas. This is further verified by looking at the critical exponents. The magnetic monopole parameter affects the phase structure of the black hole significantly.

9.1 Introduction

Ever since the pioneering work of Hawking and Bekenstein, black hole thermodynamics remains as an interesting area of research in high energy physics. Black hole being a macroscopic quantum system and a thermal system, this domain is an important way to explore the features of quantum gravity. Particularly, the study of thermodynamics of black holes in AdS space is exciting one because of AdS-CFT correspondence. Charged AdS black hole shows van der Waals like behaviour in extended phase space. An extended phase space is obtained by considering the cosmological constant as a thermodynamic variable corresponding to the fluid pressure. It's conjugate variable plays the role of volume in this approach. Only with these identifications the first law and Smarr relation are consistent with each other in AdS space. The van der Waals like critical behaviour can be seen in isotherms, Gibbs free energy plots, coexistence curves and critical exponents of the black hole, as a universal phenomena. The investigation in this regard is important because, further one may seek the answer for the underlying microscopic structure behind the critical behaviour.

A. Naveena Kumar (✉) · C. L. A. Rizwan · K. M. Ajith
Department of Physics, National Institute of Technology Karnataka (NITK), Surathkal, Mangaluru 575025, India
e-mail: naviphysics@gmail.com

A. Giri and R. Mohanta (eds.), *Workshop on Frontiers in High Energy Physics 2019*, Springer Proceedings in Physics 248,
https://doi.org/10.1007/978-981-15-6292-1_9

Monopoles are the topological defects formed during the cooling phase of the early universe. The presence of a global monopole changes the spacetime around a black hole by inducing a solid angle deficit, even though it's gravitational effects are negligible. Our motivation for current research is from the fact that any change in the surface properties will in turn be related to the thermodynamics of the black hole.

9.2 Thermodynamics of the Black Hole

The metric for a black hole which swallowed a global monopole is given by,

$$ds^2 = -f(r)dt^2 + f(r)^{-1}dr^2 + ar^2 d\Omega^2,$$

with $f(r) = 1 - \frac{2m}{r} + \frac{q^2}{r^2} + \frac{r^2}{l^2}$ and $a = 1 - \eta^2$. Where η is monopole parameter. The ADM mass is obtained by using the condition $f(r_+) = 0$,

$$M = \frac{ar_+}{2} + \frac{Q^2}{2ar_+} + \frac{ar_+^3}{2l^2}. \tag{9.1}$$

In the extended phase space cosmological constant is considered as thermodynamic pressure, $P = -\frac{\Lambda}{8\pi}$. Entropy of black hole is given by area of event horizon $S = \pi a r_+^2$. With these, the first law of thermodynamics for the black hole can be written as

$$dM = TdS + \Phi dQ + VdP. \tag{9.2}$$

The Hawking temperature can be derived from the first law as

$$T = \left(\frac{\partial M}{\partial S}\right)_{P,Q} = \frac{1}{4\pi r_+}\left(1 + \frac{3r_+^2}{l^2} - \frac{Q^2}{a^2 r_+^2}\right). \tag{9.3}$$

The physical equation of state $P = P(T, v)$ is obtained after making proper scaling,

$$P = \frac{T}{v} - \frac{1}{2\pi v^2} + \frac{2Q^2}{\pi a^2 v^4}. \tag{9.4}$$

The isotherms in $P - v$ plane are obtained from (9.4), which display the van der Waals like behaviour (Fig. 9.1). The decrease in solid angle due to monopole, reduces the critical behaviour. The vanishing first and second derivatives at the critical point gives the the critical parameters, which are dependent on monopole parameter.

$$P_c = \frac{a^2}{96\pi Q^2} \quad , \quad v_c = \frac{2\sqrt{6}Q}{a} \quad , \quad T_c = \frac{a}{3\sqrt{6}\pi Q}. \tag{9.5}$$

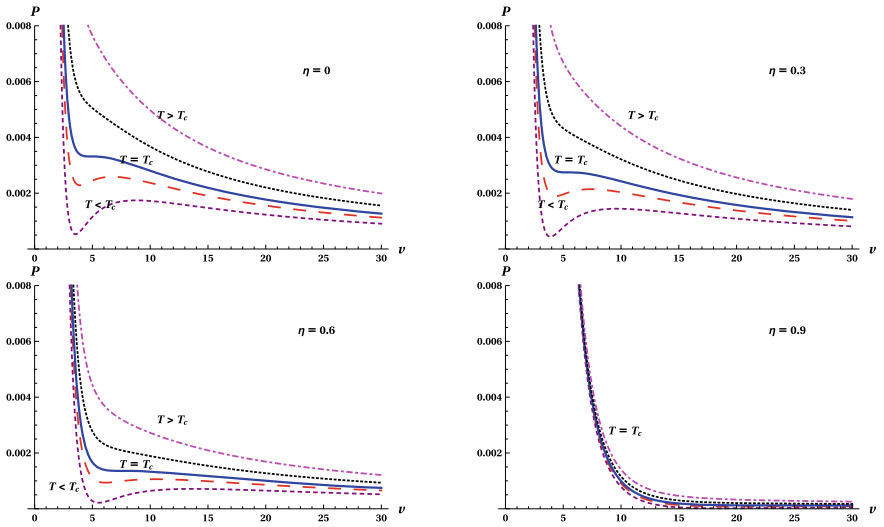

Fig. 9.1 $P - v$ isotherms in extended phase space. van der Waals like behaviour is suppressed due to the presence of monopole. ($Q = 1$ in every plot)

More about phase transitions can be studied from Gibbs free energy G, which is obtained from the Legendre transformation $G = M - TS$.

$$G(P, T) = \frac{1}{4} a r_+ \left(1 - \frac{8\pi P r_+^2}{3}\right) + \frac{3Q^2}{4ar_+}. \tag{9.6}$$

The behavior of G in terms of P is illustrated in Fig. 9.2. The solid angle deficit shrinks the swallow tail region, which in turn is a measure of change in critical behaviour. The swallow tail behaviour still remains for all values of η (enlarged in inlets).

A phase transition analogous to van der Waals liquid-gas system is observed in charged AdS black hole. Here the phase transition is between a large black hole (LBH) and small black hole (SBH). The coexistence of these phases is well depicted in a coexistence curve in $P - T$ plane (Fig. 9.3). This curve is obtained by using the fact that Gibbs free energy and temperature of SBH and LBH coincide along the coexistence curve. Coexistence line separates the LBH and SBH phases. The black hole undergoes a first order phase transition along the coexistence curve.

At the end we calculate the critical exponents which describe the behaviour of response functions near the critical point. These universal exponents are obtained as $\alpha = 0$, $\beta = 1/2$, $\gamma = 1$ and $\delta = 3$. Presence of monopole does not affect this universal result.

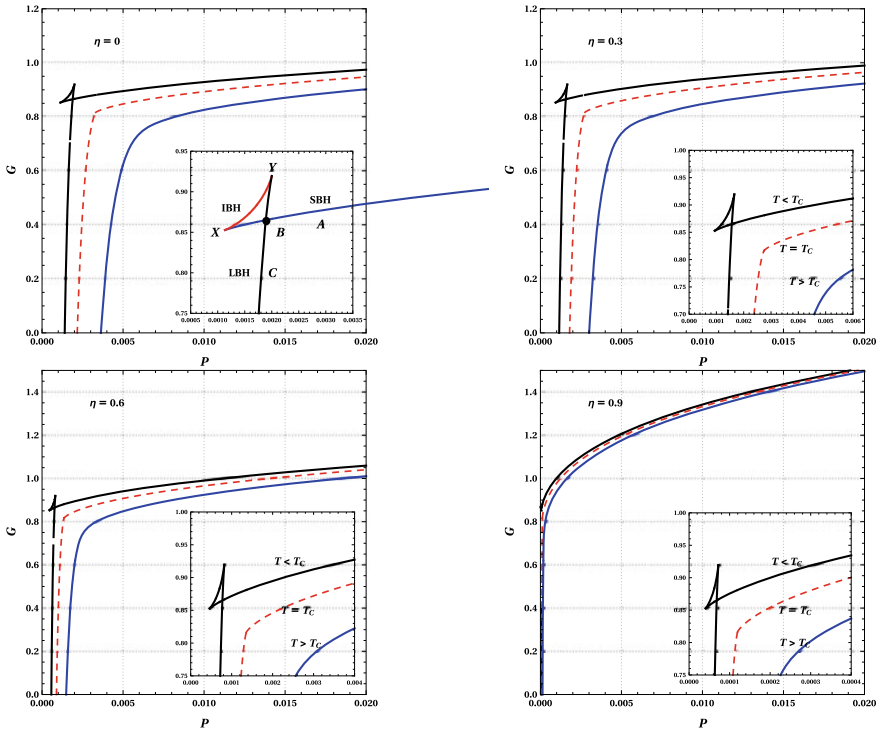

Fig. 9.2 The effect of η on the swallow tail behavior of Gibbs free energy ($Q = 1$)

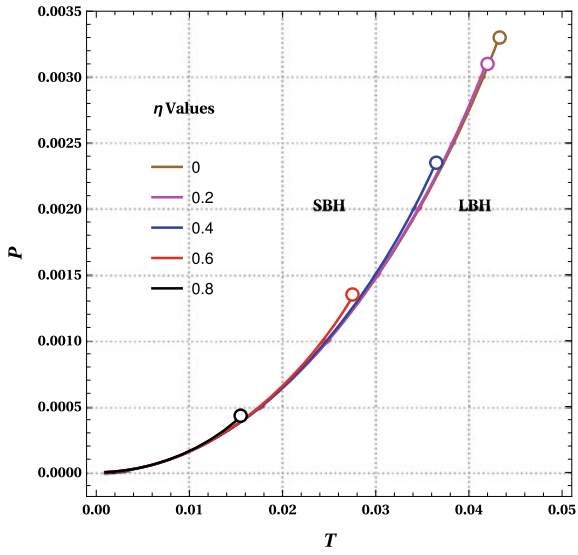

Fig. 9.3 Coexistent curves for different values of η. The circles are the termination points of first order transition

9.3 Conclusion

From this work we report that, the solid angle deficit induced by the global monopole influences the critical behaviour of charged AdS black hole. The change is observed from the $P - v$ isotherms in the extended phase space. The monopole strength dictates a consistent reduction in criticality. However the van der Waals like behaviour persists for all values of η. These are observed in Gibbs free energy plots as well. The swallow tail region reduces as monopole strength increases. The corresponding variation in coexistence curves is investigated, and it is seen that coexistence region also reduces with increasing η. These results can be interpreted as, the change in surface property due to solid angle deficit alters the thermodynamics of the black hole.

Reference

1. A. Naveena Kumara, C.L. Ahmed Rizwan, D. Vaid, K.M. Ajith, Critical behavior and microscopic structure of charged AdS black hole with a global monopole in extended and alternate phase spaces. arXiv:1906.11550

Chapter 10
Effect of Global Monopole on the Microscopic Structure of RN-AdS Black Hole

C. L. Ahmed Rizwan, A. Naveena Kumar, and K. S. Ananthram

Abstract In this work we study the microscopic structure of RN-AdS Black hole with a monopole. We utilize the connection between the thermodynamic Ruppeiner geometry and the nature of underlying microscopic interaction. The behaviour of the Ruppeiner invariant scalar is analysed in the extended space. The sign of the curvature scalar is the measure of the strength of attractive or repulsive statistical interaction. It is observed that the monopole parameter influences the microscopic structure of the black hole.

10.1 Introduction

Black hole thermodynamics has emerged as one of leading research topic in the domain of high-energy physics. This is mainly due to the exciting phenomena occurring in the black holes such as Hawking-Page transitions and van der Waals like phase structure in charged AdS black holes. Critical phenomena exhibited in AdS-BH with P-V, T-S and Gibbs energy plots showed remarkable analogy with real gas. The first order van der Waals liquid/vapour like phase transition found in black hole is interpreted as a transition between *Small* and *Large* black hole phases. In spite of these progresses, a microscopic basis for the holographic entropy is still lacking. Any information about microstructure of black holes is in the heart of quantum gravity. Hence the study of the thermodynamics and microstructure of black holes is important in a quantum gravity perspective, as it provides very useful details about the microstructure. Again from statistical mechanics we know macroscopic thermodynamics is due to its microstates. Study about microstates using *string theory*, a potential candidate for quantum gravity were limited to extremal black holes and with supersymmetry. In a completely different context, Ruppeiner and Weinhold found a way to learn information about underlying microstructure of a thermodynamic system using a

C. L. Ahmed Rizwan (✉) · A. Naveena Kumar · K. S. Ananthram
Department of Physics, National Institute of Technology Karnataka (NITK), Surathkal, Mangaluru 575025, India
e-mail: ahmedrizwancl@gmail.com

A. Giri and R. Mohanta (eds.), *Workshop on Frontiers in High Energy Physics 2019*, Springer Proceedings in Physics 248,
https://doi.org/10.1007/978-981-15-6292-1_10

phenomenological model called *thermodynamic geometry*. For any thermodynamic system, there exists equilibrium thermodynamic states which can be represented by points in the state space. The distance between arbitrary equilibrium states is inversely proportional to the fluctuations connecting the two states. A metric written in the equilibrium thermodynamic state space gives knowledge about the critical features during thermodynamic phase transitions. This innovative model then applied to study phase transitions in van der Waals gas and in various magnetic statistical models. Black holes which had already recognised as a thermodynamic system since the work of Hawking and Bekenstein are extensively studied using these geometric models.

We study the microscopic interaction of global monopole swallowed charged AdS black hole. During cosmic evolution, grand unified theory predicts different defects formation, a global monopole is one among them. Global monopoles araise from the symmetry breaking of a scalar field with global $SO(3)$ symmetry to $U(1)$. The black hole solution with a global monopole was first obtained by Barriola and Vilenkin [1]. Hence then its physical properties and phase transitions were deeply explored [2, 3]. Motivated by these studies, it is important to know the microscopic interaction responsible for its rich phase structure.

10.2 Thermodynamics

The metric for a spacetime with a global monopole is written as,

$$ds^2 = -f(r)dt^2 + f(r)^{-1}dr^2 + r^2 d\Omega^2, \tag{10.1}$$

where $f(r) = \left(1 - \frac{2m}{r} + \frac{q^2}{r^2} - \frac{\Lambda r^2}{3} - \eta^2\right)$ with m, q, and η being mass parameter, charge and global monopole parameter respectively. $\Lambda = -\frac{3}{l^2}$ is the cosmological constant for AdS space. The charge (Q) and the ADM mass (M) can be obtained as

$$Q = \left(1 - \eta^2\right) q \quad , \quad M = \left(1 - \eta^2\right) m. \tag{10.2}$$

On the event horizon r_+, $f(r)|_{r=r_+} = 0$. The ADM mass is calculated at the horizon as,

$$M = \frac{\left(1 - \eta^2\right) r_+}{2} + \frac{Q^2}{2\left(1 - \eta^2\right) r_+} + \frac{\left(1 - \eta^2\right) r_+^3}{2l^2}. \tag{10.3}$$

In the extended phase space approach of black hole thermodynamics, the cosmological constant is regarded as thermodynamic pressure P and its conjugate quantity as thermodynamic volume V. Entropy of black hole is holographic, hence can be given in terms of event horizon area.

$$P = -\frac{\Lambda}{8\pi}, \quad S = \pi\left(1-\eta^2\right) r_+^2. \tag{10.4}$$

In the extended phase space, first law of thermodynamics is,

$$dM = TdS + \Phi dQ + VdP. \tag{10.5}$$

The Hawking temperature can be obtained from surface gravity κ as,

$$T = \frac{\kappa}{2\pi} = \frac{1}{4\pi} f'(r)\big|_{r=r+} = \frac{1}{4\pi r_+}\left(1 + \frac{3r_+^2}{l^2} - \frac{Q^2}{\left(1-\eta^2\right)^2 r_+^2}\right). \tag{10.6}$$

The equation of state $P = P(T, r_+)$,

$$P = \frac{T}{2r_+} - \frac{1}{8\pi r_+^2} + \frac{Q^2}{8\pi\left(1-\eta^2\right)^2 r_+^4}. \tag{10.7}$$

The characteristic $P - r_+$ diagram obtained from this equation has van der Waals liquid/vapour like behaviour. A first-order phase transition between *Small* and *Large* black hole phase is noticed below critical points. The critical points P_c, T_c and r_{+c} are obtained from conditions,

$$\left(\frac{\partial P}{\partial r_+}\right)_T = \left(\frac{\partial^2 P}{\partial {r_+}^2}\right)_T = 0. \tag{10.8}$$

$$P_c = \frac{\left(1-\eta^2\right)^2}{96\pi Q^2} \;,\; r_{+c} = \frac{\sqrt{6}Q}{\left(1-\eta^2\right)} \;,\; T_c = \frac{\left(1-\eta^2\right)}{3\sqrt{6}\pi Q}. \tag{10.9}$$

Also, the critical exponents calculated matches with universal class ie, $\alpha = 0$, $\beta = 1/2$, $\gamma = 1$ and $\delta = 3$.

10.3 Thermodynamic Geometry

Phase structure can also be studied using thermodynamic geometry. The Ruppeiner geometry used in classical thermodynamic fluctuation theory is used to identify critical points and microscopic interactions phenomenologically. The Ruppeiner metric tensor $g_{ij}$is defined as the negative Hessian of the entropy function $g_{ij}^R = -\partial_i \partial_j S\left(M, x^\alpha\right)$ where x^α are extensive variables. The scalar curvature obtained from the metric, known as Ruppeiner scalar curvature R, contains the information about the first order phase transition. Also, the sign of R tells about the underlying interactions in the microstructure. Positive (negative) signature indicates a repulsive (attractive) interaction and zero shows a non-interacting system like in an

ideal gas. The scalar R is calculated in the coordinate space spanned by $x^{\alpha} = (S, P)$ and standard differential geometry calculation yields,

$$R = \frac{2\pi Q^2 - \left(1-\eta^2\right) S}{8PS^3 + \left(1-\eta^2\right) S^2 - \pi Q^2 S}. \tag{10.10}$$

Along the transition line, the Ruppeiner scalar is having branches and these are plotted making use of Maxwell's equal area law.

$$P_0(V_2 - V_1) = \int_{r_1}^{r_2} P dV. \tag{10.11}$$

Setting $r_1 = xr_2$ and $\chi = T/T_C$ $(0 < \chi \leq 1)$. The curvature scalar for *Small* and *Large* black hole branches is,

$$R_1 = -\frac{\left(1-\eta^2\right)\left(x^2+4x-1\right)}{4\pi Q^2 x(x+1)\left(x^2+4x+1\right)} \tag{10.12}$$

$$R_2 = \frac{\left(1-\eta^2\right) x^2 \left(x^2-4x-1\right)}{4\pi Q^2 (x+1)\left(x^2+4x+1\right)} \tag{10.13}$$

and reduced temperature, $\chi = \frac{3\sqrt{6}x(x+1)}{\left(x^2+4x+1\right)^{3/2}}$ Using these we obtain $R - \chi$ plot as shown in Fig. 10.1a, b.

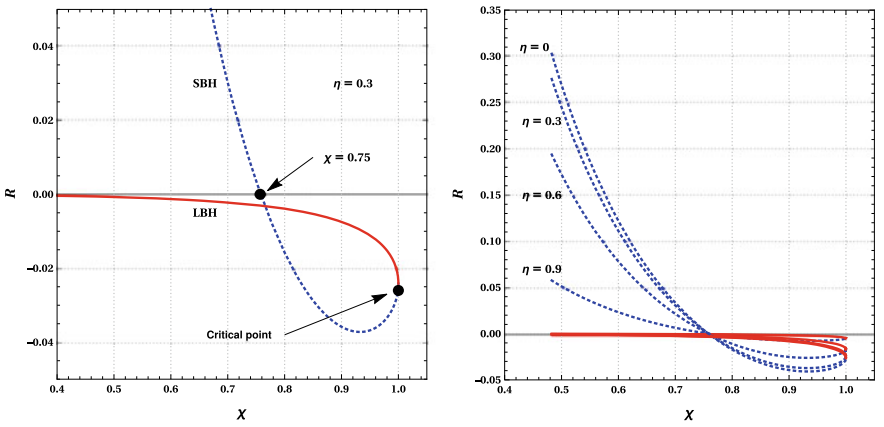

Fig. 10.1 The Ruppeiner scalar curvature R along the transition curve is plotted. The enlarged portion near the critical point and crossing point of LBH and SBH branch shown in (**a**). The red line corresponds to LBH and dotted blue line corresponds to SBH. In the second plot **b** the effect of η is shown for different values of η

10.4 Conclusion

The Fig. 10.1a, b shows that the *LBH* branch R_2 is always negative corresponds to an attractive interaction i.e, ideal Bose gas like behaviour [4].The SBH branch R_1 vanishes at $T = 0.75T_C$, negative for $T > 0.75T_C$ and positive for $T < 0.75T_C$ behaves like an anyon gas. The role of monopole parameter η can be seen as it affects only the *SBH* phase, without affecting the *LBH*.

References

1. M. Barriola, A. Vilenkin, Gravitational field of a global monopole. Phys. Rev. Lett. **63**, 341–343 (1989)
2. S. Chen, L. Wang, C. Ding, J. Jing, Holographic superconductors in the AdS black hole spacetime with a global monopole. Nucl. Phys. B **836**, 222–231 (2010)
3. G.M. Deng, J. Fan, X. Li, Y.C. Huang, Thermodynamics and phase transition of charged AdS black holes with a global monopole. Int. J. Mod. Phys. A **33**(03), 1850022 (2018)
4. A. Naveena Kumara, C.L. Ahmed Rizwan, D. Vaid, K.M. Ajith, Critical behavior and microscopic structure of charged AdS black hole with a global monopole in extended and alternate phase spaces (2019)

Chapter 11
Diffusion Coefficients and Constraints on Hadronic Inhomogeneities in the Early Universe

Sovan Sau and Soma Sanyal

Abstract After the quark hadron phase transition hadronic inhomogeneities are formed. In some regions of the plasma the number of the strange quarks are more than the up and down quarks. Besides the protons and the neutrons, the hadronization of these quarks will also produce a large number hyperons which will decay into pions, muons and their respective neutrinos. Hence in the plasma beside neutrons, protons, and electrons, there will be muons and neutrinos. Due to the decay of the hyperons muon abundance in the plasma will be very high. We study the diffusion of neutrons and protons in presence of a large number of muons immediately after the quark hadron phase transition. We find that inhomogeneities decay faster in a muon rich plasma as compared to an electron rich plasma. Thus in a muon rich plasma the size of the inhomogeneities has to be much larger to have any effect on the nucleosynthesis calculation.

11.1 Introduction

The quark hadron phase transition in the early universe resulted in the formation of hadrons at around 200 MeV. The baryon number was carried by the nearly massless quarks before the phase transition, while after the phase transition, the baryon number is carried by the heavier hadrons. The order of the phase transition is still unknown. It may be a first-order, a second order transition or a crossover. If it is of first order, it is described by the nucleation of bubbles. During this phase transition, baryon number gets concentrated in between the bubble's walls and after the phase transition, these regions form the baryon overdense regions. So there will be a baryon inhomogeneity in the plasma and this inhomogeneity can affect the nucleosynthesis calculation [1, 2]. Even if this phase transition is a crossover, there is a possibility of forming

S. Sau (✉) · S. Sanyal
University of Hyderabad, C.R. Rao Road, Hyderabad 500046, India
e-mail: sovan.sau@gmail.com

S. Sanyal
e-mail: sossp.uoh@nic.in

A. Giri and R. Mohanta (eds.), *Workshop on Frontiers in High Energy Physics 2019*, Springer Proceedings in Physics 248,
https://doi.org/10.1007/978-981-15-6292-1_11

a overdensity of quarks in different regions and generating baryon inhomogeneities. There are scenarios where collapsing Z(3) domain walls generate inhomogeneities [3, 4]. Dense inhomogeneities result in metastable quark nuggets [5]. Metastable H dibaryons have also been predicted due to the presence of s-quarks at the time of the quark-hadron transition [6]. All these scenarios lead to an inhomogeneity in the baryon number immediately after the phase transition. The ratio of neutrons and protons in the post QCD plasma play an important role in the nucleosynthesis calculations. The neutron-proton ratio basically determines the abundance of the primordial elements. If there is an inhomogeneity, the neutrons and protons diffuse through the plasma to reach an equilibrium condition [7]. The hadronization of the QGP results in some unstable hadrons also. Those unstable hadrons decay immediately to kaons, muons and muon neutrinos. The kaons too decay into muons. So finally the unstable particles will produce a large amount of muons and muon neutrinos. Previously in the literature, the diffusion of protons and neutrons have been studied in the absence of the muon. In this work we study their diffusion in the presence of muons in the plasma.

11.2 Diffusion Coefficients After the Quark-Hadron Phase Transition

The diffusion coefficient of nucleons have been studied in detail previously in [8, 9]. Since there are different kinds of particles in the plasma, the average diffusion coefficient for multi-particle diffusion is given by [10],

$$\frac{(1-x_i)}{D_i} = \sum_{i \neq j} \frac{x_j}{D_{ij}} \tag{11.1}$$

Here D_i denotes diffusion coefficient of the ith particle and D_{ij} denotes diffusion coefficient of the ith particle in presence of the jth particle. We have not considered collision of similar particles. If N be the total particle density, and n_i be the number density of the ith particle, then $x_i = \frac{n_i}{N}$. To obtain the diffusion coefficient in the plasma, we must first calculate the scattering cross-sections of the particles with one another. Once the scattering cross-sections are obtained they along with the Einstein equation give the diffusion coefficient of the neutrons and protons in the plasma. The diffusion coefficients are given by,

$$D_{ne} = \frac{M^2}{32m^3} \frac{1}{\alpha\kappa^2} \frac{e^{1/T}}{Tf(T)} \tag{11.2}$$

$$D_{n\mu} = \frac{M^2}{32m_\mu^3} \frac{1}{\alpha\kappa^2} \frac{e^{1/T'}}{T'f(T')} \tag{11.3}$$

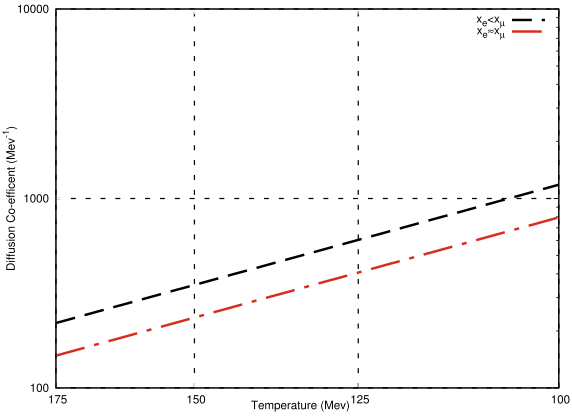

Fig. 11.1 Diffusion coefficient of neutrons in the electron, neutron and muon plasma. The dashed line denotes $x_e < x_\mu$ and the dot-dashed line denotes $x_e \approx x_\mu$

Here M is the neutron mass, m is the electron mass, and $\kappa = -1.91$ is the anomalous magnetic moment. The temperature is scaled by a factor of $m_e c^2$. We also have $f(T) = 1 + 3T + 3T^2$. $T' = \frac{T}{m_\mu c^2}$. Now from (11.1), we can get the total diffusion coefficient for the neutron and it depends on the concentration of the particles in the plasma. We can do a similar set of calculation for the proton.

We look at the diffusion coefficients at temperatures greater than 100 MeV. The number density of muons would be high around these temperatures. Diffusion coefficients of the neutrons and the protons in a muon rich plasma and a plasma with equal number densities of electron and muons have been plotted in Fig. 11.1. As the temperature decreases, the diffusion coefficients increase. So the nucleons move faster through the plasma. With the increase in number density, diffusion coefficient is also increasing. Thus the presence of muons changes the diffusion coefficient of the neutron considerably. This will definitely affect the decay of hadronic inhomogeneities at temperatures above 100 MeV. As the temperature cools to 1 MeV, the number density of muons go down. During this period, the contribution to the diffusion coefficient from the muons becomes negligible.

11.3 Decay of Inhomogeneities

We treat the inhomogeneity as a Gaussian function having a peak value of 10^{15} MeV^3 at the initial time t_0. The average number density of background plasma is of the order of 10^7 MeV^3. Baryon overdensities can be as large as 10^8 times the background density [3]. The diffusion equation is given by,

$$\frac{D(t)}{a^2}\frac{\partial^2 n(x,t)}{\partial x^2} = \frac{\partial n(x,t)}{\partial t} \tag{11.4}$$

$D(t)$ is diffusion coefficient and a is the scale factor of the expanding universe.

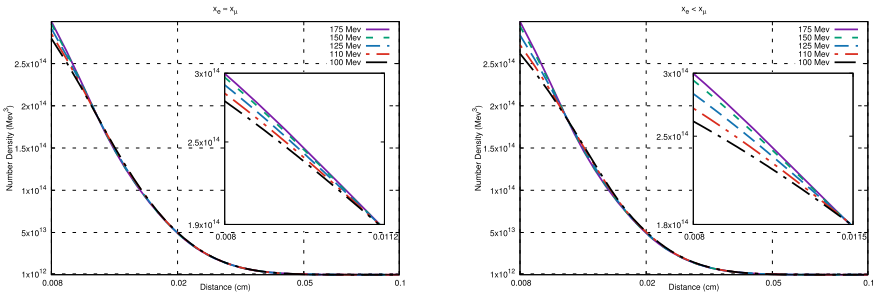

(a) (b)

Fig. 11.2 Decay of inhomogeneity in a plasma with **a** equal number of electrons and muons and **b** muon larger than electron

We use finite difference method to obtain the numerical solution of the diffusion equation. We use the standard time temperature expression to obtain the diffusion equation in terms of temperature. We consider the inhomogeneity at $T = 175\,\text{MeV}$ and evolve the inhomogeneity with a given diffusion coefficient.

We have shown how an overdensity decays in a plasma having equal numbers of electrons and muons and in a muon rich plasma in Fig. 11.2. From the two plots, it is clear that in a muon rich plasma inhomogeneities decay faster. The difference in the decay increases as the temperature cools down. The final profile of the inhomogeneity for the muon rich plasma is close to $2.5 \times 10^{14}\,\text{MeV}^3$ while in the other case overdensity is close to about $2.75 \times 10^{14}\,\text{MeV}^3$. The initial size of the inhomogeneity is considered to be the same at temperature of 175 MeV in both the cases. It indicates that the hadronic inhomogeneity decays faster, in the presence of a large muon density. This leads us to conclude that over densities which have a larger number of strange quarks will decay away faster after hadronization. Thus they will have little or no impact on the Big Bang Nucleosynthesis calculations.

11.4 Summary

We have shown that baryonic inhomogeneities in a muon rich plasma decay faster. We have obtained the diffusion coefficient of neutron and proton in a muon rich plasma. At high temperatures, it varies from the diffusion coefficient in the standard plasma. This significant change will result in the faster decay of inhomogeneities above 100 MeV. For an inhomogeneity decaying in a plasma with equal numbers of electrons and muons, the size of the inhomogeneities need to be of the order of 0.4 m for them to survive till the nucleosynthesis epoch. But in an muon rich plasma, the size of the inhomogeneity has to be at least 5% bigger to survive up to the nucleosynthesis epoch. So any mechanism that segregates the strange quarks more

than the up and down quark must generate very large inhomogeneities to have any effect on the nucleosynthesis calculations.

We would like to acknowledge discussions with Abhisek Saha and Soumen Nayak.

References

1. G.M. Fuller, G.J. Mathews, C.R. Alcock, Phys. Rev. D **37**, 1380 (1988)
2. B. Layek, S. Sanyal, A.M. Srivastava, Phys. Rev. D **63** 083512 (2001); B. Layek, S. Sanyal, A.M. Srivastava, Phys. Rev. D **67**, 083508 (2003)
3. B. Layek, A.P. Mishra, A.M. Srivastava, V.K. Tiwari, Phys. Rev. D **73**, 103514 (2006)
4. A. Atreya, A.M. Srivastava, A. Sarkar, Phys. Rev. D **85**, 014009 (2012)
5. C. Alcock, E. Farhi, Phys. Rev. D **32**, 1273 (1985)
6. J.A. de Freitas Pacheco, S. Stoica, F. Thevenin, J.E. Horvath, Phys. Rev. D **59**, 027303 (1998)
7. J.D. Barrow, R.J. Scherrer, Phys. Rev. D **98**, 043534 (2018)
8. J.H. Applegate, C.J. Hogan, R.J. Scherrer, Phys. Rev. D **35**, 1151 (1987)
9. B. Banerjee, S.M. Chitre, Phy. Lett. B **258**, 247 (1991)
10. R.B. Bird, W.E. Stewart, E.D. Lightfoot, *Transport Phenomenon* (Wiley, New York, 1960)

Chapter 12
Interacting Quintessence Model and Accelerated Expansion of the Universe

Debasis Sahu and Bibekananda Nayak

Abstract In our present work, we study the dynamics of the universe by using an interacting quintessence model, where equation of state parameter of dark energy varies between -1 and 0. First we calculated the dark energy density parameter and using that we have picturised the evolution of the deceleration parameter. From our analysis, we found that present universe is undergoing an accelerated phase of expansion where as the early time expansion was decelerated one. Our result also predicts that the transition from deceleration to acceleration would be occurred at $0.189t_0$ where t_0 is the present age of the universe.

12.1 Introduction

Along with Friedmann–Robertson–Walker metric which describes a homogeneous and isotropic universe, Einstein's field equation builds the backbone of Standard Model of Cosmology. Some of current observations [1] show that the present universe is expanding at an accelerated rate where as the Standard Model of Cosmology demands a decelerated expanding universe. For removing this controversy, in theoretical cosmology, generally two ways have been used. One is by modifying the theory of gravity like F(R) gravity and the other is by introducing an unknown form of energy having negative pressure termed as dark energy. This dark energy is homogeneous, less dense, permeate of all space, an intrinsic property of space and does not get diluted with the expansion of space. Further recent observational data [2] shows that nearly 68.3% of present universe is filled with this dark energy.

Among many models of dark energy, the most general forms of dark energy are vacuum energy, phantom energy [3] and quintessence [4] etc. Though vacuum energy,

D. Sahu (✉) · B. Nayak
P. G. Department of Applied Physics and Ballistics, Fakir Mohan University, Balasore 756019, Odisha, India
e-mail: debasissahu777@gmail.com

B. Nayak
e-mail: bibekanandafm@gmail.com

A. Giri and R. Mohanta (eds.), *Workshop on Frontiers in High Energy Physics 2019*, Springer Proceedings in Physics 248,
https://doi.org/10.1007/978-981-15-6292-1_12

explained by cosmological constant, is the simplest one, but it suffers from fine-tuning problem. So different kinds of dynamical dark energy models are proposed. Among them, Quintessence model is more popular one. Quintessence type of dark energy is characterized by its equation of state $p = \gamma_\phi \rho$ with $0 \geq \gamma_\phi \geq -1$.

In our present study, we assumed a model where quintessence type of dark energy interacts with matter during evolution of the universe such that one may grow at the expense of other and using this model, we try to explain the accelerated expansion of the universe.

12.2 Interacting Quintessence

For a spatially flat (k = 0) FRW universe filled with dust and dark energy, the Friedmann equations take the form

$$3H^2 = 8\pi G(\rho_\phi + \rho_m), \tag{12.1}$$

$$+ H^2 2\frac{\ddot{R}}{R} = -8\pi G\rho_\phi. \tag{12.2}$$

where H is the Hubble parameter, ρ_ϕ and ρ_m are considered as the densities of dark energy and matter respectively.

Assuming interaction between dark energy and matter, the energy conservation equation can be written as

$$\begin{aligned} \dot{\rho}_m + 3H\rho_m(1+\gamma_m) &= \delta, \\ \dot{\rho}_\phi + 3H\rho_\phi(1+\gamma_\phi) &= -\delta = -\Gamma\rho_\phi. \end{aligned} \tag{12.3}$$

where, $\delta = \Gamma\rho_\phi$ with Γ as the interaction rate. Considering present age of the Universe as 13.68 billion years, Γ can be calculated [5] as $\Gamma \approx 1.565\times10^{18}\ \mathrm{s}^{-1}$.

Integrating equation (12.3), one can easily get

$$(\rho_\phi)_{t<t_e} = \rho_\phi(t_e)\left(\frac{t}{t_e}\right)^{-\frac{3}{2}(1+\gamma_\phi)} e^{-\Gamma(t-t_e)} \tag{12.4}$$

and

$$(\rho_\phi)_{t>t_e} = \rho_\phi(t_0)\left(\frac{t}{t_0}\right)^{-2(1+\gamma_\phi)} e^{-\Gamma(t-t_0)} \tag{12.5}$$

where t_e is the time of matter-radiation equality and roughly equal to 10^{11} s.

12.3 Deceleration Parameter

The expansion of the universe is explained by Hubble's law. But whether the expansion is accelerating or decelerating one, is determined by deceleration parameter. The deceleration parameter is defined as, $q = -\frac{R\ddot{R}}{\dot{R}^2}$.
From (12.2),

$$q = \frac{1}{2}\left(1 + \frac{8\pi G p_\phi}{H^2}\right). \tag{12.6}$$

Using (12.4) and (12.5) in (12.6), we calculated the deceleration parameter for radiation-dominated and matter-dominated era as

$$q_{t<t_e} = \frac{1}{2} = \left[1 + 32\pi G t^2 \gamma_\phi \rho_\phi(t_e)\left(\frac{t}{t_e}\right)^{-\frac{3}{2}(1+\gamma_\phi)} e^{-\Gamma(t-t_e)}\right] \tag{12.7}$$

and

$$q_{t>t_e} = \frac{1}{2}\left[1 + 18\pi G t^2 \gamma_\phi \rho_\phi(t_0)\left(\frac{t}{t_0}\right)^{-2(1+\gamma_\phi)} e^{-\Gamma(t-t_0)}\right]. \tag{12.8}$$

Equation (12.7) implies in radiation-dominated era, deceleration parameter q can take only positive values for $-1 < \gamma_\phi < 0$ where as (12.8) tells that in matter-dominated era, q can take both positive and negative values. The variation of deceleration parameter q with equation of state parameter of dark energy γ_ϕ and time are shown in Figs. 12.1 and 12.2 respectively.

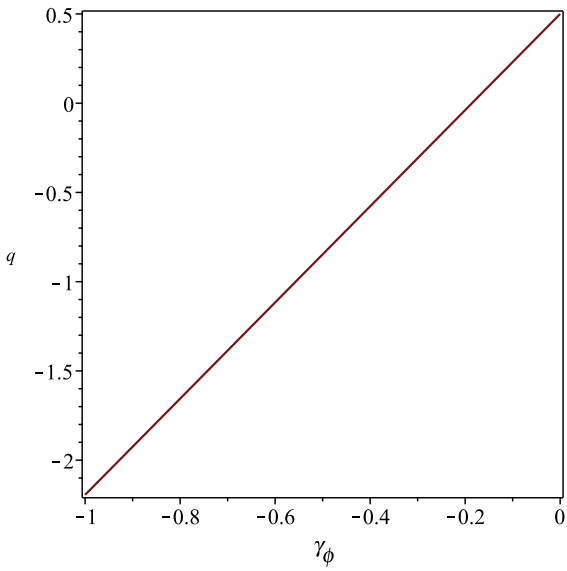

Fig. 12.1 Variation of q with γ_ϕ at $t = t_0$

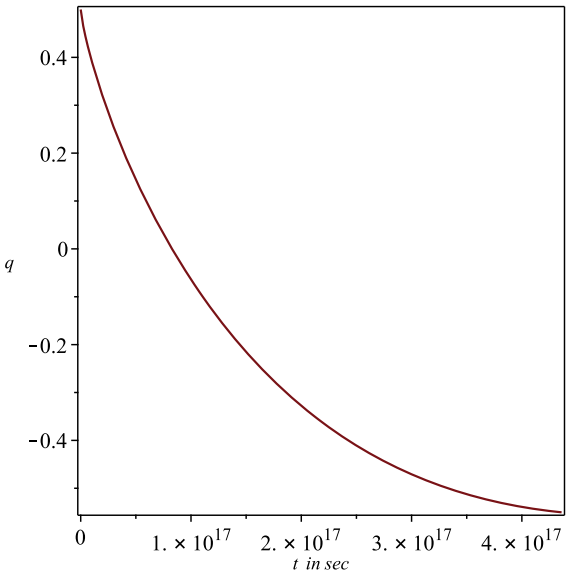

Fig. 12.2 Variation of q with t at $\gamma_\phi = -0.3898$ in matter dominated era

From Fig. 12.1, we found that deceleration parameter q takes a value of -0.55 for $t = t_0 = 4.36 \times 10^{17}$ s and $\gamma_\phi = -0.3898$ and from Fig. 12.2, we got that $q = 0$ for $t = 8.246 \times 10^{16}$ s and $\gamma_\phi = -0.3898$.

12.4 Discussion and Conclusion

We, here, used an interacting quintessence model for explaining presently observed accelerated expansion of the universe. First we calculated the dark energy density parameter and then expressed deceleration parameter in terms of it for different epochs. In the next step, we have shown the variation of deceleration parameter q with equation of state parameter γ_ϕ. Comparing with the present observational data [6] that the deceleration parameter is -0.55, the value of γ_ϕ for the present universe is found to be -0.3898. Again from our study, we found that in radiation-dominated era expansion of the universe is decelerating one since deceleration parameter q is found to be always positive. But in matter-dominated era, the universe is changing gradually from a phase of decelerated to accelerated expansion as the calculated q value shows a change from positive to negative. Also the transition time at which the decelerated expanding universe switched to accelerated one, is found to be $0.189t_0$ which is in agreement with observation [7].

References

1. A.G. Reiss et al., Observational evidence from supernovae for an accelerating universe and a cosmological constant. Astron. J. **116**, 1009–1038 (1998). https://doi.org/10.1086/300499
2. P.A.R. Ade, et al. Planck 2015 results. Astron. Astrophys. **594**, A13 (2016). https://doi.org/10.1051/0004-6361/201525830
3. R.R. Caldwell et al., Phantom energy: dark energy with $w<1$. causes a cosmic doomsday. Phys. Rev. Lett. **91**, 071301 (2003). https://doi.org/10.1103/PhysRevLett.91.071301
4. F. Cicciarella, M. Pieroni, Universality for quintessence. J. Cosmo. Astropart. Phys. **08**, 010 (2017). https://doi.org/10.1088/1475-7516/2017/08/010
5. B. Nayak, L.P. Singh, Present acceleration of the universe, holographic energy and Brans-Dicke theory. Mod. Phys. Lett. A **24**, 1785 (2009). https://doi.org/10.1142/S0217732309030205
6. M.V. dos Santos et al., Constraining the cosmic deceleration-acceleration transition with type Ia supernova, BAO/CMB and H(z) data. J. Cosmo. Astropart. Phys. **02**, 066 (2016). https://doi.org/10.1088/1475-7516/2016/02/066
7. A. Katz, A. Riotto, Baryogenesis and gravitational waves from runaway bubble collisions. J. Cosmo. Astropart. Phys. **11**, 011 (2016). https://doi.org/10.1088/1475-7516/2016/11/011

Chapter 13
Quantisation of κ-Deformed Klein–Gordon Field

E. Harikumar and Vishnu Rajagopal

Abstract We study the quantisation of real scalar field satisfying κ-deformed Klein–Gordon equation, valid upto a term. This scheme allows two choices, viz; (i) a deformed unequal time commutation relation between the field and its adjoint which leads to usual oscillator algebra, (ii) an undeformed unequal time commutation relation between field and its adjoint leading to a deformed oscillator algebra. Further we derive deformed conserved currents from κ-deformed Klein–Gordon equation.

13.1 Introduction

Most of the the quantum gravity models predict the existence of a minimal length scale [1]. Non-commutativity naturally incorporates this minimal length scale [2]. κ-deformed space-time is one such space-time where the space-time coordinates follow a Lie algebraic type commutation relation. In the low energy limits of loop gravity models space-time behaves like κ-deformed space-time. Attempts to incorporate a fundamental length scale as a frame independent quantity, extends the special relativity to Deformed/Doubly Special Relativity(DSR) [3]. The space-time associated with DSR is known to be κ space-time.

The canonical quantisation procedure requires the explicit form of the Lagrangian for quantisation, but there is an another quantisation procedure [4, 5], which uses only the equations of motion and does not require the existence Lagrangian. An unequal time commutation relation between the field and its adjoint is defined, such that it leads to commutation relations between the creation and annihilation operators appearing in the mode expansion of field operator. Using this procedure conserved currents can be constructed directly from the equation of motion, without using

E. Harikumar · V. Rajagopal (✉)
School of Physics, University of Hyderabad, Central University P.O., Hyderabad 500046, Telangana, India
e-mail: vishnurajagopal.anayath@gmail.com

E. Harikumar
e-mail: harisp@uohyd.ernet.in

A. Giri and R. Mohanta (eds.), *Workshop on Frontiers in High Energy Physics 2019*, Springer Proceedings in Physics 248,
https://doi.org/10.1007/978-981-15-6292-1_13

the Lagrangian. Using this procedure one can also derive the conserved currents corresponding to discrete symmetries [6]. Thus, this approach is suited is to study the field theory models on κ space-time as constructing a unique Lagrangian density is not easy and thus quantisation of the field theories on κ space-time is a non-trivial issue.

Here we use the above mentioned quantisation scheme for quantising the κ-deformed real Klein–Gordon(KG) field equation, valid up to first order in the deformation parameter. The equation of motion corresponding to this deformed KG field is derived using the quadratic Casimir of the undeformed κ-Poincare algebra [7]. We derive a deformed unequal time commutation relation between the field and its adjoint leading to the usual oscillator algebra. Similarly we show that the unequal time commutation relation between the field and its adjoint is undeformed if the oscillator algebra is deformed for a particular choice of deformation factor. Further we derive the deformed conserved currents for the deformed KG field theory.

Here we work with $\eta_{\mu\nu}$ =diag$(-1, +1, +1, +1)$.

13.2 Quantisation of κ-Deformed Klein–Gordon Field

In [5] it has been shown that the field theories can be quantised using their equations of motion alone (without using the explicit form of Lagrangian). Even the Conserved currents can be obtained from the equations of motion, by following this quantisation method [4, 5]. Here we use this procedure to study the quantisation of the κ-deformed KG field.

The κ-deformed space-time coordinates satisfy the Lie-algebraic type commutation relations given by

$$[\hat{x}_i, \hat{x}_j] = 0, \quad [\hat{x}_0, \hat{x}_i] = ia\hat{x}_i \tag{13.1}$$

where $a = \frac{1}{\kappa}$. Here we choose a specific realisation for $\hat{x}_\mu$ as, $\hat{x}_\mu = x_\alpha \varphi^\alpha_\mu$, where $\varphi^j_i = \delta^j_i e^{-ap_0}$, $\varphi^0_0 = 1$, $\varphi^0_i = 0$, $\varphi^i_0 = 0$ [8]. The equations of motion for κ-deformed KG field is derived using the quadratic Casimir, given by

$$D_\mu D^\mu = \left(\partial_i^2 \frac{e^{-A}}{\varphi^2} + 2\partial_0^2 \frac{(1-\cosh A)}{A^2}\right)\left(1 + \frac{a^2}{4}\left(\partial_i^2 \frac{e^{-A}}{\varphi^2} + 2\partial_0^2 \frac{(1-\cosh A)}{A^2}\right)\right). \tag{13.2}$$

Here $D_\mu = \left(\partial_0 \frac{\sinh A}{A} - ia\partial_i^2 \frac{e^{-A}}{2\varphi^2},\ \partial_i \frac{e^{-A}}{\varphi}\right)$ is the Dirac derivative that transform as 4-vector under undeformed κ-Poincare algebra [7], and $\varphi = e^{-A}$ and $A = ap_0$. Thus using (13.2) the κ-deformed KG equation valid upto a term is

$$\left(\partial_i^2 - \partial_0^2 - m^2 - ia\partial_0\partial_i^2\right)\hat{\phi}(x) = 0. \tag{13.3}$$

$\hat{\phi}(x)$ is the deformed KG field operator and $\partial_i^2 - \partial_0^2 - m^2 - ia\partial_0\partial_i^2$ is denoted as $\hat{\Lambda}(\partial)$, such that $\hat{\Lambda}(\partial)\hat{\phi}(x) = 0$. In general $\hat{\Lambda}(\partial)$ is a polynomial of derivative operators ∂_μ given as [5]

$$\hat{\Lambda}(\partial) = \sum_{l=0}^{N} \hat{\Lambda}_{\mu_1\mu_2\ldots\mu_l}\partial^{\mu_1}\partial^{\mu_2}\ldots\partial^{\mu_l} = \hat{\Lambda} + \hat{\Lambda}_\mu\partial^\mu \cdots + \hat{\Lambda}_{\mu_1\mu_2\mu_3\ldots\mu_N}\partial^{\mu_1}\partial^{\mu_2}\partial^{\mu_3}\ldots\ldots\partial^{\mu_N} \tag{13.4}$$

In this procedure the (deformed) equation of motion reduces to (deformed) KG equation, using an operator called (deformed) KG divisor, denoted by $\hat{d}(\partial)$, such that it satisfies the relations [4]

$$\hat{\Lambda}(\partial)\hat{d}(\partial) = \Box - m^2 - ia\partial_0\partial_i^2,\ [\hat{\Lambda}(\partial), \hat{d}(\partial)] = 0,\ det[d(\partial)] \neq 0 \tag{13.5}$$

For a (deformed) KG field $d(\partial)$ is $\mathbb{I}$. Now we decompose the deformed field operator using deformed creation and annihilation operators as [4, 5]

$$\hat{\phi}(x) = \int \frac{d^3p}{\sqrt{(2\pi)^3 2E_p}}\Big(\hat{u}_p(x)\hat{a}(p) + \hat{u}_p^*(x)\hat{a}^\dagger(p)\Big). \tag{13.6}$$

where, $\hat{u}_p(x)$ satisfies $\hat{\Lambda}(\partial)\hat{u}_p(x) = 0$. Now we find $\hat{u}_p(x)$ explicitly by solving this perturbatively. Hence we take $\hat{\Lambda}(\partial) = \Lambda^{(0)}(\partial) + a\Lambda^{(1)}(\partial)$ and $\hat{u}(x) = u^{(0)}(x) + a\alpha u^{(1)}(x)$, where α has the dimension of L^{-1}. By putting this in $\hat{\Lambda}(\partial)\hat{u}_p(x) = 0$, we get two equations, corresponding to a independent and a dependent coefficient. The solution to the former once (a independent) gives $u_p^{(0)}(x) = e^{-ipx}$, which is the commutative solution and the later equation (a dependent) is $\big(\Box - m^2\big)u^{(1)}(x) = \frac{1}{\alpha}E_p p_i^2 e^{-ipx}$, where E_p is the commutative energy. We use Green's function method to solve this inhomogenous differential equation. Combining this solution $\hat{u}^{(1)}(x)$ and $\hat{u}^{(0)}(x)$ we get the total solution valid up to a term as

$$\hat{u}(x) = \Big[1 + a\alpha - ia\pi(\mathbf{p})^2\Big\{-\theta(t'-t) + \theta(t-t')\Big\}\Big]e^{-ipx} = \Big(u_p^{(0)}(x) + a\alpha u_p^{(1)}(x)\Big)e^{-ipx} \tag{13.7}$$

According to this quantisation procedure the field operator and its adjoint will follow an unequal time commutation relation [5]. So here we consider a κ-deformed version of this commutation relation given as

$$[\hat{\phi}(x), \hat{\bar{\phi}}(x')] = id(\partial)\hat{\Delta}(x-x') = id(\partial)\Big(\Delta(x-x') + af(x-x')\Big) \tag{13.8}$$

where $\Delta(x-x') = \int \frac{d^3p}{(2\pi)^3 2E_p}\big(e^{-ip(x-x')} - e^{ip(x-x')}\big)$. We assume the deformed creation and annihilation operators appearing in (13.6) satisfy an undeformed commutation relation defined as

$$[\hat{a}(k), \hat{a}(k')] = [\hat{a}^\dagger(k), \hat{a}^\dagger(k')] = 0,\ \ [\hat{a}(k), \hat{a}^\dagger(k')] = \delta^3(k-k'). \tag{13.9}$$

Using (13.6), (13.7) and (13.9) in (13.8) we get $f(x-x')$ as $f(x-x') = 2\alpha\Delta(x-x')$. Hence (13.8) becomes

$$[\hat{\phi}(x), \hat{\tilde{\phi}}(x')] = i(1+2a\alpha)\Delta(x-x'). \tag{13.10}$$

Thus we find that the propagator for the deformed KG field is modified by a $(1+2a\alpha)$ factor. The consistency of this has been verified by evaluating the time ordered products for the deformed fields and we find that

$$< T\left(\hat{\phi}(x)\hat{\phi}(x')\right) >= (1+2a\alpha) < T\left(\phi(x)\phi(x')\right) >= i(1+2a\alpha)\Delta_F(x-x') \tag{13.11}$$

where $\Delta_F(x-x')$ is the propagator for KG field. Hence we say that an undeformed oscillator algebra gives a deformed unequal time commutation relation between field and its adjoint, resulting in a deformed propagator with the same deformation factor. Now let us assume the oscillator algebra to be deformed, given as

$$[\hat{a}(k), \hat{a}(k')] = [\hat{a}^\dagger(k), \hat{a}^\dagger(k')] = 0, \quad [\hat{a}(k), \hat{a}^\dagger(k')] = h(a)\delta^3(k-k'). \tag{13.12}$$

If we follow the above calculation by choosing $h(a) = 1-2a\alpha$, we find the unequal time commutation relation between field and its adjoint to be undeformed. Hence we find that for a particular choice of deformation factor in the deformed oscillator algebra, the unequal time commutation relation between field and its adjoint becomes undeformed. Thus we have

$$[\hat{a}(k), \hat{a}(k')] = [\hat{a}^\dagger(k), \hat{a}^\dagger(k')] = 0, \quad [\hat{a}(k), \hat{a}^\dagger(k')] = (1-2a\alpha)\delta^3(k-k'). \tag{13.13}$$

The vaccum state is defined as $|0\rangle$. Now the action of $\hat{a}$ and $\hat{a}^\dagger$ on a state $|n\rangle$ is evaluated with the help of (13.13) and we find that $\hat{a}(p)\,|n\rangle = \sqrt{n(1-2a\alpha)}\,|n-1\rangle$ as well as $\hat{a}^\dagger(p)\,|n\rangle = \sqrt{(n+1)(1-2a\alpha)}\,|n+1\rangle$. The deformed number operator is defined as $\hat{N}(p) = \hat{a}(p)\hat{a}^\dagger(p)$, and the action of $\hat{N}(p)$ on $|n\rangle$ is obtained as $\hat{N}(p)\,|n\rangle = n(1-2a\alpha)\,|n\rangle$. Here we find that the eigen values of all these deformed operators get modified by $(1-2a\alpha)$ factor, which is same as the deformation factor appearing in the deformed oscillator algebra [8]. This results in the modification of Unruh effect in κ space-time, calculated using Bogoliubov transformation [8].

13.3 κ-Deformed Noether Current

Here we construct the (deformed) conserved current using the (deformed) equations of motion [4–6]. For this we construct an operator $\hat{\Gamma}_\mu(\partial, -\overleftarrow{\partial})$ in the κ-deformed space-time following [4–6],

$$\hat{\Gamma}_\mu(\partial, -\overleftarrow{\partial}) = \sum_{l=0}^{N-1}\sum_{i=0}^{l} \hat{\Lambda}_{\mu\mu_1.....\mu_l}\partial_{\mu_1}.....\partial_{\mu_i}(-\overleftarrow{\partial}_{\mu_{i+1}}).....(-\overleftarrow{\partial}_{\mu_l})$$
$$= \hat{\Lambda}_\mu + \hat{\Lambda}_{\mu\nu}(\partial^\nu - \overleftarrow{\partial}^\nu) + ... \tag{13.14}$$

such that it satisfies the relation $(\partial^\mu + \overleftarrow{\partial}^\mu)\hat{\Gamma}_\mu(\partial, -\overleftarrow{\partial}) = \hat{\Lambda}(\partial) - \hat{\Lambda}(-\overleftarrow{\partial})$. This condition is used to verify that the deformed conserved current is divergenceless, i.e, $\partial_\mu \hat{J}^\mu = 0$. For a deformed KG field, $\hat{\Gamma}_\mu(\partial, -\overleftarrow{\partial})$, valid up to first order in a, is obtained to be $\hat{\Gamma}_\mu(\partial, -\overleftarrow{\partial}) = \partial_\mu - \overleftarrow{\partial}_\mu - ia\delta_{\mu 0}(\partial_i^2 - \partial_i\overleftarrow{\partial}_i + \partial_i^2)$. Using this, the expression for the deformed conserved current is obtained as

$$\hat{J}_\mu = \hat{\phi}(x)\hat{\Gamma}_\mu(\partial, -\overleftarrow{\partial})\delta\hat{\phi}(x) + h.c \tag{13.15}$$

For an infinitesimal translation in κ-deformed space-time, the coordinates of κ space-time transform as $\hat{x} \to \hat{x}'_\mu = \hat{x}_\mu + \hat{\theta}_\mu$, for the above choosen realisation, we have $\delta\hat{x}_\mu = \theta_\mu - ap_0\delta^i_\mu\theta_i$ and $\delta\hat{\phi}(x) = -\theta_0\partial_0\hat{\phi}(x) + \theta_i(1 - ap_0)\partial_i\hat{\phi}(x)$. Hence using (13.15), the deformed conserved current is

$$\hat{J}_\mu = \frac{1}{2}\hat{\phi}(x)\Big(\partial_\mu - \overleftarrow{\partial}_\mu - ia\delta_{\mu 0}(\partial_i^2 - \partial_i\overleftarrow{\partial}_i + \overleftarrow{\partial}_i^2)\Big)\Big(\theta^\nu\partial_\nu - ap_0\theta^\nu\delta_{\nu i}\partial_i\Big)\hat{\phi}(x)$$
$$- \frac{1}{2}\hat{\phi}(x)\Big(\theta^\nu\overleftarrow{\partial}_\nu - ap_0\theta^\nu\delta_{\nu i}\overleftarrow{\partial}_i\Big)\Big(\partial_\mu - \overleftarrow{\partial}_\mu - ia\delta_{\mu 0}(\partial_i^2 - \partial_i\overleftarrow{\partial}_i + \overleftarrow{\partial}_i^2)\Big)\hat{\phi}(x) \tag{13.16}$$

differentiating $\hat{J}_\mu$ with respect to θ^ν and symmetrising it, we get the energy-momentum tensor as

$$\hat{T}_{\mu\nu} = \frac{1}{2}\hat{\phi}(x)(\partial_\mu - \overleftarrow{\partial}_\mu)(\partial_\nu - \overleftarrow{\partial}_\nu)\hat{\phi}(x)$$
$$- \frac{ap_0}{4}\hat{\phi}(x)\Big[\delta_{\mu i}(\partial_\nu - \overleftarrow{\partial}_\nu)(\partial_i - \overleftarrow{\partial}_i) + \delta_{\nu i}(\partial_\mu - \overleftarrow{\partial}_\mu)(\partial_i - \overleftarrow{\partial}_i)\Big]\hat{\phi}(x)$$
$$- \frac{ia}{4}\hat{\phi}(x)\Big[\delta_{\mu 0}(\partial_\nu - \overleftarrow{\partial}_\nu)(\partial_i^2 - \partial_i\overleftarrow{\partial}_i + \overleftarrow{\partial}_i^2) + \delta_{\nu 0}(\partial_\mu - \overleftarrow{\partial}_\mu)(\partial_i^2 - \partial_i\overleftarrow{\partial}_i + \overleftarrow{\partial}_i^2)\Big]\hat{\phi}(x). \tag{13.17}$$

Now using the κ-deformed energy-momentum tensor, we obtain the κ-deformed conserved momentum as

$$\hat{P}_\nu = \int dx^3\hat{T}_{0\nu} = \frac{1}{2}\hat{\phi}(x)(\partial_0 - \overleftarrow{\partial}_0)(\partial_\nu - \overleftarrow{\partial}_\nu)\hat{\phi}(x)$$
$$- \frac{ap_0}{4}\hat{\phi}(x)\Big[\delta_{\nu i}(\partial_0 - \overleftarrow{\partial}_0)(\partial_i - \overleftarrow{\partial}_i)\Big]\hat{\phi}(x)$$
$$- \frac{ia}{4}\hat{\phi}(x)\Big[(\partial_\nu - \overleftarrow{\partial}_\nu)(\partial_i^2 - \partial_i\overleftarrow{\partial}_i + \overleftarrow{\partial}_i^2) + \delta_{\nu 0}(\partial_0 - \overleftarrow{\partial}_0)(\partial_i^2 - \partial_i\overleftarrow{\partial}_i + \overleftarrow{\partial}_i^2)\Big]\hat{\phi}(x) \tag{13.18}$$

Similarly the conserved quantities associated with the boost and rotations in the κ-deformed space-time is defined as, $\hat{M}_{\mu\nu} = \int dx^3(\hat{x}_\mu \hat{P}_\nu - \hat{x}_\nu \hat{P}_\mu)$. It can be shown that the $\hat{P}_\mu$ and $\hat{M}_{\mu\nu}$ constructed in this way, satisfy the undeformed κ-Poincare algebra.

13.4 Conclusions

In this work we have quantised the κ-deformed KG field using equations of motion alone. We have derived the deformed unequal time commutation relation between field and its adjoint, from which we have obtained the deformed propagator for deformed KG field, valid up to a term. Similarly we derived an undeformed unequal time commutation relation between field and its adjoint in κ-space-time, leading to deformed oscillator algebra. Using this deformed oscillator algebra we have shown that the eigen values of the creation, annihilation and number operators get modified by the same deformation factor which is present in the deformed oscillator algebra. We have also constructed the conserved current and energy-momentum tensor without any reference to Lagrangian.

Acknowledgements EH thanks Prof. V. Srinivasan for introducing him to the reference [4] and enlightening discussions. EH thanks SERB, Govt. of India, for support through EMR/2015/000622. VR thanks Govt. of India, for support through DST-INSPIRE/IF170622.

References

1. S. Doplicher, K. Fredenhagen, J.E. Roberts, Phys. Lett. B **39**, 331 (1994)
2. A. Connes, *Noncommutative Geometry* (Academic Press, Cambridge, 1994)
3. J. Kowalski-Glikman, *Introduction to Doubly Special Relativity* (Springer, Berlin, 2005)
4. Y. Takahashi, *An Introduction to Field Quantization* (Pergamon Press, Oxford, 1969)
5. Y. Takahashi, H. Umezawa, Nucl. Phys. **51**, 193 (1964)
6. D. Lurie, Y. Takahashi, H. Umezawa, J. Math. Phys. **7**, 1478 (1966)
7. S. Meljanac, M. Stojic, Eur. Phys. J. C **47**, 531 (2006)
8. E. Harikumar and Vishnu Rajagopal, *Eur. Phys. J.* **C 79** (2019) 735

Part II
Collider and Physics Beyond the Standard Model

Chapter 14
Recent Results in Small Systems from CMS

Prabhat R. Pujahari

Abstract The observation of a wide variety of physical phenomena in the context of the formation of a strongly interacting QCD matter in heavy-ion nuclear collisions at the LHC has drawn significant attention to the high energy heavy-ion physics community. The appearance of a varieties of similar phenomena as in heavy-ion in the high multiplicity proton-proton and proton-nucleus collisions at the LHC energies has triggered further investigation to understand the dynamics of particle production mechanism in a highly dense and small QCD medium. The CMS collaboration uses many different probes in these studies ranging from the particle production cross section to multi-particle correlations. In this proceeding, I report a few selected recent CMS results from the small systems with the main focus on the measurement of collective phenomena in high multiplicity pp and pPb collisions.

14.1 Introduction

In the context of high energy heavy-ion physics, the collisions between protons or a proton with a nucleus is commonly referred to as small system and they can provide baseline measurements for heavy-ion collisions. Traditionally, it is thought that such small systems do not show characteristics of QGP formation a priori. However, in the recent few years, this simplistic view of a small system has been challenged at the LHC—thanks to the new frontier in energies and state-of-the-art instrumentations. The individual events in a high multiplicity pp and pPb collisions can have very high charged particle multiplicity and energy density which is comparable to that of AA collisions [1].

With the advent of the LHC, high multiplicity pp and pPb collisions show unexpected phenomena which have never been observed before in such small systems.

For the CMS collaboration.

P. R. Pujahari (✉)
Physics Department, Indian Institute of Technology Madras, Chennai 600036, TN, India
e-mail: p.pujahari@cern.ch

A. Giri and R. Mohanta (eds.), *Workshop on Frontiers in High Energy Physics 2019*, Springer Proceedings in Physics 248,
https://doi.org/10.1007/978-981-15-6292-1_14

The observation of a long range rapidity ridge in the measurement of two-particle angular correlation in heavy-ion collisions is no surprise to us and this can be well explained by hydrodynamical collective flow of a strongly interacting and expanding medium [3]. However, the appearance of similar structures in a high multiplicity pp and pPb collisions has drawn a lot of attention and prompted studies to understand the cause of such behaviour in small systems. In particular, the discovery of the ridge by CMS collaboration [2] in high multiplicity pp collisions is one of such intriguing results observed in small systems [4]. Long-range, near-side angular correlations in particle production emerged in pp and subsequently in pPb collisions paved the way for a systematic investigation of the existence of the collective phenomena. Much information can also be gained by focusing on collective properties of each event, such as multi-particle correlations, or event-by-event fluctuations of such quantities. We observe signatures traditionally attributed to a collective behaviour not only in PbPb collisions but also in small systems. Since then, a wealth of new, unexpected phenomena has been observed with striking similarities to heavy-ion observations.

14.2 Transverse Energy Density

The total transverse energy, E_T, is a measure of the energy liberated by the "stopping" of the colliding nucleons in a heavy-ion or proton-nucleus collision. From Fig. 14.1 it can be seen that $dE_T/d\eta\,|_{\eta=0} \approx 22$ GeV. This is 1/40 of the value observed for the 2.5% most central PbPb collisions. However, since the cross sectional area of pPb collisions is much smaller than that of central PbPb collisions, this result implies that the maximum energy density in pPb collisions is comparable to that achieved in PbPb collisions [1]. Several modern generators are compared to these results but none is able to capture all aspects of the η and centrality dependence of the data [1].

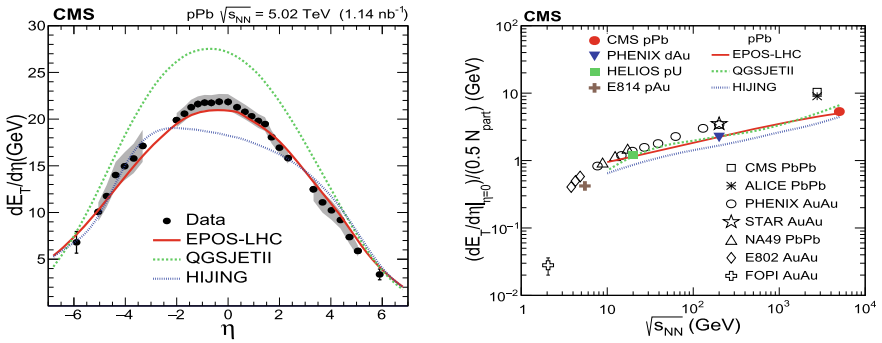

Fig. 14.1 (left) Transverse energy density versus η from minimum bias pPb collisions at $\sqrt{s_{NN}} =$ 5.02 TeV. (right) Transverse energy density per participating nucleon-nucleon pair evaluated at various $\sqrt{s_{NN}}$ for minimum bias pAu, pU, dAu, and pPb collisions [1]

14.3 Collectivity in Small Systems at the LHC

The p_{T} distributions of identified hadrons are one of the important tools to probe the collective behaviour of particle production. The p_{T} distributions in pp and pPb collisions show a clear evolution, becoming harder as the multiplicity increases [5]. As it is shown in Fig. 14.2, models including hydrodynamics describes the data better for the p_{T} spectra. Data-to-model agreement is good at higher charged particle multiplicity, N_{ch}. In addition, the evolution of the p_{T} spectra with multiplicity can be compared more directly by measuring the average transverse kinetic energy, $\langle K E_T \rangle$ [5]. If collective radial flow develops, this would result in a characteristic dependence of the shape of the transverse momentum distribution on the particle mass.

The $\langle K E_T \rangle$ for ${K_s}^0$, Λ and Ξ particles as a function of multiplicity are shown in Fig. 14.3. For all particle species, $\langle K E_T \rangle$ increases with increasing multiplicity. A theoritical Blast-wave model [6] fits have also been performed to the p_{T} spectra of strange particles in several multiplicity bins as shown in Fig. 14.2. The interpretation of the parameters of these fits, such as kinetic freeze-out temperature, T_{kin} and transverse radial flow velocity, β_T, are model dependent. In the context of the Blast-Wave model, when comparing the parameters of different systems at similar $dN_{ch}/d\eta$, it was found that β_T is larger for small systems i.e., $\beta_T(\mathrm{pp}) > \beta_T(\mathrm{pPb}) > \beta_T(\mathrm{PbPb})$. This could be an indication of a larger radial flow in small systems as a consequence of stronger pressure gradients due to a more explosive system. However, a similar decreasing trend is observed for T_{kin} and β_T as a function of multiplicity in all three collision systems.

One of the key questions about the nature of the ridge and its collectivity is whether the two-particle azimuthal correlation structures observed at large relative pseudorapidity in pp and pPb collisions result from correlations exclusively between particle pairs, or if it is a multi-particle genuine collective effect, needs to be further

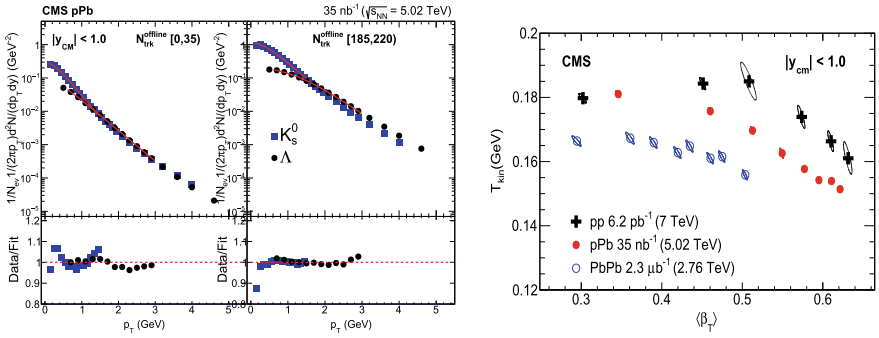

Fig. 14.2 (left) Simultaneous blast-wave fits of the p_{T} spectra of ${K_s}^0$ and Λ in low- and high-multiplicity pPb events. (right) The extracted kinetic freeze-out temperature, T_{kin}, versus the average radial-flow velocity, $\langle \beta_T \rangle$, from a simultaneous blast-wave fit to the ${K_S}^0$ and Λ p_{T} spectra at $|y_{cm}| <$ 1 for different multiplicity intervals in pp, pPb, and PbPb collisions

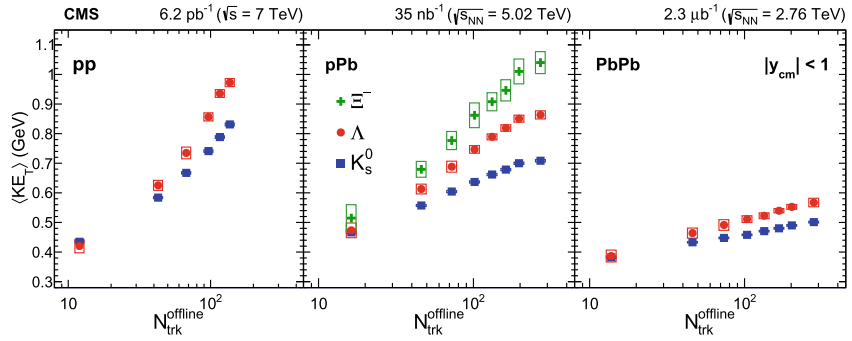

Fig. 14.3 The average transverse kinetic energy for $K_s{}^0$, Λ and Ξ particles as a function of multiplicity in pp, pPb, and PbPb collisions [5]

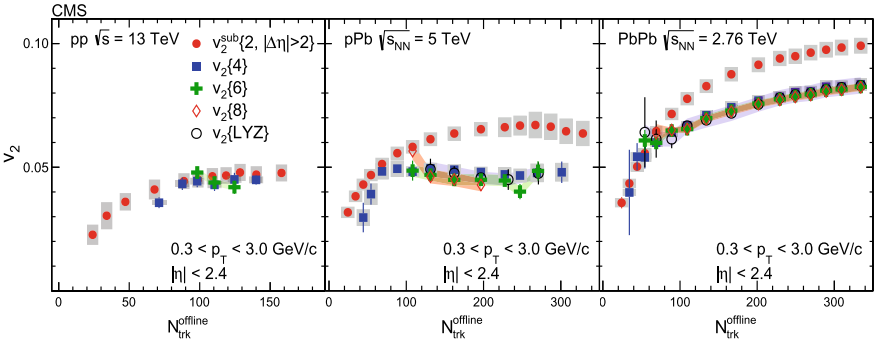

Fig. 14.4 Second-order azimuthal anisotropy Fourier harmonics, v_2 measured by CMS in pp, pPb and PbPb collisions based on multi-particle correlations [7]

understood. A strong hint for multi-particle correlations in high multiplicity pp and pPb collisions was reported by the CMS collaboration [7, 15]. Figure 14.4 shows the second-order azimuthal anisotropy Fourier harmonics (v_2) measured in pp, pPb and PbPb collisions over a wide pseudorapidity range based on correlations calculated up to eight particles. The v_2 values stay high and show similar trends in all three systems. The v_2 computed from two-particle correlations is found to be larger than that obtained with four-, six- and eight-particle correlations, as well as the Lee-Yang zeroes method. However, the v_2 obtained from multi-particle correlations, all yield to similar v_2 values i.e., $v_2\{4\} \approx v_2\{6\} \approx v_2\{8\} \approx v_2\{\text{LYZ}\}$ [7]. These observations support the interpretation of a collective origin for the observed long-range correlations in high-multiplicity pp and pPb collisions.

Another useful observable in the study of collectivity is the event-by-event correlation between Fourier harmonics of different order flow coefficients. The CMS Collaboration has measured these normalized symmetric cumulants, SC(m, n), where m and n are different order flow coefficients, in pp, pPb and PbPb collisions, as a

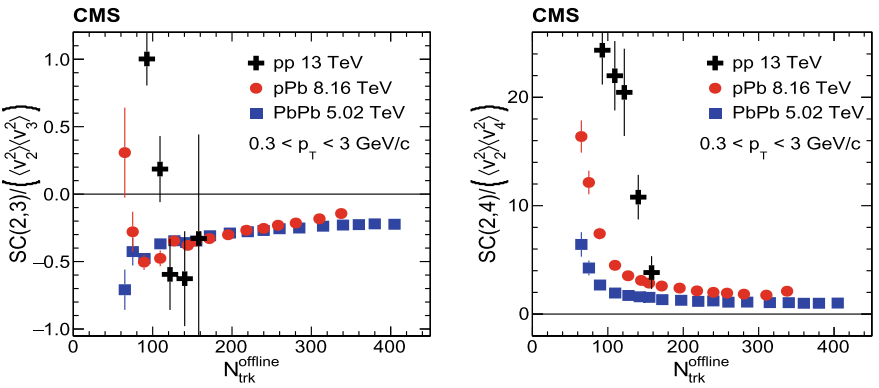

Fig. 14.5 The normalized symmetric cumulant for the second and third coefficients (left) and the second and fourth coefficients (right) are shown for pp (black cross), pPb (red circle), and PbPb (blue square). Tracks with transverse momentum between 0.3 and 3.0 GeV are used [8]

function of track multiplicity [8]. Similar observations are made in all three systems. In the case of SC(2, 3), which gauges the correlation between v_2 and v_3, an anti-correlation is found at high track multiplicity, as shown in Fig. 14.5. On the contrary, SC(2, 4) > 0: the v_2 and v_4 values are positively correlated event-by-event. Similar trends are observed in pPb and PbPb collisions, and high multiplicity pp collisions, regarding the trend of these observables as a function of track multiplicity. A long-range near-side two-particle correlation involving an identified particle is also observed [7, 9]. Results for both pPb and pp collisions are shown in Fig. 14.6. Moving to high-multiplicity events for both systems, a particle species dependence of v_2 is observed. The mass ordering of v_2 was first seen in AA collisions at RHIC

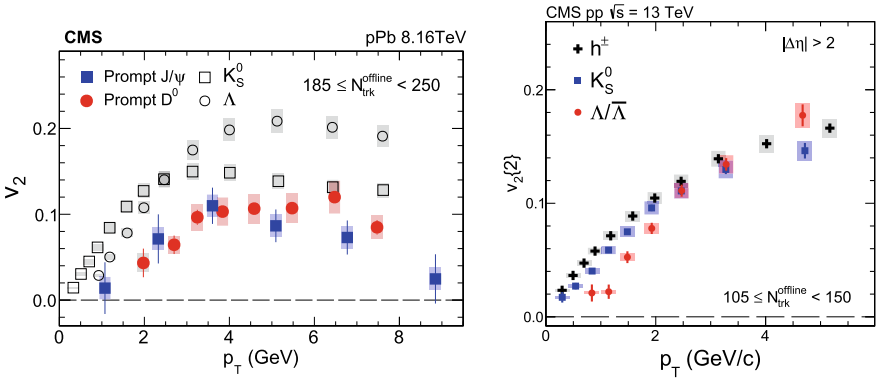

Fig. 14.6 The v_2 results for ${K_s}^0$, and Λ, prompt D^0 and prompt J/Ψ in high-multiplicity pPb (left) events. (right) The v_2 results for inclusive charged particles, ${K_s}^0$, and Λ as a function of p_T in pp collisions at $\sqrt{s} = 13$ TeV

and LHC energies [10, 11], which can be understood as the effect of radial flow pushing heavier particles towards higher p_T. This behavior is found to be qualitatively consistent with both hydrodynamic models [12] and an alternative initial state interpretation [13].

A measurement of the elliptic flow of prompt J/Ψ meson in high-multiplicity pPb collisions is reported by the CMS experiment [14]. The prompt J/Ψ results are compared with the v_2 values for open charm mesons (D^0) and strange hadrons. As shown in Fig. 14.6, positive v_2 values are observed for the prompt J/Ψ meson, as extracted from long-range two-particle correlations with charged hadrons, for $2 < p_T < 8$ GeV.

The prompt J/Ψ meson results, together with results for light-flavor and open heavy-flavor hadrons, provide novel insights into the dynamics of the heavy quarks produced in small systems that lead to high final-state multiplicities.

14.4 Conclusions

Several effects, such as mass-dependent hardening of p_{T} distributions, near-side long-range correlations, multi-particle azimuthal correlations, etc, which in nuclear collisions are typically attributed to the formation of a strongly-interacting collectively-expanding quark-gluon medium, have been observed in high-multiplicity pp and pPb collisions at the LHC. The study of small collision systems at high multiplicity is undoubtedly of considerable interest. While a lot of progress has been made towards understanding the long-range correlation phenomena in small colliding systems, there are still many open questions to be addressed by the experiemental and theoritical communities.

References

1. C.M.S. Collaboration, Phys. Rev. C **100**, 024902 (2019)
2. C.M.S. Collaboration, JINST **3**, S08004 (2008)
3. C.M.S. Collaboration, Phys. Lett. B **06**, 028 (2013)
4. C.M.S. Collaboration, Phys. Lett. B **718**, 795 (2013)
5. C.M.S. Collaboration, Phys. Lett. B **768**, 103 (2017)
6. E. Schnedermann et al., Phys. Rev. C **48**, 2462 (1993)
7. C.M.S. Collaboration, Phys. Lett. B **765**, 193 (2017)
8. C.M.S. Collaboration, Phys. Rev. Lett. **120**, 092301 (2018)
9. C.M.S. Collaboration, Phys. Rev. Lett. **121**, 082301 (2018)
10. S.T.A.R. Collaboration, Phys. Rev. C **75**, 054906 (2007)
11. PHENIX Collaboration, Phys. Rev. C **85**, 064914 (2012)
12. K. Werner et al., Phys. Rev. Lett. **112**, 232301 (2014)
13. B. Schenke et al., Phys. Rev. Lett. **117**, 162301 (2016)
14. C.M.S. Collaboration, Phys. Lett. B. **791**, 172 (2019)
15. C.M.S. Collaboration, Phys. Rev. Lett. **115**, 012301 (2015)

Chapter 15
Dark Sector Searches at the CMS Experiment

Varun Sharma

Abstract Several astrophysical observations show that about 85% of the entire universe consists of dark matter, the origin of which is unknown. Observations particularly from PAMELA, AMS, etc. have triggered light dark matter and dark sector scenarios (Adriani et al. (PAMELA Collab.) in Natue (London) 458:607, 2009, [1]). Attempts to formulate a unified theoretical framework to explain these observations have led to dark sector models. Some of the recent results for searches involving dark photons and dark-sector particles from the CMS experiment is presented Some of the recent results for searches involving dark photons and dark-sector particles from the CMS experiment is presented [2].

15.1 Introduction

Several astrophysical observations show that about 85% of the entire universe consists of dark matter, the origin of which is unknown. Observations particularly from PAMELA, AMS, etc. have triggered light dark matter and dark sector scenarios [1]. Attempts to formulate a unified theoretical framework to explain these observations have led to dark sector models. Dedicated experiments search for dark matter in the cosmos interacting directly and through annihilation. Particle colliders may also be used to search for the origin of dark matter and may provide complementary information. This paper reviews some of the recent results for searches involving dark photons and dark-sector particles from the CMS experiment.

The central feature of the CMS apparatus is a superconduction solenoid of 6 m internal diameter, providing a magnetic field of 3.8T. Within the solenoid volume are a silicon pixel and strip tracker, a lead tungstate crystal electromagnetic calorimeter,

For the CMS Collaboration.

V. Sharma (✉)
University of Wisconsin, Madison, WI, USA
e-mail: varun.sharma@cern.ch

A. Giri and R. Mohanta (eds.), *Workshop on Frontiers in High Energy Physics 2019*, Springer Proceedings in Physics 248,
https://doi.org/10.1007/978-981-15-6292-1_15

and a brass and scintillator hadron calorimeter, each composed of a barrel and two endcap sections. A more detailed description of the CMS detector can be found in [2]

15.2 Dark Photons in ZH Decays

The observation of a sizeable branching fraction of the Higgs boson to invisible or almost invisible final states would be strong sign for physics beyond the standard model (SM). A search is performed for a scalar boson H produced in association with a Z boson and decaying to an undetected particle together with a photon [3]. The analysis is based on a data set recorded by the CMS experiment in 2016–18 at a center-of-mass energy of $\sqrt{s} = 13$ TeV, corresponding to an integrated luminosity of 137 fb^{-1}.

In this search, the target final state is $\text{Z}(\rightarrow \ell\ell)\text{H}(\rightarrow \gamma\gamma_D)$, where $\ell = e, \mu$ and γ_D is a massless dark photon that couples to the Higgs boson through a charged dark sector, and is undetected in the CMS experiment. The dominant backgrounds arise from WZ and ZZ production, where an electron is mis-identified as a photon, or where additional leptons are not identified. The is significant contributions from WW, top production and small contribution from other multiboson process, such as $\text{Z}\gamma$.

Collision events for this search were collected using single-electron and single-muon trigger that require the presence of an isolated lepton (e or μ) with transverse momentum (p_T) larger than 24 and 27 GeV, respectively. The signal topology is characterized by a dilepton system ($\ell\ell$) with large p_T balanced in the transerve plane by the missing transverse energy (MET) + p_T^{γ} system from Higgs boson decay. To reject events where dilepton and photon objects are weakly correlated, transverse mass of the MET and photon system m_T must be smaller than 350 GeV. Distribution of m_T in the signal region before and after fit to data is shown in Fig. 15.1. A combination of methods based on control samples in data and simulation is used to estimate background contributions. Background contributions are categorized depending on whether they produce at least one lepton pair from the decay of a Z boson (resonant contributions) or no such lepton pair (nonresonant contributions).

The numbers of observed and expected events after applying the full selection requirements are shown in Fig. 15.2. No significant excess of events above the expectation from SM backgrounds is found. The observed and expected upper limits at 95% confidence level at $\text{m}_H = 125\,\text{GeV}$ on $\mathcal{B}(\rightarrow\text{invisible}+\gamma)$, assuming SM ZH associated production, are 4.6 and 3.6%, respectively as shown in Fig. 15.3. Allowing for deviations from SM ZH production, the product of σ_{ZH} and $\mathcal{B}(\rightarrow\text{invisible}+\gamma)$ is excluded above ~40 to ~4 fb, for m_H ranging from 125 to 300 GeV. These are the first limits on Higgs boson decays to final states that include an undetected massless dark photon.

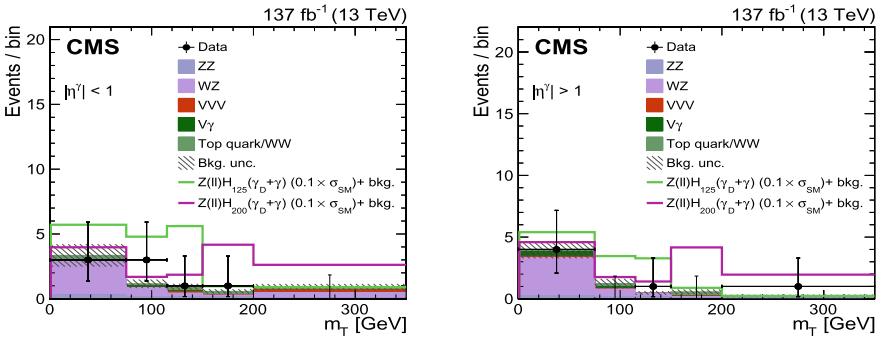

Fig. 15.1 Transverse mass distribution in the signal region for two m_H values for events with $|\eta^\gamma| < 1$ (left) and $|\eta^\gamma| > 1$ (right), after fit to data. The signal size corresponds to $0.1\sigma_{ZH}$ for both values of m_H shown

Process	Yield
Data	14
Nonresonant	2.4 ± 1.1
WZ	8.1 ± 2.0
ZZ	1.5 ± 0.3
$Z\gamma$	0.7 ± 0.7
Other	0.6 ± 0.3
Total background	13.3 ± 3.8
ZH_{125} (product of acceptance and efficiency)	17.9 ± 1.2 ($2.13 \pm 0.14\%$)
ZH_{200} (product of acceptance and efficiency)	12.3 ± 0.8 ($6.48 \pm 0.42\%$)
ZH_{300} (product of acceptance and efficiency)	3.9 ± 0.2 ($10.20 \pm 0.51\%$)

Fig. 15.2 Observed yiels, background estimates after fit to data and signal predictions after the event selection. The signal size corresponds to $0.1\sigma_{ZH}$ for all three values of m_H values shown. The values in parentheses for the signal processes correspond to the products of acceptance and selection efficiency for Z$\rightarrow \ell\ell$ events

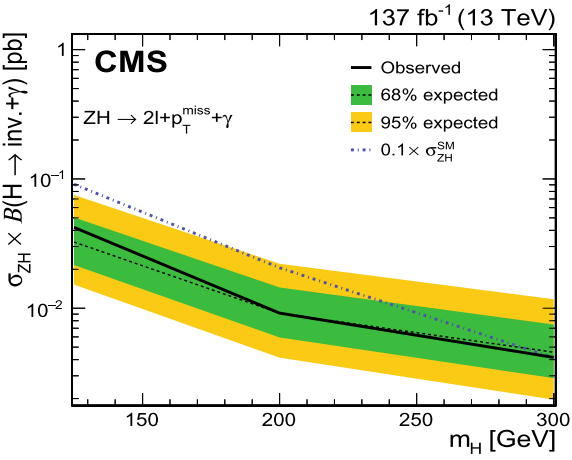

Fig. 15.3 Expected and observed upper limits at 95% CL on the product of σ_{ZH} and $\mathcal{B}$(H$\rightarrow$invisible+γ) as a function of m_H. The dot-dashed line shows the predicted signal corresponding to $0.1\sigma_{ZH}$

15.3 Emerging Jets

A search is presented for events consistent with the pair production of a heavy mediator particle that decays to a light quark and a new fermion called a dark quark, using data from proton-proton collisions at $\sqrt{s} = 13\,\text{TeV}$ corresponding to an integrated luminosity of $16.1\,\text{fb}^{-1}$ [4]. The dark quark is assumed to be charged only under a new quantum-chromodynamics-like dark force, and to form an emerging jet via a parton shower, containing long-lived dark hadrons that give rise to displaced vertices when decaying to SM hadrons.

The analysis, in particular consider the dark QCD model of Bai, Schwaller, Stolarski and Weiler (BSSW) that predicts "emerging jets" [4]. Emerging jets contain electrically charged SM particles that are produced in decays of new long-lived dark hadrons, created in a parton-shower process by dark QCD. The decay length of the lightest dark meson (dark pion) is given by

$$c\tau \approx 80\,\text{mm}\left(\frac{1}{\kappa^4}\right)\left(\frac{2\,\text{GeV}}{f_{\pi_{DK}}}\right)^2\left(\frac{100\,\text{MeV}}{m_{down}}\right)^2\left(\frac{2\,\text{GeV}}{m_{\pi_{DK}}}\right)\left(\frac{m_{X_{DK}}}{1\,\text{TeV}}\right)^4$$

where κ is the approx. element of the $N_{C_{DK}} \times 3$matrix of Yukawa couplings between the mediator particle, the quarks, and the dark quarks; $f_{\pi_{DK}}$ is the dark pion decay constant; and $m_{down}, m_{\pi_{DK}}, m_{X_{DK}}$ are the masses of the down quark, the dark pion, and the mediator particle, respectively.

The signature for this search has four high p_T jets, two from down quarks and two from dark quarks. The dark quark jets contain many displaced vertices arising from the decays of the dark pions. The main background for this search is SM four-jet production, where jet(s) are tagged as emerging either because they contain long-lived B mesons or because of track misreconstruction, and large artificial MET is created because of jet energy mismeasurement.

Events were selected if they passed a 900 GeV threshold on the scalar pT sum of all hadronic jets. An emerging jet contains multiple displaced vertices and thus multiple tracks with large impact parameters. Emerging jet candidates are required to have $|\eta| < 2.0$, corresponding to the region of the tracker where the impact parameter resolution is best. Each emerging jet candidate is required to have at least one associated track so that the impact parameter can be estimated. Four variables, defined in [4], are used to select the emerging jets. The median of the unsigned transverse impact parameters of associated tracks is correlated with the dark meson proper decay length, and should be small for SM jets and large for emerging jets. The distance between the z position of the track at its distance of closest approach to the PV and the z position of the PV is used to reject tracks from pileup vertices.

The number of events passing each selection set, along with the background expectation, are given in Fig. 15.4. The data are consistent with the expected contributions from standard model processes. Limits are set a t 95% confidence level excluding dark pion decay lengths between 5 and 225 mm for dark mediators with masses between 400 and 1250 GeV as shown in Fig. 15.5. Decay lengths smaller than

Set number	Expected	Observed	Signal	Model parameters		
				$m_{X_{DK}}$ [GeV]	$m_{\pi_{DK}}$ [GeV]	$c\tau_{\pi_{DK}}$ [mm]
1	$168 \pm 15 \pm 5$	131	36.7 ± 4.0	600	5	1
2	$31.8 \pm 5.0 \pm 1.4$	47	$(14.6 \pm 2.6) \times 10^2$	400	1	60
3	$19.4 \pm 7.0 \pm 5.5$	20	15.6 ± 1.6	1250	1	150
4	$22.5 \pm 2.5 \pm 1.5$	16	15.1 ± 2.0	1000	1	2
5	$13.9 \pm 1.9 \pm 0.6$	14	35.3 ± 4.0	1000	2	150
6	$9.4 \pm 2.0 \pm 0.3$	11	20.7 ± 2.5	1000	10	300
7	$4.40 \pm 0.84 \pm 0.28$	2	5.61 ± 0.64	1250	5	225

Fig. 15.4 Observed yields, background estimates after fit to data and signal predictions after the event selection. The signal size corresponds to $0.1\sigma_{ZH}$ for all three values of m_H values shown. The values in parentheses for the signal processes correspond to the products of acceptance and selection efficiency for Z→ $\ell\ell$ events

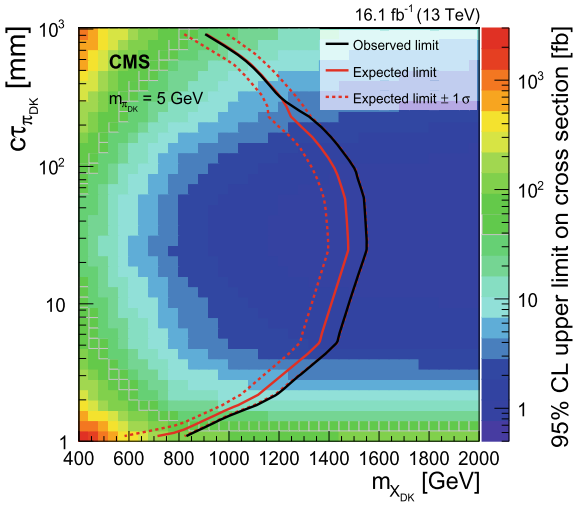

Fig. 15.5 Upper limits at 95% CL on the signal cross section and signal exclusion contours derived from theoretical cross sections for models with dark pions mass $m_{\pi_{DK}}$ of 5 GeV in the $m_{X_{DK}} - c\tau_{\pi_{DK}}$

5 and greater than 225 mm are also excluded in the lower part of this mass range. The dependence of the limit on the dark pion mass is weak for masses between 1 and 10 GeV. This analysis is the first dedicated search for the pair production of a new particle that decays to a jet and an emerging jet.

15.4 Displayed Muons

A model independent search for pair production of a light boson that decays into a pair of muons is presented. One simple example of pair production in proton-proton collisions is $pp \to h \to 2n_1 \to 2\gamma_D + 2n_D \to 4\mu + X$, where h is a Higgs boson

(either SM or non-SM), a is the new light neutral boson, and X are spectator particles that are predicted in several models [5].

Couple of benchmark models are used to design the analysis: the next-to minimal supersymmetric standard model (NMSSM) and supersymmetry (SUSY) models with hidden sectors (dark SUSY). In the dark SUSY benchmark models, breaking of a new $\mathcal{U}(1)_D$ symmetry gives rise to a massive dark photon γ_D. The lifetime, and thus the displacement of γ_D depends upon ε and the mass of the dark photon m_{γ_D}. The data used for this analysis corresponds to an integrated luminosity of 35.9 fb^{-1} of pp collisions at 13 TeV. A new trigger with increased sensitivity to displaced vertices was implemented. In addition, no cut is applied on the displacement of the muon vertex with respect to the primary vertex.

Events are selected by requiring the presence of two muons selected by the level-1 trigger, the leading muon with $p_T > 12$ GeV, the subleading muon with $p_T > 5$ GeV, and both within the tracker volume of the detector, i.e., $|\eta| < 2.4$. Each event is required to have at least four muons with $p_T > 8$ GeV (the highest one has $p_T > 15$ GeV), and $|\eta| < 2.4$, coming from

primary vertex. Dimuons are constructed from pairs of oppositely charged muons that share a common vertex. The dimuons are required to originate from the same primary vertex, $|Z_{(\mu\mu)_1} - Z_{(\mu\mu)_2}| < 0.1$ cm, where $Z_{(\mu\mu)}$ is the z position of the secondary vertex associated with the dimuon propagated back to the beamline along the dimuon direction vector. Stringent selection criterea eliminate most of the SM backgrounds with similar topology to our signal. Three SM backgrounds are found to be non-negligible: bottom quark pair production ($b\bar{b}$), prompt double J/ψ meson decays and electroweak production of four muons.

Nine events are observed in the signal region, with 7.95 ± 1.12 (stat) ± 1.45 (syst) even expected from the SM backgrounds. Their distribution in $m_{(\mu\mu)_1}$ and $m_{(\mu\mu)_2}$ is shown in Fig. 15.6. A model independent 95% confidence level upper limit on

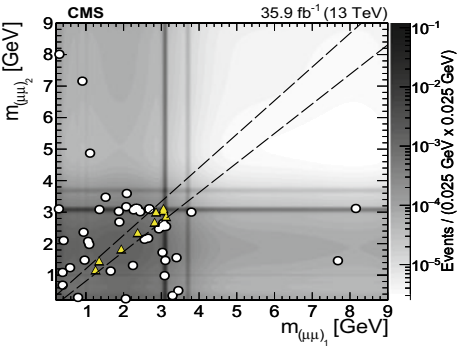

Fig. 15.6 Distribution of the invariant masses $m_{(\mu\mu)_1}$ versus $m_{(\mu\mu)_2}$ of the isolated dimuon systems; triangles represent data events passing all the selection criteria and falling in the signal region $m_{(\mu\mu)_1} \simeq m_{(\mu\mu)_2}$ (outlined by dashed lines); white bullets represent data events that pass all selection criteria but fall outside the signal region

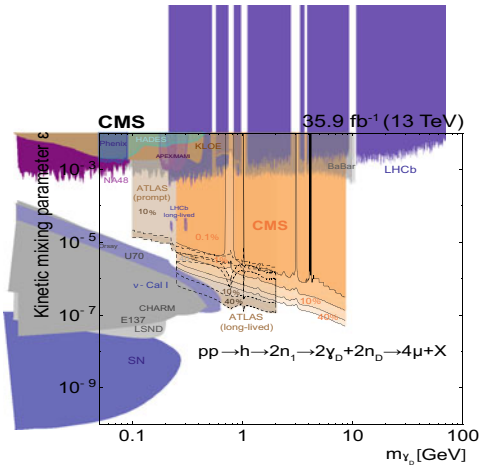

Fig. 15.7 The 90% CL upper limits (black solid curves) from this search as interpreted in the dark SUSY scenario, where the process is $pp \to h \to 2n_1 \to 2\gamma_D + 2n_D \to 4\mu + X$, with $m_{n_1} = 10\,\text{GeV}$, and $m_{n_D} = 1\,\text{GeV}$. The limits are presented in the plane of the parameters (ε and m_{γ_D}). The colored contoursfor the CMS and ATLAS limits represent different values of $\mathcal{B}(h \to 2\gamma_D + X)$ that range from 0.1 to 40%

$\sigma(h \to 2a_1) \times \mathcal{B}^2(a_1 \to 2\mu) \times A$ is set over the mass range $0.25 < m_a < 8.5\,\text{GeV}$ and is found to vary between 0.15 and 0.39 fb [5]. For dark SUSY interpretation with nonnegligible light boson lifetimes of up to $c\tau_{\gamma_D} = 100$, m_{γ_D} is contrainted from 0.25−8.5 GeV as shown in Fig. 15.7. In the context of NMSSM, the 95% CL upper limit was improved by a factor of 1.5 (3) for $m_{a_1} = 3.55(0.25)\,\text{GeV}$ over previously published limits.

15.5 Higgs Mediated

In addition to searching for evidence of the dark matter particles themselves, at colliders it is also possible to search for mediator particle decays to SM particles. Such searches are complementary to the invisible searches and are experimentally cleaner and easier to perform. If the DM particle itself is too heavy to produce or has a very weak coupling to the mediator, then searches for the mediator may be preferred to direct searches.

This section reports a search for invisible decays of a Higgs boson, using pp collision data at $\sqrt{s} = 13\,\text{TeV}$, corresponding to an integrated luminosity of $35.9\,\text{fb}^{-1}$ [6].

The search targets events when a Higgs boson is produced in association with jets from vector boson fusion (VBF). In these event, A Higgs boson is produced along with two jets that show large separation in $\Delta\eta_{jj}$ and a large dijet invariant mass (m_{jj}).

This characteristic signature allows for the suppression of SM backgrounds, making the VBF channel the most sensitive mode for invisible decays of a Higgs boson.

The signal is extracted by fitting the sum of the signal and background shapes to the binned m_{jj} distribution observed in data. The signal is expected to accumulate as an excess of events over the background at large values of mjj. The observed and

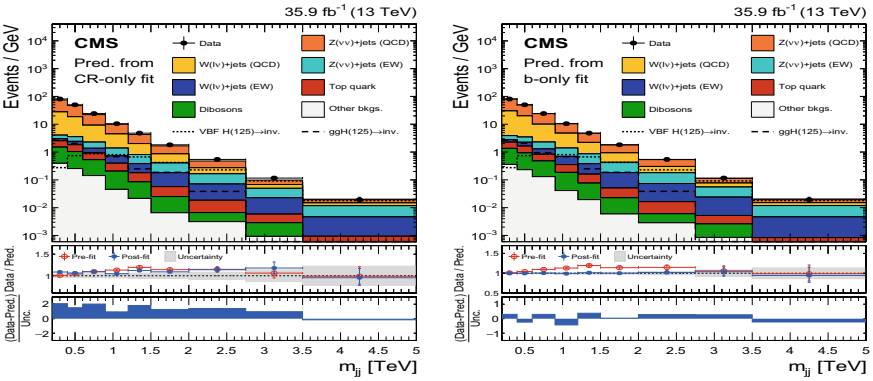

Fig. 15.8 The observed m_{jj} distribution of the shape analysis SR compared to the post-fit backgrounds from various SM processes. Predicted backgrounds obtained from data in all the CRs, excluding the SR (left), as well as in the SR (right), assuming the absence of any signal. Expected signal distributions for a 125 GeV Higgs boson ($\mathcal{B}(H \rightarrow \text{inv}) = 1$) produced through ggH and VBF modes, are overlaid

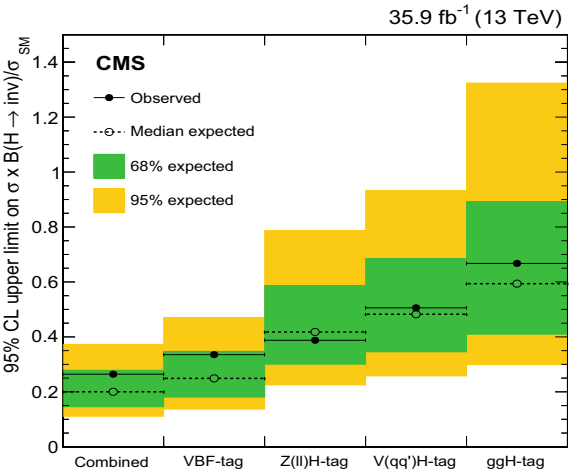

Fig. 15.9 Observed and expected 95% CL upper limits on $\sigma/\sigma_{SM}\mathcal{B}(H \rightarrow \text{inv})$ for both individual categories targeting VBF, Z($\ell\ell$)H, V(qq')H, and ggH production mode, as well as their combination

the expected m_{jj} distributions in the signal region, obtained after applying full event selection are shown in Fig. 15.8.

An observed (expected) upper limit of 0.33 (0.25) is set, at 95% CL, on $\mathcal{B}(H \rightarrow \text{inv})$, by means of a binned likelihood fit to the dijet mass distribution as shown in Fig. 15.9. A combination of across different eras, using pp collision data collected at $\sqrt{s} = 7$, 8, and 13 TeV (2015 and 2016), is also reported in Fig. 15.10. The combination yields an observed (expected) upper limit on $\mathcal{B}(H \rightarrow \text{inv})$ of 0.19 (0.15) at 95% CL.

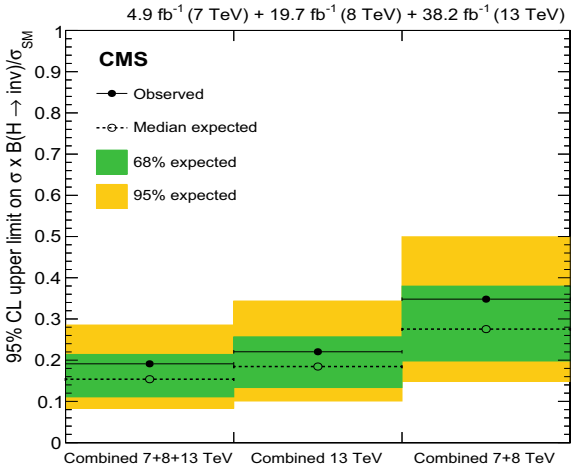

Fig. 15.10 Observed and expected 95% CL upper limits on $\sigma/\sigma_{SM}\mathcal{B}(H \rightarrow \text{inv})$ for partial combinations based either on 7+8 or 13 TeV data as well as their combinations

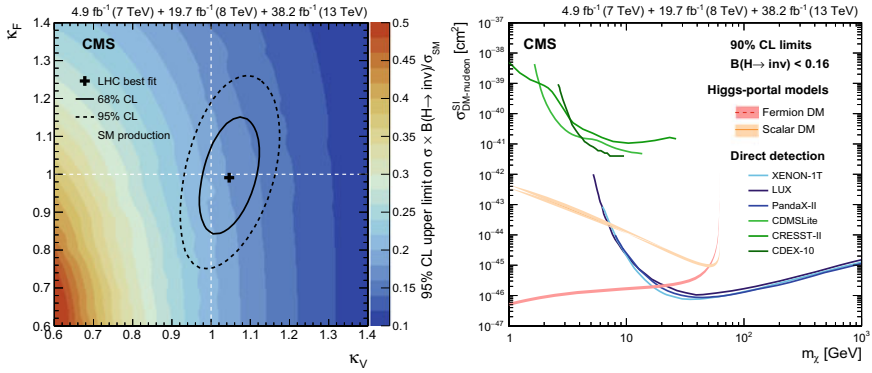

Fig. 15.11 Left: Observed 95% CL upper limits on $\sigma/\sigma_{SM}\mathcal{B}(H \rightarrow \text{inv})$ for a Higgs boson with a mass of 125.09 GeV, whose production cross section varies as a function of the coupling modifiers κ_V and κ_F. Their best estimate, along with the 68% and 95% CL contours. The SM prediction corresponds to $\kappa_V = \kappa_F = 1$. Right: 90% CL upper limits on the spin-independent DM-nucleon scattering cross section in Higgs-portal models, assuming a scalar (solid orange) or fermion (dashed red) DM candidate. Limits are computed as a function of m_χ and compared to other experiments

Constraints are placed on the spin-independent DM-nucleon interaction cross section. When compared to the upper bounds from direct detection experiments, this limit provides the strongest constraints on fermion (scalar) DM particles with masses smaller than about 18 (7) GeV as reported in Fig. 15.11.

15.6 Summary

The CMS experiment has a wide program for dark matter and dark sector searches [7]. The advanced techniques of reconstruction (displacement, timing and ionization) and triggering are used to improve sensitivity of the dark sector searches. A selection of results based on proton-proton collision data collected in Run-2 (2016–2018) has been reported.

No significant deviation with respect to standard model predictions have been found and therefore limits on dark matter masses, couplings have been set within the framework of respective models.

References

1. O. Adriani et al. (PAMELA Collab.), Natue (London) **458**, 607 (2009); M. Ackermann et al. (Fermi LAT. Collab), Phys. Rev **D82**, 092004 (2010); M. Aguilar et al. (AMS Collab.) Phys. Rev. Lett. **110**, 141102 (2013)
2. CMS collaboration, The CMS experiment at the CERN LHC. JINT **3**, S08004 (2008)
3. CMS collaboration, Search for dark photons in decays of Higgs bosons produced in association with Z bosons in proton-proton collisions at $\sqrt{s} = 13$ TeV. J. High Energ. Phys. **10**, 139 (2019). https://doi.org/10.1007/JHEP10(2019)139
4. CMS collaboration, Search for new particles decaying to a jet and an emerging jet. J. High Energ. Phys. **02**, 179 (2019). https://doi.org/10.1007/JHEP02(2019)179
5. CMS collaboration, A search for pair production of new light bosons decaying into muons in proton-proton collisions at 13 TeV. Phys. Lett. B **796**, 131 (2019). https://doi.org/10.1016/j.physletb.2019.07.013
6. CMS collaboration, Search for invisible decays of a Higgs boson produced through vector boson fusion in proton-proton collisions at $\sqrt{s} = 13$ TeV. Phys. Lett. B **793**, 520 (2019). https://doi.org/10.1016/j.physletb.2019.04.025
7. http://cms-results.web.cern.ch/cms-results/public-results/publications

Chapter 16
Dark Matter Searches at the CMS Experiment

Bhawna Gomber

Abstract The results are presented for the search for dark matter particles using data sample of proton-proton collisions at $\sqrt{s} = 13\,\text{TeV}$, collected with the CMS detector at the LHC and corresponding to an integrated luminosity of $35.9\,\text{fb}^{-1}$. Different final states with a mono-jet, mono-photon, and mono-Z signatures are considered, as well as processes with dark matter particles produced in association with a Higgs boson. The results are interpreted using the simplified models, which are then compared to the results from direct and indirect dark matter experiments.

16.1 Introduction

Several astrophysical observations [1] confirm the existence of dark matter (DM) in the universe. While, there is strong evidence for dark matter, at the moment direct observation of dark matter particles has not been confirmed. However, many theoretical models have been proposed in which DM and standard model (SM) particles interact with sufficient strength and produce DM with observable rates in high energy collisions at the CERN, LHC. In the scenario where DM would exist in the form of particles, cosmological observations strongly suggest it should be weakly interacting and massive. These Weakly Interacting Massive Particles (WIMPs) could be searched for with the CMS experiment at the CERN LHC.

The DM particles, if produced at the LHC, are not expected to leave an observable signal in the detector. However, if these particles recoil against an observable system of particles (X), they may produce a large transverse momentum imbalance (p_T^{miss}) in a collision event. This paper reviews some of the recent results for DM searches based on p_T^{miss}+X signature from the CMS experiment.

On behalf of the CMS collaboration, Supported by DST SERB.

B. Gomber (✉)
University of Hyderabad, Hyderabad, India
e-mail: bhawna.gomber@cern.ch

A. Giri and R. Mohanta (eds.), *Workshop on Frontiers in High Energy Physics 2019*, Springer Proceedings in Physics 248,
https://doi.org/10.1007/978-981-15-6292-1_16

The central feature of the CMS apparatus is a superconduction solenoid of 6 m internal diameter, providing a magnetic field of 3.8T. Within the solenoid volume are a silicon pixel and strip tracker, a lead tungstate crystal electromagnetic calorimeter, and a brass and scintillator hadron calorimeter, each composed of a barrel and two endcap sections. A more detailed description of the CMS detector can be found in [2].

Global event reconstruction follows the particle-flow (PF) algorithm [3], which aims to reconstruct and identify each individual particle in an event with an optimized combination of all subdetector information. The missing transverse momentum (p_T^{miss}) is defined as the negative vector sum of the transverse momenta of all PF candidates in an event.

16.2 Simplified Dark Matter Models

In simplified DM models, DM particles are assumed to be Dirac fermions that interact with SM particles through a spin-1 or spin-0 mediator [4]. These interactions are classified into four different types, depending on whether the mediator is a vector, axial-vector, scalar, or pseudoscalar particle. The spin-0 mediators are assumed to couple to the SM particles via Yukawa couplings. The SM Higgs boson is a specific example of a scalar mediator that may couple to the DM particles. There are 4 parameters of the Simplified Models: the dark matter mass (m_{DM}), the mediator mass (m_{med}), the strength of the coupling between mediator and SM quarks (g_q), and the strength of the coupling between the mediator and the DM particles (g_{DM}).

16.3 Monojet and Mono-V Hadronic

A search is presented for events resulting in final states with one or more energetic jets or a weak boson V which is either a W or Z boson decaying hadronically and an imbalance in p_T due to undetected particles resulting in 'monojet' and 'mono-V' final states, respectively, using data from proton-proton collisions at $\sqrt{s} = 13$ TeV corresponding to an integrated luminosity of 35.9 fb^{-1}.

Events are selected by requiring $p_T^{miss} > 200$ GeV and at least one AK4 jet jet p_T to be greater than 100 GeV in the central part of the detector $|\eta| < 2.5$. In addition events are required to have no isolated leptons, no isolated photons and no b-jets. The two categories are then distinguished by p_T and shape requirements on the jets. An event is considered to be in the mono-V category if the jet p_T is larger than 250 GeV, its invariant mass falls in the [65,105] GeV window and it has a N-subjettiness ratio τ_2/τ_1 smaller than 0.6. The N-subjettiness is a variable that catches

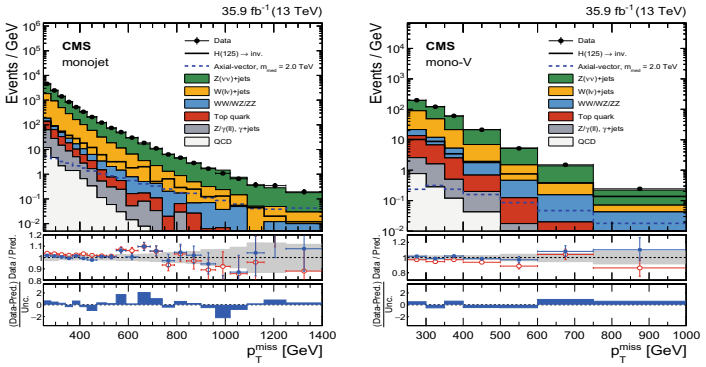

Fig. 16.1 Observed p_T^{miss} distribution in the monojet (left) and mono-V(right) signal regions compared with the post-fit background expectations for various SM processes. The last bin includes all events with $p_T^{miss} > 1250(750)$ GeV for the monojet (mono-V) category. The expected background distributions are evaluated after performing a combined fit to the data in all the control samples, not including the signal region. The fit is performed assuming the absence of any signal. Expected signal distributions for the 125 GeV Higgs boson decaying exclusively to invisible particles, and a 2 TeV axial-vector mediator decaying to 1 GeV DM particles, are overlaid. In the lower panels, ratios of data with the pre-fit background prediction (red open points) and post-fit background prediction (blue full points) are shown. The gray band in the lower panel indicates the post-fit uncertainty after combining all the systematic uncertainties. Finally, the distribution of the pulls, defined as the difference between data and the post-fit background prediction relative to the quadrature sum of the post-fit uncertainty in the prediction and statistical uncertainty in data, is shown in the lowest panel

the substructure of the jet. If the event fails the mono-V requirements, it is considered to be in the monojet category. The main backgrounds to the analysis are $Z(\nu\nu) + jets$ and $W + jets$ processes. The backgrounds are estimated using five control regions (CR) in data: dielectrons, dimuons and γ+jets (for $Z(\nu\nu)$) and single-electron and single-muon for $W + jets$.

The search is performed by extracting the signal through a combined fit of the signal and control regions. Figure 16.1 shows the p_T^{miss} distributions in the monojet and mono-V signal regions. The background prediction is obtained from a combined fit in all the control samples, excluding the signal region. Data are found to be consistent with the estimated background from the SM processes.

Upper limits are computed at 95% CL on the ratio of the measured signal cross section to the predicted one, with the CL s method [6], using the asymptotic approximation [7]. Limits are obtained as a function of the mediator mass and the DM mass. Figure 16.2 shows the exclusion contours in the m_{med} and m_{DM} plane for the vector and axial-vector mediators. Mediator masses up to 1.8 TeV, and DM masses up to 700 and 500 GeV are excluded for the vector and axial-vector models, respectively.

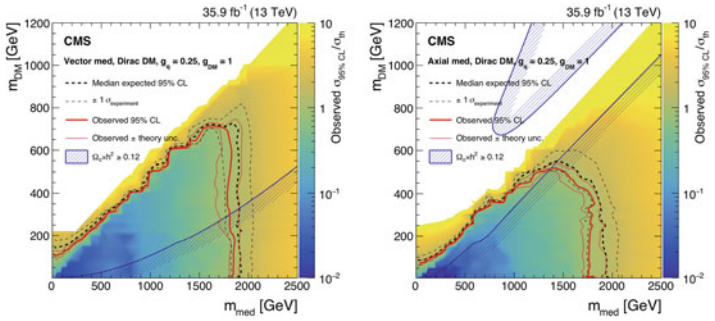

Fig. 16.2 Exclusion limits at 95% CL on μ in the m_{med} and m_{DM} plane assuming vector (left) and axial-vector (right) mediators. The solid (dotted) red (black) line shows the contour for the observed (expected) exclusion. The solid contours around the observed limit and the dashed contours around the expected limit represent one standard deviation due to theoretical uncertainties in the signal cross section and the combination of the statistical and experimental systematic uncertainties, respectively. Constraints from the Planck satellite experiment [5] are shown as dark blue contours; in the shaded area DM is overabundant

16.4 Monophoton and Mono-Z Search

The mono-photon search [8], target DM production in association with the initial state radiation of a high p_T photon. Similarly, a search is also performed in mono-Z final state, where Z bosond decays to electrons and muons. More details about mono-Z search can be found in [9].

In this search, events are selected with a high p_T photon with $p_T > 175\,\text{GeV}$ and $p_T^{miss} > 200\,\text{GeV}$. In addition events are required to have no isolated leptons, no jets. The main backgrounds to the analysis are $Z(\nu\nu) + \gamma$ and $W + \gamma$ processes. These backgrounds are estimated using four control regions (CR) in data: dielectrons, dimuons (for $Z(\nu\nu)$) and single-electron and single-muon for $W + \gamma$. This analysis also face major challenge from instrumental backgrounds i.e. spikes and beam-halo. To reject the beam halo induced EM showers, the ECAL signal in the seed crystal of the photon cluster is required to be within 3 ns of the arrival time expected for particles originating from a collision. The potential signal contribution is extracted from the data via simultaneous fits to the E_T^{γ} distributions in the signal and control regions. Predictions for $Z(\nu\nu) + \gamma$, $W + \gamma$, and the beamhalo backgrounds are varied in the fit. Beam halo is not a major background, but the extraction of its rate requires a fit to the observed distributions in the signal region. The splitting of the signal region can be thought of as a two-bin fit. Collision processes occupy the relative fractions of phase space in the horizontal (H) and vertical (V) signal regions, $C_H = 1/\pi$ and $C_V = \pi\text{-}1/\pi$, respectively.

Figure 16.3 shows the observed p_T^{miss} distribution, where data are found to be consistent with the background predictions, and hence limits are set on the DM production cross section assuming a spin-1 mediator.

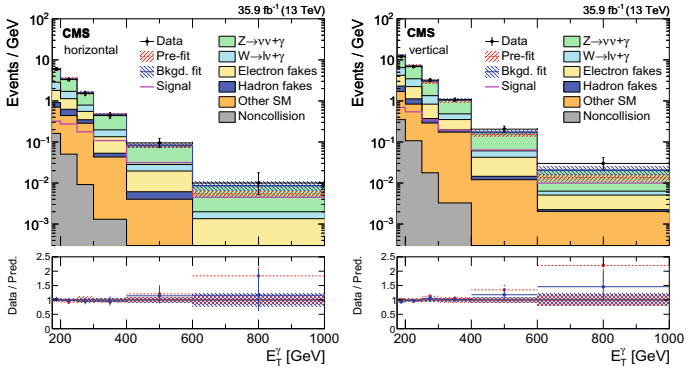

Fig. 16.3 Observed E_T^{γ} distributions in the horizontal (left) and vertical (right) signal regions compared with the post-fit background expectations for various SM processes. The last bin of the distribution includes all events with $E_T^{\gamma} > 1000\,\text{GeV}$. The expected background distributions are evaluated after performing a combined fit to the data in all the control samples and the signal region. The ratios of data with the pre-fit background prediction (red dashed) and post-fit background prediction (blue solid) are shown in the lower panels. The bands in the lower panels show the post-fit uncertainty after combining all the systematic uncertainties. The expected signal distribution from a 1 TeV vector mediator decaying to 1 GeV DM particles is overlaid

16.5 MonoHiggs

Due to the fact that the SM Higgs boson couples proportionally to the mass of the particle (Yukawa interaction), an ISR from a initial quark is not the most sensitive way to produce a mono-Higgs signature. In this final state, we consider 2 models Z'2HDM and Baryonic Z'. In Z' 2HDM model, the Z' boson is produced via a quark-antiquark interaction and then decays into a Higgs boson and a pseudoscalar mediator A, which in turn can decay to a pair of Dirac fermion DM particles χ. In Baryonic Z' model, the Z' boson acts as a DM mediator and can radiate a Higgs boson before decaying to a pair of DM particles.

The search is performed in five Higgs boson decay channels [10]: bb, $\gamma\gamma$, ZZ, $\tau\tau$ and WW. The results from the individual channels are combined to obtain the maximum sensitivity. No significant excess over the expected standard model background is observed in any of the five channels or in their combination. Limits are set on DM production in the context of two simplified models. Those channels show a nice complementarity as the bb signature has the largest branching fraction, the diphoton and di-Z signatures have the best resolution on the invariant mass of the Higgs boson and the di-τ channel has the lowest background from SM processes.

The result of the combination is shown in Fig. 16.4 for the Z'-2HDM model. It is clear that the H(bb) channel drives the limit sensitivity on most of the Z' mass range (above 700 GeV) but the other channels become competitive at lower mediator masses.

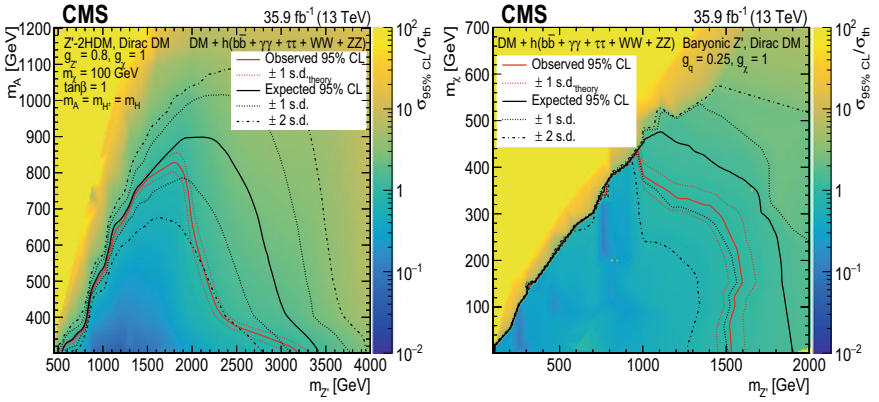

Fig. 16.4 The upper limits at 95% CL on the observed and expected σ/σ_{th} for the Z' 2HDM model (left) and Z'Baryonic model (right)

16.6 Comparison with Direct and Indirect Searches

The limits obtained from the DM searches at the LHC can be translated to limits on the DM-nucleon scattering cross section as measured by their direct detection experiments. Figure 16.5 shows the limits from the mono-Z, mono-jet and mono-γ final state for the vector and axial vector mediator case. The collider limits depend on the choice of the coupling parameters g_q and g_{DM} used in the Simplified model.

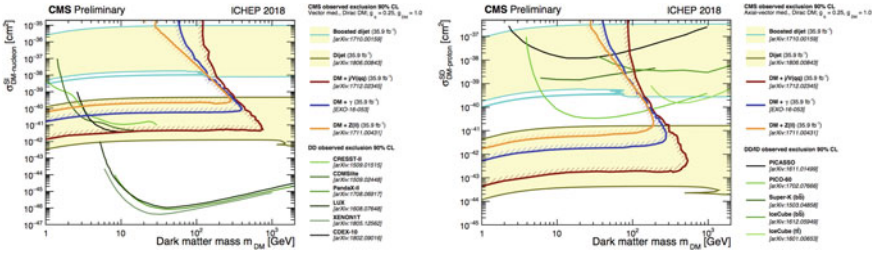

Fig. 16.5 Limits on the spin-independent DM-nucleon scattering cross section from the CMS experiment compared with the results from the direct DM detection experiments (left), and limits on the spin-dependent DM-nucleon scattering cross section from the CMS experiment compared with the results from the direct and indirect DM detection experiments (right). The CMS results are shown assuming a vector mediator and couplings, $g_q = 0.25$, and $g_{DM} = 1.0$

16.7 Summary

The CMS experiment has performed a plethora of dark matter searches [9]. A selection of results based on proton-proton collision data collected in 2016 year has been reported. No significant deviation with respect to standard model predictions have been found and therefore limits on dark matter masses and mediator masses are being set, which are further compared with direct and indirect experiments.

References

1. G. Bertone, D. Hooper, J. Silk, Particle dark matter: evidence, candidates and constraints. Phys. Rept. **405**, 279 (2005). https://doi.org/10.1146/annurev-astro-082708-101659,. arXiv:hep-ph/0404175; J.L. Feng, Dark matter candidates from particle physics and methods of detection, Ann. Rev. Astron. Astrophys. 48 (2010) 495, arXiv:1003.0904; T.A. Porter, R.P. Johnson, P.W. Graham, Dark matter searches with astroparticle data, Ann. Rev. Astron. Astrophys. **49**, 155 (2011). https://doi.org/10.1146/annurev-astro-081710-102528, arXiv:1104.2836. https://doi.org/10.1016/j.physrep.2004.08.031
2. CMS collaboration, The CMS experiment at the CERN LHC, JINT **3** S08004 (2008)
3. C.M.S. Collaboration, Particle-flow reconstruction and global event description with the CMS detector. JINST **12**, P10003 (2017). https://doi.org/10.1088/1748-0221/12/10/P10003. arXiv:1706.04965
4. O. Buchmueller, M.J. Dolan, C. McCabe, Beyond effective field theory for dark matter searches at the LHC. JHEP **01**, 025 (2014). https://doi.org/10.1103/PhysRevD.79.075020. arXiv:1308.6799; Y. Bai, J. Berger, Fermion portal dark matter, JHEP **11**, 171 (2013), arXiv:1308.0612; R. Allahverdi, B. Dutta, Natural GeV dark matter and the baryon-dark matter coincidence puzzle, Phys. Rev. D **88**, 023525 (2013), arXiv:1304.0711; J. Alwall, P. Schuster, N. Toro, Simplified models for a first characterization of new physics at the LHC, Phys. Rev. D **79**, 075020 (2009), arXiv:0810.3921
5. Planck Collaboration, Planck 2015 results. XIII. Cosmological parameters, Astron. Astrophys. **594**, A13 (2016). https://doi.org/10.1051/0004-6361/201525830, arXiv:1502.01589
6. T. Junk, Confidence level computation for combining searches with small statistics. Nucl. Instrum. Meth. A **434**, 435 (1999). https://doi.org/10.1088/0954-3899/28/10/313. arXiv:hep-ex/9902006; A. L. Read, Presentation of search results: the CLs technique, J. Phys. G 28 (2002) 2693, doi: 10.1016/S0168-9002(99)00498-2
7. G. Cowan, K. Cranmer, E. Gross, O. Vitells, Asymptotic formulae for likelihood-based tests of new physics. Eur. Phys. J. C **71**, 1554 (2011). https://doi.org/10.1140/epjc/s10052-013-2501-z]. arXiv:1007.1727. [Erratum: doi: 10.1140/epjc/s10052-011-1554-0
8. C.M.S. Collaboration, Search for new physics in final states with a single photon plus missing transverse momentum in proton-proton collisions at 13 TeV using 2016 data. JHEP **1902**, 074 (2019)
9. http://cms-results.web.cern.ch/cms-results/public-results/publications
10. CMS Collaboration, Search for dark matter particles produced in association with the Higgs boson in proton-proton collisions at 13 TeV, CMS-PAS-EXO-18-011

Chapter 17
Beyond MET: Long-Lived Particles at the LHC

Nishita Desai

Abstract Traditional searches for dark matter at the LHC rely on large missing transverse energy, or MET. I describe here, models that are inspired by co-annihilating, co-scattering or freeze-in dark matter that are not visible in MET searches, but require specialised searches to be seen. A feature of these models is the presence of a mediator particle that can be produced in large numbers at the LHC, but has a long lifetime. We therefore need a combination of different searches like displaced leptons, disappearing and heavy charged tracks to cover all interesting phase space.

17.1 Introduction

Due to the very strong implications of the presence of non-relativistic, invisible matter that pervades the Universe from astrophysical measurements a multi-pronged approach for dark matter (DM) has long been underway. Along with "direct" searches based on scattering off fixed targets and "indirect" searches that look for modification to cosmic ray spectra due to dark-matter annihilations, another possible way is to try and produce dark matter at terrestrial collision experiments like the Large Hadron Collider experiment.

The dark matter search at the LHC experiments ATLAS and CMS has matured in the nearly ten years that they have been collecting data. Initial searches were designed on the idea of an effective field theory (EFT) description of the interactions

This talk was based partly on work published in [1] (with F. Brümmer A. Bharucha) and [2] with (G. Bélanger, A. Goudelis, J. Harz, A. Lessa, J.M. No, A. Pukhov, S. Sekmen, D. Sengupta, B. Zaldivar, and J. Zurita).

N. Desai (✉)
Department of Theoretical Physics, Tata Institute of Fundamental Research, Homi Bhabha Road, Mumbai 400005, India
e-mail: nishita.desai@tifr.res.in

A. Giri and R. Mohanta (eds.), *Workshop on Frontiers in High Energy Physics 2019*, Springer Proceedings in Physics 248,
https://doi.org/10.1007/978-981-15-6292-1_17

of dark matter with quarks. While this is a very powerful method for low-energy experiments, it has been repeatedly shown that the fundamental requirement for the self-consistency of an EFT, viz that the momentum transfer be much smaller than the mass of the mediator, does not hold at LHC collision energies. The searches have therefore moved on to using "simplified models", i.e. simple UV completions of the EFT operators involving one mediator field and one DM field.

In the simplified model picture, the direct search for mediators (e.g. via di-jet and di-lepton searches) are found to give a much stronger constraint than missing energy searches for Dark Matter production. The LHC searches also provide sensitivity in the low DM-mass region which is inaccessible in direct detection due to low expected momentum-transfer. Moreover, in the case of spin-dependent interactions between DM and nucleons (which is UV completed by an axial-vector mediator), the LHC sensitivity surpasses that of direct detection experiments by several orders of magnitude.

Despite all this progress, the fact remains that we have yet to see a positive signal in any of the Dark Matter searches—direct, indirect or collider. I present here, two ideas that explain the absence of signal in all three and present two concrete models that can serve as benchmarks to design further searches. A crucial pointer to the magnitude of interactions of DM with Standard Model (SM) particles is the mechanism of achieving the right density of DM in the Universe. A well-studied and popular mechanism is via thermal freeze-out, either by direct annihilations to the SM, or annihilations in partnership with new particles (the so-called co-annihilation mechanism). Another more recent method is via "freeze-in", where the right density is achieved slowly over time, starting with a Universe with zero DM density. In both these cases, we find a large region of parameter space predicts partner particles that have a large-enough lifetime such that if they are produced at the LHC, they will decay in novel ways giving exotic signatures.

17.2 Existing Long-Lived Particle Searches

Various LLP searches are already being performed by experiments. We focus here on three kinds that we shall use to illustrate the detectability of two different Dark Matter scenarios.

17.2.1 Displaced Lepton Search

The CMS Displaced Lepton (DL) [3] search required two isolated, moderately hard leptons ($p_T > 20$ GeV) of different flavour ($e\mu$) to be present with significant impact parameter with the primary vertex to be present in the event. The search defines three signal regions—SR3 where both leptons satisfy $d_0 > 2$ mm, SR2 where either lepton

fails SR3, but both satisfy $d_0 > 1$ mm and finally SR1 where either lepton may fail SR2, but both satisfy $d_0 > 1$ mm.

Due to the very inclusive signature and very small expected SM background, the search can probe a wide range of models without prejudice, the only exception being where a compressed mass spectrum makes the leptons too soft for triggers. The first signal region is sensitive to lifetimes of LLPs as low as 0.1ns. The three signal regions being statistically independent, the upper limits are placed based on a combined likelihood defined over all three.

17.2.2 Heavy Charged Particle Search

The CMS Heavy Charged Particle (HCP) [4] search looks for a stable charged track with a long time of flight (due to lower boost) that leaves the detector. The particles are assumed to be produced via Drell–Yan process. Upper limits are provided on the cross section for masses in the range 100–800 GeV based on the charge of the particle in question.

17.2.3 Disappearing Track Search

The Disappearing Track (DT) [5, 6] search is similar to the HCP, except that the track "disappears" for exiting the tracker system. This is achieved by requiring that the track shows no hits in the outer regions of the tracker. This search is sensitive to intermediate range lifetimes of the LLP Given the dimensions of the tracker in ATLAS and CMS vary, the lifetime ranges that each experiment is sensitive to also differ.

17.3 Next-to-Minimal Dark Matter Model

A very simple calculation shows that a neutral particle with couplings and mass similar to that of Electroweak Particles naturally gives the right thermal relic density. The idea of minimal dark matter was an elegant way to ask the question: what is the minimal weakly-charged field addition that can be made to the SM such that a stable particle with the right thermal relic density can be obtained? The two viable options—an SU(2) 5-plet fermion or an SU(2) 7-plet scalar both need to be above 10 TeV in mass to satisfy the relic density requirement and will not be detectable in the near future. However, current limits on these high SU(2) multiplet particles is already several hundreds of GeV as the high multiplet implies enhanced interactions with SM gauge bosons.

We extended the idea of minimal DM to two fields instead of one, and where DM is the mixture of two states—one charged under SU(2)×U(1), one only under U(1). The presence of the non-SU(2) component allows the right relic density to be achieved for much smaller masses (of the order of 100 GeV) which will be well in range of LHC production. Moreover, it is possible for such models to simultaneously avoid direct detection limits by making the mixing parameter strong but leave the LHC production cross section untouched. Such mixed dark matter arises naturally in UV complete theories like supersymmetry and this is a more generic, model-independent formulation of the scenario. The Lagrangian for next-to-minimal dark matter with N-plet fermion ψ and singlet χ at the lowest order consists of

$$\mathcal{L} = \mathcal{L}_{\mathrm{SM}} + i\,\psi^{\dagger}\overline{\sigma}^{\mu} D_{\mu}\psi + i\,\chi^{\dagger}\overline{\sigma}^{\mu}\partial_{\mu}\chi - \left(\frac{1}{2}M\psi\psi + \frac{1}{2}m\chi\chi + \mathrm{h.c.}\right) \tag{17.1}$$

where D_{μ} is the covariant derivative with SU(2) generators appropriate to the representation of ψ. The mixing term between the N-plet and singlet state can be written in terms of a 5-dimensional operator for N = 3 and a 7-dimensional operator for N = 5

$$\mathcal{O}_{\mathrm{mix},3} = \frac{1}{\Lambda}\,(\phi^{\dagger}\phi)\psi\chi + \mathrm{h.c.} \tag{17.2}$$

$$\mathcal{O}_{\mathrm{mix},5} = \frac{1}{\Lambda^3}\,(\phi^{\dagger}\phi\phi^{\dagger}\phi)\psi\chi + \mathrm{h.c.} \tag{17.3}$$

The neutral components of the heavier, N-plet and the lighter singlet mix to form mass eigenstates we refer as $\chi_{1,2}$. We can parametrise the mixing in terms of an angle θ given by

$$\theta_3 = \sqrt{2}\frac{v^2}{\Lambda(M-m)} \tag{17.4}$$

$$\theta_5 = \sqrt{\frac{2}{3}}\frac{v^4}{\Lambda^3(M-m)} \tag{17.5}$$

The charged mass eigenstates are referred to as $\psi^{\pm(\pm)}$. Finally, the lowest order term that affects the mass splitting between the states of the N-plet are appears at dimension-7. The parameters for phenomenological study are the mass eigenstates and the mixing angle.

We find that the small mass splitting between the doubly charged $\psi^{\pm\pm}$ and singly charged $\psi^{\pm)}$ states results in a long-lived doubly charged state for the quintuplet model. Similarly, the case of a small mixing angle in the triplet model results in a long-lived $\psi^{\pm}$. The further decay of these result in leptons with significant impact parameter giving a DL signature. For longer lifetimes, the charged nature of the particles gives either a DT or HCP signature. Large portions of the parameter space can be excluded using these searches, as is shown in Fig. 17.1. Furthermore, we can also probe the breakdown of co-annihilation as the dominant mechanism of achieving

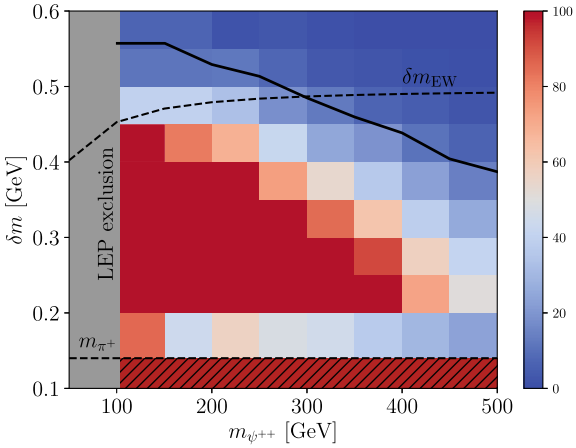

Fig. 17.1 Exclusions from the CMS displaced electron-muon pair search [7] in the $m_{\psi^{++}}$-δm plane. The dashed line corresponds to electroweak mass splitting which plateaus at 0.49 GeV. The coloured heat-map shows the value of the test statistic $\mathcal{Q}$, which is the log likelihood ratio of the signal and background. Region under solid black line (with $\mathcal{Q} > 5.99$) is excluded. The bottom hatched red area refers to limits from heavy stable charged track search whereas the grey vertical area refers to the LEP excluded region up to $m_{\psi^{++}} = 103$ GeV

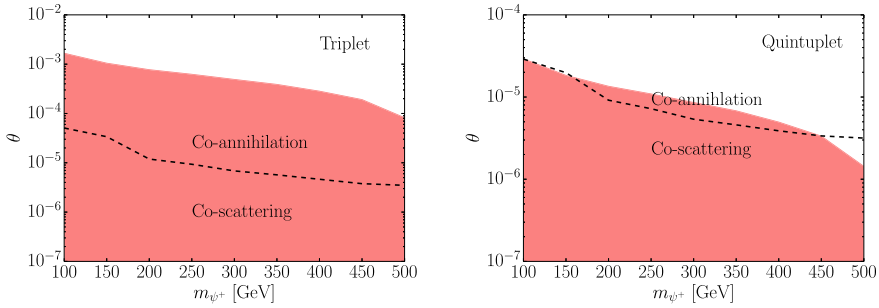

Fig. 17.2 The red shaded region shows exclusion from disappearing track search for the triplet (left) and quintuplet (right) interpreted in terms on the mixing angle θ. The dotted line corresponds to minimum values of θ required by self-consistent calculation of relic density via coannihilation

dark matter abundance as this transition coincides with lifetimes exactly in the DT region. The results from these are shown in Fig. 17.2.

17.4 Minimal Collider-Friendly Freeze-In Model

Freeze-in has recently been extensively studied as a non-thermal mechanism of DM production. One of the hallmarks of models that implement the freeze-in paradigm

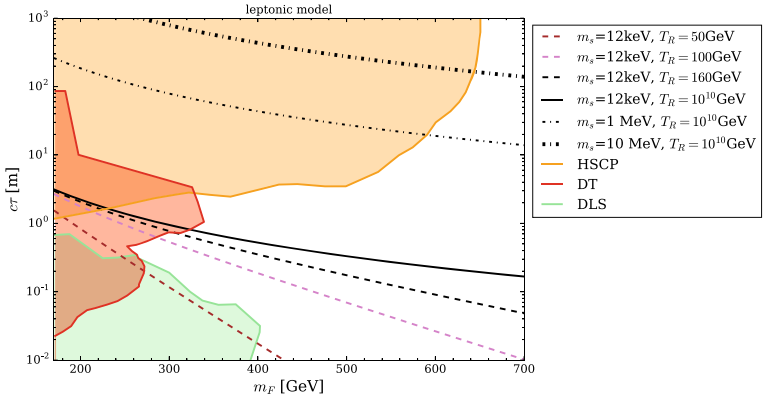

Fig. 17.3 The red shaded region shows exclusion from disappearing track search, the orange from the heavy charged particle search and the green from the displaced lepton search. The various darker lines correspond to masses of the DM particle and reheating temperatures as detailed in the figure that give the right dark matter density

is the very small interaction of the dark sector with the SM. As such, it was long believed that Freeze-in leaves no directly observable signature aside from dark matter abundance, and the dark matter particles are in turn called feebly-interacting massive particles or FIMPs. However, we find in [2], that a viable freeze-in model can be written where the FIMPs are accompanied by charged particles that can indeed be produced that the LHC. We write down a minimal model where this mechanism can be demonstrated. As the interaction of the FIMP with all SM-charged fields is required to be small, the accompanying charged particle, although produced copiously, does not decay quickly into the FIMP and becomes a LLP.

The Lagrangian of this model is as follows, with F referring to a vector like lepton, charged only under $\mathrm{U}(1)_{\mathrm{SM}}$ that couples to the right-handed SM leptons ℓ_R with corresponding Yukawa-like interaction with the scalar FIMP S, which does not carry any SM charges. We also add a Z_2 symmetry under which all new particles are charged, but SM particles are not.

$$\mathcal{L} \sim (\partial_\mu S)^2 + i\bar{F}\gamma^\mu D_\mu F - M_F \bar{F} F - (y_\ell^S S \bar{F} \ell_R + \text{h.c.}) \tag{17.6}$$

The production of E is governed by the gauge coupling whereas the decay is governed by the new Yukawa y_ℓ^s. There are of course other terms possible such as the coupling of the scalar to the Higgs etc. However, these are not relevant to the phenomenology we wish to study here. The signatures are, as before, dependent on the lifetime of the particle E and constrains can be obtained from DL, HCP and DT searches. The summary can be seen in Fig. 17.3.

17.5 Outlook

Traditional wisdom has been to look for a large missing momentum as the tell-tale sign of dark matter at the LHC. However, for a class of well-motivated models, particularly those that do not depend on the thermal freeze-out paradigm, this signature is not viable. The small couplings of these models with SM fields makes it likely that they are accompanied by other "connector" fields that are charged under SM and are naturally long-lived. We have shown how current searches for Long-lived particles can constrain such scenarios.

Two obvious gaps remain in such searches—that they require hard objects to trigger (which may be alleviated by requiring a hard initial-state radiation jet instead), and that the experimental description is such that it is still difficult for theorists to apply any but the simplest search results to their own models. Considerable study of this second problem has been done and recommendations published in the Long-Lived Particle Community Whitepaper [8].

References

1. A. Bharucha, F. Brũmmer, N. Desai, Next-to-minimal dark matter at the LHC. JHEP **11**, 195 (2018)
2. G. Bélanger et al., LHC-friendly minimal freeze-in models. JHEP **02**, 186 (2019)
3. CMS Collaboration, Search for displaced leptons in the e-mu channel (2016)
4. CMS Collaboration, Search for heavy stable charged particles with 12.9 fb^{-1} of 2016 data (2016)
5. M. Aaboud et al., Search for long-lived charginos based on a disappearing-track signature in pp collisions at $\sqrt{s} = 13$ TeV with the ATLAS detector. JHEP **06**, 022 (2018)
6. A.M. Sirunyan et al., Search for disappearing tracks as a signature of new long-lived particles in proton-proton collisions at $\sqrt{s} = 13$ TeV. JHEP **08**, 016 (2018)
7. V. Khachatryan et al., Search for displaced supersymmetry in events with an electron and a muon with large impact parameters. Phys. Rev. Lett. **114**(6), 061801 (2015)
8. J. Alimena et al., Searching for long-lived particles beyond the standard model at the large Hadron Collider (2019)

Chapter 18
UV Origin of Discrete Symmetries

Michael Ratz

Abstract We discuss the possible UV origin of discrete symmetries. We review the (i) interpretation of discrete R symmetries as discrete remnants of the Lorentz group; (ii) additional discrete transformations arising in orbifold compactifications, some of which have only been found recently; (iii) the stringy/gauge origin of family symmetries; (iv) $\mathcal{CP}$ violation from strings. These notes are based on an invited talk by the author at FHEP 2019 in Hyderabad.

18.1 Discrete Symmetries in Particle Physics

Discrete symmetries play a key role in our understanding of particle physics. The perhaps most prominent examples are the discrete transformations $\mathcal{C}$, $\mathcal{P}$ and $\mathcal{T}$. There are many more examples such as the matter parity in supersymmetric models (a.k.a. R parity), and the left–right parity of left–right symmetric and Pati–Salam models. In addition, attempts to solve the flavor puzzle often utilize discrete symmetries.

This raises several questions. How reliable are these symmetries? Are they also symmetries of the quantum theory? Our current understanding strongly suggests that all discrete symmetries need ultimately to be gauged [1]. Therefore it is imperative to seek a better understanding of the UV origin of discrete symmetries.

Mathematically all continuous gauge symmetries entail extra dimensions. That is, they correspond to "movements" along the fiber of a fiber bundle. Moreover, in strings e.g. the heterotic $E_8 \times E_8$ may be thought of being the result of 16 extra dimensions compactified on a Narain lattice [2]. These observations suggest that one may obtain a similar understanding (or interpretation) of discrete symmetries.

The original version of this chapter was revised: The corrections have been incorporated throughout the chapter. The correction to this chapter is available at https://doi.org/10.1007/978-981-15-6292-1_62

M. Ratz (✉)
Department of Physics and Astronomy, University of California, Irvine, CA 92697–4575, USA
e-mail: mratz@uci.edu

A. Giri and R. Mohanta (eds.), *Workshop on Frontiers in High Energy Physics 2019*, Springer Proceedings in Physics 248, https://doi.org/10.1007/978-981-15-6292-1_18

An obvious option is to obtain discrete symmetries by breaking a continuous gauge symmetry (spontaneously) to a discrete subgroup. The emerging discrete symmetry is then clearly gauged. This breaking can occur by a field acquiring a vacuum expectation value (VEV), or by compactification, which is also a spontaneous breaking (if done consistently), just not in four dimensions.

18.2 Discrete Symmetries to Complete the MSSM

Let us start with a discussion of the role of discrete symmetries in the context of the minimal supersymmetric extension of the standard model (MSSM). Discrete R symmetries are instrumental for supersymmetric phenomenology. To see this, consider the most general superpotential that is consistent with the standard model gauge symmetries up to dimension 5,

$$\begin{aligned}\mathscr{W}_{\text{gauge invariant}} \;=\; & \mu\, \boldsymbol{h}_d \boldsymbol{h}_u + \kappa_i\, \boldsymbol{\ell}_i \boldsymbol{h}_u \\ & + Y_e^{gf}\, \boldsymbol{\ell}_g \boldsymbol{h}_d \boldsymbol{e}_f^{\mathcal{C}} + Y_d^{gf}\, \boldsymbol{q}_g \boldsymbol{h}_d \boldsymbol{d}_f^{\mathcal{C}} + Y_u^{gf}\, \boldsymbol{q}_g \boldsymbol{h}_u \boldsymbol{u}_f^{\mathcal{C}} \\ & + \lambda_{gfk}\, \boldsymbol{\ell}_g \boldsymbol{\ell}_f \boldsymbol{e}_k^{\mathcal{C}} + \lambda'_{gfk}\, \boldsymbol{\ell}_g \boldsymbol{q}_f \boldsymbol{d}_k^{\mathcal{C}} + \lambda''_{gfk}\, \boldsymbol{u}_g^{\mathcal{C}} \boldsymbol{d}_f^{\mathcal{C}} \boldsymbol{d}_k^{\mathcal{C}} \\ & + \kappa_{gf}\, \boldsymbol{h}_u \boldsymbol{\ell}_g \boldsymbol{h}_u \boldsymbol{\ell}_f + \kappa^{(1)}_{gfk\ell}\, \boldsymbol{q}_g \boldsymbol{q}_f \boldsymbol{q}_k \boldsymbol{\ell}_\ell + \kappa^{(2)}_{gfk\ell}\, \boldsymbol{u}_g^{\mathcal{C}} \boldsymbol{u}_f^{\mathcal{C}} \boldsymbol{d}_k^{\mathcal{C}} \boldsymbol{e}_\ell^{\mathcal{C}} \;. \end{aligned} \tag{18.1}$$

Here, the boldface math letters represent the MSSM superfields in a suggestive convention. The κ_i terms in the first line have to vanish, or at least to be very small. The so–called μ parameter needs to be roughly of the order of the electroweak scale, and will be discussed below in more detail. The couplings in the second line need to be all present since they are (up to threshold corrections and multiplication by the ratio of Higgs VEVs $\langle \boldsymbol{h}_u \rangle / \langle \boldsymbol{h}_d \rangle$) given by the Yukawa couplings of the standard model. On the other hand, the terms in the third line need to vanish or to be very small.[1] All the κ_i, λ_{gfk}, λ'_{gfk} and λ''_{gfk} terms may be forbidden by imposing R parity [3].[2] This raises the question of where this $\mathbb{Z}_2$ symmetry, which we will denote $\mathbb{Z}_2^{\mathcal{M}}$ in the following, comes from. What is more, and what is sometimes not appreciated very much, $\mathbb{Z}_2^{\mathcal{M}}$ is *not* the full story. Rather, some of the $\kappa^{(i)}_{gfk\ell}$ terms in the last line need to be suppressed as much as $\lesssim 10^{-8}/M_{\text{P}}$ [5]. On the other hand, the $\kappa_{gf}\, \boldsymbol{h}_u \boldsymbol{\ell}_g \boldsymbol{h}_u \boldsymbol{\ell}_f$ term is the so–called Weinberg operator, and the leading candidate for an operator that gives rise to realistic, suppressed neutrino masses.

This raises the question of how one can control the dangerous operators while keeping the desired ones. It turns out that, under arguably rather moderate assumptions, the choices are highly restricted. In detail, let us make the following assumptions and requirements:

1. SO(10) unification of matter is not an accident;
2. the μ term is forbidden by a symmetry but appears after SUSY breaking;
3. want to preserve gauge coupling unification;

[1] One may allow one of the λ_{gfk}, λ'_{gfk} or λ''_{gfk} to be relatively unsuppressed.

[2] Despite its name, this symmetry is not a true R symmetry, but equivalent to matter parity [4].

Table 18.1 $\mathbb{Z}_4^R$ charges

	q	u^C	d^C	ℓ	e^C	h_u	h_d	ν^C
$\mathbb{Z}_4^R$	1	1	1	1	1	0	0	1

4. standard model Yukawa couplings and Weinberg operator are allowed.

It turns out that, under these assumptions, the symmetry is unique [6, 7]: it is an order four R symmetry, $\mathbb{Z}_4^R$, which has been first proposed in [8].[3] The charge assignment is very simple, see Table 18.1.

They are obviously consistent with SO(10) grand unification, where matter fields sit in one irreducible representation, the **16**–plet, and the Higgs fields come from the **10**–plet.

It is instructive to see how anomaly matching [10, 11] works for $\mathbb{Z}_4^R$, or, more generally, $\mathbb{Z}_M^R$ symmetries. Assume you start from a unified gauge group, SU(5) or higher. Then, at this level there is only one anomaly coefficient,

$$A_{\mathrm{SU}(5)^2-\mathbb{Z}_M^R} = A^{\mathrm{matter}}_{\mathrm{SU}(5)^2-\mathbb{Z}_M^R} + A^{\mathrm{extra}}_{\mathrm{SU}(5)^2-\mathbb{Z}_M^R} + 5q_\theta \ , \tag{18.2}$$

where $A^{\mathrm{matter}}_{\mathrm{SU}(5)^2-\mathbb{Z}_M^R}$ is the contribution from the matter fields, $A^{\mathrm{extra}}_{\mathrm{SU}(5)^2-\mathbb{Z}_M^R}$ a possible extra contribution, and $5q_\theta$ the contribution from the gauginos.[4] Now assume some mechanism breaks SU(5) (or larger) down to the standard model gauge symmetry $G_{\mathrm{SM}} = \mathrm{SU}(3)_C \times \mathrm{SU2}_{\mathrm{L}} \times \mathrm{U}(1)_Y$. Then the anomaly coefficients become

$$A^{\mathrm{SU}(5)}_{\mathrm{SU}(3)^2-\mathbb{Z}_M^R} = A^{\mathrm{matter}}_{\mathrm{SU}(3)^2-\mathbb{Z}_M^R} + A^{\mathrm{extra}}_{\mathrm{SU}(3)^2-\mathbb{Z}_M^R} + 3q_\theta + g2\frac{1}{2}\cdot 2\cdot 2\cdot q_\theta \ , \tag{18.3a}$$

$$A^{\mathrm{SU}(5)}_{\mathrm{SU}(2)^2-\mathbb{Z}_M^R} = A^{\mathrm{matter}}_{\mathrm{SU}(2)^2-\mathbb{Z}_M^R} + A^{\mathrm{extra}}_{\mathrm{SU}(2)^2-\mathbb{Z}_M^R} + 2q_\theta + g4\frac{1}{2}\cdot 2\cdot 3\cdot q_\theta \ . \tag{18.3b}$$

Here we have kept but crossed out the contributions from the extra gauginos which are in SU(5) but not G_{SM} (and which are sometimes called X and Y bosons). We see that if something breaks SU(5) down to G_{SM}, and removes the contributions from the extra gauginos, due to anomaly matching we need to have massless fields that do not come in complete GUT representations. That is, 't Hooft anomaly matching for (discrete) R symmetries implies the presence of split multiplets below the GUT scale!

Where can such R symmetries come from? It can be shown with elementary group–theoretical methods that they can *not* arise from 4–dimensional models of grand unification [12]. In more detail, assuming (i) a GUT model in four dimensions based on $G \supset \mathrm{SU}(5)$, (ii) GUT symmetry breaking is spontaneous, and (iii) there is

[3] The fact that only R symmetries can forbid the μ term has been motivated in [9].

[4] Our conventions are such that the superpotential has R charge 2.

only finite number of fields, one can show that one either has to break the R symmetry at the high scale, or has light exotic charged states.

What does light mean? Light means of the order of R symmetry breaking. Why and how is the R symmetry broken? R symmetries are necessarily broken because, in order to warrant an almost vanishing vacuum energy, the superpotential needs to acquire a VEV. This VEV determines the gravitino mass,

$$\langle \mathscr{W} \rangle \sim m_{3/2} M_{\rm P}^2 \quad \curvearrowright \quad m_{3/2} \sim \frac{\langle \mathscr{W} \rangle}{M_{\rm P}^2} \,. \tag{18.4}$$

However, as the superpotential carries R charge 2, there is a residual $\mathbb{Z}_2$ symmetry, which, in the case of $\mathbb{Z}_4^R$, coincides with matter parity. Let us briefly discuss the implications for the $\mathscr{W}_{\text{gauge invariant}}$ of (18.1). We see that the R parity violating couplings κ_i, λ_{gfk}, λ'_{gfk} and λ''_{gfk} are zero because of the exact residual symmetry. By construction, the standard model Yukawa couplings and Weinberg operator are allowed, and one can easily check that each of these terms carries R charge 2. What about the μ term and the $\kappa^{(i)}_{gfk\ell}$ couplings? They appear after R symmetry breaking. However, since the order parameter of R symmetry breaking is the gravitino mass, one finds that, in the framework of gravity mediation,

$$\mu \sim m_{3/2} \quad \text{and} \quad \kappa^{(i)}_{gfk\ell} \sim \frac{m_{3/2}}{M_{\rm P}^2} \ll \frac{10^{-8}}{M_{\rm P}} \,. \tag{18.5}$$

The statement on the μ term can be thought of as the Kim–Nilles [13] and Giudice–Masiero [14] mechanisms being at work, but the $\mathbb{Z}_4^R$ offers an explanation for why these are the *only* contributions.

Where can one get this $\mathbb{Z}_4^R$ from? As already mentioned, not from 4D GUTs. However, they do arise in orbifold compactifications of the heterotic string [15, 16], which we discuss in what follows.

18.3 Orbifold Compactifications of the Heterotic String

A toroidal orbifold emerges by dividing a torus by some of its non–freely acting symmetries. The resulting space is smooth everywhere except for the orbifold fixed points (cf. Fig. 18.1). In general, these fixed points are special points at which (a) the gauge symmetry gets broken (b) localized "matter" fields live. Just by looking at Fig. 18.1 it is tempting to suspect that orbifold compactifications have plenty of discrete symmetries. In fact, as we shall discuss in Sect. 18.4, additional discrete transformations arise, some of which have only been noted recently; 2. Section 18.5, family symmetries appear naturally; 3. Section 18.6, some compacifications have built–in $\mathcal{CP}$ violation. With regards to the discussion in Sect. 18.2, discrete R symmetries emerge as discrete remnants of the Lorentz group. The so–called H–momentum conservation rule [17, 18] can be interpreted as an R symmetry [19]. It turns out that it is

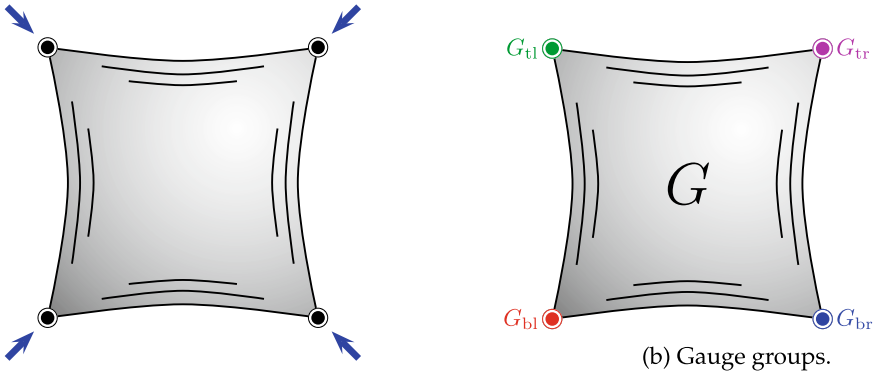

(a) Fixed points. (b) Gauge groups.

Fig. 18.1 Cartoon of an orbifold

rather straightforward to construct an explicit string model with the exact spectrum of the MSSM and a residual $\mathbb{Z}_4^R$ symmetry [20, 21]. As discussed in Sect. 18.2, this symmetry is instrumental to understand why the Higgs pair is massless prior to supersymmetry breaking. The alert reader may wonder how a discrete remnant of the Lorentz symmetry may appear anomalous. This is because some the residual symmetries in orbifolds are diagonal subgroups of the symmetries of the upstairs theory. Of course, in string theory, these anomalous looking symmetries are never really anomalies, but cancelled by the Green–Schwarz mechanism [22].

18.4 Discrete Remnants of Orbifolding

Given the phenomenological success of the orbifold models, it is imperative to carefully analyze the residual symmetries these constructions have. The standard lore used to be that the surviving symmetry consists of the transformations that commute with the orbifold action. This turns out to be not entirely correct [23].

Consider a higher–dimensional gauge theory with gauge fields $V_a^\mu(x, y)\,\mathsf{T}_a^{(\mathrm{CW})}$, where $\mathsf{T}_a^{(\mathrm{CW})}$ denote the generators in the Cartan–Weyl basis. Now compactify on an orbifold with action on the extra coordinates y and generators

$$y \overset{P}{\mapsto} \vartheta\, y \quad \text{and} \quad \mathsf{T}_a^{(\mathrm{CW})} \overset{P}{\mapsto} P\,\mathsf{T}_a^{(\mathrm{CW})}\,P^{-1}\,. \tag{18.6}$$

We demand that performing first a gauge transformation and then the orbifold transformation, or reversing the order of the operations leads to the result,

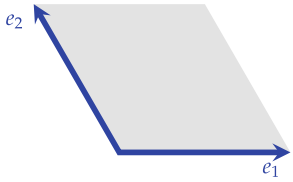

Fig. 18.2 Simple roots of SU(3)

$$\begin{array}{ccc} V_a^\mu(x,y)\,\mathsf{T}_a^{(\mathrm{CW})} & \xrightarrow{P\in O} & V_a^\mu(x,\vartheta^{-1}y)\,P\,\mathsf{T}_a^{(\mathrm{CW})}\,P^{-1} \\ \Big\downarrow{\scriptstyle U\in G} & & \Big\downarrow{\scriptstyle U\in G} \\ V_a^\mu(x,y)\,U\,\mathsf{T}_a^{(\mathrm{CW})}\,U^{-1} & \xrightarrow{P\in O} & V_a^\mu(x,\vartheta^{-1}y)\,P\,U\,\mathsf{T}_a^{(\mathrm{CW})}\,U^{-1}\,P^{-1}\,. \end{array} \tag{18.7}$$

Using Schur's lemma, this leads to the condition that $P^{-1}U^{-1}P\,U$ is in the center of the group G [23], which is weaker than the traditional condition that P commutes with U.

Note that even if one demands that P commutes with U, some important symmetries have been missed in the past, with the perhaps most important example being the so–called left–right parity or D–parity of the Pati–Salam [24] or left–right symmetric model [25],

$$[\mathrm{SU}(4)\times\mathrm{SU}(2)_\mathrm{L}\times\mathrm{SU}(2)_\mathrm{R}]\rtimes\mathbb{Z}_2\,. \tag{18.8}$$

It is known that this $\mathbb{Z}_2$ can be obtained in 4D SO(10) GUTs by giving a VEV to a **54**–plet [26, 27]. However, it has been only noted recently that this symmetry is automatically there if one breaks SO(10) by the action of a $\mathbb{Z}_2$ orbifold [23]. This symmetry illustrates a generic feature of these discrete remnants: they are typically outer automorphisms of the continuous residual gauge symmetry.

An example in which the fact that the "survival" condition is weaker than previously assumed is important in the $\mathbb{T}^2/\mathbb{Z}_3$ orbifold with an SU(3) gauge symmetry. Here the torus lattice coincides with the root lattice of SU(3) (Fig. 18.2). The associated gauge embedding is

$$P\;=\;\begin{pmatrix}\omega & 0 & 0\\ 0 & \omega^2 & 0\\ 0 & 0 & 1\end{pmatrix}\;\in\;\mathrm{SU}(3)\,, \tag{18.9}$$

where $P^3\;=\;\not\Vdash$. The condition for unbroken gauge symmetries is

$$[P,U_{(k)}]\;=\;\exp\left(\frac{2\pi\mathrm{i}\,k}{3}\right)\not\Vdash\quad\text{where}\quad k\;\in\;\{0,1,2\}\,. \tag{18.10}$$

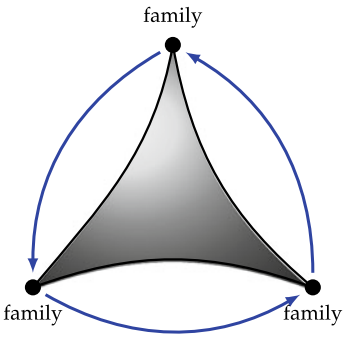

Fig. 18.3 Geometric origin of family symmetries

Therefore, the residual symmetries are

$$U_{(0)} = \begin{pmatrix} e^{i(\alpha+\beta)} & 0 & 0 \\ 0 & e^{i(\alpha-\beta)} & 0 \\ 0 & 0 & e^{-2i\alpha} \end{pmatrix} \quad \text{and} \quad U_{(1)} = \begin{pmatrix} 0\,0\,1 \\ 1\,0\,0 \\ 0\,1\,0 \end{pmatrix} . \tag{18.11}$$

So $\mathrm{SU}(3) \xrightarrow{\mathbb{Z}_3^{\mathrm{orb.}}} \Big[\mathrm{U}(1) \times \mathrm{U}(1)\Big] \rtimes \mathbb{Z}_3$. The explanation of the additional $\mathbb{Z}_3$ factor in terms of gauge symmetries completes the analysis by Beye et al. [28, 29], who explore the gauge origin of family symmetries in string theory. Away from the critical radius R_{crit} the U(1) symmetries get broken to $\mathbb{Z}_3$ subgroups such that

$$\mathrm{SU}(3) \xrightarrow{\mathbb{Z}_3^{\mathrm{orb.}}} \Big[\Big[\mathrm{U}(1) \times \mathrm{U}(1)\Big] \rtimes \mathbb{Z}_3\Big] \rtimes \mathbb{Z}_2 \xrightarrow{R \neq R_{\mathrm{crit}}} \Big[\Big[\mathbb{Z}_3 \times \mathbb{Z}_3\Big] \rtimes \mathbb{Z}_3\Big] \rtimes \mathbb{Z}_2 = \Delta(54) .$$

The $\mathbb{Z}_2$ factor is the outer automorphism of SU(3). This explicitly demonstrates the gauge origin of the full $\Delta(54)$ flavor symmetry. This will be discussed in more detail elsewhere.

18.5 Family Symmetries

As discussed in the previous section, family symmetries can arise from orbifolding. In fact, they arise very naturally in heterotic orbifolds [30, 31]. One way to understand how whey arise is to look at the geometry of compact space. As illustrated in Fig. 18.3 for the $\mathbb{Z}_3$ orbifold plane, the repetition of families may be related to the geometrical properties of the orbifold such as the existence of equivalent fixed points. It is then not too surprising that certain permutation symmetries arise. To obtain the full symmetry group, one has to work a bit harder. In general, they are obtained as the outer automorphism group of the space group [32, 33]. Even though the discussion at the end of Sect. 18.4 only concerns the $\Delta(54)$ symmetry, it strongly

suggests that all the other flavor symmetries derived from string compactifications originate completely from gauge symmetries.

In what follows, we will discuss that the string–derived $\Delta(54)$ symmetry has another, rather surprising property.

18.6 $\mathcal{CP}$ Violation from Strings

It has been pointed out that there is a deep, group–theoretical connection between flavor symmetries and $\mathcal{CP}$ violation [34]. Certain discrete groups clash with $\mathcal{CP}$ conservation [34, 35] (see [36] for a recent review). There are simple group–theoretic indicators that allow one to tell $\mathcal{CP}$–violating groups from those which are consistent with $\mathcal{CP}$ apart [35]. All odd order non–Abelian finite groups clash with $\mathcal{CP}$, yet there are also even–order groups of that type, and intererestingly the above–mentioned $\Delta(54)$ symmetry belongs to this class.

As discussed above, the $\Delta(54)$ flavor symmetry emerges from the $\mathbb{Z}_3$ orbifold plane. Already the very first string–derived 3–generation models [37] have this symmetry (although this has not been spelled out at the time when these models were found), so this is not at all an exotic property. One therefore expects that these models have a built–in means of $\mathcal{CP}$ violation, which has been confirmed in [38]. That is, these flavor symmetries, which have been explicitly shown to be gauged and can be understood as outer automorphisms of the so–called space group, "destroy" $\mathcal{CP}$, an outer automorphism of the Lorentz group.

18.7 Summary

Given all the strong arguments that all symmetries, including discrete ones, need to be gauged, in these proceedings we studied to which extent this is the case the discrete symmetries in string compactifications. While this is straightforward to see for most of the discrete symmetries, it is a bit harder to make this explicit for flavor symmetries. Only after a recent careful reanalysis of the residual symmetries of orbifolding the gauge origin of all symmetry factors could be established.

Altogether we have reviewed the conceivable roles of explicitly string–derived discrete symmetries in physics beyond the standard model. In particular:

1. Discrete R symmetries can be understood as discrete remnants of the Lorentz symmetry of compact space. They appear to be instrumental to solve the problems of supersymmetric extensions of the standard model.
2. There are symmetries after orbifolding that have been missed until recently. These symmetries comprise the left–right parity of left–right symmetric and Pati–Salam models, and other outer automorphism symmetries of the low–energy continuous gauge group.

3. Discrete flavor symmetries can be completely traced back to continuous gauge symmetries in higher dimensions. They also provide a possible origin of $\mathcal{CP}$ violation.

Acknowledgements Big thanks go to the organizers of FHEP 2019 for putting together such nice conference, and to Patrick Vaudrevange for comments. This work is supported by NSF Grant No. PHY-1719438.

References

1. E. Witten, Nature Phys. **14**, 116 (2018), arXiv:1710.01791 [hep-th]
2. K.S. Narain, Phys. Lett. **169B**, 41 (1986)
3. P. Fayet, Phys. Lett. B **69**, 489 (1977)
4. S. Dimopoulos, S. Raby, F. Wilczek, Phys. Lett. B **112**, 133 (1982)
5. I. Hinchliffe, T. Kaeding, Phys. Rev. D **47**, 279 (1993)
6. H.M. Lee, S. Raby, M. Ratz, G.G. Ross, R. Schieren, et al. Phys. Lett. **B694**, 491 (2011), arXiv:1009.0905 [hep-ph]
7. H.M. Lee, S. Raby, M. Ratz, G.G. Ross, R. Schieren, et al., Nucl. Phys. **B850**, 1 (2011).arXiv:1102.3595 [hep-ph]
8. K. Babu, I. Gogoladze, K. Wang, Nucl. Phys. **B660**, 322 (2003), arXiv:hep-ph/0212245 [hep-ph]
9. L.J. Hall, Y. Nomura, A. Pierce, Phys. Lett. **B538**, 359 (2002), arXiv:hep-ph/0204062
10. G. 't Hooft, Phys. Rev. Lett. **37**, 8 (1976)
11. C. Csáki, H. Murayama, Nucl. Phys. **B515**, 114 (1998), arXiv:hep-th/9710105
12. M. Fallbacher, M. Ratz, P.K. Vaudrevange, Phys. Lett. **B705**, 503 (2011), arXiv:1109.4797 [hep-ph]
13. J.E. Kim, H.P. Nilles, Phys. Lett. B **138**, 150 (1984)
14. G. Giudice, A. Masiero, Phys. Lett. B **206**, 480 (1988)
15. L.J. Dixon, J.A. Harvey, C. Vafa, E. Witten, Nucl. Phys. B **261**, 678 (1985)
16. L.J. Dixon, J.A. Harvey, C. Vafa, E. Witten, Nucl. Phys. B **274**, 285 (1986)
17. S. Hamidi, C. Vafa, Nucl. Phys. B **279**, 465 (1987)
18. L.J. Dixon, D. Friedan, E.J. Martinec, S.H. Shenker, Nucl. Phys. B **282**, 13 (1987)
19. T. Kobayashi, S. Raby, R.-J. Zhang, Nucl. Phys. **B704**, 3 (2005), arXiv:hep-ph/0409098
20. R. Kappl, B. Petersen, S. Raby, M. Ratz, R. Schieren, P.K. Vaudrevange, Nucl. Phys. **B847**, 325 (2011), arXiv:1012.4574 [hep-th]
21. M.-C. Chen, M. Fallbacher, M. Ratz, Mod. Phys. Lett. **A27**, 1230044 (2012), arXiv:1211.6247 [hep-ph]
22. M.B. Green, J.H. Schwarz, Phys. Lett. B **149**, 117 (1984)
23. S. Biermann, A. Mütter, E. Parr, M. Ratz, P.K.S. Vaudrevange, Phys. Rev. **D100**(6), 066030 (2019), arXiv:1906.10276 [hep-ph]
24. J.C. Pati, A. Salam, Phys. Rev. **D10**, 275 (1974) [Erratum: Phys. Rev. D **11**, 703 (1975)]
25. R.N. Mohapatra, G. Senjanovic, Phys. Rev. Lett. **44**, 912 (1980)
26. T.W.B. Kibble, G. Lazarides, Q. Shafi, Phys. Rev. D **26**, 435 (1982)
27. D. Chang, R.N. Mohapatra, M.K. Parida, Phys. Rev. Lett. **52**, 1072 (1984)
28. F. Beye, T. Kobayashi, S. Kuwakino, Phys. Lett. **B736**, 433 (2014), arXiv:1406.4660 [hep-th]
29. F. Beye, T. Kobayashi, S. Kuwakino, JHEP **03**, 153 (2015), arXiv:1502.00789 [hep-ph]
30. T. Kobayashi, H.P. Nilles, F. Plöger, S. Raby, M. Ratz, Nucl. Phys. **B768**, 135 (2007), arXiv:hep-ph/0611020
31. H.P. Nilles, M. Ratz, P.K. Vaudrevange, Fortsch. Phys. **61**, 493 (2013), arXiv:1204.2206 [hep-ph]

32. H.P. Nilles, S. Ramos-Sánchez, M. Ratz, P.K. Vaudrevange, Phys. Lett. **B726**, 876 (2013), arXiv:1308.3435 [hep-th]
33. A. Baur, H. P. Nilles, A. Trautner, and P. K. S. Vaudrevange, arXiv:1901.03251 [hep-th]
34. M.-C. Chen, K. Mahanthappa, Phys. Lett. **B681**, 444 (2009). arXiv:0904.1721 [hep-ph]
35. M.-C. Chen, M. Fallbacher, K. Mahanthappa, M. Ratz, A. Trautner, Nucl. Phys. **B883**, 267 (2014), arXiv:1402.0507 [hep-ph]
36. M.-C. Chen, M. Ratz, arXiv:1903.00792 [hep-ph]
37. L.E. Ibáñez, J.E. Kim, H.P. Nilles, F. Quevedo, Phys. Lett. B **191**, 282 (1987)
38. H.P. Nilles, M. Ratz, A. Trautner, P.K.S. Vaudrevange, arXiv:1808.07060 [hep-th]

Chapter 19
Pathways to Unification with Vector Like Fermions

Biplob Bhattacherjee, Ashwani Kushwaha, Pritibhajan Byakti, and Sudhir K. Vempati

Abstract We present a minimal extensions of Standard Model with TeV scale vector like fermions which leads to unification of gauge couplings. Model has been constraints from proton decay, Higgs stability and perturbativity. The simplest models contain copies of vector like fermions in two different (incomplete) representations. Some models enclose SU(2) triplet, Type III seesaw mechanism for neutrino masses whereas some others have a dark matter candidate. In all the models, at least one of the candidates has non-trivial representation under $SU(3)_{color}$. In the limit of vanishing Yukawa couplings, new QCD bound states are formed, which can be probed at LHC. The present limits based on results from 13 TeV already probe these particles for masses around a TeV.

19.1 Introduction

Grand Unification the one of the elegant solutions which could explain the hierarchy between the strong, weak and electromagnetic forces. The three separate gauge couplings unify in to a single one at some high scale $\sim 10^{(15-16)}$ GeV; a single gauge group like $SU(5)$ would suffice to explain all the three interactions at those scales. GUTs (Grand Unified theories) have been very popular due to various other features they predicted like proton decay, fermion mass relations including top-bottom yukawa unification, charge quantisation, weak mixing angle etc. It has been noticed

B. Bhattacherjee · A. Kushwaha · P. Byakti · S. K. Vempati (✉)
Centre for High Energy Physics, Indian Institute of Science, C. V. Raman Avenue, Bangalore 560012, India
e-mail: vempati@iisc.ac.in

A. Kushwaha
INFN-Sezione di Napoli, Complesso Universitario di Monte S. Angelo, Via Cintia Edificio 6, 80126 Napoli, Italy

P. Byakti
Department of Physics, Pandit Deendayal Upadhyaya Adarsha Mahavidyalaya (PDUAM) Eraligool, Karimganj 788723, Assam, India

A. Giri and R. Mohanta (eds.), *Workshop on Frontiers in High Energy Physics 2019*, Springer Proceedings in Physics 248,
https://doi.org/10.1007/978-981-15-6292-1_19

that Grand Unified theories have a hierarchy problem which manifests itself as large uncontrolled quantum corrections to the Standard Model Higgs boson mass of the order of GUT scale. Furthermore it has been noticed after the results from CERN's LEP-I, the Standard Model gauge couplings do not unify precisely at the GUT scale.

Supersymmetric Grand Unified theories on the other hand offer a resolution to these problems. They solve the hierarchy problem by cancelling the dangerous quadratic and large logarithmic corrections and furthermore lead to a precise unification of the Standard Model gauge coupling constants. The supersymmetric grand unification has been pursued in great detail over the last few decades and is still perhaps the most popular physics beyond standard model (BSM). It also ties naturally with String theory. While supersymmetric grand unification still remains the most attractive path, it is still important to keep an open eye for other possibilities especially given that LHC has so far not seen any signature of supersymmetric particles.

In the recent years, there have been other solutions for the hierarchy problem. Perhaps one of the most radical and remarkable of them is the relaxion solution [1] which uses a cosmological evolution of the Higgs particle in a potential generated by an axion like field, leading it to be trapped at a particular point. While this is indeed an interesting idea, it leads to no new physics around the weak scale. In this kind of scenarios, there will be a desert at least up to 10^6 GeV and further beyond. Depending on the variations of the mechanism, there need not be no new physics to solve the hierarchy problem all the way up to the GUT scale.

We are interested in the extensions of the Standard Model with this kind of the solutions to the hierarchy problem in mind. The question we asked is how to realise Grand Unification in this set up. Gauge coupling unification will not be possible unless there is some extension of the Standard Model matter spectrum. We consider vector-like fermions which lead to precision gauge coupling unification (for earlier works in this direction, please see [2–16]). There are other features of these models which makes them appealing. The constraints from electroweak precision parameters remain small, especially from S and T parameters [17, 18], as long as the mixing between vector-like fermions and SM fermions is small. There are no gauge anomalies as they are vector in nature. And further, they can be tested directly at the collider experiments like LHC. In these models as we will see the Higgs potential naturally remains stable all the up to the GUT scale. In the view that the primary existence of these vector particles is unification of gauge couplings, we dub them "unificons" [19]. However, as we will see later, these models do not restrict themselves only to unification. In some models, we find solutions with a provision for Type III seesaw mechanism for neutrino masses, and in some others there is a dark matter candidate. Thus "unificon" models can indeed have wide phenomenological reach solving other problems in Standard Model like neutrino masses and dark matter.

As a search for all possible models with extra vector-like fermions would be a herculean task, we resort to minimality. We assume unification of gauge couplings á la SU(5). Additional vector-like particles appear as incomplete representations of SU(5). We have looked at all possible incomplete decompositions emanating from SU(5) representations up to dimension 75. The number of copies in each representation is taken to be n which is an integer between 1 and 10. The mass range of these

additional vector-like fermions is chosen to be $m \sim k$ TeV, where k is a $\mathcal{O}(1)$ number taken to be approximately between 1/4–5.

19.2 Renormalization Group Equation

19.2.1 One Loop Gauge Unification

The gauge couplings do not unify precisely in the Standard Model. If one insists on unification of the guage couplings at the GUT scale, the required $\sin^2\theta_W(M_Z^2)$ is 0.204 (for one loop beta functions) instead of the current experimental value of $\sin^2\theta_W(M_Z^2) = 0.23129 \pm 0.00005$ [20]. We look for additional vector-like matter fermions, close to the weak scale, which can compensate the deviation and lead to successful gauge coupling unification. At the 1-loop level, the beta functions for the three gauge couplings are given as

$$\frac{dg_l}{dt} = -\frac{1}{16\pi^2} b_l g_l^3, \text{ where } t = \ln\mu, \tag{19.1}$$

where is $l = \{U(1), SU(2), SU(3)\}$ runs over all the three gauge groups. The b_l functions have the general form:

$$b_l = \Big[\frac{11}{3}C(V_l) - \frac{2}{3}T(F_l) - \frac{1}{3}T(S_l)\Big]. \tag{19.2}$$

Here $C(R)$ is quadratic Casimir and $T(R)$ is Dynkin index of representation R. V, F and S represents vector, Weyl fermion and complex scalar field respectively. For U(1) group $T(R_1)$ and $C(R_1)$ are

$$T(R_1) = C(R_1) = \frac{3}{5}Y^2. \tag{19.3}$$

In the presence of a vector-like fermion V_1 at the scale M_1 greater than weak scale, given the gauge coupling unification at M_{GUT}, the (19.1) take the form:

$$\alpha_l^{-1}(\mu_{in}) = \frac{b_l^0}{2\pi}\ln\frac{\mu_{in}}{M_{GUT}} + \frac{b_l^{V_1}}{2\pi}\ln\frac{M_1}{M_{GUT}} + \alpha_l^{-1}(M_{GUT}), \tag{19.4}$$

where $\alpha_l = \dfrac{g_l^2}{4\pi}$ and $b_l^{V_1}$ capture effect of addition of vector-like fermions at the scale M_1. The parameter $\bar{b}$ is an useful measure of unification of gauge couplings. It is defined as

$$\bar{b}(\mu_{in}) = \frac{\alpha_3^{-1}(\mu_{in}) - \alpha_2^{-1}(\mu_{in})}{\alpha_2^{-1}(\mu_{in}) - \alpha_1^{-1}(\mu_{in})} \tag{19.5}$$

$$= \frac{\triangle b_{32}^0 + \left(\triangle b_{32}^{V_1}\right) \ln(M_1/M_{GUT})/\ln(\mu_{in}/M_{GUT})}{\triangle b_{21}^0 + \left(\triangle b_{21}^{V_1}\right) \ln(M_1/M_{GUT})/\ln(\mu_{in}/M_{GUT})}. \tag{19.6}$$

where the second line can be derived from (19.4) assuming unification at M_{GUT}. The parameters Δb_{lk} are defined as $b_l - b_k$. In the absence of new vector-like particles, $\bar{b}$ is independent of the running scale μ. In their presence however, there is a μ dependence but it is typically mild. For the case where the new particles are close to weak scale $\sim$ TeV, and when $\mu_{in} = M_Z$, the log factor, $\ln(M_1/M_{GUT})/\ln(\mu/M_{GUT})$ is close to one. In this case, the expression for unified theories is given by

$$\bar{b} = \frac{\triangle b_{32}^0 + \triangle b_{32}^{V_1}}{\triangle b_{21}^0 + \triangle b_{21}^{V_1}} \tag{19.7}$$

Note that the (19.5) can purely be determined from experiments at M_Z. Its value is given by

$$\bar{b}(M_Z) = 0.718, \tag{19.8}$$

In the SM, if we insist on unified gauge couplings at M_{GUT}, at the weak scale, $\bar{b}$ takes the value 0.5 clearly in conflict with experiments. In MSSM, $\bar{b}$ turns out to be 5/7. Of course, these arguments are valid only at one loop. There is deviation in (19.7) when higher loops are considered.

19.2.2 Two Loop RG Evolution of Gauge Couplings

To improve the precision in unification of gauge couplings, we consider two loop beta functions. At the two loop level, the beta functions involve Yukawa couplings which makes them model dependent. In the present analysis, we restrict ourselves to models with minimal or zero vector-like fermion and SM mixing through the Higgs mechanism. With this assumption, we can safely neglect the Yukawa contribution from the new sector to the gauge coupling unification. The RG equations at the two loop level are given by [21, 22]:

$$\frac{dg_l}{dt} = -b_l \frac{g_l^3}{16\pi^2} - \sum_k m_{lk} \frac{g_l^3 g_k^2}{(16\pi^2)^2} - \frac{g_l^3}{(16\pi^2)^2} Tr\left\{C_{lu} Y_u^\dagger Y_u + C_{ld} Y_d^\dagger Y_d + C_{le} Y_e^\dagger Y_e\right\}, \tag{19.9}$$

where the first term in the right hand side is due to one-loop which was discussed in the previous subsection. The second term is purely from gauge interactions whereas

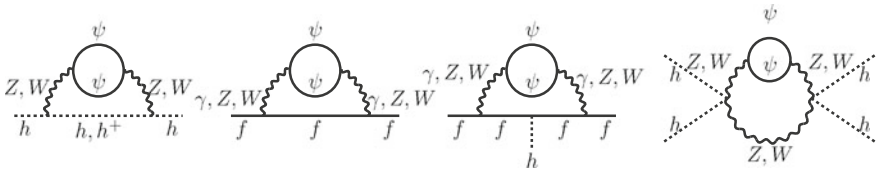

Fig. 19.1 Diagrams contributing in two loop RG of Yukawa and Higgs quartic couplings, through new Fermion fields (ψ). Here f is any standard model fermion. First two diagrams correspond to anomalous dimension and the last two diagrams are giving vertex corrections

the third terms involves the Yukawa terms $Y_{u,d,e}$ where the suffixes mean the up-type, down-type and lepton-type couplings. The expression for the coefficients appearing in the second term of the above equation are as follows [21]:

$$m_{lk} = \left(2C(F_k)d(F_k)T(F_l)d(F_m) + 4C(S_k)d(S_k)T(S_k)d(S_m)\right) \text{ where } l \neq k \tag{19.10}$$

$$m_{ll} = \left[\frac{10}{3}C(V_l) + 2C(F_l)\right]T(F_l)d(F_m)d(F_k) + \left[\frac{2}{3}C(V_l) + 4C(S_l)\right]T(S_l)d(S_m)d(S_k) - \frac{34}{3}[C(V_l)^2], \tag{19.11}$$

where $d(R)$ means dimension of the representation R and other factors C(R) and T(R) are already defined in (19.2).

As we are considering the Yukawa couplings between the vector-like fermions with Higgs boson to be negligible,[1] the contribution of vector-like particles to C_{lf} coefficient can be taken as zero. On the other hand $\delta m_{ij} \neq 0$, where δ is used to indicate contribution from additional vector-like fermions. The explicit values of δm_{ij} for each of the viable models can be found in [19].

Two-loop RG running for the Yukawa couplings is given as

$$Y_{u,d,e}^{-1}\frac{dY_{u,d,e}}{dt} = \frac{1}{16\pi^2}\beta_{u,d,e}^{(1)SM} + \frac{1}{(16\pi^2)^2}\beta_{u,d,e}^{(2)SM} \tag{19.12}$$

The SM RG for these Yukawa couplings are shown in [19]. Two loop beta functions get contributions from the diagrams shown in Fig. 19.1, which results in the following terms:

$$\begin{aligned}
\delta\beta_u^{(2)V} &= \frac{40}{9}g_3^4T(F_3)d(F_2)d(F_1) + \frac{29}{90}g_1^4T(F_1)d(F_3)d(F_2) + \frac{1}{2}g_2^4T(F_2)d(F_3)d(F_1)\\
\delta\beta_d^{(2)V} &= \frac{40}{9}g_3^4T(F_3)d(F_2)d(F_1) - \frac{1}{90}g_1^4T(F_1)d(F_3)d(F_2) + \frac{1}{2}g_2^4T(F_2)d(F_3)d(F_1)\\
\delta\beta_e^{(2)V} &= \frac{11}{10}g_1^4T(F_1)d(F_3)d(F_2) + \frac{1}{2}g_2^4T(F_2)d(F_3)d(F_1)
\end{aligned} \tag{19.13}$$

[1] This can be organised by imposing discrete symmetries distinguishing SM partners from vector-like fermions.

Higgs Self Coupling The modification of the gauge beta functions in the presence of additional vector-like particles can have implications on the evolution of the Higgs self coupling. The evolution of the SM Yukawa couplings is itself modified in these models. We followed [23], beta function of the λ at the two loop and put a condition that λ is always positive at all scales of evolution. Two-loop RG running for the Higgs quartic coupling are

$$\frac{d\lambda}{dt} = \frac{1}{16\pi^2}\beta_\lambda^{(1)SM} + \frac{1}{(16\pi^2)^2}\beta_\lambda^{(2)SM}, \tag{19.14}$$

where beta functions for SM Higgs quartic couplings are defined in [19]. The effect of new fermion fields in RG of Higgs quartic couplings are:

$$\begin{aligned}\delta\beta_\lambda^{(2)V} = &-\frac{1}{25}g_1^4\left(12g_1^2 + 20g_2^2 - 25\lambda\right)T(F_1)d(F_3)d(F_2)\\ &-\frac{1}{5}g_2^4\left(4g_1^2 + 20g_2^2 - 25\lambda\right)T(F_2)d(F_3)d(F_1)\end{aligned} \tag{19.15}$$

To solve the RG equations we need boundary values of the coupling constants and masses at the top mass (M_t) scale. The quantities of interest are Higgs quartic coupling (λ), Yukawa couplings and gauge coupling, which can be calculated in terms of physical observables W-boson mass (M_W), Z-boson mass (M_Z), Higgs mass (M_h) and $\alpha_3(M_Z)$ at the two loop level. The input parameters are calculated in the $\overline{MS}$-scheme. More detailed can be found in [19, 23].

Proton Decay For these models, using the simple decay width formulae, $\Gamma \sim \alpha_{Gut}\frac{m_{proton}^5}{M_{GUT}^4}$ we estimate the life time of the proton, where the current experimental value is of order $> 10^{32} - 10^{34}$ years [24].

Threshold Corrections at GUT Scale To study the impact of threshold corrections on gauge coupling unification, we define the following parameters: $\alpha_{ave.}(\mu) = (\alpha_1(\mu) + \alpha_2(\mu) + \alpha_3(\mu))/3$ and $\bar{\Delta}_i(\mu) = (\alpha_i(\mu) - \alpha_{avg}(\mu))/\alpha_{ave}(\mu)$. Note that α_{ave} coincides with α_{GUT} when all $\bar{\Delta}_i \to 0$, at the scale M_{GUT}. In the presence of threshold corrections, one could allow for deviations in α_{GUT} in terms of $\bar{\Delta}_i$ at the GUT scale. Defining $\Delta = max(\bar{\Delta}_i)$, we see that Δ is as large as 6% in the Standard Model. In our survey of models below, we have allowed for variations in Δ up to 1.2%.

19.3 Gauge Coupling Unification with Vector-Like Fermions

In our search, we focus on vector-like matter in incomplete representations of SU(5). We have considered (incomplete) representations [25] up-to dimension 75. The full list of incomplete representations is presented in Appendix A. As can be seen from

the Table 19.2, there are 40 representations which we have considered. We found no successful models for $i = 1$ even with $n_1 = 6$. The simplest solutions we found contain at least two different representation content each with a different number of copies. We call these solutions "minimal unificon models". These are listed in Table 19.1. The two representations considered are called Rep.1 and Rep2. The representation is described as $n_i(R_{SU(3)}, R_{SU(2)}, R_{U(1)})$, where n_i introduced earlier is the number of copies of the representation, R_G is the representation of the field under the gauge group G of the SM.

Furthermore, in the above, we mentioned only one part of the representation instead of the complete vector multiplet for brevity. The second last column, entries are written in units of 10^{16} GeV. All models appeared as the solution of one loop RG equation. Third and fifth columns show's the mass range of the vector-like fields.

The list of such of models is given in Table 19.1. Several interesting features are evident. The minimalist model is model 7, with only two vector-like fermions. These model are constraints from direct searches of vector-like quarks at LHC and elsewhere if there is significant mixing with SM particles. In its absence, as we assumed here, the bound will be different. We would discuss one of the model in detail.

19.3.1 Model 2

We got six copies of Rep1 $= \left(1, 2, \frac{1}{2}\right)$ in mass range between 250–2000 GeV and two copies of Rep2 $= (8, 1, 0)$ with mass range from 500 GeV to 5 TeV. Rep1 field is lepton doublet like field, lightest neutral component of these fermions can be a dark matter candidate. Rep2 is gluino like and at the renormalisation level, it can interact with the gluons only and does not have any decay chain.

In the model, M_{Rep1} is always less than M_{Rep2}. A sample unification point is shown in Fig. 19.2a, six copies of lepton like vector fermions with degenerate mass of 620 GeV and two copy of Rep2 with a mass of 4310 GeV is considered. The figure shows unification of gauge couplings as well as running of y_t and λ. Mass distribution in Rep1-Rep2 mass plane is shown in Fig. 19.2b.

19.4 Collider Signature of Minimal Vector-Like Fermion Models

In this section we will show the pair-produced colored particles from BSM senarios can be constrained through the non- observation of dijet and other resonances arising from their QCD bound states. In the following we will concentrate on the strongly interacting exotic sector; which appears in all the successful models.

Table 19.1 Model with two vector-like fermions representation satisfying gauge coupling unification and vacuum stability condition, considering $\triangle$ of 1.2%

Mod No.	Rep 1	M_{Rep1} GeV	Rep 2	M_{Rep2} GeV	One loop	Two loop	Vaccum stability	M_{GUT} $\times 10^{16}$ GeV	α_{GUT}
1	$6\left(1, 2, \frac{1}{2}\right)$	$(250 - 5000)$	$1\left(6, 1, \frac{1}{3}\right)$	$(250 - 5000)$	✓	✓	✓	∼0.11	∼0.038
2	$6\left(1, 2, \frac{1}{2}\right)$	$(250 - 2000)$	2 (8, 1, 0)	$(500 - 5000)$	✓	✓	✓	∼2.34	∼0.040
3	2 (1, 3, 0)	$(250 - 5000)$	$4\left(3, 1, \frac{1}{3}\right)$	$(250 - 5000)$	✓	✓	✓	∼2.29	∼0.030
4	$2\left(3, 1, \frac{2}{3}\right)$	$(250 - 5000)$	$2\left(3, 2, \frac{1}{6}\right)$	$(250 - 4500)$	✓	✓	✓	∼ 4.79	∼0.040
5	3 (1, 3, 0)	$(1800 - 5000)$	$1\left(6, 1, \frac{2}{3}\right)$	$(250 - 950)$	✓	✓	✓	∼1.08	∼0.037
6	$1\left(1, 4, \frac{1}{2}\right)$	$(250 - 2000)$	$2\left(6, 1, \frac{2}{3}\right)$	$(1000 - 5000)$	✓	✓	✓	∼8.58	∼0.107
7	$1\left(3, 1, \frac{1}{3}\right)$	$(250 - 5000)$	$1\left(3, 2, \frac{1}{6}\right)$	$(250 - 5000)$	✓	✓	✓	∼2.20	∼0.028
8	$4\left(1, 2, \frac{1}{2}\right)$	$(300 - 5000)$	1 (8, 1, 0)	$(300 - 5000)$	✓	✓	✓	∼0.10	∼0.030
9	3 (1, 3, 0)	$(1100 - 5000)$	$6\left(3, 1, \frac{1}{3}\right)$	$(250 - 1800)$	✓	✓	✓	∼25.0	∼0.037

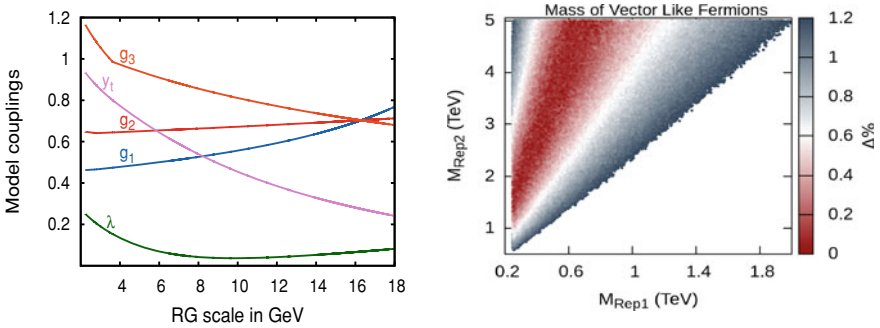

(a) (b)

Fig. 19.2 Model 2: Fig. **a** Gauge couplings (g_1,g_2,g_3) unification and vacuum stability ($\lambda > 0$) plot, considering vector-like fermion in Rep1 of mass 620 GeV and Rep2 of mass 4310 GeV. Figure **b** Mass range allowed for vector-like fermions in Rep1 and Rep2 for gauge unification and vacuum stability

19.4.1 Formalism for Bound State

We investigate the possibility of producing bound states of the colour vector-like fermions. For the formation of bound state, we assume the new vector-like fermion (ψ) is long lived. The bound state formalism has been studied in [26, 27], where they focus on pair-produced colour particle Beyond the Standard Model by the observation of diphoton, dijet etc. resonances arising from QCD bound state.

A pair of $\psi\bar{\psi}$ near threshold can form a QCD bound state, which we defined as $\mathcal{O}$. For particles (ψ) of mass $m_\psi \gg \Lambda_{QCD}$, we can estimate bound state as modified hydrogenic approximation. For a particle ψ in the colour representation R, the potential between ψ and $\bar{\psi}$ depends on the colour representation $\mathcal{R}$ of the $\psi\bar{\psi}$ pair through the casimirs of R and $\mathcal{R}$ as

$$V(r) = -C\frac{\bar{\alpha}_s}{r}, \qquad C = C(R) - \frac{1}{2}C(\mathcal{R}) \tag{19.16}$$

where $\bar{\alpha}_s$ is defined as the running coupling at the scale of the average distance between the two particle in the corresponding hydrogenic state, which is order of the Bohr radius $a_0 = 2/(C\bar{\alpha}_s m_\psi)$. The production cross-section of any narrow resonance $\mathcal{O}$ of mass M and spin J from parton x and y, and the decay rate of bound state to x and y, are related by

$$\hat{\sigma}_{xy\to\mathcal{O}} = \frac{2\pi(2J+1)d_{\mathcal{O}}(\mathcal{R})}{D_x D_y}\frac{\Gamma_{\mathcal{O}\to xy}}{M}2\pi\delta(\hat{s} - M^2) \qquad (\times 2 \text{ for x = y}) \tag{19.17}$$

where $D_{\mathcal{O}}$ denotes the colour representation of particle $\mathcal{O}$.

In the next subsection we will strict ourself to study the colour singlet and spin zero ($J = 0$) bound state system. Assuming the production cross-section of $\psi\bar{\psi}$ is dominated by gluon fusion. The gluon fusion partonic production cross-section of of bound state is given by

$$\hat{\sigma}_{gg\to\mathcal{O}} = \frac{\pi^2}{8}\frac{\Gamma_{\mathcal{O}\to gg}}{M}\delta(\hat{s} - M^2) \tag{19.18}$$

Depending on the quantum number of ψ, bound state $\mathcal{O}$ can decay to diphoton, dijet, $Z\gamma$, ZZ and W^+W^- channels. The production of preceding pair events produced in proton-proton collisions in LHC can be predicted as $\sigma(pp \to \mathcal{O}) \times BR(\mathcal{O} \to X_1X_2)$.

19.4.2 Signals $\gamma\gamma$ and Dijet Chennel

Any spin half particle can be produced in pairs (in gg collisions) in an S-wave $J = 0$ colour singlet bound state, which can decay as typically narrow $\gamma\gamma$, ZZ, $Z\gamma$ and gg resonance. There has been searches in $Z\gamma$, ZZ and WW resonances from these bound states. They all remain less sensitive than $\gamma\gamma$ channel. Hence, we show here the channel $\gamma\gamma$. The decay width of the $\gamma\gamma$ signal due to spin $J = 0$ bound state is given as:

$$\Gamma(\mathcal{O}^{\mathcal{R}}_{J=0} \to \gamma\gamma) = \frac{Q^4 C(R)^3 d_R}{2}\alpha^2\bar{\alpha}_s^3 m_\psi \tag{19.19}$$

S-wave bound state with spin $J = 0$ can be produced via $gg \to \mathcal{O}$ and annihilating mostly to gg. For $j = 1/2$ there is also a comparable contribution from S-wave $J = 1$ colour octet bound states produced via $q\bar{q} \to \mathcal{O}$ and annihilating to $q\bar{q}$, which we will not discuss here.

The decay width of gg signal due to spin $J = 0$ colour singlet bound state is,

$$\Gamma(\mathcal{O}^{\mathcal{R}=1}_{J=0} \to gg) = \frac{C(R)^5 d_R}{32}\alpha_s^2\bar{\alpha}_s^3 m_\psi \tag{19.20}$$

($\times 2$ for Complex Representation of constituent fermion)

19.4.3 Limits on Signals from CMS and ATLAS

In next section we examine the constraints on masses of bound state from dijet and diphoton bounds considering one copy of constituent vector-like fermions. We have used the recent limits of ATLAS and CMS for diphoton resonance at centre of energy

$\sqrt{s} = 13$ TeV from 2015 and as well as 2016 data. Dijet bounds has been considered for centre of energy $\sqrt{s} = 8$ and 13 TeV from both ATLAS and CMS.

19.4.3.1 Dijet Bounds

In Fig. 19.3a, b we present the $\sigma(pp \to \mathcal{O}) \times BR(\mathcal{O} \to gg)$ as a function of the mass of the $\mathcal{O}$ resonance considering one copy of constituent vector-like fermions. The black line is the upper limit on this cross-section from ATLAS [28] 8 TeV and blue line is from CMS [29] 8 TeV data in Fig. 19.3a. Figure 19.3b shows the dijet limits from ATLAS(black) [30] 13 TeV and CMS(blue) [31] 13 TeV data. We can clearly say that the dijet limits are not strong enough to rule any of the models, if they have only one copy of constituent fermions.

19.4.3.2 Diphoton Bounds

We present the production of diphoton channel as a function of the resonance mass considering one copy of constituent vector-like fermions in Fig. 19.4. Black line is the upper limit on this cross-section from ATLAS [32] 13 TeV and blue line is from CMS [33] 13 TeV data. It can be observed that the upper limits on cross-section can give stringent bound on the masses of vector-like fermions ($m_\psi = M/2$).

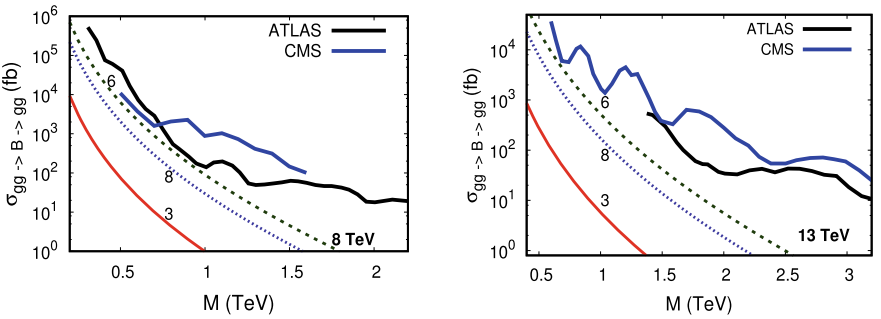

Fig. 19.3 Cross section of Dijet events at $\sqrt{s} = 8$ TeV (left) and $\sqrt{s} = 13$ TeV (right) for bound state of representation $\mathcal{R} = 1$ and $J = 0$, from constituent particle of representation $R = 3, 6, 8$. Limits from ATLAS 8 and 13 TeV are shown in thick black and CMS 8 and 13 TeV are shown in thick blue

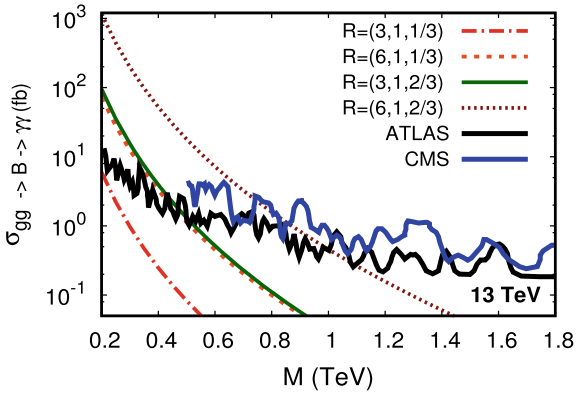

Fig. 19.4 Cross section of diphoton event w.r.t bound state mass at $\sqrt{s} = 13$ TeV for bound state of representation $\mathcal{R} = 1$ and $J = 0$ from constituent particle of color representation $R = 3, 6$. The red line(dash dot) shows the fermion with $R = 3$ and $Q = 1/3$, green line(solid) correspond to $R = 3$ and $Q = 2/3$, purple line(dotted) shows the fermion with $R = 6$ and $Q = 2/3$ and orange line(dashed) shows the $R = 6$ and $Q = 1/3$ fermion. Limits are from ATLAS 13 TeV black line and CMS 13 TeV blue line

19.5 Summary and Outlook

Grand Unified theories seems one of the most promising physics, beyond SM. We look for models with extra vector-like fermions at the weak scale which can lead to successful unification of gauge couplings. With two representation, we find a class of nine models leading to successful unification of gauge couplings. The coloured set of the vector-like fermions can be probed at LHC by looking for bound states formed by them and their probable decays. We have listed the present bounds from LHC for each successful model. Recently another work [34] has followed a similar direction and our results are consistent with each other.

Acknowledgements S. K. Vempati thanks the organisers of the conference FHEP-2019, at Hyderabad, India for a wonderful atmosphere. This work is supported by the CNRS LIA (Laboratoire International Associé) THEP (Theoretical High Energy Physics) and the INFRE-HEPNET (IndoFrench Network on High Energy Physics) of CEFIPRA/IFCPAR (Indo-French Centre for the Promotion of Advanced Research). SKV and AK are supported also CEFIPRA project "Glimpses of New physics" and Department of Science and Technology, Govt of India, Project "Nature of New Physics".

Appendix: Representations and Dynkin Indices

We considered all the $SU(3) \times SU(2) \times U(1)$ representations coming from $SU(5)$ representations upto dimension 75. In Table 19.2, we listed those forty representations

Table 19.2 Representation of fields considered in this paper. In the column entitled with "SM Rep" we put incomplete multiplets of $SU(5)$ and the entries inside the brackets are $SU(3)$, $SU(2)$ and $U(1)$ representations respectively. In the column with title we'd written the $SU(5)$ representations from which those representations are coming. Dynkin indices are calculated assuming the fields are scalar fields. Note that we had considered up the SU(5) representation of dimension 75. There are some extra representations as well

S.No.	SM Rep	Source	Dynkin indices	S.No.	SM Rep	Source	Dynkin indices
1	$(1, 1, 1)$	10	$\left(0, 0, -\frac{1}{5}\right)$	21	$\left(3, 2, \frac{7}{6}\right)$	$\overline{45}, \overline{50}$	$\left(-\frac{1}{3}, -\frac{1}{2}, -\frac{49}{30}\right)$
2	$(1, 1, 2)$	$\overline{50}$	$\left(0, 0, -\frac{4}{5}\right)$	22	$\left(3, 3, -\frac{1}{3}\right)$	45, 70	$\left(-\frac{1}{2}, -2, -\frac{1}{5}\right)$
3	$(1, 1, 3)$		$\left(0, 0, -\frac{9}{5}\right)$	23	$\left(3, 3, \frac{2}{3}\right)$	$\overline{35}, \overline{40}$	$\left(-\frac{1}{2}, -2, -\frac{4}{5}\right)$
4	$(1, 1, 4)$		$\left(0, 0, -\frac{16}{5}\right)$	24	$\left(\bar{3}, 3, \frac{4}{3}\right)$	70	$\left(-\frac{1}{2}, -2, -\frac{16}{5}\right)$
5	$(1, 1, 5)$		$(0, 0, -5)$	25	$\left(3, 4, \frac{7}{6}\right)$	$\overline{70'}$	$\left(-\frac{2}{3}, -5, -\frac{49}{15}\right)$
6	$\left(1, 2, \frac{1}{2}\right)$	5, 45, 70	$\left(0, -\frac{1}{6}, -\frac{1}{10}\right)$	26	$\left(6, 1, \frac{1}{3}\right)$	$\overline{45}$	$\left(-\frac{5}{6}, 0, -\frac{2}{15}\right)$
7	$\left(1, 2, -\frac{3}{2}\right)$	40	$\left(0, -\frac{1}{6}, -\frac{9}{10}\right)$	27	$\left(6, 1, -\frac{2}{3}\right)$	15	$\left(-\frac{5}{6}, 0, -\frac{8}{15}\right)$
8	$(1, 3, 0)$	24	$\left(0, -\frac{2}{3}, 0\right)$	28	$\left(6, 1, \frac{4}{3}\right)$	50	$\left(-\frac{5}{6}, 0, -\frac{32}{15}\right)$
9	$(1, 3, 1)$	15	$\left(0, -\frac{2}{3}, -\frac{3}{5}\right)$	29	$\left(\bar{6}, 2, \frac{1}{6}\right)$	35, 40	$\left(-\frac{5}{3}, -1, -\frac{1}{15}\right)$
10	$\left(1, 4, \frac{1}{2}\right)$	70	$\left(0, -\frac{5}{3}, -\frac{1}{5}\right)$	30	$\left(6, 2, \frac{5}{6}\right)$	75	$\left(-\frac{5}{3}, -1, -\frac{5}{3}\right)$
11	$\left(1, 4, -\frac{3}{2}\right)$	35	$\left(0, -\frac{5}{3}, -\frac{9}{5}\right)$	31	$\left(6, 2, -\frac{7}{6}\right)$	70	$\left(-\frac{5}{3}, -1, -\frac{49}{15}\right)$
12	$(1, 5, -2)$	$70'$	$\left(0, -\frac{10}{3}, -4\right)$	32	$\left(6, 3, \frac{1}{3}\right)$	$\overline{50}, \overline{70'}$	$\left(-\frac{5}{2}, -4, -\frac{2}{5}\right)$
13	$(1, 5, 1)$		$\left(0, -\frac{10}{3}, -1\right)$	33	$(8, 1, 0)$	24	$(-1, 0, 0)$
14	$(1, 5, 0)$		$\left(0, -\frac{10}{3}, 0\right)$	34	$(8, 1, 1)$	40	$\left(-1, 0, -\frac{8}{5}\right)$
15	$\left(3, 1, -\frac{1}{3}\right)$	5, 45, 50, 70	$\left(-\frac{1}{6}, 0, -\frac{1}{15}\right)$	35	$\left(8, 2, \frac{1}{2}\right)$	45, 50, 70	$\left(-2, -\frac{4}{3}, -\frac{4}{5}\right)$
16	$\left(\bar{3}, 1, -\frac{2}{3}\right)$	10, 40	$\left(-\frac{1}{6}, 0, -\frac{4}{15}\right)$	36	$(8, 3, 0)$	75	$\left(-3, -\frac{16}{3}, 0\right)$

(continued)

Table 19.2 (continued)

S. No.	SM Rep	Source	Dynkin indices	S. No.	SM Rep	Source	Dynkin indices
17	$\left(\bar{3}, 1, \frac{4}{3}\right)$	45	$\left(-\frac{1}{6}, 0, -\frac{16}{15}\right)$	37	$\left(\overline{10}, 1, 1\right)$	35	$\left(-\frac{5}{2}, 0, -2\right)$
18	$\left(3, 1, \frac{5}{3}\right)$	75	$\left(-\frac{1}{6}, 0, -\frac{5}{3}\right)$	38	$\left(\overline{10}, 2, \frac{1}{2}\right)$	$70'$	$\left(-5, -\frac{5}{3}, -1\right)$
19	$\left(3, 2, \frac{1}{6}\right)$	10, 15, 40	$\left(-\frac{1}{3}, -\frac{1}{2}, -\frac{1}{30}\right)$	39	$\left(15, 1, -\frac{1}{3}\right)$	70	$\left(-\frac{10}{3}, 0, -\frac{1}{3}\right)$
20	$\left(3, 2, -\frac{5}{6}\right)$	24, 75	$\left(-\frac{1}{3}, -\frac{1}{2}, -\frac{5}{6}\right)$	40	$\left(15, 1, \frac{4}{3}\right)$	$70'$	$\left(-\frac{10}{3}, 0, -\frac{16}{3}\right)$

[25] with their contribution to beta function (i.e. Dynkin index) considering them as scalar fields.

References

1. P.W. Graham, D.E. Kaplan, S. Rajendran, Cosmological relaxation of the electroweak scale. Phys. Rev. Lett. **115**(22), 221801 (2015)
2. C. Liu, Z.-H. Zhao, θ_{13} and the Higgs mass from high scale supersymmetry. Commun. Theor. Phys. **59**, 467–471 (2013)
3. T.G. Rizzo, Desert guts and new light degrees of freedom. Phys. Rev. D **45**, 3903–3905 (1992)
4. D.E. Morrissey, C.E.M. Wagner, Beautiful mirrors, unification of couplings and collider phenomenology. Phys. Rev. D **69**, 053001 (2004)
5. V. Barger, J. Jiang, P. Langacker, T. Li, String scale gauge coupling unification with vector-like exotics and non-canonical U(1)(Y) normalization. Int. J. Mod. Phys. A **22**, 6203–6218 (2007)
6. L. Calibbi, L. Ferretti, A. Romanino, R. Ziegler, Gauge coupling unification, the GUT scale, and magic fields. Phys. Lett. B **672**, 152–157 (2009)
7. I. Donkin, A. Hebecker, Precision gauge unification from extra Yukawa couplings. JHEP **09**, 044 (2010)
8. L.J. Hall, Y. Nomura, A finely-predicted higgs boson mass from a finely-tuned weak scale. JHEP **03**, 076 (2010)
9. R. Dermisek, Unification of gauge couplings in the standard model with extra vectorlike families. Phys. Rev. D **87**(5), 055008 (2013)
10. L.-F. Li, F. Wu, Coupling constant unification in extensions of standard model. Int. J. Mod. Phys. A **19**, 3217–3224 (2004)
11. R. Shrock, Variants of the standard model with electroweak-singlet quarks. Phys. Rev. D **78**, 076009 (2008)
12. I. Dorsner, P. Fileviez Perez, Unification without supersymmetry: neutrino mass, proton decay and light leptoquarks. Nucl. Phys. **B723**, 53–76 (2005)
13. J.L. Chkareuli, I.G. Gogoladze, A.B. Kobakhidze, Natural nonSUSY SU(N) GUTs. Phys. Lett. B **340**, 63–66 (1994)
14. R. Dermisek, Insensitive unification of gauge couplings. Phys. Lett. B **713**, 469–472 (2012)
15. I. Dorsner, S. Fajfer, I. Mustac, Light vector-like fermions in a minimal SU(5) setup. Phys. Rev. D **89**(11), 115004 (2014)
16. M.-L. Xiao, J.-H. Yu, Stabilizing electroweak vacuum in a vectorlike fermion model. Phys. Rev. D **90**(1), 014007 (2014). [Addendum: Phys. Rev. D **90**(1), 019901 (2014)]
17. F. del Aguila, J. de Blas, M. Perez-Victoria, Effects of new leptons in electroweak precision data. Phys. Rev. D **78**, 013010 (2008)
18. S.A.R. Ellis, R.M. Godbole, S. Gopalakrishna, J.D. Wells, Survey of vector-like fermion extensions of the standard model and their phenomenological implications. JHEP **09**, 130 (2014)
19. B. Bhattacherjee, P. Byakti, A. Kushwaha, S.K. Vempati, Unification with vector-like fermions and signals at LHC. JHEP **05**, 090 (2018)
20. C. Patrignani and P. D. Group, Review of particle physics. Chinese Phys. C **40**(10), 100001 (2016)
21. D.R.T. Jones, The two loop beta function for a G(1) x G(2) gauge theory. Phys. Rev. D **25**, 581 (1982)
22. H. Arason, D.J. Castano, B. Keszthelyi, S. Mikaelian, E.J. Piard, P. Ramond, B.D. Wright, Renormalization group study of the standard model and its extensions. 1. The standard model. Phys. Rev. D **46**, 3945–3965 (1992)
23. D. Buttazzo, G. Degrassi, P.P. Giardino, G.F. Giudice, F. Sala, A. Salvio, A. Strumia, Investigating the near-criticality of the Higgs boson. JHEP **12**, 089 (2013)

24. V. Takhistov, Review of nucleon decay searches at super-Kamiokande, in *51st Rencontres de Moriond on EW Interactions and Unified Theories La Thuile, Italy, March 12–19, 2016* (2016)
25. R. Slansky, Group theory for unified model building. Phys. Rep. **79**, 1–128 (1981)
26. Y. Kats, M.J. Strassler, Probing colored particles with photons, leptons, and jets. JHEP **11**, 097 (2012). [Erratum: JHEP 07,009 (2016)]
27. Y. Kats, M.D. Schwartz, Annihilation decays of bound states at the LHC. JHEP **04**, 016 (2010)
28. G. Aad et al., Search for new phenomena in the dijet mass distribution using $p - p$ collision data at $\sqrt{s} = 8$ TeV with the ATLAS detector. Phys. Rev. D **91**(5), 052007 (2015)
29. V. Khachatryan et al., Search for narrow resonances in dijet final states at sqrt(s) = 8 TeV with the novel CMS technique of data scouting. Phys. Rev. Lett. **117**, 031802 (2016)
30. Search for New Phenomena in Dijet Events with the ATLAS Detector at $\sqrt{s}$ = 13 TeV with 2015 and 2016 data, Technical report. ATLAS-CONF-2016-069, CERN, Geneva (2016)
31. A.M. Sirunyan et al., Search for dijet resonances in proton-proton collisions at $\sqrt{s} = 13$ TeV and constraints on dark matter and other models (Phys. Lett. B, Submitted to, 2016)
32. Search for scalar diphoton resonances with 15.4 fb^{-1} of data collected at $\sqrt{s}$ = 13 TeV in 2015 and 2016 with the ATLAS detector, Technical report. ATLAS-CONF-2016-059, CERN, Geneva (2016)
33. V. Khachatryan et al., Search for high-mass diphoton resonances in proton-proton collisions at 13 TeV and combination with 8 TeV search (Phys. Lett. B, Submitted to, 2016)
34. K. Kowalska, D. Kumar, Road map through the desert: unification with vector-like fermions. JHEP **12**, 094 (2019)

Chapter 20
Higgs Vacuum Stability with Vector-Like Fermions

Shrihari Gopalakrishna

Abstract Recent studies including two-loop renormalization group equations indicate that in the standard model, the Higgs electroweak vacuum is meta-stable with a decay lifetime much larger than the age of the Universe. Beyond the standard model states coupled to the Higgs could change this conclusion. Vector-like fermions are such states present in many beyond the standard model theories, and their effects are particularly important as they could potentially destabilize the Higgs vacuum. Here we discuss this issue, and show regions of the parameter space, namely vector-like fermion mass and Yukawa coupling to the Higgs, in which the electroweak vacuum is stable, meta-stable, or unstable.

20.1 Introduction

As reviewed for example in [1], the stability of the Higgs electroweak (EW) vacuum can be analyzed using the renormalization group improved Higgs effective potential, and recent analyses at the NNLO level in [2–5] has indicated that the standard model (SM) Higgs vacuum is meta-stable with a decay life-time much larger than the age of the Universe. Thus, although in the SM the EW vacuum decays, since the life-time is so large, it may not present any problem.

However, when new beyond the standard model (BSM) states are coupled to the Higgs, the situation could be altered. For example, new vector-like fermions (VLF) are present in many BSM models and can potentially destabilize the EW vacuum. Generically, fermions coupled to the Higgs tend to destabilize the vacuum, while bosons do the opposite. Along with the VLFs, if new bosonic states are also present in those models, the conclusion has to be revisited after including those states. In [6], we analyzed the effect of VLFs on Higgs vacuum stability in a model-independent

S. Gopalakrishna (✉)
Institute of Mathematical Sciences (IMSc), Chennai 600 113, India
e-mail: shri@imsc.res.in
URL: https://www.imsc.res.in/~shri/index.html

Homi Bhabha National Institute (HBNI), Anushaktinagar, Mumbai 400 094, India

A. Giri and R. Mohanta (eds.), *Workshop on Frontiers in High Energy Physics 2019*, Springer Proceedings in Physics 248,
https://doi.org/10.1007/978-981-15-6292-1_20

way, and we summarize in this article the main results of that study. All the content presented here is drawn from [6] and references therein.

We write the quantum Higgs effective potential as

$$V_{\rm eff}(h) = \frac{m^2_{h\,\rm eff}}{2} h^2 + \frac{\lambda_{\rm eff}(h)}{4} h^4 \,, \tag{20.1}$$

where $\lambda_{\rm eff}$ depends on the Higgs field value h, in the form $\ln(h/M)$, with a subtraction scale M. For $h \gg m_h$, the mass-term has a negligible effect and we omit it. We denote the field-value as $h \equiv \mu$, and $\lambda_{\rm eff}(\mu)$ as $\lambda(\mu)$. As shown for example in [7], $\lambda(\mu)$ obeys a renormalization group equation (RGE) equation of the form

$$\frac{d\,\lambda(\mu)}{d\ln\mu} = \beta_\lambda\left(\lambda(\mu), y_t(\mu), g_3(\mu), g_2(\mu), g_1(\mu), \ldots\right) \,. \tag{20.2}$$

where the RGE is now an evolution with field value $h = \mu$. The β_λ is the usual β-function for the coupling λ, and integrating the RGE resums the leading logs of the form $\log^n(\mu/M)$. We show in β_λ the dependence on λ, and on other significant couplings such as the top Yukawa coupling y_t and the $SU(3), SU(2), U(1)$ gauge couplings $g_a = \{g_3, g_2, g_1\}$ of the SM, but omit other small couplings that contribute insignificantly. All these couplings evolve with renormalization scale, with the corresponding β-functions β_{y_t}, β_{g_a}, etc. When we add VLFs, β_λ (and the other beta-functions) will also depend on the new couplings to the VLF. From (20.1), we can see that for $h \gg m_h$, the vacuum becomes unstable at the scale when $\lambda(\mu)$ becomes negative. Fermions that are coupled to the Higgs contribute with a negative sign to β_λ and tend to destabilize the Higgs vacuum, although the full situation including the wave-function renormalizations and the coupled nature of the RGEs is not so simple to state. In the following, we show the effect of including VLF contributions to the β-functions. We numerically integrate the RGEs to determine $\lambda(\mu)$ (and the other couplings), and ask if $\lambda(\mu)$ becomes negative at some field value μ, signalling vacuum instability.

If $\lambda(\mu)$ becomes negative, it indicates that the EW vacuum at $h = v = 246\,\text{GeV}$, may tunnel away to a lower minimum at much larger field values. We compute the tunneling rate (inversely related to the time-scale) by working in Euclidean space and computing the action for the 'bounce' configuration of the Higgs field, which we elaborate on later. If the tunneling time-scale is smaller than the age of the Universe, we deem this unacceptable since we would fail to get an understanding as to why we still find ourselves in the EW vacuum. As mentioned earlier, recent studies indicate that in the SM, the EW vacuum is meta-stable but with a tunneling life-time much larger than the age of the Universe. We reconfirm this with our analysis and then move-on to analyzing the situation with VLFs present. The VLF parameters must be such that the tunneling life-time remains larger than the age of the Universe. Curiously, we find that for some VLF parameters, the EW vacuum can be absolutely stable also, i.e. $\lambda(\mu)$ never becomes negative for any (large) μ. We demonstrate

these aspects with simple VLF models that are either in the trivial or fundamental representations of $SU(3)$, $SU(2)$ and $U(1)$. We call an $SU(3)$ triplet as a vector-like quark (VLQ), and an $SU(3)$ singlet as a vector-like lepton (VLL).

20.2 The Renormalization Group Equations (RGE)

In the notation of [6], we write the SM Lagrangian density as

$$\mathcal{L} \supset \bar{t} i \partial\!\!\!/ t - \lambda (H^\dagger H)^2 - (y_t \bar{q}_L \cdot H^* t_R + h.c.) \,, \tag{20.3}$$

where the $\cdot$ denotes the anti-symmetric combination of $SU(2)$ indices, $q_L = (t_L \; b_L)^T$ is the $SU(2)$ doublet, and, $t = (t_L \; t_R)^T$ and $b = (b_L \; b_R)^T$ are the top-quark and bottom-quark Dirac fermions. Here we show only the relevant terms that are sizeable.

We introduce VLFs via an effective model, taking an $SU(2)$ doublet VLF $\chi = (\chi_1 \; \chi_2)^T$ and an $SU(2)$ singlet VLF ξ, and write the VLF mass-terms and Higgs Yukawa couplings as

$$\mathcal{L} \supset -M_\chi \bar{\chi}\chi - M_\xi \bar{\xi}\xi - (\tilde{y}\, \bar{\chi} \cdot H^* \xi + h.c.) \,. \tag{20.4}$$

χ is a VLQ if it is an $SU(3)$ triplet, else if it is trivial, it is a VLL. The VLQ have gluon interactions, while VLL do not. We denote the hypercharge of χ as Y_χ, and that of ξ as Y_ξ. For simplicity, we do not turn-on mixed Yukawa couplings with one VLF and one SM fermion (SMF), which could be present for SM-like hypercharge assignments to the VLF.

Reference [6] reviews in detail the derivation of the SM fermion contributions to the RGE at 1-loop, using which the VLF contributions to the RGEs are derived. To improve the precision, the dominant 2-loop VLF contributions are included in the β-functions, obtained from the package 'SARAH' [8, 9]. The dominant non-fermionic 2-loop contributions are taken from the literature (for example, [4]). For the full set of RGEs we refer the reader to [6] and do not reproduce them here.

We take the input parameters as follows and as compiled in [4], choosing the renormalization point as the top mass scale $\tilde{m}_t$:

- The EW VEV: $v = 246.2\,\text{GeV}$,
- The Higgs quartic: $\tilde{\lambda} = 0.12710$ (NNLO),
- The top Yukawa coupling: $\tilde{y}_t = 0.93558$ (partial 3-loop),
- The $SU(3)_c$ coupling constant: $\tilde{g}_3 = 1.1666$ (partial 4-loop),
- The $SU(2)_L$ coupling constant: $\tilde{g}_2 = 0.64755$ (NLO),
- The $U(1)$ coupling constant: $\tilde{g}_1 = \sqrt{5/3}\, g' = \sqrt{5/3} \times 0.35937$ (NLO).

We take the top mass as $\tilde{m}_t = \tilde{y}_t v/\sqrt{2}$, and the Higgs mass as $\tilde{m}_h = \sqrt{2\tilde{\lambda}}\, v$.

We numerically integrate the RGE using the package *Mathematica*. As a cross-check, we compute the scale at which $\lambda(\mu)$ becomes zero (before going negative) in the SM and find excellent agreement to that in the literature.

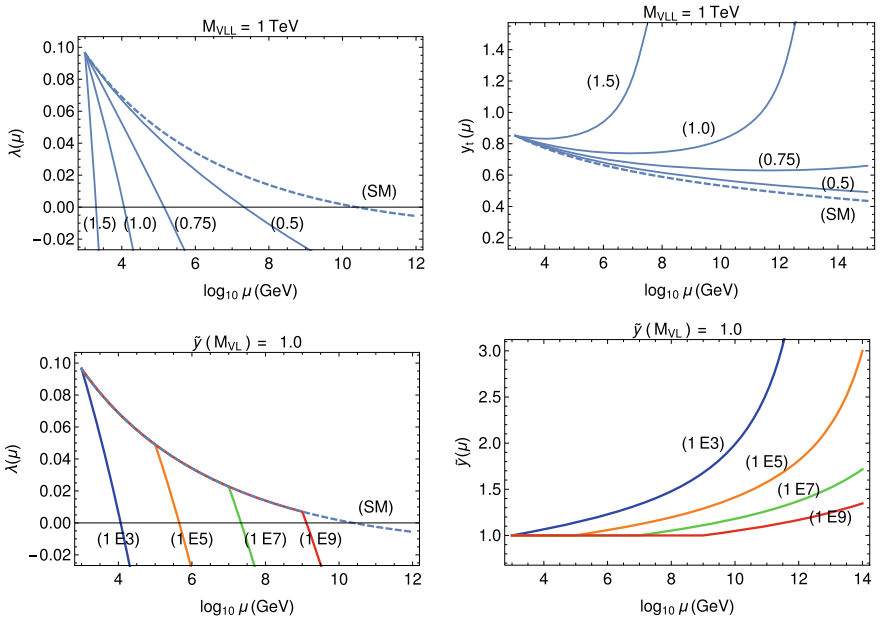

Fig. 20.1 From [6]. The evolution of λ, y_t, and $\tilde{y}$ with Higgs field value μ for a degenerate family of one SU(2) doublet VLL and one singlet VLL, for $M_{VL} = 1$ TeV and various $\tilde{y}$ (first two plots), and for $\tilde{y}(M_{VL}) = 1$ and various M_{VL} (in GeV) (last two plots)

We present the RGE evolution of the couplings for the SM, and also for a VLF family of one $SU(2)$ doublet VLL and one singlet VLL. For various M_{VL} and $\tilde{y}$, in Fig. 20.1 we show the evolution for a VLL generation, while we show in Fig. 20.2 the evolution for a VLQ. In all figures, the dashed lines are for the SM (no VLFs), and the solid lines are with the VLFs. In the SM, $\lambda(\mu)$ becomes zero at the field value $\mu \sim 10^{10.5}$ GeV, in good agreement with the results in the literature.

Figure 20.1 shows how the couplings evolve with Higgs field value $h \equiv \mu$ for a mass-degenerate VLL family of one $SU(2)$ doublet and one singlet VLL. $\tilde{y}$ and the M_{VL} values are shown as $(rEm) \equiv r \times 10^m$ GeV respectively. λ becomes negative at a smaller field value as $\tilde{y}$ increases or as M_{VL} decreases.

Figure 20.2 shows how the couplings evolve with Higgs field value μ for a mass-degenerate VLQ family of one $SU(2)$ doublet VLQ and one singlet VLQ, for different M_{VL} and $\tilde{y}$ values. For $M_{VL} = 3$ TeV, if $\tilde{y} > 0.35$, λ becomes negative at a smaller field value as $\tilde{y}$ increases or as M_{VL} decreases, and is lesser when compared to the value in the SM. However, if $\tilde{y} < 0.35$, the vacuum instability is pushed to higher field values as compared to the SM. Curiously, for $\tilde{y} < 0.3$, λ remains positive for field values all the way up to M_{Pl}, i.e. the EW vacuum is the global minimum and is absolutely stable. For example, when $\tilde{y} = 0.1$, λ stays always positive for M_{VL} values slightly less than about 10^5 GeV.

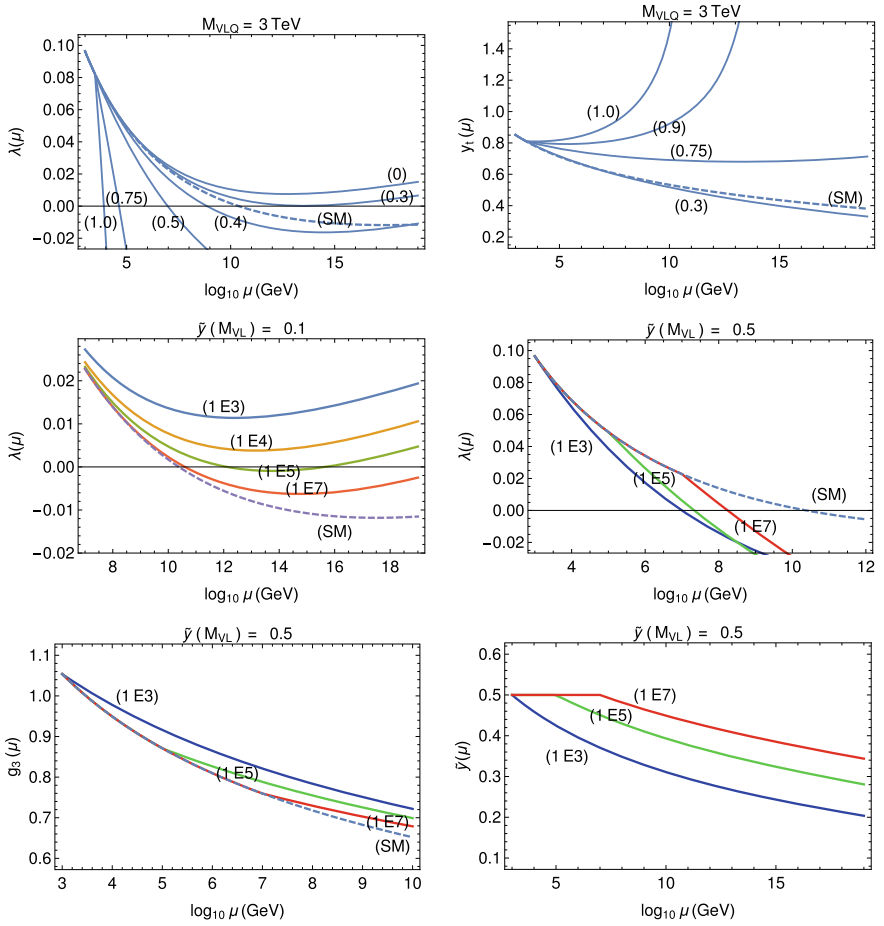

Fig. 20.2 From [6]. λ, y_t, g_3 and $\tilde{y}$ evolution with μ for a VLQ family, for $M_{VLQ} = 3$ TeV (top-most row), and, for different M_{VL} (in GeV) for $\tilde{y}(M_{VL}) = \{0.1, 0.5\}$ (bottom four plots)

These examples show the effect of a VLL and VLQ generation on the evolution of the couplings. More examples are presented in [6]. If λ does become negative, then the EW vacuum can tunnel away from the EW vacuum, and we discuss next the tunneling life-time for such cases.

20.3 Tunneling from the EW Vacuum

The meta-stable electroweak Higgs vacuum can tunnel into a deeper true vacuum via quantum mechanical barrier penetration. To compute the probability of tunneling, we follow the method reviewed in [10]. Here, we outline only the main points, drawing from the full details of the procedure given in [6].

We formulate the problem in Euclidean space-time coordinates ρ^i, with $\rho^2 \equiv \rho^i \rho^i$. We obtain the 'bounce' configuration ($h_B(\rho)$) as stationary points of the Euclidean action, which are solutions of the equation of motion (EOM)

$$\frac{d^2h}{d\rho^2} + \frac{3}{\rho}\frac{dh}{d\rho} = \frac{\partial V_{\text{eff}}}{\partial h} , \tag{20.5}$$

subject to the boundary conditions (BC) $(dh/d\rho)(\rho{=}0) = 0$ and $h(\rho \to \infty) = v$. We compute the bounce configuration using the RGE evolved couplings of Sect. 20.2. We denote by S_B the value of the Euclidean action in this bounce configuration, which is

$$S_B = 2\pi^2 \int_0^\infty d\rho\, \rho^3 \left[\frac{1}{2}\left(\frac{dh_B}{d\rho}\right)^2 + V_{\text{eff}}(h_B)\right] . \tag{20.6}$$

In terms of the bounce action S_B, the tunneling probability P_{tunl} is given by

$$P_{\text{tunl}} = (h_0/m_t)^4\, e^{(404-S_B)} , \tag{20.7}$$

where h_0 is the initial field value of the bounce. P_{tunl} essentially indicates the probability that we would have tunneled out of the EW vacuum by today (i.e. over the age of the Universe). Thus, if $P_{\text{tunl}} \ll 1$ we are fine, but if $P_{\text{tunl}} \gtrsim 1$ we lose understanding of why we still find ourselves in the EW vacuum, and we consider disfavored the BSM model parameter-space that led to this situation. This then imposes a constraint on BSM parameter-space points, which in our case are VLF mass and coupling.

We solve the EOM in (20.5) numerically using *Mathematica*. subject to the BC $h(\rho = 0) = h_0$, $(dh/d\rho)(\rho = 0) = 0$. We pick h_0 iteratively, searching for a h_0 that will lead to $h(\rho_{\text{end}}) = v$ and $(dh/d\rho)(\rho_{\text{end}}) = 0$. The numerical solution is tricky to obtain due to the large dynamical range of field values in the bounce, but we have managed to obtain a solution using an iterative search strategy, details of which are in [6]. In Fig. 20.3, we show the quantum effective potential $V_{\text{eff}}(h \equiv \mu)$, and the bounce solution $h_B(\hat{\rho})$ obtained numerically, where we have defined $\hat{\rho} \equiv \rho \tilde{m}_t$. We see that

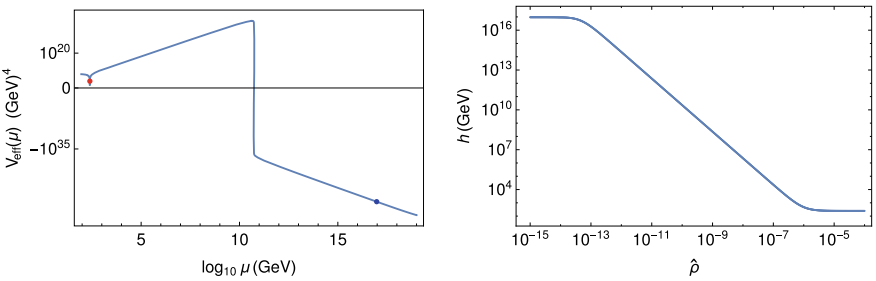

Fig. 20.3 From [6]. For the SM, the quantum effective potential $V_{\text{eff}}(h \equiv \mu)$, and the bounce configuration $h_B(\hat{\rho})$

$V_{\rm eff}(\mu)$ crosses zero at about $\mu \approx 10^{10.75}$ GeV, and is negative for larger μ. The blue dot shows the starting field value (h_0) of the bounce and the red dot the ending field value (v). By numerical integration of (20.6) we obtain S_B for this $h_B(\rho)$. For the SM, we find $S_B = 2866$ (in $\hbar = 1$ units), and using this in (20.7), we obtain the probability to tunnel away from the EW vacuum to be $P_{\rm tunl} \sim 10^{-1013}$, an incredibly tiny probability. Thus, as stated earlier, in the SM, the EW vacuum is meta-stable with a tunneling life-time much larger than the age of the Universe. This is in very good agreement with the result obtained in [4].

Following an identical procedure, we compute numerically $h_B(\rho)$, S_B and $P_{\rm tunl}$ with VLF states also added. We add a VLL family with an $SU(2)$ singlet with hypercharge -1 and an $SU(2)$ doublet with hypercharge $-1/2$, with a common mass M_{VL} and various $\tilde{y}$. For a VLL family with $M_{VL} = 10^3$ GeV and $\tilde{y} = 0.6$, we find $S_B = 472$ and $P_{\rm tunl} \sim 10^{-6}$. With such a VLL present, the tunneling probability is dramatically enhanced compared to the SM, but this parameter-space point is still allowed since $P_{\rm tunl} \ll 1$. As another example, we consider a VLL with $M_{VL} = 10^3$ GeV and $\tilde{y} = 0.61$, for which we find $S_B = 422$ and $P_{\rm tunl} \sim 10^{17}$. Since $P_{\rm tunl} \gg 1$, this parameter-space point is excluded. From these examples, we see the extreme sensitivity of $P_{\rm tunl}$ on $\tilde{y}$.

Next, we add a VLQ family with a color triplet VLQ family with an $SU(2)$ singlet VLQ with hypercharge $2/3$ and an $SU(2)$ doublet VLQ with hypercharge $1/6$. For such a VLQ, in Fig. 20.4 we show the regions of stability, meta-stability, and instability, in the M_{VL} (in GeV) and $\tilde{y}$ parameter-space. The Higgs electroweak minimum is the absolute minimum in the region marked "stable", there is a lower minimum at large field values with $P_{\rm tunl} \lesssim \mathcal{O}(1)$ in the region marked "meta-stable", and $P_{\rm tunl} \gtrsim \mathcal{O}(1)$ in the region marked "unstable". For $\tilde{y} \gtrsim 0.5$ we find that the $P_{\rm tunl} \gtrsim \mathcal{O}(1)$, almost independently of M_{VL}, excluding such regions of parameter-space.

These examples illustrate the effects VLFs have on the question of Higgs vacuum stability. An interesting possibility we notice is that for some VLF representations and parameter values, $\lambda(\mu)$ never goes negative, implying that the EW vacuum is a

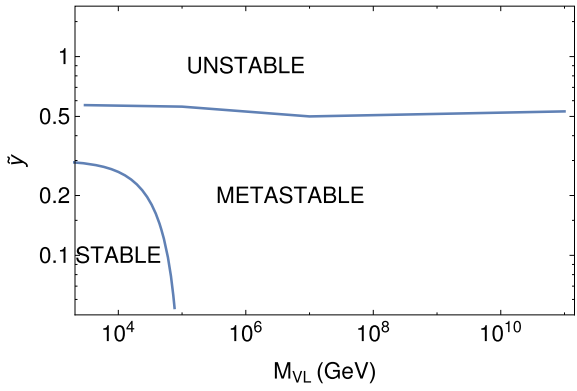

Fig. 20.4 From [6]. With a VLQ family added, the regions of stability, meta-stability and instability

global minimum and absolutely stable, unlike in the SM where it is meta-stable. More examples are presented in [6], including the case when there is a second minimum (in addition to the EW minimum) at large field values.

20.4 Comparison with the Analytical Approximation of S_B

An analytical approximation has been developed in [11, 12] for the Euclidean action evaluated for the bounce configuration, which is,

$$S_B^{\text{approx}} = \frac{8\pi^2}{3(-\lambda(t))}\,, \tag{20.8}$$

where t is the scale where the bounce makes a transition from large field values to v. We compare next our numerical results for S_B obtained in Sect. 20.3 to this analytical approximation. As explained in [6], this analytical expression works well when $\beta_\lambda(\mu) \approx 0$ for some μ, and we set t to this μ. Such is the case in the SM. For the SM, the S_B computed numerically as in Sect. 20.3 gives us 2866. Using the analytical approximation of (20.8), with $t \approx 10^{17}$ GeV (the scale at which $\beta_\lambda \approx 0$), where $\lambda = -0.009$, we find $S_B^{\text{approx}} = 2848$. These are indeed quite close and will yield similar P_{tunl} values, and (20.8) thus provides a good approximation. However as explained in [6], with VLFs present, there may be no scale at which $\beta_\lambda(\mu) \approx 0$, i.e. there is no unique scale at which the bounce makes the transition, and we cannot apply the analytical approximation. We have to then rely on the numerical computations of the tunneling probability that we have presented.

20.5 Conclusions

We discuss the issue of the stability of the electroweak vacuum in the presence of vector-like fermions, using the renormalization group improved Higgs quantum effective potential. For illustration, we consider simple VLF models, namely, a family of singlet and double vector-like quarks or leptons, coupled to the Higgs via the Yukawa coupling $\tilde{y}$.

We present results of numerically integrating the renormalization group equations, and ask if $\lambda(\mu)$ becomes zero at any field value μ, signalling vacuum instability. When this happens, we present numerical computations of the tunneling probability from the electroweak vacuum to large field values, got by computing the bounce configuration that are stationary points of the Euclidean action.

We show that the standard model electroweak vacuum is meta-stable, but with an incredibly tiny tunneling probability, in good agreement with results in the literature. With VLFs present, the situation can dramatically change with the tunneling rate even becoming of order unity, disfavoring such points.

We compare our numerical evaluation of the bounce configuration and its Euclidean action with an analytical approximation present in the literature. We show that for the standard model, the analytical approximation is very good, but in the case when VLFs are present, it may not be applicable. One has to then resort to a numerical computation as we have done.

References

1. M. Sher, Phys. Rep. **179**, 273 (1989). https://doi.org/10.1016/0370-1573(89)90061-6
2. F. Bezrukov, M.Y. Kalmykov, B.A. Kniehl, M. Shaposhnikov, JHEP **1210**, 140 (2012). https://doi.org/10.1007/JHEP10(2012)140, arXiv:1205.2893 [hep-ph]
3. G. Degrassi, S. Di Vita, J. Elias-Miro, J.R. Espinosa, G.F. Giudice, G. Isidori, A. Strumia, JHEP **1208**, 098 (2012). https://doi.org/10.1007/JHEP08(2012)098, arXiv:1205.6497 [hep-ph]
4. D. Buttazzo, G. Degrassi, P.P. Giardino, G.F. Giudice, F. Sala, A. Salvio, A. Strumia, JHEP **1312**, 089 (2013). https://doi.org/10.1007/JHEP12(2013)089, arXiv:1307.3536 [hep-ph]
5. F. Bezrukov, M. Shaposhnikov, J. Exp. Theor. Phys. **120**, 335 (2015); [Zh. Eksp. Teor. Fiz. **147**, 389 (2015)]. https://doi.org/10.1134/S1063776115030152, arXiv:1411.1923 [hep-ph]
6. S. Gopalakrishna, A. Velusamy, Phys. Rev. D **99**(11), 115020 (2019). https://doi.org/10.1103/PhysRevD.99.115020, arXiv:1812.11303 [hep-ph]
7. S. Weinberg, *The Quantum Theory of Fields: Modern Applications*, vol. 2 (Cambridge University Press, Cambridge, 1995)
8. F. Staub, arXiv:0806.0538 [hep-ph]
9. F. Staub, Comput. Phys. Commun. **185**, 1773 (2014). https://doi.org/10.1016/j.cpc.2014.02.018, arXiv:1309.7223 [hep-ph]
10. S. Coleman, *Aspects of Symmetry: Selected Erice Lectures* (Cambridge University Press, Cambridge, 1985). https://doi.org/10.1017/CBO9780511565045
11. K.M. Lee, E.J. Weinberg, Nucl. Phys. B **267**, 181 (1986). https://doi.org/10.1016/0550-3213(86)90150-1
12. P.B. Arnold, Phys. Rev. D **40**, 613 (1989). https://doi.org/10.1103/PhysRevD.40.613

Chapter 21
Phenomenology of Two Higgs Doublet Model with Flavor Dependent $U(1)$ Symmetry

Takaaki Nomura

Abstract We propose a generation dependent lepton/baryon Abelian gauge symmetry, $U(1)_X$, as a possible solution for the $b \to s\mu^+\mu^-$ anomalies. Introducing two Higgs doublet fields, we can reproduce the observed CKM matrix, and generate flavor changing Z' interactions in the quark sector due to flavor dependent charge assignment. One thus can explain observed anomalies in $b \to s\ell^+\ell^-$ decay with the lepton non-universal $U(1)_X$ charge assignments. Taking into account experimental constraints of B_s–$\bar{B}_s$ mixing we show parameter region explaining the anomalies and discuss dark matter physics.

21.1 Introduction

An introduction of new $U(1)$ gauge symmetry is one of the simple extension of the standard model (SM) of particle physics which can provide rich phenomenological consequences. In particular flavor dependent $U(1)$ gauge symmetry is interesting since it can constrain structure of Yukawa couplings generating masses for quarks, charged leptons and neutrinos [1–6]. In this kind of approaches to the flavor problem, these models may generate flavor changing neutral current (FCNC) processes through Z' boson exchange.

One can apply flavor dependent local $U(1)$ to explain recent indication of anomalies in B physics measurements for $b \to s\ell^+\ell^-$ process. The angular observable P_5' in decay of B meson, $B \to K^*\mu^+\mu^-$ [7], indicates 3.4σ deviations from the data with integrated luminosity of 3.0 fb^{-1} at the LHCb [8], confirming an earlier observation with 3.7σ deviations [9]. In addition, 2.1σ deviations were reported for the same observable by Belle [10, 11]. Furthermore, an anomaly in the measurement of lepton flavor universality by the ratio $R_K = BR(B^+ \to K^+\mu^+\mu^-)/BR(B^+ \to K^+e^+e^-)$ [12, 13] at the LHCb shows 2.6σ deviations from the SM prediction [14].

T. Nomura (✉)
School of Physics, Korea Institute for Advanced Studay (KIAS),
Seoul 02455, Republic of Korea
e-mail: nomura@kias.re.kr

A. Giri and R. Mohanta (eds.), *Workshop on Frontiers in High Energy Physics 2019*, Springer Proceedings in Physics 248,
https://doi.org/10.1007/978-981-15-6292-1_21

Moreover the LHCb collaboration also reported an anomaly in the ratio $R_{K^*} = BR(B \to K^* \mu^+ \mu^-)/BR(B \to K^* e^+ e^-)$ where the observed values are deviated from the SM prediction by $\sim 2.4\sigma$ as $R_{K^*} = 0.660^{+0.110}_{-0.070} \pm 0.024 (0.685^{+0.113}_{-0.069} \pm 0.047)$ for $(2m_\mu^2) < q^2 < 1.1\ \text{GeV}^2$ $(1.1\ \text{GeV}^2 < q^2 < 6\ \text{GeV}^2)$ [15].

Here we review a model based on flavor dependent Abelian gauge symmetry $U(1)_{B_3 - x_\mu L_\mu - x_\tau L_\tau}$, which is anomaly-free for $x_\mu + x_\tau = 1$ motivated by $b \to s\ell^+\ell^-$ anomalies [16]. In this model we introduce two Higgs doublet fields to generate the realistic CKM matrix, where small mixings associated with third generation quarks can be obtained naturally as shown in [17]. In the reference it is also shown that $Z'bs$ interaction is induced after electroweak symmetry breaking in a model with flavor dependent $U(1)_{L_\mu - L_\tau - a(B_1+B_2-2B_3)}$ gauge symmetry where a can be arbitrary real number. Then, $b \to s\ell^+\ell^-$ anomalies can be explained by the effective operator induced by exchange of a TeV scale Z' boson. We will also discuss constraint form B_s–$\bar{B}_s$ mixing and dark matter physics.

21.2 A Model

Here we review a model based on flavor dependent local $U(1)_X$ symmetry. For fermions, $U(1)_X$ charges are assigned as Table 21.1 where it is chosen to cancel gauge anomalies. In this model we introduce two Higgs doublets in order to induce the realistic CKM mixing matrix:

$$\Phi_1 : (\mathbf{1}, \mathbf{2})(1/2, -1/3), \quad \Phi_2 : (\mathbf{1}, \mathbf{2})(1/2, 0), \quad (SU(3)_C, SU(2)_L)(U(1)_Y, U(1)_X) \tag{21.1}$$

We also introduce two $SU(2)_L$ singlet scalar fields developing vacuum expectation values (VEVs):

$$\varphi_1 : (\mathbf{1}, \mathbf{1})(0, 1/3), \quad \varphi_2 : (\mathbf{1}, \mathbf{1})(0, 1), \tag{21.2}$$

where φ_1 is also necessary to induce $\Phi_1^\dagger \Phi_2$ terms while φ_2 is added for generating the 23(32) element of Majorana mass matrix of right-handed neutrino. The VEVs of these scalar fields spontaneously break electroweak and $U(1)_X$ gauge symmetries. In our set up, the full scalar potential for scalar fields in our model is given by

Table 21.1 Charge assignment for the SM fermions and right-handed neutrinos where the indices $i = 1, 2$ indicate the first and second generations

Fermions	Q_{iL}	u_{iR}	d_{iR}	Q_{3L}	t_R	b_R	L_{1L}	L_{2L}	L_{3L}	e_R	μ_R	τ_R	ν_{1R}	ν_{2R}	ν_{3R}
$SU(3)_C$	**3**	**3**	**3**	**3**	**3**	**3**	**1**	**1**	**1**	**1**	**1**	**1**	**1**	**1**	**1**
$SU(2)_L$	**2**	**1**	**1**	**2**	**1**	**1**	**2**	**2**	**2**	**1**	**1**	**1**	**1**	**1**	**1**
$U(1)_Y$	$\frac{1}{6}$	$\frac{2}{3}$	$-\frac{1}{3}$	$\frac{1}{6}$	$\frac{2}{3}$	$-\frac{1}{3}$	$-\frac{1}{2}$	$-\frac{1}{2}$	$-\frac{1}{2}$	-1	-1	-1	0	0	0
$U(1)_X$	0	0	0	$\frac{1}{3}$	$\frac{1}{3}$	$\frac{1}{3}$	0	$\frac{1}{3}$	$-\frac{4}{3}$	0	$\frac{1}{3}$	$-\frac{4}{3}$	0	$\frac{1}{3}$	$-\frac{4}{3}$

$$
\begin{aligned}
V = &- \mu(\Phi_1^\dagger \Phi_2 \varphi_1^* + \text{h.c.}) + \mu_{11}^2 |\Phi_1|^2 + \mu_{22}^2 |\Phi_2|^2 + \mu_{\varphi_1}^2 |\varphi_1|^2 + \mu_{\varphi_2}^2 |\varphi_2|^2 \\
&+ \frac{\lambda_1}{2} |\Phi_1|^4 + \frac{\lambda_2}{2} |\Phi_2|^4 + \lambda_3 |\Phi_1|^2 |\Phi_2|^2 + \lambda_4 |\Phi_1^\dagger \Phi_2|^2 + \lambda_{\varphi_1} |\varphi_1|^4 + \lambda_{\varphi_2} |\varphi_2|^4 \\
&+ \lambda_{\Phi_1 \varphi_1} |\Phi_1|^2 |\varphi_1|^2 + \lambda_{\Phi_2 \varphi_1} |\Phi_2|^2 |\varphi_1|^2 + \lambda_{\Phi_1 \varphi_2} |\Phi_1|^2 |\varphi_2|^2 + \lambda_{\Phi_2 \varphi_2} |\Phi_2|^2 |\varphi_2|^2 \\
&+ \lambda_{\varphi_1 \varphi_2} |\varphi_1|^2 |\varphi_2|^2 - \lambda_X (\varphi_1^3 \varphi_2^* + h.c.),
\end{aligned} \tag{21.3}
$$

where we assumed all the coupling constants are real for simplicity. We also introduce additional Dirac fermion χ with $U(1)_X$ charge 5/6 where its stability is guaranteed by remnant Z_2 symmetry.

The Yukawa couplings for quarks are given by

$$
\begin{aligned}
-\mathcal{L}_Q = &\, y_{ij}^u \bar{Q}_{iL} \tilde{\Phi}_2 u_{jR} + y_{ij}^d \bar{Q}_{iL} \Phi_2 d_{jR} + y_{33}^u \bar{Q}_{3L} \tilde{\Phi}_2 t_R + y_{33}^d \bar{Q}_{3L} \Phi_2 b_R \\
&+ \tilde{y}_{3i}^u \bar{Q}_{3L} \tilde{\Phi}_1 u_{iR} + \tilde{y}_{i3}^d \bar{Q}_{iL} \Phi_1 b_R + \text{h.c.},
\end{aligned} \tag{21.4}
$$

where $i = 1, 2$ and $\tilde{\Phi}_i = i\sigma_2 \Phi_i^*$. Φ_2 is the Higgs doublet with vanishing $U(1)_X$ charge, and is the SM-like Higgs doublet. After two Higgs doublet fields get the non-zero vacuum expectation values (VEVs) $\langle \Phi_{1,2} \rangle = (0 \; v_{1,2}/\sqrt{2})^T$, we obtain the following forms of quark mass matrices:

$$
\begin{aligned}
M^u &= \frac{1}{\sqrt{2}} \begin{pmatrix} v_2 y_{11}^u & v_2 y_{12}^u & 0 \\ v_2 y_{21}^u & v_2 y_{22}^u & 0 \\ 0 & 0 & v_2 y_{33}^u \end{pmatrix} + \begin{pmatrix} 0 & 0 & 0 \\ 0 & 0 & 0 \\ (\xi_u)_{31} & (\xi_u)_{32} & 0 \end{pmatrix}, \\
M^d &= \frac{1}{\sqrt{2}} \begin{pmatrix} v_2 y_{11}^d & v_2 y_{12}^d & 0 \\ v_2 y_{21}^d & v_2 y_{22}^d & 0 \\ 0 & 0 & v_2 y_{33}^d \end{pmatrix} + \begin{pmatrix} 0 & 0 & (\xi_d)_{13} \\ 0 & 0 & (\xi_d)_{23} \\ 0 & 0 & 0 \end{pmatrix}.
\end{aligned} \tag{21.5}
$$

Note that the matrices $\left(\xi_{u,d}\right)_{ij} \equiv \tilde{y}_{ij}^{u,d} v_1/\sqrt{2}$ have the same structure as those discussed in [17]. We shall assume the second terms with $\xi_{u,d}$ are small perturbation effects generating realistic 3×3 CKM mixing matrix where the (33) elements are $v_2 y_{33}^{u(d)} \sim \sqrt{2} m_{t(b)}$ following the discussion in [17]. As in the SM, the quark mass matrices are diagonalized by unitary matrices $U_{L,R}$ and $D_{L,R}$ which change quark fields from interaction basis to mass basis: $u_{L,R} \to U_{L,R}^\dagger u_{L,R}$ ($d_{L,R} \to D_{L,R}^\dagger d_{L,R}$). Then the CKM matrix is given by $V_{CKM} = U_L^\dagger D_L$. In this model, taking small ξ_d values, CKM matrix can be approximated as $V_{CKM} \simeq D_L$, and $D_R \simeq \mathbf{1}$, as obtained in [17].

Then Z' interactions to the SM fermions are written as

$$
\begin{aligned}
\mathcal{L} \supset &\frac{g_X}{3} \left(\bar{\mu} \gamma^\mu \mu - 4 \bar{\tau} \gamma^\mu \tau + \bar{\nu}_\mu \gamma^\mu P_L \nu_\mu - 4 \bar{\nu}_\tau \gamma^\mu P_L \nu_\tau + \bar{\nu}_2 \gamma^\mu P_R \nu_2 - 4 \bar{\nu}_3 \gamma^\mu P_R \nu_3 \right) Z'_\mu \\
&+ \frac{g_X}{3} \bar{t} \gamma^\mu t Z'_\mu + \frac{g_X}{3} \left(\bar{d}_\alpha \gamma^\mu P_L d_\beta \Gamma_{\alpha\beta}^{d_L} + \bar{d}_\alpha \gamma^\mu P_R d_\beta \Gamma_{\alpha\beta}^{d_R} \right) Z'_\mu \,,
\end{aligned} \tag{21.6}
$$

where g_X is the gauge coupling constant associated with the $U(1)_X$ and the lepton sector is given in the flavor basis here. The coupling matrices Γ^{d_R} and Γ^{d_L} for down-type quarks are given approximately by

$$\Gamma^{d_L} \simeq \begin{pmatrix} |V_{td}|^2 & V_{ts}V_{td}^* & V_{tb}V_{td}^* \\ V_{td}V_{ts}^* & |V_{ts}|^2 & V_{tb}V_{ts}^* \\ V_{td}V_{tb}^* & V_{ts}V_{tb}^* & |V_{tb}|^2 \end{pmatrix}, \quad \Gamma^{d_R} \simeq \begin{pmatrix} 0\,0\,0 \\ 0\,0\,0 \\ 0\,0\,1 \end{pmatrix}, \tag{21.7}$$

where $V_{qq'}$'s are the CKM matrix elements. We have applied the relation $V_{CKM} \simeq D_L$, as we discussed above. In our model the Z' mass, $m_{Z'}$, is dominantly given by the VEV of SM singlet scalar field as discussed below.

21.3 Phenomenology

In this section, we discuss phenomenology in the model such as explanation of $b \to s\mu^+\mu^-$ anomalies, B_s–$\bar{B}_s$ mixing and dark matter.

21.3.1 Effective Interaction for $b \to S\mu^+\mu^-$

Gauge interactions in (21.6) induce the effective Hamiltonian for $b \to s\mu^+\mu^-$ process such that

$$\begin{aligned} \Delta H_{\text{eff}} &= \frac{g_X^2 V_{tb}V_{ts}^*}{9m_{Z'}^2}(\bar{s}\gamma^\mu P_L b)(\bar{\mu}\gamma_\mu\mu) + h.c. \\ &= -\frac{g_X^2}{9m_{Z'}^2}\left(\frac{\sqrt{2}\pi}{G_F\alpha_{em}}\right)\left(\frac{-4G_F}{\sqrt{2}}\frac{\alpha_{em}}{4\pi}V_{tb}V_{ts}^*\right)(\bar{s}\gamma^\mu P_L b)(\bar{\mu}\gamma_\mu\mu) + h.c., \end{aligned} \tag{21.8}$$

where G_F is the Fermi constant and α_{em} is the electromagnetic fine structure constant. We thus obtain the Z' contribution to Wilson coefficient ΔC_9^μ as

$$\Delta C_9^\mu = -\frac{g_X^2}{9m_{Z'}^2}\left(\frac{\sqrt{2}\pi}{G_F\alpha_{em}}\right) \simeq 2.78 \times \frac{-1}{3}\left(\frac{g_X}{0.62}\right)^2\left(\frac{1.5\ \text{TeV}}{m_{Z'}}\right)^2. \tag{21.9}$$

In order to obtain $\Delta C_9^\mu \sim -1$, x_μ should be negative and g_X is required to be ~ 0.6 for $m_{Z'} = 1.5$ TeV. Figure 21.1 shows the contour of ΔC_9^μ in the $(m_{Z'}, g_X)$ plane where the yellow(light-yellow) region corresponds to 1σ (2σ) region from global fit in [18].

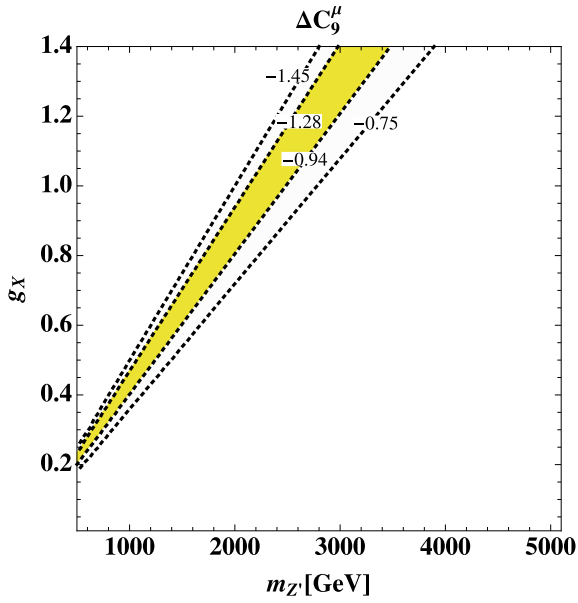

Fig. 21.1 The contours showing Z' contribution to ΔC_9^μ on the $m_{Z'}$-g_X plane where yellow(light-yellow) region corresponds to 1σ (2σ) region from global fit in [18]. The figure is taken from [16]

21.3.2 Constraint from B_s–$\bar{B}_s$ Mixing

In our model, Z' and neutral scalar bosons induce flavor changing neutral current (FCNC) interactions. The neutral scalar bosons include the SM Higgs h, CP-even heavy Higgs H and CP-odd Higgs A. Here we consider constraints from B_s–$\bar{B}_s$ mixing where other $\Delta F = 2$ processes are more suppressed by CKM factors.

The effective Hamiltonian for the B_s–$\bar{B}_s$ mixing is given by

$$H_{eff} = C_1(\bar{s}\gamma^\mu P_L b)(\bar{s}\gamma_\mu P_L b) + C_2'(\bar{s}P_R b)(\bar{s}P_R b). \tag{21.10}$$

The relevant Wilson coefficients are

$$C_1 = \frac{1}{2}\frac{g_X^2}{9m_{Z'}^2}(\Gamma_{sb}^{d_L})^2, \quad C_2' = \sum_{\eta=h,H,A}\frac{-1}{2m_\eta^2}(\Gamma_{sb}^{\eta})^2, \tag{21.11}$$

where $\Gamma_{qq'}^{\eta}$ is couplings for $\eta\bar{q}q'$ interactions ($\eta = h, H, A$), the explicit expressions of which are given in [16]. Using these Wilson coefficients we obtain ratio between Δm_{B_s} in our model and the SM prediction $\Delta m_{B_s}^{SM}$, under large $\tan\beta$ and small α, such that

$$R_{B_s} = \frac{\Delta m_{B_s}}{\Delta m_{B_s}^{SM}} \simeq \frac{g_X^2 (V_{tb} V_{ts}^*)^2}{9 m_{Z'}^2} (8.2 \times 10^{-5}\ \mathrm{TeV}^{-2})^{-1} + \left[0.12 \cos^2(\alpha - \beta) \tan^2\beta + 0.19 \tan^2\beta \left(\frac{(200\ \mathrm{GeV})^2}{m_H^2} - \frac{(200\ \mathrm{GeV})^2}{m_A^2} \right) \right], \tag{21.12}$$

where the first and second terms in the right-hand side corresponds to contributions from Z' and scalars, respectively [17, 19, 20]. The allowed range of R_{B_s} is estimated by [19, 20]

$$0.83 < R_{B_s} < 0.99. \tag{21.13}$$

We find that R_{B_s} will be deviated from the allowed range by Z' contribution when $\Delta C_9^\mu \simeq -1$ is required. Thus cancellation between Z' and scalar contribution is necessary to satisfy the experimental constraint. Here we derive allowed parameter region on $\{m_H, m_A - m_H\}$ plane satisfying B_s–$\bar{B}_s$ constraints when we fit C_9^μ to explain $b \to s\ell^+\ell^-$ anomalies choosing $\tan\beta = 10$ and $\cos(\alpha - \beta) \sim 0$ as reference values. In Fig. 21.2, we show the allowed parameter region where the yellow(light yellow) region corresponds to that in Fig. 21.1.

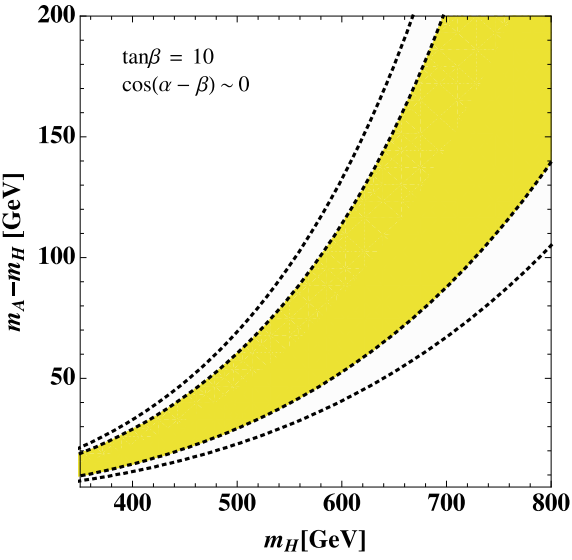

Fig. 21.2 The allowed region on $\{m_H, m_A - m_H\}$ plane satisfying B_s–$\bar{B}_s$ constraints with fitting C_9 to explain $b \to s\ell^+\ell^-$ anomalies where the yellow(light yellow) region corresponds to that in Fig. 21.1. Here we take $\tan\beta = 10$ and $\cos(\alpha - \beta) \sim 0$ as reference values. The figure is taken from [16]

21.3.3 Dark Matter

We consider a Dirac fermion χ as our DM candidate, and the relic density is determined by the DM annihilation process $\chi\bar{\chi} \to Z' \to f_{SM}\bar{f}_{SM}/HA/H^+H^-$ where f_{SM} is a SM fermion and/or $\chi\bar{\chi} \to Z'Z'$ depending on kinematic condition. Then we estimate relic density of our DM using `micrOMEGAs 4.3.5` [21] implementing relevant interactions.

Then we scan parameters in the range of

$$m_X \in [200, 3100]\ \text{GeV}, \quad m_{Z'} \in [500, 7000]\ \text{GeV}, \quad g_X \in [0.01, 1.5], \quad (21.14)$$

with assuming that $\tan\beta = 10$ and $\cos(\alpha - \beta) = 0$ as reference values. We note that the effects of scalar bosons are subdominant. The left panel of Fig. 21.3 shows the parameter region which accommodates the observed relic density of DM, $\Omega h^2 = 0.1206 \pm 0.0063$, taking 3σ range of observed value by the Planck collaboration [22]. Moreover the right panel of the figure indicates the region in which both observed relic density and $b \to s\ell^+\ell^-$ anomalies are explained within 2σ. In addition DM-nucleon scattering cross section by Z' exchange is suppressed by CKM factor and the allowed region is not constrained by the DM direct detection experiments.

Before closing this section we discuss possibility of indirect detection of our DM. In this model DM pair annihilates mainly through $\chi\bar{\chi} \to Z' \to \tau^+\tau^-$ and/or $\chi\bar{\chi} \to Z'Z' \to 2\tau^+\tau^-$ and gamma-ray search gives the strongest constraint on the annihilation cross section by Fermi-LAT observation [23, 24]. In our parameter region of $m_{Z'} > 500$ GeV, DM annihilation cross section explaining the relic density is well below the constraint for the $\tau^+\tau^-$ dominant case [23, 24] unless there is large enhancement factor; constraint on cross section for four τ mode would be similar. Thus our model is safe from indirect detection cross section and will be tested with larger amount of data in future.

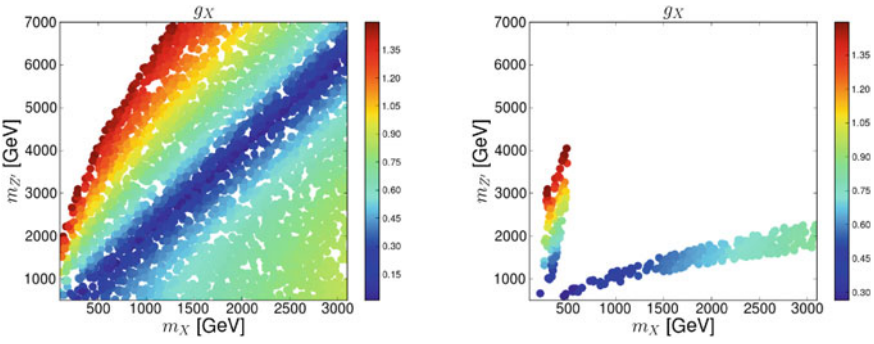

Fig. 21.3 (Left): parameter region which accommodates the observed DM relic density. (Right): parameter region which explains both DM relic density and $b \to s\ell^+\ell^-$ anomalies. The figures are taken from [16]

21.4 Summary

We have reviewed a model based on flavor dependent local $U(1)$ symmetry which can explain $b \to s\ell^+\ell^-$ anomalies. The flavor changing Z' interactions appear after electroweak symmetry breaking via fermion mixing. Then we obtain effective interaction via Z' exchange inducing $b \to s\ell^+\ell^-$ process. Taking into account B_s–$\bar{B}_s$ mixing constraint, we have shown parameter region explaining $b \to s\ell^+\ell^-$ anomalies. We also discuss dark matter physics in the model.

References

1. T. Nomura, H. Okada, Phys. Lett. B **761**, 190 (2016). arXiv:1606.09055 [hep-ph]
2. P. Ko, T. Nomura, H. Okada, Phys. Lett. B **772**, 547 (2017). arXiv:1701.05788 [hep-ph]
3. P. Ko, T. Nomura and H. Okada, Phys. Rev. D **95**(11), 111701 (2017). arXiv:1702.02699 [hep-ph]
4. S. Lee, T. Nomura, H. Okada, Nucl. Phys. B **931**, 179 (2018). arXiv:1702.03733 [hep-ph]
5. T. Nomura, H. Okada, Phys. Dark Univ. **21**, 90 (2018). arXiv:1712.00941 [hep-ph]
6. T. Nomura, H. Okada, arXiv:1806.09957 [hep-ph]
7. S. Descotes-Genon, J. Matias, M. Ramon, J. Virto, JHEP **1301**, 048 (2013). arXiv:1207.2753 [hep-ph]
8. R. Aaij et al., [LHCb Collaboration], JHEP **1602**, 104 (2016). arXiv:1512.04442 [hep-ex]
9. R. Aaij et al., [LHCb Collaboration], Phys. Rev. Lett. **111**, 191801 (2013). arXiv:1308.1707 [hep-ex]
10. A. Abdesselam et al., [Belle Collaboration], arXiv:1604.04042 [hep-ex]
11. S. Wehle et al., [Belle Collaboration], arXiv:1612.05014 [hep-ex]
12. G. Hiller, F. Kruger, Phys. Rev. D **69**, 074020 (2004). [hep-ph/0310219]
13. C. Bobeth, G. Hiller, G. Piranishvili, JHEP **0712**, 040 (2007). arXiv:0709.4174 [hep-ph]
14. R. Aaij et al., [LHCb Collaboration], Phys. Rev. Lett. **113**, 151601 (2014). arXiv:1406.6482 [hep-ex]
15. R. Aaij et al., [LHCb Collaboration], arXiv:1705.05802 [hep-ex]
16. P. Ko, T. Nomura, C. Yu, JHEP **1904**, 102 (2019). arXiv:1902.06107 [hep-ph]
17. A. Crivellin, G. D'Ambrosio, J. Heeck, Phys. Rev. D **91**(7), 075006 (2015). arXiv:1503.03477 [hep-ph]
18. B. Capdevila, A. Crivellin, S. Descotes-Genon, J. Matias, J. Virto, JHEP **1801**, 093 (2018). arXiv:1704.05340 [hep-ph]
19. P. Arnan, L. Hofer, F. Mescia, A. Crivellin, JHEP **1704**, 043 (2017). arXiv:1608.07832 [hep-ph]
20. A. Bazavov et al., [Fermilab Lattice and MILC Collaborations], Phys. Rev. D **93**(11), 113016 (2016). arXiv:1602.03560 [hep-lat]
21. G. Belanger, F. Boudjema, A. Pukhov, A. Semenov, Comput. Phys. Commun. **192**, 322 (2015). arXiv:1407.6129 [hep-ph]
22. N. Aghanim et al., [Planck Collaboration]. arXiv:1807.06209 [astro-ph.CO]
23. A. Albert et al., [Fermi-LAT and DES Collaborations], Astrophys. J. **834**(2), 110 (2017). arXiv:1611.03184 [astro-ph.HE]
24. S. Hoof, A. Geringer-Sameth, R. Trotta, arXiv:1812.06986 [astro-ph.CO]

Chapter 22
Signatures of GW from an Extended Inert Doublet Model

Debasish Majumdar, Avik Paul, and Biswajit Banerjee

Abstract We explore the emission of Gravitational waves (GWs) from a first order phase transition. To this end, we extend the scalar sector of Standard Model of particle physics (SM) by an additional scalar dublet and a scalar singlet. While the added doublet is Z_2 odd, the singlet is Z_2 even and on spontaneous symmetry breaking while the added singlet acquires a vacuum expectation value (VEV), the additional doublet does not develop any VEV. We explore in detail the phenomenology of the model and study the first order phase transition within the framework of this model. We then compute the consequent production of GWs and investigate the detection possibilities of such GWs at the future space borne detectors such as eLISA, ALIA, DECIGO etc.

22.1 Introduction

The study of Gravitational waves (GWs) has received a boost after the discovery of GWs by LIGO [1] from the collision of two black holes. Subsequently, other GW events from such collisions as well as collision with neutron stars are also detected by LIGO [2]. But the primordial GWs from the early Universe could have been generated from quantum fluctuations, topological defects, cosmic strings, first order phase transitions etc. In this work, we address the GW production from elecgtroweak first order phase transition by simple extension of the standard model of particle physics (SM) by an additional doublet scalar and a singlet scalar.

D. Majumdar (✉) · A. Paul · B. Banerjee
Astroparticle Physics and Cosmology Division, Saha Institute of Nuclear Physics, HBNI, 1/AF Bidhannagar, Kolkata 700064, India
e-mail: debasish.majumdar@saha.ac.in

A. Paul
e-mail: avik.paul@saha.ac.in

B. Banerjee
e-mail: biswajit.banerjee@saha.ac.in

A. Giri and R. Mohanta (eds.), *Workshop on Frontiers in High Energy Physics 2019*, Springer Proceedings in Physics 248,
https://doi.org/10.1007/978-981-15-6292-1_22

The electroweak phase transition as explained by SM following the spontaneous breakdown of $SU(2)_L \times U(1)_Y$ symmetry via Higgs mechanism whereby the SM scalar Higgs acquires a vacuum expectation value or VEV, is a smooth crossover and not a first order transition. In this work, we extend the SM by an additional doublet scalar and an additional singlet scalar. On spontaneous symmetry breaking (SSB), the extra doublet does not acquire any VEV (and thus termed as inert doublet) while the singlet develops a VEV on SSB. Discrete Z_2 symmetry is imposed on the additional doublet and singlet such that while the inert doublet is Z_2 odd, the additional singlet is Z_2 even. In the present model, after SSB, the SM scalar and the added singlet scalar mix and after diagonalisation of the mass matrix one of the two CP even eigenstate is attributed to the physical Higgs. This model has been discussed earlier in the context of particle Dark Matter [3, 4]. We demonstrate that this model also induces a strong first order phase transition and subsequently we explore the emission and strength of GW from this transition. The GWs may be produced from strong first order phase transition by the process of bubble collisions [5, 6]. In brief, when the Universe makes a transition from one metastable minimum to the global minimum, due to the existence of a barrier between these to minima, the Universe tunnels through these two minima causing first order electroweak phase transition. This process progresses through nucleation of electroweak bubbles that collide, coalesce and also undergo expansion to lead the Universe to the electroweak broken phase.

In the present work, we chose some benchmark set of points from the allowed model parameter space [3, 4] and computed the GW intensities. These are then compared with the expected sensitivities of different future space-based primordial GW detection experiments such as Big Bang Observer (BBO) [7], Evolved Laser Interferometer Space Antenna (eLISA) [7], Advanced Laser Interferometer Antenna (ALIA) [8], DECi-hertz Interferometer Gravitational wave Observatory (DECIGO) [7], Ultimate-DECIGO (U-DECIGO) [9] and ground-based detector Advanced LIGO (aLIGO) [7].

22.2 Formalism

22.2.1 The Model

As mentioned earlier, the model in the present work is an extension of the Standard Model with an inert doublet Φ_I and a real scalar singlet S. While the inert doublet is Z_2 odd, the singlet S is Z_2 even. The potential of the scalar sector of the model is given as

$$
\begin{aligned}
V = & m_1^2 \Phi_H^\dagger \Phi_H + m_2^2 \Phi_I^\dagger \Phi_I + \frac{1}{2} m_s^2 S^2 + \lambda_1 \left(\Phi_H^\dagger \Phi_H\right)^2 + \lambda_2 \left(\Phi_I^\dagger \Phi_I\right)^2 \\
& + \lambda_3 \left(\Phi_H^\dagger \Phi_H\right) \left(\Phi_I^\dagger \Phi_I\right) \lambda_4 \left(\Phi_I^\dagger \Phi_H\right) \left(\Phi_H^\dagger \Phi_I\right) \\
& + \frac{\lambda_5}{2} \left[\left(\Phi_I^\dagger \Phi_H\right)^2 + \left(\Phi_H^\dagger \Phi_I\right)^2 \right] + \rho_1 \left(\Phi_H^\dagger \Phi_H\right) S \\
& + \rho_1' \left(\Phi_I^\dagger \Phi_I\right) S + \rho_2 \left(\Phi_H^\dagger \Phi_H\right) S^2 + \rho_2' \left(\Phi_I^\dagger \Phi_I\right) S^2 + \frac{\rho_3}{3} S^3 + \frac{\rho_4}{4} S^4.
\end{aligned}
\tag{22.1}
$$

In the above (22.1). Φ_H denotes the Higgs field. After SSB, Φ_I does not acquire any VEV and with v and v_s as the VEVs acquired by the SM Higgs and the added scalar singlet, we have

$$
\phi_H = \begin{pmatrix} 0 \\ \frac{1}{\sqrt{2}} (v + h) \end{pmatrix}, \ \phi_I = \begin{pmatrix} H^+ \\ \frac{1}{\sqrt{2}} (H_0 + i A_0) \end{pmatrix}, \ S = v_s + s, \tag{22.2}
$$

After minimising the scalar potential represented in (22.1), we obtain

$$
\begin{aligned}
m_1^2 + \lambda_1 v^2 + \rho_1 v_s + \rho_2 v_s^2 = 0, \\
m_s^2 + \rho_3 v_s + \rho_4 v_s^2 + \frac{\rho_1 v^2}{2 v_s} + \rho_2 v^2 = 0.
\end{aligned}
\tag{22.3}
$$

By evaluating the second order derivatives of the scalar potential (after SSB), the elements of the mass matrix can be obtained.

As h and s mix, diagonalising the mass matrix in h, s basis by a unitary matrix U, the physical mass eigenstates are obtained as

$$
h_1 = h \ \cos\theta - s \ \sin\theta, \ h_2 = h \ \sin\theta + s \ \cos\theta, \tag{22.4}
$$

where θ is the mixing angle that can be computed from

$$
\tan\theta = \frac{y}{1 + \sqrt{1 + y^2}}, \quad \text{where } y = \frac{2\mu_{hs}^2}{\mu_h^2 - \mu_s^2} \ . \tag{22.5}
$$

The mass eigenstates are

$$
m_{h_1, h_2}^2 = \frac{\left(\mu_h^2 + \mu_s^2\right)}{2} \pm \frac{\left(\mu_h^2 - \mu_s^2\right)}{2} \sqrt{1 + y^2}, \tag{22.6}
$$

where the '+' sign is for h_1 and '$-$' sign is for h_2, and h_1 is the physical (SM like) Higgs with mass $m_{h_1} = 125.09$ GeV [10] and h_2 is the other scalar. Both the cases namely $m_{h_2} > m_{h_1}$ and $m_{h_2} < m_{h_1}$ are considered here. We mention as an aside that

in this model H_0 can be the lightest stable particle and hence a viable dark matter candidate when the coupling $\lambda_5 < 0$ (in (22.1)).

The expressions for other couplings (and model parameters) can be obtained from the minimisation conditions and using the elements of the mass matrix.

22.2.2 Electroweak Phase Transition and Gravitational Waves Production

The finite temperature effective potential is given by [11]

$$V_{\text{eff}} = V_{tree-level} + V_{1-loop}^{T=0} + V_{1-loop}^{T\neq 0}, \tag{22.7}$$

where $V_{1-loop}^{T=0}$ and $V_{1-loop}^{T\neq 0}$ are the one-loop corrected potential at zero temperature and at finite temperature respectively. The one-loop effective potential at zero temperature is given by [11]

$$V_{1-loop}^{T=0} = \pm\frac{1}{64\pi^2}\sum_i n_i m_i^4\left[\log\frac{m_i^2}{Q^2} - C_i\right], \tag{22.8}$$

where '+'('−') are for bosons(fermions). The degrees of freedom of these particle species are $n_{W^\pm} = 6, n_Z = 3, n_t = 12$ and $n_{h,H_0,A_0,H^+,H^-,s} = 1$. In the Landau gauge ($\xi = 0$), the Goldstone masses become zero at $T = 0$ and also there are no ghost contributions [12]. The renormalisable scale Q is taken to be $Q = 246.22$ GeV. In (22.8), C_i represents a numerical constant. The numerical constants C_i for different particles are $C_{W,Z} = 5/6$ and $C_{h,H_0,A_0,H^\pm,s,t} = 3/2$. The one-loop effective potential at finite temperature has the form [11]

$$V_{1-loop}^{T\neq 0} = \frac{T^4}{2\pi^2}\sum_i n_i J_\pm\left[\frac{m_i^2}{T^2}\right], \tag{22.9}$$

where

$$J_\pm\left(\frac{m_i^2}{T^2}\right) = \pm\int_0^\infty dy\ y^2\log\left(1 \mp e^{-\sqrt{y^2+\frac{m_i^2}{T^2}}}\right). \tag{22.10}$$

We use the CosmoTransitions package [11] for computation of the finite temperature corrections to the tree-level potential.

The intensity $\Omega_{\text{GW}}\text{h}^2$ of GW as a function of frequency is the sum of the contributing three components [5–16]

$$\Omega_{\text{GW}}\text{h}^2 = \Omega_{\text{col}}\text{h}^2 + \Omega_{\text{SW}}\text{h}^2 + \Omega_{\text{turb}}\text{h}^2. \tag{22.11}$$

The component from the bubbles collision $\Omega_{\text{col}}\text{h}^2$ is given by

$$\Omega_{\rm col}h^2 = 1.67\times10^{-5}\left(\frac{\beta}{H}\right)^{-2}\frac{0.11v_w^3}{0.42+v_w^2}\left(\frac{\kappa\alpha}{1+\alpha}\right)^2\left(\frac{g_*}{100}\right)^{-\frac{1}{3}}\frac{3.8\left(\frac{f}{f_{col}}\right)^{2.8}}{1+2.8\left(\frac{f}{f_{\rm col}}\right)^{3.8}}\,, \tag{22.12}$$

with the parameter β

$$\beta = \left[HT\frac{d}{dT}\left(\frac{S_3}{T}\right)\right]\Big|_{T_n}, \tag{22.13}$$

where T_n is the nucleation temperature and H_n is the Hubble parameter at T_n. The Euclidean action S_3 is given by

$$S_3 = 4\pi\int dr\; r^2\left[\frac{1}{2}\left(\partial_r\phi\right)^2 + V_{eff}\right], \tag{22.14}$$

where $\phi = (h, H_0, s)$.
The bubble wall velocity v_w follows from the expression [17]

$$v_w = \frac{1/\sqrt{3}+\sqrt{\alpha^2+2\alpha/3}}{1+\alpha}. \tag{22.15}$$

The parameter κ in (22.12) represents the fraction of latent heat deposited in a thin shell which is given by

$$\kappa = 1-\frac{\alpha_\infty}{\alpha}, \tag{22.16}$$

with [18]

$$\alpha_\infty = \frac{30}{24\pi^2 g_*}\left(\frac{v_n}{T_n}\right)^2\left[6\left(\frac{m_W}{v}\right)^2+3\left(\frac{m_Z}{v}\right)^2+6\left(\frac{m_t}{v}\right)^2\right], \tag{22.17}$$

v_n is the VEV of Higgs at T_n. The parameter α is defined as the ratio of vacuum energy density $\rho_{\rm vac}$ released by the electroweak phase transition to the background energy density of the plasma $\rho_*^{\rm rad}$ at T_n. The expression of α has the form

$$\alpha = \left[\frac{\rho_{\rm vac}}{\rho^*_{\rm rad}}\right]\Big|_{T_n}. \tag{22.18}$$

with

$$\rho_{\rm vac} = \left[\left(V_{\rm eff}^{\rm high}-T\frac{dV_{\rm eff}^{\rm high}}{dT}\right)-\left(V_{\rm eff}^{\rm low}-T\frac{dV_{\rm eff}^{\rm low}}{dT}\right)\right], \tag{22.19}$$

and

$$\rho^*_{\rm rad} = \frac{g_*\pi^2T_n^4}{30}. \tag{22.20}$$

The quantity $f_{\rm col}$ in (22.12) is the peak frequency produced by the bubble collisions which takes the form

$$f_{\rm col} = 16.5 \times 10^{-6}\ {\rm Hz} \left(\frac{0.62}{v_w^2 - 0.1 v_w + 1.8}\right) \left(\frac{\beta}{H}\right) \left(\frac{T_n}{100\ {\rm GeV}}\right) \left(\frac{g_*}{100}\right)^{\frac{1}{6}}. \tag{22.21}$$

The sound wave (SW) component of the gravitational wave (22.11) is given by

$$\Omega_{\rm SW} {\rm h}^2 = 2.65 \times 10^{-6} \left(\frac{\beta}{H}\right)^{-1} v_w \left(\frac{\kappa_v \alpha}{1+\alpha}\right)^2 \left(\frac{g_*}{100}\right)^{-\frac{1}{3}} \left(\frac{f}{f_{\rm SW}}\right)^3 \left[\frac{7}{4 + 3\left(\frac{f}{f_{\rm SW}}\right)^2}\right]^{\frac{7}{2}}, \tag{22.22}$$

where κ_v is the faction of latent heat transformed into the bulk motion of the fluid which has the following form

$$\kappa_v = \frac{\alpha_\infty}{\alpha} \left[\frac{\alpha_\infty}{0.73 + 0.083\sqrt{\alpha_\infty} + \alpha_\infty}\right]. \tag{22.23}$$

The peak frequency $f_{\rm SW}$ produced by the sound wave mechanisms takes the form

$$f_{\rm SW} = 1.9 \times 10^{-5}\ {\rm Hz} \left(\frac{1}{v_w}\right) \left(\frac{\beta}{H}\right) \left(\frac{T_n}{100\ {\rm GeV}}\right) \left(\frac{g_*}{100}\right)^{\frac{1}{6}}. \tag{22.24}$$

The component $\Omega_{\rm turb} {\rm h}^2$ (from the turbulence in plasma) is

$$\Omega_{\rm turb} {\rm h}^2 = 3.35 \times 10^{-4} \left(\frac{\beta}{H}\right)^{-1} v_w \left(\frac{\epsilon \kappa_v \alpha}{1+\alpha}\right)^{\frac{3}{2}} \left(\frac{g_*}{100}\right)^{-\frac{1}{3}} \frac{\left(\frac{f}{f_{\rm turb}}\right)^3 \left(1 + \frac{f}{f_{\rm turb}}\right)^{-\frac{11}{3}}}{\left(1 + \frac{8\pi f}{h_*}\right)}, \tag{22.25}$$

where $\epsilon = 0.1$ and the peak frequency $f_{\rm turb}$ is

$$f_{\rm turb} = 2.7 \times 10^{-5}\ {\rm Hz} \left(\frac{1}{v_w}\right) \left(\frac{\beta}{H}\right) \left(\frac{T_n}{100\ {\rm GeV}}\right) \left(\frac{g_*}{100}\right)^{\frac{1}{6}}. \tag{22.26}$$

In (22.25) the parameter h_* has the following form

$$h_* = 16.5 \times 10^{-6}\ {\rm Hz} \left(\frac{T_n}{100\ {\rm GeV}}\right) \left(\frac{g_*}{100}\right)^{\frac{1}{6}}. \tag{22.27}$$

22.3 Calculations and Results

We calculate gravitational wave intensity from the model using the (22.11)–(22.27). The calculations are performed for three chosen sets of benchmark points for several model parameters. The sets are chosen from the allowed parameter space. The allowed parameter space is obtained from theoretical constraints such as vacuum stability and perturbativity as also the experimental constraints given by collider bounds, the PLANCK dark matter relic density and the upper bound for the dark matter direct detection scattering cross-sections. Although not explored here, but note that the inert doublet component H_0 can be a viable dark matter candidate in this model as mentioned earlier. The chosen benchmark points are given in Table 22.1. The computed values of the parameters (v_n, T_c, T_n, α, β/H) corresponding to each of the three BPs to be used for the calculations of GW intensity are furnished in Table 22.2. These values are computed using the package CosmoTransitions [11].

Using the computed numerical values for each of the three sets given in Table 22.2 (corresponding to the BPs given in Table 22.1), the GW intensities for different GW frequencies from the first-order phase transitions are now calculated from (22.11)–(22.27) for each of the sets. The variations of GW intensities with the frequen-

Table 22.1 The chosen three benchmarks points (BPs). (Reproduced from Avik Paul, Biswajit Banerjee, Debasish Majumdar, Journal of Cosmology and Astroparticle Physics, **10**, 062 (2019), published 28 October 2019 • ©IOP publishing Ltd. and SISSA Medialab. Reproduced by permission of IOP Publishing. All rights reserved. DOI: https://doi.org/10.1088/1475-7516/2019/10/062)

BP	m_{H_0} in GeV	m_{h_2} in GeV	v_s in GeV	$\sin\theta$	ρ_1 in GeV	ρ_3 in GeV	λ_L	λ_s	λ_2	$\Omega_{\rm DM}h^2$	$\sigma_{\rm SI}$ cm^2
1	30	100	300	0.01	−3	0.01	0.001	0.0012	0.2	0.1220	9.41×10^{-48}
2	68	150	400	0.06	−7	0.2	0.002	0.033	0.031	0.1208	3.69×10^{-48}
3	76	200	500	0.03	−1	0.1	0.0016	0.0033	0.01	0.1195	3.56×10^{-48}

Table 22.2 The phase transition parameters obtained from three benchmark points (BPs) in Table 22.1 (Reproduced from Avik Paul, Biswajit Banerjee, Debasish Majumdar, Journal of Cosmology and Astroparticle Physics, **10**, 062 (2019), published 28 October 2019 • ©IOP publishing Ltd. and SISSA Medialab. Reproduced by permission of IOP Publishing. All rights reserved. DOI: https://doi.org/10.1088/1475-7516/2019/10/062)

BP	v_n in GeV	T_c in GeV	T_n in GeV	α	$\frac{\beta}{H}$
1	226.89	135.68	119.86	0.24	317.86
2	191.03	146.89	132.14	0.25	402.89
3	209.95	170.92	158.24	0.19	783.65

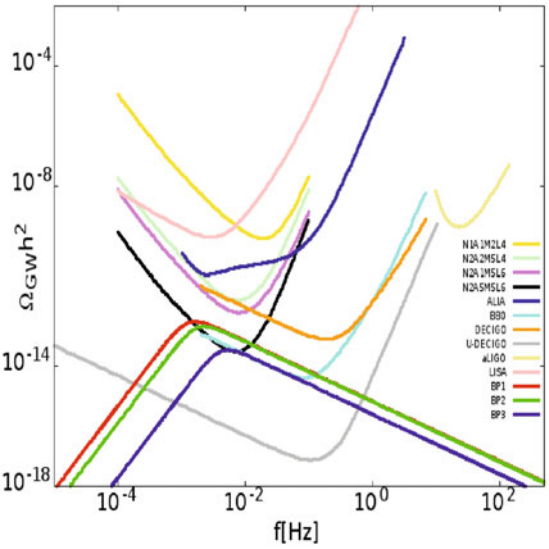

Fig. 22.1 Comparison of the chosen three BPs with the sensitivity curves of N1A1M2L4, N2A2M5L4, N2A1M5L6 and N2A5M5L6 configurations of eLISA, ALIA, BBO, DECIGO, U-DECIGO, aLIGO and LISA detectors (Reproduced from Avik Paul, Biswajit Banerjee, Debasish Majumdar, Journal of Cosmology and Astroparticle Physics, **10**, 062 (2019), published 28 October 2019 • ©IOP publishing Ltd. and SISSA Medialab. Reproduced by permission of IOP Publishing. All rights reserved. DOI: https://doi.org/10.1088/1475-7516/2019/10/062)

cies for different BPs are shown in Fig. 22.1. The results are then compared with the detectability of such GWs at the future detectors such as BBO, eLISA, ALIA, DECIGO, U-DECIGO, aLIGO and LISA. For this purpose, the sensitivities of these detectors are also plotted in Fig. 22.1. It can be seen from Fig. 22.1 that the peaks of the calculated GW frequencies in this model for the three BPs are within the sensitivity limits of eLISA, BBO and U-DECIGO.

22.4 Summary and Discussions

In this work, we have considered an extended Standard Model and explore the possibility of first order electroweak phase transition with this model and subsequent production of Gravitational Waves. In the model, the SM is extended by an inert doublet and a scalar singlet. It may also be mentioned that with suitable imposition of Z_2 symmetry and assuming that the added singlet scalar acquires a VEV (along with the SM Higgs), this inert doublet model component can be a viable particle dark matter candidate. The intensities of hte GWs are then computed with three sets of benchmark points for the parameters of the model. These calculated GW inten-

sities are then compared with the projected sensitivities of future space based (as also ground based) GW detectors for detection of such primordial GWs. We calculated and plotted the variations of GW intensities with GW frequencies for the GW emissions from the 1st order electroweak phase transitions in the framework of the present model. Our calculations show that the peak values of such GWs are within the detectable ranges of the future detectors BBO, eLISA and U-DECIGO.

References

1. Virgo, LIGO Scientific Collaboration, B. P. Abbott et al., Phys. Rev. Lett. **116**, 241103 (2016)
2. B.P. Abbott et al., [LIGO Scientific and Virgo Collaborations], Phys. Rev. Lett. **119**, 161101 (2017)
3. A. Dutta Banik, D. Majumdar, Eur. Phys. J. C **74**, 3142 (2014)
4. A. Dutta Banik, D. Majumdar, Phys. Lett. B **743**, 420 (2015)
5. A. Kosowsky, M.S. Turner, R. Watkins, Phys. Rev. D **45**, 4514 (1992)
6. S.J. Huber, T. Konstandin, JCAP **09**, 022 (2008)
7. C.J. Moore, R.H. Cole, C.P.L. Berry, Class. Quant. Grav. **32**, 015014 (2015)
8. X. Gong et al., J. Phys. Conf. Ser. **610**, 012011 (2015)
9. H. Kudoh, A. Taruya, T. Hiramatsu, Y. Himemoto, Phys. Rev. D **73**, 064006 (2006)
10. C. Patrignani et al., [Particle Data Group], Chin. Phys. C **40**, 100001 (2016)
11. C.L. Wainwright, Comput. Phys. Commun. **183**, 2006 (2012)
12. P. Basler, M. Krause, M. Muhlleitner, J. Wittbrodt, A. Wlotzka, JHEP **02**, 121 (2017)
13. M. Hindmarsh, S.J. Huber, K. Rummukainen, D.J. Weir, Phys. Rev. Lett. **112**, 041301 (2014)
14. M. Hindmarsh, S.J. Huber, K. Rummukainen, D.J. Weir, Phys. Rev. D **92**, 123009 (2015)
15. C. Caprini, R. Durrer, Phys. Rev. D **74**, 063521 (2006)
16. T. Kahniashvili, L. Kisslinger, T. Stevens, Phys. Rev. D **81**, 023004 (2010)
17. P.J. Steinhardt, Phys. Rev. D **25**, 2074 (1982)
18. V.R. Shajiee, A. Tofighi, Eur. Phys. J. C **79**, 360 (2019)

Chapter 23
Relaxed Constraints on Masses of New Scalars in 2HDM

Siddhartha Karmakar

Abstract 'Alignment without decoupling' in two-Higgs-doublet model (2HDM) is particularly important as it allows for new scalars of masses $\sim \mathcal{O}(100)$GeV with sizable decay to SM particles even after the discovery of the SM-like Higgs. In light of measurement of Higgs signal strengths and direct exotic scalar searches at LHC, the constraints on the masses and couplings of the new scalars in 2HDM are rather significant. We have investigated the sacrosanctity of these constraints when any new physics beyond a tree-level 2HDM at a ∼TeV scale is introduced. It is found that, for cascade decays of new scalars in 2HDM at LHC, the constraints on masses can be significantly changed.

23.1 Introduction

Since the discovery of the standard model (SM)-like Higgs boson (h_{125}) at the LHC, a plethora of beyond-SM (BSM) theories have been significantly constrained. 2HDM is one of the simplest yet prospective extensions of SM, which can address the phenomenological issues that SM cannot explain. In the framework of 2HDM, one can explain baryon asymmetry via electroweak baryogenesis, neutrino mass in presence of right-handed Majorana neutrinos and dark matter through an additional Z_2 symmetry. 2HDM is the simplest extension beyond the SM which simultaneously accommodates a SM-like Higgs and new scalars of masses $\sim \mathcal{O}(100)$ GeV with sizable couplings with the SM particles in the regime of 'alignment without decoupling' [1, 2]. Thus, it is a rather promising scenario in the wake of BSM scalar searches at the LHC. The measurements of signal strengths of the SM-like Higgs boson alone constrain the mixing between the two doublets significantly. Moreover, the direct searches of the new scalars in the 2HDM also put stringent bounds on the masses and couplings of these scalars even in the alignment limit [3].

S. Karmakar (✉)
Indian Institute of Technology Indore, Khandwa Road, Simrol, Indore 453552, India
e-mail: phd1401251010@iiti.ac.in

A. Giri and R. Mohanta (eds.), *Workshop on Frontiers in High Energy Physics 2019*, Springer Proceedings in Physics 248,
https://doi.org/10.1007/978-981-15-6292-1_23

2HDMs often constitute the scalar sector of even more complicated models such as supersymmetry (SUSY), composite/little Higgs, which address the issue of Higgs mass hierarchy. The direct searches of the additional particles like superpartners in SUSY models, top partner in composite models, etc. has pushed the masses of these particles beyond $\sim$1 TeV. But typically, if the new scalars in these models mix with the SM Higgs, these scalars must have masses $\lesssim$1 TeV to preserve perturbative unitarity in gauge boson scattering processes. Thus, we are looking at a BSM landscape with scalars with mass of few hundreds of GeVs and heavier degrees of freedom beyond $\sim$1 TeV taking care of the hierarchy problem. Hence, the effects of these TeV scale particles can be encoded in higher dimensional operators consisting of the SM fields and the second scalar doublet. It is commonly presumed that any new physics at $\sim$ TeV scale might drastically change the constraints in a 2HDM at the tree-level. Thus, we investigate the sacrosanctity of these constraints against the inclusion of new physics encoded in higher dimensional operators in the framework of 2HDM effective field theory (2HDMEFT), while remaining agnostic about any specific origin for such new physics. A complete and non-redundant basis for such operators was introduced for the first time in [4]. In the following, we study the changes in the allowed values of masses and mixing angles of the scalars in 2HDM in presence of bosonic dim-6 perators.

23.2 2HDM and Dimension-Six Operators

First we review some basic aspects of a generic 2HDM. The two scalar doublets can be defined as:

$$\varphi_I = \begin{pmatrix} \phi_I^+ \\ \frac{1}{\sqrt{2}}(v_I + \rho_I) + i\,\eta_I \end{pmatrix}, \tag{23.1}$$

where, $I = 1, 2$. The generic 2HDM potential is gives by:

$$\begin{aligned} V(\varphi_1, \varphi_2) = {} & m_{11}^2|\varphi_1|^2 + m_{22}^2|\varphi_2|^2 - (\mu^2\varphi_1^\dagger\varphi_2 + h.c.) + \lambda_1|\varphi_1|^4 + \lambda_2|\varphi_2|^4 \\ & + \lambda_3|\varphi_1|^2|\varphi_2|^2 + \lambda_4|\varphi_1^\dagger\varphi_2|^2 + \frac{\lambda_5}{2}\Big((\varphi_1^\dagger\varphi_2)^2 + h.c.\Big). \end{aligned} \tag{23.2}$$

Here the hard Z_2-violating terms have been neglected as they lead to tree-level flavour-changing neutral currents which are rather constrained. The charged scalars ($\phi_I^\pm$), CP-even neutral scalars (ρ_I) and pseudoscalars (η_I) pertaining to the two doublets mix after the electroweak symmetry breaking. These three mass matrices are diagonalised by orthogonal rotations characterised by angles α and β:

$$\begin{pmatrix} H \\ h \end{pmatrix} = \mathcal{R}(\alpha)\begin{pmatrix} \rho_1 \\ \rho_2 \end{pmatrix}, \quad \begin{pmatrix} W_L^\pm \\ H^\pm \end{pmatrix} = \mathcal{R}(\beta)\begin{pmatrix} \phi_1^\pm \\ \phi_2^\pm \end{pmatrix}, \quad \begin{pmatrix} Z_L \\ A \end{pmatrix} = \mathcal{R}(\beta)\begin{pmatrix} \eta_1 \\ \eta_2 \end{pmatrix}, \tag{23.3}$$

where, $\mathcal{R}(\theta) = \begin{pmatrix} \cos\theta & \sin\theta \\ -\sin\theta & \cos\theta \end{pmatrix}$ and $\beta = \tan^{-1}(v_2/v_1)$, $v_{1,2}$ being the vacuum expectation values (vev) of $\varphi_{1,2}$. The physical basis of 2HDM parameters consists of the following set of variables: $\{m_h = 125\,\text{GeV}, m_H, m_A, m_{H^\pm}, \tan\beta, \cos(\beta-\alpha), m_{12}^2\}$. The theoretical constraints, such as stability, perturbativity and unitarity put constraints on both the masses and mixing angles, which we do not discuss here in detail. The coupling of the SM-like Higgs boson h to SM vector bosons $V = W, Z$ are rescaled compared to the SM case by a factor: $\kappa_{hVV} = \sin(\beta-\alpha)$. Similarly, the $hf\bar{f}$ couplings are also modified by certain multipliers depending on the Yukawa type. For example, in type-II 2HDM, $\kappa_{hdd} = \kappa_{hll} = (s_{\beta-\alpha} - t_\beta c_{\beta-\alpha})$ and $\kappa_{huu} = (s_{\beta-\alpha} + c_{\beta-\alpha}/t_\beta)$. The measurement of the signal strengths of h_{125} dictates that the observed values of most of its couplings to the SM bosons and fermions are close to the SM values within $\sim 20\%$ uncertainty. In 2HDM, all couplings of h approach their SM values in the so-called 'alignment limit': $c_{\beta-\alpha} \to 0$. Depending on the value of t_β, the allowed range of $c_{\beta-\alpha}$ can at the most go up to $-0.05 \lesssim c_{\beta-\alpha} \lesssim 0.1$ at 95%CL [3]. This also restricts the couplings of the new scalars: For example, vertices like AZH, $H^\pm HW^\pm$, etc. are proportional to $s_{\beta-\alpha}$, whereas AZh, $H^\pm HW^\pm$, etc. are proportional to $c_{\beta-\alpha}$. Moreover, there are direct constraints on the masses of new scalar from LHC searches of $A \to Zh(H)$, $A(H) \to \tau\bar{\tau}$, VV, $b\bar{b}$ etc.

Now we investigate whether these constraints might change in presence of new physics at ~TeV. As mentioned earlier, the effects of these new physics can be encoded in higher dimensional operators in the scenario of 'alignment without decoupling' [4]. Let us consider a couple of bosonic dim-6 operators, such as, $O_1 = c_1(\partial_\mu|\varphi_1|^2)^2/f^2$, $O_2 = c_2(\partial_\mu|\varphi_2|^2)^2/f^2$, where $c_{1,2}$ are the Wilson coefficients, and new physics scale $f = 1$ TeV. In presence of the above operators the kinetic terms of the fields pertaining to the two doublets become non-canonical and subsequently, the fields must be redefined in the following manner:

$$h \to (1-x_1)h + yH, \qquad H \to (1-x_2)H + yh, \tag{23.4}$$

with, $x_1 = (v^2/f^2)(c_1 s_\alpha^2 c_\beta^2 + c_2 c_\alpha^2 s_\beta^2)$, $x_2 = (v^2/f^2)(c_1 c_\alpha^2 c_\beta^2 + c_2 s_\alpha^2 s_\beta^2)$, $y = (v^2/2f^2)(c_1 s_{2\alpha} s_{2\beta} - c_{2\alpha} c_\beta^2)$. Thus, the couplings involving h and H are accordingly rescaled. At this point we define a suitable benchmark point: **BP1** $\{m_{12}^2 = m_A^2 s_\beta c_\beta$, $c_1 = 1, c_2 = -3/2\}$. On inclusion of dim-6 operators with Wilson coefficients as in **BP1**, the couplings of h to the SM quarks becomes: $\kappa'_{hqq} = (1-x_1)\kappa_{hqq} + y\kappa_{Hqq}$. Thus, the gluon-fusion production cross-section of h also changes in **BP1** compared to 2HDM at the tree-level. In Fig. 23.1a we have shown the region allowed from the measurement of signal strengths of h_{125} on the $c_{\beta-\alpha} - t_\beta$ plane. Here, it can be seen that the Higgs signal strength marginally excludes the tree-level alignment limit for $t_\beta \gtrsim 2.5$ at 95% CL [5].

For $t_\beta = 1.5$, assuming a degenerate mass spectra for the new scalars, $m_H = m_{H^\pm} = m_A$, the region excluded from exotic scalar searches on the $c_{\beta-\alpha} - m_H$ plane has been shown in Fig. 23.1b. In this limit, decays of these new scalars into one another is kinematically prohibited and only decays to SM particles are allowed.

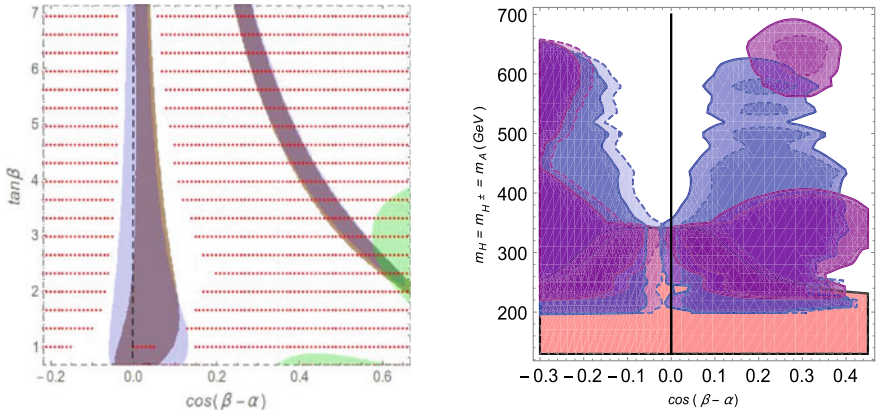

Fig. 23.1 **a** Constraints from h_{125} signal strengths at 95% CL. Blue (brown) region is allowed in case of 2HDM at tree-level (in presence of dim-6 terms as in **BP1**). Red dotted (green) region are ruled out from theoretical constraints (direct search of $A \to Zh(b\bar{b})$). **b** Blue, purple, pink region are ruled out from direct searches $H \to WW$, $A \to Zh(b\bar{b})$ and $A \to \tau\bar{\tau}$. Regions enclosed by solid (dashed) lines correspond to the cases of 2HDM at tree-level (in presence of dim-6 terms as in **BP1**)

Decay processes like $H \to WW$, $A \to Zh$ are always vanishing at the alignment limit in tree-level 2HDM. However, here it can be seen that in presence of dim-6 operators, these processes can be non-vanishing at $c_{\beta-\alpha} = 0$, thus ruling out the tree-level alignment limit for certain range of $m_{H,A}$. Even for a hierarchical mass spectrum: $m_A = m_{H^\pm} \geqslant m_H$ (dubbed Case **C1**) and type-I Yukawa couplings, as it is shown in Fig. 23.2a, the bound on the masses of the new scalars can be significantly relaxed at $c_{\beta-\alpha} = 0$ and $t_\beta \sim 1.5$. Here, the non-observation of $A \to ZH(b\bar{b})$ puts the most stringent constraint. As Fig. 23.2b shows, upon the inclusion of dim-6 operators as in **BP1**, the branching ratio for $H \to b\bar{b}$ significantly decreases due to the increase in Br($H \to WW$). This in turns reduces the decay rate of $A \to ZH(b\bar{b})$, leading to a relaxed constraint on m_H [6]. This effect can also be seen in type-IV 2HDM where the couplings of scalars to down-type quarks are similar to type-I 2HDM. Though, for type-II and -III 2HDM, the branching ratio of $H \to b\bar{b}$ is quite large at the tree-level itself. For these cases, the percentage changes in BR($H \to b\bar{b}$) upon including dim-6 operators are not as large as in type-I or type-IV 2HDM, leading to milder changes in the bounds on m_H.

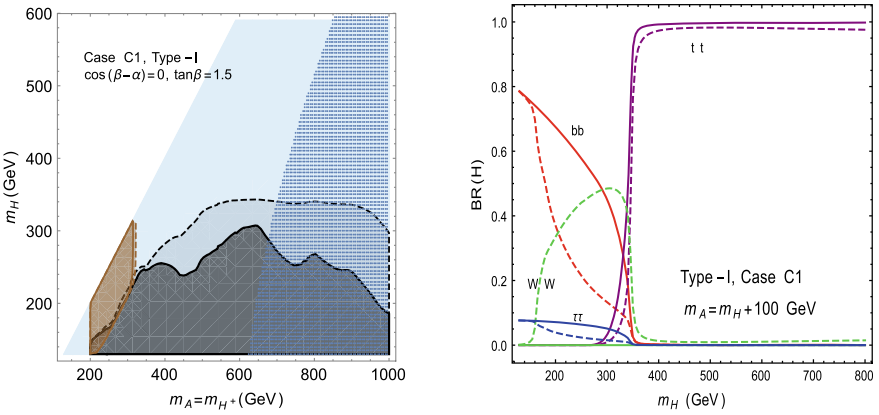

Fig. 23.2 **a** Light (dark) grey regions with dotted (solid) boundary are ruled out from $pp \to A \to ZH(b\bar{b})$ in 2HDM at tree-level and **BP1** of 2HDMEFT. Blue dotted region is ruled out from unitarity and perturbativity. **b** Change in the branching ratios of H with m_H. Solid (dashed) lines correspond to the case of 2HDM at tree-level (**BP1** of 2HDMEFT)

23.3 Conclusion

Extended scalar sectors can address the open questions of the Universe, such as neutrino mass, baryon asymmetry, dark matter, etc. After the discovery of SM-like Higgs, all the models with extended scalar sectors are pushed towards the 'alignment limit'. Alignment is easily achieved when the new scalars are decoupled from the SM particle spectrum. This scenario is not quite predictive in light of new scalar searches and can have significant constraints from unitarity and perturbativity. On the other hand, the case of 'alignment without decoupling' can be rather predictive at LHC as it allows for new scalars of mass $\sim \mathcal{O}(100)$ GeV with significant coupling to SM fermions.

2HDM sometime appear as integral parts of more complicated theories like supersymmetry, little/composite Higgs, which are deployed to solve the Higgs mass hierarchy problem. But the LHC searches of have pushed the mass scale of superpartners or the heavy top partners, etc., which soften the Higgs mass divergence beyond ∼TeV. Thus, the effect of these heavy particles can be encoded in higher dimensional operators, while considering 2HDM as a low-energy theory. We check the validity of the constraints on 2HDM parameter space from Higgs data and direct new scalar searches in presence of these higher dimensional operators of 2HDMEFT. By considering the bosonic operators of dim-6 we show that the constraints on new scalar masses from LHC direct searches can be significantly relaxed for cascade decay of scalars in case of hierarchical mass spectra. We also show that, though the tree-level

alignment limit in 2HDM is robust against most of the dim-6 operators, for type-II 2HDM, the tree-level alignment limit may be ruled out at 95% CL from both Higgs signal strengths and direct scalar searches.

References

1. J.F. Gunion, H.E. Haber, Phys. Rev. D **67**, 075019 (2003). arXiv:hep-ph/0207010
2. M. Carena, I. Low, N.R. Shah, C.E.M. Wagner, JHEP **1404**, 015 (2014). arXiv:1310.2248 [hep-ph]
3. G.C. Dorsch, S.J. Huber, K. Mimasu, J.M. No, Phys. Rev. D **93**(11), 115033 (2016). arXiv:1601.04545 [hep-ph]
4. S. Karmakar, S. Rakshit, JHEP **1710**, 048 (2017). arXiv:1707.00716 [hep-ph]
5. S. Karmakar, S. Rakshit, JHEP **1809**, 142 (2018). arXiv:1802.03366 [hep-ph]
6. S. Karmakar, S. Rakshit, Phys. Rev. D **100**(5), 055016 (2019). arXiv:1901.11361 [hep-ph]

Chapter 24
Charged Higgs Discovery Prospects

Baradhwaj Coleppa, Agnivo Sarkar, and Santosh Kumar Rai

Abstract We study the discovery prospects of the charged Higgs boson in the context of multi Higgs models in certain BSM scenarios. We classify models into three categories based on the charged Higgs coupling properties: gaugophobic, fermiophobic, and chromophobic. We will present the detailed collider phenomenology of a chromophobic charged Higgs in the context of 14 TeV LHC.

24.1 Overview and Current Limits

The extension of SM, which comes under the collective banner of "Beyond the Standard Model" (BSM) theories can categorized into a few broad classes: one enlarging the gauge group of SM, one enlarging the scalar sector or ones that enlarge the matter content. Depending upon the model building strategies many models fall under more than one class as mentioned. In this study we will engage ourselves in those BSM scenarios which contain an enlarged scalar sector. Principally these can also have an enlarged gauge sector and/or matter sector, however we will focus on simple cases where the gauge symmetry and fermionic content of the model is SM-like. Typically charged Higgs Bosons ($H^{\pm}$) appears in the particle spectrum where the scalar sector of the model contains additional Higgs multiplets along with the SM Higgs doublet. There are numerous possibilities for the Charged Higgs to couple with the SM particles and one can classify these models based on the nature of the charged Higgs coupling. In this spirit we sort the models which contains charged Higgs in three broad categories: Gaugophobic models, where $H^{\pm}$ does not couple with the SM electro-weak gauge bosons, Leptophobic models where $H^{\pm}$ does not couples to the

B. Coleppa · A. Sarkar (✉)
Physics Discipline, Indian Institute of Technology Gandhinagar, Gandhinagar 382355, Gujarat, India
e-mail: agnivo.sarkar@iitgn.ac.in

S. Kumar Rai
Regional Center for Accelerator-based Particle Physics, Harish-Chandra Research Institute, HBNI, Chhatnag Road, Jhusi, Prayagraj, Allahabad 211019, India

A. Giri and R. Mohanta (eds.), *Workshop on Frontiers in High Energy Physics 2019*, Springer Proceedings in Physics 248,
https://doi.org/10.1007/978-981-15-6292-1_24

leptons in the SM and Chromophobic models where couplings between SM coloured particles and $H^{\pm}$ are absent. Depending on the nature of its couplings, the charged Higgs will have rather different decays and production mechanisms. Searches for the charged higgs have largely been restricted to its production via $gb \to H^{+}t$, or via top decay: $t \to H^{+}b$ if $m_{H^{\pm}} < m_t$. In the former case, the predominant decay is to tb while in the latter it could be $H^{+} \to \tau\nu$. While other channels like $AW^{\pm}$ have been explored, to a large extent either the production or the decay have been one of the "standard" cases. This is clearly untenable in a general search strategy if, for example, the charged Higgs is chromophobic and the $H^{+}tb$ vertex does not exist.

– **Chromophobic**: Since the $H^{\pm}$ does not couple to colored particles, the production channel $pp \to H^{\pm}t$ is absent and we need to look for the $H^{\pm}$ as a decay product of a heavier particle like a heavy neutral scalar H. The possible s channel mode $u\bar{d} \to H^{+}$ is suppressed by the small masses of the quarks, and hence would not be viable. Thus, in this case, we look at $pp \to H \to W^{\pm}H^{\mp}$ with $H^{\pm} \to AW^{\mp}$.

In what follows, we will concentrate only in the chromophobic case. For a detailed study of the other scenario, one can look into [1].

Before moving to collider phenomenology we want to briefly present current status regarding charged Higgs searches. The ATLAS and CMS experiments have collected data independently from various phases of the collider run and searched for $H^{\pm}$ in both the low mass i.e. $m_{H^{\pm}} < m_t$ and high mass i.e. $m_{H^{\pm}} > m_t$ regions and thus far there is no evidence in support of the existence of a $H^{\pm}$ scalar. If mass of $H^{\pm}$ is lower than top-quark mass, then the major production channel for $H^{\pm}$ is via top-quark decay. This $H^{\pm}$ can further decay via light quark channels like $H^{\pm} \to c\bar{s}/c\bar{b}$ or via leptons $H^{\pm} \to \tau\nu_{\tau}$. Combining all the data collected from these above mentioned search channels excludes the mass range 80–160 GeV. For the heavy $H^{\pm}$ depending upon mass and coupling there are various dominant production channels available i.e. associated production channel ($pp \to H^{\pm}t$), VBF production process and s-channel production. These $H^{\pm}$ can further decay via leptonic, hadronic channel as well as via electro-weak gauge bosons. Combining all these results one can exclude the mass range from 200 GeV–3 TeV. For details regarding results, please refer [2–18].

While the direct collider limit puts a stringent bound on the $H^{\pm}$ mass, but these limits are valid within the context of specific search strategies, where one assume 100% BR to a desired channel. Thus experimental search which involves $g_{H^{\pm}tb}$ coupling either in production or decay process does not put a mass bound on a Chromophobic $H^{\pm}$.

24.2 Chromophobic $H^{\pm}$ Search Prospects at the LHC

In this we will discuss $H^{\pm}$ search prospects in Chromophic models at the 14 TeV LHC. In this work we will present the phenomenology in a model independent fashion: we will choose the optimal channels for the chromophobic class of models and do a signal versus background study for an optimized choice of cuts. We will not be

using any specific couplings or branching ratio (BR) which are in general dependent upon model specifics. Thus, for a chosen fiducial cross-section, we determine an optimal cut-flow chart that can suppress the corresponding SM background without substantially affecting the signal cross-section. We will then use the number of events which remains after imposing the cuts to back-calculate the minimum signal cross-section require for a 5σ discovery.

Since the associated production channel is not viable option, we will produce $H^{\pm}$ via cascade decay of neutral heavy Higgs H^0 i.e. ($pp \to H^0 \to H^{\pm}W^{\mp}$). After the production of $H^{\pm}$ further decays into a light neutral Higgs A^0 and $W^{\pm}$. The complete process under consideration is—($pp \to H^0 \to H^{\pm}W^{\mp} \to W^{\pm}A^0\ell^-\bar{\nu} \to jjb\bar{b}\ell^-\bar{\nu}$). To proceed we choose benchmark points $m_{H^{\pm}} = 300\,\text{GeV}$, 500 GeV to perform the analysis. In addition we fix the mass of H^0 and A^0 to be 800 GeV and 150 GeV respectively. Due to the presence of the multi jet final state, the major experiment search challenges comes from the dominant SM process like $t\bar{t} + jets$, WZ + jets. The presence of $\ell\nu$ in the final state helps in suppressing a large number of pure QCD background events particularly for a signal with appreciable lepton p_T. Also the signal events has only one source of missing energy, which makes ZZ + jets background insignificant. We performed the data simulation using MadGraph5_aMC@NLO [19] event generator. The relevant SM backgrounds are generated via the in-built SM model file in the MadGraph repository [20]. To generate the signal distribution we build a BSM model file using FeynRules [21] which exhibits an enlarged scalar sector with appropriate assumption mentioned above. Parton level events generated from MadGraph are passed on to Pythia 6 [22] for showering and hadronization. After that Delphes 3 [23] performed the simulation of detector level effects. For subsequent reconstruction of the events followed by a detailed cut-based analysis, we have used the MadAnalysis 5 [24, 25] framework.

To eliminate any soft jets and leptons we have employed the set of following basic identification cut—

$$p_T^j > 20\,\text{GeV}, \qquad p_T^{\ell} > 10\,\text{GeV}, \qquad |\eta^j| \leq 5 \qquad \text{and} \qquad |\eta^{\ell}| \leq 2.5$$

We have chosen a wider window for the pseudo rapidity for the jets compared to the leptons to ensure that we do not lose many signal events. Further we demand that all pairs of particles are optimally separated:

$$\Delta R_{jj} = \Delta R_{bb} = \Delta R_{jl} = \Delta R_{bj} = 0.4$$

We start by imposing an event selection cut of (N(j) $\geq$ 2, N(b) = 2 and N(ℓ) = 1). This will reduce more than 90% of the background but as collateral damage we will also lose a large number of signal events. Next we will use the following kinematic cuts to eliminate the SM background significantly.

$$H_T > 400\,\text{GeV}, P_T(j_1) > 75\,\text{GeV}, P_T(b_1) > 75\,\text{GeV}$$

Table 24.1 The cross-sections required for the 5σ and 2σ exclusion of the $m_{H^\pm}$ for the chromophobic signal scenarios for different values of integrated luminosity

Production channel	Benchmark points	2σ significance		5σ significance	
		$\mathcal{L} = 500\,\text{fb}^{-1}$	$\mathcal{L} = 1000\,\text{fb}^{-1}$	$\mathcal{L} = 500\,\text{fb}^{-1}$	$\mathcal{L} = 1000\,\text{fb}^{-1}$
Chromophobic	300 GeV	2.997	2.073	7.526	5.31
	500 GeV	2.75	1.939	6.899	4.866

Notice that for chromophobic signal, a pair of b-jets originated from the 150 GeV light Higgs and further the 2b+2j combination should reconstruct the charged Higgs. Based on this observation, we choose the cuts $120\,\text{GeV} \leq m_{b\bar{b}} \leq 180\,\text{GeV}$ and $(m_{H^\pm} - 100)\,\text{GeV} \leq m_{b\bar{b}jj} \leq (m_{H^\pm} + 100)\,\text{GeV}$. After this model independent analysis more than 99% background events eliminated and it is simple enough to take the remaining events to estimate the actual number of signal events necessary to obtain a 5σ discovery. These numbers are presented in Table 24.1.

24.3 Model Implication

In Table 24.1 we have presented the signal strength required for a 5σ discovery. To truly judge the efficiency of our approach, we needs to analyse the feasibility to realise the signal cross-section in a particular model with an enlarged scalar sector containing a charged Higgs. While one should strictly use model where charged Higgs is chromophobic in nature, our goal here is not to give an overview of models. Thus we will follow a simple route of choosing a particular model—the Type II Two Higgs-doublet model (2HDM)—and turning of the coupling between charged Higgs and color particle. Note that 2HDM in general does not fall into the category of chromophobic class, but this analysis will able to give a sense of the number involved and the efficiency of the cuts we have deduced in the process of collider phenomenology. Also we will only modify the coupling between $H^\pm$ and coloured particle of 2HDM model, all the other couplings involving neutral Higgs and gauge bosons will remains unchanged in our calculation. With the basic structure now in place, we present in Fig. 24.1 the 5σ discovery or a 2σ exclusion of the parameter space in the Type II 2HDM (with appropriate coupling modifications as discussed earlier).

We point out at the outset that there are many constraints on this model on both the theoretical (vacuum stability, perturbativity etc.) and experimental (observation of the 125 GeV Higgs, $\Delta\rho$, $b \to s\gamma$ etc.) fronts, and these together constrain the available parameter space of the model. A complete analysis of all such constraints is beyond the scope of this paper (see for example [26]), and thus we present the discovery and exclusion regions on the entire parameter space of Type II 2HDM. However, one

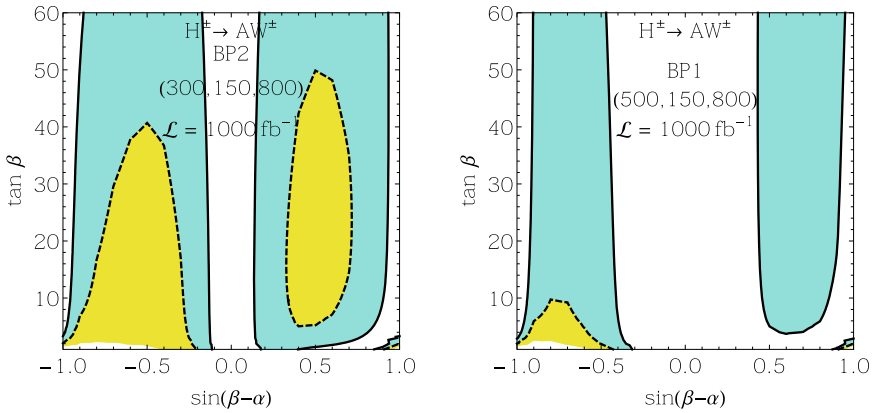

Fig. 24.1 The 95% exclusion regions (cyan regions) and the 5-σ discovery reach (yellow regions) for the chromophobic signal in the $\sin(\beta - \alpha)$ verses $\tan\beta$ plane for the benchmark points 300 GeV (left) and 500 GeV (right)

should note that some of this parameter space might already be ruled out owing to the aforementioned considerations. However, our aim here is to try and understand the maximal available discovery regions for the particular collider analysis detailed in the previous section. We conclude this study by pointing out that it is imperative to probe for non-standard signatures of BSM physics in cases of extended scalar sectors. It is possible that depending on the nature of the charged Higgs couplings, the discovery of these particles can be effective in channels involving not one, but even two new physics couplings—a case which is usually dismissed as non-viable might indeed turn out to be the dominant discovery mode. In fact, a discovery of the charged Higgs in one of these exotic channels might prove to be an efficient way of narrowing down the possibilities of new physics models at the TeV scale.

Acknowledgements BC acknowledges support from the Department of Science and Technology, India, under Grant YSS/2015/001771. The work of SKR is partially supported by funding available from the Department of Atomic Energy, Government of India, for the Regional Centre for Accelerator-based ParticlePhysics (RECAPP), Harish-Chandra Research Institute. SKR would like to thank the Theory Division of CERN while the work was being completed. We thank Satendra Kumar for collaboration during the early stages of this project.

References

1. B. Coleppa, A. Sarkar, S.K. Rai, arXiv:1909.11992 [hep-ph]
2. G. Aad et al., ATLAS Collaboration, JHEP **1206**, 039 (2012). https://doi.org/10.1007/JHEP06(2012)039, arXiv:1204.2760 [hep-ex]
3. G. Aad et al., ATLAS Collaboration, JHEP **1303**, 076 (2013). https://doi.org/10.1007/JHEP03(2013)076, arXiv:1212.3572 [hep-ex]

4. G. Aad et al., ATLAS Collaboration, Eur. Phys. J. C **73**(6), 2465 (2013). https://doi.org/10.1140/epjc/s10052-013-2465-z, arXiv:1302.3694 [hep-ex]
5. G. Aad et al., ATLAS Collaboration, JHEP **1503**, 088 (2015). https://doi.org/10.1007/JHEP03(2015)088. arXiv:1412.6663 [hep-ex]
6. G. Aad et al., ATLAS Collaboration, Phys. Rev. Lett. **114**(23), 231801 (2015). https://doi.org/10.1103/PhysRevLett.114.231801, arXiv:1503.04233 [hep-ex]
7. G. Aad et al., ATLAS Collaboration, JHEP **1603**, 127 (2016). https://doi.org/10.1007/JHEP03(2016)127, arXiv:1512.03704 [hep-ex]
8. M. Aaboud et al., ATLAS Collaboration, Phys. Lett. B **759**, 555 (2016). https://doi.org/10.1016/j.physletb.2016.06.017, arXiv:1603.09203 [hep-ex]
9. M. Aaboud et al., ATLAS Collaboration, Phys. Lett. B **787**, 68 (2018). https://doi.org/10.1016/j.physletb.2018.10.021, arXiv:1806.01532 [hep-ex]
10. M. Aaboud et al., ATLAS Collaboration, JHEP **1809**, 139 (2018). https://doi.org/10.1007/JHEP09(2018)139, arXiv:1807.07915 [hep-ex]
11. M. Aaboud et al., ATLAS Collaboration, JHEP **1811**, 085 (2018). https://doi.org/10.1007/JHEP11(2018)085, arXiv:1808.03599 [hep-ex]
12. S. Chatrchyan et al., CMS Collaboration, JHEP **1207**, 143 (2012). https://doi.org/10.1007/JHEP07(2012)143, arXiv:1205.5736 [hep-ex]
13. V. Khachatryan et al., CMS Collaboration, JHEP **1511**, 018 (2015). https://doi.org/10.1007/JHEP11(2015)018, arXiv:1508.07774 [hep-ex]
14. V. Khachatryan et al., CMS Collaboration, JHEP **1512**, 178 (2015). https://doi.org/10.1007/JHEP12(2015)178, arXiv:1510.04252 [hep-ex]
15. CMS Collaboration, CMS-PAS-HIG-16-031
16. A.M. Sirunyan et al., CMS Collaboration, Phys. Rev. Lett. **119**(14), 141802 (2017). https://doi.org/10.1103/PhysRevLett.119.141802, arXiv:1705.02942 [hep-ex]
17. A.M. Sirunyan et al., CMS Collaboration, JHEP **1811**, 115 (2018). https://doi.org/10.1007/JHEP11(2018)115, arXiv:1808.06575 [hep-ex]
18. V. Khachatryan et al., CMS Collaboration, JHEP **1504**, 025 (2015). https://doi.org/10.1007/JHEP04(2015)025, arXiv:1412.6302 [hep-ex]
19. J. Alwall et al., JHEP **1407**, 079 (2014). https://doi.org/10.1007/JHEP07(2014)079, arXiv:1405.0301 [hep-ph]
20. C. Degrande, C. Duhr, B. Fuks, D. Grellscheid, O. Mattelaer, T. Reiter, Comput. Phys. Commun. **183**, 1201 (2012). https://doi.org/10.1016/j.cpc.2012.01.022, arXiv:1108.2040 [hep-ph]
21. N.D. Christensen, P. de Aquino, C. Degrande, C. Duhr, B. Fuks, M. Herquet, F. Maltoni, S. Schumann, Eur. Phys. J. C **71**, 1541 (2011). https://doi.org/10.1140/epjc/s10052-011-1541-5, arXiv:0906.2474 [hep-ph]
22. T. Sjostrand, S. Mrenna, P.Z. Skands, JHEP **0605**, 026 (2006). https://doi.org/10.1088/1126-6708/2006/05/026, arXiv:hep-ph/0603175
23. J. de Favereau et al., DELPHES 3 Collaboration, JHEP **1402**, 057 (2014). https://doi.org/10.1007/JHEP02(2014)057, arXiv:1307.6346 [hep-ex]
24. E. Conte, B. Fuks, G. Serret, Comput. Phys. Commun. **184**, 222 (2013). https://doi.org/10.1016/j.cpc.2012.09.009, arXiv:1206.1599 [hep-ph]
25. E. Conte, B. Dumont, B. Fuks, C. Wymant, Eur. Phys. J. C **74**(10), 3103 (2014). https://doi.org/10.1140/epjc/s10052-014-3103-0, arXiv:1405.3982 [hep-ph]
26. B. Coleppa, F. Kling, S. Su, JHEP **1401**, 161 (2014). https://doi.org/10.1007/JHEP01(2014)161, arXiv:1305.0002 [hep-ph]

Chapter 25
Some Compelling Overview of Charged Particle Multplicity Distribution in pp Collisions at the LHC

Ritu Aggarwal and Manjit Kaur

Abstract In this paper we report the oscillatory behavior observed in the modified combinants when Shifted-Gompertz distribution is used to define the phenomenology of the multi-particle production for the pp collisions. These oscillatory behavior in the modified combinants C_j, were first reported using the modified NBD. In this paper we have considered a 2-component and a 3-component Shifted-Gompertz distribution to explain the multiplicity data. The agreement with the experimental multiplicity distribution is observed to improve and the oscillations in the combinants, C_j are observed to get more pronounced.

25.1 Introduction

In a particle collision at high energies, charged particle multiplicity is the simplest variable that can be reconstructed in the products from the final state. Also, it is one of the most important quantities that gives insight about the mechanism of particle production in the high energy collisions. The charged particle multiplicity probability distribution, $P(N)$, where N is the number of charged particles produced in an interation, was thought to obey KNO scaling [1] and was successfully defined using a Poisson distribution [2] or a Negative Binomial distribution (MBD) [3], until it's violation was observed in the results published by UA5 collaboration [4]. Several other theoretical distributions [5–8] and a combination of two or more NBDs [9] were used to improve the agreement between theoretical and experimental distributions. Recently a new distribution, i.e. Shifted Gompertz distribution (SGD) has been used [10] to define the experimental $P(N)$ distribution. It was observed that using a modified form of SGD in which a combination of two SGDs are taken, i.e. taking

R. Aggarwal (✉)
Savitribai Phule Pune University, Pune, India
e-mail: ritu.aggarwal1@gmail.com

M. Kaur
Panjab University, Chandigarh, India
e-mail: manjit@pu.ac.in

A. Giri and R. Mohanta (eds.), *Workshop on Frontiers in High Energy Physics 2019*, Springer Proceedings in Physics 248,
https://doi.org/10.1007/978-981-15-6292-1_25

one SGD for a fraction of soft component of events and another SGD for the hard component of events, further improved the agreement to data. In the present paper a single SGD is used and it's scale parameter variable, b, is proposed to be dependent on N. The details are given in Sect. 25.2.

Recently oscillations in the modified combinants [11], that are used to define the multi-particle distributions using a recurrence relation, have been reported in pp collision data collected by the CMS detector at the LHC. It has also been reported there, that a single NBD fails to explain such oscillations theoretically and they can be closely reproduced when a modified NBD is used, where parameter m is taken to be dependent on N. In the present paper, the oscillations in the modified combinants are studied using the SGD and it's modified forms, and are presented in Sect. 25.2. The dependence of oscillations on the $P(0)$ values are studied and the sensitivity of the oscillations to any fluctuations in $P(N)$ are also probed.

25.2 Shifted-Gompertz Distributions and Its Modified Forms

The SGD distribution is a widely used theoretical distribution outside High Energy Physics Community [12] and is used to study the weather forecast systems, market responses etc. Recently it has also been used successfully [10] to explain the $P(N)$ distributions in the high energy particle collisions. It's functional form is given as below,

$$P(n; b, \zeta) = be^{-(bn+\zeta e^{-bn})}(1 + \zeta(1 - e^{-bn})), n > 0 \tag{25.1}$$

where ζ is the shape parameter and b is the scale parameter. In [10], a modified form of SGD is also used which is a combination of two SGDs as shown below.

$$P(n; \alpha, b_1, \zeta_1, b_2, \zeta_2) = \alpha P^{SGD}_{soft}(N) + (1 - \alpha) P^{SGD}_{semi-hard}(N). \tag{25.2}$$

Here α represents the fraction of soft events.

In the present paper two new modified form of SGD are proposed. In the first one, the shape parameter is proposed to depend on N as shown below and is referred to as 2-component SGD,

$$b = b(N) = ce^{a_1|N-d|}. \tag{25.3}$$

In the second type, the shape paramter is taken to be dependent on N following the relation given below, and is referred as 3-component SGD,

$$b = b(N) = ce^{(a_1|N-d|+(a_2|N-d|)^4)}. \tag{25.4}$$

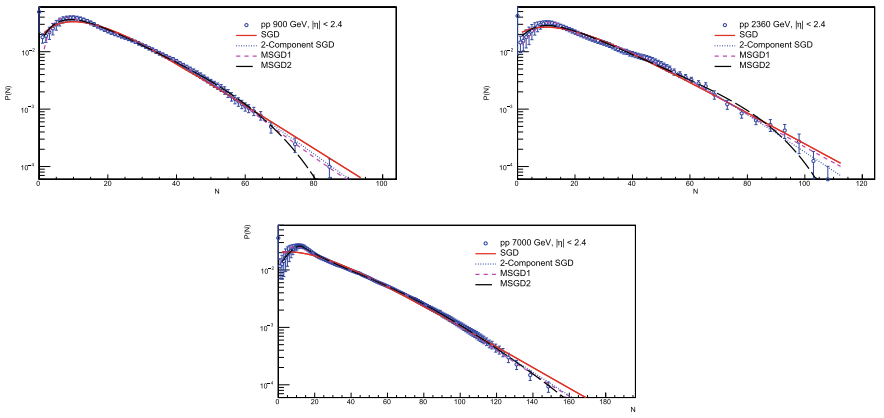

Fig. 25.1 The charged multiplicity distribution, $P(N)$ for pp data collected using CMS detector at the LHC shown at 900, 2360 and 7000 GeV at $|\eta| < 2.4$. The $P(N)$ distribution is fitted using SGD, MSGD, 2-component SGD and 3-component SGD as defined in the text

25.2.1 Comparison to Data

The $P(N)$ distribution for pp collision data collected by the CMS collaboration [13] at the LHC at various center-of-mass (c.m.) energies is fitted with SGD, MSGD, 2-component SGD and 3-component SGD distributions. It is observed that using MSGD the data-fit agreement improves. Figure 25.1 shows the $P(N)$ distribution for pp collisions for center-of-mass energies of 900, 2360 and 7000 GeV with η range $|2.4|$. Different theoretical fits as discussed above are shown. It is observed that SGD fails to follow the experimental distribution at low and at high multiplicities. Using a MSGD, fit improves the agreement with data, which is further improved when a 3-component SGD is used.

25.3 Modified Combinants

The probability of producing $N+1$ particles, $P(N+1)$, is linked to the probability of producing N particles, $P(N)$, using the relation shown below

$$(N+1)P(N+1) = g(N)P(N) \tag{25.5}$$

where $g(N)$ is the generating function for the given theoretical distribution used to analyze the experimental $P(N)$ distribution. The probability of producing $N+1$ particles can be further written as a combination of probabilities of producing lower multiplicities as shown below:

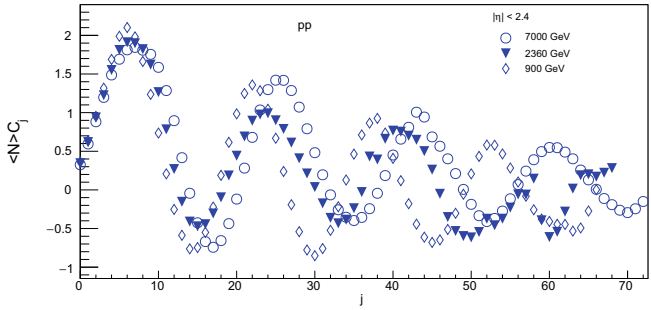

(a)

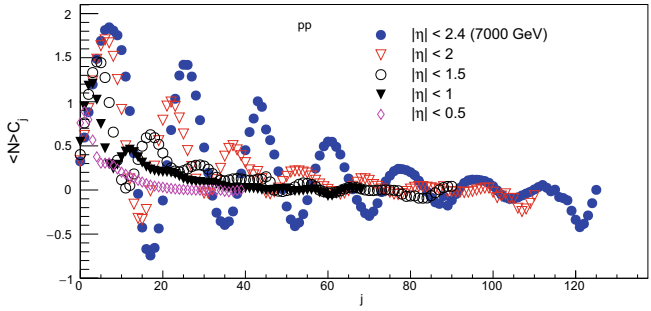

(b)

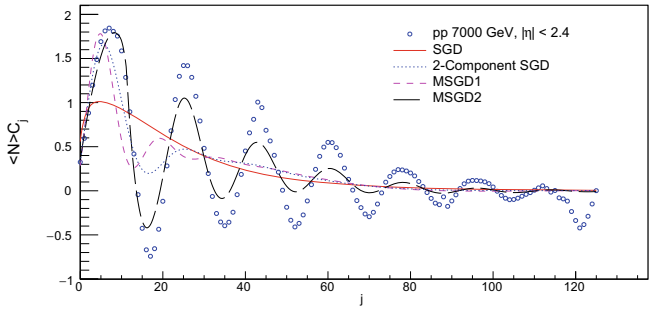

(c)

Fig. 25.2 **a** Oscillations in coefficients $< N > C_j$ at various c.m. energies for $|\eta| < 2.4$. **b** $< N > C_j$s calculated for 7000 GeV pp data and compared at various η values. **c** Comparison of $< N > C_j$s for various theoretical fits with data

$$(N+1)P(N+1) =< N > \sum_{j=0}^{N} C_j P(N-j) \tag{25.6}$$

where C_j are the combination coefficients. The above relation can be inverted to find C_js in terms of the multiplicity distributions using the following equation

$$< N > C_j = (j+1)[\frac{P(j+1)}{P(0)}] - < N > \sum_{j=0}^{j-1} C_i[\frac{P(j-i)}{P(0)}] \tag{25.7}$$

The modified combinants, $< N > C_j$s are calculated for the pp collision data at η of $|2.4|$ at various c.m. energies as shown in Fig. 25.2a. It is observed that for different c.m. energies the modified combinants oscillate as a function of rank j, the amplitude of which dies out rapidly with rank j. The oscillations are observed at all c.m. energies. Figure 25.2b shows the oscillations in the combinant coefficients observed for the c.m. energy, 7000 GeV and in different pseudo-rapidity windows. It is observed that the amplitude of oscillations increase with the increase in the η range. Figure 25.2c shows the combination coefficients calculated using different theoretical fits as discussed above. The fit using SGD fails to show the oscillations, where as MSGD and 3-component SGD show oscillations in the C_js. This is also because these describe the $P(N)$ distribution in data very well.

25.3.1 Sensitivity of Oscillations in C_js

The value of $P(0)$ is required for calculation of C_js as shown in equation (7). However $P(0)$ is associated with large uncertainties, and often is not included in the multiplicity distribution analysis. As a check of dependence of C_js on the $P(0)$ value, $P(0)$ is varied with $\pm\delta$, where δ is the uncertainty quoted on $P(0)$. The C_js are recalculated and shown in Fig. 25.3a, where a change in time period of the oscillations is observed. To test the sensitivity of the oscillations further, values of $P(N)$ at $N = 10$ and 11 are varied by 2% up and down respectively and C_js are recalculated. A 2% change in $P(N)$ values resulted a large change in the C_j's values as shown in Fig. 25.3b.

25.4 Summary and Discussion

The charged multiplicity distributions from pp collision data collected at the LHC at c.m. energies 900, 2360 and 7000 GeV have been fitted with SGD and its modified forms, namely MSGD, 2-component SGD and 3-component SGD. It is observed that MSGD and 3-component SGD describes the $P(N)$ distribution from data very

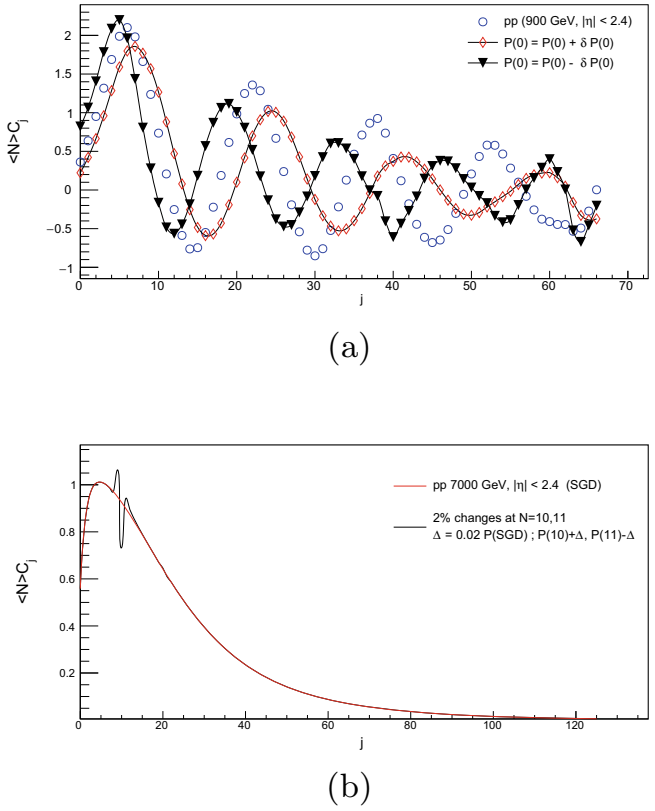

Fig. 25.3 **a** Variation in $< N > C_j$s when $P(0)$ is varied by the quoted uncertainty on $P(0)$. **b** $< N > C_j$s calculated using SGD for pp data at 7000 GeV c.m. energy, also shown are the result of variation in $< N > C_j$s obtained when $P(10)$ and $P(11)$ are varied by 2% as described in the text

well. The oscillations in the modified combinants are observed in pp collision data at all c.m. energies. The amplitude of these oscillations are dependent on the rapidity window selected for the analysis. Simple SGD is not found to show these oscillations, which on the other hand are shown by MSGD, 2-component and 3-component SGD.

References

1. Z. Koba, H.B. Nielsen, P. Olesen, Nucl. Phys. B **40**, 317 (1972)
2. M. Althoff et al., Z. Phys. **C22**(307) 1098 (1984); M. Derrick et al., Phys. Rev. **D34** 3304 (1986)
3. P. Carruthers, C.C Shih, Int. J. Mod. Phys. **A2**, 1447 (1987); A. Giovannini, R. Ugoccioni, Z. Phys. **C30** 391, (1986); *Proceedings of International Symposium on Multiparticle Dynamics, Italy, Sept. 8–12* (1997)

4. R.E. Ansorge, B. Asman et al., Z. Phys., **C43**, 357 (1989); G.J. Alner et al., Phys. Lett. **B160**, 193 (1985)
5. R. Szwed et al., Mod. Phys. Lett. A **5**, 1851 (1990)
6. C. Tsallis, J. Stat. Phys. **52**, 479 (1988)
7. C.E. Agiar, T. Kodama, Phys. A **320**, 271 (2003)
8. S. Dash et al., Phys. Rev. D **94**, 074044 (2016)
9. I.J. Zborovsky, J. Phys. **G40**, 055005 (2013); I.J. Zborovsky, Eur. Phys. J. **C78**, 816 (2018)
10. R. Chawla, M. Kaur, Adv. High Energy Phys. 5129341 (2018)
11. G. Wilk, Z. Wlodarczyk, Int. J. Mod. Phys. **A33**, 1830008 (2018); J. Phys. G: Nucl. Part. Phys. **44**, 015002 (2017); M. Rybczynski, G. Wilk, Z. Wlodarczyka (2018), arXiv:1811.07197v1 [hep-ph]
12. D. Juki, D. Markovi, Eur. J. Pure Appl. Math. **10**, 157 (2017); F. Jimenez, P. Jodra, Commun. Stat. Theory Methods **38**, 75 (2009); F. Jimenez Torres, J. Comput. Appl. Math. **255**, 867 (2014)
13. V. Khachatryan, A.M. Sirunyan et al., CMS collaboration. J. High Energy Phys. JHEP **01**, 79 (2011)

Chapter 26
Polarization of Z Boson as a Probe of Anomalous Gauge-Higgs Couplings

Priyanka Sarmah, Kumar Rao, and Saurabh D. Rindani

Abstract We study possible new physics interactions in the ZZH vertex contributing to the Higgsstrahlung process $e^+e^- \to ZH$ at proposed future e^+e^- colliders using the polarization of the Z as a probe. We estimate the limits on the anomalous couplings using the angular asymmetries of charged leptons from Z decay which are simply related to the Z polarization asymmetries at centre of mass energies of 250 and 500 GeV and various combinations of polarized e^+ and e^- beams.

26.1 Introduction

While the discovery of a Higgs like boson (h) at the LHC completes the particle spectrum of the standard model, a confirmation of the electroweak symmetry breaking mechanism requires a precise measurement of the Higgs boson to the EW gauge bosons and the SM fermions. Future measurements of the couplings and other properties of the higgs boson would involve going beyond simple cross sections and decay rate measurements. Of particular interest are the polarization parameters of the spin-1 Z boson. An electron-positron collider is better suited to this task than the LHC, while providing the possibility of longitudinally polarized e^+e^- beams. In this work we consider probing anomalous couplings of the Z boson with the Higgs in the process $e^-e^+ \to ZH$. We adopt the formalism which connects the asymmetries from the angular distribution of the decay products of the Z to its polarization parameters [1–3]. Measurement of these polarization parameters will give insight into the

P. Sarmah (✉) · K. Rao
Indian Institute of Technology Bombay, Mumbai 400076, India
e-mail: pami@phy.iitb.ac.in

K. Rao
e-mail: kumar.rao@phy.iitb.ac.in

S. D. Rindani
Theoretical Physics Division, Physical Research Laboratory,
Navrangpura, Ahmedabad 380009, India
e-mail: saurabh@prl.res.in

A. Giri and R. Mohanta (eds.), *Workshop on Frontiers in High Energy Physics 2019*, Springer Proceedings in Physics 248,
https://doi.org/10.1007/978-981-15-6292-1_26

production mechanism and also provide information about the nature of the tensorial structure as well as the strength of anomalous couplings in the ZZH interaction. We consider the process $e^-e^+ \to ZH$, where the vertex $Z_\mu(k_1) \to Z_\nu(k_2)H$ has the Lorentz structure

$$\Gamma^V_{\mu\nu} = \frac{g}{\cos\theta_W} m_Z \left[a_Z g_{\mu\nu} + \frac{b_Z}{m_Z^2}\left(k_{1\nu}k_{2\mu} - g_{\mu\nu}k_1.k_2\right) + \frac{\tilde{b}_Z}{m_Z^2}\epsilon_{\mu\nu\alpha\beta}k_1^\alpha k_2^\beta \right] \quad (26.1)$$

where g is the $SU(2)_L$ coupling and θ_W is the weak mixing angle. The form factors a_Z, b_Z and $\tilde{b}_Z$ are in general complex. The first two couplings would correspond to CP-even terms in the interaction, while the third term is odd under CP. In the SM, the coupling a_Z is unity at tree level, whereas the other two couplings b_Z, $\tilde{b}_Z$ vanish at tree level, denoting the deviation from the tree-level SM value. Such anomalous couplings could arise from loop corrections in the SM or in any extension of SM with some new particles. Anomalous interactions in the HVV vertex have been searched for by the CMS collaboration [4–6] and although the current data are consistent with the SM predictions, the constraints are still weak to allow for beyond the SM contributions to the vertex.

26.2 *Z* Polarization and Lepton Asymmetries

We compute the helicity amplitudes for the process

$$e^-(p_1) + e^+(p_2) \to Z^\alpha(p) + H(k) \quad (26.2)$$

in the massless limit of the initial particles, with the ZZH vertex given in (26.1). The spin-density matrix for Z production expressed in terms of the helicity amplitudes M is given by

$$\rho(i,j) = \overline{\sum}_{\lambda,\lambda'} M(\lambda,\lambda',i)M^*(\lambda,\lambda',j) \quad (26.3)$$

the average being over the initial helicities λ, λ' of the electron and positron respectively and the Z polarization the indices i, j can take values $\pm, 0$. Apart from the diagonal elements, it is also necessary to know the off-diagonal elements to include the spin information in a coherent way in the combination of the Z production and decay processes. Then, on integrating over the phase space, the full density matrix (26.3) would lead to the eight independent vector and tensor polarization components, known as the *polarization parameters* of the Z [7].

These eight independent vector(P_x, P_y and P_z) and tensor polarization(5 $T'_{ij}s$) observables can be extracted using appropriate linear combinations of the integrated density matrix elements $\sigma(i, j)$ defined in [8]

$$P_x = \frac{\{\sigma(+,0)+\sigma(0,+)\}+\{\sigma(0,-)+\sigma(-,0)\}}{\sqrt{2}\sigma},$$
$$P_y = \frac{-i\{[\sigma(0,+)-\sigma(+,0)]+[\sigma(-,0)-\sigma(0,-)]\}}{\sqrt{2}\sigma}$$

$$P_z = \frac{[\sigma(+,+)]-[\sigma(-,-)]}{\sigma},$$
$$T_{xz} = \frac{\sqrt{3}\{[\sigma(+,0)+\sigma(0,+)]-[\sigma(0,-)+\sigma(-,0)]\}}{4\sigma}$$

$$T_{xy} = \frac{-i\sqrt{6}[\sigma(-,+)-\sigma(+,-)]}{4\sigma},$$
$$T_{yz} = \frac{-i\sqrt{3}\{[\sigma(0,+)-\sigma(+,0)]-[\sigma(-,0)-\sigma(0,-)]\}}{4\sigma}$$

$$T_{xx}-T_{yy} = \frac{\sqrt{6}[\sigma(-,+)+\sigma(+,-)]}{2\sigma},$$
$$T_{zz} = \frac{\sqrt{6}}{2}\left\{\frac{[\sigma(+,+)]+[\sigma(-,-)]}{\sigma}-\frac{2}{3}\right\}$$

where $\sigma(i,\,j)$ is the integral of $\rho(i,\,j)$, and σ is the production cross section. Experimentally, the spin information of the Z is obtained from kinematic distributions of its decay products. References [2, 8] describe the formalism that connects all the spin observables of the Z to the various leptonic angular asymmetries constructed in the rest frame of the Z,

$$A_x = \frac{3\alpha P_x}{4} \equiv \frac{\sigma(\cos\phi^* > 0)-\sigma(\cos\phi^* < 0)}{\sigma(\cos\phi^* > 0)+\sigma(\cos\phi^* < 0)}$$
$$A_y = \frac{3\alpha P_y}{4} \equiv \frac{\sigma(\sin\phi^* > 0)-\sigma(\sin\phi^* < 0)}{\sigma(\sin\phi^* > 0)+\sigma(\sin\phi^* < 0)}$$

$$A_z = \frac{3\alpha P_z}{4} \equiv \frac{\sigma(\cos\theta^* > 0)-\sigma(\cos\theta^* < 0)}{\sigma(\cos\theta^* > 0)+\sigma(\cos\theta^* < 0)}$$
$$A_{xy} = \frac{2}{\pi}\sqrt{\frac{2}{3}}T_{xy} \equiv \frac{\sigma(\sin 2\phi^* > 0)-\sigma(\sin 2\phi^* < 0)}{\sigma(\sin 2\phi^* > 0)+\sigma(\sin 2\phi^* < 0)}$$

$$A_{xz} = \frac{-2}{\pi}\sqrt{\frac{2}{3}}T_{xz} \equiv \frac{\sigma(\cos\theta^*\cos\phi^* < 0) - \sigma(\cos\theta^*\cos\phi^* > 0)}{\sigma(\cos\theta^*\cos\phi^* > 0) + \sigma(\cos\theta^*\cos\phi^* < 0)}$$
$$A_{yz} = \frac{2}{\pi}\sqrt{\frac{2}{3}}T_{yz} \equiv \frac{\sigma(\cos\theta^*\sin\phi^* > 0) - \sigma(\cos\theta^*\sin\phi^* < 0)}{\sigma(\cos\theta^*\sin\phi^* > 0) + \sigma(\cos\theta^*\sin\phi^* < 0)}$$

$$A_{x^2-y^2} = \frac{1}{\pi}\sqrt{\frac{2}{3}}(T_{xx} - T_{yy}) \equiv \frac{\sigma(\cos 2\phi^* > 0) - \sigma(\cos 2\phi^* < 0)}{\sigma(\cos 2\phi^* > 0) + \sigma(\cos 2\phi^* < 0)}$$
$$A_{zz} = \frac{3}{8}\sqrt{\frac{3}{2}}T_{zz} \equiv \frac{\sigma(\sin 3\theta^* > 0) - \sigma(\sin 3\theta^* < 0)}{\sigma((\sin 3\theta^* > 0) + \sigma((\sin 3\theta^* < 0)}$$

Here, $\alpha = \frac{R_\ell^2 - L_\ell^2}{R_\ell^2 + L_\ell^2}$ is the Z boson polarization analyser, given in terms of its left and right handed couplings to charged leptons, L_ℓ and R_ℓ respectively. The angles θ^* and ϕ^* are polar and azimuthal angles of the lepton in the rest frame of the Z.

26.3 Results and Discussion

We present numerical values for the sensitivities of the asymmetries to the various anomalous couplings. We consider two possibilities for the collider parameters,*viz.*,c.m. energy $\sqrt{s} = 250$ GeV, with integrated luminosity $\int \mathcal{L}dt = 2\ ab^{-1}$ and c.m. energy 500 GeV with integrated luminosity $\int \mathcal{L}dt = 500\ \text{fb}^{-1}$[9]. We evaluate the limit considering one coupling to be non-zero at a time and list it in the tables below for unpolarized and oppositely polarized initial beams neglecting systematic errors (Table 26.1).

Table 26.1 1σ limit obtained from various leptonic asymmetries for unpolarized and polarized beams at $\sqrt{s} = 250$ GeV(Left) and $\sqrt{s} = 500$ GeV(Right)

Observable	Coupling	Limit ($\times 10^{-3}$) for $P_L = 0$, $\bar{P}_L = 0$	Limit ($\times 10^{-3}$) for $P_L = -0.8$, $\bar{P}_L = 0.3$
σ	$Re\ b_z$	1.36	1.15
A_x	$Re\ b_z$	3480	478
A_y	$Re\ \tilde{b}_z$	303	41.7
A_z	$Im\ \tilde{b}_z$	32.3	27.2
A_{xy}	$Re\ \tilde{b}_z$	22.7	19.2
A_{yz}	$Im\ b_z$	189	26.1
A_{xz}	$Im\ \tilde{b}_z$	107	14.7
$A_{x^2-y^2}$	$Re\ b_z$	94.5	80.2
A_{zz}	$Re\ b_z$	26.8	22.8

Observable	Coupling	Limit ($\times 10^{-3}$) for $P_L = 0$, $\bar{P}_L = 0$	Limit ($\times 10^{-3}$) for $P_L = -0.8$, $\bar{P}_L = 0.3$
σ	$Re\ b_z$	3.32	2.8
A_x	$Re\ b_z$	394	54.2
A_y	$Re\ \tilde{b}_z$	204	28.2
A_z	$Im\ \tilde{b}_z$	47.9	40.4
A_{xy}	$Re\ \tilde{b}_z$	33.7	28.5
A_{yz}	$Im\ b_z$	77.7	10.7
A_{xz}	$Im\ \tilde{b}_z$	72.0	9.93
$A_{x^2-y^2}$	$Re\ b_z$	46.7	39.4
A_{zz}	$Re\ b_z$	12.8	10.8

It is observed that apart from the total cross section which provides the best limit on the coupling $Re\ b_z$, the observable A_{zz} is also capable of placing a better limit on the same and it becomes more stringent for the combination ($P_L = -0.8$, $\bar{P_L} = 0.3$) at $\sqrt{s} = 500$ GeV. Although it seems that the total cross section is enough for probing the coupling $Re\ b_z$, one will require the other angular asymmetries to explore the couplings which do not appear in the total cross section.

The best limit on $Im\ \tilde{b}_z$ is 9.93×10^{-3}, which comes from A_{xz} whereas the best limit of 19.2×10^{-3} on $Re\ \tilde{b}_z$ can be obtained from the observable A_{xy} for a reduced beam energy of 250 GeV. Similarly the best bound of 10.7×10^{-3} on the coupling $Im\ b_z$ can be achieved from the observable A_{yz}, which gets improved as one increases the c.m. energy to 500 GeV. As can be seen from the tables, the use of opposite sign beam polarization puts stronger constraints on the anomalous couplings, in some cases upto an order of magnitude better. Further we find that a systematic uncertainty of 1% for the asymmetries worsens the limits on couplings by a factor lying between 1.5 and 3 in the case of c.m. energy of 250 GeV,still leaving them in the same ball park as the limits estimated without systematic uncertainty. However, the change in the limits for the case of c.m energy of 500 GeV is much smaller, only around 5–10%. Similarly, a 1% uncertainty in the measurement of the cross section leads to a change in the limits for the cross sections by 5–7% at 500 GeV, for unpolarized and polarized beams respectively, whereas the corresponding limits worsen by a factor between 1.6–1.8 for the case of 250 GeV.

Hence, we see that most of the 1σ limits on the anomalous couplings, derived from the polarization observables are of the order of a few times 10^{-3}. Also we notice one important feature that oppositely polarized beams provides much tighter bounds on the couplings than the same sign polarized and unpolarized beams, which further gets improved as one increases the c.m. energy.

References

1. J.A. Aguilar-Saavedra et al., Eur. Phys. J. C **77**(4), 234 (2017)
2. F. Boudjema, R.K. Singh, JHEP **0907**, 028 (2009)
3. J. Nakamura, JHEP **1708**, 008 (2017)
4. A.M. Sirunyan et al., [CMS Collaboration], arXiv:1901.00174 [hep-ex]
5. A.M. Sirunyan et al., [CMS Collaboration], arXiv:1903.06973 [hep-ex]
6. ATLAS Collaboration, ATLAS-CONF-2018-053
7. E. Leader, Camb. Monogr. Part. Phys. Nucl. Phys. Cosmol. **15** (2011)
8. R. Rahaman, R.K. Singh, Eur. Phys. J. C **76**(10), 539 (2016)
9. K. Rao, S.D. Rindani, P. Sarmah, Nucl. Phys. B **950**, 114840 (2020)

Part III
Astroparticles, Neutrinos and Dark Matter

Chapter 27
Astronomical Probes of Ultra Light Dark Matter

Subhendra Mohanty and Tanmay Kumar Poddar

Abstract Ultra light particles of mass $m \lesssim 10^{-19}$eV can be probed from binary pulsar timing experiments if they are radiated from compact binary systems such as neutron star-neutron star (NS-NS) and neutron star-white dwarf (NS-WD) binary systems. The orbital period decay of the compact binary system is mainly due to gravitational wave radiation which matches with the observational data to within one percent accuracy. Ultra light particles can also emit from the compact binary systems and contribute to about one percent of the observed orbital period decay. For radiation, the mass of the ultra light particles should be less than the orbital frequency of the binary system. In this paper, we consider massless scalar or ultralight pseudoscalar axion like particles radiate from compact binary systems and put bounds on the coupling constant from pulsar timing data. These ultra light particles can be a candidate of fuzzy dark matter (FDM) and from the constraints of NS-WD, we conclude that if ALPs are FDM, then they do not couple with quarks. Astrophysical objects like neutron stars contain muons and they can mediate long range $L_\mu - L_\tau$ force between the compact binary systems. The ultra light vector gauge bosons can also radiate from the binary systems and contribute to the orbital period decay.

27.1 Ultra Light Dark Matter

The standard model of particle physics does not explain the experimental evidence of dark matter. In this paper we consider the fuzzy dark matter (FDM) model which can solve the small scale structure problem. The FDM consists of ultra light scalar or axion like pseudoscalar particles of mass $m_a \sim 10^{-21}\text{eV} - 10^{-22}\text{eV}$. The de Broglie wavelength of the FDM particles is comparable to the size of the dwarf galaxy so that all the FDM particles can contained in the dwarf galaxy. The Lagrangian of the axion like particle is [1, 2]

S. Mohanty (✉) · T. Kumar Poddar
Theoretical Physics Division, Physical Research Laboratory, Ahmedabad 380009, India
e-mail: mohanty@prl.res.in

A. Giri and R. Mohanta (eds.), *Workshop on Frontiers in High Energy Physics 2019*, Springer Proceedings in Physics 248,
https://doi.org/10.1007/978-981-15-6292-1_27

$$\mathcal{L} = \sqrt{g}\Big[g^{\mu\nu}\partial_\mu a \partial_\nu a + \mu^4\Big(\cos\frac{a}{f} - 1\Big)\Big], \tag{27.1}$$

where a is the axion field, f is the axion decay constant and μ is a parameter which is related with the axion mass. The equation of motion of the axion field for non relativistic or zero modes becomes

$$\ddot{a} + 3H\dot{a} + m^2 \sin\frac{a}{f} = 0, \tag{27.2}$$

where the axion mass is $m = \frac{\mu^2}{f}$. The axion field solution is damped harmonic oscillatory. For the Hubble parameter $H > m$, the axion field takes a constant value which fixes the initial misalignment angle. The oscillation of the axion field starts when $H \sim m$. The oscillation modes are damped as $R^{-\frac{3}{2}}$ for $H < m$ and the energy density of the axion field redshifts like a cold dark matter. Here R is the scale factor. Hence the relic density of FDM is

$$\Omega_a \sim 0.1\Big(\frac{f}{10^{17}\text{GeV}}\Big)\Big(\frac{m}{10^{-22}\text{eV}}\Big)^{1/2}. \tag{27.3}$$

From (27.3), we conclude that FDM particles satisfy the present relic density if the mass of the particle is 10^{-22}eV and the decay constant $f \sim 10^{17}$GeV.

27.2 Orbital Period Decay of Binary Pulsars and Graviton Radiation

The observed value of the orbital period decay agrees well with the gravitational wave radiation. The orbital period decay of Hulse Taylor binary pulsar over time is shown in Fig. 27.1.

The interaction between the graviton and matter is denoted by the Lagrangian [3, 4]

$$\mathcal{L} = \frac{1}{2}\partial_\alpha h'^{\mu\nu}\partial^\alpha h'_{\mu\nu} + \frac{1}{2}\kappa h'^{\mu\nu}T^{\mu\nu}, \tag{27.4}$$

where, $h'_{\mu\nu} = \kappa^{-1}h_{\mu\nu}$ and $\kappa = \sqrt{32\pi G}$. The matter field is

$$T_{\mu\nu}(x') = M\delta^3(\mathbf{x}' - \mathbf{x}(t))U_\mu U_\nu, \tag{27.5}$$

where G is the universal gravitational constant, $M = m_1m_2/(m_1 + m_2)$ is the reduced mass of the binary system and U_μ is the four velocity of the reduced mass of the binary system in the Kepler orbit. m_1 and m_2 are the masses of the two stars in the binary system. Using the Peter–Mathews formula, we obtain the energy loss due to graviton emission is

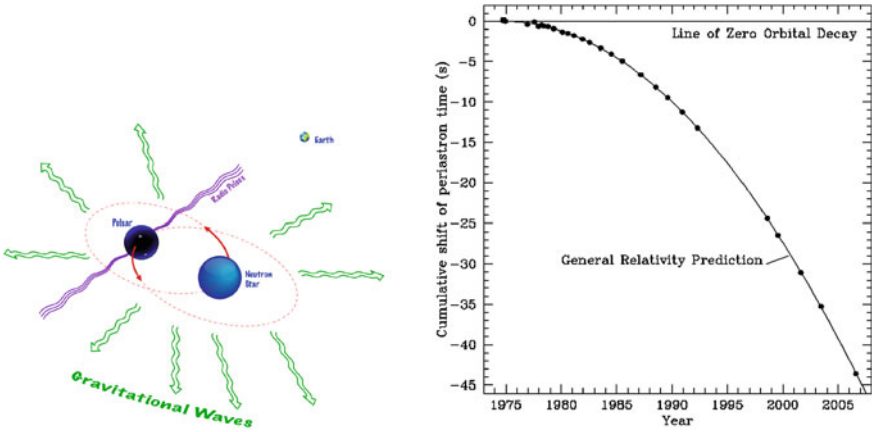

Fig. 27.1 The left plot denotes the emission of gravitational wave radiation from Hulse-Taylor binary pulsar and the right plot denotes the orbital period decay over time

$$\frac{dE}{dt} = \frac{32}{5} G\Omega^6 \Big(\frac{m_1 m_2}{(m_1+m_2)}\Big)^2 a^4 (1-e^2)^{-7/2}\Big(1+\frac{73}{24}e^2+\frac{37}{96}e^4\Big), \tag{27.6}$$

where e is the eccentricity of the binary orbit, Ω is the orbital frequency, and a is the semi major axis of the binary orbit. The orbital period (P_b) decay is related with the rate of energy loss by

$$\frac{dP_b}{dt} = -6\pi G^{-3/2}(m_1 m_2)^{-1}(m_1+m_2)^{-1/2} a^{5/2}\Big(\frac{dE}{dt}\Big). \tag{27.7}$$

Putting the values of all the quantities in (27.6) we obtain the energy loss due to graviton radiation for the Hulse-Taylor (HT) binary pulsar

$$\frac{dE}{dt} = 3.2 \times 10^{33} \text{erg/sec}, \tag{27.8}$$

and the rate of orbital period decay becomes $\dot{P}_b = -2.40263 \pm 0.0005 \times 10^{-12} ss^{-1}$ which agrees well with the observed value $\dot{P}_{b\,observed} = -2.40262 \pm 0.0005 \times 10^{-12} ss^{-1}$.

27.3 Radiation of Long Range Fifth Force Scalar from Compact Binary System

The orbital period decay due to gravitational wave radiation agrees well with the observed value for HT binary pulsar, however there is less than one percent mismatch

between the observed and the GR predicted value. We consider massless scalars can emit from the binary system and contribute to the orbital period decay. The interaction Lagrangian between the massless scalar (ϕ) and the baryon (ψ) is [4]

$$\mathcal{L} = g_s \phi \bar{\psi} \psi = g_s \phi n(x), \tag{27.9}$$

where $n(x)$ is the baryon number density, and g_s is the coupling constant. Following the same procedure as above we obtain the rate of energy loss due to massless scalar radiation

$$\frac{dE}{dt} = \frac{1}{24\pi}\left[\left(\frac{N_1}{m_1} - \frac{N_2}{m_2}\right) M g_s\right]^2 \Omega^4 a^2 \frac{(1+\frac{e^2}{2})}{(1-e^2)^{5/2}}, \tag{27.10}$$

where N_1 and N_2 are the number of baryons in the two stars of the binary system. Assuming this massless scalar radiation contributes to the uncertainty, we obtain the upper bound on the coupling constant

$$g_s < 3 \times 10^{-19}. \tag{27.11}$$

27.4 ALPs Radiation from Compact Binary System

For ultralight axion like particles (ALPs) radiation from compact binary system to take place, the orbital frequency of the binary orbit should be greater than the mass of the emitted particle. Hence the orbital frequency of the binary orbit is

$$\Omega = \left[G\frac{(m_1+m_2)}{a^3}\right]^{1/2} \sim 10^{-19}\text{eV}. \tag{27.12}$$

Hence, compact binary system can emit particles of mass less than 10^{-19}eV. It has been discussed in [5] that if compact stars such as neutron star (NS) and white dwarf (WD) are immersed in a very low mass axionic potential then the axion field solution falls off like Yukawa interaction with distance outside of the compact star. Assuming the spacetime outside of the compact star is Schwarzschild, the axion filed solution inside and outside of the compact star becomes [6]

$$a(r) = 4\pi f, \qquad r < R, \tag{27.13}$$

$$= -\frac{q_{eff}}{2GM}\ln\left(1 - \frac{2GM}{r}\right), \qquad r > R, \tag{27.14}$$

where q_{eff} is the effective axion charge of the compact star and is given as

$$q_{eff} = -\frac{8\pi GMf}{\ln\left(1-\frac{2GM}{R}\right)}. \tag{27.15}$$

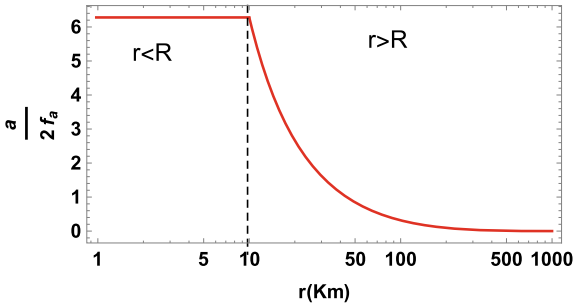

Fig. 27.2 Inside of the compact star ($r < R$), the axion field is constant. Outside of the compact star ($r > R$), the axion field has a long range behaviour

Table 27.1 Summary of the upper bounds on the axion decay constant f for four compact binaries. For all the binaries we assume $m < 10^{-19}$ eV [6]

Compact binary system	f_a (GeV)
PSR J0348+0432	$\lesssim 1.66 \times 10^{11}$
PSR J0737–3039	$\lesssim 9.76 \times 10^{16}$
PSR J1738+0333	$\lesssim 2.03 \times 10^{11}$
PSR B1913+16	$\lesssim 2.12 \times 10^{17}$

The axion field inside and outside of a compact star is shown in Fig. 27.2.

So the power loss due to ultralight ALPs dipole radiation is

$$\frac{dE}{dt} = \frac{\Omega^4 p^2}{24\pi} \frac{(1 + e^2/2)}{(1 - e^2)^{\frac{5}{2}}} \left(1 - \frac{m^2}{\Omega^2}\right)^{3/2}, \tag{27.16}$$

where p is called the dipole moment and is given by

$$p = 8\pi G f \mu a \left[\frac{1}{\ln\left(1 - \frac{2Gm_2}{R}\right)} - \frac{1}{\ln\left(1 - \frac{2Gm_1}{R}\right)} \right]. \tag{27.17}$$

In this paper we consider four compact binary systems and put upper bounds on the axion decay constant if we assume ALPs contribute to the less than one percent of the orbital period decay. In Table 27.1, we put upper bounds on the axion decay constant for four compact binary systems.

So the stronger bound comes from the NS-WD binary system which is $f \lesssim \mathcal{O}(\sim 10^{11}\text{GeV})$ and it implies FDM which couples with quarks are ruled out.

Table 27.2 Summary of the upper bounds on gauge boson-muon coupling g for four compact binary systems. We take $M'_Z < 10^{-19}$ eV

Compact binary system	g (orbital period decay)
PSR B1913+16	$\leq 2.21 \times 10^{-18}$
PSR J0737–3039	$\leq 2.17 \times 10^{-19}$
PSR J0348+0432	$\leq 9.02 \times 10^{-20}$
PSR J1738+0333	$\leq 4.24 \times 10^{-20}$

27.5 $L_\mu - L_\tau$ Vector Gauge Boson Radiation from Compact Binary System

In the standard model, one can gauge one of the three global symmetries ($L_e - L_\mu$, $L_e - L_\tau$, and $L_\mu - L_\tau$) in an anomaly free way. This can give rise to long range Yukawa type force. The $L_e - L_{\mu,\tau}$ long range force from the electrons can be probed in neutrino oscillation experiments but it is difficult to probe $L_\mu - L_\tau$ long range force from neutrino oscillation experiment. Due to large chemical potential of degenerate electrons, the muon decay is forbidden, and hence, neutron star contains large muon charge. For white dwarf, Fermi suppression does not really apply and white dwarfs do not contain muon charge. In NS, there are approximately 10^{55} number of muons. A $L_\mu - L_\tau$ vector gauge boson exchange between muons in two neutron stars generate a long range fifth force between two NS in the binary system. The energy loss due to $L_\mu - L_\tau$ gauge boson radiation from the compact binary system is [7]

$$\frac{dE}{dt} = \frac{g^2}{6\pi} M^2 \Big(\frac{Q_1}{m_1} - \frac{Q_2}{m_2}\Big)^2 \Omega^4 a^2 \frac{(1 + \frac{e^2}{2})}{(1 - e^2)^{5/2}}, \tag{27.18}$$

where g is the gauge boson muon coupling constant, Q_1 and Q_2 are the muon charges of the two stars in the binary system. If the vector gauge boson contributes to less than one percent of the orbital period decay apart from gravitational wave radiation, then we can put upper bound on the coupling constant from the available data. For vector gauge boson radiation to take place, the mass of the particle should be less than the orbital frequency which restricts the mass spectrum of the radiated particles to $M'_Z \lesssim 10^{-19}$eV. In Table 27.2, we put upper bounds on the gauge coupling for four compact binary systems. The stronger bound of the gauge coupling is $g \lesssim \mathcal{O}(10^{-20})$.

The exclusion plot for gauge boson coupling is shown in Fig. 27.3.

27.6 Conclusions and Discussions

In this paper, we discuss that apart from gravitational quadrupole radiation, the scalar or pseudoscalar ALPs radiation, $L_\mu - Ł_\tau$ vector gauge boson radiation also con-

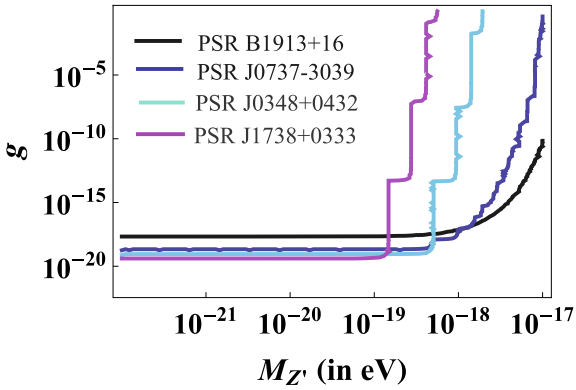

Fig. 27.3 Exclusion plots to constrain the coupling of the gauge field in a gauged $L_\mu - L_\tau$ scenario for four compact binary systems. The regions above the coloured lines are excluded

tribute to the orbital period decay. From binary pulsar timing data we put bounds on the coupling constants. The particles which are emitted from the binary system have mass $\lesssim 10^{-19}$eV. These ultralight particles can be a candidate for FDM. From the bound from NS-WD binary system, we conclude that if ALPs are FDM, then they do not couple with quarks.

References

1. W. Hu, R. Barkana, A. Gruzinov, Cold and fuzzy dark matter. Phys. Rev. Lett. **85**, 1158–1161 (2000)
2. L. Hui, J.P. Ostriker, S. Tremaine, E. Witten, Ultralight scalars as cosmological dark matter. Phys. Rev. D **95**, 043541 (2017)
3. P.C. Peters, J. Mathews, Gravitational radiation from point masses in a Keplerian orbit. Phys. Rev. **131**, 435 (1963)
4. S. Mohanty, P.K. Panda, Particle physics bounds from the Hulse- Taylor binary. Phys. Rev. D **53**, 5723–5726 (1996)
5. A. Hook, J. Huang, Probing axions with neutron star inspirals and other stellar processes. J. High Energy Phys. **2018**, 36 (2018)
6. T.K. Poddar, S. Jana, S. Mohanty, Phys. Rev.D **101**, 8 083007 (2020)
7. T.K. Poddar, S. Mohanty, S. Jana, Phys. Rev. D **100**, 123023 (2019)

Chapter 28
Extragalactic Neutrinos: A Window to New Physics

Siddhartha Karmakar, Sujata Pandey, and Subhendu Rakshit

Abstract Starting with a brief review of IceCube experiment, we discuss the potential of IceCube in probing physics beyond the domain of the standard model of particle physics. Here we concentrate on the possible neutrino-dark matter interactions as the high energy astrophysical neutrinos travel through the cosmos. We also compare the potential of IceCube with LHC in probing non-standard neutrino-nucleon interactions.

28.1 Introduction

The IceCube detector at Antarctica has recorded several high energy neutrino events that do not originate from our galaxy. One of these neutrinos has even been identified to originate from a distant blazar. With this heralds an era of neutrino astronomy. We would like to observe far away astrophysical objects with the help of neutrinos, understand the mechanisms of generation of various particles at different energy regimes. This will complement other modes of observations, for example, with photons at different wavelengths, by observing cosmic rays, detecting the associated gravitational waves, etc. We have already studied the Sun detecting the neutrinos produced in weak interactions that drive Sun's thermonuclear power generation processes. This has helped establish the standard solar model. We need to proceed in the same fashion for the astrophysical objects like Active Galactic Nuclei (AGN), Gamma Ray Bursts (GRB), etc.

In this talk, we would like to discuss another aspect of such observations. IceCube has proven its worth to probe physics beyond the standard model (BSM): For example, some of the constraints on neutrino-nucleus interactions from IceCube are

S. Rakshit (✉)
FHEP 2019, Hyderabad, India
e-mail: rakshit@iiti.ac.in

S. Karmakar · S. Pandey · S. Rakshit
Discipline of Physics, Indian Institute of Technology Indore,
Khandwa Road, Simrol, Indore 453 552, India

A. Giri and R. Mohanta (eds.), *Workshop on Frontiers in High Energy Physics 2019*, Springer Proceedings in Physics 248,
https://doi.org/10.1007/978-981-15-6292-1_28

more stringent than those offered by LHC. Various features of the extragalactic neutrino spectrum may be reflective of neutrino-dark matter interactions, as the neutrino passes through dark matter halos on its way to the Earth. Such interactions might help us to do neutrino astronomy as well.

Now the question is due to the two apparently contradictory prospects of such an experiment, given the uncertainty of the incoming neutrino flux, can we at all be able to find definitive new physics signatures at IceCube? The answer is surprisingly affirmative! Before we delve into such specific aspects of BSM search at IceCube, we first review the neutrino generation processes at these astrophysical sources and their detection at the IceCube.

28.2 A Brief Overview

Protons in the aforesaid astrophysical objects are believed to undergo Fermi acceleration, a non-thermal process, moving through the shock waves that have moving magnetic inhomogeneities acting as magnetic mirrors. After sufficient acceleration, the protons may interact with the surrounding protons or photons to churn out charged pions which eventually decay to give birth to neutrinos. Along with the charged pions, neutral pions also get produced, which promptly decay into a pair of photons. These processes also produce cosmic rays. Both the neutrinos and their anti-particles are produced according to the flavour ratio $1 : 2 : 0$.

We have observed cosmic rays up to an energy $\sim 10^{11}$ GeV. In detectors like Auger, one can do astronomy with these particles for energies more than 10^9 GeV, as charged particles with lower energies deflect in the interstellar magnetic field, and fails us to point back towards its source. We have done astronomy with photons ranging from radio waves to gamma rays. Gamma ray photons interact with the cosmic microwave background (CMB) photons. For energies more than a few tens of TeV, the cross-section becomes substantial, and such gamma rays get absorbed. So the astronomy based on photons do not work beyond such energies. As we have observed cosmic rays of extreme energies, taking a cue from the production mechanisms mentioned above, it is naturally expected to observe neutrinos of energies around this range as well. This prompted the construction of Amanda, which was then superseded by the IceCube, which will receive a further upgrade to IceCube-Gen2.

In the standard scenario, these neutrinos oscillate as they travel. As the distance travelled is much larger than the length of oscillation, it gets averaged out to lead to the probability of flavour conversion from ν_α to ν_β as

$$P_{\alpha\beta} = \sum_k |U_{\alpha k}|^2 \, |U_{\beta k}|^2 \,,$$

where U stands for the PMNS matrix.

Neutrinos undergo charged-current (CC) and neutral-current (NC) interactions in the Antarctic ice. CC interaction of ν_e and NC interactions of all flavours of neutrinos

produce showers, whereas CC interactions of ν_μ and ν_τ lead to track events in the photomultipliers of IceCube. ν_τs of energy more than a PeV can exhibit 'double-bang' events, a characteristic signature of tau flavoured neutrinos, which are yet to be observed at the IceCube. Neutrinos and anti-neutrinos are not distinguishable as at the IceCube one cannot differentiate charged leptons from its anti-particles, with only one exception: $\bar{\nu}_e$s can interact with electrons in the detector to undergo a Glashow resonance. As a result for a $\bar{\nu}_e$ of energy 6.3 PeV, the cross-section is large. No event of this kind has been reported so far. In general, low energy neutrinos penetrate through the Earth. However, high energy astrophysical neutrinos, having a much larger cross-section with Earth's matter, finds it opaque. For $E \sim 10^{12}$ GeV, the mean free path is less than a metre! This ensures that although one expects less number of extremely energetic neutrinos, the probability of their detection at the IceCube is substantial.

The observed neutrino spectrum is shown in Fig. 28.1b. Around a PeV, very few events have been observed so far, while below ∼160 TeV, there is a slight excess. In between 400 TeV–1 PeV, only a few events have been detected, perhaps indicating a dip in the spectrum. It is debatable as the statistics are rather poor. Although the uncertainties in the flux of astrophysical neutrinos are rather large, there is however a guaranteed flux, originating from the interactions of cosmic rays with CMB photons. Their energies are expected to peak around 10^9 GeV. With IceCube, one expects at least an event per year, which is yet to be observed. This might be indicative of a sharp cut-off after a few PeVs. IceCube-Gen2, having a volume ten times larger than the present IceCube, after a few years of operation will be able to substantially reduce such statistical uncertainties in the observed neutrino spectrum and put the debates to rest.

In passing, we note that IceCube offers probing new physics beyond the standard model due to the following: A neutrino of energy hitting a proton or a neutron at rest probes physics of scale

$$E_{\rm CM} = \sqrt{2 m_{\rm N} E} \sim 14 \sqrt{\frac{E}{10^{17}{\rm eV}}}\ {\rm TeV}.$$

Hence, it can compete with LHC and even go much beyond to probe non-standard neutrino-nucleon interactions.

28.3 ν-DM Interactions

As mentioned earlier, cosmic rays are observed up to an energy 3×10^{11} GeV. But, the non-observation of cosmogenic neutrinos and, in fact, any neutrino after a few PeVs might indicate a sharp cut-off in the neutrino spectra. Moreover, IceCube has observed [1] a neutrino event originating from a blazar TXS 0506+056 1.75Gpc away from the Earth, which ensures that AGNs are indeed a source for such highly energetic astrophysical neutrinos. But, as most of the AGN models predict substantial

neutrino flux above a PeV [2], this leads to a contradiction, unless such neutrinos somehow disappear on their way to the Earth. CMB neutrinos, having lower number densities, cannot lead to suppressions of such an extent unless one takes BSM s-channel resonant interactions into account! Hence, it is interesting to ask ourselves if neutrino absorption in dark matter (DM) can do the job.

Weakly interacting massive particle (WIMP) is not fit for the job as it also suffers from the same problem: The lack of significant number density. Dark matter of mass less than an eV can account for the required number density. But usually, they are regarded as 'hot', which is responsible for only about 1% of the DM relic density. Sub-eV scalar DM, forming a Bose-Einstein condensate [3] turns out to be a perfect candidate as it also offers solutions to the other problems in astrophysics, namely the missing satellite and cusp-core problems. A further bottleneck comes from the fact that it is quite challenging to build a particle physics model that allows substantial interaction between high energy neutrinos and an ultralight scalar DM particle. A wide variety of interactions have been enlisted in [4], and only a few interactions were found to offer significant cross-section [5]. A renormalisable model based on a Z' exchange has been presented, which we outline in the following.

The Z' in this model couples to the third generation leptons only, so that the bounds from anomalous magnetic moments of electron and muon are evaded. The Lagrangian is given by,

$$\mathcal{L} \supset ig(\phi^* \partial_\mu \phi - \phi\, \partial_\mu \phi^*) Z'^\mu + if\, \bar{\nu}_\tau \gamma_\mu \nu_\tau Z'^\mu \,. \tag{28.1}$$

$m_{Z'}$ is taken to be 10 MeV, to keep the standard big-bang nucleosynthesis unperturbed. The measurements on Z decay-width put the most stringent constraint on the $Z'\tau\tau$ coupling, $f < 0.022$. The resulting ν-DM cross-section, driven by a t-channel process, is given by

$$\sigma \simeq \begin{cases} \frac{g^2 f^2}{2\pi} \frac{m_{\rm DM} E}{m_{Z'}^4} & \text{if } E < m_{Z'}^2/m_{\rm DM} \\ \frac{g^2 f^2}{4\pi} \frac{1}{m_{Z'}^2} & \text{if } E > m_{Z'}^2/m_{\rm DM} \,, \end{cases}$$

and is plotted in Fig. 28.1a.

While travelling through a uniform DM distribution of number density $n = 1.2 \times 10^{-6}$ GeV/cc over a distance L, the neutrino flux gets attenuated as $F_0(E)$ $\exp(-n\sigma L)$, where $F_0(E)$ stands for the initial flux. However, as the neutrino scatters off a DM particle, its energy degrades—a process known as regeneration. This leads to an alteration of the resulting neutrino flux, which is obtained by solving an integro-differential equation. Due to the peculiar shape of the cross-section, a dip appears in the final flux. Keeping in mind that the interaction occurs via the t-channel [7], and hence, is not caused by any resonance, it is remarkable! Fig. 28.1a illustrates this mechanism. All fluxes are multiplied by E^2, expressed in units of GeV cm^{-2} s^{-1} str^{-1}, and are scaled by a factor 3×10^9. ν-DM cross-section σ is plotted in units of eV^{-2} and is scaled by 3×10^{21}. In Fig. 28.1b, we put this mechanism to the test by comparing with the real data. A diffuse neutrino flux that goes

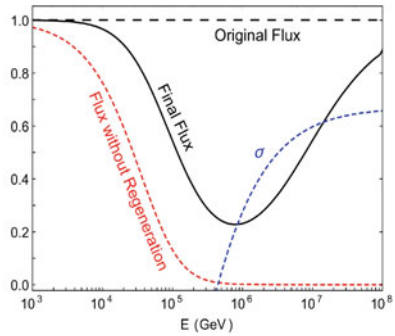

An illustration of the mechanism causing a dip. Here $m_{\rm DM} = 0.3$ eV and $gf = 7 \times 10^{-3}$.

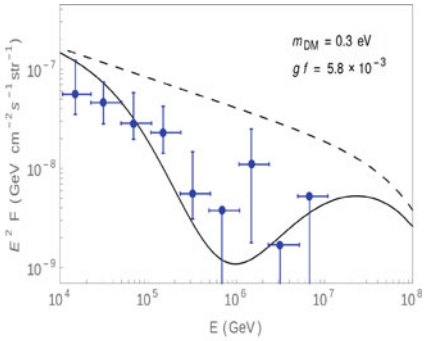

Absorption dip due to ν-DM interaction for an $E^{-2.3}$ diffuse neutrino flux.

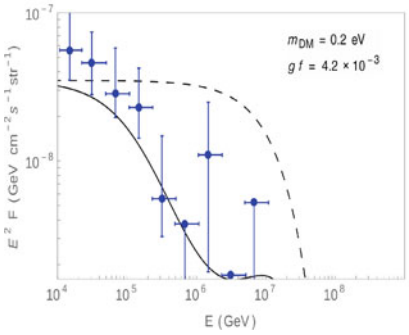

An early cut-off in a diffuse neutrino flux. The dashed line represents an E^{-2} original flux with a cut-off at 12 PeV.

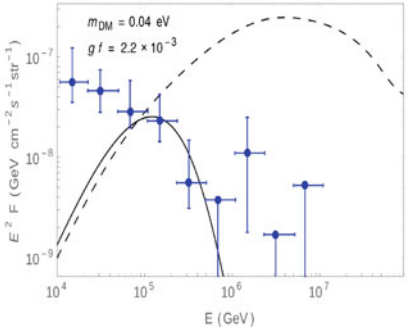

Attenuation of the diffuse neutrino flux for the AGN core model S05.

Fig. 28.1 Absorption of neutrinos due to ν-DM interaction. The dashed black lines indicate the original flux. The solid black lines represent the same flux after absorption in DM halo. The blue points represent the fitted diffuse astrophysical flux to the 7-year IceCube data [6]. For all plots $m_{Z'} = 10$ MeV, $m_\nu = 0.1$ eV, and $L = 200$ Mpc

as $E^{-2.3}$, is used to validate the mechanism. For another benchmark, we show in Fig. 28.1c that the dip now takes a different shape to account for an early cut-off. As mentioned earlier, this mechanism also helps explain the non-observation of a large neutrino flux at higher energies. In Fig. 28.1d the dashed curve stands for the neutrino flux as predicted by the AGN core model S05 [8]. Our mechanism helps it to reconcile with the observations, resulting in a 'low-energy excess', as this adds to the standard-fit only at low energies. With only one dark matter candidate, it is not possible to explain all the features. However, one can envisage a multi-component DM scenario to alleviate this shortcoming. At present, it is not justified to fit the data in our proposed scheme with a single component DM, given the large uncertainties in the flux. Such ν-DM interactions are harmless to the standard neutrino cosmology as at low energies the cross-section is negligible. Another interesting fact is that in

the case of such ν-DM interactions the $E_{\rm CM} = \sqrt{2m_{\rm DM}E}$ for sub-eV DM can be rather small—suitable to probe new physics at an energy ∼MeV or even less!

28.4 Non-standard ν-Nucleon Interactions

High energy astrophysical neutrino experiments like IceCube offer a probe for neutrino interactions with matter at unprecedented energies. At these energies, ∼PeV or less, these deep inelastic interactions are not affected by partonic uncertainties as the relevant domain of Bjorken–Paschos 'x' is by and large well tested at HERA and is accessible to LHCb. Then can the non-standard neutrino-quark interactions (NSI) be tested at these energies? In fact, LHC also offers similar opportunities. Which one is better? One can write quite a few such NSI. Many of them are severely constrained by low energy neutrino scattering or oscillation experiments. Can we then obtain better constraints using these astrophysical neutrinos at IceCube or at LHC? We stumbled on these questions and addressed them in [9].

In general, NSIs are defined as

$$\mathcal{L}_{\rm NSI} = 2\sqrt{2}\epsilon_{ij}^{qC} G_F (\bar{\nu}^i \gamma_\mu \nu^j)(\bar{q}\gamma^\mu P_C q), \qquad C = L, R\,. \tag{28.2}$$

Here, we consider NSIs of type $\bar{\nu}\nu\bar{q}q$ only. SU(2) invariance implies presence of NSIs of type $\bar{\ell}\ell\bar{q}q$, which are tightly constrained from other experiments. But, it is not that difficult to encounter situations where such NSIs with the charged counterparts of $\bar{\nu}\nu\bar{q}q$ are absent. For example, $\mathcal{O}_8 = (\bar{L}H\gamma_\mu H^\dagger L)(\bar{q}\gamma^\mu q)$ leads to an interaction of the form $\bar{\nu}\nu\bar{q}q$, but not to its counterpart involving charged leptons $\bar{\ell}\ell\bar{q}q$ [10–12]. Hence, we do not consider bounds on $\bar{\nu}\nu\bar{q}q$ implied from the constraints on $\bar{\ell}\ell\bar{q}q$. By the same token, we also do not consider NSIs of type $\bar{\nu}\ell\bar{q}q'$.

LHC and IceCube compete with each other to put constraints on the NSIs. Here we illustrate this in a particular scenario where these non-standard interactions are generated by the exchange of a Z' gauge boson.

$$\mathcal{L} \supset g_\nu(\bar{\nu}\gamma_\mu P_L \nu)Z'^\mu + g_q(\bar{q}\gamma^\mu q)Z'_\mu. \tag{28.3}$$

Stringent experimental constraints exist [13] on the couplings g_ν and g_q for $m_{Z'} \lesssim 1$ GeV. For larger masses, these are quite relaxed. We need to check if IceCube and LHC can do a better job in that regime.

Up-going events at the IceCube reach the detector from different directions traversing different amount of earth's matter. This leads to a sensitivity of the neutrino flux to the total neutrino-nucleon cross-section. CC cross-section is measured rather precisely from the observation of track events. This enables one to put bounds on the NC cross-section $\sigma_{\rm NC}$. Thus the NSIs considered in this paper can be constrained from the uncertainties in $\sigma_{\rm NC}$. Constraints for 28.3 are shown in Fig. 28.2. These interactions contribute to the process $pp \to \nu\bar{\nu}j$. The ensuing constraint from LHC monojet+$\not{E}_T$ searches [17] at $\sqrt{s} = 8$ TeV on the interaction in (28.3) comes out to

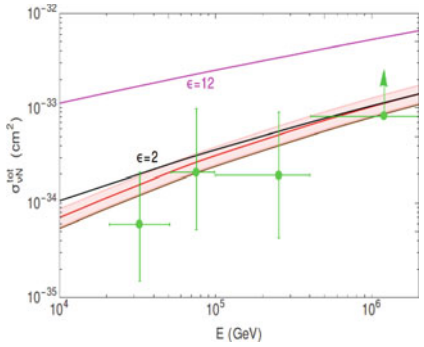

Constraints on NSI for $m_{Z'} = 5$ GeV.

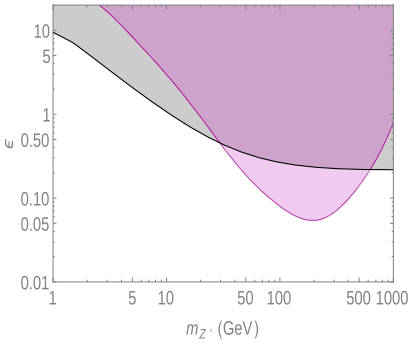

$m_{Z'}$ dependence of the constraints.

Fig. 28.2 LHC versus IceCube: In **a**, the brown line represents the total SM neutrino-nucleon cross-section [14]. The red line and the light red band denote the central value and 1σ allowed range of $\sigma^{tot}_{\nu N}$ from IceCube observation of track events respectively [15]. Similarly, the green points and related error bars in the y-direction stand for the central values and 1σ allowed ranges in $\sigma^{tot}_{\nu N}$ measured from the IceCube observation of shower events at different energy bins respectively [16]. The magenta line depicts the value of $\sigma^{tot}_{\nu N}$ with the NSI parameter ϵ set at its maximum allowed value from LHC, $\epsilon = 12$. The black line represents the value of $\sigma^{tot}_{\nu N}$ with ϵ set at its maximum allowed value from IceCube, $\epsilon = 2$. In **b**, the pink and grey regions are excluded from LHC and IceCube respectively

be, $g_q g_\nu \lesssim 9.9 \times 10^{-3}$, implying $\epsilon \equiv g_q g_\nu (v^2/2m^2_{Z'}) \lesssim 12$ for $m_{Z'} = 5$ GeV. This is more significant than the Borexino bound. For the same $m_{Z'}$, the observation of the cascade events at IceCube offers a slightly better bound than the LHC monojet+$\not{E}_T$ searches, $g_q g_\nu \lesssim 1.65 \times 10^{-3}$, implying $\epsilon \lesssim 2$.

Bounds on ϵ can be read off Fig. 28.2b for different values of $m_{Z'}$. Except the range $m_{Z'} \sim 35-500$ GeV, the IceCube provides a better constraint than the LHC [9, 18]. This happens due to the LHC's sizable acceptance in the channel $pp \to j + \not{E}_T$ for such range of $m_{Z'}$ with renormalisable interactions [19]. In [9], this analysis has been extended to include several other NSIs, both Z'-mediated and contact-type effective interactions. For the latter, LHC constraints are always better than the IceCube ones. Future experiments, like MATHUSLA, SHiP, FASER, can put better bounds on NSIs for $m_{Z'} \sim 1$ GeV. Significant constraints can also come from neutrino-nucleon scattering experiments at COHERENT and neutrino oscillation experiments like DUNE. However, one needs to keep in mind that while these bounds are flavour-specific, the constraints offered by IceCube and LHC, as discussed in [9], are applicable to all flavours of neutrino NSI!

28.5 Summary

The IceCube has proven itself to be an impressive facility to probe physics beyond the standard model of particle physics. Even with its limited exposure, it can already compete with LHC. The future upgrade IceCube-Gen2 will help improve the statistics. The features of the observed spectra of high energy neutrino spectra will be more conspicuous by then. If some of the existing features persist, then the explanations offered by ν-DM interactions can be tested further to unravel the nature and further observable consequences of such interactions. One may note that with one DM component it is not possible to explain all the features—one needs to look for models with multi-component dark sector.

Such ν-DM interactions can be useful to explore interiors of astrophysical objects. Our new findings [20] suggest that the DM density profile might get imprinted in the energy dependence of neutrino flavour ratios, that can be observed in IceCube-Gen2. This will mark the beginning of another new era of neutrino astronomy. Stay tuned!

Acknowledgements This work is supported by the Department of Science and Technology, India *via* DST-DAAD grant no. INT/FRG/DAAD/P-22/2018 and DST-SERB grant no. CRG/2019/002354.

References

1. M.G. Aartsen et al., Science **361**(6398), eaat1378 (2018)
2. K. Murase, J.F. Beacom, Phys. Rev. D **81**, 123001 (2010)
3. W. Hu, R. Barkana, A. Gruzinov, Phys. Rev. Lett. **85**, 1158 (2000)
4. S. Pandey, S. Karmakar, S. Rakshit, JHEP **1901**, 095 (2019)
5. For the literature on ν-DM interactions and the resulting neutrino absorption, please see the references [17–34] of Ref. [4]
6. A. Karle, Talk presented at La Palma 2018 on behalf of IceCube collaboration
7. S. Karmakar, S. Pandey, S. Rakshit, arXiv:1810.04192 [hep-ph]
8. F.W. Stecker, Phys. Rev. D **88**(4), 047301 (2013)
9. S. Pandey, S. Karmakar, S. Rakshit, JHEP **1911**, 046 (2019)
10. M.B. Gavela, D. Hernandez, T. Ota, W. Winter, Phys. Rev. D **79**, 013007 (2009)
11. S. Davidson, V. Sanz, Phys. Rev. D **84**, 113011 (2011)
12. S. Davidson, C. Pena-Garay, N. Rius, A. Santamaria, JHEP **0303**, 011 (2003)
13. W. Altmannshofer, M. Tammaro, J. Zupan, JHEP **1909**, 083 (2019)
14. R. Gandhi, C. Quigg, M.H. Reno, I. Sarcevic, Phys. Rev. D **58**, 093009 (1998)
15. M.G. Aartsen et al., IceCube collaboration. Nature **551**, 596 (2017)
16. M. Bustamante, A. Connolly, Phys. Rev. Lett. **122**(4), 041101 (2019)
17. G. Aad et al., [ATLAS collaboration], Eur. Phys. J. C **75**(7), 299 (2015), Erratum: [Eur. Phys. J. C **75**(9), 408 (2015)]
18. D. Buarque Franzosi, M.T. Frandsen, I.M. Shoemaker, Phys. Rev. D **93**(9), 095001 (2016)
19. A. Friedland, M.L. Graesser, I.M. Shoemaker, L. Vecchi, Phys. Lett. B **714**, 267 (2012)
20. S. Pandey, S. Rakshit, Work in progress

Chapter 29
UV-IR Freeze-In of a Fermionic Dark Matter and Its Possible X-Ray Signature

Anirban Biswas, Sougata Ganguly, and Sourov Roy

Abstract We discuss the production of a non-thermal fermion dark matter χ through ultraviolet (UV), infrared (IR) and mixed UV-IR freeze-in mechanism in a minimal extension of the standard model (SM) with two gauge singlet fields. In addition to the gauge singlet fermion χ, there is a gauge singlet pseudo scalar field $\tilde{\phi}$. We have found that for 10^{10} GeV $\leq \Lambda \leq 10^{15}$ GeV, χ is dominantly produced via UV and mixed UV-IR freeze-in when reheat temperature $T_{\rm RH} \gtrsim 10^4$ GeV and below which the production is dominated by IR and mixed freeze-in. Moreover, we have considered the cascade annihilation $\chi\bar{\chi} \to \tilde{\phi}\tilde{\phi} \to 4\gamma$ to address the longstanding $\sim$3.5 keV X-ray line observed from various galaxies and galaxy clusters.

29.1 Introduction

Non-thermal origin of dark matter is one of such frameworks where dark matter possesses extremely weak interaction with other particles in the thermal bath. In this framework, it is assumed that the initial abundance of dark matter is almost negligible compared to other particles maintaining thermal equilibrium among themselves. Here, dark matter particles are produced gradually from the decay as well as scattering of bath particles. This is known as the Freeze-in mechanism [2]. Moreover, there are two types of freeze-in depending on the time of maximum production of dark matter. One of them is the ultra-violet (UV) freeze-in [2, 3] where dark and visible sectors

Invited talk (based on [1]) given by Sourov Roy at FHEP 2019, Hyderabad, India.

A. Biswas · S. Ganguly · S. Roy (✉)
School of Physical Sciences, Indian Association for the Cultivation of Science, 2A & 2B Raja S.C. Mullick Road, Kolkata 700032, India
e-mail: tpsr@iacs.res.in

A. Biswas
e-mail: tpab3@iacs.res.in

S. Ganguly
e-mail: tpsg4@iacs.res.in

A. Giri and R. Mohanta (eds.), *Workshop on Frontiers in High Energy Physics 2019*, Springer Proceedings in Physics 248,
https://doi.org/10.1007/978-981-15-6292-1_29

are connected by the higher dimensional operators only. As a result, abundance of dark matter becomes extremely sensitive to the initial history such as the reheat temperature ($T_{\rm RH}$) of the Universe. In this situation production of dark matter occurs only through scatterings. On the other hand, renormalisable interaction between dark and visible sectors leads to another kind of dark matter production which is dominated at around the temperature $T \sim$ mass of the initial state particles, when latter are in thermal equilibrium. Unlike the previous case, this kind of freeze-in is mostly effective at the lowest possible temperature for a particular production process (i.e. either decay or scattering or both) hence this is known as the infrared (IR) freeze-in [2, 4]. Moreover, freeze-in can also be possible when initial state particles themselves remain out of thermal equilibrium [5].

In this talk, based on [1], we discuss both the UV freeze-in and IR freeze-in in a single framework and also discuss a possible signature of our dark matter candidate via ∼3.5 keV X-ray line. Non-thermal production of $\tilde{\phi}$ from UV processes and its subsequent decay into $\chi\bar{\chi}$ via a dimension four operator is dubbed as mixed UV-IR freeze-in scenario of χ. In addition, the pseudo scalar $\tilde{\phi}$ may also act as a decaying dark matter component.

The observation of ∼3.5 keV X-ray line by the XMM Newton X-ray observatory from various galaxy clusters including Perseus, Coma, Centaurus etc. was first reported in [6]. Afterwards, there are studies by various groups claiming the presence of this *line* in the X-ray spectrum from the Andromeda galaxy [7] and also from the centre of our Milky Way galaxy [8]. There are several studies providing possible explanations of the origin of this x-ray line signal, in physics beyond the SM. A comprehensive list of references can be found in [1].

Here we provide an explanation in terms of annihilating dark matter where the dark matter candidate χ undergoes a cascade annihilation in which first a pair of $\chi\bar{\chi}$ annihilates into $\tilde{\phi}\tilde{\phi}$ and thereafter each $\tilde{\phi}$ decays into two γs. This type of dark matter annihilation produces a "box" shaped photon spectrum [9] which gets a *line* shape as $m_\chi \to m_{\tilde{\phi}}$.

Rest of this article is organized as follows. A brief discussion of the model is presented in Sect. 29.2. Dark matter production via UV and IR freeze-in is discussed in Sect. 29.3. Possibility of $\tilde{\phi}$ as a decaying dark matter candidate is discussed in Sect. 29.4. An indirect signature of the dark matter candidate χ is discussed in Section 29.5. Our conclusions are given in Sect. 29.6.

29.2 Model

We have extended the fermionic sector as well as the scalar sector of the SM by adding a Dirac fermion χ and a pseudo scalar $\tilde{\phi}$. Both χ and $\tilde{\phi}$ are singlet under the SM gauge group $\mathrm{SU}(3)_c \otimes \mathrm{SU}(2)_L \otimes \mathrm{U}(1)_Y$. Additionally, we have imposed a $\mathbb{Z}_2$ symmetry in the Lagrangian and we demand that only χ is odd under $\mathbb{Z}_2$. Due to this, the Dirac fermion χ cannot have any interaction with the SM fields up to the level of dimension four. The minimal operator describing interaction of χ with SM Higgs doublet Φ is a five dimensional operator suppressed by a mass scale Λ. However,

Table 29.1 Field content of our model and their charges under $SU(3)_c \otimes SU(2)_L \otimes U(1)_Y \otimes \mathbb{Z}_2$

Field content	Charge under $SU(3)_c \otimes SU(2)_L \otimes U(1)_Y \otimes \mathbb{Z}_2$ symmetry
$\ell_L = \begin{pmatrix} \nu_e \\ e \end{pmatrix}_L, \begin{pmatrix} \nu_\mu \\ \mu \end{pmatrix}_L, \begin{pmatrix} \nu_\tau \\ \tau \end{pmatrix}_L$	$(1,\ 2,\ -1,\ +)$
$\ell_R = e_R,\ \mu_R,\ \tau_R$	$(1,\ 1,\ -2,\ +)$
$Q_L = \begin{pmatrix} u \\ d \end{pmatrix}_L, \begin{pmatrix} c \\ s \end{pmatrix}_L, \begin{pmatrix} t \\ b \end{pmatrix}_L$	$(3,\ 2,\ \frac{1}{3},\ +)$
$U_R = u_R,\ c_R,\ t_R$	$(1,\ 1,\ \frac{4}{3},\ +)$
$D_R = d_R,\ s_R,\ b_R$	$(1,\ 1,\ -\frac{2}{3},\ +)$
$\Phi = \begin{pmatrix} \phi^+ \\ \phi^0 \end{pmatrix}$	$(1,\ 2,\ 1,\ +)$
χ	$(1,\ 1,\ 0,\ -)$
$\tilde{\phi}$	$(1,\ 1,\ 0,\ +)$

χ has renormalisable interaction with the remaining non-standard particle $\tilde{\phi}$. On the other hand, being a pseudo scalar, the CP invariance restricts interactions of $\tilde{\phi}$ as well. Although unlike χ, $\tilde{\phi}$ has interaction with the SM Higgs doublet at dimension four level, beyond that one can have interactions between $\tilde{\phi}$ and SM gauge bosons which have very rich phenomenology. Because of the unbroken $\mathbb{Z}_2$ symmetry, the Dirac fermion χ is absolutely stable and is considered to be the dark matter candidate. On the other hand, when the mass of $\tilde{\phi}$ is less than $m_\chi/2$, $\tilde{\phi}$ is very long-lived and it can act as a decaying dark matter candidate. The lifetime of $\tilde{\phi}$ is controlled by the cut-off scale Λ.

The charges of all the fields under $SU(3)_c \otimes SU(2)_L \otimes U(1)_Y \otimes \mathbb{Z}_2$ symmetry are listed in Table 29.1.

The gauge invariant and CP conserving Lagrangian of our model is given by

$$\begin{aligned}
\mathcal{L} = \mathcal{L}_{SM} &+ \overline{\chi}(i\,\partial\!\!\!/ - m_\chi)\chi + \frac{1}{2}(\partial^\mu\tilde{\phi})(\partial_\mu\tilde{\phi}) - \frac{1}{2}m_{\tilde{\phi}}\tilde{\phi}^2 \\
&- \frac{\tilde{\phi}\, B_{\mu\nu}\tilde{B}^{\mu\nu}}{2\,\Lambda} - \frac{\tilde{\phi}\, W^a_{\mu\nu}\tilde{W}^{\mu\nu}_a}{2\,\Lambda} - \frac{\tilde{\phi}\, G^b_{\mu\nu}\tilde{G}^{\mu\nu}_b}{2\,\Lambda} \\
&- \frac{y^\ell_{\alpha\beta}}{\Lambda}(i\,\overline{\ell_{L\alpha}}\,\Phi\,\gamma_5\,\ell_{R\beta}\,\tilde{\phi} + h.c) - \frac{y^d_{\alpha\beta}}{\Lambda}(i\,\overline{Q_{L\alpha}}\,\Phi\,\gamma_5\,D_{R\beta}\tilde{\phi} + h.c) \\
&- \frac{y^u_{\alpha\beta}}{\Lambda}(i\,\overline{Q_{L\alpha}}\,\tilde{\Phi}\,\gamma_5\,U_{R\beta}\tilde{\phi} + h.c) \\
&- \frac{\overline{\chi}\chi\,\Phi^\dagger\Phi}{\Lambda} - g\,\overline{\chi}\gamma_5\chi\tilde{\phi} + \frac{\lambda}{2}\tilde{\phi}^2\Phi^\dagger\Phi\,,
\end{aligned} \tag{29.1}$$

where $\alpha,\ \beta$ are the generation indices and Λ is a mass scale representing the cut-off scale of our effective theory.

29.3 Dark Matter Production via UV and IR Freeze-In

Our dark matter candidate χ always stays out of thermal equilibrium and behaves as a non-thermal relic. In this case UV freeze-in is possible due to the presence of higher dimensional interactions between χ and SM fermions, gauge bosons and in this process maximum χ production occurred when the temperature of the Universe was equal to $T_{\rm RH}$, the reheat temperature. On the other hand, after electroweak symmetry breaking (EWSB) additional χ particles are produced from the scatterings and decays of the SM particles via IR freeze-in mechanism. We have calculated both the UV and IR contributions to the relic density of our dark matter candidate χ. The required interaction terms which are responsible for the UV contribution are given by,

$$\begin{aligned}\mathcal{L} \supset & -\frac{\overline{\chi}\chi\Phi^{\dagger}\Phi}{\Lambda} - \frac{\epsilon^{\mu\nu\alpha\beta}\left(\partial_\mu B_\nu\right)\left(\partial_\alpha B_\beta\right)\tilde{\phi}}{\Lambda} \\ & - \frac{\epsilon^{\mu\nu\alpha\beta}\left(\partial_\mu W^a_\nu\right)\left(\partial_\alpha W^a_\beta\right)\tilde{\phi}}{\Lambda} - \frac{\epsilon^{\mu\nu\alpha\beta}\left(\partial_\mu G^b_\nu\right)\left(\partial_\alpha G^b_\beta\right)\tilde{\phi}}{\Lambda} \\ & - \frac{i}{\Lambda}\sum_{i=1}^{3}\left\{\sum_{\alpha=u,d} y^{\alpha}_{ii}\,\overline{q_i}_L\,\gamma_5\,q_{i\,R}\,\phi^{0*} + y^{\ell}_{ii}\,\overline{\ell_i}_L\,\gamma_5\,\ell_{i\,R}\,\phi^{0*} + h.c.\right\}\tilde{\phi} - g\,\bar{\chi}\gamma_5\chi\,\tilde{\phi}\,.\end{aligned} \tag{29.2}$$

Since UV freeze-in occurs well above the electroweak symmetry breaking, during UV freeze-in B_μ, W^a_μ $(a = 1,\ 2,\ 3)$ and G^b_μ $(b = 1 \ldots . 8)$ are physical gauge bosons and χ is produced from their annihilations mediated by pseudo scalar $\tilde{\phi}$. Moreover, χ can also be produced from the annihilations of $T_3 = \frac{1}{2}$ and $-\frac{1}{2}$ components of the Higgs doublet Φ. Furthermore, one can also have the following scattering processes $t\,\bar{t} \to \Phi\,\tilde{\phi}$, $t\,\Phi \to t\,\tilde{\phi}$ and $\bar{t}\,\Phi \to \bar{t}\,\tilde{\phi}$, which are dominant in the UV regime, with subsequent $\tilde{\phi} \to \bar{\chi}\,\chi$ decay leading to mixed UV-IR freeze-in. The relevant Feynman diagrams can be found in [1]. On the other hand, IR freeze-in becomes effective only after the EWSB. The interaction terms which govern IR production of χ are given by

$$\begin{aligned}\mathcal{L} \supset & -\frac{\epsilon^{\mu\nu\alpha\beta}\left(\partial_\mu W^-_\nu\right)\left(\partial_\alpha W^+_\beta\right)\tilde{\phi}}{\Lambda} - \frac{\epsilon^{\mu\nu\alpha\beta}\left(\partial_\mu W^+_\nu\right)\left(\partial_\alpha W^-_\beta\right)\tilde{\phi}}{\Lambda} - \frac{\epsilon^{\mu\nu\alpha\beta}\left(\partial_\mu Z_\nu\right)\left(\partial_\alpha Z_\beta\right)\tilde{\phi}}{\Lambda} \\ & - \frac{\epsilon^{\mu\nu\alpha\beta}(\partial_\mu A_\nu)(\partial_\alpha A_\beta)\tilde{\phi}}{\Lambda} - \frac{\epsilon^{\mu\nu\alpha\beta}\left(\partial_\mu G^b_\nu\right)\left(\partial_\alpha G^b_\beta\right)\tilde{\phi}}{\Lambda} - \frac{i}{\Lambda}\sum_j m_{f_j}\,\overline{f_j}\gamma_5 f_j\tilde{\phi} \\ & - \frac{v}{\Lambda}\overline{\chi}\chi h - \frac{1}{2\Lambda}\overline{\chi}\chi\,h^2 - g\,\overline{\chi}\gamma_5\chi\,\tilde{\phi}\,,\end{aligned} \tag{29.3}$$

where m_{f_j} is the mass of the SM fermion f_j and the summation index j is taken over all the SM fermions.

Therefore, our dark matter candidate χ has IR contributions to its relic density from the following scattering processes: $gg \to \overline{\chi}\chi$, $W^+W^- \to \overline{\chi}\chi$, $ZZ \to \overline{\chi}\chi$, $\bar{f}_j f_j \to \overline{\chi}\chi$, $hh \to \overline{\chi}\chi$ and $\tilde{\phi}\tilde{\phi} \to \overline{\chi}\chi$. Apart form these scatterings, χ can also be produced from the decays of Higgs boson h and pseudo scalar $\tilde{\phi}$ if such processes are kinematically allowed. Feynman diagrams for all these processes can be found in [1]. Note that in this work we are considering $m_{\tilde{\phi}} \leq 100$ GeV, this choice does not allow $\tilde{\phi}$ to be generated thermally [1].

In order to calculate the relic abundance of χ produced via freeze-in, we solve the Boltzmann equation of χ, taking into account all possible interactions into the collision term. The Boltzmann equation of χ is given by

$$\frac{dn_\chi}{dt} + 3Hn_\chi \simeq \sum_i n_i^{\rm eq}\, n_i^{\rm eq} \langle \sigma\, {\rm v}_{\rm rel}\rangle_{i\,i\to\overline{\chi}\chi} + n_h^{\rm eq} \langle \Gamma_{h\to\overline{\chi}\chi}\rangle + \frac{g_{\tilde{\phi}} m_{\tilde{\phi}} \Gamma_{\tilde{\phi}\to\chi\bar{\chi}}}{2\pi^2} \int_0^\infty f(p,T) \frac{p^2 dp}{\sqrt{p^2 + m_{\tilde{\phi}}^2}} + \mathcal{F}_{2\to3}(T) + \mathcal{F}_{2\to4}(T)\,, \tag{29.4}$$

where, n_i is the number density of species i and the corresponding equilibrium number density is denoted by $n_i^{\rm eq}$.

In the right hand side of the above equation, we have the usual collision term of the Boltzmann equation. Since χ has an insignificant initial number density, we have neglected inverse processes proportional to n_χ^2. The first term in the right hand side indicates the production of χ from scattering of particles i which are in thermal equilibrium. The second part of the collision term represents the increase in number density of χ from decay of the SM Higgs (h). The third part of the collision term indicates the production of χ via mixed freeze-in. The momentum distribution function of $\tilde{\phi}$ is denoted by $f(p,T)$. The fourth and fifth terms in (29.4) indicate the production of χ from $2 \to 3$ and $2 \to 4$ processes via off-shell $\tilde{\phi}$ [1].

The relic density ($\Omega_\chi h^2$) of χ is given by

$$\Omega_\chi h^2 = 2.755 \times 10^8 \frac{m_\chi}{\rm GeV}\, Y_\chi(T_0)\,. \tag{29.5}$$

where $Y_\chi(T_0)$ is the comoving number density defined as $Y_\chi \equiv \dfrac{n_\chi}{s}$, where the quantity s is the entropy density of the Universe.

29.3.1 Numerical Results of the Boltzmann Equation

In this section, we present the allowed parameter space that we have obtained by computing dark matter relic density and comparing this with the reported range of $\Omega_{\rm DM}h^2 = 0.120 \pm 0.001$ by the Planck experiment. In order to do this, we have

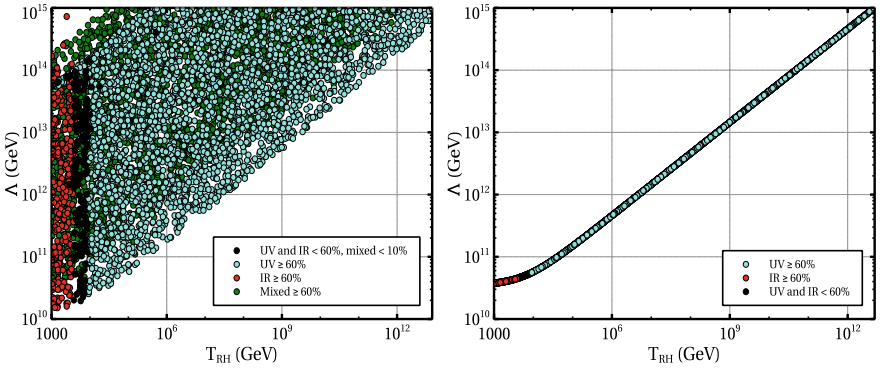

Fig. 29.1 Left panel: The $T_{\rm RH} - \Lambda$ parameter space reproducing correct dark matter relic density via freeze-in mechanism for $m_{\tilde{\phi}} = 100$ GeV and $1\,{\rm keV} \leq m_\chi \leq 100$ GeV. Right panel: Corresponding values of $T_{\rm RH}$ and Λ for $m_{\tilde{\phi}} \simeq m_\chi = 7.06$ keV. Figure taken from [1]

varied the independent parameters Λ, $T_{\rm RH}$, m_χ, g and λ within the following ranges. $10^{10}\,{\rm GeV} \leq \Lambda \leq 10^{15}\,{\rm GeV}$, $10^3\,{\rm GeV} \leq T_{\rm RH} \leq 10^{13}\,{\rm GeV}$, $10^{-6}\,{\rm GeV} \leq m_\chi \leq 10^2\,{\rm GeV}$, $10^{-8} \leq g \leq 10^{-2}$, $10^{-12} \leq \lambda \leq 10^{-8}$. The allowed parameter space in the $T_{\rm RH} - \Lambda$ plane by the relic density constraint is shown in the left panel of Fig. 29.1.

From Fig. 29.1 it is clearly visible that UV freeze-in contributes maximally for large reheat temperature i.e. $T_{\rm RH} > 10^4$ GeV. This is because the UV effect on $Y_\chi(T_0)$ is proportional to $T_{\rm RH}$. In addition, the contribution of UV freeze-in to $Y_\chi(T_0)$ has a $1/\Lambda^2$ suppression, as a result one needs larger Λ for higher $T_{\rm RH}$ such that $\Omega_\chi h^2$ does not exceed 1σ allowed range of $\Omega_{\rm DM} h^2$.

For $T_{\rm RH} < 10^4$ GeV, scatterings of W, Z, h and decay of the Higgs boson are the dominant sources of IR freeze-in. An additional source of significant production of χ is via mixed freeze-in. As a result, $\tilde{\phi}$ production from the scatterings involving top quark and subsequent decay of $\tilde{\phi}$ into $\bar{\chi}\chi$ pair gives substantial contribution to $\Omega_\chi h^2$. Furthermore, the variation of Λ for a particular value of $T_{\rm RH}$ is mostly due to g and m_χ where the latter is varying between 1 keV to 100 GeV.

The same parameter space for $m_{\tilde{\phi}} \simeq m_\chi = 7.06$ keV is shown in the right panel of Fig. 29.1. Here we get UV freeze-in dominance for higher values of $T_{\rm RH}$ and Λ whereas for low reheating temperature ($T_{\rm RH} < 10^4$ GeV) IR freeze-in becomes superior. Also note that here we get a line and this is mainly due to the reason that in the present plot we have kept m_χ fixed at 7.06 keV.

29.4 Possibility of $\tilde{\phi}$ as a Dark Matter

Let us discuss the possibility of having $\tilde{\phi}$ as another dark matter component. $\tilde{\phi}$ can be produced thermally via the Primakoff process, $f + \gamma \to f + \tilde{\phi}$. It can also be produced from the Primakoff like processes where photons are replaced by other SM

gauge bosons Z and $W^{\pm}$. We have found that the freeze-out temperature T_f of $\tilde{\phi}$ always remains larger than 100 GeV as long as $\Lambda \gtrsim 10^9$ GeV [10]. This implies $\tilde{\phi}$ (of mass $m_{\tilde{\phi}} \lesssim 100$ GeV) freezes-out relativistically when $\Lambda \gtrsim 10^9$ GeV, which is the range of Λ we are considering in this work. In this case the relic density of $\tilde{\phi}$ is given by [11]

$$\Omega_{\tilde{\phi}} h^2 = 0.12 \times \left(\frac{m_{\tilde{\phi}}}{163\,\text{eV}}\right) \times \left(\frac{106.75}{g_s(T_f)}\right) . \tag{29.6}$$

Therefore, $\tilde{\phi}$ with mass larger than 163 eV will overclose the Universe. In order to avoid this unpleasant situation, one needs the freeze-out temperature T_f of $\tilde{\phi}$ to be larger than the reheat temperature (T_{RH}) of the Universe such that $\tilde{\phi}$ will never be produced thermally from the Primakoff process.

However, $\tilde{\phi}$ will be produced dominantly via UV-freeze-in from the processes like $t\,\bar{t} \to \Phi\,\tilde{\phi}, t\,\Phi \to t\,\tilde{\phi}$ and $\bar{t}\,\Phi \to \bar{t}\,\tilde{\phi}$ where the abundance of $\tilde{\phi}$ depends on T_{RH} and Λ. Assuming the mass of $\tilde{\phi}$ to be $\sim$7 keV and $m_\chi \gtrsim m_{\tilde{\phi}}$, $\tilde{\phi}$ has only $\gamma\,\gamma$ decay mode available. Therefore, the way to make $\tilde{\phi}$ partially stable is by increasing Λ. However, the required value of Λ in the range between 10^{12} GeV and 10^{17} GeV is strongly disfavored from extragalactic background light (EBL) and X-ray observations.

29.5 Indirect Signature of χ via $\sim$ 3.5 keV X-Ray Line

In this model, the dark matter candidate χ can annihilate into a pair of $\tilde{\phi}$, which further decays into $\gamma\gamma$ final state i.e. $\bar{\chi}\chi \to \tilde{\phi}\tilde{\phi} \to 4\gamma$. Such cascade annihilation of χ results in a box shaped diffuse γ-ray spectrum [9], with each emitted photon has energy $m_{\tilde{\phi}}/2$ in the rest frame of $\tilde{\phi}$. The width of the spectrum is given by,

$$\Delta E = \sqrt{m_\chi^2 - m_{\tilde{\phi}}^2}\,, \tag{29.7}$$

which depends on the mass splitting between dark matter χ and pseudo scalar $\tilde{\phi}$.

The excess X-ray flux observed from centre of the Milky Way galaxy within an angle of 14′ is $(29 \pm 5) \times 10^{-6}$ cts/sec/cm^2 at an energy $E_\gamma = 3.539 \pm 0.011$ keV [8]. Therefore, we have considered $m_\chi = 7.06$ keV and $\delta = (m_\chi - m_{\tilde{\phi}})/m_\chi \sim 10^{-5}$ to match with the observed line like X-ray spectrum. For $m_{\tilde{\phi}} \simeq m_\chi$ and $m_{\tilde{\phi}} \sim 7$ keV, we have considered the mass scale 10^{10} GeV$\leq \Lambda \leq 10^{12}$ GeV. In this range of Λ, $\tilde{\phi}$ is long-lived but not stable over the cosmological time scale and χ is the only dark matter candidate.

The differential photon flux from the cascade annihilation of dark matter is given by,

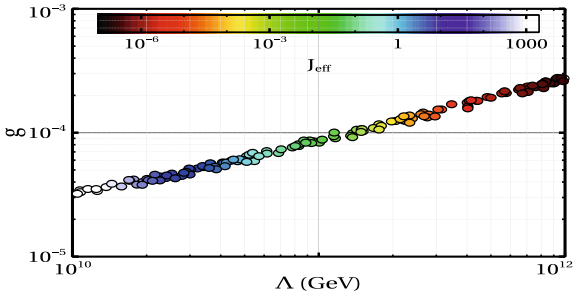

Fig. 29.2 Allowed values of Λ and g which reproduce observed X-ray flux (19×10^{-6}cts/cm$^2/s \leq \Phi_\gamma \leq 39 \times 10^{-6}cts/cm^2/s$ in 2σ range) from the centre of Milky Way galaxy. Figure taken from [1]

$$\frac{d\Phi_\gamma}{dE_\gamma} = 2 \times \frac{1}{4}\frac{r_\odot}{4\pi}\left(\frac{\rho_\odot}{m_\chi}\right)^2 \langle\sigma \mathrm{v}_{\mathrm{rel}}\rangle_{\bar{\chi}\chi\to\tilde{\phi}\tilde{\phi}} \frac{dN_\gamma}{dE_\gamma} J_{\mathrm{eff}} \Delta\Omega \,, \tag{29.8}$$

where, $\rho_\odot = 0.3$ GeV/cm^3 is the dark matter density at the solar neighbourhood, $r_\odot = 8.5$ kpc is the distance of the solar location from the galactic centre and $\Delta\Omega$ is the solid angle corresponding to an angle $14'(\sim 0.25^0)$ around the galactic centre. $\langle\sigma \mathrm{v}_{\mathrm{rel}}\rangle_{\bar{\chi}\chi\to\tilde{\phi}\tilde{\phi}}$ is the thermally averaged annihilation cross section for $\bar{\chi}\chi \to \tilde{\phi}\tilde{\phi}$. $\frac{dN_\gamma}{dE_\gamma}$ is just a Dirac delta function.

The effect of large lifetime of $\tilde{\phi}$ modifies the J-factor, which is a measure of amount of dark matter present in the region of interest, into an effective one that depends on effective dark matter density (ρ_{eff}) [1].

Finally, we have computed the X-ray flux from cascade annihilation of $\bar{\chi}\chi$ to explain the 3.53 keV X-ray line which has been observed by XMM Newton from the galactic centre [8], The allowed parameter space in the $\Lambda - g$ plane is shown in Fig. 29.2. The corresponding values of J_{eff} are depicted by the colour bar.

29.6 Conclusion

In this work, we have considered a minimal extension of the Standard Model by a gauge singlet $\mathbb{Z}_2$-odd fermion χ which couples to the SM Higgs boson by a dimension five effective operator. The production of χ at the early Universe occurs through UV, IR and UV-IR mixed freeze-in mechanism. We have also presented a discussion on the possibility of an indirect signature of our non-thermal dark matter χ in the light of the unexplained $\sim$3.5 keV X-ray line from various galaxies including our own Milky Way galaxy and also from galaxy clusters. For this we have introduced a SM gauge singlet pseudo scalar $\tilde{\phi}$ in the particle spectrum. Our dark matter χ of mass $\sim$7 keV pair annihilates into a pair of long lived $\tilde{\phi}$ and each $\tilde{\phi}$ thereafter decays into two photons. Finally, we have identified the allowed parameter space which reproduces the XMM Newton observed X-ray flux from the galactic centre of Milk way in 2σ range.

References

1. A. Biswas, S. Ganguly, S. Roy, arXiv:1907.07973 [hep-ph]. JCAP **03**, 043 (2020)
2. L.J. Hall, K. Jedamzik, J. March-Russell, S.M. West, JHEP **1003**, 080 (2010). https://doi.org/10.1007/JHEP03(2010)080
3. F. Elahi, C. Kolda, J. Unwin, JHEP **1503**, 048 (2015). https://doi.org/10.1007/JHEP03(2015)048
4. N. Bernal, M. Heikinheimo, T. Tenkanen, K. Tuominen, V. Vaskonen, Int. J. Mod. Phys. A **32**(27), 1730023 (2017). https://doi.org/10.1142/S0217751X1730023X
5. A. Biswas, A. Gupta, JCAP **1703**, 033 (2017), Addendum: [JCAP **1705**, A02 (2017)], https://doi.org/10.1088/1475-7516/2017/03/033, https://doi.org/10.1088/1475-7516/2017/05/A02
6. E. Bulbul, M. Markevitch, A. Foster, R.K. Smith, M. Loewenstein, S.W. Randall, Astrophys. J. **789**, 13 (2014). https://doi.org/10.1088/0004-637X/789/1/13
7. A. Boyarsky, O. Ruchayskiy, D. Iakubovskyi, J. Franse, Phys. Rev. Lett. **113**, 251301 (2014). https://doi.org/10.1103/PhysRevLett.113.251301
8. A. Boyarsky, J. Franse, D. Iakubovskyi, O. Ruchayskiy, Phys. Rev. Lett. **115**, 161301 (2015). https://doi.org/10.1103/PhysRevLett.115.161301
9. A. Ibarra, S. Lopez Gehler, M. Pato, JCAP **1207**, 043 (2012). https://doi.org/10.1088/1475-7516/2012/07/043
10. D. Cadamuro, J. Redondo, JCAP **1202**, 032 (2012). https://doi.org/10.1088/1475-7516/2012/02/032
11. E.W. Kolb, M.S. Turner, Front. Phys. **69**, 1 (1990)

Chapter 30
Recent Results from GRAPES-3 Observatory

P. K. Mohanty

Abstract The GRAPES-3 is a high density extensive air shower array experiment located in Ooty, India. It is operating with an array of 400 scintillator detectors in conjunction with a 560 m^2 tracking muon telescope. It is designed to observe cosmic rays and gamma rays in the TeV-PeV energy range. The design of the muon telescope allows multi-rigidity observations of galactic cosmic rays (GCRs) from a near equatorial location at a cut off rigidity of 17 GV. It provides a real-time monitoring of the GCR intensity over a field of view of 2.3 sr with a direction resolution of 4°. A record of 4×10^9 muons per day allows GRAPES-3 to probe various solar phenomena through modulation of GCR intensity with unprecedented sensitivity (1 part in 10^4). The discovery of a transient weakening of Earth's magnetic field through the detection of a muon burst was a highlight from the GRAPES-3 experiment. This is extremely important from space weather perspective. The discovery of a record break potential of 1.3 GV during a thunderstorm using muon imaging is another highlight result from the GRAPES-3 experiment which may provide better understanding of the high energy particle acceleration in the closest natural accelerator. At present the expansion of the muon telescope is underway to increase its area by 560 m^2 to significantly enhance its capability.

30.1 Introduction

Cosmic rays have been observed over an extraordinary range of energies (10^8–10^{20} eV). They have provided the widest window to probe the high energy phenomena in the universe. The presence of these very high energy particles in nature is difficult to explain since it is contrary to any kind of stable or thermal equilibrium. Therefore, the existence of non-thermal and/or non-equilibrium conditions becomes necessary

On Behalf of the GRAPES-3 Collaboration.

P. K. Mohanty (✉)
Tata Institute of Fundamental Research, Mumbai 400005, India
e-mail: pkm@tifr.res.in

A. Giri and R. Mohanta (eds.), *Workshop on Frontiers in High Energy Physics 2019*, Springer Proceedings in Physics 248,
https://doi.org/10.1007/978-981-15-6292-1_30

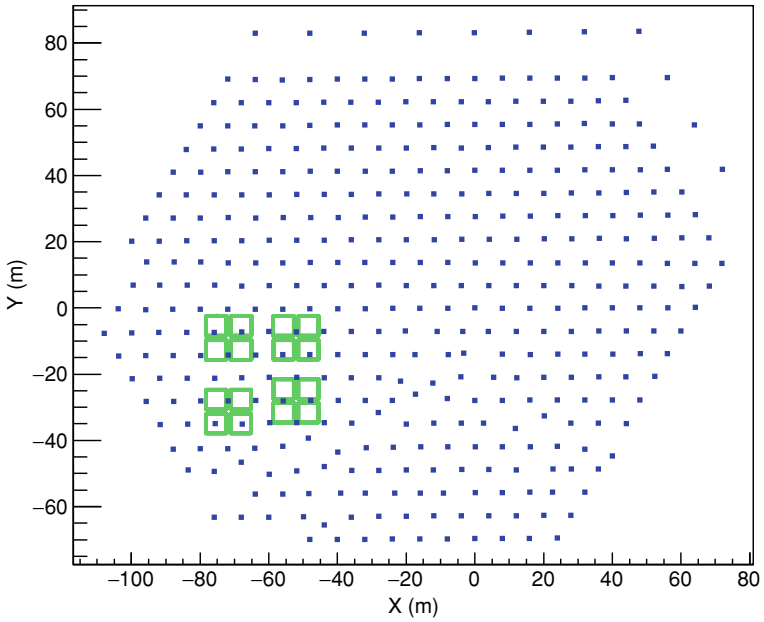

Fig. 30.1 GRAPES-3 EAS array in Ooty, India (11.4 °N, 76.7 °E, 2200 m altitude). Small filled squares represent scintillator detectors of 1 m^2 area each separated by 8 m and the 16 big squares represent muon modules of 35 m^2 area each

to explain their presence. Some of the scenarios proposed to explain the acceleration of particles to high energies require extreme physical conditions that may even necessitate modifications of the existing understanding of physics. Despite the discovery of cosmic rays more than a century ago, the origin of these particles is still to be understood. The primary objective of the GRAPES-3 is to obtain a better understanding the acceleration of high energy particles in the universe through sensitive measurements.

The GRAPES-3 (**G**amma **R**ay **A**stromony at **P**eV **E**nergie**S** Phase-**3**) is a major cosmic ray extensive air shower (EAS) experiment located in Ooty, India (11.4°N latitude, 76.7°E longitude, 2200 m altitude). It comprises two major detector components which include; (1) an array of 400 plastic scintillator detectors of 1 m^2 area each, separated by 8 m deployed over an area of 25,000 m^2 [1, 2], and (2) a large area (560 m^2) tracking muon telescope [3] as shown in the schematic in Fig. 30.1.

The Interaction of primary cosmic rays (PCRs) in the atmosphere generates a cascade of secondary particles which is known as extensive air shower (EAS). At the ground level, the secondaries constitute an electromagnetic component which include electrons and photons (∼90%), a muonic component (∼8–9%), and a hadronic component which include pions, kaons, protons, neutrons (∼1%). The number of secondary particles and their lateral spread on the ground is proportional to the energy of the PCRs. Each scintillator detector in the GRAPES-3 expriment is designed to

measure the density and relative arrival time of EAS particles which in turn are used to reconstruct the EAS to obtain the energy and incident direction of PCR respectively. Due to the smaller inter-detector spacing, the array triggers low energy showers down below to 1 TeV in contrast to most of the traditional EAS arrays with energy threshold typically above 100 TeV. Therefore, the GRAPES-3 measurements could bridge the gap between the direct measurements of PCRs using satellite and balloon based experiments in space and indirect measurements at the ground. The energy sensitivity of the array is between 1 TeV and 10 PeV. It records 3×10^6 EAS events per day. The EAS information from the scintillator array along with the muon component from the muon telescope are used to study the energy spectrum and mass composition of primary cosmic rays [4, 5].

The muon telescope records muons in the EAS with a threshold energy of 1 GeV. It comprises 16 individual modules of 35 m^2 area each based on proportional counters (PRCs) as the basic detector. Each PRC is a steel tube of 6 m long with a square cross section of 10 cm $\times$ 10 cm. It is filled with a mixture of Argon (90%) and Methane (10%) called P10 which serves as an active detection medium for the charged particles. Each module contains four layers of PRCs of 58 PRC in each layer arranged in a grid configuration that allows to obtain the arrival direction of each muon incident at zenith angle up to 60° covering a field of view of 2.3 sr [6]. An absorber in form of concrete of 550 g cm^{-2} thickness has been placed above the PRC layers that allows penetrating muons of above 1 GeV to be recorded. The reconstructed muons are recorded in 13×13 (169) directional bins with an average angular resolution of 4°. The muon telescope provides a two dimensional real-time monitor of the muon flux. It records $\sim 5 \times 10^4$ muons per second providing a high temporal measurement of the galactic cosmic ray intensity variation caused by various solar phenomena.

The unique combination of high statistics and high angular resolution measurement of muon flux makes GRAPES-3 an incredibly sensitive probe for exploring new domains such as solar physics, space weather and atmospheric acceleration. Several interesting measurements have been obtained from GRAPES-3 on solar phenomena and space weather driven by transient solar events such as flares and coronal mass ejections (CMEs) [6–13]. Space weather is a major concern since it can cause significant disruptions in our immediate space environment, affecting a whole host of technologies such as the global positioning system, satellite operations, communication, aviation and the electrical power grids that we routinely rely on [14].

30.2 Results on Solar Storms

During the active phase of the solar cycle, frequent eruptions from the solar corona takes place, ejecting out billion tons of solar material into the interplanetary space called coronal mass ejections (CME). Depending on the speed of the CME, it can take less than a day to several days to reach on the earth. During the passage of the CME over the earth, the magnetic field in the CME shields the low energy galactic

cosmic rays causing reduction in the cosmic ray flux observed on the earth and this phenomena is known as Forbush decreases. Satellites placed at the first Lagrangian point called L1 at a distance of 1.5 million km from the earth along the sun-earth line measures the plasma parameters including the interplanetary magnetic field (IMF) and the velocity of the plasma. This information is relayed to the ground station through radio signal which takes about 5 s, providing advance information on the arrival of the solar storm.

During the period of 18–25 June 2015, a series of solar flares and CMEs occurred from the active sunspot region namely NOAA AR2371. The IMF measurements by the WIND spacecraft located at L1 point showed that three CMEs arrived on the earth in succession on 21 June at 16:45 UT, 22 June at 5:45 UT and 22 June at 18:40 UT [15]. These arrivals were marked by jumps in the solar wind velocity (V_{sw}) and the total IMF (|B|) as shown in Fig. 30.2a and b respectively. When the third CME struck at 18:40 UT, the V_{sw} jumped from 440 kms^{-1} to 700 kms^{-1} and the |B| jumped from 10 nT to 44 nT. The z component of the IMF i.e. B_z was strongly aligned to south, opposite to that of the earth's magnetic field orientation. The GRAPES-3 muon telescope recorded a sudden increase in the muon flux of about a magnitude of 1% in coincident with IMF parameters lasting for two hours between 19:00 h and 21:00 h as can be seen from Fig. 30.2. The phenomenon subsequently referred as the cosmic ray burst occurred in the midst of a continuing FD. An excess of 9.2×10^5 on a background of 2.9×10^8 muons during the two hour interval implies a significance in excess of 50 σ.

As mentioned in Sect. 30.1, the muon telescope consists 16 identical modules where each module provides 169 directional measurement of the muon flux. The 169 directions were grouped into 9 coarser directions of ~0.3 sr to enhance statistical accuracy. Figure 30.3 shows the burst observation in 16 modules in total $16 \times 9 = 144$ directions. Out of these, the burst was detected with more than 5 σ in 42 directions, 4–5 σ in 37 directions and 3–4 σ in 40 directions. Further, the burst was observed simultaneously in all directions indicating its occurrence close to the earth.

After inverting the polarity of the IMF B_z, it was superimposed with the burst profile as shown in Fig. 30.4. A correlation coefficient of 0.94 suggested that the both IMF and the burst are strongly related. Since the IMF B_z and earth's magnetic field were oppositely oriented, we started with a hypothesis that there could be a weakening of the earth's magnetic field due to interactions of these two fields. This could have caused in lowering of the cutoff rigidity allowing low energy GCRs to enter into the earth's atmosphere which otherwise were forbidden due to the magnetic field. To test this hypothesis, simulations were carried out to calculate the cutoff rigidity in 9 directions just with the earth's magnetic field and then superimposing IMF on earth's magnetic field. This was performed by back-tracing method where an antiproton is launched upward in the earth's magnetic fields modelled by the international geomagnetic reference field (IGRF11). Cosmic rays of rigidity above the cutoff rigidity were simulated in the earth's atmosphere using the CORSIKA code for the production of muons and finally their detection in the muon telescope. The reproduction of the muon burst in 9 directions has validated the hypothesis of the transient weakening of earth's magnetic field [11, 12].

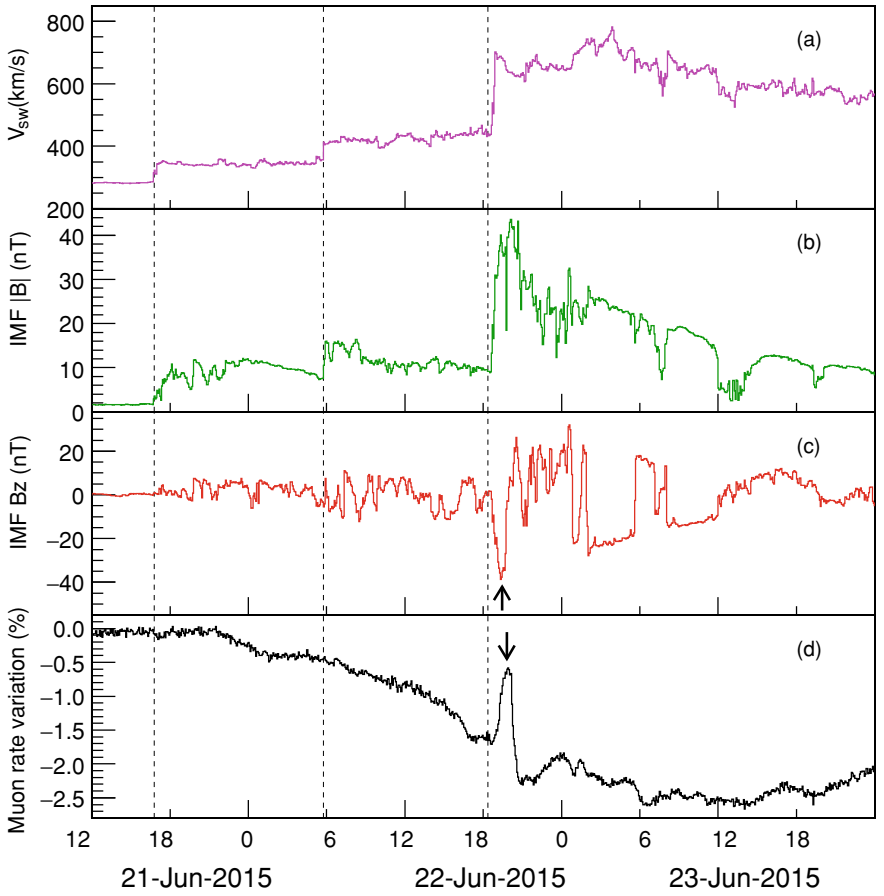

Fig. 30.2 Top 3 panels show solar wind and IMF data from WIND spacecraft time shifted to the bow shock nose: **a** V_{SW}, **b** |B|, **c** B_z, **d** GRAPES-3 muon rate. Vertical dashed lines indicate CME arrival times (UT)

Further an in-depth study of this event revealed that the arrival time of geomagnetic storm predicted by the satellites was not accurate. Our analysis shows that the storm was delayed by an additional 28 min, which was obtained by a cross correlation study of GRAPES-3 data with the simulated profile based on magnetic field information from satellites. A search effort with 20 years of GRAPES-3 archival data has identified >70 burst-like events which show varying delays from event to event. The detailed analysis of these events could address the problem of identifying the dependence of the arrival time delay as a function of geomagnetic storm parameters. This is extremely important for accurate prediction of geomagnetic storms, a challenging problem in space-weather research.

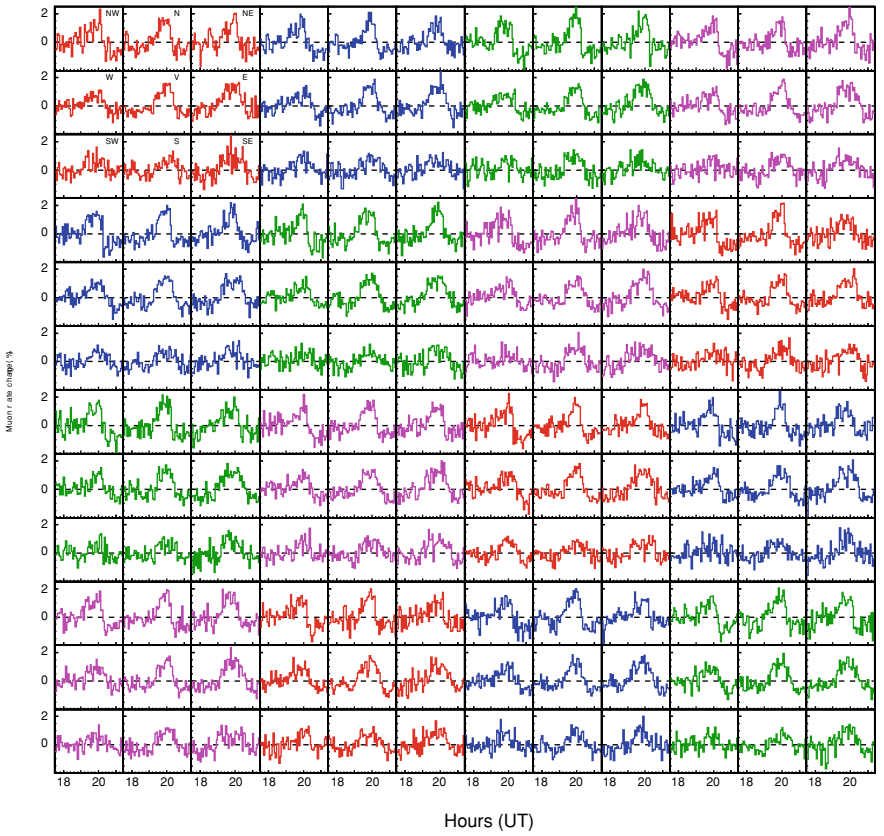

Fig. 30.3 Muon-rate variation in nine directions of each of the 16 muon telescope module observed by GRAPES-3 on 22 June 2015. Each module is represented by a different color

30.3 Results on Thunderstorm Acceleration

Study of acceleration of charged particles in the atmosphere by the large scale electric fields present in thunderstorms is a new emerging area. Nobel laureate C. T. R. Wilson had predicted generation of electric potentials of $\sim$1 GV in thunderclouds 90 years ago [16]. Discovery of terrestrial gamma-ray flashes (TGFs) containing MeV photons by Compton Gamma-Ray Observatory gave signature of electric potential in thunderclouds [17]. The detection of highest γ-ray energy of 100 MeV by the AGILE satellite would require bremsstrahlung of very high-energy electrons and presence of potentials of hundreds of MV [18].

The GRAPES-3 records rapid variation in muon intensity correlated with the variation of the electric field during thunderclouds measured by four electric field monitors which are widely spaced within 6 km distance from its location. In Ooty, thunderstorms mostly occurs during the month of March-June and September-

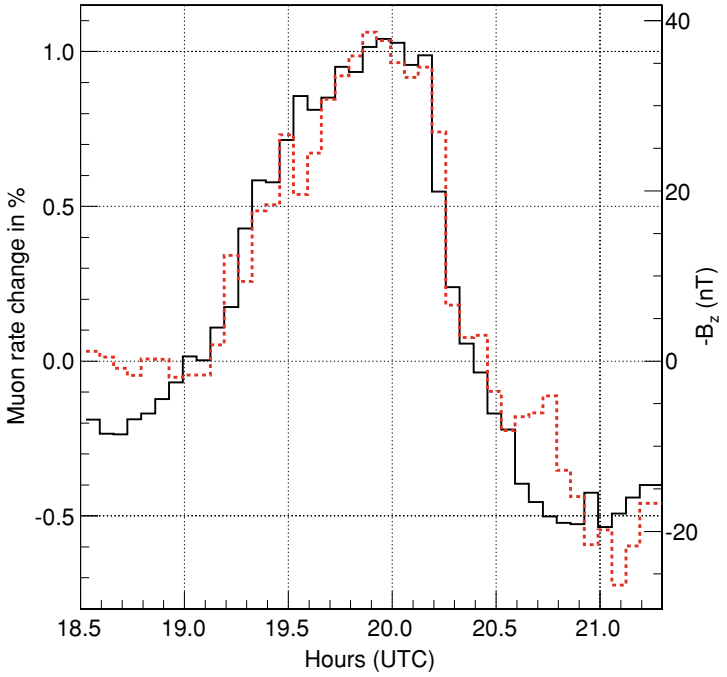

Fig. 30.4 Correlation between muon rate (solid line) and IMF B_z (broken line) during the 22 June 2015 burst event. Correlation coefficient $R = -0.94$

October. Analysis of data recorded during 2011–2014 found 184 events with muon intensity variations of 0.3–2.0% associated with electric field variations lasting for 10–30 mins. Out of these events, the one on 1 December 2014 was spectacular and had a clean profile. Therefore it was investigated in detail to estimate the potential of the thundercloud. The variation of muon intensity lasting over 18 min starting 10:42 UT on 1 December 2014 is shown in Fig. 30.5. The image of the muon intensity variation in the field of view of the muon telescope is shown in Fig. 30.6.

In thunderclouds, charge separation occurs while the bottom part of the cloud attains negative polarity and the top of the cloud can attain positive polarity. Within the charged cloud, if positive muons get decelerated, negative muons get accelerated. Since the positive muon number is more than negative muons, a reduction of total muon is expected and an increase is expected if the polarity of the cloud is reversed. An extensive simulation was carried out to estimate the potential during this thunderstorm using CORSIKA code. Electric potential was set up in atmosphere at a height between 8 to 10 km and the muons response to electric field was simulated. Muons produced by the atmospheric interaction of primary cosmic ray protons and reaching to the detector were passed through the muon telescope module. Only those muons with 1 GeV reaching to the bottom layer of proportional counters were counted. The maximum potential estimated for the event was 1.3 GV [19]. This possibly is the

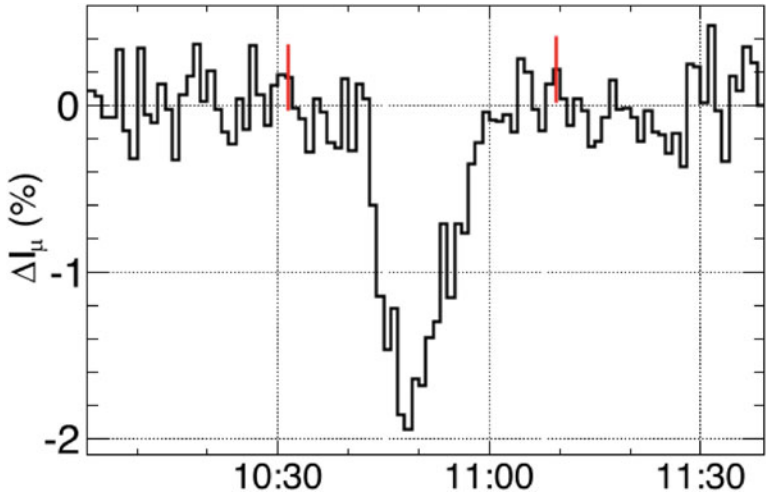

Fig. 30.5 Muon intensity variation observed on 1 December 2014 during a thunderstorm, starting at 10:42 UT and lasting 18 min. Vertical bars represent $\pm 1\sigma$ error [19]

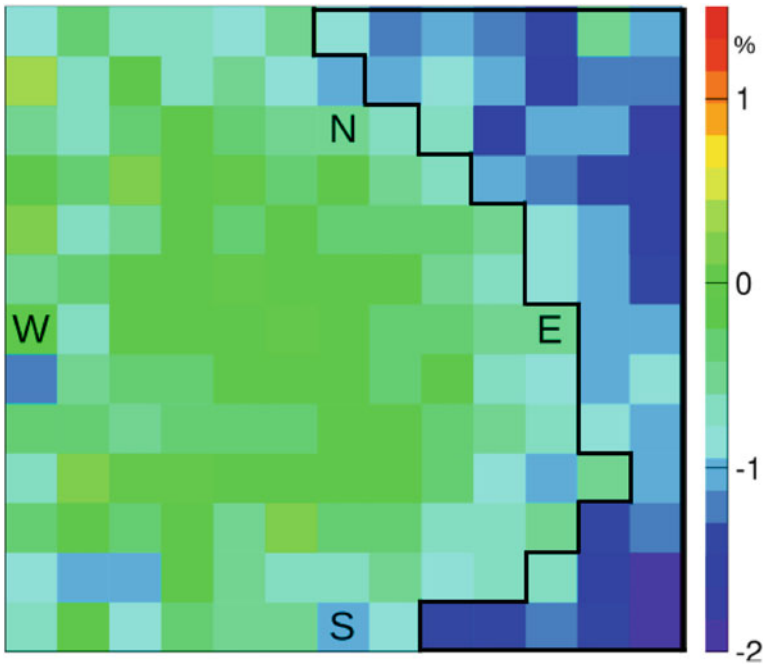

Fig. 30.6 Image of the muon intensity variation during 18 min thunderstorm on 1 December 2014 in the field of view of the GRAPES-3 muon telescope. 45 out of 169, thunderstorm contiguous directions are enclosed by dark boundary [19]

first direct evidence for the generation of GV potentials in thunderclouds, consistent with the prediction of C. T. R. Wilson, 90 years ago [16]. The existence of GV potentials could explain the production of highest energy γ-rays in terrestrial γ-ray flashes discovered 25 years back [17].

References

1. S.K. Gupta et al., Nucl. Instrum. Meth. A **540**, 311 (2005)
2. P.K. Mohanty et al., Astropart. Phys. **31**, 24–26 (2009)
3. Y. Hayashi et al., Nucl. Instrum. Meth. A **545**, 643 (2005)
4. H. Tanaka et al., J. Phys. G: Nucl. Part. Phys. **39**, 025201 (2012)
5. F. Varsi et al., PoS (ICRC 2019) **449** (2019)
6. T. Nonaka et al., Phys. Rev. D **74**, 052003 (2006)
7. K.P. Arunbabu et al., Astron. Astrophys. **555**, A139 (2013)
8. K.P. Arunbabu et al., Astron. Astrophys. **580**, A41 (2015)
9. H. Kojima et al., Astroparticle Phys. **62**, 21 (2015)
10. H. Kojima et al., Phys. Rev. D **62**, 121303(R) (2015)
11. P.K. Mohanty et al., Phys. Rev. Lett. **117**, 171101 (2016)
12. P.K. Mohanty et al., Phys. Rev. D **97**, 082001 (2018)
13. H. Kojima et al., Phys. Rev. D **98**, 022004 (2018)
14. Ferguson et al., IEEE Trans. Plasma Sci. **43**, 3086 (2015)
15. http://omniweb.gsfc.nasa.gov/form/omni_min.html
16. C.T.R. Wilson, Nucl. J. Franklin Inst. **208**, 1 (1929)
17. G.J. Fishman et al., Science **264**, 1313 (1994)
18. M. Tavani et al., Phy. Rev. Lett. **106** 018501 (2011)
19. B. Hariharan et al., Phy. Rev. Lett. **122**, 105101 (2019)

Chapter 31
Dark Matter Mass in Extra $U(1)$ Gauge Model

Imtiyaz Ahmad Bhat and Rathin Adhikari

Abstract Alongwith $SU(2) \times U(1)$ group of Standard Model an extra $U(1)$ gauge group has been considered in a model in which dark matter field could be present. In such models there is also extra $U(1)$ gauge boson apart from neutral Z boson which is present in Standard Model. PLANCK collaboration has obtained experimental bound on dark matter relic density. On the other hand, LHC has obtained constraint on such extra gauge boson mass and its gauge coupling. Based on these constraints we have discussed the allowed region of masses of extra gauge boson and the dark matter which is the lightest one among other right-handed Majorana fermions present in the model. From other experiments we have discussed in brief the possibility of further constraining such parameter space.

31.1 Introduction

In Standard Model of Particle Physics there is no dark matter field. However, there are some experimental evidences in support of dark matter [1–3]. For a viable model for dark matter an extra $U(1)$ gauge group has been considered together with $SU(2) \times U(1)$ group of Standard Model [4–6]. In such models there is one extra neutral gauge boson X apart from Standard model type neutral Z boson. There could be mixing of X boson with standard Z boson. However, to keep photon mass zero and to avoid the stringent phenomenological constraint this mixing has been assumed to be zero here.

PlANCK experiment [7] has constrained dark matter relic density as

$$\Omega_{DM} h^2 = 0.1200 \pm 0.0012$$

I. A. Bhat · R. Adhikari (✉)
Centre for Theoretical Physics, Jamia Millia Islamia (Central University),
Jamia Nagar, New Delhi 110025, India
e-mail: rathin@ctp-jamia.res.in

A. Giri and R. Mohanta (eds.), *Workshop on Frontiers in High Energy Physics 2019*, Springer Proceedings in Physics 248,
https://doi.org/10.1007/978-981-15-6292-1_31

where Ω_{DM} is the density parameter for dark matter and $h = H_0/(100\,\mathrm{km\,s^{-1}\,Mpc^{-1}}$. Also there are stringent bound on the mass and gauge coupling associated with the extra $U(1)$ gauge boson. This has recently been obtained by CMS and ATLAS [8–10] collaboration at LHC.

We have used these experimental constraints to find the allowed parameter space of dark matter mass and X boson mass. To study this particularly we have considered an extra $U(1)$ gauge model which is anomaly free [11]. We have considered both annihilation and co-annihilation channel of dark matter with other heavier right handed Majorana fermion for evaluating dark matter relic density. Such annihilation and co-annihilation lead to final states of standard model fermion and antifermion pairs.

31.2 The Extra $U(1)$ Gauge Model

The model [11] which is an $U(1)$ extension of SM, has four neutral fermions Σ^0_{1R}, Σ^0_{2R}, S_{1R} and S_{2R}. The fermionic fields Σ^0_{1R} and Σ^0_{2R} are $SU(2)_L$ triplets and do not couple to Z and S_{1R} and S_{2R} are singlets.These different fermionic field plays some role to cancel anomalies. Also they could play the role of dark matter with their odd Z_2 values. The mass eigenstates of these four Majorana fermions is written as ψ_k with mass m_{ψ_k}. We have considered the dark matter field as ψ_1 which has the lightest mass among above four possible states. We consider ψ_2 as the next to lightest among these four mass eigenstates and the masses m_{ψ_1} and m_{ψ_2} are not far apart. Because of this there could be annihilation of pair of ψ_1 to standard model fermion and anti-fermion pair as well as there could be co-annihilation of ψ_1 and ψ_2.

The fermionic and the scalar particle content of the model are given in Table 31.1 and Table 31.2 respectively.

Using anomaly cancellation conditions the various different $U(1)_X$ charges of various fields can be expressed in terms of the other two $U(1)_X$ charges n_1 and n_4, corresponding to quark doublet and lepton doublet respectively. Under Z_2 symmetry, odd and even fields are specified in the last column of the above tables.

We consider the vacuum expectation values (vev) of various neutral scalars fields be $\langle\phi^0\rangle = v_1$ and $\langle\chi^0_{1,2}\rangle = u_{1,2}$. One can write then the mass-squared elements, in the basis of Z and X boson (in which photon and Z boson is already diagonal) as,

$$
\begin{aligned}
M^2_{ZZ} &= \frac{1}{2} g_Z^2 \left(v_1^2\right) \; ; \\
M^2_{ZX} &= M^2_{XZ} = \frac{3}{8} g_Z g_X \left(n_1 - n_4\right) v_1^2 \; ; \\
M^2_{XX} &= \frac{1}{2} g_X^2 \left(3n_1 + n_4\right)^2 \left(u_1^2 + 9u_2^2\right) + \frac{9}{8} g_X^2 \left(n_1 - n_4\right)^2 v_1^2
\end{aligned}
$$

As stated earlier to avoid photon to have any non-zero mass and also to avoid the constraints from electroweak precision measurements we consider $M^2_{ZX} = 0$ which

Table 31.1 Fermion fields in the model

particle	$U(1)_X$	Z_2
$(u,d)_L$	n_1	+
u_R	$\frac{1}{4}(7n_1 - 3n_4)$	+
d_R	$\frac{1}{4}(n_1 + 3n_4)$	+
$(\nu, l)_L$	n_4	+
l_R	$\frac{1}{4}(-9n_1 + 5n_4)$	+
$\Sigma_{1R,2R}^{(+,0,-)}$	$\frac{3}{8}(3n_1 + n_4)$	–
N_R	$-\frac{3}{4}(3n_1 + n_4)$	+
S_{1R}	$\frac{1}{8}(3n_1 + n_4)$	–
S_{2R}	$\frac{5}{8}(3n_1 + n_4)$	–

Table 31.2 Scalar fields in the model

particle	$U(1)_X$	Z_2
$\phi^{(+,0)}$	$\frac{3}{4}(n_1 - n_4)$	+
$\eta_1^{(+,0)}$	$\frac{1}{8}(3n_1 - 7n_4)$	–
$\eta_2^{(+,0)}$	$\frac{1}{8}(9n_1 - 5n_4)$	–
χ_1^0	$\frac{1}{4}(3n_1 + n_4)$	+
χ_2^0	$\frac{3}{4}(3n_1 + n_4)$	+
χ_3^0	$\frac{1}{8}(3n_1 + n_4)$	–
χ_4^+	$\frac{3}{8}(n_1 - 5n_4)$	–
$\xi^{(++,+,0)}$	$\frac{1}{8}(9n_1 - 13n_4)$	–

gives the condition on two independent $U(1)_X$ charges as $n_1 = n_4$. Then the mass of the extra $U(1)_X$ gauge boson is

$$M_X^2 = M_{XX}^2 = \frac{1}{2} g_X^2 (4n_1)^2 \left(u_1^2 + 9u_2^2\right)$$

and is related to its gauge coupling and the vev of two scalar singlets.

In considering interactions of extra gauge boson X with S_{1R} and S_{2R} in the mass basis of ψ_k, we are considering for simplicity that the corresponding mixing matrix elements Z_{ij} has non-zero 1–2 block with mixing angle θ involving S_{1R} and S_{2R} and this block is decoupled from 3–4 block involving other two neutral fermions Σ_{1R}^0 and Σ_{2R}^0. The mass gap between the dark matter ψ_1 and the next lightest neutral fermion ψ_2 is defined in terms of the parameter $\Delta = (m_{\psi_2} - m_{\psi_1})/m_{\psi_1}$. In the next section, we will be analysing the constraints on dark matter mass with reference to the mixing angle θ and mass gap parameter Δ.

31.3 Dark Matter Mass from Relic Density Constraints and LHC Constraints

Using the Boltzmann equation [12] governing the evolution of number density of the dark matter (DM) with the thermally averaged cross section for the process $\psi_1\psi_1 \rightarrow f\bar{f}$, one can obtain the relic density where Boltzman equation is given by:

$$\dot{n_{\psi_1}} + 3Hn_{\psi_1} = < \sigma v > ((n_{\psi_1}^{eqb})^2 - n_{\psi_1}^2)$$

where n_{ψ_1} and $n_{\psi_1}^{eqb}$ are the number density and thermal equillibrium number density respectively of the DM particle. Here, H is Hubble expansion rate of the universe and $\langle \sigma v \rangle$ is the thermally averaged cross section for the process $\psi_1\psi_1 \rightarrow f\bar{f}$. The thermally averaged cross section can be expanded in powers of relative velocity of two dark matter particle to be scattered and is expressed as $< \sigma v >= a + bv^2$. The solution of the above Boltzmann equation can be written numerically as [13]

$$\Omega_{\psi_1} h^2 \approx \frac{1.04 \times 10^9 x_f}{M_{pl}\sqrt{g_*}(a + 3b/x_f)}$$

where $x_f = m_{\psi_1}/T_f$, T_f is the freeze-in temperature, g_* is the number of relativistic degrees of freedom at the time of freeze in. The parameter x_f can be obtained numerically from the following equation:

$$x_f = \ln \frac{0.038\ M_{Pl}\ m_{\psi_1} < \sigma v >}{g_*^{1/2} x_f^{1/2}}.$$

The pair of lighter ψ_1 will be annihilated to standard model fermions and anti-fermions through the mediator X boson at the tree level Feynman diagram. However, such process will not be mediated through Z boson because of our consideration of zero $Z - X$ mixing. Due to the Majorana nature of the dark matter, its vector coupling with X boson is zero and it has only non-zero axial-vector coupling with X. The annihilation cross section of Majorana fermion to Standard Model $f\bar{f}$ will occur through S-channel mediated by X boson. The a and b parameter in $< \sigma v >$ corresponding to the process $\psi_1\psi_1 \rightarrow f\bar{f}$ can be written respectively as

$$a = \frac{n_c\, g_{fa}^2\, m_f^2\, g_{11}^2\, m_{\psi_1}}{24\pi\left[(M_X^2 - 4m_{\psi_1}^2)^2 + M_X^2\Gamma_X^2\right]}\sqrt{1 - \frac{m_f^2}{m_{\psi_1}^2}}\left(12 - 96\frac{m_{\psi_1}^2}{M_X^2} + 192\frac{m_{\psi_1}^4}{M_X^4}\right),$$

$$b = a\left[-\frac{1}{4} + \frac{m_f^2}{8(m_{\psi_1}^2 - m_f^2)} - \frac{M_X^4 - 16M_X^2 m_{\psi_1}^2 + 48m_{\psi_1}^4}{4((M_X^2 - 4m_{\psi_1}^2)^2 + M_X^2\Gamma_X^2)}\right.$$

$$+\frac{\left(-4+2\frac{g_{fv}^2}{g_{fa}^2}+4\frac{m_{\psi_1}^2}{m_f^2}+4\frac{g_{fv}^2 m_{\psi_1}^2}{g_{fa}^2 m_f^2}-24\frac{m_{\psi_1}^2}{M_X^2}+96\frac{m_{\psi_1}^4}{M_X^4}\right)}{\left(12-96\frac{m_{\psi_1}^2}{M_X^2}+192\frac{m_{\psi_1}^4}{M_X^4}\right)}\Bigg].$$

where $n_c = 3$ when f stands for quarks and $n_c = 1$ when f stands for leptons. There could be co-annihilation of ψ_1 with ψ_2 also. The dark matter relic density [14, 15] will depend on both annihilation and co-annihilation cross sections of ψ_1. To take into account co-annihilation some modifications of the above Boltzman equation is necessary. This has been discussed in detail in [16].

If there is very large mass difference between ψ_1 and ψ_2, in that case ψ_2 will be out of thermal equilibrium much earlier than ψ_1. There will not be much effect of co-annihilation on the number density of ψ_1. However, while taking into account co-annihilation we have considered cases where mass gap parameter Δ is nearer to 1.

There are resonant as well as non-resonant new phenomena searched by Large Hadron Collider (LHC) operating at $\sqrt{s} = 13$ TeV [8–10] in which the final state is dilepton/dijet. ATLAS Collaboration at LHC has obtained allowed region of coupling g_X of quarks and leptons with extra gauge boson mass M_X in figure (4) of [8] and figure (5a) of [9] at 95% confidence level. We have considered the allowed region of g_X and M_X obtained by ATLAS at LHC in figure (5a) of [9] in our numerical analysis. g_X coupling in our paper is related to coupling $\gamma^{'}$ of this figure as $g_X \approx 0.463\gamma^{'}$.

To find the allowed region in the M_X and m_{ψ_1} plane numerically we have fixed $U(1)$ charges by considering $n_1 = n_4 = 1/\sqrt{2}$ (normalizing $n_1^2 + n_4^2 = 1$) satisfying zero mixing condition of X with Standard Model Z boson. We have considered $\Delta = 1$ in the TeV mass range of dark matter.

The allowed region of $M_X - m_{\psi_1}$ plane has been shown in Fig. 31.1 after considering the variation of g_X over the range (0.005–0.7) and M_X upto 5 TeV as considered by LHC ATLAS collaboration. This analysis is done only for annihilation channel present i.e. $\psi_1\psi_1 \rightarrow f\bar{f}$. In this case no co-annihilation channel has been considered and the other two parameters θ and Δ are zero. Here, we have used the constraint coming from relic abundance on dark matter from Planck 2017 $\Omega h^2 \in (0.1188, 0.1212)$ [7]. The allowed parameter space in Fig. 31.1b is less as there is further constraint on g_X and M_X as given by ATLAS [8, 9] at LHC. In Fig. 31.1b the allowed region in the M_X -m_{ψ_1} plane increases for higher values of M_X and m_{ψ_1}.

In Fig. 31.2 the allowed region of $M_X - m_\psi$ plane have been shown in which the co-annihilation channel alongwith annihilation channel have been considered for $\theta = \pi/4$ and $\Delta = 1$. In this case the allowed region is further reduced in comparison to only annihilation channel. We have also studied the variation of allowed parameter space between M_X and m_ψ under different combination of θ and Δ values. Particularly with the variation of θ there is very little change in the parameter space. With the decrease in Δ values the allowed parameter space decreases to some extent.

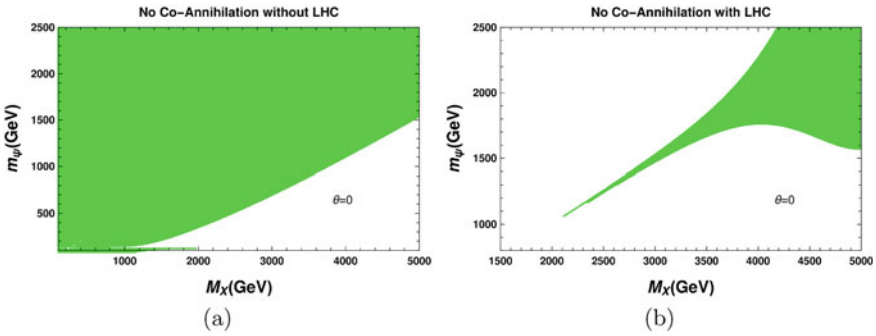

Fig. 31.1 Allowed region in the M_X and m_{ψ_1} plane for no co-annihilation channel. The left figure and right figure corresponds to no LHC constraints and LHC constraints on M_X and g_X respectively

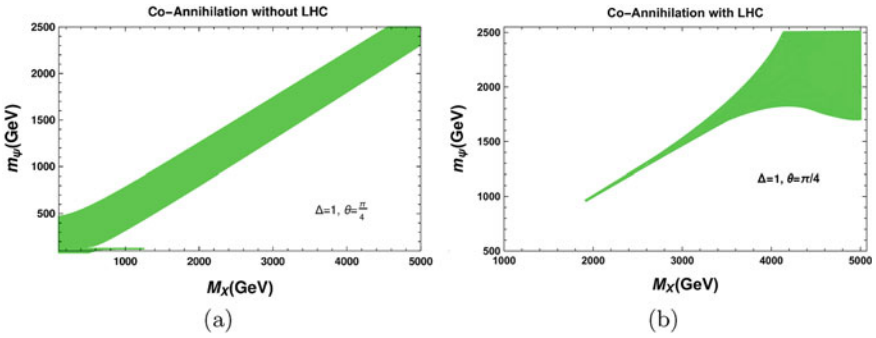

Fig. 31.2 Allowed region in the M_X and m_{ψ_1} plane for co-annihilation channels with $\Delta = 1$ and $\theta = \pi/4$. The left figures and right figures corresponds to no LHC constraints and LHC constraints on M_X and g_X respectively

31.4 Summary and Outlook

We have shown the allowed dark matter mass depending on extra $U(1)$ gauge boson mass. For this we have taken into account the relic density constraint from PLANCK data and LHC constraint on X boson mass and its gauge coupling. We have considered zero mixing of X boson with standard model neutral gauge boson Z.

In the extra $U(1)$ gauge model considered here [11] apart from three light active neutrinos, N_R plays the role of fourth neutrino as sterile. The active and sterile neutrino mixing is possible here because of interaction $S_{1R} S_{2R} \bar{\chi}_2^0$. So there is scope to impose constraints from light neutrino mass as well as active sterile neutrino mixing as discussed in [16].

In future if experiment at LHC improves the constraint on extra gauge boson mass and its gauge coupling it could be possible to further constrain the allowed parameter space for dark matter mass.

Acknowledgements I. A. Bhat likes to thank Department of Science and Technology (DST), Govt. of India for financial support through Inspire Fellowship (DST/INSPIRE Fellowship/2014/IF140038).

References

1. G. Bertone, D. Hooper, J. Silk, Phys. Rep. **405**, 279 (2005). [hep-ph/0404175]
2. F. Zwicky, Helv. Phys. Acta **6**, 110 (1933) [Gen. Rel. Grav. **41**, 207 (2009)]
3. WMAP Collaboration, D.N. Spergel et al. Astrophys. J. **148**, 175 (2003); SDSS Collaboration, M. Tegmark et al., Phys. Rev. **D69**, 103501 (2004)
4. P. Langacker, Rev. Mod. Phys. **81**, 1199 (2009). [arXiv:0801.1345 [hep-ph]]
5. D. Suematsu, Y. Yamagishi, Int. J. Mod. Phys. **A10** (1995) [hep-ph/9411239]; M. Cvetic, S. Godfrey, [hep-ph/9504216], A. Leike, Phys. Rep. **317** (1999) [hep-ph/9805494]; M. Cvetic, P. Langacker, [hep-ph/9707451], D.A. Demir, Phys. Rev. **D59**, 015002 (1999), [hep-ph/9809358]; J. L Diaz-Cruz, J.M. Hernandez-Lopez, J.A. Orduz-Ducuara, J. Phys G **40**, 125002 (2013)
6. E. Ma, Phys. Rev. D **73**, 077301 (2006)
7. N. Aghanim et al., [Planck Collaboration] (2018), arXiv:1807.06209 [astro-ph.CO]
8. M. Aaboud et al., [ATLAS Collaboration], Phys. Rev. D **96**, 052004 (2017), arXiv:1703.09127 [hep-ex]
9. M. Aaboud et al., [ATLAS Collaboration], JHEP **1710**, 182 (2017), arXiv:1707.02424 [hep-ex]
10. A.M. Sirunyan et al., [CMS Collaboration], Phys. Lett. B **769**, 520 (2017); Erratum: [Phys. Lett. B **772**, 882 (2017)] arXiv:1611.03568 [hep-ex]
11. R. Adhikari, D. Borah, E. Ma, Phys. Lett. B **755**, 414 (2016). [arXiv:1512.05491] [hep-ph]
12. M. Beltran, D. Hooper, E.W. Kolb, Z.C. Krusberg, Phys. Rev. D **80**, 043509 (2009). [arXiv:0808.3384] [hep-ph]
13. E.W. Kolb, M.S. Turner, Front. Phys. **69**, 1 (1990)
14. K. Griest, D. Seckel, Phys. Rev. D **43**, 3191 (1991)
15. M. Cannoni, Eur. Phys. J. C **76**(3), 137 (2016), arXiv:1506.07475 [hep-ph]
16. I.A. Bhat, R. Adhikari, arXiv:1906.10185 [hep-ph]

Chapter 32
$0\nu\beta\beta$ Signature in LRSM with Higgs Bidoublet and Doublets

Chayan Majumdar, Sudhanwa Patra, Supriya Senapati, and Urjit A. Yajnik

Abstract We consider a version of Left-Right Symmetric Model in which the scalar sector consists of a Higgs bidoublet (Φ) with $B - L = 0$, doublets ($H_{L,R}$) with $B - L = 1$ and a charged scalar (δ^+) with $B - L = 2$ leading to radiatively generated Majorana masses for neutrinos and thereby, leads to new physics contributions to neutrinoless double beta decay ($0\nu\beta\beta$) saturating the present experimental bounds. We show that such a novel framework can be embedded in a non-SUSY $SO(10)$ GUT leading to successful gauge coupling unification at around 10^{16} GeV with the scale of left-right symmetry breaking around 10^{10} GeV. The model can also be extended to have left-right symmetry breaking at TeV scale, enabling detection of W_R, Z_R bosons in LHC and future collider searches.

32.1 Introduction

The Standard Model (SM) is an elegant theory for elementary Particle Physics which has now been successfully verified including the Higgs Mechanism. However several open problems persist. Two such problems are the parity asymmetry seen in low-energy weak-interactions and the theoretical origin of neutrino mass for which we have a convincing evidence from neutrino oscillation experiment [1, 2]. In the framework of the left-right symmetric models (LRSM) [3–5], both these questions receive a satisfactory answer pointing to unification. In this work, we consider a version of

C. Majumdar · S. Senapati · U. A. Yajnik
Indian Institute of Technology Bombay, Mumbai 400076, India
e-mail: chayan@phy.iitb.ac.in

S. Senapati
e-mail: supriya@phy.iitb.ac.in

U. A. Yajnik
e-mail: yajnik@phy.iitb.ac.in

S. Patra (✉)
Department of Physics, IIT Bhilai, GEC Campus, Raipur, India
e-mail: sudhanwa@iitbhilai.ac.in

A. Giri and R. Mohanta (eds.), *Workshop on Frontiers in High Energy Physics 2019*, Springer Proceedings in Physics 248,
https://doi.org/10.1007/978-981-15-6292-1_32

LRSM in which the scalar sector consists of a Higgs bidoublet (Φ) with $B - L = 0$, Higgs doublets ($H_{L,R}$) with $B - L = 1$. However this version of LRSM implies no Majorana mass terms and therefore no lepton number violation in the theory. In order to have lepton number violating theory [6], the model can be extended by adding a charged scalar δ^+ with $B - L$=2. This extra addition will allow us to radiatively generate the Majorana mass terms for neutrinos at loop-level. This was first pointed out by Fileviez Perez et al. [7].

The experimental observation of lepton number violating rare process Neutrinoless double beta decay ($0\nu\beta\beta$) would reveal the Majorana nature of light neutrinos and can provide information on the absolute scale of neutrino mass. The Lepton number violating $0\nu\beta\beta$ process could arise either from the standard mechanism due to exchange of light neutrinos or by some new physics beyond SM (BSM). In the present scenario, we aim to discuss the new physics contribution to $0\nu\beta\beta$ and also intend to examine the resulting contributions to $0\nu\beta\beta$ transition which can saturate the current experimental bounds.

Grand Unified Theories (GUTs) [4] based on the gauge group $SO(10)$ are very appealing prospect to unify the three fundamental forces in nature i.e, strong, weak and electromagnetism. Unlike the $SU(5)$ GUT, $SO(10)$ admits intermediate symmetry breaking scale like left-right symmetry or Pati-Salam symmetry. Our goal here is also to embed our LRSM framework into such a non-SUSY $SO(10)$ GUT scenario. Such left-right symmetry breaking occuring at the scale of a few TeV can give rise to interesting weak collider phenomenology in near future.

32.2 Description of the Model and Generation of Majorana Masses

The left-right symmetric model [3–5] is based on the gauge group,

$$\mathcal{G}_{LR} \equiv SU(2)_L \times SU(2)_R \times U(1)_{B-L} \times SU(3)_C \tag{32.1}$$

with the electric charge defined as $Q = T_{3L} + T_{3R} + \frac{B-L}{2}$. The fermion sector of this model is given by,

$$q_L = \begin{pmatrix} u_L \\ d_L \end{pmatrix} \equiv [2, 1, 1/3, 3]\,,\ q_R = \begin{pmatrix} u_R \\ d_R \end{pmatrix} \equiv [1, 2, 1/3, 3]\,,$$
$$\ell_L = \begin{pmatrix} \nu_L \\ e_L \end{pmatrix} \equiv [2, 1, -1, 1]\,,\ \ell_R = \begin{pmatrix} \nu_R \\ e_R \end{pmatrix} \equiv [1, 2, -1, 1]\,.$$

In the version of left-right symmetric model with Higgs doublets and bidoublets, all the fermions including neutrinos are getting Dirac type masses and thus, have no lepton number violation in the model. The lepton number violation can be accomodated minimally with the inclusion of a charged scalar $\delta^+(1_L, 1_R, 2_{B-L}, 1_C)$ which

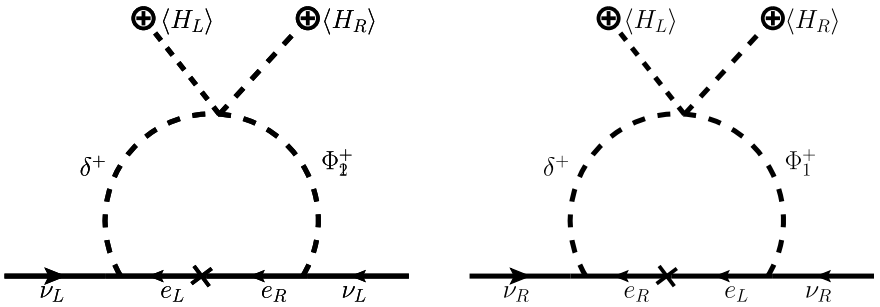

Fig. 32.1 Generation of Majorana masses for left-handed and right-handed neutrinos at one loop level

will allow the generation of Majorana masses for both left-handed and right-handed neutrinos at one-loop level. Thus, the complete scalar sector of the model is as follows [7]

$$\Phi \equiv [2, 2, 0, 1]\,, H_L \equiv [2, 1, 1, 1]\,, H_R \equiv [1, 2, 1, 1]\,, \delta^+ \equiv [1, 1, 2, 1]. \quad (32.2)$$

The symmetry breaking pattern for this left-right symmetric model is given by

$$SO(10) \xrightarrow{M_U} \mathcal{G}_{2_L 2_R 1_{B-L} 3_C} \xrightarrow{M_R} \mathcal{G}_{2_L 1_Y 3_C}\,(\mathrm{SM}) \xrightarrow{M_Z} \mathcal{G}_{1_Q 3_C}\,.$$

The one-loop generated Majorana masses for left-handed and right-handed neutrinos in this model (pointed out in [7]) as shown in Fig. 32.1 as,

$$\begin{aligned} M_L^{\text{1-loop}} &\simeq \frac{\lambda' \langle H_L \rangle \langle H_R \rangle}{16\pi^2} \frac{\lambda^L M_\ell Y_\ell^T}{M^2} \mathscr{I}\,, \\ M_R^{\text{1-loop}} &\simeq \frac{\lambda' \langle H_L \rangle \langle H_R \rangle}{16\pi^2} \frac{\lambda^R M_\ell Y_\ell^T}{M^2} \mathscr{I}\,, \end{aligned} \quad (32.3)$$

where $M = max(M_{\delta^+}, M_\Phi)$, M_ℓ is the mass of the lepton and $\mathscr{I}$ is the loop factor, can be found as,

$$\mathscr{I} = \frac{log[\frac{M_\ell^2}{M_{\delta^+}^2}] M_{\delta^+}^2}{M_{\delta^+}^2 - M_\ell^2} - \frac{log[\frac{M_\ell^2}{M_\phi^2}] M_\phi^2}{M_\phi^2 - M_\ell^2}.$$

32.3 Embedding the Framework in SO(10) Framework and Gauge Coupling Unification

To predict the scale of left-right symmetry breaking scale, we embed this version of left-right symmetric model within a non-supersymmetric $SO(10)$ GUT [9, 10] with the breaking chain as described in the previous section. The gauge coupling unifications with the help of relevant one-loop RG equation [11] for this version of LRSM and also an extended version of that are given in Fig. 32.2.

Now in view to embed our framework in non-SUSY $SO(10)$ GUT, we can consider the breaking chain

$$SO(10) \xrightarrow{M_U} \mathcal{G}_{2_L 2_R 1_{B-L} 3_C} \xrightarrow{M_R} \mathcal{G}_{2_L 1_Y 3_C} \left(\text{SM}\right) \xrightarrow{M_Z} \mathcal{G}_{1_Q 3_C} \,.$$

The symmetry breaking from $SO(10)$ to LRSM can be achieved by assigning non-zero vev to a Higgs field $\langle \Sigma(1,1,15)\rangle \in \{45_H\}$. The LR-symmetry breaking Higgs H_R belongs to the representation 16_H. For the generation of SM fermion masses the Higgs multiplets are limited as $16 \times 16 = 10_s + 120_a + \overline{126}_s$. The Higgs field $H_\Phi \in \{10_H\}$ can be decompossed under LR gauge group as,

$$H_\Phi(10) = \Phi(1,2,2,0) \oplus \left(3,1,1,-\frac{1}{3}\right) \oplus \left(\overline{3},1,1,\frac{1}{3}\right).$$

Also, the extra charged scalar δ^+ belongs to 120-dimensional representation of $SO(10)$. To break the $SO(10)$ gauge group to LRSM, one needs Higgs field either $A(210)$ or $B(45)$. The decomposition of these fields under Pati-Salam group $(SU(2)_L \otimes SU(2)_R \otimes SU(4)_C)$ are as follows,

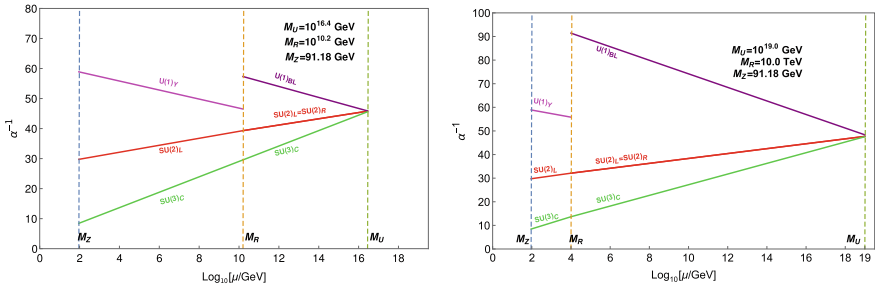

Fig. 32.2 Left: Gauge coupling running and unification in the minimal left-right symmetric model for lepton number violation with $M_{\text{GUT}} = 10^{16.4}$ GeV and the left-right symmetry breaking scale $M_{\text{R}} = 10^{10.2}$ GeV. Right: Gauge coupling running and unification in case 2, with the model of Fig. 32.2 enhanced by addition of four copies of charged scalar $\delta^+(1_L, 1_R, 2_{BL}, 1_C)$ and one copy of $\xi(1_L, 1_R, 4/3_{BL}, 6_C)$ at mass scale M_R and above. This results in M_U being pushed close to Planck scale 10^{19}GeV however the left-right symmetry breaking scale M_{R} becomes $= 10^4$ GeV

$$A(210) = (1,1,1) \oplus (1,1,15) \oplus (2,2,6) \oplus (3,1,15) \oplus (1,3,15) \oplus (2,2,10) \oplus (2,2,\overline{10}) \tag{32.4}$$

$$B(45) = (3,1,1) \oplus (1,3,1) \oplus (1,1,15) \oplus (2,2,6) \tag{32.5}$$

Now, we can embed the Higgs doublets in spinorial representation $C(16) \oplus \overline{C(16)}$. Using these representations, we can embed our LRSM framework to find the most general $SO(10)$ invariant Higgs potential as,

$$\begin{aligned} V = {} & \mu_B^2 B_{ab} B_{ba} + \mu_h^2 h_a h_a + \mu_C^2 (\overline{C}C) + \mu_\delta^2 (\delta^+)^2 + \lambda_\delta (\delta^+)^4 + \lambda_B B^2 B^2 + \lambda'_B B^4 \\ & + \lambda_h h^4 + \lambda_C (\overline{C}C)^2 + \lambda'_C (C^4 + \overline{C}^4) + h_a g_{hB} B_{ab} B_{bc} h_c + g'_{hB} B^2 h^2 \\ & + (g_{hC} h^2 + g_{BC} B^2) \overline{C}C + g_{\delta hC} (\delta^+)^2 h (CC + \overline{C}\overline{C}) \end{aligned} \tag{32.6}$$

Now including the $\xi \in \{54_H\}$ particle in $SO(10)$ GUT scenario decomposed as

$$D(54) = (1,1,1) \oplus (3,3,1) \oplus (1,1,20) \oplus (2,2,6)$$

we have gauge-invariant Higgs potential as,

$$\begin{aligned} V' = {} & V + \mu_D^2 D_{ab} D_{ba} + \lambda_D D^4 + g_{BD} B^2 D^2 + g'_{BD} B_{ab} B_{bc} D_{cd} D_{da} + g''_{BD} B_{ab} D_{bc} B_{cd} D_{da} \\ & + h_a g_{hD} D_{ab} D_{bc} h_c + g_{DC} D^2 \overline{C}C \end{aligned} \tag{32.7}$$

32.4 Results and Discussion on $0\nu\beta\beta$

From gauge coupling unification plots discussed in Sect. 32.3, we have two different prediction of the left-right symmetry breaking scale as (i) $M_R = 10^{10}$ GeV and (ii) $M_R = 10^4$ GeV. Now, for the determination of neutrino masses the benchmark points in this model is tabulated as in Table 32.1 (give citation to table). Here we have used

Table 32.1 Estimated values of physical masses for light and heavy neutrinos using derived values of M_D and radiatively generated $M_{L,R}^{1-\text{loop}}$ using representative set of input model parameters

λ'	λ^R	Y^ℓ	$M_R^{\text{1-loop}}$(keV)	M_D(eV)	M_ν(eV)
10^{-2}	10^{-3}	5.86×10^{-11}	12.67	0.1	10^{-6}
1	0.5	5.86×10^{-12}	6.3	0.1	1.59×10^{-6}
1	0.5	4.63×10^{-10}	1000	10	10^{-4}
10^{-2}	10^{-3}	5.86×10^{-10}	126.7	1	10^{-4}

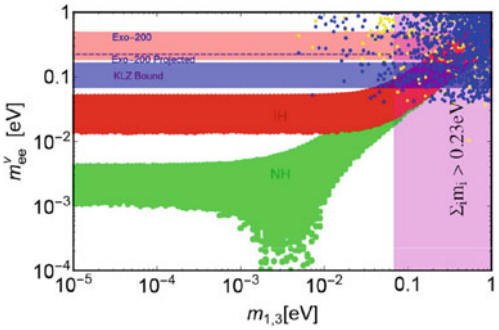

Fig. 32.3 Plots for effective Majorana mass due to standard mechanism for neutrinoless double beta decay due to exchange of light neutrinos for normal hierarchy (horizontal green shaded colour) and for inverted hierarchy (horizontal red shaded colour). The limit on sum of light neutrino masses from cosmological data is displayed in vertical shaded region. The other horizontal shaded coloured regions are displayed for bounds coming from different neutrinoless double beta decay experiments. The yellow and blue dots represent new physics contributions arising from so called λ and η diagrams

$\langle \Phi \rangle = v_1 = 170.572$ GeV, $\langle H_L \rangle = v_L = 34.114$ GeV, $M_{\delta^+} \simeq$ TeV, and the two possible values $\langle H_R \rangle \simeq 10^{10}$ GeV and 10^4 GeV.

For $M_R = 10^{10}$ GeV left-right breaking scale, the masses of right-handed gauge bosons W_R, Z_R will be around the same scale, the scenario is far away from the reach of LHC or any future proposed colliders. Also the ratio $\frac{M_{W_L}}{M_{W_R}}$ and $W_L - W_R$ mixing i.e, $\tan\xi$ are negligible, and thus the new physics contributions to $0\nu\beta\beta$ arising from purely right-handed currents and mixed current effects like λ and η-diagrams are negligible. And due to negligible heavy-light neutrino sector mixing, $\frac{M_D}{M_R^{\text{1-loop}}} \sim 10^{-5}$ the contributions arising from purely left-handed currents with the exchange of light as well as heavy neutrinos are also negligible which actually forbids this case to find out any new physics contribution to $0\nu\beta\beta$ (Fig. 32.3).

On the other hand, having considered $M_R \sim 10^4$ GeV with the masses of Z_R, W_R around few TeV, we can have rich collider phenomenology. In addition, the new physics contributions arising from purely right-handed currents and mixed current effects like λ and η-diagrams are sizeable enough as are the contributions arising from large light-heavy neutrino mixing. In fact for the same range of input parameters, the effective mass parameter comes out as, $\mathbf{m}_{\text{ee},\lambda} \simeq 62.37$ eV. Thus, the new physics contributions are indeed large enough to saturate the experimental bound like GERDA [12] and KamLAND-Zen [13] experiments.

Also, in the connection to cosmological scenario [14], the discussed negligible mixing between light and heavy neutrinos in our framework can explain how the over-abundance of keV RH neutrino (warm) DM through the regeneration of heavy neutrinos via neutrino oscillation around the BBN epoch can be forbidden.

References

1. S. Fukuda et al., Super-Kamiokande, Constraints on neutrino oscillations using 1258 days of Super-Kamiokande solar neutrino data. Phys. Rev. Lett. **86**, 5656–5660 (2001)
2. Q.R. Ahmad et al., SNO, Direct evidence for neutrino flavor transformation from neutral current interactions in the Sudbury Neutrino Observatory. Phys. Rev. Lett. **89**, 011301 (2002)
3. R. Mohapatra, J.C. Pati, A natural left-right symmetry. Phys. Rev. D **11**, 2558 (1975)
4. J.C. Pati, A. Salam, Lepton number as the fourth color. Phys. Rev. D **10**, 275–289 (1974)
5. G. Senjanović, R.N. Mohapatra, Exact left-right symmetry and spontaneous violation of parity. Phys. Rev. D **12**, 1502 (1975)
6. W.-Y. Keung, G. Senjanović, Majorana neutrinos and the production of the right-handed charged gauge boson. Phys. Rev. Lett. **50**, 1427 (1983)
7. P. Fileviez Perez, C. Murgui, S. Ohmer, Simple left-right theory: lepton number violation at the LHC. Phys. Rev. **D94**(5), 051701 (2016)
8. H. Georgi, S.L. Glashow, Unity of all elementary particle forces. Phys. Rev. Lett. **32**, 438–441 (1974)
9. J.R. Bhatt, P-H. Gu, U. Sarkar, S.K. Singh, Neutrino dark energy in grand unified theories. Phys. Rev. **D80**, 073013 (2009)
10. T. Fukuyama, A. Ilakovac, T. Kikuchi, S. Meljanac, N. Okada, $SO(10)$ group theory for the unified model building. J. Math. Phys. **46**, 033505 (2005)
11. D.R.T. Jones, The two loop beta function for a G(1) x G(2) gauge theory. Phys. Rev. D **25**, 581 (1982)
12. M. Agostini et al., GERDA, Results on neutrinoless double-β Decay of ^{76}Ge from phase I of the GERDA experiment. Phys. Rev. Lett. **111**(12), 122503 (2013)
13. A. Gando et al., KamLAND-Zen, Limit on neutrinoless $\beta\beta$ Decay of ^{136}Xe from the first phase of KamLAND-Zen and comparison with the positive claim in ^{76}Ge. Phys. Rev. Lett. **110**(6), 062502 (2013)
14. M. Nemevsek, G. Senjanovic, Y. Zhang, Warm dark matter in low scale left-right theory. JCAP **1207**, 006 (2012)

Chapter 33
Sterile Neutrino in Minimal Extended Seesaw with A_4 Flavour Symmetry

Kalpana Bora and Neelakshi Sarma

Abstract In this work, we first review the status of evidences in support of existence of sterile neutrinos. Then, after revisiting one of the most minimal seesaw (MES) model that gives rise to a $(3 + 1)$ light neutrino mass matrix, we include A_4 flavour symmetry in the theory. Considering the generic vacuum alignments of A_4 triplet flavons, we classify the resulting mass matrices based on their textures, and predict interesting correlations between neutrino oscillation in the allowed cases. We also find that all of these allowed cases prefer normal hierarchical pattern of light neutrino masses over inverted hierarchy.

33.1 Introduction

Existence of non-zero neutrino masses and large mixings have now become a well established fact, as guided by several experimental results [1]. Along with precise values of the solar and atmospheric mixing angles and mass squared differences, relatively recent experiments like MINOS, T2K, NOνA, Double ChooZ, Daya-Bay and RENO (for details, please see [1]) have established the large value of reactor mixing angle. Apart from the currently unknown issues in the neutrino sector, like mass hierarchy, Dirac CP violating phase as the global fit data suggest, another interesting question in the neutrino sector is the possibility of additional neutrino species with eV scale mass. In fact, this has turned out to be not just a speculation, but has gathered considerable attention in the last two decades following some anomalies reported by a few experiments. The first such anomaly was reported by the Liquid Scintillator Neutrino Detector (LSND) experiment in their anti-neutrino flux measurements. The LSND experiment searched for $\bar{\nu}_\mu \to \bar{\nu}_e$ oscillations in the appearance mode and reported an excess of $\bar{\nu}_e$ interactions that could be explained by incorporating at least

K. Bora (✉) · N. Sarma
Gauhati University, Guwahati, Assam, India
e-mail: kalpana.bora@gmail.com

N. Sarma
e-mail: nsarma25@gmail.com

A. Giri and R. Mohanta (eds.), *Workshop on Frontiers in High Energy Physics 2019*, Springer Proceedings in Physics 248,
https://doi.org/10.1007/978-981-15-6292-1_33

one additional light neutrino with mass in the eV range. This result was supported by the subsequent measurements at the MiniBooNE experiment. Similar anomalies have also been observed at reactor neutrino experiments as well as gallium solar neutrino experiments. These anomalies received renewed attention recently after the MiniBooNE collaboration reported their new analysis incorporating twice the size data sample than before (please see the [1]), confirming the anomaly at 4.8σ significance level which becomes $>6\sigma$ effect if combined with LSND. Although an eV scale neutrino can explain this anomaly, such a neutrino can not have gauge interactions in the standard model (SM) from the requirement of being in agreement with precision measurement of Z boson decay width at LEP experiment [1]. Hence such a neutrinos is often referred to as a sterile neutrino while the usual light neutrinos are known as active neutrinos. Status of this framework with three active and one sterile or $3 + 1$ framework with respect to such short baseline neutrino anomalies can be found in several global fit studies [2–4]. It is worth mentioning that the latest cosmology results from the Planck collaboration [1] constrains the effective number of relativistic degrees of freedom $N_{\text{eff}} = 2.99 \pm 0.17$ at 68% confidence level (CL), which is consistent with the SM prediction $N_{\text{eff}} = 3.046$ for three light neutrinos. Similarly, the constraint on the sum of absolute neutrino masses $\sum_i |m_i| < 0.12$ eV (at 95% CL) does not leave any room for an additional light neutrino with mass in eV order. Although this latest bound from the Planck experiment cannot accommodate one additional light sterile neutrino at eV scale within the standard ΛCDM model of cosmology, one can evade these tight bounds by considering the presence of some new physics beyond the standard model (BSM).

Several BSM proposals that can account for an eV scale sterile neutrino having non-trivial mixing with active neutrinos can be found in literature. While the usual seesaw mechanisms like type I, type II and type III [1] explaining the lightness of active neutrinos were studied in details for a long time, their extensions to the $3 + 1$ case was not very straightforward primarily due to the gauge singlet nature of the sterile neutrino. Yet, there have been several proposals to generate a 4×4 light neutrino mass matrix within different seesaw frameworks in recent times [5–12]. Here we adopt a minimal framework known as the minimal extended seesaw proposed in the $3 + 1$ neutrino context by [5, 6] and study different possible realisations within the framework of non-abelian discrete flavour symmetry A_4. Flavour symmetry is needed to explain the observed flavour structure of different particles of the standard model. In the original proposal [6] also, the A_4 flavour symmetry was utilised but within the limited discussion the issue of non-zero reactor mixing angle as well as different A_4 vacuum alignments were not addressed. In another recent work based on the same model with A_4 flavour symmetry (see [56] of [1]), some details of the associated neutrino phenomenology was discussed by sticking to the effective 3×3 active neutrino mass matrix which can be generated by integrating out the sterile neutrino. In our present work, we consider the full 4×4 mass matrix and do not integrate out the sterile neutrino as its mass may not lie far above the active ones always, as hinted by experiments mentioned above. We also classify different possible textures of the 4×4 neutrino mass matrix based on generic A_4 vacuum alignments for triplet flavons. Similar but not texture specific work in three neutrino

cases to constrain different A_4 vacuum alignments from three neutrino data which was further constrained from successful leptogenesis (see [57] of [1]). Here we extend such studies to the $3+1$ neutrino cases. Texture zeros in $3+1$ neutrino scenarios were discussed in different contexts earlier using flavour symmetries like Z_N, $U(1)$ etc. [8, 10, 11] but here we show that some of these textures can be realised (upto a few more constraints) just from the vacuum alignment of A_4 triplet flavons. We first make the classifications for allowed and disallowed textures based on already known texture results in $3+1$ neutrino frameworks [8, 10, 13] and then numerically analyse some of the textures which have not been studied before. To be more specific, we categorise our textures based on $\mu-\tau$ symmetric cases, texture zero cases, hybrid cases and disallowed ones. Out of them, we numerically analyse all the textures belonging to $\mu-\tau$ symmetric and texture zero cases leaving the discussion on hybrid textures to future works. It should be noted that, although the discovery of non-zero reactor mixing angle has ruled out $\mu-\tau$ symmetry in the three neutrino scenarios, it is possible to retain it in a $3+1$ scenario where the 3×3 neutrino block retains this symmetry while the active-sterile sector breaks it. This interesting but much less explored idea to generate non-zero θ_{13} by allowing the mixing of three active neutrinos with a eV scale sterile neutrino was proposed earlier in [14, 15] and was also studied in details recently in [12]. We find that many of the textures belonging to these categories are already ruled out by neutrino data while the ones which are allowed give interesting correlations between neutrino parameters which can be tested at ongoing and future experiments. This article is organised starting with description of the model, then classification of textures, numerical analysis along with results and discussions, lastly we have given a conclusion.

33.2 The Model

As mentioned before, we adopt the model first proposed in [6] but discuss it from a more general perspective taking all the allowed terms in the Lagrangian and all possible generic vacuum alignments of A_4 triplets. We note that the discrete non-abelian group A_4 is the group of even permutations of four objects or the symmetry group of a tetrahedron. It has twelve elements and four irreducible representations with dimensions n_i such that $\sum_i n_i^2 = 12$. These four representations are denoted by $\mathbf{1}$, $\mathbf{1}'$, $\mathbf{1}''$ and $\mathbf{3}$ respectively. The particle content of the model along with their transformations under the symmetries of the model are shown in Table 33.1. Apart from the SM gauge symmetry and A_4 flavour symmetry, an additional discrete symmetry Z_4 is also chosen in order to forbid certain unwanted terms. For example, the chosen Z_4 charge of the singlet neutrino S keeps a bare mass term away from the Lagrangian. This is important because a bare mass term will be typically large, at least of electroweak scale and hence will not help us generate a 4×4 light neutrino mass matrix with all terms at or below the eV scale. To have a seesaw mechanism at place, three right handed neutrinos ν_{Ri}, $i=1,2,3$ are included into the model. Apart from the usual Higgs field H responsible for electroweak symmetry breaking,

Table 33.1 Fields and their transformations under the chosen symmetries

	l	e_R	μ_R	τ_R	H	ϕ	$\phi^{'}$	$\phi^{''}$	ξ	$\xi^{'}$	χ	ν_{R1}	ν_{R2}	ν_{R3}	S
$SU(2)_L$	2	1	1	1	2	1	1	1	1	1	1	1	1	1	1
A_4	3	1	$1^{''}$	$1^{'}$	1	3	3	3	1	$1^{'}$	1	1	$1^{'}$	1	1
Z_4	1	1	1	1	1	1	i	-1	1	-1	$-i$	1	$-i$	-1	i

there are six flavon fields ϕ, $\phi^{'}$, $\phi^{''}$, ξ, $\xi^{'}$, χ responsible for spontaneous breaking of the flavour symmetries and generating the desired leptonic mass matrices. The leading order Lagrangian for the leptons can be written as

$$\begin{aligned}\mathcal{L}_Y \supset\ & \frac{y_e}{\Lambda}(\bar{l}H\phi)_{\underline{1}}e_R + \frac{y_\mu}{\Lambda}(\bar{l}H\phi)_{\underline{1'}}\mu_R + \frac{y_\tau}{\Lambda}(\bar{l}H\phi)_{\underline{1''}}\tau_R + \frac{y_1}{\Lambda}(\bar{l}H\phi)_{\underline{1}}\nu_{R1} + \\ & \frac{y_2}{\Lambda}(\bar{l}H\phi')_{\underline{1''}}\nu_{R2} + \frac{y_3}{\Lambda}(\bar{l}H\phi'')_{\underline{1}}\nu_{R3} + \frac{1}{2}\lambda_1\xi\overline{\nu_{R1}^{c}}\nu_{R1} \\ & + \frac{1}{2}\lambda_2\xi'\overline{\nu_{R2}}^{c}\nu_{R2} + \frac{1}{2}\lambda_3\xi\overline{\nu_{R3}}^{c}\nu_{R3} + \frac{1}{2}\rho\chi\overline{S^c}\nu_{R1} + y_4\xi\overline{S^c}\nu_{R2} + y_5\chi^{\dagger}\overline{S^c}\nu_{R3} + \text{h.c.}\end{aligned} \tag{33.1}$$

where Λ is the cut-off scale of the theory, y_e, y_μ, y_τ, y_1, y_2, y_3, y_4, y_5, λ_1, λ_2, λ_3, ρ are the dimensionless Yukawa couplings. It is worth noting that the last two terms were not included in the original model [6] although they are allowed by the chosen symmetry of the model. We include them here as they contribute non-trivially to the neutrino mass matrix as well as the generation of correct neutrino mixing. We denote a generic vacuum alignment of the flavon fields as follows - $\langle\phi\rangle = v(n_1, n_2, n_3)$, $\langle\phi'\rangle = v(n_4, n_5, n_6)$,

$$\langle\phi''\rangle = v(n_7, n_8, n_9), \quad \langle\xi\rangle = \langle\xi'\rangle = v, \quad \langle\chi\rangle = u \tag{33.2}$$

where n_i, $i = 1 - 9$ are dimensionless numbers which we choose to take values as $n_i \in (-1, 0, 1)$, which are natural choices for alignments in such flavour symmetric models. Here v or u denotes the vacuum expectation value (VEV) of the flavon fields which typically characterises the scale of flavour symmetry breaking. Similar but more restricted alignments are chosen in the original proposal [6]. The charged lepton mass matrix can be written as

$$m_l = \frac{\langle H\rangle v}{\Lambda}\begin{pmatrix} n_1 y_e & n_2 y_\mu & n_3 y_\tau \\ n_3 y_e & n_1 y_\mu & n_2 y_\tau \\ n_2 y_e & n_3 y_\mu & n_1 y_\tau \end{pmatrix}. \tag{33.3}$$

The neutral fermion mass matrix in the basis (ν_L, ν_R, S) can be written as

$$\mathcal{M} = \begin{pmatrix} 0 & M_D & 0 \\ M_D^T & M_R & M_S^T \\ 0 & M_S & 0 \end{pmatrix} \tag{33.4}$$

where M_D, the Dirac neutrino mass matrix is

$$M_D = \frac{\langle H \rangle v}{\Lambda} \begin{pmatrix} y_1 n_1 & y_2 n_5 & y_3 n_7 \\ y_1 n_3 & y_2 n_4 & y_3 n_9 \\ y_1 n_2 & y_2 n_6 & y_3 n_8 \end{pmatrix} = \sqrt{A} \begin{pmatrix} y_1 n_1 & y_2 n_5 & y_3 n_7 \\ y_1 n_3 & y_2 n_4 & y_3 n_9 \\ y_1 n_2 & y_2 n_6 & y_3 n_8 \end{pmatrix} \tag{33.5}$$

with $A = \frac{\langle H \rangle^2 v^2}{\Lambda^2}$. The right-handed neutrino mass matrix takes the diagonal form, and M_S in the basis (S, ν_R) is given by - $M_S = (\rho u, y_4 v, y_5 u)$. In the case where $M_R \gg M_S > M_D$, the effective 4×4 light neutrino mass matrix in the basis (ν_L, ν_s) can be written as given in [6]. Using the expressions for M_D, M_R, M_S mentioned above, the 4×4 active-sterile mass matrix can be written as

$$m_\nu^{4\times4} = \begin{pmatrix} -Aa_7 & -Aa_8 & -Aa_9 & -\sqrt{A}a_1 \\ -Aa_{10} & -Aa_{11} & -Aa_{12} & -\sqrt{A}a_2 \\ -Aa_{13} & -Aa_{14} & -Aa_{15} & -\sqrt{A}a_3 \\ -\sqrt{A}a_4 & -\sqrt{A}a_5 & -\sqrt{A}a_6 & -a_0 \end{pmatrix} \tag{33.6}$$

where constants a_is can be expressed in terms of various yukawa couplings and VEVs [1]. This is a 4×4 complex symmetric mass matrix, in general having ten independent elements. However, depending upon the vacuum alignments or the specific values of $n_i \in (-1, 0, 1)$, the mass matrix can have interesting textures which we discuss in details in the next section.

33.2.1 Classification of Textures

We choose to work in the basis where the charged lepton mass matrix is diagonal. This allows the leptonic mixing matrix to be directly related to the diagonalising matrix of the light neutrino mass matrix. As discussed in the previous section, this corresponds to the VEV of the flavon field ϕ to be $\langle \phi \rangle = v(n_1, n_2, n_3)$, with $n_1 = 1$, $n_2 = n_3 = 0$. In the most general case of the vacuum alignments of the flavon fields ϕ' and ϕ'', each of $n_4, n_5, n_6, n_7, n_8, n_9$ can take 3 values, i.e. 0, 1, -1. Therefore we have $3^6 = 729$ possible cases of different vacuum alignments, which will generate 729 different 4×4 neutrino mass matrices. We first single out the disallowed textures based on the known results from previous analysis [8–10, 13] which are given in details in [1]. **Allowed cases:**

1. $\mu - \tau$ symmetry in 3×3 active neutrino block. Total number of such textures is 40.
2. One zero texture mass matrix. Total number of such textures is 96.
3. Two zero texture mass matrix. Total number of such textures is 64.
4. Three zero texture mass matrix. Total number of such textures is 8.
5. Hybrid texture mass matrix with no zeros but some constraints relating different elements. Total number of such textures is 296.

Total number of such allowed mass matrices is 504. We further classify each of these allowed categories into different sub-categories based on the constraints relating different elements of the light neutrino mass matrix [1].

33.2.2 Classification of Allowed Textures

33.2.2.1 ($\mu - \tau$) Symmetric Texture, Texture 1 Zero and Texture 3 Zero

The 40 $\mu - \tau$ symmetric textures can be classified into 4 sub-categories depending upon the constraints that they satisfy. We have also classified all the 96 texture 1 zero cases into 12 categories depending upon constraints satisfied by them. For representative purpose, we have mentioned one such VEV alignment and the corresponding mass matrix in [1]. All 8 texture 3 zero cases can be classified into the category with 3 complex constraints i.e. $M_{e\mu} = 0, \quad M_{e\tau} = 0, \quad M_{\mu\tau} = 0.$

33.2.2.2 Texture 2 Zero Case

All 64 texture 2 zero cases can be classified into 8 categories. For example, one of them is 8 matrices with 3 complex constraints i.e. $M_{e\mu} = 0, \quad M_{e\tau} = 0, \quad M_{\mu\mu} = M_{\mu\tau}$. For other categories, please see [1].

33.2.3 Numerical Analysis, Results and Discussion

Next, we present the method adopted for numerical analysis for ($\mu - \tau$) symmetric textures, texture 1, texture 2 and texture 3 zero cases, in order to check their consistency with 3 + 1 neutrino data. It is well known that 4 × 4 unitary mixing matrix can be parametrised [1, 15] as

$$U = R_{34}\tilde{R}_{24}\tilde{R}_{14}R_{23}\tilde{R}_{13}R_{12}P \tag{33.7}$$

$$\tilde{R}_{14} = \begin{pmatrix} c_{14} & 0 & 0 & s_{14}e^{-i\delta_{14}} \\ 0 & 1 & 0 & 0 \\ 0 & 0 & 1 & 0 \\ -s_{14}e^{i\delta_{14}} & 0 & 0 & c_{14} \end{pmatrix} \tag{33.8}$$

with $c_{ij} = \cos\theta_{ij}$, $s_{ij} = \sin\theta_{ij}$, δ_{ij} being the Dirac CP phases, and

$$P = \text{diag}(1, e^{-i\frac{\alpha}{2}}, e^{-i(\frac{\beta}{2}-\delta_{13})}, e^{-i(\frac{\gamma}{2}-\delta_{14})})$$

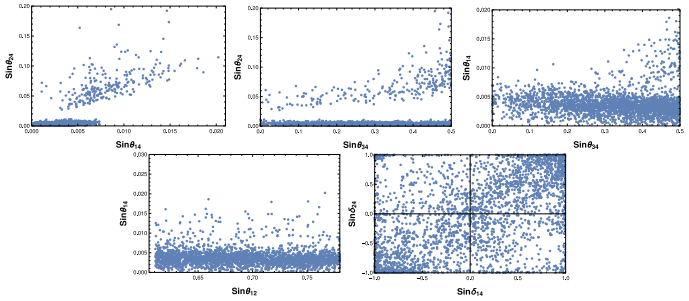

Fig. 33.1 Neutrino oscillation parameters in active-sterile sector for case (i) from texture 2 zero category for NH

is the diagonal phase matrix containing the three Majorana phases α, β, γ. In this parametrisation, the six CP phases vary from $-\pi$ to π. The 4×4 complex symmetric Majorana light neutrino mass matrix is written in [1]. One can analytically write down the 4×4 light neutrino mass matrix in terms of three mass squared differences, lightest neutrino mass $m_1(m_3)$, six mixing angles i.e., θ_{13}, θ_{12}, θ_{23}, θ_{14}, θ_{24}, θ_{34}, three Dirac type CP phases i.e., δ_{13}, δ_{14}, δ_{24} and three Majorana type CP phases i.e., α, β, γ [1]. For each class of neutrino mass matrix with textures that we analyse, there exists several constraints relating the mass matrix elements or equating some of them to zero. Depending upon the number of constraints, we choose the set of input parameters and solve for the remaining ones. We have varied our input parameters for the usual three neutrino part in the 3σ allowed range as given in the global analysis of the world neutrino data [1] and varied Δm^2_{LSND} from 0.7 eV^2 to 2.5 eV^2. Only some of the sub-classes give solutions and correlations in the range of parameters allowed by the global best fit values. For details, please see [1]. As an example, for the two zero texture case, the correlations corresponding to the solutions for subclass (i) are shown in Fig. 33.1.

33.3 Conclusion

To summarise, we first reviewed the status of existence of sterile neutrino, with reference to various data available in literature. Then, we summarised the findings of our work [1], in which we had studied the viability of different possible textures in light neutrino mass matrix within the framework of $3 + 1$ neutrino scenario by considering an A_4 flavour symmetric minimal extended seesaw mechanism (with an additional discrete symmetry Z_4). While the minimal extended seesaw mechanism naturally explains $3 + 1$ light neutrino scenario in an economical way predicting the lightest neutrino to be massless, presence of the A_4 flavour symmetry dictates the flavour structure of the 4×4 light neutrino mass matrix. We chose general VEV alignments for the triplet flavon VEVs, and obtained texture zero and $\mu - \tau$ symmetry

forms of neutrino mass matrices. Though the existence an additional light neutrino having mass around the eV scale is yet to be confirmed by other neutrino experiments, our analysis show how difficult it is to realise such a scenario in the minimal extended seesaw if A_4 flavour symmetry with generic vacuum alignment is present. If the existence of such light sterile neutrino gets well established later, the predictions for unknown neutrino parameters obtained in our analysis can be tested for further scrutiny of the model, in a way similar to [16] where the possibility of probing texture zeros in three neutrino scenarios at neutrino oscillation experiments was studied.

Acknowledgements We sincerely thank the organisers of the International workshop FHEP 2019, for giving the opportunity to give a talk, and for warm hospitality. Financial support from Govt. of India, under the DST-SERB project $DST/SERB/2014/000296$ is deeply acknowledged. We also thank Debasish Borah, with whom this work was done.

References

1. N. Sarma, K. Bora, D. Borah, Eur. Phys. J. C79(2), 129 (2019). Accessed 11 Feb 2019. https://doi.org/10.1140/epjc/s10052-019-6584-z, arXiv:1810.05826 [hep-ph]
2. J. Kopp, P.A.N. Machado, M. Maltoni, T. Schwetz, JHEP **1305**, 050 (2013)
3. C. Giunti, M. Laveder, Y.F. Li, H.W. Long, Phys. Rev. D **88**, 073008 (2013)
4. S. Gariazzo, C. Giunti, M. Laveder, Y.F. Li, E.M. Zavanin, J. Phys. **G43**, 033001 (2016)
5. J. Barry, W. Rodejohann, H. Zhang, JHEP **1107**, 091 (2011)
6. H. Zhang, Phys. Lett. B **714**, 262 (2012)
7. J. Barry, W. Rodejohann, H. Zhang, JCAP **1201**, 052 (2012)
8. D. Borah, M. Ghosh, S. Gupta, S. Prakash, S.K. Raut, Phys. Rev. **9D4**(11), 113001 (2016)
9. D. Borah, Phys. Rev. D **94**, 075024 (2016)
10. D. Borah, M. Ghosh, S. Gupta, S.K. Raut, Phys. Rev. D **96**(5), 055017 (2017)
11. N. Nath, M. Ghosh, S. Goswami, S. Gupta, JHEP **1703**, 075 (2017)
12. D. Borah, Phys. Rev. D **95**, 035016 (2017)
13. N. Nath, M. Ghosh, S. Gupta, Int. J. Mod. Phys. A **31**(24), 1650132 (2016)
14. R.N. Mohapatra, S. Nasri, H.-B. Yu, Phys. Rev. D **72**, 033007 (2005)
15. J. Barry, W. Rodejohann, H. Zhang, JHEP **1107**, 091 (2011); J. Barry, W. Rodejohann, H. Zhang, JCAP **01**, 052 (2012)
16. K. Bora, D. Borah, D. Dutta, Phys. Rev. D **96**, 075006 (2017)

Chapter 34
Origin of Dark Matter and Baryon Asymmetry of the Universe in an A_4 Flavor Symmetric Neutrino Mass Model

Ananya Mukherjee

Abstract We have explored the possibility of explaining baryogenesis via leptogenesis in an A_4 flavor symmetric framework considering type I seesaw as the origin of neutrino mass. Generation of a non-zero reactor mixing angle is brought out by the fifth generation right handed neutrino. We have calculated the matter-antimatter asymmetry for both vanilla and flavor dependent leptogenesis for a considerably wider choice of right handed neutrino mass. Finally, we found a narrow region of parameter space where both baryon asymmetry and neutrino mixing parameters can be placed together.

34.1 Introduction

Despite the fact that the Standard Model (SM) continues to stand with its enormous success after the milestone discovery of the Higgs Boson, there exists some unaddressed phenomena like origin of neutrino mass and dark matter, matter-antimatter asymmetry etc. This fact motivates us towards building a framework where all of these issues can be addressed. Existence of tiny neutrino mass has been well established by the neutrino oscillation experiments [1, 2]. At the same time there are several field theoretical schemes dedicated to explain this tiny nature of neutrino mass. Seesaw mechanism constitutes one such scheme which beautifully explains small neutrino mass. As it is well known that the SM gauge group do not provide an explanation in support of neutrino mass, in this context extension of the SM particle sector has now become a necessity rather a choice. In this regard, inclusion of the heavy right handed neutrinos (RHN) provide us a way to implement the seesaw mechanism offering a tiny Majorana neutrino mass. One of the direct consequences of the type I seesaw mechanism is Leptogenesis through which one can estimate the baryon asymmetry of the Universe (BAU).

A. Mukherjee (✉)
Theoretical Physics Division, Physical Research Laboratory,
Ahmedabad 380009, Gujarat, India
e-mail: ananya@prl.res.in

A. Giri and R. Mohanta (eds.), *Workshop on Frontiers in High Energy Physics 2019*, Springer Proceedings in Physics 248,
https://doi.org/10.1007/978-981-15-6292-1_34

Although there are plenty of evidences that show the tiny excess of matter over antimatter in the present Universe yet its origin remains illusive. With this growing evidence there has been proposed several ways for realizing this matter-antimatter asymmetry. Among them baryogenesis via leptogenesis is familiar as one of the most popular ways as proposed by Fukugita and Yanagida [3]. In such a scenario the L violating out of equilibrium decay of the singlet heavy Majorana neutrinos with mass larger than the critical temperature creates an initial excess of lepton number L (for detail one may refer to [4]). This excess in lepton number gets partially converted into the BAU (Y_B) via (B+L) violating sphaleron transition [5]. In principle, the inclusion of the RHNs makes it possible to explain the tiny neutrino mass in addition with the matter-antimatter asymmetry via the process of leptogenesis. The lepton asymmetry is dynamically generated by the L violating out of equilibrium decay of the lightest RHN satisfying Sakharov's conditions [6–8] which is required for a nonzero BAU. The Lagrangian for neutrino mass generation permits the lepton-number-violating decays of N_i (for i = 1, 2) via: $N_i \rightarrow l + H^c$ and $N_i \rightarrow l^c + H$. Since each decay mode can take place at both tree and one-loop levels, the interference of two decay amplitudes contributes to a CP-violating asymmetry ϵ_i between $N_i \rightarrow l + H^c$ and its CP-conjugated process $N_i \rightarrow l^c + H$. If Sakharov's third condition is satisfied the out-of-equilibrium decays of the lightest RHN N_i, ϵ_i may result in a net lepton number asymmetry which later on may convert into the observed baryon asymmetry. Such an elegant baryogenesis-via-leptogenesis mechanism offers a viable interpretation of the cosmological baryon number asymmetry, which is a ratio of the difference in number densities of baryons (n_B) and anti baryons ($n_{\bar{B}}$) to the entropy density of the universe, $Y_B = (8.55 - 8.77) \times 10^{-11}$, which has recently been reported by Planck 2015 [9].

On the other hand in the neutrino sector there is a considerable progress in the measurement of the parameters which constitute the mixing matrix transforming neutrino flavor eigenstate to the mass eigenstates. However the value of the Dirac CP phase and the octant of the atmospheric mixing angle θ_{23} is yet to be determined precisely. There have been extensive theoretical as well as experimental studies which are dedicated in order to resolve these two issues in the neutrino sector. Generation of nonzero reactor angle θ_{13} can be achieved by several mechanisms as already available in the literature. Among them the most popular one is through breaking the symmetry which the neutrino mass matrix is following. As already available in the literature there are various mixing patterns like TBM, BM, HM, GRM all of which predict the θ_{13} to be zero. Now, one can produce $\theta_{13} \neq 0$ by breaking these symmetries by several mechanisms. In this particular model this is achieved by the introduction of a fifth number of RHN, which in turn modifies the light neutrino mass matrix in such a way that results into a non vanishing θ_{13}. In addition, the presence of this fifth RHN also helps us in explaining the the tiny excess of matter over antimatter via the process of leptogenesis. This model also provides some textures among the elements of the light neutrino mass matrix, which constrains the Majorana phases. The complex Dirac Yukawa couplings of this model give rise to a nonzero lepton asymmetry which in turn yields the observed BAU. We have computed the lepton asymmetry generated over a range of right handed neutrino mass for exploring the possibility of having both

flavored and unflavored leptogenesis. There has been several BSM frameworks [10–13] where baryon asymmetry is produced by thermal leptogenesis with hierarchical RHNs. In addition with neutrino mass and a source of matter-antimatter asymmetry this model also accommodates a scalar dark matter candidate ϕ which falls within the WIMP paradigm. This model produces the mixing angles and the mass squared splittings in agreement with the recent neutrino and cosmology data. Using the global fit oscillation data, we determine the value of the model parameters which later on are used to compute the lepton asymmetry parameter.

34.2 The Model

Role of the non-Abelian discrete flavor symmetry groups are of great importance in particle physics, specially in the context of building neutrino mass models. Among all the non-Abelian discrete symmetry groups A_4 is the most appealing one which is the smallest group having a triplet irreducible representation. To explain the large mixing angles in the leptonic sector and the underlying symmetry behind any mixing pattern the flavor symmetry plays a crucial role. To introduce A_4 is the first alternating group which has four irreducible representations, among them there are three singlets $1, 1', 1''$ and one triplet 3. The group A_4 has 12 elements, which can be written in terms of the generators of the group S and T. Where the generators satisfy the following relation (for detail one may refer to [14])

$$S^2 = (ST)^3 = (T)^3 = 1$$

We explore the model discussed in [15] for the purpose of estimating baryogenesis via leptogenesis through the CP violating decay of the lightest RHN present in the model. The model has a total of five right handed neutrinos, among them three are the components of N_T which transform as an A_4 triplet and hence are degenerate. The other two viz., N_4 and N_5 transform as A_4 singlets $1'$ and $1''$ respectively. Therefore the SM fermion sector has been extended by the inclusion of three $SU(2)$ fermion singlets. At the same time there is an extra flavon ϕ which transforms as an $SU(2)$ doublet and a A_4 triplet. The full particle content of the model has been shown in Table 34.1. The Yukawa Lagrangian for the neutrino sector can be written as

$$\begin{aligned}\mathcal{L}_Y = {} & Y_1^{\nu} L_e (N_T \phi)_1 + Y_2^{\nu} L_\mu (N_T \phi)_1'' + Y_3^{\nu} L_\tau (N_T \phi)_1' + Y_4^{\nu} L_\tau N_4 H + Y_5^{\nu} L_\mu N_5 H \\ & + M_1 N_T N_T + M_2 N_4 N_5 + h.c.\end{aligned}$$

Following the A_4 product rules as mentioned in [14] we can arrive at the following structures for the Dirac and Majorana neutrino mass matrices as follows. For a consistent choice of vev alignment of $\langle \phi \rangle \sim v_\phi (1, 0, 0)$

Table 34.1 Quantum numbers under $SU(2)$ and A_4 symmetry groups

	L_e	L_μ	L_τ	l_e^c	l_μ^c	l_τ^c	N_T	N_4	N_5	H	ϕ
$SU(2)$	2	2	2	1	1	1	1	1	1	2	2
A_4	1	$1'$	$1''$	1	$1''$	$1'$	3	$1'$	$1''$	1	3

$$m_D = \begin{pmatrix} y_1^\nu v_\phi & 0 & 0 & 0 & 0 \\ y_2^\nu v_\phi & 0 & 0 & 0 & y_5^\nu v_h \\ y_3^\nu v_\phi & 0 & 0 & y_4^\nu v_h & 0 \end{pmatrix}, M_R = \begin{pmatrix} M_1 & 0 & 0 & 0 & 0 \\ 0 & M_1 & 0 & 0 & 0 \\ 0 & 0 & M_1 & 0 & 0 \\ 0 & 0 & 0 & 0 & M_2 \\ 0 & 0 & 0 & M_2 & 0 \end{pmatrix}. \tag{34.1}$$

34.3 Type I Seesaw Mechanism and Its Consequence Leptogenesis

For the particle content of this model mentioned in the previous section one can obtain the low energy neutrino mass matrix using the type I seesaw scheme as given below.

$$-m_\nu \sim m_D^T M_R^{-1} m_D \tag{34.2}$$

We get the following light neutrino mass matrix (34.1).

$$m_\nu = \begin{pmatrix} a^2 & ab & ac \\ ab & b^2 & bc+k \\ ac & bc+k & c^2 \end{pmatrix} \tag{34.3}$$

where, the elements are defined as $a = \frac{y_1^\nu v_\phi}{\sqrt{M_1}}, b = \frac{y_2^\nu v_\phi}{\sqrt{M_1}}, c = \frac{y_3^\nu v_\phi}{\sqrt{M_1}}, k = \frac{y_4^\nu y_5^\nu v_h^2}{M_2}$. We have following textures arising due to the structure of light neutrino mass matrix which put constraints on some neutrino parameters.

$$m_\nu^{11}.m_\nu^{22} = (m_\nu^{12})^2,\ m_\nu^{11}.m_\nu^{33} = (m_\nu^{13})^2$$

34.3.1 Lepton Asymmetry Parameter

It is to note that all the Dirac Yukawa couplings coming from the type I seesaw are complex and hence can act as a source of CP-violation, as there are no CP-violating phase associated with RHNs. Therefore it can be said that the sole contribution to CP-asymmetry is provided by the complex Dirac Yukawa couplings. With the help of

the lepton asymmetry formula taken from [12] we compute the asymmetry produced in the leptonic sector. There are three domains of baryogenesis depending on the scale of the decaying right handed neutrino mass. Prescription on lepton asymmetry for these three regime is different [10, 12]. Using the formulas mentioned therein one can determine the baryon asymmetry as shown in Fig. 34.2.

34.4 Numerical Analysis and Results

For numerical analysis we have diagonalised the right handed neutrino mass matrix for getting the eigenvalues of M_R. The Dirac mass matrix has been chosen in a basis where RH neutrino mass matrix is diagonal. For that one can write $m_{LR} = m_D U_R$, where $U_R^* M_{RR} U_R^\dagger = \text{diag}(M_1, M_2, M_3, M_4, M_5)$. Authors in [15] has explained the reason of why only normal hierarchy is favored by this model. Thus we have calculated the lepton asymmetry only for the parameter space where neutrino mass follow normal hierarchy. It is to note that due to the structure of M_R made by the A_4 product rules, diagonalization of M_R gives rise to two distinct hierarchical eigenvalues of the RH neutrino mass matrix. Among them we may chose any one to be slightly lighter than the other, CP-violating decay of which to SM leptons and Higgs is creating the lepton asymmetry. For numerical computation we redefine some of the model parameters as mentioned below and the neutrino mass matrix takes the following structure.

$$m_\nu = \begin{pmatrix} a^2 & ab & ac \\ ab & b^2 & de^{i\phi_d} \\ ac & de^{i\phi_d} & c^2. \end{pmatrix} \tag{34.4}$$

The model is consisted of a total of five model parameters, which can be numerically evaluated using the global fit oscillation data taken from [16]. We vary the parameters $d,\ \phi_d$ in the range $d \in [-1, 1]$, and $\phi_d \in [-\pi, \pi)$ while determining $a,\ b,\ c$. Since this analysis is only restricted to normal hierarchy mass pattern thus we can have $m_1, m_2 = \sqrt{\Delta m^2_{\text{sol}} + m_1^2}, m_3 = \sqrt{\Delta m^2_{\text{sol}} + \Delta m^2_{\text{atm}} + m_1^2}$ as the three light neutrino masses. We choose $m_1, \Delta m^2_{\text{sol}}, \Delta m^2_{\text{atm}}$ as the independent parameters and are randomly varied within their 3σ range as reported by [16] for numerical computation. On the other hand among the model parameters d and ϕ_d have been chosen for random scan within the interval mentioned below.

For studying the effect of flavor projection on lepton asymmetry we choose the mass scales of RHN to be of three ranges [12]. We choose the parameter M_2 to be slightly larger than M_1 in the Majorana mass matrix by denoting. For two flavor leptogenesis the RHN mass has been chosen around 10^{10} GeV. As demanded by the corresponding mass regime for RHN, M_i, M_j have been chosen less than 10^9 GeV. We have calculated the lepton asymmetry ϵ_i^α by changing the ratio of RHN mass squared $\frac{M_j^2}{M_i^2}$ for each regime of leptogenesis. We choose the RHN masses as required for different region of leptogenesis as shown in Table 34.2. To start with, we first

Table 34.2 Key ingredients for required lepton asymmetry in order to account for the observed Y_B and outcomes

	M_i (GeV)	M_j (GeV)	$x_j = \frac{M_j^2}{M_i^2}$	Y_B	Y_B, $\theta_{13} \neq 0$ at a time
One flavor	8×10^{12}	10^{13}	1.5625	✓	×
Two flavor	10^{10}	1.0009×10^{10}	1.0018	✓	✓
Three flavor	10^{8}	1.000009×10^{8}	1.00002	✓	✓

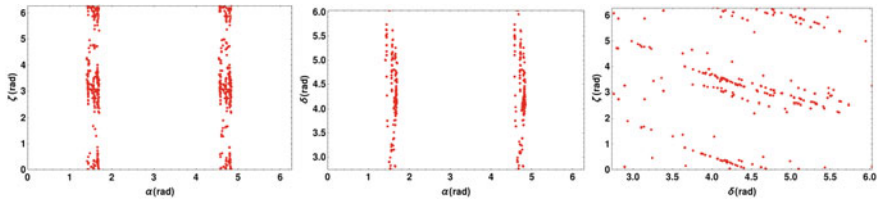

Fig. 34.1 Constraint on Majorana and Dirac phases

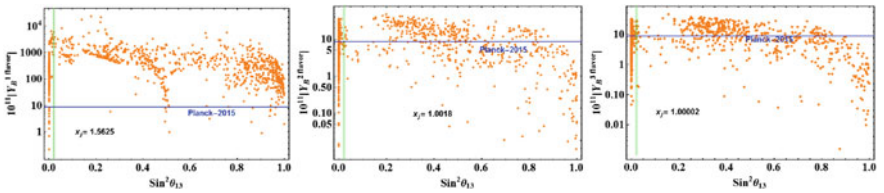

Fig. 34.2 Parameter space for Y_B and $\theta_{13} \neq 0$. The green vertical band presents the latest experimental bound for $\mathrm{Sin}^2\theta_{13}$ with the blue horizontal band for the Planck bound for $\mathrm{Y}_B = (8.55 - 8.77) \times 10^{-11}$

evaluate the model parameters a, b and c by randomly varying the mass splittings in their allowed 3σ ranges. After numerically evaluating these model parameters we feed them to the lepton asymmetry ϵ_i^α calculation. Using that value of ϵ_i^α one can find the baryon to photon ratio. We present here the Y_B as a function of the model parameters. In Fig. 34.1 we plot for the constrained Majorana and Dirac phases due to the presence of the texture present in the neutrino mass matrix. In Fig. 34.2 we plotted for Y_B as a function of the model parameters and the predicted reactor mixing angle. This figure shows Y_B for two different values of the Majorana mass splittings x_j, one for $\mathrm{x}_j = 1.018$ and another for $\mathrm{x}_j = 1.0018$ making it clear that, as the mass squared ratio decreases we can have more parameter space for Y_B. In the lower panel of Fig. 34.2 we present the common parameter space for Y_B and $\theta_{13} \neq 0$ and notice that for two and three flavor regime the parameter space matches, while for the unflavored regime there is no exact matching.

34.5 Conclusion

We have presented an analysis on baryogenesis via thermal leptogenesis scenario in an extension of the SM with A_4 flavor symmetry where type I seesaw is offering the tiny neutrino mass. The model parameter space is determined using the latest global fit neutrino oscillation data for two mass squared splittings in their allowed 3σ range and found relations among the various model parameters. It is also to note that, the textures of the light neutrino mass matrix put constrains on the Dirac and Majorana phases. Taking these values of model parameters we have investigated the possibility of addressing both flavored and unflavored leptogenesis by considering different possible mass regimes concerned with the right handed neutrinos. It is clear from the results that the model addressed leptogenesis at all the possible scales of RHN mass as mentioned in Table 34.2. Interesting is to note that the RHN mass squared ratio (x_j) for a particular mass regime plays a crucial role in obtaining a sufficient amount of lepton asymmetry which would account for the observed matter-antimatter asymmetry. We presented a Table 34.2 summarizing the various RHN mass scales and the mass squared ratios which are demanded by the model under consideration in order to explain matter-antimatter asymmetry. The important findings of the present analysis is provided in the following Table 34.2.

References

1. Y. Fukuda et al., Super-Kamiokande Collaboration
2. Q.R. Ahmad et al., SNO Collaboration, Phys. Rev. Lett. **89**, 011301 (2002)
3. M. Fukugita, T. Yanagida, Phys. Lett. B **174**, 45 (1986)
4. A. Riotto, M. Trodden, Ann. Rev. Nucl. Part. Sci. **49**, 35 (1999)
5. A. Pilaftsis, Int. J. Mod. Phys. A **14**, 1811 (1999)
6. A.D. Sakharov, Pisma. Zh. Eksp. Teor. Fiz. **5**, 32 (1967)
7. S. Davidson, E. Nardi, Y. Nir, Phys. Rep. **466**, 105 (2008)
8. M. Flanz, E.A. Paschos, Phys. Rev. D **58**, 113009 (1998)
9. P.A.R. Ade et al., Planck Collaboration, Astron. Astrophys. **594**, A13 (2016)
10. A. Mukherjee, M.K. Das, J.K. Sarma,. arXiv:1803.08239
11. B. Karmakar, A. Sil, Phys. Rev. D **91**, 013004 (2015)
12. R. Samanta, P. Roy, A. Ghosal, JHEP **06**, 085 (2018)
13. D. Borah, M.K. Das, Phys. Rev. D **90**(1), 015006 (2014)
14. H. Ishimori, T. Kobayashi, H. Ohki, Y. Shimizu, H. Okada, M. Tanimoto, Prog. Theor. Phys. Suppl. **183**, 1 (2010)
15. D. Meloni, S. Morisi, E. Peinado, Phys. Lett. B **697**, 339 (2011)
16. P.F. de Salas et al., arXiv:1708.01186 [hep-ph]

Chapter 35
eV Scale Sterile Neutrino and Dark Matter Phenomenology in $A_4 \times U(1)_{B-L}$ Model

Subhasmita Mishra, Mitesh Behera, Rukmani Mohanta, Sudhanwa Patra, and Shivaramakrishna Singirala

Abstract We discuss an A_4 flavor extended B − L model to realize an eV scale sterile neutrino, which is evident from both particle physics and cosmology experiments. The current framework includes a gauged B − L extension of standard model, where three exotic fermions with B − L charges −4, −4 and 5 are introduced to cancel gauge anomalies. Absence of usual Dirac Yukawa couplings between the SM neutrinos and the exotic fermions allows natural realization of eV scale sterile-like neutrino and its mixing by invoking the A_4 flavor symmetry. We demonstrate the neutrino phenomenology by perturbing the TBM mixing to obtain a large θ_{13}. We also explored the extra contribution to the effective neutrino mass in neutrinoless double beta decay in the presence of eV scale sterile neutrino. On the other hand the interesting feature of the model is that two of three exotic fermions are stable dark matter candidates. We constrain the gauge parameters associated with $U(1)$ gauge extension, using relic density and collider bounds.

S. Mishra (✉)
IIT Hyderabad, Hyderabad, India
e-mail: subhasmita.mishra92@gmail.com

M. Behera · R. Mohanta
University of Hyderabad, Hyderabad, India
e-mail: miteshbehera1304@gmail.com

R. Mohanta
e-mail: rmsp@uohyd.ac.in

S. Patra
IIT Bhilai, Bhilai, India
e-mail: sudhanwa@iitbhilai.ac.in

S. Singirala
IIT Indore, Indore, India
e-mail: krishnas542@gmail.com

A. Giri and R. Mohanta (eds.), *Workshop on Frontiers in High Energy Physics 2019*, Springer Proceedings in Physics 248,
https://doi.org/10.1007/978-981-15-6292-1_35

35.1 Introduction

The standard model (SM) being very successful theory till date, fails to address certain experimental discrepancies. Among them, we focus on the neutrino masses and mixing in the presence of eV scale sterile neutrino, which is recently evident from LSND and MiniBooNE from the measured excess flux of muon to electron type neutrino oscillation. There are several attempts made by the phenomenologist to account for these issues by extending the standard model particle spectrum, where A_4 flavor symmetry has been proven to be very successful to explain neutrino phenomenology with simple tri-bi-maximal (TBM) mixing [1, 2]. Apart from the masses and mixing, the Majorana nature of neutrinos is still doubtful, which can only be evident from neutrinoless double beta decay experiment. On the other hand, the existence of dark sector is still an unsolved mystery and many experiments like LUX, XENON, PICO, PandaX, Fermi-LAT, Magic,AMS etc are curiously searching for the direct or indirect signature of the dark matter [5]. In this framework, we tried to address the neutrino and dark matter phenomenology with an eV scale sterile like neutrino and Majorana dark matter in an A_4 extended $U(1)_{\mathrm{B-L}}$ model.

35.2 The Model

The present framework includes a $\mathrm{U(1)_{B-L}}$ gauge extension of SM with additional $\mathrm{A_4}$ flavor symmetry, where three new neutral fermions N_i's ($i = 1, 2, 3$) with exotic $\mathrm{B-L}$ charges -4, -4 and $+5$ are considered to cancel the triangle gauge anomalies. Three SM singlet flavon fields ϕ_T, χ, ζ are introduced to break the $\mathrm{A_4}$ flavor symmetry at high scale. Assignment of non-zero vacuum expectation to three singlet scalars (ϕ_2, ϕ_4 and ϕ_8) leads to spontaneous breaking of $U(1)_{\mathrm{B-L}}$ symmetry and generate mass terms to all exotic fermions and the new gauge boson. Z_3 symmetry can be imposed to remove unwanted terms in the Lagrangian.

Exotic charges of the new fermions forbid the tree level interaction with SM particles. Therefore the higher dimension interaction Lagrangian for charged and neutral leptons is given by

$$\begin{aligned}\mathscr{L}_\ell &= -H\left[\frac{y_e}{\Lambda}\left(\overline{L_L}\phi_T\right)_1 \otimes e_R + \frac{y_\mu}{\Lambda}\left(\overline{L_L}\phi_T\right)_{1'} \otimes \mu_R + \frac{y_\tau}{\Lambda}\left(\overline{L_L}\phi_T\right)_{1''} \otimes \tau_R\right] + H.c. \\ &= -\frac{v v_T}{2\Lambda}\left[y_e(\overline{e_L}e_R) + y_\mu(\overline{\mu_L}\mu_R) + y_\tau(\overline{\tau_L}\tau_R)\right], \end{aligned} \tag{35.1}$$

$$\begin{aligned}\mathscr{L}_{\nu,\mathscr{N}} &= -\frac{y_1}{\Lambda^2}[LLHH]_1 \otimes \phi_2 - \frac{y_\chi}{\Lambda^3}[LLHH]_3 \otimes \chi \otimes \phi_2 - \frac{y_s}{\Lambda^3}\overline{L}HN_1(\phi_4\phi_2)^\dagger\chi \\ &\quad -\frac{y_p}{\Lambda^3}[LLHH]_{1''} \otimes (\zeta)_{1'} \otimes \phi_2 - \frac{y_{11}}{\Lambda}N_1N_1\phi_8^\dagger\phi_2^\dagger + \mathrm{H.c.} \end{aligned} \tag{35.2}$$

The VEV alignment of the scalar fields are denoted as follows.

$$\langle H\rangle = \frac{v}{\sqrt{2}}\begin{pmatrix}0\\1\end{pmatrix},\ \langle\phi_2\rangle = \frac{v_2}{\sqrt{2}},\ \langle\phi_4\rangle = \frac{v_4}{\sqrt{2}},\ \langle\phi_8\rangle = \frac{v_8}{\sqrt{2}},\ \langle\phi_T\rangle = \frac{v_T}{\sqrt{2}}\begin{pmatrix}1\\0\\0\end{pmatrix}\ \langle\chi\rangle = \frac{v_\chi}{\sqrt{2}}\begin{pmatrix}1\\1\\1\end{pmatrix}.$$

Hence the mass matrix of neutrinos can be constructed from the above Lagrangian and can be analytically diagonalized by the orthogonal transformation $U^T M_\nu U = \text{Diag}(m_{\nu_1},\ m_{\nu_2},\ m_{\nu_3})$. Here U is the mixing matrix, which is constructed from the normalized eigenvectors.

$$\mathscr{M}_\nu = \begin{pmatrix} a+\frac{2d}{3} & -\frac{d}{3} & -\frac{d}{3}+b & e\\ -\frac{d}{3} & \frac{2d}{3}+b & a-\frac{d}{3} & e\\ -\frac{d}{3}+b & a-\frac{d}{3} & \frac{2d}{3} & e\\ e & e & e & m_s\end{pmatrix},\ U = \begin{pmatrix} \frac{-p_+}{l_{p+}} & \frac{1}{6e}\frac{K_{p-}}{N_{p-}} & \frac{-p_-}{l_{p-}} & \frac{1}{6e}\frac{K_{p+}}{N_{p+}}\\ \frac{q_+}{l_{p+}} & \frac{1}{6e}\frac{K_{p-}}{N_{p-}} & \frac{q_-}{l_{p-}} & \frac{1}{6e}\frac{K_{p+}}{N_{p+}}\\ \frac{1}{l_{p+}} & \frac{1}{6e}\frac{K_{p-}}{N_{p-}} & \frac{1}{l_{p-}} & \frac{1}{6e}\frac{K_{p+}}{N_{p+}}\\ 0 & \frac{1}{N_{p-}} & 0 & \frac{1}{N_{p+}}\end{pmatrix}. \tag{35.3}$$

Here,$a = \frac{y_1 v_2 v^2}{2\sqrt{2}\Lambda^2}$ and $d = \frac{y_\chi v_\chi v^2 v_2}{2\sqrt{2}\Lambda^3}, e = \frac{y_s v v_4 v_2 v_\chi}{2\sqrt{2}\Lambda^3}, m_s = \frac{y_{11} v_2 v_8}{2\Lambda}, b = \frac{y_p v^2 v_\xi v_2}{\Lambda^3}$. The term b introduces the perturbation in TBM mixing to opt for a nonzero θ_{13}, consistent with the observation. The elements of the mixing matrix are denoted as following,

$$\begin{aligned} K_{p\pm} &= a+b-m_s \pm \sqrt{12e^2+(a+b-m_s)^2},\ p_\pm = \frac{a \pm \sqrt{a^2-ab+b^2}}{a-b}\\ N^2_{p\pm} &= 1+\frac{\left(a+b-m_s \pm \sqrt{12e^2+(a+b-m_s)^2}\right)^2}{12e^2},\\ q_\pm &= \frac{b \pm \sqrt{a^2-ab+b^2}}{a-b},\ l^2_{p\pm} = 1+(p_\pm)^2+(q_\pm)^2. \end{aligned} \tag{35.4}$$

And the mass eigenvalues of the 4×4 neutrino mixing matrix are stated as

$$\begin{aligned} m_{\nu_1} &= d+\sqrt{a^2-ab+b^2},\ m_{\nu_2} = \frac{1}{2}[a+b+m_s-\sqrt{12e^2+(a+b-m_s)^2}],\\ m_{\nu_3} &= d-\sqrt{a^2-ab+b^2},\ m_{\nu_4} = \frac{1}{2}[a+b+m_s+\sqrt{12e^2+(a+b-m_s)^2}]. \end{aligned} \tag{35.5}$$

Comparing the current mixing matrix in (35.3) with the standard 4×4 neutrino mixing matrix, we can have the mixing angles as follows (Figs. 35.1 and Table 35.1)

$$\sin^2\theta_{12} \simeq \frac{1}{3}\left[1-2\left(\frac{e}{m_s}\right)^2\right],\ \sin^2\theta_{23} \simeq \frac{1}{2}\left[1+\left(\frac{e}{m_s}\right)^2\right], \tag{35.6}$$

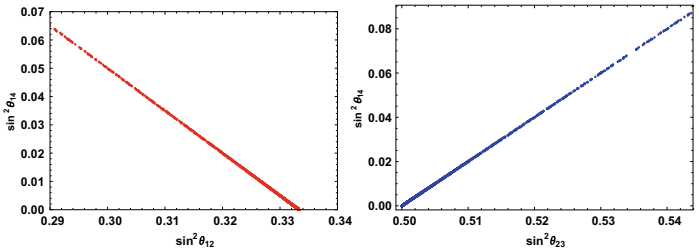

Fig. 35.1 Correlation of the active-sterile mixing angle θ_{14} with solar mixing angle θ_{12} (left panel) and with atmospheric mixing angle θ_{23} (right panel)

Table 35.1 SM field content of lepton and Higgs sectors alongwith their corresponding charges

Field	L	e_R	μ_R	τ_R	H	N_1	N_2	N_3	ϕ_2	ϕ_4	ϕ_8	ϕ_T	χ	ζ
$SU(2)_L$	2	1	1	1	2	1	1	1	1	1	1	1	1	1
A_4	3	1	$1''$	$1'$	1	1	1	1	1	1	1	3	3	$1'$
$U(1)_{B-L}$	-1	-1	-1	-1	0	5	-4	-4	2	4	8	0	0	0
Z_2	+	+	+	+	+	+	−	−	+	+	+	+	+	+

$$\sin^2\theta_{14} \approx \sin\theta_{34} \approx \sin^2\theta_{24} \approx \left(\frac{e}{m_s}\right)^2, \tag{35.7}$$

$$\sin^2\theta_{13} = \frac{|U_{e3}|^2}{(1-\sin^2\theta_{23})(1-\sin^2\theta_{14})} = \frac{b^2}{4a^2}\left(1+2\frac{e^2}{m_s^2}\right). \tag{35.8}$$

35.2.1 Numerical Analysis

To perform numerical analysis in a systematic way, we define $\lambda_1 = \frac{b}{a}$, $\lambda_2 = \frac{d}{a}$ and $\lambda_3 = \frac{e^2}{m_s a}$ with ϕ_{ba}, ϕ_{da}, ϕ_{ea} as the phases of λ_1, λ_2 and λ_3 respectively. The expressions of mass eigenvalues in (35.5) can thus be written as

$$\begin{aligned}
|m_{\nu_1}| &= |a|\Big[(\lambda_2\cos\phi_{da}+C)^2+(\lambda_2\sin\phi_{da}+D)^2\Big]^{\frac{1}{2}},\\
|m_{\nu_2}| &= |a|\Big[(1+\lambda_1\cos\phi_{ba}-3\lambda_3\cos\phi_{ea})^2+(\lambda_1\sin\phi_{ba}-3\lambda_3\sin\phi_{ea})^2\Big]^{\frac{1}{2}},\\
|m_{\nu_3}| &= |a|\Big[(\lambda_2\cos\phi_{da}-C)^2+(\lambda_2\sin\phi_{da}-D)^2\Big]^{\frac{1}{2}},\\
|m_{\nu_4}| &= |a|\Big[(\frac{m_s}{a}+3\lambda_3\cos\phi_{ea})^2+(3\lambda_3\sin\phi_{ea})^2\Big]^{\frac{1}{2}},
\end{aligned} \tag{35.9}$$

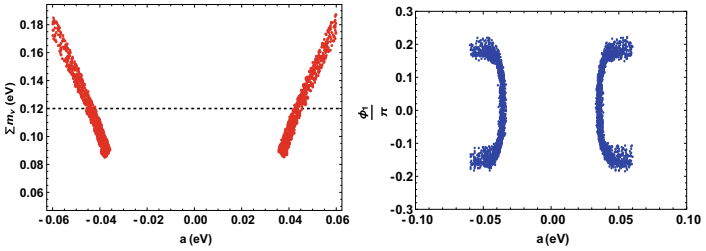

Fig. 35.2 Left panel shows the variation of a with the total active neutrino masses and the right panel represents the correlation of a with phase associated with λ_1. The variables are randomly generated as $a \in [-0.06, 0.06]$ eV, $\lambda_1 \in [0.01, 0.3]$, $\phi_{ba} \in [-\pi, \pi]$

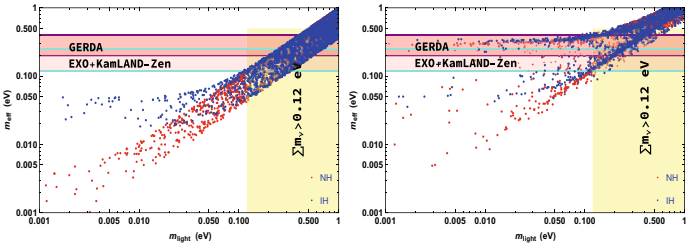

Fig. 35.3 Left Panel and right panel represent the Variation of effective Majorana mass as a function of the lightest neutrino mass, m_1 (m_3) for NH (IH) for SM and the present model respectively, the shaded region compatible with GERDA and EXO+KamLAND-Zen experiments

here,

$$C = \left(\frac{A + \sqrt{A^2 + B^2}}{2}\right)^{\frac{1}{2}}, \quad D = \left(\frac{-A + \sqrt{A^2 + B^2}}{2}\right)^{\frac{1}{2}},$$
$$A = 1 - \lambda_1 \cos\phi_{ba} + \lambda_1^2 \cos 2\phi_{ba}, \quad B = -\lambda_1 \sin\phi_{ba} + \lambda_1^2 \sin 2\phi_{ba} \quad (35.10)$$

Here, we try to show the impact of non-zero δ_{13} on the model parameters by considering the corresponding phase of λ_1, ϕ_{ba} to vary from $-\pi$ to π and $\lambda_2 = 0.5$. Left panel of the Fig. 35.2 displays the allowed parameter space for the model parameter a as per the cosmological observation of total active neutrino mass, which lies from ± 0.035 to ± 0.045 eV in first and second quadrant respectively. The right panel represents the correlation of a with the phase of λ_1.

35.3 Neutrinoless Double Beta Decay

Presence of eV scale sterile like neutrino helps to obtain a large active-sterile mixing and therefore provides an effective contribution to the Majorana mass as per the

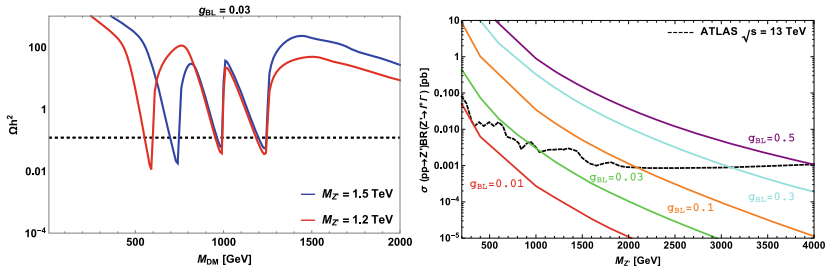

Fig. 35.4 Variation of relic density as a function of DM mass for varying Z' mass (left panel) and $g_{\rm BL}$ (right panel). The benchmark for the masses of the scalars are $(M_{H'_1}, M_{H'_2}, M_{H'_3}, M_{A'_1}, M_{A'_2}) = (2.2, 2, 2.5, 2.1, 0.9)$ (in TeV). Horizontal dashed lines represent 3σ range of Planck limit on relic density. Colored lines in right panel represent the dilepton signal cross section as a funciton of $M_{Z'}$ for different values of $g_{\rm BL}$ with the black dashed line points to ATLAS bound [6]

allowed range of GERDA and KamLAND-Zen [4]. The effective neutrino mass in the present framework is given by (Fig. 35.3)

$$m_{ee}^{\rm tot} = m_{ee}^{\nu} + m_{ee}^{N} = \left(\sum_{i=1}^{3} U_{ei}^2 m_i + \sum_{i\in {\rm eV}} U_{e4}^2 m_{si}\right), \tag{35.11}$$

35.4 Dark Matter Phenomenology

The model includes two heavy Majorana neutrinos N_2 and N_3, exotic B − L charges forbid the interaction with SM particles and the stability is ensured by the standard Z_2 symmetry. The Lagrangian for the odd fermions is provided as following

$$\mathscr{L}_{\rm DM} = \sum_{\alpha=2,3} i\overline{N_\alpha}\gamma_\mu D_\mu N_\alpha - \sum_{\alpha,\beta=2,3} y_{\alpha\beta} N_\alpha N_\beta \phi_8 + H.c, \tag{35.12}$$

The dark matter relic density consistent with 3σ observation of Planck data, is obtained in scalar and gauge portal, shown in the left panel of Fig. 35.4. The collider bounds on the new gauge parameters are discussed from the dilepton channel of ATLAS and represented in the right panel.

35.5 Conclusion

In this article, we discussed neutrino and dark matter phenomenology along with the effect of neutrinoless double beta decay by extending the standard model with $U(1)_{\rm B-L}$ gauge symmetry and A_4 flavor symmetry. The exotic B − L charges of

the new Majorana fermions makes the phenomenology interesting with eV scale sterile like neutrino and the odd being the dark matter candidates. The scenario of $3 + 1$ like models is well explored in this framework in compatible with the current neutrino oscillation data. Large active-sterile mixing provided a new direction to the NDBD with an effective contribution to the Majorana mass within the experimental bounds of GERDA and KamaLAND-Zen. Apart from this, the Majorana dark matter phenomenology is explained with a correct relic density as per the Planck data and the collider constraints on new gauge parameters from ATLAS are discussed. The detail explanation of the model is discussed in [7].

Subhasmita Mishra and Mitesh Behera acknowledge DST Inspire for its financial support.

References

1. J. Kopp, M. Maltoni, T. Schwetz, Phys. Rev. Lett. 107, 091801 (2011). https://doi.org/10.1103/PhysRevLett.107.091801, arXiv:1103.4570 [hep-ph]
2. J. Barry, W. Rodejohann, H. Zhang, JHEP **1107**, 091 (2011). https://doi.org/10.1007/JHEP07(2011)091, arXiv:1105.3911 [hep-ph]
3. M. Tanabashi et al., [Particle Data Group], Phys. Rev. D **98**(3), 030001 (2018). https://doi.org/10.1103/PhysRevD.98.030001
4. A. Gando et al. [KamLAND-Zen Collaboration], Phys. Rev. Lett. **110**(6), 062502 (2013) https://doi.org/10.1103/PhysRevLett.110.062502, arXiv:1211.3863 [hep-ex]
5. E. Ma, R. Srivastava, Phys. Lett. B **741**, 217 (2015). https://doi.org/10.1016/j.physletb.2014.12.049, arXiv:1411.5042 [hep-ph]
6. The ATLAS collaboration, ATLAS-CONF-2015-070
7. S. Mishra, M. Kumar Behera, R. Mohanta, S. Patra, S. Singirala, arXiv:1907.06429 [hep-ph]

Chapter 36
Type III Seesaw and Two-Component Dark Matter in $U(1)_{B-L}$ Model

Anirban Biswas, Debasish Borah, and Dibyendu Nanda

Abstract We have studied gauged $U(1)_{B-L}$ extension of the Standard Model where neutrino masses are generated from type III seesaw mechanism. Instead of three right handed neutrinos having unit lepton number each, which is so called the minimal $B - L$ model, the model with three fermion triplets will introduce new anomaly in the theory. Two neutral Dirac fermions having fractional $B - L$ charges, both of which are naturally stable by virtue of a remnant $\mathbb{Z}_2 \times \mathbb{Z}_2'$ symmetry, will also be necessary to cancel the leftover triangle anomalies. We have shown that the model can be constrained from various relevant phenomenological bounds. Another interesting property of this model is that due to the presence of additional neutral gauge bosons there can be an enhanced production of the fermion triplet in collider experiments.

36.1 Introduction

Standard model (SM) has failed to explain the presence of dark matter (DM) in our universe which remains as the most important puzzle of particle physics today. Recent data from PLANCK 2018 [1] has suggests that DM gives rise to around 26% of the present Universe's energy content. Although all the evidences [2–4] so far are only based on the gravitational interactions, there are enormous efforts to hunt for the other type of interactions with the SM particles. The most popular BSM framework is known as weakly interacting massive particle (WIMP) paradigm. However,

A. Biswas
School of Physical Sciences, Indian Association for the Cultivation of Science, 2A & 2B Raja S.C. Mullick Road, Kolkata 700032, India
e-mail: anirban.biswas.sinp@gmail.com

D. Borah · D. Nanda (✉)
Department of Physics, Indian Institute of Technology, Guwahati, Assam 781039, India
e-mail: dibyendu.nanda@iitg.ac.in

D. Borah
e-mail: dborah@iitg.ac.in

A. Giri and R. Mohanta (eds.), *Workshop on Frontiers in High Energy Physics 2019*, Springer Proceedings in Physics 248,
https://doi.org/10.1007/978-981-15-6292-1_36

experiments like XENON [8, 9], PANDA [6, 7], LUX [5] , have not been able to produce any positive signal putting strong upper bounds on DM interactions with the SM particles (quarks). Due to the null results reported by different experiments, people have started to think about different scenarios where dark sector can have two-component instead of having one. Such two-component scenarios can help one to explain the null results in different direct detection experiments.

Similar to the BSM proposals of DM, there have been may proposals to explain the non-zero mass and mixing in the neutrino sector. Popular seesaw mechanisms can be categorised as type I seesaw [10–13], type II seesaw [14–16, 18], type III seesaw [19]. It is highly motivating to look for a common framework that can explain both DM as well as neutrino mass problem. Motivated from these facts, we have studied a very well motivated gauged $U(1)_{B-L}$ extension of SM where B and L correspond to baryon and lepton numbers, respectively. In this model light neutrino masses arise from a type III seesaw mechanism along with two stable DM candidate. Unlike the usual type I seesaw models where the anomaly can be canceled by three right handed neutrinos with $B - L$ charge -1 each, here the presence of three triplet fermions introduces more anomaly. Out of many possible solutions we have discussed one which naturally predicts the presence of two stable DM candidate in the model. The presence of new gauge boson dictates the ralic abundance as well as helps to enhance the production cross-section of the charged triplet fermions in proton proton collider at the LHC.

36.2 The Model

To implement type III seesaw mechanism we have added two copies of triplet fermions (Σ_{1R}, Σ_{2R}) and with charge (1, 3, 0, -1). The non vanishing anomalies are,

$$\begin{aligned} \left[SU(2)_L\right]^2 U(1)_{B-L} &= 4 \\ \left[U(1)_{B-L}\right]^3 &= 3 \\ \left[U(1)_{B-L}\right] &= 3 \end{aligned} \tag{36.1}$$

The first anomaly is due to the non-trivial transformation of the triplet fermions under $SU(2)_L$. To cancel the anomaly in the $SU(2)_L$ sector we have added one more triplet (Σ_{3R}) with charge (1, 3, 0, 2) and (36.1) becomes,

$$\begin{aligned} \left[SU(2)_L\right]^2 U(1)_{B-L} &= 0 \\ \left[U(1)_{B-L}\right]^3 &= -21 \\ \left[U(1)_{B-L}\right] &= -3 \end{aligned} \tag{36.2}$$

There are various possible solutions for (36.2) out of which we have studied one where we need four chiral fermions

$$N_{1L}\left(1,1,0,-\frac{7}{5}\right),\quad N_{1R}\left(1,1,0,-\frac{2}{5}\right),\quad N_{2L}\left(1,1,0,\frac{6}{5}\right),\quad N_{2R}\left(1,1,0,-\frac{14}{5}\right) \tag{36.3}$$

To generate masses for all the new fermions we also have added three singlet scalars along with SM higgs (H)

$$\phi_1(1,1,0,1),\quad \phi_2(1,1,0,4),\quad \phi_3(1,1,0,2),\quad H\left(1,2,\frac{1}{2},0\right) \tag{36.4}$$

The Lagrangian of the model is given by

$$\mathcal{L} = \mathcal{L}_{SM} - \frac{1}{4}B'_{\alpha\beta}\,B'^{\alpha\beta} + \mathcal{L}_{scalar} + \mathcal{L}_{fermion}\ . \tag{36.5}$$

where $\mathcal{L}_{SM}$ represents the SM Lagrangian, the second term shows the kinetic terms of $B-L$ gauge bosons, third and fourth terms represent the Lagrangian for scalar and new fermion sector of the model. The $\mathcal{L}_{scalar}$ can be written as

$$\begin{aligned}\mathcal{L}_{scalar} = {} & \left(D_{H\,\mu}H\right)^{\dagger}\left(D_H{}^{\mu}H\right) + \sum_{i=1}^{3}\left(D_{\phi_i\,\mu}\phi_i\right)^{\dagger}\left(D_{\phi_i}{}^{\mu}\,\phi_i\right) - \Big[-\mu_H^2(H^{\dagger}H) + \lambda_H(H^{\dagger}H)^2 \\ & + \sum_{i=1}^{3}\left(-\mu_{\phi_i}^2(\phi_i^{\dagger}\phi_i) + \lambda_{\phi_i}(\phi_i^{\dagger}\phi_i)^2\right) + \sum_{i,j=1(i\neq j)}^{3}\lambda_{\phi_i\phi_j}(\phi_i^{\dagger}\phi_i)(\phi_j^{\dagger}\phi_j) \\ & + \sum_{i=1}^{3}\lambda_{H\phi_i}(H^{\dagger}H)(\phi_i^{\dagger}\phi_i) + \left(\beta\,\phi_1\phi_1\phi_3\phi_2^{\dagger} + \delta\,\phi_1\phi_1\phi_3^{\dagger} + \zeta\,\phi_3\phi_3\phi_2^{\dagger} + h.c.\right)\Big],\end{aligned} \tag{36.6}$$

The Lagrangian for the new fermionic fields can be written as

$$\mathcal{L}_{fermion} = \mathcal{L}_{singlet} + \mathcal{L}_{triplet} \tag{36.7}$$

The Lagrangian for the singlet fields can be written as

$$\begin{aligned}\mathcal{L}_{Singlet} = {} & i\sum_{\kappa=1}^{2}[\overline{N_{\kappa\,L}}\not{D}(Q_{\kappa}^{L})N_{\kappa\,L} + \overline{N_{\kappa\,R}}\not{D}(Q_{\kappa}^{R})N_{\kappa\,R}] \\ & -\left(\mathcal{Y}_1\,\overline{N_{1\,L}}N_{1\,R}\,\phi_1^{\dagger} + \mathcal{Y}_2\,\overline{N_{2\,L}}N_{2\,R}\,\phi_2 + \text{h.c.}\right).\end{aligned} \tag{36.8}$$

One can see that the Yukawa interactions are exactly diagonal in the basis $\xi_1 = N_{1L} + N_{1R}$ and $\xi_2 = N_{2L} + N_{2R}$ and can be written as

$$\mathcal{L}_{\text{Singlet}} = i\,\overline{\xi_1}\,\partial\!\!\!/\,\xi_1 + i\,\overline{\xi_2}\,\partial\!\!\!/\,\xi_2 + \frac{g_{BL}}{10}\,\overline{\xi_1}\,Z\!\!\!/_{BL}\,(9-5\gamma_5)\,\xi_1 + \frac{2\,g_{BL}}{5}\,\overline{\xi_2}\,Z\!\!\!/_{BL}\,(2+5\gamma_5)\,\xi_2$$
$$-\mathcal{Y}_1\,\overline{\xi_1}\,P_R\,\xi_1\,\phi_1^\dagger - \mathcal{Y}_2\,\overline{\xi_2}\,P_R\,\xi_2\,\phi_2 - \mathcal{Y}_1\,\overline{\xi_1}\,P_L\,\xi_1\,\phi_1 - \mathcal{Y}_2\,\overline{\xi_2}\,P_L\,\xi_2\,\phi_2^\dagger\,, \tag{36.9}$$

Finally the Lagrangian for the triplet fermions can be written as,

$$\mathcal{L}_{\text{Triplet}} = \frac{i}{2}\sum_{k=1}^{3}\left(\text{Tr}[\overline{\Sigma_{kR}}\,\partial\!\!\!/\,\Sigma_{kR}] + \text{Tr}[\overline{\Sigma_{kR}{}^c}\,\partial\!\!\!/'\,\Sigma_{kR}{}^c]\right) - \frac{1}{2}\left(\text{Tr}[\overline{\Sigma_{1R}{}^c}\sqrt{2}\,Y_{\Sigma_1\phi_3}\,\Sigma_{1R}]\phi_3\right.$$
$$+\,\text{Tr}[\overline{\Sigma_{2R}{}^c}\sqrt{2}\,Y_{\Sigma_2\phi_3}\,\Sigma_{2R}]\phi_3 + \text{Tr}[\overline{\Sigma_{3R}{}^c}\sqrt{2}\,Y_{\Sigma_3\phi_2}\,\Sigma_{3R}]\phi_2^\dagger + h.c.\Big) - \frac{1}{2}\Big\{\left(\text{Tr}[\overline{\Sigma_{1R}{}^c}\sqrt{2}\,Y_{\Sigma_{13}\phi_1}\,\Sigma_{3R}]\right.$$
$$\left.+\text{Tr}[\overline{\Sigma_{3R}{}^c}\sqrt{2}\,Y_{\Sigma_{13}\phi_1}\,\Sigma_{1R}]\right)\phi_1^\dagger + \left(\text{Tr}[\overline{\Sigma_{2R}{}^c}\sqrt{2}\,Y_{\Sigma_{23}\phi_1}\,\Sigma_{3R}] + \text{Tr}[\overline{\Sigma_{3R}{}^c}\sqrt{2}\,Y_{\Sigma_{23}\phi_1}\,\Sigma_{2R}]\right)\phi_1^\dagger$$
$$+\left(\text{Tr}[\overline{\Sigma_{1R}{}^c}\sqrt{2}\,Y_{\Sigma_{12}\phi_3}\,\Sigma_{2R}] + \text{Tr}[\overline{\Sigma_{2R}{}^c}\sqrt{2}\,Y_{\Sigma_{12}\phi_3}\,\Sigma_{1R}]\right)\phi_3 + h.c.\Big\} +$$
$$\left(\sum_{\alpha=1,2,3,\ \beta=1,2}\sqrt{2}y_\Sigma^{\alpha\beta}\,\overline{l_{\alpha L}}\,\Sigma_{\beta R}\,\tilde{\Phi} + h.c.\right), \tag{36.10}$$

Where the last term in (36.10) is the interaction with the triplet fermions and SM leptons through SM higgs which is responsible for generating neutrino mass through type III seesaw mechanism. For more details please see [20]

36.3 Results and Discussion

As we have already mentioned that we have two stable DM candidates in our model, so the total relic abundance of DM will be sum of individual DM candidates. In the left panel of Fig. 36.1 we have shown the variation of relic density as a function of DM mass by keeping all the other parameters fixed. The horizontal line represents the bound from PLANCK [1] data. The resonances due to different s-channel diagrams have reduced the relic abundances as expected.

In the right panel of Fig. 36.1 we have shown the allowed parameter space of our model in g_{BL} vs $M_{Z_{BL}}$ plane and the variation of the other parameters have shown in the Table 36.1. The cyan points are those which are allowed from the bounded from below criteria and as well as give correct relic density. However, in this model parameter space can also be constrained from direct detection (DD) as DM can scatter off the nucleons either through Z_{BL} or through the mixing between the SM higgs and the singlet scalars. If we apply the DD bound, the allowed points becomes very small and the red points in Fig. 36.1 represent those points which are allowed from all relevant experimental bounds.

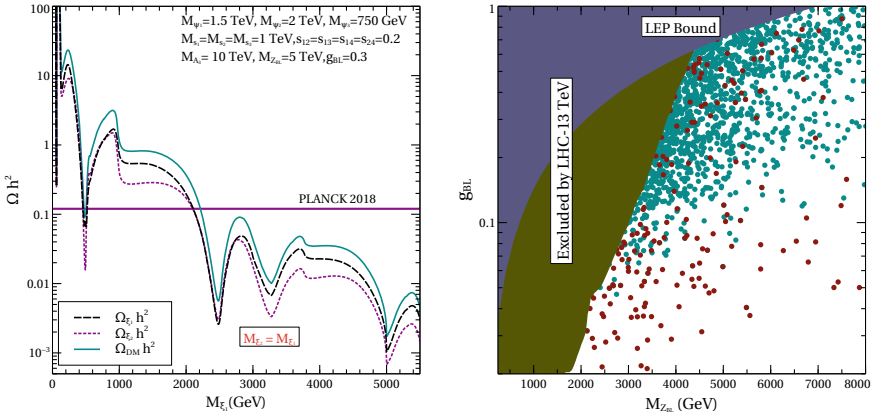

Fig. 36.1 Left panel: Relic abundance of two DM candidates with degenerate masses keeping all other model parameters fixed to benchmark values. Right panel: Summary plot showing the allowed points with and without applying the direct detection bounds from XENON1T experiment

Table 36.1 The parameters of our model and ranges used in the random scan

Parameters	Range
M_{ξ_1}	(10 GeV, 8 TeV)
M_{ξ_2}	(10 GeV, 8 TeV)
M_{s_1}	(100 GeV, 10 TeV)
M_{s_2}	(100 GeV, 10 TeV)
M_{s_3}	(100 GeV, 10 TeV)
$M_{Z_{BL}}$	(100 GeV, 10 TeV)
g_{BL}	(0.0001, 1)
M_{ψ_3}	(1 TeV, 2.5 TeV)
M_{ψ_2}	750 GeV + M_{ψ_3}
M_{ψ_1}	1.5 TeV + M_{ψ_3}
M_{A_3}	(1 TeV, 20 TeV)
M_{A_2}	$\sqrt{\frac{3}{7}}\, M_{A_3}$

In Fig. 36.2 we have shown the collider prospects of our model. The left panel is representing the production cross-section of the charged components of the triplet fermions as function of it mass for two different center of mass energy. It clearly shows that there is an enhancement in the production. If one can produce these charged fermions they will then decay to the neutral components and a $\pi^{\pm}$ and will show the disappearing charged track kind of signature in the collider. Right panel of Fig. 36.2 shows the decay length of the charged triplet fermions as function of its mass.

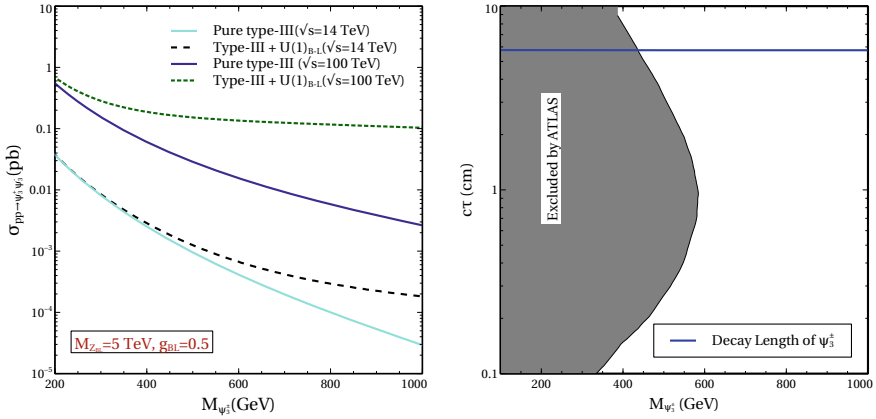

Fig. 36.2 Left panel: Plot showing improvement in production cross-section of the $\psi_3^{\pm}$ pairs due to Z_{BL} mediation for two choices of centre of mass energies in proton proton collisions. Right panel: Decay length of $\psi_3^{\pm}$ versus its mass compared with the ATLAS bound on disappearing charge track searches at 13 TeV centre of mass energy

In conclusion, we have proposed a new version of gauged $U(1)_{B-L}$ model which naturally predicts two stable DM candidate with out any add-hoc symmetry and also gives rise light neutrino mas through type III seesaw mechanism. The relic density of DM is dictated by both Z_{BL} as well as singlet scalars. We find the allowed parameter space form the relevant experimental bounds and also shown the collider predictions of our model.

References

1. N. Aghanim et al., [Planck Collaboration], arXiv:1807.06209 [astro-ph.CO]
2. F. Zwicky, Die Rotverschiebung von extragalaktischen Nebeln. Helv. Phys. Acta **6**, 110–127 (1933). [Gen. Rel. Grav. **41**, 207 (2009)]
3. V.C. Rubin, W.K. Ford Jr., Rotation of the andromeda nebula from a spectroscopic survey of emission regions. Astrophys. J. **159**, 379–403 (1970)
4. D. Clowe, M. Bradac, A.H. Gonzalez, M. Markevitch, S.W. Randall, C. Jones, D. Zaritsky, A direct empirical proof of the existence of dark matter. Astrophys. J. **648**, L109–L113 (2006). [astro-ph/0608407]
5. D.S. Akerib et al., LUX Collaboration, Results from a search for dark matter in the complete LUX exposure. Phys. Rev. Lett. **118**(2), 021303 (2017). arXiv:1608.07648
6. A. Tan et al., PandaX-II Collaboration, Dark matter results from first 98.7 days of data from the PandaX-II experiment. Phys. Rev. Lett. **117**(12), 121303 (2016). arXiv:1607.07400
7. X. Cui et al., PandaX-II Collaboration, Dark matter results from 54-ton-day exposure of PandaX-II experiment, arXiv:1708.06917
8. **XENON** Collaboration, E. Aprile et al., *First Dark Matter Search Results from the XENON1T Experiment*, arXiv:1705.06655
9. E. Aprile et al., Dark matter search results from a one tonne × year exposure of XENON1T, arXiv:1805.12562

10. P. Minkowski, $\mu \to e\gamma$ at alut of 10^9 muon decays? Phys. Lett. **67B**, 421–428 (1977)
11. M. Gell-Mann, P. Ramond, R. Slansky, Complex spinors and unified theories. Conf. Proc. C **790927**, 315–321 (1979). [arXiv:1306.4669]
12. R.N. Mohapatra, G. Senjanovic, Neutrino mass and spontaneous parity violation. Phys. Rev. Lett. **44**, 912 (1980)
13. J. Schechter, J.W.F. Valle, Neutrino masses in SU(2) x U(1) theories. Phys. Rev. D **22**, 2227 (1980)
14. R.N. Mohapatra, G. Senjanovic, Neutrino masses and mixings in gauge models with spontaneous parity violation. Phys. Rev. D **23**, 165 (1981)
15. G. Lazarides, Q. Shafi, C. Wetterich, Proton lifetime and fermion masses in an SO(10) model. Nucl. Phys. B **181**, 287–300 (1981)
16. C. Wetterich, Neutrino masses and the scale of B-L violation. Nucl. Phys. B **187**, 343–375 (1981)
17. J. Schechter, J.W.F. Valle, Neutrino decay and spontaneous violation of lepton number. Phys. Rev. D **25**, 774 (1982)
18. B. Brahmachari, R.N. Mohapatra, Unified explanation of the solar and atmospheric neutrino puzzles in a minimal supersymmetric SO(10) model. Phys. Rev. D **58**, 015001 (1998). [hep-ph/9710371]
19. R. Foot, H. Lew, X.G. He, G.C. Joshi, Seesaw neutrino masses induced by a triplet of leptons. Z. Phys. C **44**, 441 (1989)
20. A. Biswas, D. Borah, D. Nanda, JHEP **1912**, 109 (2019). https://doi.org/10.1007/JHEP12(2019)109, arXiv:1908.04308 [hep-ph]

Chapter 37
$\Delta(27)$ Flavor Model Within Type–II Seesaw and Associated Phenomenology

Itishree Sethi and Sudhanwa Patra

Abstract In this article, we studied the extension of Standard Model (SM) to scrutinize the phenomenology of type-II seesaw mechanism with the inclusion of two Higgs doublets, three scalar triplets and one scalar singlets additionally invoked with $\Delta(27)$ flavor discrete symmetry, which helps to explain the non-zero neutrino masses and mixings, matter-antimatter asymmetry and lepton flavor violation. Here, we have investigated the detailed numerical analysis of neutrino oscillation data like non-zero reactor mixing angle, δ_{CP}, the sum of the light neutrino masses, two mass squared differences and its implication to neutrino-less double beta decay. We also discuss on the matter-antimatter asymmetry of the universe through leptogenesis with the decay of TeV scale scalar triplets and variation of CP-asymmetry with input model parameters. Finally, we comment on implication to lepton flavor violating decays like $\mu \to e\gamma$, $\mu \to 3e$ processes.

37.1 Introduction

The non-zero neutrino masses directly specify the existence of physics beyond the SM (BSM). From experiment, the precise measurement of neutrino oscillation provide the possibility to probe various BSM theories. SO that, we can go BSM in two different way, one is either we have to add new particles in the SM or we have to add some new symmetry.

I. Sethi (✉)
Department of Physics, IIT Hyderabad, Kandi 502285, India
e-mail: ph15resch11004@iith.ac.in

S. Patra
Department of Physics, IIT Bhilai, GEC Campus, Raipur, India
e-mail: sudhanwa@iitbhilai.ac.in

A. Giri and R. Mohanta (eds.), *Workshop on Frontiers in High Energy Physics 2019*, Springer Proceedings in Physics 248,
https://doi.org/10.1007/978-981-15-6292-1_37

37.2 Framework of the Model

We discussed the extension of SM with additional symmetry $\Delta(27)$, which includes three Higgs doublets along and three additional scalar triplets. The Lagrangian for neutrino mass can be written as

$$\begin{aligned} -\mathcal{L}^{\nu}_{\text{Yuk}} &= f^{ij}_{\alpha}\overline{\ell^{c}_{L_i}}\ell_{L_j}\otimes\Delta_{\alpha} + f^{ij'}_{\alpha}\overline{\ell^{c}_{L_i}}\otimes\ell_{L_j}\otimes\Delta_{\alpha} \\ &+ f^{ij''}_{\alpha}\overline{\ell^{c}_{L_i}}\otimes\ell_{L_j}\otimes\Delta_{\alpha} + \frac{h_k}{\Lambda}[\overline{\ell^{c}_{iL}}\ell_{jL}\otimes\Delta_k]\cdot\chi \end{aligned} \tag{37.1}$$

After the VEV gain, the neutrino mass matrix will be

$$\mathbb{M}_{\nu} \simeq \begin{pmatrix} a+\epsilon & c & b \\ c & b+\epsilon & a \\ b & a & c+\epsilon \end{pmatrix}. \tag{37.2}$$

Notifying, $\alpha_1 = \mid \frac{b}{a} \mid$, $\alpha_2 = \mid \frac{c}{a} \mid$, $\alpha_3 = \mid \frac{\epsilon}{a} \mid$, the physical light neutrinos masses are given by,

$$\begin{aligned} m_1 &= |a|\Big[\,(\alpha_3\cos\phi_{\epsilon a}+C)^2+(\alpha_3\sin\phi_{\epsilon a}+D)^2\,\Big]^{\frac{1}{2}}, \\ m_2 &= |a|\Big[\,(1+\alpha_1\cos\phi_{ba}+\alpha_2\cos\phi_{ca}+\alpha_3\cos\phi_{\epsilon a})^2 \\ &\quad +(\alpha_1\sin\phi_{ba}+\alpha_2\sin\phi_{ca}+\alpha_3\sin\phi_{\epsilon a})^2\,\Big]^{\frac{1}{2}}, \\ m_3 &= |a|\Big[\,(\alpha_3\cos\phi_{\epsilon a}-C)^2+(\alpha_3\sin\phi_{\epsilon a}-D)^2\,\Big]^{\frac{1}{2}}. \end{aligned}$$

Using the model parameters, the square of masses and their differences are derived to be (Table 37.1), $r = \frac{\Delta m^2_{\odot}}{|\Delta m^2_{A}|}$.

$$= \frac{(K^2-G^2+2(K-G)\alpha_3\cos\phi_{\epsilon a})(\alpha_3^2+K^2-2K\alpha_3\cos\phi_{\epsilon a})}{4K\alpha_3\cos\phi_{\epsilon a}(G^2+\alpha_3^2+2G\alpha_3\cos\phi_{\epsilon a})}. \tag{37.3}$$

where

$$K = \sqrt{1+\alpha_1^2+\alpha_2^2-(\alpha_1+\alpha_1\alpha_2+\alpha_2)},\ G = 1+\alpha_1+\alpha_2. \tag{37.4}$$

Table 37.1 Complete field content with their corresponding charges of the proposed model

Field	L_{iL}	e_{iR}	H_1	H_2	H_3	$\{\Delta_1, \Delta_2, \Delta_3\}$	χ
$SU(2)_L$	2	1	2	2	2	3	1
$\Delta(27)$	3	3^*	1_1	1_2	1_3	3	1_1

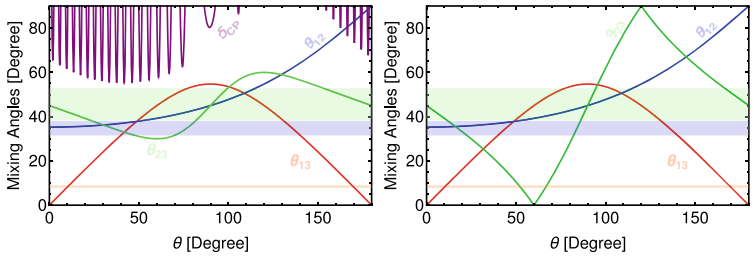

Fig. 37.1 This plot shows the correlation between (**a**) total neutrino mass with ϕ_1 (**b**) total neutrino mass with effective neutrino mass (**c**) total neutrino mass with a

37.2.1 Correlations Between Neutrino Mixing Angles

The model mixing matrix can be written as

$$\mathbb{U} = \begin{pmatrix} \frac{2}{\sqrt{6}}\cos\theta & \frac{1}{\sqrt{3}} & \frac{2}{\sqrt{6}}\sin\theta e^{-i\delta} \\ -\frac{1}{\sqrt{6}}\cos\theta + \frac{1}{\sqrt{2}}\sin\theta e^{i\delta} & \frac{1}{\sqrt{3}} & -\frac{1}{\sqrt{6}}\sin\theta e^{-i\delta} - \frac{1}{\sqrt{2}}\cos\theta \\ -\frac{1}{\sqrt{6}}\cos\theta - \frac{1}{\sqrt{2}}\sin\theta e^{i\delta} & \frac{1}{\sqrt{3}} & -\frac{1}{\sqrt{6}}\sin\theta e^{-i\delta} + \frac{1}{\sqrt{2}}\cos\theta \end{pmatrix} \cdot \begin{pmatrix} 1 & 0 & 0 \\ 0 & e^{\frac{i\alpha}{2}} & 0 \\ 0 & 0 & e^{\frac{i\beta}{2}} \end{pmatrix}.$$

The mixing angle relations are found as

$$\begin{aligned} \sin^2\theta_{13} &= \frac{2}{3}\sin^2\theta, \\ \sin^2\theta_{12} &= \frac{1}{2+\cos 2\theta}, \\ \sin^2\theta_{23} &= \frac{1}{2}\left(1 + \frac{\sqrt{3}\sin 2\theta\cos\delta}{2+\cos 2\theta}\right). \end{aligned} \tag{37.5}$$

The Jarlskog rephrasing invariant is given by (Fig. 37.1)

$$J_{\rm CP} = \frac{\sin\theta_{13}}{3\sqrt{2}}\sin\delta\sqrt{1 - \frac{3}{2}\sin^2\theta_{13}}\,, \tag{37.6}$$

37.2.2 Comment on Neutrino-Less Double Beta Decay

The measure of lepton number violation in neutrino-less double beta decay is called effective Majorana parameter with following form,

$$m_{\rm ee} = \left|\mathbb{U}_{e1}^2 m_1 + \mathbb{U}_{e2}^2 m_2 e^{i\sigma/2} + \mathbb{U}_{e3}^2 m_3 e^{i\beta/2}\right|$$
$$= \left|\frac{2}{3} m_1 cos^2\theta + \frac{1}{3} m_2 e^{i\alpha/2} + \frac{2}{3} m_3 sin^2\theta e^{i\beta/2}\right|, \tag{37.7}$$

37.3 Leptogenesis with Scalar Triplet

Out-of-equilibrium decay of scalar triplets in the early Universe can produce lepton asymmetry.The expression for CP-asymmetry due to decay of lightest scalar triplets (assuming $m_{\Delta_1} \simeq$ TeV and other two triplets around 10 TeV so that $g(x) \to x$) is given by

$$\epsilon_{\Delta_1}^{\ell_i} \simeq -\frac{1}{2\,\pi\,v^2} \frac{m_{\Delta_\beta}^2}{m_{\Delta_1}} \frac{\sqrt{B_\ell^1 B_H^1}}{\widetilde{m}_{\Delta_1}} \text{Im}\Big[\left(\mathbb{M}_\nu^\dagger \mathbb{M}_\nu\right)_{ii}\Big]. \tag{37.8}$$

Here, $\mathbb{M}_\nu = \sum_\alpha f_\alpha \frac{\mu_{\Delta_\alpha} v^2}{2m_{\Delta_\alpha}^2}$ and with B_α^ℓ and B_α^H standing for the Δ_α triplet decay branching ratios to lepton and scalar final states. The above expression is the lepton asymmetry, from which one can calculate the baryon asymmetry. Finally, in this model, part we have studied the Lepton Flavor Violation for two decays $\mu \to e\gamma$ and $\mu \to 3e$.

37.4 Conclusion

In this article, we have discussed the generation of nonzero θ_{13} in a $\Delta(27)$ symmetric framework. For which, we have extended the particle content of the SM model by adding two Higgs doublets in the Model, which corrects the charged lepton mass and three Higgs triplets, that accounts for the mass to the neutrinos via type-II seesaw mechanism as well as one scalar singlet also. The choice of these particles helped us to calculate the neutrino mass matrix as well as the neutrino Yukawa matrices dictated by the flavor symmetry imposed $\Delta(27)$ which helps in studying the mixing angles involved in the U_{PMNS} matrix. This model also describes the non-zero δ_{CP} and J_{CP}. Also the effective Majorana parameter is studied in terms of two Majorana phases α and β. We have also discussed on the leptogenesis with the decay of TeV scale scalar triplets. Finally, this model explained LFV decays like $\mu \to e\gamma$, $\mu \to 3e$ processes.

Acknowledgements IS would like to acknowledge the Ministry of Human Resource Development (MHRD) for its financial support. IS would also like to thank Dr. Biswaranjan Behera for the initial discussion on the project.

References

1. I. Sethi, S. Patra, arXiv:1909.01560 [hep-ph]
2. B. Karmakar, A. Sil, Phys. Rev. D **91**, 013004 (2015). https://doi.org/10.1103/PhysRevD.91.013004, arXiv:1407.5826 [hep-ph]
3. M. Sruthilaya, R. Mohanta, S. Patra, Eur. Phys. J. C **78**(9), 719 (2018). https://doi.org/10.1140/epjc/s10052-018-6181-6, arXiv:1709.01737 [hep-ph]
4. I. de Medeiros Varzielas, D. Emmanuel-Costa, Phys. Rev. D **84**, 117901 (2011). https://doi.org/10.1103/PhysRevD.84.117901, arXiv:1106.5477 [hep-ph]
5. G. Altarelli, D. Meloni, J. Phys. G **36**, 085005 (2009). https://doi.org/10.1088/0954-3899/36/8/085005, arXiv:0905.0620 [hep-ph]

Chapter 38
Mass and Life Time of Heavy Dark Matter Decay into IceCube PeV Neutrinos

Madhurima Pandey, Debasish Majumdar, Ashadul Halder, and Shibaji Banerjee

Abstract We consider a superheavy dark matter (SHDM) decaying into ultrahigh energy (UHE) neutrinos that may account for upgoing muon neutrino events ($\sim$ PeV energy region) detected by IceCube. From our analysis of IceCube PeV neutrinos assuming to have possibly originated from SHDM, we constrain the mass as well as the decay lifetime for such decaying dark matter.

38.1 Introduction

The sources of the ultrahigh energy (UHE) neutrino events observed at the IceCube detector in the TeV-PeV energy range is by and large unknown. We can understand the nature of the sources from which these high energetic neutrino originates by analysing the data coupled with the multi-messenger astronomy results. The very popular as well as diverse sources of these UHE neutrinos are Gamma Ray Bursts (GRBs) [1], stellar remnants [2, 3], Supernovae and Hypernovae remnants [4], Active Galactic Nuclei (AGN) [5, 6] etc. The IceCube data having neutrino energy >20 TeV are refered to as the HESE (high energy starting events) data by the IceCube

Speaker.

M. Pandey (✉) · D. Majumdar
Astroparticle Physics and Cosmology Division, Saha Institute of Nuclear Physics, HBNI, 1/AF Bidhannagar, Kolkata 700064, India
e-mail: madhurima.pandey@saha.ac.in

D. Majumdar
e-mail: debasish.majumdar@saha.ac.in

A. Halder · S. Banerjee
Department of Physics, St. Xavier's College, 30, Mother Teresa Sarani, Kolkata 700016, India
e-mail: ashadul.halder@gmail.com

S. Banerjee
e-mail: shiva@sxccal.edu

A. Giri and R. Mohanta (eds.), *Workshop on Frontiers in High Energy Physics 2019*, Springer Proceedings in Physics 248,
https://doi.org/10.1007/978-981-15-6292-1_38

Collaborartion (IC). The HESE data have been fitted with the single power law $\sim E^{-\gamma}$ and γ is obtained as $2.92^{+0.33}_{-0.29}$ by the IC. A second component, which is more softer than the HESE one component fit, has also been appeared in Fig. 2 of [7] in and around PeV region. This region above 120 TeV exhibits the different power law and this is designated as the pink band with the band thickness indicating 1σ error (Fig. 2 of [7]). We consider this pink band in and around PeV energy range and explore that the rare or long lived decay of superheavy dark matter (SHDM) in the Universe could have created these UHE neutrinos (in the pink band). SHDM could be produced during a spontaneous symmetry breaking in Grand Unified Scale and thus their production is nonthermal in nature. They can also be created by the process of gravitational production. To explain the decay procedure of SHDM one needs to consider two decay channels, one is the hadronic decay channel and the other is the leptonic decay channel. In the hadronic decay channel SHDM could be produced via the cascading QCD partons, where that dark matter has been obtained by the the deay process such as $\chi \to \bar{q}q$, which is followed by the production of the leptons as the final decay products through the hadronization. We obtain the neutrino spectrum/flux as the final product of the numerical evolution of Dokshitzer-Grivov-Lipatov-Altarelli-Parisi (DGLAP) equations [8, 9] and the Monte Carlo (MC) studies. Similarly in the leptonic decay channel the decay proceeds through the electroweak cascade. In this work, we try to estimate the best fit values of the mass (m_χ) and the decay lifetime (τ) of SHDM by making a χ^2 fit with the IC data, which undergoes via the hadronic channel. Also for the fixed value of the dark matter mass we calculate the best fit value of the dark matter decay lifetime (τ) when both hadronic and leptonic decay channel are considered.

38.2 Formalism

The neutrino spectrum from the decay of such SHDM can be written as [10]

$$\frac{\mathrm{d}N_\nu}{\mathrm{d}x} = 2R \int_{xR}^{1} \frac{\mathrm{d}y}{y} \mathrm{D}^{\pi^\pm}(y) + 2 \int_x^1 \frac{\mathrm{d}z}{z} f_{\nu_i}\left(\frac{y}{z}\right) \mathrm{D}^{\pi^\pm}(z) \ , \tag{38.1}$$

where $R = \dfrac{1}{1-r}$, $r = (m_\mu/m_\pi)^2 \simeq 0.573$. We can define $\mathrm{D}^\pi(x,s)$ as $\mathrm{D}^\pi \equiv [\mathrm{D}^\pi_q(x,s) + \mathrm{D}^\pi_g(x,s)]$, where the fraction of the dimensionless energy of SHDM transferred to the hadron can be represented as $x (\equiv 2E/m_\chi)$ and the functions $f_{\nu_i}(x)$ are given as [11]

$$
\begin{aligned}
f_{\nu_i}(x) &= g_{\nu_i}(x)\Theta(x-r) + (h^{(1)}_{\nu_i}(x) + h^{(2)}_{\nu_i}(x))\Theta(r-x) \ , \\
g_{\nu_\mu}(x) &= \frac{3-2r}{9(1-r)^2}(9x^2 - 6\ln x - 4x^3 - 5) \ , \\
h^{(1)}_{\nu_\mu}(x) &= \frac{3-2r}{9(1-r)^2}(9r^2 - 6\ln r - 4r^3 - 5) \ , \\
h^{(2)}_{\nu_\mu}(x) &= \frac{(1+2r)(r-x)}{9r^2}[9(r+x) - 4(r^2 + rx + x^2)] \ , \\
g_{\nu_e}(x) &= \frac{2}{3(1-r)^2}[(1-x)(6(1-x)^2 + r(5+5x-4x^2)) + 6r\ln x] \\
h^{(1)}_{\nu_e}(x) &= \frac{2}{3(1-r)^2}[(1-r)(6-7r+11r^2-4r^3) + 6r\ln r] \ , \\
h^{(2)}_{\nu_e}(x) &= \frac{2(r-x)}{3r^2}(7r^2 - 4r^3 + 7xr - 4xr^2 - 2x^2 - 4x^2 r) \ .
\end{aligned} \tag{38.2}
$$

We obtain the neutrino spectrum for different values of m_χ by computing (38.1). The two possible channels through which SHDM decays are hadronic and leptonic. The contribution to the neutrino spectrum due to the decay of SHDM via leptonic channel is very small (less than $\sim 10\%$) for the chosen range of m_χ which we have found in this work. Therefore the main focus of our work is to study the contribution of the hadronic channel.

The neutrino flux can be of two type; galactic and extragalactic. The galactic neutrino flux from the decay of SHDM having mass m_χ and decay lifetime τ is given as

$$
\frac{\mathrm{d}\Phi_{\mathrm{G}}}{\mathrm{d}E}(E_\nu) = \frac{1}{4\pi m_\chi \tau}\int_V \frac{\rho_\chi(R[r])}{4\pi r^2}\frac{\mathrm{d}N}{\mathrm{d}E}(E, l, b)\mathrm{d}V \ , \tag{38.3}
$$

where the dark matter density is indicated by $\rho_\chi(R[r])$ and we consider the Navarro-Frenk-White (NFW) profile for the dark matter density. The neutrino spectrum from decaying SHDM is defined as $\frac{\mathrm{d}N}{\mathrm{d}E}(E, l, b)$, l and b represent the galactic coordinate.

For the similar decay, the isotropic extragalactic flux can be written as

$$
\frac{\mathrm{d}\Phi_{\mathrm{EG}}}{\mathrm{d}E}(E_\nu) = \frac{1}{4\pi m_\chi \tau}\int_0^\infty \frac{\rho_0 c/H_0}{\sqrt{\Omega_m(1+z^3) + (1-\Omega_m)}}\frac{\mathrm{d}N}{\mathrm{d}E}[E(1+z)]\mathrm{d}z \ . \tag{38.4}
$$

In the above equation (38.4), c/H_0 ($= 1.37 \times 10^{28}$ cm) is the Hubble radius, ρ_0 ($= 1.15 \times 10^{-6}$ GeV/cm^3) is the cosmological dark matter density at the present epoch and $\Omega_m = 0.316$. The injected neutrino spectrum due to the decay of SHDM ($\frac{\mathrm{d}N}{\mathrm{d}E}$) is a function of particle energy at redshift z, $E(z) = (1+z)E$. For both the cases (galactic and extragalactic) we have assumed that the neutrinos are reaching the Earth with the flavour ratio of three active neutrinos (ν_e, ν_μ, ν_τ) 1:1:1.

The total contribution of the galactic and the extagalactic flux can be obtained as

$$\phi^{\text{th}}(E_\nu) = \frac{\mathrm{d}\Phi_{\text{EG}}}{\mathrm{d}E}(E_\nu) + \frac{\mathrm{d}\Phi_{\text{G}}}{\mathrm{d}E}(E_\nu) \ . \tag{38.5}$$

38.3 Calculatons and Results

In our analysis we consider the energy range $\sim 10^5$ GeV– $\sim 5 \times 10^6$ GeV and this region is designated by the pink band with 1σ uncertainty (in Fig. 2 of [7]) for upgoing UHE neutrinos obtained by the analysis of the IceCube Collaboration. We have considered this pink band along with the three observational points. In addition to these three experimental points we also choose another 9 points from the pink band with their 1σ spread. The chosen data sets of 12 points for the fit are enlisted in Table 38.1.

We have made a χ^2 fit to find the best fit values of SHDM mass (m_χ) and the decay lifetime (τ) which goes into UHE neutrinos through the decay process. We can define the χ^2 for our fit as

$$\chi^2 = \sum_{i=1}^{n} \left(\frac{E_i^2 \phi_i^{\text{th}} - E_i^2 \phi_i^{\text{Ex}}}{(\text{err})_{\text{i}}} \right)^2 \ , \tag{38.6}$$

Table 38.1 We use the data points (12 in all) for the χ^2 fit from the pink band (with 1σ error), where the points marked with "*" are the observational points obtained by the analysis of the IceCube Collaboration as shown in the (Fig. 2 of [7]). See text for details

Energy (in GeV)	Neutrino Flux $\left(E_\nu^2 \frac{d\Phi}{dE}\right)$ (in GeV cm^{-2} s^{-1} sr^{-1})	Error
2.51189e+06*	4.16928e−09*	8.2726e−09*
1.19279e+06*	5.03649e−09*	7.5383e−09*
2.68960e+05*	7.50551e−09*	8.1583e−09*
3.54813e+06	5.25248e−09	4.1258e−09
2.30409e+06	5.71267e−09	4.1600e−09
1.52889e+06	6.21317e−09	3.9882e−09
1.05925e+06	6.61712e−09	3.7349e−09
7.18208e+05	7.04733e−09	3.9777e−09
4.46684e+05	7.66476e−09	3.6478e−09
2.86954e+05	8.16308e−09	4.1571e−09
1.90409e+05	8.87827e−09	6.2069e−09
1.43818e+05	9.65612e−09	6.8856e−09

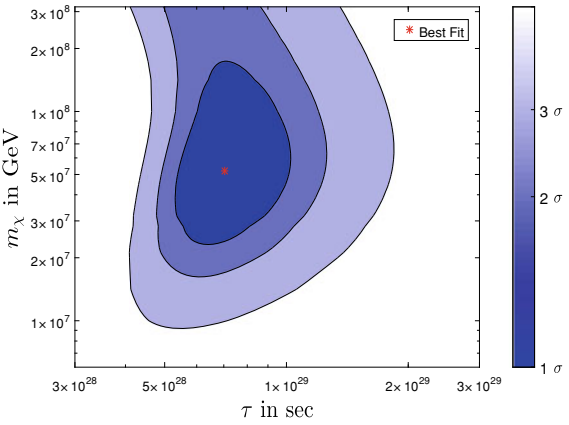

Fig. 38.1 $m_\chi - \tau$ (two parameter) χ^2 fit. 1σ, 2σ, and 3σ level of confidence have been shown. Figure reproduced from M. Pandey et al., Phys. Lett. B **797**, 134910 (2019)

where $n(=12)$ defines the number of chosen points, ϕ_i^{th} is the theoretical flux obtained from (38.5) having energies of the chosen data points E_i, $E_i^2\phi_i^{\text{Ex}}(E_\nu)$ $(=E_\nu^2\frac{\mathrm{d}\Phi}{\mathrm{d}E})$ corresponding to experimental data, which are tabulated in Table 38.1 and $(\text{err})_i$ is the ith chosen experimental points (Table 38.1).

By minimizing the χ^2 analysis we obtain the best values of m_χ and τ as $m_\chi = 5.2 \times 10^7$ GeV, $\tau = 7.05 \times 10^{28}$ sec. Therfore this is a two parameter χ^2 fit and for this two parameter fit we obtain the 1σ, 2σ and 3σ regions by adopting the range of χ^2 to be $\chi^2_{\text{min}} + 2.30$, $\chi^2_{\text{min}} + 4.61$, $\chi^2_{\text{min}} + 9.21$ respectively. We have shown the results in Fig. 38.1. Only hadronic channel is considered here for the study of the best fit values of the mass and decay lifetime of SHDM decaying into UHE neutrinos. In addition to this we also explore that how much the leptonic channel contributes in SHDM decay process when we consider the pink band region. In this regard, we fix one parameter such as the mass of SHDM at its best value ($m_\chi = 5.2 \times 10^7$ GeV) and make a one parameter χ^2 fit shown in Fig. 38.2 using the same set of values from Table 38.1. We obtain the best fit value of the decay lifetime τ as $\tau = 8.57 \times 10^{28}$ sec, which indicates that the contribution of the leptonic channel is very marginal.

38.4 Summary and Discussions

We consider the decay of SHDM as the source of UHE neutrinos in and around PeV energy region (pink band with 1σ error as the width of the band). We then obtain the best fit values of the mass and decay life time of SHDM by making a χ^2 analysis. In this two parameter fit we consider only the hadronic channel for SHDM decay. We have also shown that the contribution of the leptonic channel is very small. Therefore for UHE neutrinos in and around PeV energy region, the hadronic channel suffices and the leptonic channel has very little role to play.

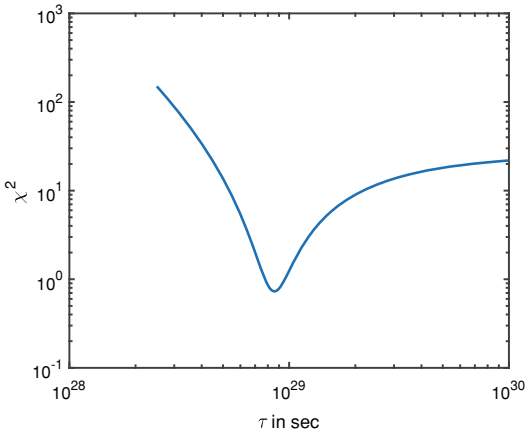

Fig. 38.2 Variation of χ^2 with τ for a fixed value of m, (fixed at the best value of m_x) reproduced M. Pandey et al., Phys. Lett. B **797**, 134910 (2019)

References

1. E. Waxman, J.N. Bahcall, Phys. Rev. lett. **78**, 2292 (1997)
2. A. Loeb, E. Waxman, JCAP **0605**, 003 (2006)
3. N. Murase, M. Ahlers, B.C. Lacki, Phys. Rev. D. **88**, 121301 (2013)
4. S. Chakraborty, I. Izaguirre, Phys. Lett. B **745**, 35 (2015)
5. F.W. Stecker, C. Done, M.H. Salamone, P. Somners, Phys. Rev. Lett. **66**, 2697 (1991), Erratum: Phys. Rev. Lett. **69**, 2738 (1992)
6. O. Kalashev, D. Semikoz, I. Tkachev, J. Exp. Theor. Phys. **120**, 541 (2015)
7. The IceCube Collaboration,*35th International Cosmic Ray Conference - ICRC2017*, PoS (ICRC2017) 981
8. V.N. Gribov, L.N. Lipatov, Sov. J. Nucl. Phys. **15**, 438 (1972), **15**, 675 (1972)
9. G. Altarelli, G. Parisi, Nucl. Phys. **B126**, 298 (1977), Yu. L. Dokshitzer, Sov. Phys. JETP **46**, 641 (1977)
10. M. Kacherlriess, O.E. kalashev, M. Yu. Kuznetsov, Phys. Rev. D. **98**, 083016 (2018)
11. S.R. Kelner, F.A. Aharonian, V.V. Bugayov, Phys. Rev. D. **74**, 034018 (2006) [Erratum: Phys. Rev. D. **79**, 039901 (2009)]

Chapter 39
Constraints on Ultra Light Dark Matter from Compact Binary Systems

Tanmay Kumar Poddar, Subhendra Mohanty, and Soumya Jana

Abstract The decay of orbital period of a compact binary system (neutron star-neutron star, neutron star-white dwarf) is primarily due to gravitational wave radiation which agrees with the observation. However, there is about one percent mismatch with the GR prediction. In this paper we consider the radiation of axion like particles (ALPs) which can contribute about one percent of the observed decay of the orbital period. If a compact star is immersed in such a low mass axionic potential, it develops a long range field outside the star. For ALPs radiation to take place, the mass of those particles should be less than the orbital frequency of the periodic motion of the binary system. This implies, for most of the observed binaries, particles with mass $m_a < 10^{-19} eV$ can be radiated which includes fuzzy dark matter (FDM) particles. In this paper, we consider four compact binary systems and we obtain bound on axion decay constant, $f_a \lesssim \mathcal{O}(10^{11} GeV)$ from the observation of orbital period decay. This implies that if ALPs has to be FDM then they do not couple with gluons.

39.1 Axion Profile for an Isolated Neutron Star/white Dwarf

It has been pointed out in [1, 2] that compact stars (neutron stars (NS) and white dwarfs (WD)) can be possible sources of axions and if a compact star is immersed in a very low mass axionic potential then the solution of the axion field outside of the neutron star falls off with distance like Yukawa interaction. Including the GR correction, the axion field solutions inside and outside of the compact star are [2],

T. K. Poddar (✉) · S. Mohanty
Theoretical Physics Division, Physical Research Laboratory, Ahmedabad 380009, India
e-mail: tanmay@prl.res.in

S. Jana
Département de Physique Théorique, Université de Genève, 24 quai Ernest Ansermet, 1211 Genève, Switzerland

A. Giri and R. Mohanta (eds.), *Workshop on Frontiers in High Energy Physics 2019*, Springer Proceedings in Physics 248,
https://doi.org/10.1007/978-981-15-6292-1_39

$$a(r) = 4\pi f_a, \qquad r < R, \tag{39.1}$$

$$= -\frac{q_{eff}}{2GM} \ln\left(1 - \frac{2GM}{r}\right), \qquad r > R, \tag{39.2}$$

where f_a is the axion decay constant, G is the universal gravitational constant, M is the mass of the compact star, R is the radius of the compact star and q_{eff} is the effective axion charge or the effective coupling of the Yukawa type interaction and is defined by [2],

$$q_{eff} = -\frac{8\pi GMf_a}{\ln\left(1 - \frac{2GM}{R}\right)} \tag{39.3}$$

We assume that the spacetime metric outside the neutron star is Schwarzchild, because for a typical neutron star ($M = 1.4M_\odot$, $R = 10\,\text{Km}$), GM/R is not negligible to one. However if $GM/R \ll 1$ (for white dwarf), then $q_{eff} \sim 4\pi f_a R$ and the axion profile outside the neutron star is $a \sim q_{eff}/r$ [1]. The new effective axion charge (39.3) is smaller than $4\pi f_a R$ by 21.46%. The plot of axion profile inside and outside of a neutron star is shown in Fig. 39.1.

39.2 Axionic Fifth Force and Scalar Radiation for the Compact Binaries

The long range axion field mediates a fifth force $F_5 = \frac{q_1 q_2}{4\pi D^2}$ between the two stars in a binary system, where q_1 and q_2 are the effective axion charges and D is the separation between them. The Kepler's law is modified due to fifth force [3]

$$\omega^2 = \frac{G(m_1 + m_2)}{D^3}(1 + \alpha), \qquad \alpha = \frac{q_1 q_2}{4\pi G m_1 m_2}, \tag{39.4}$$

where ω is the orbital frequency of the binary system, m_1 and m_2 are the masses of the two stars in the binary system and α is the ratio of the fifth force to the gravitational force.

The total power radiated for such quasi periodic motion of a binary system is [1]

$$\frac{\mathrm{d}E}{\mathrm{d}t} = -\frac{32}{5} G\mu^2 D^4 \omega^6 (1 - e^2)^{-\frac{7}{2}} \left(1 + \frac{73}{24}e^2 + \frac{37}{96}e^4\right) - \frac{\omega^4 p^2}{24\pi} \frac{(1 + e^2/2)}{(1 - e^2)^{\frac{5}{2}}}, \tag{39.5}$$

where e is the eccentricity of the orbit, μ is the reduced mass of the system, and p is dipole moment of the system and is given by [2]

$$p = 8\pi G f_a \mu D \left[\frac{1}{\ln\left(1 - \frac{2Gm_2}{r_{NS}}\right)} - \frac{1}{\ln\left(1 - \frac{2Gm_1}{r_{NS}}\right)}\right]. \tag{39.6}$$

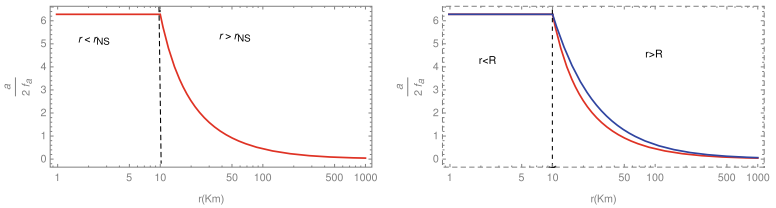

Fig. 39.1 **a** Plot of the axion field a as the function of r. The typical mass of a neutron star $M = 1.4M_{\odot}$ and radius $R = r_{NS} = 10\,\text{km}$. **b** The blue curve stands for the axion field $a \sim q_{eff}/r$ and the red curve stands for the axion field $a \sim -q_{eff}/2GM\ln(1 - 2GM/r)$ outside of the neutron star. For blue curve, the effective axion charge is $q_{eff} = 4\pi f_a R$ and for the red curve q_{eff} is given by (39.3)

The decay of the orbital period is given by [2, 4]

$$\dot{P}_b = 6\pi G^{-\frac{3}{2}}(1+\alpha)^{-\frac{3}{2}}(m_1 m_2)^{-1}(m_1+m_2)^{-\frac{1}{2}} D^{\frac{5}{2}} \left(\frac{\mathrm{d}E}{\mathrm{d}t}\right). \tag{39.7}$$

39.3 Results

The behaviour of the axionic potential as a function of the axionic field and distance [2] and the nature of the axionic field as we go from inside to outside of a compact star is also shown in Fig. 39.1.

39.4 Implication for the Axionic Fuzzy Dark Matter (FDM)

The fuzzy dark matter relic density is [5]

$$\Omega_{DM} \sim 0.1\left(\frac{a_0}{10^{17}GeV}\right)^2\left(\frac{m_a}{10^{-22}eV}\right)^{\frac{1}{2}}, \tag{39.8}$$

where a_0 is the initial value of the axion field and m_a is the mass of the axion. For the NS-WD binaries PSR J0348+0432 and PSR J1738+0333, the bound on $f_a(\lesssim 10^{11}GeV)$ is well below the GUT scale and this gives the stronger bound (Table 39.1) [2]. This implies if ultra light ALPs ($m_a \sim 10^{-21}eV - 10^{-22}eV$) are FDM then they do not couple with gluons.

Table 39.1 Summary of the upper bounds on the axion decay constant f_a from compact binaries. For all the binaries we assume $m_a < 10^{-19}$ eV

Compact binary system	f_a (GeV)	α
PSR J0348+0432	$\lesssim 1.66 \times 10^{11}$	$\lesssim 5.73 \times 10^{-10}$
PSR J0737-3039	$\lesssim 9.76 \times 10^{16}$	$\lesssim 9.21 \times 10^{-3}$
PSR J1738+0333	$\lesssim 2.03 \times 10^{11}$	$\lesssim 8.59 \times 10^{-10}$
PSR B1913+16	$\lesssim 2.12 \times 10^{17}$	$\lesssim 3.4 \times 10^{-2}$

39.5 Conclusions and Discussions

In this paper, we have discussed that ALPs can contribute to the decay in orbital period for the above four compact binaries if the mass is smaller than $10^{-19} eV$. We have obtained upper bounds on the axion decay constant of ALPs for the four binary systems. The bound $f_a \lesssim \mathcal{O}(10^{11} GeV)$ from WD binaries do not favour ALPs as the FDM.

References

1. A. Hook, J. Huang, JHEP06(2018)036
2. T.K. Poddar, S. Mohanty, S. Jana, Phys. Rev. D **101**, 8, 083007 (2020)
3. S. Jana, S. Mohanty, Phys. Rev. D **99**, 044056 (2019)
4. P.C. Peters, J. Mathew, Phys. Rev. **131**, 435 (1963)
5. L. Hui, J.P. Ostriker, S. Tremaine, E. Witten, Phys. Rev. D **95**, 043541 (2017)

Chapter 40
Viscous Dark Matter and Its Implication for 21 cm Signal

Arvind Kumar Mishra

Abstract We explore the effect of the dark matter (DM) viscosity on the cosmic evolution. The DM viscosity dissipates energy and increases the DM temperature. We propose that the energy dissipation from the Viscous dark matter, can generate photons that populate the low energy tail of the Cosmic Microwave Background (CMB) radiation. We argue that the produced photons are large enough to explain the anomaly in the 21 cm global signal observed by the EDGES collaboration.

40.1 Introduction

Viscous dark matter contains a rich physics and leads to some interesting consequences in contrast to the perfect DM fluid description in standard cosmology. It has been argued that VDM can explain the present cosmic acceleration [1–3] and also resolve the tensions between Planck and local measurements [4]. For a recent review on the DM viscosity, see [5].

In this work, we explore the effect of the DM viscosity and discuss the photon production from the VDM via the viscous energy dissipation. We also investigate the different possibilities from which the VDM can generate photons and examine their consequences in the cosmic evolution.

A. Kumar Mishra (✉)
Theoretical Physics Division, Physical Research Laboratory, Navrangpura 380009, Ahmedabad, India
e-mail: arvind@prl.res.in

Indian Institute of Technology Gandhinagar, Palaj, Gandhinagar 382355, Gujarat, India

A. Giri and R. Mohanta (eds.), *Workshop on Frontiers in High Energy Physics 2019*, Springer Proceedings in Physics 248,
https://doi.org/10.1007/978-981-15-6292-1_40

40.2 Viscous Dark Matter Cosmology

We assume that the DM is a viscous fluid with bulk viscosity. The presence of viscosity produce the entropy and heats the DM fluid. The heat energy per unit time per unit volume generated via the VDM dissipation is given as [6]

$$\frac{dQ_{\rm v}}{dV\,dt} = T_\chi \nabla_\mu S^\mu \,. \tag{40.1}$$

Here $\nabla_\mu S^\mu = \frac{\zeta_\chi}{T_\chi} (\nabla_\mu u^\mu)^2$, where ζ_χ and T_χ corresponds to the DM viscosity and its temperature, respectively. Here S^μ and u^μ represent the entropy and velocity four vector, respectively. In the comoving frame, i.e. $u^\mu = (1, 0, 0, 0)$, the above equation simplifies as

$$\frac{dQ_{\rm v}}{dV\,{\rm d}t} = 9\zeta_\chi H^2 \,. \tag{40.2}$$

In order to study the effects of DM bulk viscosity on cosmic evolution, we consider a power-law form of the DM bulk viscosity as [7]

$$\zeta_\chi(z) = \zeta_0 \left(\frac{\rho_\chi(z)}{\rho_{\chi 0}}\right)^\alpha \,, \tag{40.3}$$

where ζ_0 and α are the viscosity parameters. Here $\rho_\chi(z)$ and $\rho_{\chi 0} \equiv \rho_\chi(0)$ represent the DM energy density at redshift z, and at present, i.e. $z = 0$, respectively.

Further using the above (40.2), the energy density dissipated by viscous DM is given as a function of a redshift as [8]

$$q_{\rm vis}(z_{\rm s} \to z_{\rm e}) = 5.36 \times 10^{-43} \left(\frac{H_0\, m_{Pl}^2}{24\pi}\right) \left(\frac{\bar{\zeta}}{2\alpha+1}\right) \left[(z_{\rm s}+1)^{3(\alpha+\frac{1}{2})} - (z_{\rm e}+1)^{3(\alpha+\frac{1}{2})}\right] , \tag{40.4}$$

where $\alpha \neq -0.5$. Here $z_{\rm s}$ and $z_{\rm e}$ represent the starting and ending redshift between which the DM dissipates its energy.

Furthermore, the presence of the DM viscosity modifies its temperature evolution equation by supplying energy from the viscous dissipation (as given in (40.2)). Thus the temperature of the VDM evolves as [9]

$$\frac{dT_\chi}{dz} = 2\,\frac{T_\chi}{1+z} - \frac{2}{3(1+z)H}\left(\frac{m_\chi}{\rho_\chi}\right)\left(\frac{dQ_{\rm v}}{dV\,{\rm d}t}\right) \,, \tag{40.5}$$

where m_χ and ρ_χ represent the mass and energy density of the VDM, respectively. We are interested in the matter dominated era, then $H(z) \approx H_0 \left[\Omega_{M0}\,(1+z)^3\right]^{1/2}$, where Ω_{M0} and H_0 ($H_0 = 100h$ km-s^{-1}MPc^{-1}) represents the present value of matter content (DM and baryon) and the Hubble rate, respectively. We assume $h = 0.674$, $\Omega_{B0}h^2 = 0.0224$, $\Omega_{M0}h^2 = 0.142$ from Planck 2018 data [10].

The solution for VDM temperature (using (40.5)) is given by [8]

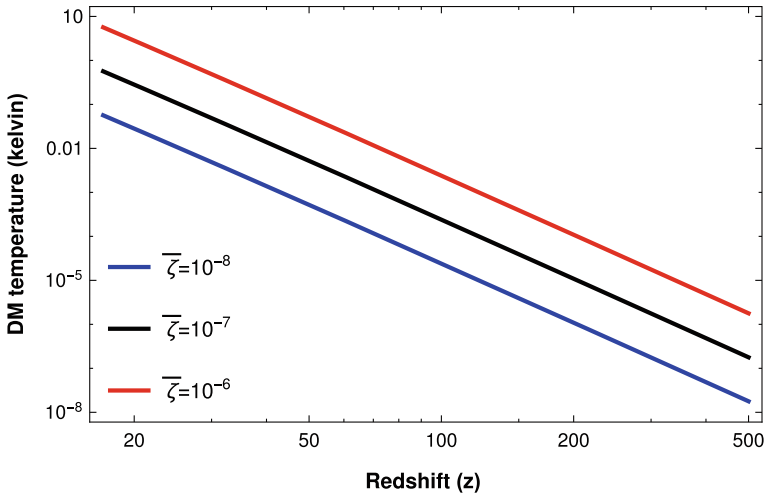

Fig. 40.1 The DM temperature evolution as a function of redshift for different values of the DM viscosity parameters. Here we assume $\alpha = -1$ and $m_\chi = 1$ GeV

$$T_\chi(z) = A(1+z)^2 - \frac{4.2}{24\pi}\left(\frac{H_0^2\, m_{\rm Pl}^2}{\rho_c}\right)\left(\frac{m_\chi\, \bar{\zeta}}{\alpha - 1.16}\right)[1+z]^{3(\alpha-\frac{1}{2})}\ , \qquad (40.6)$$

where A is the constant of integration and ρ_c is the present critical energy density of the Universe. Here, $\bar{\zeta} = \frac{24\pi G\zeta_0}{H_0}$ is a dimensionless viscosity parameter and $m_{\rm Pl} = \frac{1}{\sqrt{G}}$ is the Planck mass. In order to calculate A, we consider the initial condition as $T_\chi(z = 1300) = 0$ [8].

To see the effect of the DM viscosity on its temperature, we plot $T_\chi(z)$ as a function of the redshift in Fig. 40.1. Here we assume $\alpha = -1$, $m_\chi = 1$ GeV and plot $T_\chi(z)$ for $\bar{\zeta} = 10^{-6}$ (red line), $\bar{\zeta} = 10^{-7}$ (black line), $\bar{\zeta} = 10^{-8}$ (blue line). We see that as the DM viscosity increases, its temperature also increases and this effect becomes prominent at the late time (small redshift).

Furthermore, as we have seen that as the DM viscosity increases its temperature increases but for sufficiently large DM viscosity, the VDM temperature becomes large and can conflict with the DM coldness paradigm. In order to maintain the DM coldness in the redshift interval $z_{\rm dec} \geq z \gg 1$, the condition on T_χ/m_χ is given by [11]

$$\frac{T_\chi}{m_\chi} \leq 1.07 \times 10^{-14}\,(1+z)^2\ , \qquad (40.7)$$

where $z_{\rm dec}$ corresponds for the redshift at which the DM decouples with the thermal plasma kinematically. Then using (40.6) and (40.7), one can find a condition on the DM viscosity for which the viscous DM follow the coldness criteria at the redshift, z is given by [8]

$$\bar{\zeta} \;\leq\; 1.92 \times 10^{-13} \left(\frac{\rho_c}{H_0^2\, m_{\rm Pl}^2}\right)\left(\alpha - 1.16\right)\left[\left(1300\right)^{3\alpha-\frac{7}{2}} - \left(1+z\right)^{3\alpha-\frac{7}{2}}\right]^{-1} \;, \tag{40.8}$$

where $z_{\rm dec} \gg 1300 > z \gg 1$. We point out that the above DM coldness criteria is applied only for the linear regime of the structure formation and fails to hold for the late time where the structures are found in form of the collapsed object such as galaxies and clusters.

40.3 Photons Production From the Viscous Energy Dissipation

As we have seen that the VDM dissipates energy. We propose that the energy dissipation from the DM viscosity can produce the Standard Model (SM) particles, specifically the SM photons (from now only photons). In this work, we assume that energy dissipation can generate the photons by two possible ways, which we will discuss below.

40.3.1 When the Viscous Dissipation Directly Leads to the Photons

In this case, we assume that the viscous energy dissipation produces the photons directly and the photons are in thermal equilibrium with the DM (i.e. $T_\chi = T_A$). Then the number density of the generated photons is given as

$$n_{\chi\to A} = \frac{1}{\pi^2}\int_0^\infty \frac{\omega_A^2}{\exp\left(\frac{\omega_A}{T_A}\right)-1}\, d\omega_A \;. \tag{40.9}$$

In the low energy limit (upto $\omega_A = \omega_{\rm max}$) and integrating (40.9), we get

$$n_{\chi\to A} \approx \frac{T_\chi\, \omega_{\rm max}^2}{2\pi^2} \;. \tag{40.10}$$

40.3.2 When Viscous Dissipation Produces Dark Radiation Which Generate Photons Via Kinetic Mixing

In this case, we assume that the DM dissipates into the dark radiation, A' which is in thermal equilibrium with the DM, i.e. $T_{A'} = T_\chi$. Then the number density of the produced dark radiation can be given by

$$n_{A'} = \frac{g_{A'}}{2\pi^2}\int_{m_{A'}}^{\infty}\left(\frac{\omega_{A'}}{\exp\left(\frac{\omega_{A'}-\mu_{A'}}{T_{A'}}\right)-1}\right)\sqrt{\omega_{A'}^2 - m_{A'}^2}\; d\omega_{A'}\;, \tag{40.11}$$

where $g_{A'}$, $\mu_{A'}$ and $m_{A'}$ represent the relativistic degree of freedom, the chemical potential and mass of the dark radiation, respectively. We further assume that the DR can convert into the photons via a kinetic mixing for which the Lagrangian density is given by

$$\mathcal{L}_{\mathcal{A}'\mathcal{A}} = -\frac{1}{4}F_{\mu\nu}F^{\mu\nu} - \frac{1}{4}F'_{\mu\nu}F'^{\mu\nu} - \frac{\epsilon}{2}F_{\mu\nu}F'^{\mu\nu} + \frac{1}{2}m_{A'}^2 A'_{\mu}A'^{\mu}\;, \tag{40.12}$$

where ϵ is the kinetic mixing parameter. The probability of conversion from the DR to photons becomes maximum at the time of resonance, when $m_{A'} = m_A(z)$, where $m_A(z)$ is the plasma mass of the photon at redshift z, given as [12]

$$m_A(z) \simeq 1.7 \times 10^{-21}\,(1+z)^{3/2}\,x_e^{1/2}(z)\;\text{GeV}\;. \tag{40.13}$$

Here $x_e(z)$ is the electron fraction which we calculate from the RECFAST code [13]. The conversion probability of DR into the SM photon at the resonance is given by [12]

$$P_{A'\longrightarrow A} = \frac{\pi\epsilon^2 m_{A'}^2}{\omega_{A'}}\left|(1+z)\,H(z)\,\frac{dm_A^2}{dz}\right|^{-1}_{z=z_{\rm res}}\;. \tag{40.14}$$

where $z_{\rm res}$ is the redshift at which the resonance occures. Further, the differential number density of the photon produced from the DR to photons is given by

$$\frac{dn_{A'\to A}}{d\omega_{A'}} = \left(\frac{dn_{A'}}{d\omega_{A'}}\right)P_{A'\to A}\;. \tag{40.15}$$

Thus using the (40.11) and (40.14) in (40.15), the number density of the produced photons in the low energy limit (upto $\omega_{A'} = \omega_{\rm max}$) is obtained as [8]

$$n_{A'\to A} = \frac{\pi\epsilon^2 g_{A'} m_{A'}^2 T_\chi}{2\pi^2}\left[\sqrt{\omega_{\rm max}^2 - m_{A'}^2} + m_{A'}\tan^{-1}\left(\frac{m_{A'}}{\sqrt{\omega_{\rm max}^2 - m_{A'}^2}}\right) - \frac{\pi m_{A'}}{2}\right]\left|(1+z)\,H\frac{dm_A^2}{dz}\right|^{-1}_{z=z_{res}}\;. \tag{40.16}$$

40.4 Viscous Dissipation Explain the EDGES Anomaly

The EDGES collaboration has detected an anomaly in a global signal of the 21 cm line at the redshift $z \sim 17$ [15]. The possible explanation of the anomaly requires a DM-gas interaction [16], large photons in the CMB tail [14], 21 cm axion [17] or an early dark energy [18].

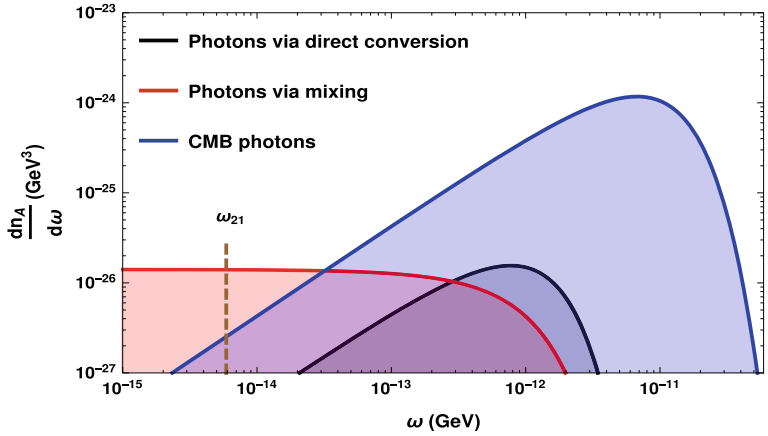

Fig. 40.2 The spectrum of the photon produced by the viscous dissipation and the CMB photons. We consider $\alpha = -1$, $\bar{\zeta} = 10^{-6}$, $m_\chi = 1$ GeV and $\epsilon = 2.1 \times 10^{-7}$ [14]. Here brown dashed vertical line, ω_{21} represents the energy of 21 cm signal. The photons obtained from the kinetic mixing populate the numbers of RJ photons but directly converted photons fail to do so [8]

In this work, we propose that the viscous energy dissipation into the photons can explain the EDGES anomaly. From Fig. 40.2 it is clear that the photons obtained from the kinetic mixing with the DR (red region) can significantly increase the number density of the CMB photons in the small frequency region, but does not alter the number density of the high-frequency photons by an appreciable amount. For the case of directly produced photons (black region), there is an increase in the CMB photons only at large frequency region and hence this case is inappropriate to address the EDGES anomaly.

We also find that for the DM viscosity considered here, the produced radiation is not large to change the Hubble expansion rate. For example, in case of $\alpha = -1$ and $\bar{\zeta} = 10^{-7}$, $\frac{q_{\rm vis}(1300\to 17)}{\rho_{\rm CMB}} = 2 \times 10^{-8}$. Hence the VDM will not modify the CMB observations. The EDGES constraint on DM viscosity, see [9].

40.5 Conclusion

The presence of the dark matter viscosity leads to the energy dissipation in the DM fluid and increases its temperature. For large DM viscosity, DM temperature becomes high and may conflict with the DM coldness criteria. In light of the assumption that the DM is cold fluid, we derive the condition on the DM viscosity parameters throughout the cosmic evolution.

In this work, we have discussed the photon production from the viscous energy dissipation in two ways; when VDM dissipates into photons directly and when VDM firstly dissipates into dark radiation and then converts into the photons via the kinetic

mixing. We find that the photons produce from the kinetic mixing increase the low energy photons and explain the EDGES anomaly but the directly converted photons do not.

References

1. J.C. Fabris, S.V.B. Goncalves, R. de Sa Ribeiro, Gen. Rel. Grav. **38**, 495 (2006)
2. A. Atreya, J.R. Bhatt, A. Mishra, JCAP **1802**(02), 024 (2018)
3. A. Atreya, J.R. Bhatt, A.K. Mishra, JCAP **1902**(02), 045 (2019)
4. S. Anand, P. Chaubal, A. Mazumdar, S. Mohanty, JCAP **1711**(11), 005 (2017)
5. I. Brevik, . Grn, J. de Haro, S.D. Odintsov, E.N. Saridakis, Int. J. Mod. Phys. D **26**(14), 1730024 (2017)
6. S. Weinberg, Gravitation and Cosmology: Principles and Applications of the General Theory of Relativity (Wiley, Hoboken, 1972)
7. H. Velten, D.J. Schwarz, J.C. Fabris, W. Zimdahl, Phys. Rev. D **88**(10), 103522 (2013)
8. A.K. Mishra, arXiv:1907.04238 [astro-ph.CO]
9. J.R. Bhatt, A.K. Mishra, A.C. Nayak, Phys. Rev. D **100**(6), 063539 (2019)
10. N. Aghanim et al. [Planck Collaboration], arXiv:1807.06209 [astro-ph.CO]
11. C. Armendariz-Picon, J.T. Neelakanta, JCAP **1403**, 049 (2014)
12. A. Mirizzi, J. Redondo, G. Sigl, JCAP **0903**, 026 (2009)
13. S. Seager, D.D. Sasselov, D. Scott, Astrophys. J. Suppl. **128**, 407 (2000)
14. M. Pospelov, J. Pradler, J.T. Ruderman, A. Urbano, Phys. Rev. Lett. **121**(3), 031103 (2018)
15. J.D. Bowman, A.E.E. Rogers, R.A. Monsalve, T.J. Mozdzen, N. Mahesh, Nature **555**(7694), 67 (2018)
16. R. Barkana, Nature **555**(7694), 71 (2018)
17. G. Lambiase, S. Mohanty, The 21 cm axion, arXiv:1804.05318 [hep-ph]
18. J.C. Hill, E.J. Baxter, JCAP **1808**(08), 037 (2018)

Chapter 41
Implications of Neutrino Mixing Data on Hierarchical Texture 2 Zero Mass Matrices

Neelu Mahajan

Abstract The recent results from atmospheric and accelerator neutrino experiments favored normal mass ordering i.e. m1 < m2 < m3, maximal lepton Dirac CP violating phase δ along with maximal θ_{23} mixing angle. In the light of these recent results we have carried out analysis for texture 2 zero hierarchical neutrino mass matrices. One finds that the aforementioned texture mass matrix is able to reproduce mixing data at 3σ C.L. Further, we have calculated the numerical values of several neutrino parameters such as neutrino mass spectrum, sum of absolute neutrino masses, Majorana neutrino mass, CP violating phases.

41.1 Introduction

The discovery of neutrino oscillations has opened up the door of opportunity to explore new physics and unravelling the mysteries of flavor structure. Neutrino physics is going through the precision era as far as the physical parameters are concerned. The reactor neutrino experiments [14] Daya Bay, Double Chooz and RENO, not only open up the possibilities to explore the leptonic CP violation but also helps to pin down the octant of the atmospheric angle θ_{23}. Also, T2K, Superkomiokande and NovA experiments [2] have shown significant improvements regarding Dirac CP violating phase which is a measure of leptonic Dirac CP violation. The latest data available from these experiments favors maximal CP violation. Refering to the global analysis of neutrino oscillation [7], indicates a preference for the upper octant $\theta_{23} > 45°$ and also reported preference of normal hierarchy as compared to inverted hierarchy. Cosmological data from Planck Collaboration [3] has presented a limit on sum of neutrino masses $\Sigma < 0.12\,\text{eV}$ at 95% C.L. The upper limit on neutrinoless double beta decay $\langle m_{ee} \rangle < (0.06-0.2)$ eV has been achieved from the GERDA [4], EXO [6] and KamLAND-Zen [11] at 90% C.L. The latest experimental upper bound of $\langle m_e \rangle < 1.1$ eV is set by the KATRIN [5] Collaboration at 90% C.L.

N. Mahajan (✉)
Department of Physics, G.G.D.S.D College, Chandigarh, India
e-mail: neeluggdsd@gmail.com

A. Giri and R. Mohanta (eds.), *Workshop on Frontiers in High Energy Physics 2019*, Springer Proceedings in Physics 248,
https://doi.org/10.1007/978-981-15-6292-1_41

The present precision statistical data helps in exploring the flavor structure of neutrino mass matrix. Since the flavor structure is dictated by the fermion mass matrices, it is desirable to focus attention on these in the hope of getting clues for fermion mass matrices. Thus, the construction of mass matrix is necessary for model building and may unravel the underlying dynamics of neutrino masses, mixing and CP violation.

The confirmation of Higgs Boson by ATLAS and CMS Collaboration completes the SM. Interestingly, within this model quark masses and elements of CKM matrix observe a hierarchical pattern. Ver ma et al. [21] investigated that the quark mixing data indeed permit quark mass matrices to have a natural and hierarchical structure provided $(M_{ij}) \approx O(\sqrt{m_i m_j})$ or i, j = 1,2,3, $i \neq j$, such structures are referred as natural mass matrices [16]. Such naturalness lead to the absence of parallel texture structure. In literature [21], hierarchical structures referred as non parallel texture structure, have achieved greater importance as they offer a natural translation of the observed strong hierarchies in the quark masses and mixing angles onto the corresponding mass matrix i.e. predict very simple and compelling relations among the elements. Thus these texture zeros not only make the theory more predictive and minimal but could also indicate the presence of additional symmetries behind them.

As compared with the quark sector, mass spectrum for leptonic sector is quite different. The charged lepton masses $m_e < m_\nu < m_\tau$ show hierarchical pattern while at least two of the neutrinos have same order of mass. Taking into account the quark lepton unification [18], similar analyis has been done for a hierarchical texture structure in the leptonic sector in accordance with the naturalness criterion [16]. Not only one but several viable sets of hierarchical hermitian mass matrices provide possible clues for model building [20]. In the present work we extend the parameter space of one such hierarchical texture two zero mass matrices and examine the implications of recent precision neutrino oscillation data on them.

41.2 Methodology

To begin with, we consider the following hermitian mass matrices

$$M_f = \begin{pmatrix} E_f & A_f & F_f \\ A_f^* & D_f & B_f \\ F_f & B_f & C_f \end{pmatrix}, \tag{41.1}$$

which,without loss of generality, are related to the most general mass matrices [12]. As a next step, one can introduce texture zeros in these matrices using the WB transformations [8], in particular, one can find a matrix W transforming

$$M_l = W^\dagger M_l W, \qquad M_\nu = W^\dagger M_\nu W \tag{41.2}$$

leading to

$$M_l = \begin{pmatrix} 0 & A_l & 0 \\ A_l^* & D_l & B_l \\ 0 & B_l & C_l \end{pmatrix}, \qquad M_{\nu D} = \begin{pmatrix} 0 & 0 & A_\nu \\ 0 & D_\nu & B_\nu \\ A_\nu^* & B_\nu^* & C_\nu \end{pmatrix}, \tag{41.3}$$

M_l and $M_{\nu D}$ respectively corresponding to Dirac-like charged lepton and neutrino mass matrices. Further, in order to incorporate the condition of 'naturalness' on these mass matrices, we have considered the following hierarchy for the elements of the matrices [16]

$$(1, i) < (2, j) \leqslant (3, 3); \quad i = 1, 2, 3, \, j = 1, 2, 3. \tag{41.4}$$

Therefore, the matrices given in equation (41.3) can now be considered as most general and their analysis can lead to very broad and interesting consequences. Before getting into the details of the analysis, we first present some of the essentials pertaining to the construction of the PMNS matrix from these mass matrices. Details of diagonalizing transformation can be looked in our previous paper [15]. To facilitate the diagonalization of M_k, where $k = l, \nu D$, the complex mass matrix M_k can be expressed as

$$M_k = Q_k M_k^r P_k \tag{41.5}$$

or

$$M_k^r = Q_k^\dagger M_k P_k^\dagger , \tag{41.6}$$

where M_k^r is a real symmetric matrix with real eigenvalues and Q_k and P_k are diagonal phase matrices. For the hermitian mass matrix $Q_k = P_k^\dagger$. In general, the real matrix M_k^r is diagonalized by the orthogonal transformation O_k, e.g.,

$$M_k^{diag} = {O_k}^T M_k^r O_k , \tag{41.7}$$

which on using equation (41.6) can be rewritten as

$$M_k^{diag} = {O_k}^T Q_k^\dagger M_k P_k^\dagger O_k . \tag{41.8}$$

The case of leptons is fairly straight forward, whereas in the case of neutrinos, the diagonalizing transformation is hierarchy specific as well as requires some fine tuning of the phases of the right handed neutrino mass matrix M_R. Assuming fine tuning of the phase matrices $Q_{\nu D}^T$ and $Q_{\nu D}$ as well as using the orthogonality of $O_{\nu D}$, it can be shown that the effective neutrino mass matrix can be expressed as

$$M_\nu = P_{\nu D} O_{\nu D} \frac{(M_{\nu D}^{diag})^2}{m_R} O_{\nu D}^T P_{\nu D}. \tag{41.9}$$

The lepton mixing matrix or the Pontecorvo-Maki-Nakagawa-Sakata (PMNS) matrix [17] U can be obtained from the matrices used for diagonalizing the mass matrices M_l and M_ν and is expressed as

$$U = (Q_l O_l \xi_l)^\dagger (P_{\nu D} O_{\nu D}). \tag{41.10}$$

Eliminating the phase matrix ξ_l by redefinition of the charged lepton phases, the above equation becomes

$$U = O_l^\dagger Q_l P_{\nu D} O_{\nu D}\,, \tag{41.11}$$

where $Q_l P_{\nu D}$, without loss of generality, can be taken as $(e^{i\phi_1},\ e^{i\phi_2},\ e^{i\phi_3})$; ϕ_1, ϕ_2 and ϕ_3 being related to the phases of mass matrices and can be treated as free parameters.

In case of Majorana neutrinos, the neutrino mass matrix M_ν is given by seesaw mechanism, for example,

$$M_\nu = -M_{\nu D}^T \,(M_R)^{-1}\, M_{\nu D}, \tag{41.12}$$

where $M_{\nu D}$ and M_R are respectively, the Dirac neutrino mass matrix and the right-handed Majorana neutrino mass matrix. Following Fukugita et al. [10] we consider the structure of $M_R = m_R I$ as simple as possible to keep the number of parameters under control, where I is the unity matrix and m_R denotes a very large mass scale.

41.3 Inputs Used for Analysis

The inputs for masses and mixing angles used in the present analysis at 3σ C.L. are as follows [7],

$$\Delta m_{12}^2 = (6.79 - 8.01) \times 10^{-5}\ \text{eV}^2, \quad m_{23}^2 = (2.431 - 2.622) \times 10^{-3}\ \text{eV}^2, \tag{41.13}$$

$$\sin^2\theta_{12} = 0.275 - 0.350, \quad \sin^2\theta_{23} = 0.428 - 0.624, \quad \sin^2\theta_{13} = 0.0204 - 0.0244. \tag{41.14}$$

The masses and mixing angles, used in the analysis, have been constrained by the data given in equations (41.13) and (41.14). For the purpose of calculations, we have taken the lightest neutrino mass and the phases ϕ_1 and ϕ_2 as free parameters. The other two masses are constrained by $\Delta m_{12}^2 = m_{\nu_2}^2 - m_{\nu_1}^2$ and $\Delta m_{23}^2 = m_{\nu_3}^2 - m_{\nu_2}^2$ in the normal hierarchy case defined as $m_{\nu_1} < m_{\nu_2} \ll m_{\nu_3}$.The explored range of lightest neutrino mass m_{ν_1} is taken to be $0.0001\,\text{eV} - 1.0\,\text{eV}$ as our results remain unaffected even if the range is extended further. In the absence of any constraints on the phases ϕ_1, and ϕ_2 these have been given full variation from 0 to 2π.

41.4 Results and Discussion

Considering preference for normal hierarchy as reported by [7],we check the compatibility of equation (41.3) for normal hierarchy of Majorana neutrinos by constraining mixing angles. Using equation (41.11), the PMNS matrix [17] obtained for this particular combination is

$$U = \begin{pmatrix} 0.78 - 0.84 & 0.52 - 0.58 & 0.14 - 0.15 \\ 0.42 - 0.46 & 0.45 - 0.51 & 0.74 - 0.76 \\ 0.31 - 0.39 & 0.67 - 0.69 & 0.62 - 0.69 \end{pmatrix}, \tag{41.15}$$

in good agreement with the ranges of mixing matrix element given by Esteban et al. [7]at 3σ C.L.

In order to have a better understanding of the above mentioned results as well as for the sake of completion, we have presented plots of various neutrino parameters by putting a constraint on mixing angles.

In upper left panel Fig. 41.1a we plot the available parameter space represented by dots for $\sin^2\theta_{13}$ and $\sin^2\theta_{23}$ by constraining mixing angles. The solid black rectangular region corresponds to experimental 3 σ values of mixing angles. One finds that the aforementioned case is viable as data is present in that black rectangular experimental region showing the viability of the texture. The allowed range of $\sin^2\theta_{13}$ is

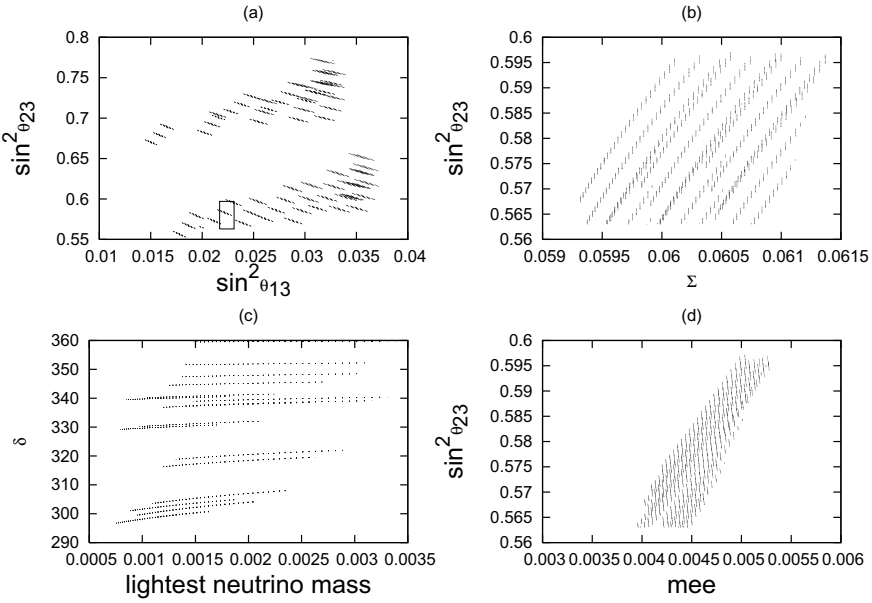

Fig. 41.1 Predicted correlation between neutrino parameters for 3 σ allowed ranges of mixing angles

0.0204–0.0244 and corresponding range of $\sin^2\theta_{23}$ is 0.5630–0.5970. It is important to note that the predictions for θ_{13} includes the best fit value. The value of $\sin^2\theta_{23}$ also includes the best fit value, is maximal and lies in the second octant. Further, resolving the atmospheric octant will require an improved measurement of reactor angle. Being precise, this correlation is easily testable in future and ongoing experiments such as LBNE, PINGU, Hyper-K [13].

In upper right panel Fig. 41.1b shows the variation of atmospheric mixing angle $\sin^2\theta_{23}$ and sum of neutrino masses Σ. One finds that there is a strong corelation between the two observables. The allowed value of Σ is 0.0593–0.0613 eV. Our predictions are well within the reach of the cosmological data from Planck Collaboration [3].

In lower left panel Fig. 41.1c shows the dependence of CP violating phase δ on the lightest neutrino mass. The allowed value of δ is $295^\circ - 352^\circ$, is quite closer to the special case 270°, suggest a kind of flavor symmetry that underlies the observed pattern of lepton flavor mixing. Further, in lower right panel Fig. 41.1d shows the variation of atmospheric mixing angle $\sin^2\theta_{23}$ and effective neutrino mass $\langle m_{ee}\rangle$ .The allowed value of $\langle m_{ee}\rangle$ is 0.0465–0.0592 eV. Hence, our prediction is well within the reach of the KATRIN experiment [5].

Further, for completion, the texture is analyzed and find it compatible with an oscillation data even at 1σ C.L. level. But, an inverted hierarchy of light neutrino mass spectrum can not be accommodated, which is an interesting prediction that will undergo tests in several ongoing and near future experiments. The confirmation of these correlations would be a strong signal of an underlying dynamics having a common origin of quark-lepton mixing.

Acknowledgements N.M. would like to thank Principal, GGDSD College, Chandigarh for providing facilities to work.

References

1. P. Adamson et al., [MINOS Collaboration], Phys. Rev. Lett. **107**, 181802 (2011), K. Abe et al. (T2K), Phys. Rev. D. **91**, 072010 (2015)
2. P. Adamson et al., Phys. Rev. Lett. **118**, 231801 (2017)
3. N.Aghanim, et al., Planck 2018 results, arXiv:1807.06209
4. M. Agostini, et al., Pjys. Rev. Lett. **111**(12), 122503 (2013)
5. M. Aker, et al., arXiv: 1909.06048
6. J.B. Albert et al., Nature **510**, 229–234 (2014)
7. I.Esteban, M.C.Gonzalez- Garcia, A. Hernandez-Cabezudo, M.Maltoni, T. Schwetz, JHEP 01, 106 (2019)
8. H. Fritzsch, Z. Z. Xing, Phys. Lett. B **413**, 396 (1997), Nucl. Phys. B **556**, 49 (1999)
9. H. Fritzsch, S. Zhou, Phys. Lett. B **718**, 1457 (2013)
10. M. Fukugita, Y. Shimizu, M. Tanimoto, T. Yanagida, Phys. Lett. B **716**, 294 (2012)
11. A. Gando et al., Phys. Rev. Lett **117**(8), 082503 (2016)
12. M. Gupta, G. Ahuja, Int. J. Mod. Phys. A **27**, 1230033 (2012), ibid **26**, 2973, (2011)
13. E. Kearns et al., arxiv:1309.0184
14. S.-B. Kim, Phys. Rev. Lett. **118**, 231801 (2017)

15. N. Mahajan, M. Randhawa, M. Gupta, P.S. Gill, Prog. Theor. Exp. Phys. **2013**, 083B02 (2013)
16. R. Pecci, K. Wang, Phys. Rev D **53**, 2712 (1996)
17. B. Pontecorvo, Zh. Eksp. Teor. Fiz. (JETP) **33**, (1957) 549, ibid 53, 1717 (1967), Z. Maki, M. Nakagawa, S. Sakata, Prog. Theor. Phys. **28**, 870 (1962)
18. Michael A. Schmidt, Yu. Alexei, Smirnov. Phys. Rev. D **74**, 113003 (2006)
19. G.'t Hooft, Naturalness, Chiral symmetry, https://doi.org/10.1007/978-1-4684-7571-5-9.
20. R. Verma, arXiv: 1607.00958v1 [hep-ph]
21. R. Verma, S. Zhou, Eur. Phys. J. C **76**, 272 (2016). arXiv:1512.06638v3 [hep-ph]

Chapter 42
Study of Texture Zeros of $M_\nu^{4\times4}$ in Minimal Extended Seesaw Mechanism

Priyanka Kumar and Mahadev Patgiri

Abstract In this chapter, we study the phenomenology of zero textures of $M_\nu^{4\times4}$ in the context of Minimal Extended Seesaw (MES) mechanism which is an extended version of type-I seesaw mechanism with an additional singlet 'S'. MES deals with 3×3 form of Dirac neutrino mass matrix M_D and right-handed Majorana neutrino mass matrix M_R along with 1×3 form of M_S which couples the right-handed neutrinos and the sterile singlet 'S'. In this work, we realize the two-zero textures of $M_\nu^{4\times4}$ considering MES mechanism and $(4 + 4)$ scheme, that is, 4 zeros in M_D and 4 zeros in M_R. Realization of the textures lead to certain constraint correlations which are then examined within 1σ range of neutrino oscillation data. We consider 1σ range for Dirac CP phase δ_{13} while all the other five CP phases are kept unconstrained. We present scatter plots as a viability check for the textures.

42.1 Introduction

Experimental observation of the anomalous oscillation mode $\bar{\nu_\mu} - \bar{\nu_e}$ in the LSND experiment [1], corresponds to squared mass difference of eV^2 which hints towards the existence of an additional eV scale sterile neutrino apart from the three active neutrinos. Similar discrepancies were observed by a number of other experiments thereby hinting towards the presence of an additional flavor of neutrino. From the theoretical front, the admixtures of the three active neutrinos with one sterile neutrino have been studied in the Minimal Extended Seesaw (MES) mechanism [2] which is an extension of the type-I seesaw mechanism. Here, the Standard Model (SM) is extended by including one gauge singlet chiral field 'S'. MES mechanism gives rise to an eV-scale sterile neutrino naturally without needing to insert any tiny Yukawa couplings or mass scale. In $(3 + 1)$ scheme, that is, three active and one light sterile

P. Kumar (✉) · M. Patgiri
Cotton University, Guwahati 781001, Assam, India
e-mail: prianca.kumar@gmail.com

M. Patgiri
e-mail: mahadevpatgiri@mail.com

A. Giri and R. Mohanta (eds.), *Workshop on Frontiers in High Energy Physics 2019*, Springer Proceedings in Physics 248,
https://doi.org/10.1007/978-981-15-6292-1_42

neutrino, neutrino mass matrix takes 4×4 form, where the fourth row and column represents the active-sterile mixing sector. The 4×4 MES neutrino mass matrix consists of 3×3 form of Dirac neutrino mass matrix M_D and right-handed Majorana neutrino mass matrix M_R along with 1×3 row matrix M_S which couples the singlet 'S' with the three right-handed neutrinos.

In this chapter we shall study the two-zero textures of $M_\nu^{4\times4}$ [3] by considering four-zero textures of M_D and M_R ($4+4$ scheme) and one-zero texture of M_S, which will finally propagate as zeros in $M_\nu^{4\times4}$ via MES mechanism. Texture zero models [4] have been extensively studied in literature both in three and $(3+1)$ neutrino regime [3, 5] for their usefulness in increasing the predictivity of the mass matrix by reducing the number of free parameters. We also check the viability of each of the textures by means of scatter plots wherein the correlations obtained by imposing zeros, are plotted against $\sin\theta_{34}$. While doing so, we have considered 1σ range of experimental values [6] while the five CP phases are kept unconstrained.

The chapter is organised as follows: Two-zero textures of $M_\nu^{4\times4}$ are discussed in Sect. 42.2. In Sect. 42.3 we present realization of the 12 two-zero textures and their corresponding correlations. Also scatter plots for 4 two-zero textures are shown as representative cases. Finally we conclude in Sect. 42.4.

42.2 Two-Zero Textures of 4 × 4 Neutrino Mass Matrix

Considering charged lepton mass matrix to be diagonal, the 4×4 Majorana neutrino mass matrix takes the form

$$M_\nu^{4\times4} = \begin{pmatrix} m_{ee} & m_{e\mu} & m_{e\tau} & m_{es} \\ m_{e\mu} & m_{\mu\mu} & m_{\mu\tau} & m_{\mu s} \\ m_{e\tau} & m_{\mu\tau} & m_{\tau\tau} & m_{\tau s} \\ m_{es} & m_{\mu s} & m_{\tau s} & m_{ss} \end{pmatrix}, \tag{42.1}$$

Out of a large number of possibilities only 15 two-zero textures of $M_\nu^{4\times4}$ [3] are found to be viable. In this work we realize the viable two-zero textures in the context of MES mechanism. The 4×4 neutrino mass matrix in MES mechanism takes the form [2]

$$M_\nu^{4\times4} = -\begin{pmatrix} M_D M_R^{-1} M_D^T & M_D M_R^{-1} M_S^T \\ M_S (M_R^{-1})^T M_D^T & M_S M_R^{-1} M_S^T \end{pmatrix}. \tag{42.2}$$

Here M_D, M_R are of 3×3 form while M_S is a 1×3 row matrix. The general form of M_D, M_R and M_S are

$$M_D = \begin{pmatrix} a & b & c \\ d & e & f \\ g & h & i \end{pmatrix}, \qquad M_R = \begin{pmatrix} A & B & C \\ B & D & E \\ C & E & F \end{pmatrix}, \qquad M_S = (s_1 \quad s_2 \quad s_3) \tag{42.3}$$

Table 42.1 Table shows the form of M_D, M_R and M_S for each texture along with their corresponding correlation

Texture	M_D	M_R	M_S	Correlation
A_1	$(b, c, f, h = 0)$	$(C, D \neq 0)$	$(0 \quad s_2 \quad s_3)$	$\frac{m_{\tau\tau}}{m_{e\tau}} = 2\left(\frac{m_{\tau s}}{m_{es}}\right)$
A_2	$(a, c, f, g = 0)$	$(B, F \neq 0)$	$(s_1 \quad 0 \quad s_3)$	$\frac{m_{\mu\mu}}{m_{\mu s}} = 2\left(\frac{m_{e\mu}}{m_{es}}\right)$
B_3	$(c, e, f, h = 0)$	$(C, D \neq 0)$	$(s_1 \quad 0 \quad s_3)$	$m_{e\tau}m_{\mu s} = m_{es}m_{\mu\tau}$
B_4	$(c, d, h, i = 0)$	$(C, D \neq 0)$	$(s_1 \quad 0 \quad s_3)$	$m_{ss}m_{\mu\tau} = 2m_{\tau s}m_{\mu s}$
C	$(e, f, g, h = 0)$	$(C, D \neq 0)$	$(s_1 \quad 0 \quad s_3)$	$m_{ss}m_{\mu\tau} = 2m_{\mu s}m_{\tau s}$
D_1	$(c, d, f, g = 0)$	$(B, F \neq 0)$	$(s_1 \quad 0 \quad s_3)$	$m_{ee}m_{\mu s} = 2m_{es}m_{e\mu}$
D_2	$(a, e, h, i = 0)$	$(B, F \neq 0)$	$(s_1 \quad s_2 \quad 0)$	$m_{e\tau}m_{ss} = 2m_{\tau s}m_{es}$
E_1	$(a, c, e, f = 0)$	$(B, F \neq 0)$	$(s_1 \quad s_2 \quad 0)$	$m_{\tau s}m_{e\mu} - m_{e\tau}m_{\mu s} = m_{\mu\tau}m_{es}$
E_2	$(a, c, h, i = 0)$	$(B, F \neq 0)$	$(s_1 \quad s_2 \quad 0)$	$\frac{m_{\mu s}}{m_{\tau s}} - \frac{m_{e\mu}}{m_{e\tau}} = \frac{m_{\mu\tau}m_{es}}{m_{\tau s}m_{e\tau}}$
F_1	$(a, c, e, h = 0)$	$(C, D \neq 0)$	$(s_1 \quad s_2 \quad 0)$	$2m_{\mu\tau}m_{\mu s}m_{\tau s} - m_{\mu\mu}m_{\tau s}^2 = m_{\mu s}^2 m_{\tau\tau}$
F_2	$(b, d, f, h = 0)$	$(C, D \neq 0)$	$(0 \quad s_2 \quad s_3)$	$m_{\mu\mu}m_{ss} = m_{\mu s}^2$
F_3	$(c, f, g, h = 0)$	$(B, F \neq 0)$	$(0 \quad s_2 \quad s_3)$	$2\left(\frac{m_{e\tau}}{m_{es}}\right) - \frac{m_{\tau\tau}}{m_{\tau s}} = \frac{m_{ee}m_{\tau s}}{m_{es}^2}$

It has been found that out of 15 only 12 two-zero textures can be realized in the $(4 + 4)$ scheme: Texture A_1 with $ee = 0, e\mu = 0$; Texture A_2: $ee, e\tau = 0$; B_3 : $e\mu, \mu\mu = 0$; $B_4 : e\tau, \tau\tau = 0$; $C = \mu\mu, \tau\tau = 0$, $D_1 : \mu\mu, \mu\tau = 0$; $D_2 : \mu\tau, \tau\tau = 0$, $E_1 = ee, \mu\mu = 0$, $E_2 = ee, \tau\tau = 0$, $F_1 = e\mu, e\tau = 0$, $F_2 = e\mu, \mu\tau = 0$, $F_3 = e\tau, \mu\tau = 0$ [3]. In our work we shall realize these 12 textures considering $(4 + 4)$ scheme and 4×4 form of MES mass matrix in (42.2).

42.3 Realization of Two-Zero Textures Under (4 + 4) Scheme

We present the realization of the 12 two-zero textures along with their respective correlations in Table 42.1. Here the second, third and fourth column represents four-zero elements of M_D, two non-zero elements of M_R and one-zero texture of M_S respectively. The fifth column represents the correlation that are generated when zeros are imposed on $M_\nu^{4\times4}$.

In order to test the survivability of the textures, we scan the correlations of each texture under 1σ range of oscillation data. We keep the Dirac $(\delta_{14}, \delta_{24})$ and Majorana (α, β, γ) CP phases unconstrained, that is, $0 - 2\pi$. In our analysis we consider 1σ range of $\delta_{13} = (212^0 - 290^0)$ for normal hierarchy(NH) and $\delta_{13} = (202^0 - 292^0)$ for inverted hierarchy (IH) case [6]. Constraints on sterile neutrino parameters are from [7–9]. As a representative case we present the scatter

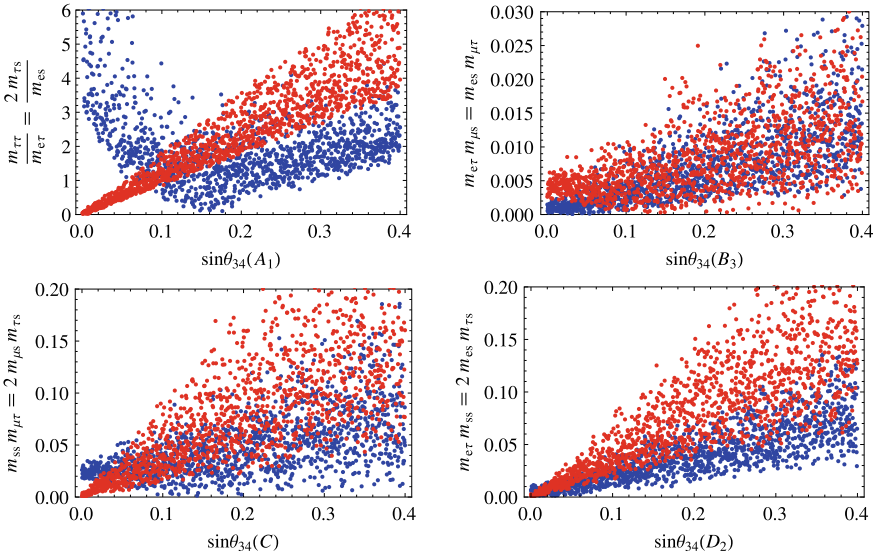

Fig. 42.1 Scatter plots for texture A_1 (upper left), B_3 (upper right), C (lower left), D_2 (lower right). Blue and red dots represent the lhs and rhs of a correlation respectively

plots for texture A_1, B_3, C, D_2 in Fig. 42.1 for NH case. The correlations are plotted against $\sin\theta_{34} = (0 - 0.4)$. From the figure for texture A_1 (upper left plot) it is evident that, overlapping between the left hand side (lhs) and right hand side (rhs) of the correlation persists only for values of $\sin\theta_{34} = (0.08 - 0.22)$ and thus the texture is allowed only within that range of $\sin\theta_{34}$. Similarly, the textures B_3, C are allowed for values of $\sin\theta_{34} = (0.04 - 0.4)$ while texture D_2 is allowed for all values of $\sin\theta_{34} = (0 - 0.4)$. Allowed values of $\sin\theta_{34}$ for the remaining textures are found to be $A_2 : (0.04 - 0.4)$, $B_4 : (0.08 - 0.4)$, D_1, $F_2 : (0.08 - 0.34)$, E_1, $E_2 = (0.04 - 0.08)$, F_1, $F_3 : (0 - 0.4)$.

42.4 Conclusion

In this chapter we have studied the phenomenology of two-zero textures of $M_\nu^{4\times4}$ and found that out of 15 only 12 two-zero textures can be realized in the context of $(4 + 4)$ scheme and MES mechanism. Realization of the textures have led to some correlations which have been examined under 1σ range of oscillation data. We have found that the some textures are viable for some selective range of $\sin\theta_{34}$ while certain textures are allowed for all range of $\sin\theta_{34} = (0 - 0.4)$.

References

1. C. Athanassopoulos et al., Phys. Rev. Lett. **77**, 3082 (1996); A. Aguilar et al., Phys. Rev. D **64**, 112007 (2001)
2. J. Barry, W. Rodejohann, H. Zhang, JHEP **1107**, 091 (2011). arXiv:1105.3911
3. M. Ghosh, S. Goswami, S. Gupta, JHEP **1304**, 103 (2013). arXiv:1211.0118
4. L. Lavoura, J. Phys. G **42**, 105004 (2015). arXiv:1502.0300
5. M. Patgiri, P. Kumar, D. Sarma, Study of texture zeros of fermion mass matrices in minimal extended seesaw mechanism and symmetry realization. Int. J. Mod. Phys. A **32**(27), 1750168 (2017)
6. F. Capozzi, E. Di Valentino, E. Lisi, A. Marrone, A. Melchiorri, A. Palazzo, Global constraints on absolute neutrino masses and their ordering. Phys. Rev. D **95**, 096014 (2017). arXiv:1703.04471
7. S. Gariazzo, C. Giunti, M. Laveder, Y.F. Li, E.M. Zavanin, Light sterile neutrinos. J. Phys. **G43**, 033001 (2016). arXiv:1507.0820
8. C. Giunti, Oscillations beyond three-neutrino mixing, in *Talk given at Proceedings of Neutrino 2016*, London UK (2016)
9. T. Schwetz, Global oscillation fits with sterile neutrinos, in *Talk given at Proceedings of Sterile Neutrino Crossroads, 2011* (Virginia Tech, USA, 2011)

Chapter 43
Effects of Nonstandard Interactions on Coherence in Neutrino Oscillations

Khushboo Dixit and Ashutosh Kumar Alok

Abstract We study the effects of non-standard neutrino matter interactions on the coherence of oscillating neutrino-system in a model independent way in the context of upcoming DUNE experiment. We find that the LMA-LIGHT solution (with normal ordering of mass eigenstates) decreases the coherence in the system in comparison to the standard model prediction for almost all values of neutrino energy E and CP violating phase δ. However, a large enhancement in coherence parameter in the entire $(E - \delta)$ plane is possible for the DARK octant of θ_{12} for inverted ordering, with a protuberant enhancement at $E \sim 4\,\text{GeV}$, where maximum neutrino flux is expected in the DUNE experiment. Such features make neutrino a promising candidate for carrying out quantum information theoretic tasks.

43.1 Introduction

The phenomenon of neutrino oscillation is a consequence of the quantum superposition principle which makes the quantum coherence an indispensable part of the system. The coherence is a fundamental concept in quantum mechanics and reflects the degree of quantumness of the system. The system of oscillating neutrinos can maintain quantum coherence over a large distance which can be detected in long baseline experiments. Hence, neutrinos can prove to be promising candidates for various tasks related to quantum information. Therefore, it is pertinent to quantify the quantumness of the oscillating neutrino system.

The phenomena of neutrino oscillation implies physics beyond the standard model (SM) suggesting non-zero mass of neutrino. A hint of lepton flavor non-universality, in disagreement with the SM, has been observed in the decays induced by the quark level transitions $b \to c l \nu$ $(l = e, \mu, \tau)$ and $b \to s\, l^+ l^-$ $(l = e, \mu)$. Lorentz structures

Speaker: Khushboo Dixit.

K. Dixit (✉) · A. Kumar Alok
Indian Institute of Technology Jodhpur, Jodhpur 342037, India
e-mail: dixit.1@iitj.ac.in

A. Giri and R. Mohanta (eds.), *Workshop on Frontiers in High Energy Physics 2019*, Springer Proceedings in Physics 248,
https://doi.org/10.1007/978-981-15-6292-1_43

of possible new physics in these decay modes [1–4] can be generated in new physics models, such as Z' and leptoquark models. The existence of these new particles can also affect the pattern of neutrino oscillations. A convenient way to describe these new physics effects in neutrino interactions in the electroweak broken phase are the so called non-standard interaction (NSI) parameters. In view of recent updates on oscillation parameters [5, 6], we study the effects of NSI on the quantum coherence of the neutrino system in a model-independent approach within the context of DUNE experimental set-up [7].

43.2 Dynamics of Neutrino System with NSI Effect

We consider the neutral-current (NC) interactions driven by NSI relevant to neutrino propagation in matter. The Lagrangian can be written as

$$\mathcal{L}_{NSI} = -2\sqrt{2}G_F \sum_{f,P,\alpha,\beta} \epsilon_{\alpha,\beta}^{f,P} (\bar{\nu}_\alpha \gamma^\mu P_L \nu_\beta)(\bar{f}\gamma_\mu P f), \tag{43.1}$$

where G_F is the Fermi constant, α and β are flavor indices, P_L & P_R are the projection operators and f is the charged fermion. Here, $\epsilon_{\alpha,\beta}^{f,P} \sim \mathcal{O}(G_x/G_F)$ represents the strength of the new interaction with respect to the SM interaction. If the flavor of neutrinos participating in the interaction is considered to be independent of the charged fermion type, one can write

$$\epsilon_{\alpha\beta}^{f,P} \equiv \epsilon_{\alpha\beta}^{\eta}\, \xi^{f,P}, \tag{43.2}$$

where matrix elements $\epsilon_{\alpha\beta}^{\eta}$ correspond to the coupling between neutrinos and the coefficients $\xi^{f,P}$ represent the coupling to the charged fermions. The Hamiltonian for the evolution of neutrino-state, in mass eigenstate basis, including NSI effect can be written as $\mathcal{H}_m = H_m + U^{-1} V_f U$, where $H_m = \text{diag}(\text{E}_1, \text{E}_2, \text{E}_3)$ and U is the 3×3 unitary (PMNS) matrix which differs from the usual one by an overall phase matrix $P = \text{diag}(\text{e}^{\text{i}\delta}, 1, 1)$. The matter part V_f of the Hamiltonian including the operators corresponding to the NSI effect is given as

$$V_f = A \begin{pmatrix} 1+\epsilon_{ee}(x) & \epsilon_{e\mu}(x) & \epsilon_{e\tau}(x) \\ \epsilon_{e\mu}^*(x) & \epsilon_{\mu\mu}(x) & \epsilon_{\mu\tau}(x) \\ \epsilon_{e\tau}^*(x) & \epsilon_{\mu\tau}^*(x) & \epsilon_{\tau\tau}(x) \end{pmatrix}, \tag{43.3}$$

with $A = \sqrt{2}G_F N_e(x)$. and $\epsilon_{\alpha\beta} = \sum_{f=e,u,d} \frac{N_f(x)}{N_e(x)} \epsilon_{\alpha\beta}^f$, $N_f(x)$ is the number density of fermion f as a function of the distance x traveled by neutrino and we can write $N_u(x) = 2N_p(x) + N_n(x)$ and $N_d(x) = N_p(x) + 2N_n(x)$. Therefore, we can write $\epsilon_{\alpha\beta} = (2 + Y_n)\epsilon_{\alpha\beta}^u + (1 + 2Y_n)\epsilon_{\alpha\beta}^d$, with $Y_n = N_n/N_e$, N_e is the number density of

electrons and $N_p = N_e$. In order to obtain the evolution operator U_f, we use the formalism given in [8] and it is obtained as

$$U_f(L) = e^{-i\mathcal{H}_f L} = U e^{-i\mathcal{H}_m L} U^{-1} = \phi \sum_{a=1}^{3} e^{-iL\lambda_a} \frac{1}{3\lambda_a^2 + c_1} \left[(\lambda_a^2 + c_1)\mathbf{I} + \lambda_a \tilde{T} + \tilde{T}^2\right], \tag{43.4}$$

where $\phi = e^{-iL\mathrm{Tr}(\mathcal{H}_m/3)}$, $T = \mathcal{H}_m - \mathrm{Tr}(\mathcal{H}_m)\mathbf{I}/3$, $\mathrm{Tr}(\mathcal{H}_m) = E_v + A(1 + \epsilon_{ee} + \epsilon_{\mu\mu} + \epsilon_{\tau\tau})$, $\tilde{T} \equiv UTU^{-1}$, λ_a (eigenvalues of T), $a = 1, 2, 3$ and $c_1 = \det(T)\ \mathrm{Tr}(T^{-1})$.

The CPT-transformation of $\mathcal{H}_f$ involves the change of the octant of θ_{12} (DARK octant with $\theta_{12} > 45°$) and the change in the sign of Δ_{31} that is responsible to generate the LMA-DARK solution, (besides the usual LMA-LIGHT solution), of solar neutrino problem.

43.3 Quantum Coherence in Neutrino System

Among several measures, we use the l_1-norm of coherence [9] which is expressed as the sum of the absolute values of off-diagonal elements of the density matrix $\rho = |\psi\rangle\langle\psi|$

$$\chi = \sum_{i \neq j} |\rho_{ij}|. \tag{43.5}$$

This measure is a positive, convex function and is monotonic under incoherent operations. For a completely incoherent state (often called as *mixed states*), the off-diagonal elements are zero. Recently, in [10], the parameter χ has been expressed in terms of neutrino survival and transition probabilities. Thus, it is the most feasible measure of coherence from the viewpoint of current neutrino experimental facilities. The maximum attainable value of χ is $d - 1$ where d is the dimension of the system. For three flavor neutrino system, $|\psi(t)\rangle \equiv |\nu_\alpha(t)\rangle = \sum_{i=1,2,3} U_{fij}(t)|\nu_\beta\rangle$, with $\{j, \beta\} = \{\{1, e\}, \{2, \mu\}, \{3, \tau\}\}$. Here U_{fij} are elements of the evolution operator in flavor basis.

43.4 Results and Discussions

In Fig. 43.1, we studied χ^{SM} and χ^{NSI} in the context of DUNE experiment. The oscillation parameters are $\theta_{12} = 33.82°$ (for both SM as well as LMA-LIGHT solution) and 56.18° (for LMA-DARK solution), $\theta_{23} = 49.6°$, $\theta_{13} = 8.61°$, $\Delta_{21} = 7.39 \times 10^{-5}\,\mathrm{eV}^2$ and $|\Delta_{32}| = 2.525 \times 10^{-3}\,\mathrm{eV}^2$ [11]. We obtain $0.1 \leq \chi^{SM} \leq 1.67$ with $\chi^{SM} \geq 1.5$ in the range $E \in (4 - 6)\,\mathrm{GeV}$ for $+\Delta_{31}$. Using [5], we found that LMA-L+NO solution reduces χ^{NSI} as compared to the SM, except in the region $\delta \in (0 - 2)$ and $(5 - 6)$ for $E \in (4 - 6)\,\mathrm{GeV}$. The LMA-L+IO solution enhances

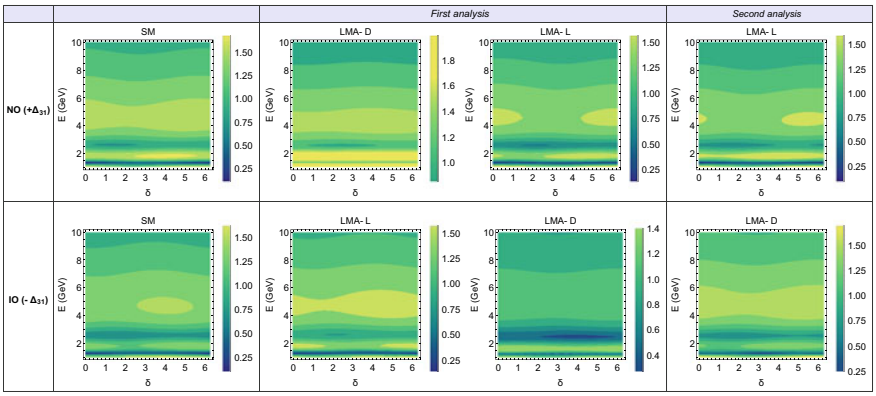

Fig. 43.1 Coherence parameter χ plotted in the $E - \delta$ plane in the context of DUNE experiment

χ^{NSI} with prominent enhancement in the region $E \in (4-6)\,\text{GeV}$ for $\delta \in [0, 2\pi]$ and at $E \approx 2\,\text{GeV}$ for $\delta \in (0-2)$ and $(4-6)$. For LMA-D+NO, we get large enhancement for $E \leq 2\,\text{GeV}$ and marginal suppression of χ_f^{NSI} for $E \geq 2\,\text{GeV}$ while for LMA-D+IO overall suppresses χ_f^{NSI} for all $\delta \in [0, 2\pi]$. Using results of [6], we found that the LMA-L+NO solution marginally decreases the value of coherence parameter in comparison to the SM. For the LMA-D+IO solution, the coherence in the system is enhanced around $E \approx 4\,\text{GeV}$ (this energy correspond to the maximum neutrino flux at DUNE), for almost all values of $\delta \in [0, 2\pi]$.

43.5 Conclusions

In the DUNE experimental set-up, we find that the LMA-LIGHT+NO solution marginally decreases the value of coherence parameter in comparison to the SM. For the LMA-DARK+IO solution the coherence in the system is enhanced around $E \approx 4\,\text{GeV}$, the energy corresponding to maximum neutrino flux at DUNE, for almost all values of CP violating phase. It is observed that the SM interaction with normal hierarchy (and NSI with inverted hierarchy (LMA-D)) show an increase in the degree of coherence. These features, along with the fact that neutrinos interact very feebly, make it a promising candidate for carrying out the quantum information tasks.

References

1. M. Algueró, B. Capdevila, A. Crivellin, S. Descotes-Genon, P. Masjuan, J. Matias, J. Virto, Eur. Phys. J. C **79**(8), 714 (2019)
2. A.K. Alok, A. Dighe, S. Gangal, D. Kumar, JHEP **1906**, 089 (2019)

3. J. Aebischer, W. Altmannshofer, D. Guadagnoli, M. Reboud, P. Stangl, D.M. Straub, arXiv:1903.10434 [hep-ph]
4. A.K. Alok, D. Kumar, J. Kumar, S. Kumbhakar, S.U. Sankar, JHEP **1809**, 152 (2018)
5. I. Esteban, M.C. Gonzalez-Garcia, M. Maltoni, I. Martinez-Soler, J. Salvado, JHEP **1808**, 180 (2018)
6. I. Esteban, M.C. Gonzalez-Garcia, M. Maltoni, JHEP **1906**, 055 (2019)
7. K. Dixit, A.K. Alok, arXiv:1909.04887 [hep-ph]
8. T. Ohlsson, H. Snellman, Phys. Lett. B **474**, 153 (2000)
9. T. Baumgratz, M. Cramer, M.B. Plenio, Phys. Rev. Lett. **113**, 140401 (2014)
10. X.K. Song, Y. Huang, J. Ling, M.H. Yung, Phys. Rev. A **98**, 050302(R) (2018)
11. I. Esteban, M.C. Gonzalez-Garcia, A. Hernandez-Cabezudo, M. Maltoni, T. Schwetz, JHEP **1901**, 106 (2019)

Chapter 44
Lorentz Invariance Violation and Long Baseline Experiments

Rudra Majhi, C. Soumya, and Rukmani Mohanta

Abstract Neutrinos interact only through weak interaction. This property will help us to study Planck suppressed physics, as neutrinos can propagate very long distances without any deviation and any small deviation to the Planck scale physics during the propagation can be detected through Long Baseline experiments. So, in this study we have used neutrino oscillation as a testing ground to test the CPT violation through Lorentz invariance violation (LIV) in long baseline experiment NOνA. We have shown the effects of the Lorentz violating operators at Probability level and on CP violation sensitivity of the experiment and also obtained constraints on the parameters.

44.1 Introduction

CPT is the basic symmetry of the nature and it is based on the Hermiticity, Locality and Lorentz invariance of the theory. CPT violation is possible through the Lorentz Invariance violation. CPT violation and Lorentz violation are the small scale physics which are tiny deviation from the relativity. Neutrinos are more suitable particle to probe CPT violation through Long baseline experiments. Although, experimental bounds are there from Kaon and Lepton sector on CPT and Lorentz violation, which are quite stringent. Lorentz violation demands a universal length scale, which will contradict with the special theory of relativity. The apparent solution to this contradiction is the modification of the dispersion relation. This modification will affect

R. Majhi (✉) · R. Mohanta
University of Hyderabad, Hyderabad 500 046, India
e-mail: rudra.majhi95@gmail.com

R. Mohanta
e-mail: rukmani98@gmail.com

C. Soumya
Institute of Physics, Sachivalaya Marg, Bhubaneswar 751005, India
e-mail: soumyac20@gmail.com

A. Giri and R. Mohanta (eds.), *Workshop on Frontiers in High Energy Physics 2019*, Springer Proceedings in Physics 248,
https://doi.org/10.1007/978-981-15-6292-1_44

Table 44.1 The values of oscillation parameters that we consider in our analysis [4]

Parameter	$\sin^2\theta_{12}$	$\sin^2\theta_{13}$	$\sin^2\theta_{23}$	δ_{CP}	Δm^2_{12}	Δm^2_{31}
True values	0.310	0.02240	0.5	$-\pi/2$	$7.39 \times 10^{-5}\,\text{eV}^2$	$2.5 \times 10^{-3}\,\text{eV}^2$
3σ range	NA	NA	$0.4 \rightarrow 0.6$	$[-\pi, \pi]$	NA	$(2.36 \rightarrow 2.64) \times 10^{-3}\,\text{eV}^2$

the neutrino oscillation probability as well as the unknowns in the neutrino sector as discussed in the [1].

Perturbation terms can be add to the standard neutrino physics to include the LIV effect. The Hamiltonian for neutrinos, including LIV is

$$H = H_{vac} + H_{mat} + H_{LIV} \tag{44.1}$$

Where H_{vac} and H_{mat} corresponds to the Hamiltonian for vacuum and matter effect, while H_{LIV} is the Lorentz violating Hamiltonian.

$$H_{LIV} = \begin{pmatrix} a_{ee} & a_{e\mu} & a_{e\tau} \\ a^*_{e\mu} & a_{\mu\mu} & a_{\mu\tau} \\ a^*_{e\tau} & a^*_{\mu\tau} & a_{\tau\tau} \end{pmatrix} - \frac{4}{3}E \begin{pmatrix} c_{ee} & c_{e\mu} & c_{e\tau} \\ c^*_{e\mu} & c_{\mu\mu} & c_{\mu\tau} \\ c^*_{e\tau} & c^*_{\mu\tau} & c_{\tau\tau} \end{pmatrix} \tag{44.2}$$

The dimensions of $a_{\alpha\beta}$ and $c_{\alpha\beta}$ are different, $a_{\alpha\beta}$ and $c_{\alpha\beta}$ are proportional to baseline L and LE respectively. In this study we have considered only $a_{\alpha\beta}$ parameters for the analysis, then it is quite similar to the presence of NSI during propagation.

44.2 Simulation Details

As our analysis focused on currently running long baseline experiments NOνA, we simulate the experiment using GLoBES software package along with snu plugin [2, 3]. Implementation of LIV have done similar to the NSI case. In our analysis, we use the values of oscillation parameters as given in Table 44.1.

The value for all the diagonal LIV elements considered as $|a_{\alpha\alpha}| = 1 \times 10^{-22}\,\text{GeV}$ and for the off-diagonal elements as $|a_{\alpha\beta}| = 2 \times 10^{-23}\,\text{GeV}$. The LIV phases are in the allowed region $[-\pi, \pi]$.

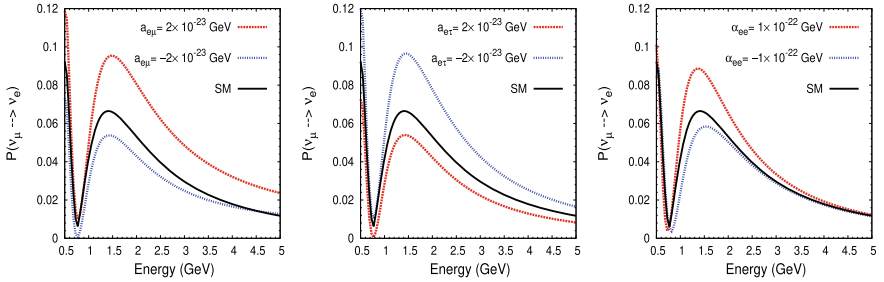

Fig. 44.1 Probability as a function of Energy for different $a_{\alpha\beta}$ for NOνA experiment

44.3 Result

The long-baseline experiments are mainly looking for the $\nu_\mu \to \nu_e$ and $\overline{\nu}_\mu \to \overline{\nu}_e$ channels. Analytical expression for the ν_e appearance and disappearance channel ($\nu_\mu \to \nu_\mu$) can be found in [5]. In Fig. 44.1 top panel represent the ν_e appearance probability. LIV parameters a_{ee}, $a_{e\mu}$ and $a_{e\tau}$ contribute in leading order to the appearance probability, have shown in the figure. In each plot black curve is for the standard three flavor oscillation probabilities and red (blue) dotted curve corresponds to positive (negative) values of the LIV parameters. In all cases significant effect of Lorentz violation have been observed.

We have shown the potential of NOνA experiment to constrain the LIV parameters as shown in Fig. 44.2. The bounds for the parameters (in GeV) at 2σ C.L. are:

$$|a_{e\mu}| < 4.6 \times 10^{-23}\ , \quad |a_{e\tau}| < 1.71 \times 10^{-22}, \quad |a_{\mu\tau}| < 9.35 \times 10^{-23}\ ,$$
$$[-5.9, 3.8] \times 10^{-22} \approx a_{ee}\ , [-1.1, 1.2] \times 10^{-22} \approx a_{\mu\mu}\ , [-1.2, 0.96] \times 10^{-22} \approx a_{\tau\tau} \tag{44.3}$$

CP violating phase plays a crucial role in Neutrino sector. We have shown the sensitivity to exclude the CP conserving value as a function of true δ_{CP} in Fig. 44.3. The black curve represents the standard matter effect case in each panel. The diagonal elements a_{ee}, $a_{\mu\mu}$ and $a_{\tau\tau}$ are shown as blue, green and red curve respectively as in top left panel of Fig. 44.3. Rest of the panels are for the off-diagonal elements $a_{e\mu}$, $a_{e\tau}$ and $a_{\mu\tau}$. Due to the extra phases of the off diagonal parameters, by varying the phase in the allowed region $[-\pi, \pi]$, we are getting the band structure. In all the cases of diagonal and non diagonal LIV parameters, significant impact on CPV sensitivities observed. Also, for some values of the non-diagonal phase of the LIV parameters, the CPV sensitivity can be enhanced compared to the standard case. One can obtain a significant sensitivity in presence of Lorentz violation where there is no such or very small sensitivities in standard case.

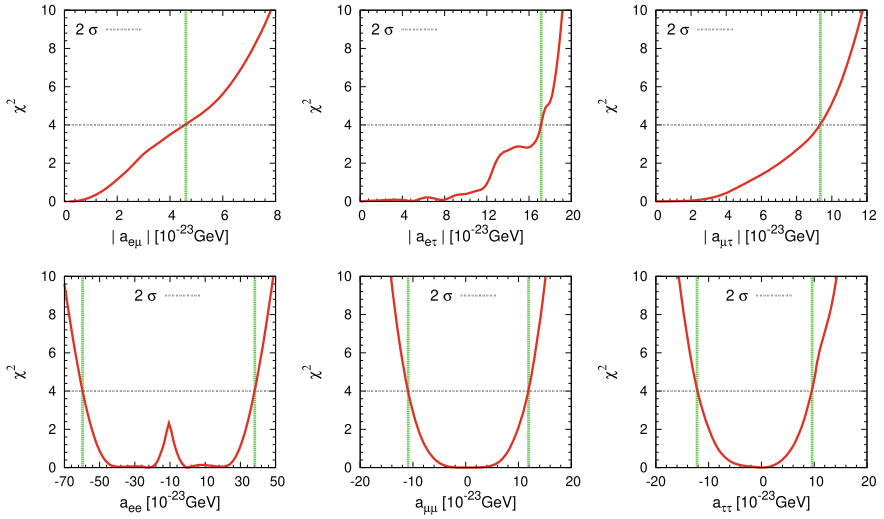

Fig. 44.2 Bounds on LIV parameters from NOνA experiment

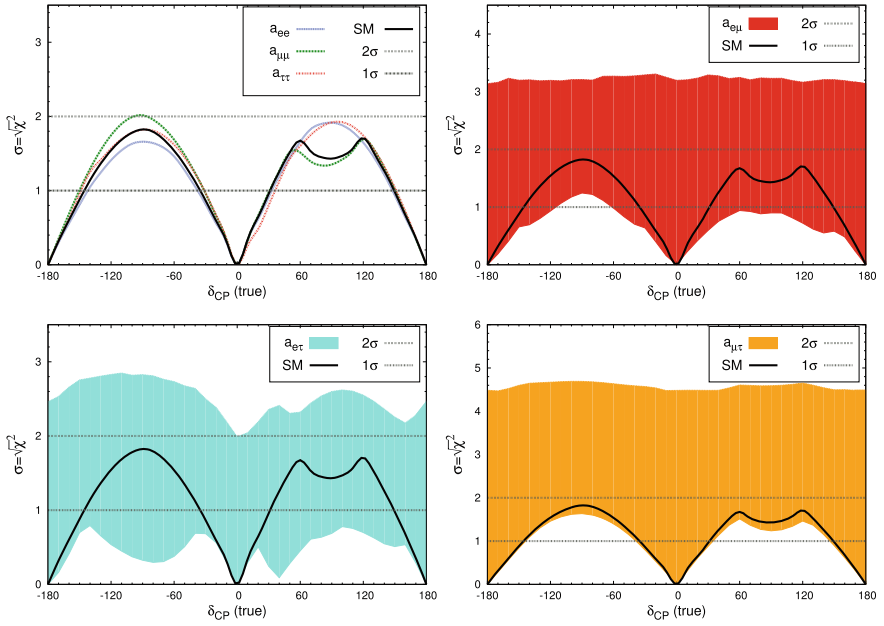

Fig. 44.3 CP violation sensitivity for NOνA experiment

44.4 Conclusion

CPT violation can be possible by including the Lorentz violation in the theory, which are small scale physics effects. Such effects can be probed in Long baseline experiments. Lorentz violating parameters have impact at probability and CPV sensitivity level. The CP violation sensitivities may enhance or deteriorate depending on the absolute value and phases of the Lorentz violating parameter. Also the impacts on the mass hierarchy and octant sensitivities due to the Lorentz violation can be studied in long baseline experiments. Precise bounds on the LIV parameters can be obtained from long baseline neutrino oscillation experiments.

Acknowledgements We would like to thank DST INSPIRE and SERB, Govt. of India for financial support.

References

1. G. Barenboim, M. Masud, C.A. Ternes, M. Tórtola, Phys. Lett. B **788**, 308 (2019). https://doi.org/10.1016/j.physletb.2018.11.040, arXiv:1805.11094 [hep-ph]
2. P. Huber, M. Lindner, W. Winter, Comput. Phys. Commun. **167**, 195 (2005). https://doi.org/10.1016/j.cpc.2005.01.003, arXiv:hep-ph/0407333
3. P. Huber, J. Kopp, M. Lindner, M. Rolinec, W. Winter, Comput. Phys. Commun. **177**, 432 (2007). https://doi.org/10.1016/j.cpc.2007.05.004, arXiv:hep-ph/0701187
4. I. Esteban, M.C. Gonzalez-Garcia, A. Hernandez-Cabezudo, M. Maltoni, T. Schwetz, JHEP **1901**, 106 (2019). https://doi.org/10.1007/JHEP01(2019)106, arXiv:1811.05487 [hep-ph]. NuFIT 4.0 (2018), www.nu-fit.org
5. R. Majhi, C. Soumya, R. Mohanta, Eur. Phys. J. C **80** no.5, 364 (2020) https://doi.org/10.1140/epjc/s10052-020-7963-1, arXiv:1907.09145 [hep-ph]

Part IV
QCD and Heavy Ion Physics

Chapter 45
Do Proton+Proton Collisions at the LHC Energies Produce Droplets of Quark-Gluon Plasma?

Raghunath Sahoo

Abstract The proton-proton (pp) collisions at the Large Hadron Collider (LHC), CERN, Switzerland has brought up new challenges and opportunities in understanding the experimental findings in contrast to the conventional lower energy pp collisions. Usually pp collisions are used as the baseline measurement at the GeV and TeV energies in order to understand a possible high density QCD medium formation in heavy-ion collisions. However, the TeV pp collisions have created a new domain of research, where scientists have started observing heavy-ion-like features (signatures) in high-multiplicity pp collisions. This warrants a relook into TeV pp collisions, if at all QGP-droplets are produced in such collisions. In this presentation, I discuss some of the new findings and concepts emerging out in pp collisions at the LHC energies along with some of the new emergent phenomena in particle production.

45.1 Introduction

Relativistic heavy-ion collisions aim at producing the primordial matter in the laboratory, thermodynamics of which is governed by partons – quarks and gluons, instead of the usual hadrons. The Universe at its infancy, was believed to be filled with such a deconfined matter of quarks and gluons. To recreate and characterize such a system in the laboratory, proton-proton (pp) collisions are usually used as baseline measurements assuming no such creation of partonic medium and deconfinement transition in these collisions. This is the case till the Relativistic Heavy Ion Collider (RHIC), Brookhaven National Laboratory, USA pp collisions at a center-of-mass energy, $\sqrt{s} = 200\,\text{GeV}$. However, going from RHIC to the CERN Large Hadron Collider (LHC), where there is 35–65 times higher collision energies available in hadronic (pp) collisions, a new domain of particle production has possibly been created. This is because of new observations like strangeness enhancement, long-range

R. Sahoo (✉)
Discipline of Physics, School of Basic Sciences, Indian Institute of Technology Indore, Indore 453552, India
e-mail: Raghunath.Sahoo@cern.ch

A. Giri and R. Mohanta (eds.), *Workshop on Frontiers in High Energy Physics 2019*, Springer Proceedings in Physics 248,
https://doi.org/10.1007/978-981-15-6292-1_45

correlations, collectivity in small systems (pp) etc., which are initially perceived to be signatures of Quark-Gluon Plasma (QGP) and expected to be seen in central heavy-ion collisions [1]. The LHC energy frontier opens up new challenges in understanding the multiplicity dependent experimental data and further characterizing the produced systems using differential variables.

A deconfined state of partons is expected either at very high temperatures and energy densities pertaining to an early universe scenario (LHC) or through the compression of nuclei so that the physical boundaries of the hadrons vanish so as to create a free domain in which the partons seem to roam around, the volume of which is higher than the hadronic volume. The latter is expected to happen at lower collision energies, possibly at the FAIR or NICA. When the former points to a net-baryon free regime, the latter is baryon-rich domain of the Quantum Chromodynamics (QCD) phase diagram. For the present discussions, we shall stay close to the early universe scenario, which is the LHC energy domain. The chemical freeze-out temperature where all the inelastic particle producing interactions stop and the initial energy density measured at the LHC energies are much higher than the lattice QCD prediction for a deconfinement transition. These are the two basic requirements after which, one looks for all the possible indirect signatures of QGP, as it is highly short-lived. The kinetic freeze-out temperature, $T_{\rm kin}$ measured from the simultaneous Blastwave model fitting to the low-p_T multi-strange particle data taken by the ALICE experiment in pp collisions at $\sqrt{s} = 7\,\text{TeV}$ reveals that $T_{\rm kin}$ is comparable to that one obtains in p-Pb and Pb-Pb collisions. This is found to be higher than the critical temperature ($T_{\rm c}$) for the deconfinement transition [2].

45.2 Basic Requirements for the Formation of QGP

It is well-known that high energy accelerators help us to revisit the earlier and hotter history of our Universe searching for a new simplicity by observing phenomena and particles no longer observed in our everyday experience. In this regards, three small and fundamental equations of Physics play a crucial role. Those are the famous de Broglie equation: $E \propto 1/size$, Einstein's equation: $E = (\sum_i m_i)c^2$ and Boltzmann equation: $E = k_B T$. Higher collision energies thus help in probing lower length scales, producing a spectrum of new particles and also creating very high temperatures, which pertain to an early time scenario. Through the head-on collisions of heavy nuclei like Au+Au or Pb+Pb one creates very high temperature (almost 10^5 times the core of the Sun) and energy density (order of magnitude higher than the normal nuclear matter density) in the laboratory. Our theoretical estimations driven by lattice QCD for a deconfinement transition to happen are the critical temperature, $T_c \sim 150 - 170\,\text{MeV}$ and the critical energy density, $\epsilon_c \sim 1\,\text{GeV/fm}^3$ [3, 4]. It is also seen that near this criticality the degrees of freedom of the system rises sharply [5]. The new deconfined phase of partons is highly short-lived (lifetime $\sim 10^{-23}$ s) and hence the signatures of such a plasma are all indirect in nature. The major signatures of QGP are: strangeness enhancement, elliptic flow (and the higher

order harmonics), suppression of quarkonia, long-range correlations, higher degree of collective radial expansion etc. QGP is perceived to be a thermally equilibrated (local) state of partons in a domain of volume, which is higher than the hadronic dimension. Thermalization is a requirement for the QGP formation and this can happen through mutual interactions of the system quanta given the volume of the fireball is sufficient enough or in a smaller volume like that of pp collisions, this could possibly also happen through multiple interactions leading to the phenomenon of multipartonic interactions (MPI), if the quanta have sufficient momentum. This also goes inline with the requirement of a hydrodynamic scenario in pp collisions, where one expects the mean free path of the system to be less than the system size and the space-time variation of local thermodynamic quantities should be less than the thermalization rate of the system, which is controlled by microscopic interactions. Although it was expected from the start of the RHIC at BNL that QGP will behave like an ideal gas and would approach the Stefan–Boltzmann limit of different thermodynamic observables, after the discoveries are made, it was revealed that it behaves like a "*perfect fluid*", with minimum shear viscosity to entropy ratio, η/s seen in nature [6]. Although QGP was discovered at the RHIC energies, the LHC heavy-ion runs were expected to bring new domains of particle production and some of the QGP signatures would depend on collision energy, like that was seen for the degree of quarkonia suppression at the LHC, which was found to be smaller than that of RHIC. The LHC pp collisions, however has brought up new scaling laws in the final state irrespective of the collision energy and collision species, showing the final state multiplicity is the driving (scaling) observable. Let's now look into some of the important observations in LHC pp collisions before drawing any conclusion or giving any outlook for the possible formation of QGP-droplets in such hadronic collisions at the LHC [7].

45.3 Proton-Proton Collisions at the LHC

The ALICE experiment has observed the enhancement of multi-strange particles in high-multiplicity pp collisions and the enhancement is found to be comparable with p-Pb and Pb-Pb collisions at similar multiplicities [2]. A simultaneous fitting of Blastwave model to the low-p_T (bulk) of the spectra of multi-strange particles shows a degree of collective radial flow ($< \beta >= 0.49 \pm 0.02$) and kinetic freeze-out temperature ($T_{\text{kin}} = 163 \pm 10$ MeV), which is comparable to the critical temperature, T_c, while hardening of the spectra is also seen towards higher multiplicity classes [2]. The CMS experiment has parallely come up with a highly interesting observation of near-side long-range ridge-like two particle correlations in high-multiplicity pp collisions [10], which was first observed in heavy-ion collisions at the RHIC energies. There are attempts to understand these heavy-ion-like observations in LHC pp high-multiplicity events in order to conclude if these indicate to a new physics or QGP-droplets are formed in these hadronic collisions. In view of this, there are explorations through different theoretical models to confront to these experimental observations.

The strangeness enhancement in high-multiplicity pp collisions is explained by theoretical models like DIPSY, where the interactions between gluonic strings are allowed to form color ropes and through the mechanism of "rope hadronization", strangeness is produced. In addition, the radial flow observed in pp collisions is also explained through "color reconnection" mechanism in PYTHIA8. In the direction of small systems and thermalization, which is always a matter of great debate, if one assumes the availability of sufficient energy leading to the participating partons to have enough momentum to go through multiple interactions, the emerging phenomenon, MPI happens to explain some of the features observed in experiments. For instance MPI seems to explain the forward rapidity J/ψ production in pp collisions at the LHC [11]. Although long-range near-side ridge in two particle correlation has a hydrodynamic origin, small system hydrodynamics is a question by itself. As explained above, one can expect hydrodynamic collectivity at the partonic level possibly through multipartonic interactions and this could be a reality at TeV energies, when one starts to see the dominance of gluons and sea quarks in the system. As explained in [12], the observed ridge-like structure in high-multiplicity pp events by the CMS experiment could be the evidence for the collision of aligned high-intensity flux tubes connecting the valence quarks of the colliding protons. The possible formation of a high density QCD medium however warrants the observation of elliptic flow and possibly higher order flow harmonics in pp collisions. In addition, we also observe the inelastic pp cross section, σ_{pp} to show a different functional behavior at the LHC energies compared to the top RHIC energy [13]. This possibly invokes a new domain of particle production which not only involves hard-QCD processes at the partonic level, but also phenomena like initial and final state radiation (ISR, FSR), underlying events (UE), color reconnection (CR), multipartonic interactions (MPI), different hadronization phenomena like rope hadronization.

45.4 Event Topology Studies in Proton-Proton Collisions

The event topology of proton-proton collisions at GeV energies is usually a back-to-back emission of momentum conserving dijet structure as shown in Fig. 45.1. However, at the LHC energies the event multiplicity in pp collisions grows towards higher track densities in the phase space, as shown in Fig. 45.2. The underlying physics of these high-multiplicity events are yet to be fully understood. At the meantime, as we know particle production has soft (low-p_T transfer) and hard components (dominated by pQCD high-p_T processes), one needs to devise new observables to study the event topology and thus disentangle event types to make deeper studies. In this direction, transverse spherocity (S_0) and R_T (a self-normalized measurement of number of charged tracks in the transverse region: $N_T / < N_T >$ [14]) are some of the new event shape observables. Transverse spherocity is defined as:

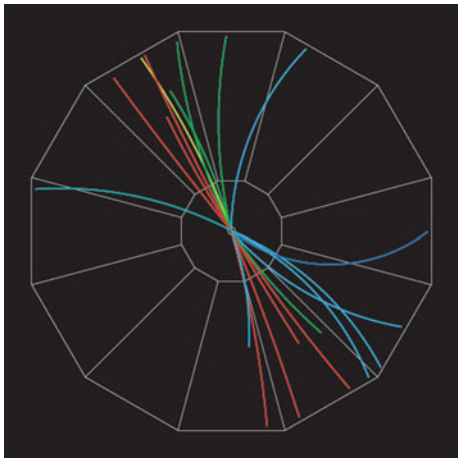

Fig. 45.1 (Color Online) Event topology of pp collisions at $\sqrt{s} = 200\,\text{GeV}$ in RHIC. The event shows a back-to-back jet structure. Figure courtesy: STAR Experiment@RHIC [8]

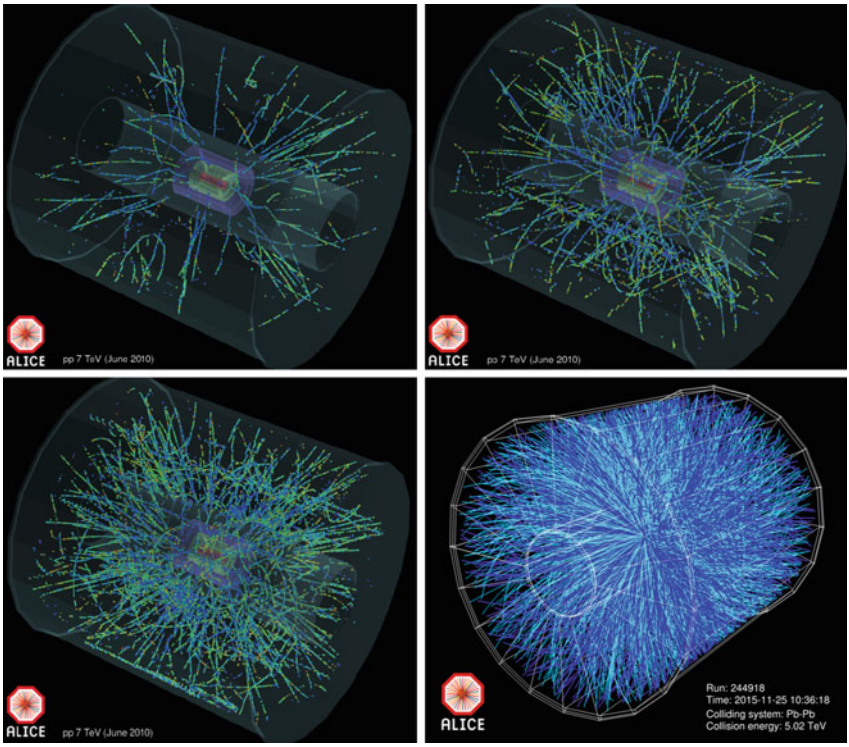

Fig. 45.2 (Color Online) Event topology of pp collisions at the LHC energies showing the evolution of particle density in phase space: top to bottom—low-multiplicity, medium-multiplicity and high-multiplicity pp collisions compared with heavy-ion collisions at the TeV energies. Figure courtesy: ALICE Experiment@CERN [9]

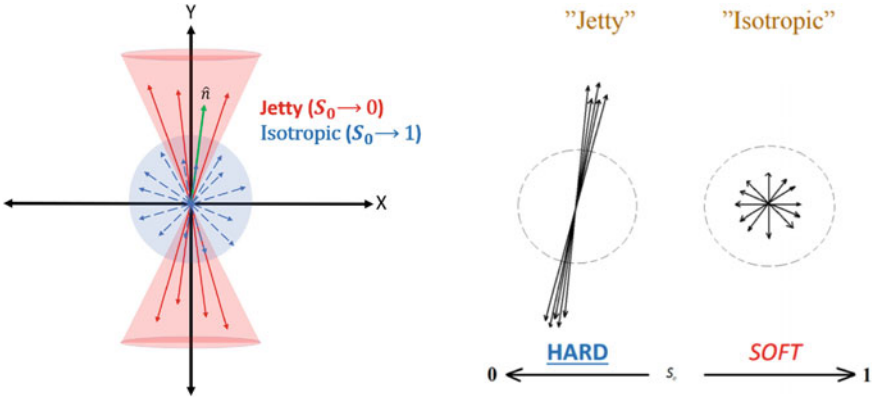

Fig. 45.3 (Color Online) A schematic of event topology of pp collisions showing jetty and isotropic events

$$S_T^{spherocity} = S_0 = \frac{\pi^2}{4} \min_{\mathbf{n}=(n_x,n_y,0)} \left(\frac{\sum_i |\mathbf{p}_{Ti} \times \mathbf{n}|}{\sum_i |\mathbf{p}_{Ti}|} \right)^2, \tag{45.1}$$

where the values of S_0 which define the structure in the transverse plane runs from 0 (for jetty) to 1 (for isotropic). In spherocity there is only ϕ dependence and only back-to-back dijet shapes can be selected. A schematic picture showing the selection of event topology using spherocity in pp collisions is shown in Fig. 45.3. The spherocity distribution of minimum bias events as a function of charged particle multiplicity in pp collisions at $\sqrt{s} = 5.02$ [15] is shown in Fig. 45.4 (left). One observes here that the high-multiplicity events have a higher degree of having isotropic event topology.

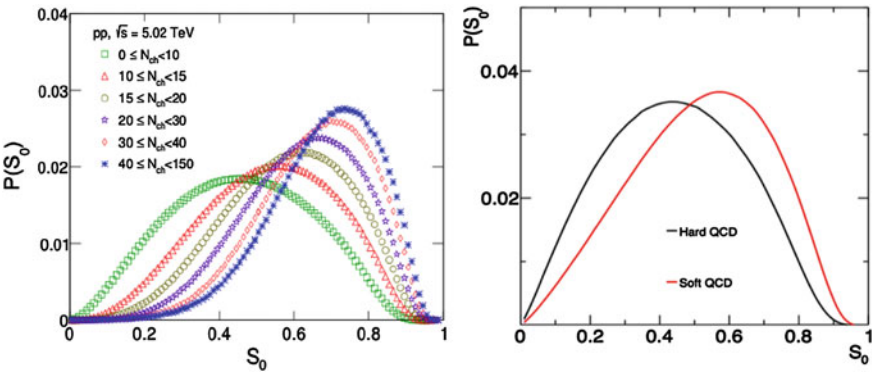

Fig. 45.4 (Color Online) (Left) The spherocity distribution of minimum bias events as a function of charged particle multiplicity in pp collisions at $\sqrt{s} = 5.02$ [15]. High-multiplicity events have a higher degree of isotropic event topology. (Right) Isotropic events are dominated by soft QCD processes, whereas the jetty topology is hard QCD driven

The right panel of the figure shows isotropic events are dominated by soft QCD processes, whereas the jetty topology is hard QCD driven. These are obtained from PYTHIA8 simulated events [15]. Moving from pp to p+Pb and Pb+Pb collisions, it becomes evident to presume a smooth evolution of final state multiplicity and also the process of isotropization, given that more and more particles are produced as the system size grows. Event shape studies are highly helpful in separating the event types and thereby the underlying particle production dynamics. Differential studies using final state multiplicity and event topology would be very useful in understanding the pp physics at the LHC energies [16].

45.5 Some Emerging Phenomena in Proton-Proton Physics

Some of the emergent physics aspects in view of the pp collisions at the TeV energies are outlined below.

1. Particle multiplicity seems to drive the system properties. Threshold of $N_{\mathrm{ch}} \sim 20$ for MPI to be dominant is observed, which is also seen as a thermodynamic limit where statistical ensembles give similar results [11, 17]. $p_{\mathrm{T}} \sim 8$ GeV/c indicates a new domain of particle production [18].
2. Multipartonic interactions, Color reconnection, Rope Hadronization seem to explain some of the features observed in experiments.
3. Small system QGP-like behaviour is a future direction of research and needs more explorations both theoretically and through new observables in experiments to conclude about possible formation of QGP-droplets in pp collisions at the TeV energies.
4. Connecting particle production from hadronic to nuclear collisions using various theoretical models involving transport equations are necessary.
5. Application of non-extensive statistical mechanics in hadronic collisions is driven by particle spectra and this indicates to a new domain of studies on systems away from thermodynamic equilibrium.
6. QCD thermodynamics: pp versus heavy-ion collisions and the multiplicity dependence of thermodynamic parameters.
7. Event topology studies using different observables like transverse spherocity, R_T etc. and their experimental biases are some of the ongoing directions of research.

Although this is a small list, we anticipate this to be populated with time, when a deeper understanding of underlying physics is made.

45.6 Summary

In this contribution, we have tried to summarize some of the important heavy-ion-like observations in pp collisions at the LHC energies. The present theoretical understandings are also discussed, along with some outlook on the event topology and the idea of looking into high-multiplicity pp events in order to explore the possibilities of formation of QGP-droplets at the LHC energies. This presentation leaves out with some of the open questions in pp physics, which need a deeper understanding.

Acknowledgements The author would like to acknowledge the financial supports under the projects: ALICE Project No. SR/MF/PS- 01/2014-IITI(G) of Department of Science & Technology, Government of India and DAE-BRNS Project No. 58/14/29/2019-BRNS of Government of India.

References

1. H. Heiselberg, Phys. Rep. **351**, 161 (2001)
2. J. Adam et al., ALICE collaboration, Nat. Phys. **13**, 535 (2017)
3. S. Borsanyi et al., J. High Energy Phys. **2010**, 77 (2010)
4. S. Borsanyi et al., Phys. Lett. B **730**, 99 (2014)
5. F. Karsch, Nucl. Phys. A **698**, 199 (2002)
6. J. Adam et al., STAR collaboration, Nucl. Phys. A **757**, 102 (2005)
7. R. Sahoo, AAPPS Bull. **29**, 16 (2019)
8. www.star.bnl.gov
9. https://cds.cern.ch/
10. V. Khachatryan et al., CMS collaboration, JHEP **1009**, 091 (2010)
11. D. Thakur, S. De, R. Sahoo, S. Dansana, Phys. Rev. D **97**, 094002 (2018)
12. J.D. Bjorken et al., Phy. Letts. B **726**, 344 (2013)
13. G. Antchev et al., TOTEM collaboration, Eur. Phys. J. C **79**, 103 (2019)
14. T. Martin, P. Skands, S. Farrington, Eur. Phys. J. C **76**, 299 (2016)
15. A. Khatun, D. Thakur, S. Deb, R. Sahoo, J. Phys. G: Nucl. Part. Phys. **47**, 055110 (2020)
16. A. Ortiz, G. Paić, E. Cuautle, Nucl. Phys. A **941**, 78 (2015)
17. N. Sharma, J. Cleymans, B. Hippolyte, M. Paradza, Phys. Rev. C **99**, 044914 (2019)
18. R. Rath, A. Khuntia, R. Sahoo, J. Cleymans, J. Phys. G: Nucl. Part. Phys. **47**, 055111 (2020)

Chapter 46
Parton Distributions and Spin Structure of Hadrons

Harleen Dahiya

Abstract We have investigated the quark distributions of the spin-0 pseudoscalar mesons in light cone quark model (LCQM). In particular, we have studied the parton distribution function (PDF) of the pion. We have also focussed on the generalized parton distributions (GPDs) of the pions obtained from the overlap of light-cone wavefunctions (LCWFs). We have obtained the results for the transverse momentum distributions (TMDs) of the pion and kaon.

46.1 Introduction

The nonperturbative structure of the hadron is well described by the distribution of partons inside the hadron in both position and momentum space. The distribution amplitudes (DAs) are among the most basic quantities not only providing important information on bound states in QCD but also play an essential role in describing the various hard exclusive processes [1, 2] of QCD. The parton distribution functions (PDFs) [3, 4], which are accessible in deep inelastic scattering (DIS) or Drell–Yan processes, encode the distribution of longitudinal momentum and polarization carried by the constituents. The generalized parton distributions (GPDs) [5–8] reveal the parton distribution in the direction transverse to the hadron motion providing the knowledge of 3-dimensional (3D) spatial structure of hadron. One can obtain the form factors, charge distributions, PDFs etc. from GPDs under certain conditions [9–11]. The momentum distributions of hadrons are described by the transverse momentum-dependent parton distributions (TMDs) which are functions of longitudinal momentum fraction x and transverse momentum possessed by the parton ($\mathbf{k}_\perp$).

To understand the relativistic effects of the motion of quarks and gluons in the hadrons, light-cone formalism is used which is a convenient frame to study the appli-

H. Dahiya (✉)
Department of Physics, Dr. B.R. Ambedkar National Institute of Technology, Jalandhar 144011, India
e-mail: dahiyah@nitj.ac.in

A. Giri and R. Mohanta (eds.), *Workshop on Frontiers in High Energy Physics 2019*, Springer Proceedings in Physics 248,
https://doi.org/10.1007/978-981-15-6292-1_46

cations to the exclusive processes. The advantage of using the light-front dynamics is that the Wigner rotation related to the spin states is unity in different frames under the Lorentz transformation. The light-cone quark model (LCQM) finds application in QCD low-scale regime. The pion has chiral symmetry constraints, particularly the explicit chiral and spontaneous symmetry breaking, leading to the pion structure being the simplest valence-quark substructure to study. The LCQM is successful in explaining the electromagnetic form factors of pion and kaon.

46.2 Light-Cone Quark Model (LCQM)

The hadron eigenstate $|M(P^+, \mathbf{P}_\perp, S_z)\rangle$ in connection with multi-particle Fock eigenstates $|n\rangle$ is defined as [12]

$$|M(P^+, \mathbf{P}_\perp, S_z)\rangle = \sum_{n,\lambda_i} \int \prod_{i=1}^{n} \frac{\mathrm{d}x_i \mathrm{d}^2\mathbf{k}_{\perp i}}{\sqrt{x_i}\, 16\pi^3} 16\pi^3 \delta\left(1 - \sum_{i=1}^{n} x_i\right) \delta^{(2)}\left(\sum_{i=1}^{n} \mathbf{k}_{\perp i}\right) \times |n : x_i P^+, x_i \mathbf{P}_\perp + \mathbf{k}_{\perp i}, \lambda_i\rangle \psi_{n/M}(x_i, \mathbf{k}_{\perp i}, \lambda_i), \tag{46.1}$$

where $P = (P^+, P^-, \mathbf{P}_\perp)$ is considered as the total momentum of meson and S_z is the longitudinal spin projection. The momenta of meson having mass M and its constituents having masses m_1 and m_2 in light-cone frame are defined as

$$P = \left(P^+, \frac{M^2}{P^+}, \mathbf{0}_\perp\right),\ k_1 = \left(xP^+, \frac{\mathbf{k}_\perp^2 + m_1^2}{xP^+}, \mathbf{k}_\perp\right),\ k_2 = \left((1-x)P^+, \frac{\mathbf{k}_\perp^2 + m_2^2}{(1-x)P^+}, -\mathbf{k}_\perp\right). \tag{46.2}$$

The light-cone wavefunction in LCQM is written as

$$\psi^F_{S_z}(x, \mathbf{k}_\perp, \lambda_1, \lambda_2) = \varphi(x, \mathbf{k}_\perp)\ \chi^F_{S_z}(x, \mathbf{k}_\perp, \lambda_1, \lambda_2), \tag{46.3}$$

where φ and χ correspond to the momentum space and spin wavefunctions respectively and superscript F stands for the front form. The LCWF of pion (or kaon) can be obtained through the transformation of the instant-form SU(6) wavefunctions using Melosh–Wigner rotation.

The light-cone spin wavefunction of pseudoscalar '$\mathscr{P}$' meson, which can be pion or kaon depending on their composition, has the form

$$\chi^{\mathscr{P}}(x, \mathbf{k}_\perp) = \sum_{\lambda_1, \lambda_2} \kappa^F_{S_z}(x, \mathbf{k}_\perp, \lambda_1, \lambda_2) \chi_1^{\lambda_1}(F) \chi_2^{\lambda_2}(F), \tag{46.4}$$

with S_z and λ being the spin projection of pion (or kaon) and quark helicity, respectively. Since for pion (kaon) having masses m (m_1 and m_2), the z-component of spin

is zero ($S_z = 0$), therefore, the component coefficients $\kappa^F_{S_z=0}(x, \mathbf{k}_\perp, \lambda_1, \lambda_2)$ in spin wavefunction are indicated as

$$\begin{aligned}
\kappa^F_0(x, \mathbf{k}_\perp, \uparrow, \downarrow) &= \omega_1\omega_2[(q_1^+ + m_1)(q_2^+ + m_2) - q_\perp^2]/\sqrt{2}, \\
\kappa^F_0(x, \mathbf{k}_\perp, \downarrow, \uparrow) &= -\omega_1\omega_2[(q_1^+ + m_1)(q_2^+ + m_2) - q_\perp^2]/\sqrt{2}, \\
\kappa^F_0(x, \mathbf{k}_\perp, \uparrow, \uparrow) &= \omega_1\omega_2[(q_1^+ + m_1)q_2^L - (q_2^+ + m_2)q_1^L]/\sqrt{2}, \\
\kappa^F_0(x, \mathbf{k}_\perp, \downarrow, \downarrow) &= \omega_1\omega_2[(q_1^+ + m_1)q_2^R - (q_2^+ + m_2)q_1^R]/\sqrt{2},
\end{aligned} \tag{46.5}$$

where $q_1^+ = q_1^0 + q_1^3 = x_1\mathscr{M}$, $q_2^+ = q_2^0 + q_2^3 = x_2\mathscr{M}$, and $\mathbf{k}_\perp = \mathbf{q}_\perp$, with

$$\mathscr{M}^2 = \frac{m_1^2 + \mathbf{k}_\perp^2}{x_1} + \frac{m_2^2 + \mathbf{k}_\perp^2}{x_2}. \tag{46.6}$$

Here x_i $(i = 1, 2)$ is the light-cone quark momentum fraction.

The momentum space wavefunctions $\varphi^{\pi(K)}(x, \mathbf{k}_\perp)$ in (46.3) are adopted using Brodsky–Huang–Lepage (BHL) prescription. For pion we have

$$\varphi^\pi(x, \mathbf{k}_\perp) = A^\pi \exp\Big[-\frac{1}{8\beta_\pi^2}\frac{\mathbf{k}_\perp^2 + m^2}{x(1-x)}\Big], \tag{46.7}$$

where A^π is the normalization constants for pion.

46.3 Parton Distribution Functions (PDFs)

The pion (kaon) PDF gives the probability of finding the quark in the pion (kaon) where the quark carries a longitudinal momentum fraction $x = k^+/P^+$. At fixed light-front time, the PDF can be expressed as [13]

$$f^{\mathscr{P}}(x) = \frac{1}{2}\int \frac{dz^-}{4\pi} e^{ik^+z^-/2}\langle \mathscr{P}^+(P); S|\bar{\Psi}(0)\Gamma\Psi(z^-)|\mathscr{P}^+(P); S\rangle|_{z^+=\mathbf{z}_\perp=0} \tag{46.8}$$

Since the spin is zero ($S = 0$) in both the cases, we deal with the unpolarized parton distribution function which comes from the above relation by substituting $\Gamma = \gamma^+$. The overlap form of PDF is defined as

$$\begin{aligned}
f^{\pi(K)}(x) = \int \frac{d^2\mathbf{k}_\perp}{16\pi^3}\Big[&| \psi_0^{\pi(K)}(x, \mathbf{k}_\perp, \uparrow, \uparrow) |^2 + | \psi_0^{\pi(K)}(x, \mathbf{k}_\perp, \uparrow, \downarrow) |^2 \\
&+ | \psi_0^{\pi(K)}(x, \mathbf{k}_\perp, \downarrow, \uparrow) |^2 + | \psi_0^{\pi(K)}(x, \mathbf{k}_\perp, \downarrow, \downarrow) |^2 \Big].
\end{aligned} \tag{46.9}$$

If we study the quark distribution function $f^{\pi(K)}(x)$ for pion (kaon) as a function of x we find that the probability of finding the quark along x in pion is more near the

center, while in kaon, it is maximum at a slightly lower value of quark momentum fraction in the longitudinal direction. The peak is broader in the case of pion as compared to kaon. The distribution peak has higher amplitude in case of kaon as compared to pion.

46.4 Generalized Parton Distributions (GPDs)

We calculate the GPDs of quark for pion and kaon in LCQM. GPDs have support region $x\epsilon[-1, 1]$ [5, 14]. However, for present calculations we restrict ourself to only DGLAP region i.e. $\zeta < x < 1$. One can define the correlation to evaluate unpolarized GPD $H(x, \zeta = 0, t)$ as [5, 15]

$$H^{\mathscr{P}}(x,0,t) = \frac{1}{2}\int \frac{dz^-}{4\pi} e^{ixP^+z^-/2}\langle \mathscr{P}^+(P')\bar{\Psi}(0)\gamma^+\Psi(z)\mathscr{P}^+(P)\rangle|_{z^+=\mathbf{z}_\perp=0}. \quad (46.10)$$

For the case of pion we have

$$\begin{aligned} &H^{\pi}(x,0,t) \\ &= \int \frac{d^2\mathbf{k}_\perp}{16\pi^3}\Big[\big((x\mathscr{M}^{\pi}+m)((1-x)\mathscr{M}'^{\pi}+m)-\mathbf{k}'^2_\perp\big)\big((x\mathscr{M}^{\pi}+m)((1-x)\mathscr{M}^{\pi}+m)-\mathbf{k}^2_\perp\big) \\ &+\big(\mathscr{M}'^{\pi}+2m\big)\big(\mathscr{M}^{\pi}+2m\big)\Big]\frac{\varphi^{\pi *}(x,\mathbf{k}'_\perp)\varphi^{\pi}(x,\mathbf{k}_\perp)}{\omega'_1\omega'_2\omega_1\omega_2}, \end{aligned} \quad (46.11)$$

with

$$\mathscr{M}^{\pi} = \sqrt{\frac{m^2+\mathbf{k}^2_\perp}{x(1-x)}}, \quad \mathscr{M}'^{\pi} = \sqrt{\frac{m^2+\mathbf{k}'^2_\perp}{x(1-x)}}, \quad (46.12)$$

in initial and final states, respectively.

For the case of kaon we have

$$\begin{aligned} &H^{K}(x,0,t) \\ &= \int \frac{d^2\mathbf{k}_\perp}{16\pi^3}\Big[\big((x\mathscr{M}'^{K}+m_1)((1-x)\mathscr{M}'^{K}+m_2)-\mathbf{k}'^2_\perp\big)\big((x\mathscr{M}^{K}+m_1)((1-x)\mathscr{M}^{K}+m_2)-\mathbf{k}^2_\perp\big) \\ &+\big(\mathscr{M}'^{K}+m_1+m_2\big)\big(\mathscr{M}^{K}+m_1+m_2\big)\Big]\frac{\varphi^{K *}(x,\mathbf{k}'_\perp)\varphi^{K}(x,\mathbf{k}_\perp)}{\omega'_1\omega'_2\omega_1\omega_2}, \end{aligned} \quad (46.13)$$

with

$$\mathscr{M}^{K} = \sqrt{\frac{m_1^2+\mathbf{k}^2_\perp}{x}+\frac{m_2^2+\mathbf{k}^2_\perp}{1-x}}, \quad \mathscr{M}'^{K} = \sqrt{\frac{m_1^2+\mathbf{k}'^2_\perp}{x}+\frac{m_2^2+\mathbf{k}'^2_\perp}{1-x}}, \quad (46.14)$$

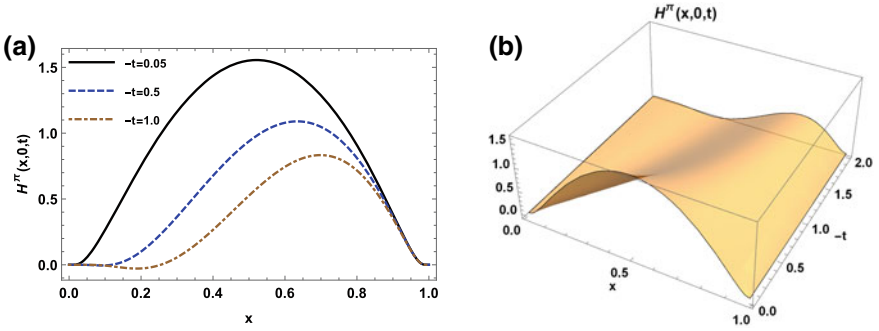

Fig. 46.1 The GPD $H(x, 0, t)$ of u quark in case of pion **a** at different values of $-t$ (in GeV^2), **b** with respect to x and $-t$

in the initial and the final states, respectively. Here, $t = -\mathbf{q}_\perp^2$ is denoted as the total momentum transferred to the meson. The detailed discussion on graphical representation of GPD in case of kaon has been already explained in [16].

Using input parameters we calculate the GPDs $H(x, 0, t)$ of u-quark in pion (π^+ meson). To understand the dependence of the GPD on x, in Fig. 46.1a, we give the graphical representation of H as a function of x in pion with fixed values of $-t$. The quark distribution in pion with respect to x is maximum at the center for a comparatively lower value of $-t$ which implies that the longitudinal momentum fraction is maximum at the center when the momentum transferred to the pion in lower. As the value of momentum transferred $-t$ increases, the peak shifts towards higher values of x which is away from the centre. By increasing the $-t$ to the higher values, the distribution peaks shift towards the higher values of x and the magnitude of distribution becomes lower. It signifies that when the momentum transferred to the final state of meson is higher, the quark spread is low at the higher values of x. For a more complete distribution with respect to the momentum fraction (x) and the total momentum transferred to the π^+ ($-t$), we present the 3-dimensional plot of GPD $H(x, 0, t)$ for π^+ in Fig. 46.1b.

46.5 Transverse Momentum-Dependent Parton Distributions (TMDs)

TMDs provide the distribution of partons in momentum space and are functions of longitudinal momentum fraction $x = k^+/P^+$ and transverse momentum $\mathbf{k}_\perp$ carried by the struck quark. To evaluate the pion and the kaon TMDs, the unintegrated quark-quark correlator can be defined as [17, 18].

$$\Phi^{\mathscr{P}}(x, \mathbf{k}_\perp; S) = \frac{1}{2}\int \frac{dz^-}{2\pi}\frac{d^2\mathbf{z}_\perp}{(2\pi)^2} e^{ik.z/2}\langle \mathscr{P}^+(P), S|\bar{\Psi}(0)\Gamma\Psi(z)|\mathscr{P}^+(P), S\rangle|_{z^+=0}. \tag{46.15}$$

Since the spin is zero ($S = 0$) for the pion and the kaon, we are left with only the TMD which comes from the combination where meson is taken to be unpolarized. After putting the states of respective mesons and $\Gamma = \gamma^+$, we get the explicit expressions of unpolarized pion TMD $f_1^\pi(x, \mathbf{k}_\perp^2)$ and unpolarized kaon TMD $f_1^K(x, \mathbf{k}_\perp^2)$. The overlap form of unpolarized TMD $f_1(x, \mathbf{k}_\perp^2)$ is given as

$$f_1^{\pi(K)}(x, \mathbf{k}_\perp^2) = \frac{1}{16\pi^3}\Big[\,|\,\psi_0^{\pi(K)}(x, \mathbf{k}_\perp, \uparrow, \uparrow)\,|^2 + |\,\psi_0^{\pi(K)}(x, \mathbf{k}_\perp, \uparrow, \downarrow)\,|^2 + |\,\psi_0^{\pi(K)}(x, \mathbf{k}_\perp, \downarrow, \uparrow)\,|^2 + |\,\psi_0^{\pi(K)}(x, \mathbf{k}_\perp, \downarrow, \downarrow)\,|^2\,\Big]. \tag{46.16}$$

In Fig. 46.2a, b, we show the distribution f_1 of a unpolarized quark in the unpolarized meson (pion or kaon) with respect to the longitudinal momentum fraction respectively for different values of $\mathbf{k}_\perp^2$. The probability of finding the quark in pion is more as compared to kaon, if the momentum fraction carried by that quark is higher in the longitudinal direction. As we increase the $\mathbf{k}_\perp^2$), the momentum distribution starts lowering down in both cases. We also present the plots of TMD $f_1(x, \mathbf{k}_\perp^2)$ as a function of quark transverse momentum squared for different values of x in Fig. 46.3. The distribution decreases when the transverse momentum carried by quark increases. The probability to find the quark in pion and kaon starts decreasing and eventually becomes zero by the increase in the quark transverse momentum. For a more clear picture, we present the 3-D plots for both the cases, which provide the combined information with respect to longitudinal momentum fraction and transverse momentum carried by active u quark in Fig. 46.4.

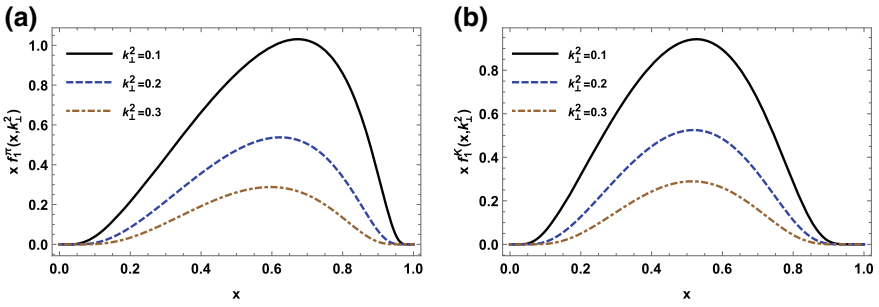

Fig. 46.2 (color online) The unpolarized TMD $xf_1(x, \mathbf{k}_\perp^2)$ w.r.t x for different values of $\mathbf{k}_\perp^2$ (in GeV^2) for **a** pion, and **b** kaon

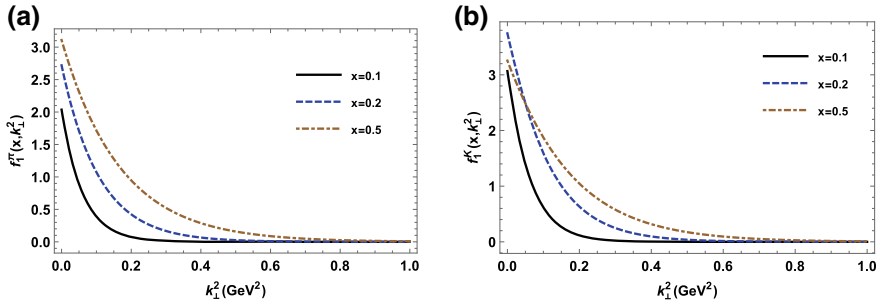

Fig. 46.3 The unpolarized TMD $f_1(x, \mathbf{k}_\perp^2)$ w.r.t $\mathbf{k}_\perp^2$ (in GeV^2) for different values of x for **a** pion, and **b** kaon

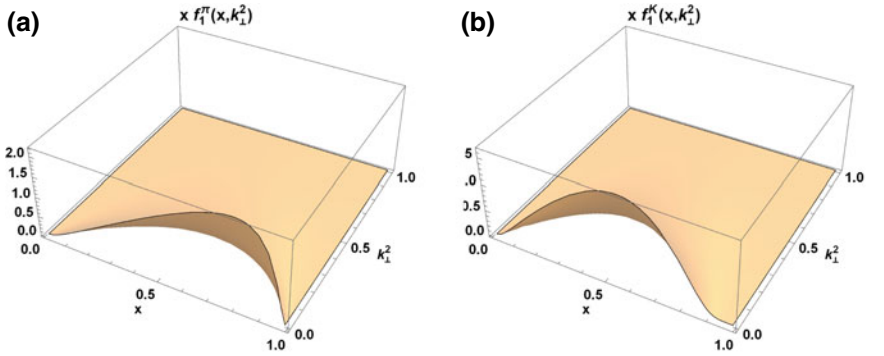

Fig. 46.4 The 3-D plots of unpolarized TMD $f_1(x, \mathbf{k}_\perp^2)$ as a function of x and $\mathbf{k}_\perp^2$ for **a** pion, and **b** kaon

46.6 Conclusions

We have studied the distributions of quark in pion and kaon in light-cone quark model where the light-cone wavefunctions have been obtained by transforming the instant-form wavefunctions through the Melosh–Wigner rotation. We have used the overlap representation of LCWFs to perform the calculations for the distributions. The quark distribution functions have been evaluated for pion and kaon, and observed that the probability of finding the quark with respect to the quark longitudinal momentum fraction is more at the center in case of pion. Further, we have performed the calculations for GPDs in DGLAP region for zero skewness i.e. $0 < x < 1$, which provide us the pure transverse structure of meson. It is impossible to obtain the purely transverse structure experimentally. For both pseudoscalar mesons, depending upon the total momentum transferred to the composite system, we observe the change in distribution with respect to active quark longitudinal momentum fraction. The quark distribution in case of kaon is more concentrated than in pion with respect to x. The transverse structure of pion and kaon has also been examined. We studied the TMDs

with respect to the momentum fraction carried by the quark in longitudinal direction (x) at different values of transverse momentum $\mathbf{k}_\perp^2$ and vice-versa. To observe the combined effect, we have shown the 3D picture of TMD w.r.t x and $\mathbf{k}_\perp^2$.

Acknowledgements H.D. would like to thank the Department of Science and Technology (Ref No. EMR/2017/001549) Government of India for financial support.

References

1. S.J. Brodsky, G.P. Lepage, Adv. Ser. Dir. High Energy Phys. **5**, 93 (1989)
2. V.L. Chernyak, A.R. Zhitnitsky, Nucl. Phys. B **201**, 492 (1982); Erratum: [Nucl. Phys. B **214**, 547 (1983)]
3. D.E. Soper, Nucl. Phys. B **53**, 69 (1997)
4. A.D. Martin, W.J. Stirling, R.S. Thorne, G. Watt, Eur. Phys. J. C **63**, 189 (2009)
5. M. Diehl, Phys. Rep. **388**, 41 (2003)
6. M. Garcon, Eur. Phys. J. A **18**, 389 (2003)
7. K. Geoke, M.V. Polyakov, M. Vanderhaeghen, Prog. Part. Nucl. Phys. **47**, 401 (2001)
8. A.V. Belitsky, A.V. Radyushkin, Phys. Rep. **418**, 1 (2005)
9. M. Guidal, M.V. Polyakov, A.V. Radyushkin, M. Vanderhaeghen, Phys. Rev. D **72**, 054013 (2005)
10. N.S. Nikkhoo, M.R. Shojaei, Phys. Rev. C **97**, 055211 (2018)
11. G.A. Miller, Phys. Rev. Lett. **99**, 112001 (2007)
12. W. Qian, B.-Q. Ma, Phys. Rev. D **78**, 074002 (2008)
13. T. Maji, D. Chakrabarti, Phys. Rev. D **94**, 094020 (2016)
14. S.J. Brodsky, M. Diehl, D.S. Hwang, Nucl. Phys. B **596**, 99 (2001)
15. D. Chakrabarti, X. Zhao, H. Honkanen, R. Manohar, P. Maris, J.P. Vary, Phys. Rev. D **89**, 116004 (2014)
16. S. Kaur, H. Dahiya, Phys. Rev. D **100**, 074008 (2019)
17. B. Pasquini, P. Schweitzer, Phys. Rev. D **90**, 014050 (2014)
18. S. Meissner, A. Metz, K. Goeke, Phys. Rev. D **76**, 034002 (2007)

Chapter 47
A Study of Transverse Single Spin Asymmetry in Hadroproduction and Electroproduction of J/ψ

Bipin Sonawane, Anuradha Misra, and Vaibhav Rawoot

Abstract We present a study of transverse single spin asymmetry (TSSA) and gluon Sivers function in the process $p + p^{\uparrow} \to J/\psi + X$ and $e + p^{\uparrow} \to e + J/\psi + X$ using generalised parton model (GPM) formalism. We have used the color evaporation model for the J/ψ production. We estimate TSSA for COMPASS (17.33 GeV), e-RHIC (31.6 GeV) and RHIC (200 GeV) energy scales. The present study is suitable for understanding gluon dynamics considering initial state interaction and final state interaction within GPM approach.

47.1 Introduction

Three dimensional structure of a nucleon is studied by probing transverse single spin asymmetry and transverse momentum dependent functions (TMDs). TMDs provide one of the interesting methods to understand the inner dynamics of a nucleon. In simple quark-parton model, the quarks inside the fast hadrons are assumed to be collinear i.e. their momentum is assumed to be parallel to the momentum of the hadron. One dimensional picture of the nucleon in terms of collinear parton distribution function (PDF) $f(x_a, Q)$ does not specify inner dynamics of the hadron.

A complete description of the nucleon structure needs transverse degrees of freedom involving the correlation of spin and momentum of parton [1, 2]. It is hardly possible to know the spin structure of the nucleon without taking into account the transverse motion of the inner partons. The transverse motion of the partons usually integrated over in the nucleon dynamics but spin-$k_{\perp}$ dependent correlations are needed to compute carefully. To understand 3-D structure of the hadron, a new class of PDFs, transverse momentum dependent PDFs, $f_{a/A}(x_a, k_a, Q)$ and transverse momentum dependent fragmentation function, $D_{C/c}(Z, P_{\perp c}, Q)$ have been

B. Sonawane (✉) · V. Rawoot
Amity School of Applied Sciences, Amity University Mumbai, Mumbai, India
e-mail: bipinsonawane2010@gmail.com

A. Misra
Department of Physics, University of Mumbai, Mumbai, India

A. Giri and R. Mohanta (eds.), *Workshop on Frontiers in High Energy Physics 2019*, Springer Proceedings in Physics 248,
https://doi.org/10.1007/978-981-15-6292-1_47

introduced and collectively known as TMDs, These TMDs are depend upon light cone momentum fraction and intrinsic transverse motion of the inner partons.

The Spin dependent PDFs are explored in the scattering experiments involving polarised beams. The gluon Sivers function (GSF) [3, 4] is one such function which is interpreted as the probability of finding unpolarised parton inside transversely polarised proton. The GSF can be probed using an observable quantity transverse single spin asymmetry (TSSA). TSSA arise in the production of J/ψ in the collision of transversely polarised proton beams off an unpolarised proton or an electron. The spin-orbit coupling in the nucleons is associated with quark transverse momentum and bound state structure of the nucleons and leads to TSSA. The orbital angular momentum leading to spin orbit coupling could be a prime candidate to explain large TSSAs.

Transverse Single Spin Asymmetry arises in polarised $p-p$ process like $pp^{\uparrow} \rightarrow \pi X$. In this process, the cross section depends on the proton spin orientation with respect to the production plane, giving rise to an observable quantity called single spin asymmetry. It is defined as

$$A_N = \frac{d\sigma^{\uparrow} - d\sigma^{\downarrow}}{d\sigma^{\uparrow} + d\sigma^{\downarrow}} = \frac{\Delta d\sigma}{2d\sigma^{unpol}} \tag{47.1}$$

where, $d\sigma^{\uparrow}$ and $d\sigma^{\downarrow}$ represent differential cross-sections for scattering of a transversely polarised proton off an unpolarised proton (or lepton) with one of the protons being upwards (downwards) polarised with respect to the production plane.

47.2 TSSA in $e + p^{\uparrow} \rightarrow e + J/\psi + X$

In this section we present the calculations of TSSA in elctroproduction of J/ψ process. Here, we use generalisation of Color evaporation model of J/ψ production [5]. We obtained the expression by taking into account the transverse momentum dependence of Weizsacker–William function ($f_{\gamma/e}$) and parton distribution function ($f_{g/p^{\uparrow}}$). The expressions for numerator is [6, 7]

$$d\sigma^{\uparrow} - d\sigma^{\downarrow} = F_{J/\psi} \int_{4m_c^2}^{4m_D^2} dM \int d^2k_{\perp g} \Delta^N f_{g/p^{\uparrow}}(x_g, k_{\perp g}) f_{\gamma/e}(x_{\gamma}, k_{\perp \gamma}) \hat{\sigma}_0(M^2) \tag{47.2}$$

The expression for the denominator is

$$d\sigma^{\uparrow} + d\sigma^{\downarrow} = 2F_{J/\psi} \int_{4m_c^2}^{4m_D^2} dM \int d^2k_{\perp g} f_{g/p^{\uparrow}}(x_g, k_{\perp g}) f_{\gamma/e}(x_{\gamma}, k_{\perp \gamma}) \hat{\sigma}_0(M^2) \tag{47.3}$$

where, $d\sigma^{\uparrow(\downarrow)} = \frac{d\sigma^{\uparrow(\downarrow)}}{dyd^2q_T}$ and $k_{\perp\gamma} = q_T - k_{\perp g}$. Parameter $F_{J/\psi}$ gives the probability of J/ψ production below $D\bar{D}$ threshold and $d\hat{\sigma}$ is partonic cross-section for sub-process $\gamma g \to c\bar{c}$. Unpolarised distribution function is assumed to have a gaussian form and parametrization used for the gluon Sivers function is [8]

$$f_{g/p}(x, k_\perp) = f_{g/p}(x, Q)\frac{1}{\pi\langle k_\perp^2\rangle}e^{-k_\perp^2/\langle k_\perp^2\rangle}. \tag{47.4}$$

$$\Delta^N f_{g/p^\uparrow}(x, k_\perp; Q) = 2\mathcal{N}_g(x) f_{g/p}(x, Q)h(k_\perp)\frac{e^{-k_\perp^2/\langle k_\perp^2\rangle}}{\pi\langle k_\perp^2\rangle}$$

where

$$\mathcal{N}_g(x) = N_i x^{\alpha_i}(1-x)^{\beta_g}\frac{(\alpha_g+\beta_g)^{\alpha_g+\beta_g}}{\alpha_g^{\alpha_g}\beta_g^{\beta_g}}, \qquad h(k_\perp) = \sqrt{2e}\frac{k_\perp}{M_1}e^{-k_\perp^2/M_1^2}. \tag{47.5}$$

47.3 TSSA in $pp^\uparrow \to J/\psi X$

In this section we present the formalism of TSSA in $pp^\uparrow \to J/\psi X$ using color evaporation model (CEM) [6, 9–11]. In this calculation, partonic sub processes which contribute in lowest order are $q\bar{q} \to c\bar{c}$ and $gg \to c\bar{c}$.

In color evaporation model, the total cross-section for the production of J/ψ at leading order (LO) is obtained by convolution of the partonic cross section for $c\bar{c}$ production with PDFs and integrating over the invariant mass-squared from $4m_c^2$ to $4m_D^2$:

$$\sigma^{p+p\to J/\psi+X} = F_Q\int_{4m_c^2}^{4m_D^2} dM_{c\bar{c}}^2\int dx_a dx_b\Bigg[f_{g/p}(x_a)f_{g/p}(x_b)\frac{d\hat{\sigma}^{gg\to c\bar{c}}}{dM_{c\bar{c}}^2} + \sum_q f_{q/p}(x_a)f_{\bar{q}/p}(x_b)\frac{d\hat{\sigma}^{q\bar{q}\to c\bar{c}}}{dM_{c\bar{c}}^2}\Bigg], \tag{47.6}$$

The numerator of TSSA using CEM is,

$$\frac{d^3\sigma^\uparrow}{dyd^2\mathbf{q}_T} - \frac{d^3\sigma^\downarrow}{dyd^2\mathbf{q_T}} = \frac{F_Q}{s}\int[dM_{c\bar{c}}^2 d^2\mathbf{k}_{\perp a}d^2\mathbf{k}_{\perp b}]\delta^2(\mathbf{k}_{\perp a}+\mathbf{k}_{\perp b}-\mathbf{q}_T) \times\Bigg\{\Delta^N f_{g/p^\uparrow}(x_a, \mathbf{k}_{\perp a})f_{g/p}(x_b, \mathbf{k}_{\perp b})\hat{\sigma}_0^{gg\to c\bar{c}}(M_{c\bar{c}}^2) + \sum_q\Bigg[\Delta^N f_{q/p^\uparrow}(x_a, \mathbf{k}_{\perp a})f_{\bar{q}/p}(x_b, \mathbf{k}_{\perp b})\hat{\sigma}_0^{q\bar{q}\to c\bar{c}}(M_{c\bar{c}}^2)\Bigg]\Bigg\}, \tag{47.7}$$

The denominator of TSSA is,

$$\frac{d^3\sigma^{\uparrow}}{dyd^2\mathbf{q}_T}+\frac{d^3\sigma^{\downarrow}}{dyd^2q_T}=\frac{2F_Q}{s}\int[dM^2_{c\bar{c}}d^2\mathbf{k}_{\perp a}d^2\mathbf{k}_{\perp b}]\delta^2(\mathbf{k}_{\perp a}+\mathbf{k}_{\perp b}-\mathbf{q}_T)$$
$$\times\left\{f_{g/p^{\uparrow}}(x_a,\mathbf{k}_{\perp a})f_{g/p}(x_b,\mathbf{k}_{\perp b})\hat{\sigma}_0^{gg\to c\bar{c}}(M^2_{c\bar{c}})\right.$$
$$\left.+\sum_q\left[f_{q/p^{\uparrow}}(x_a,\mathbf{k}_{\perp a})f_{\bar{q}/p}(x_b,\mathbf{k}_{\perp b})\hat{\sigma}_0^{q\bar{q}\to c\bar{c}}(M^2_{c\bar{c}})\right]\right\}.\times \quad (47.8)$$

q are contributing partons (Figs. 47.1, 47.2 and 47.3).

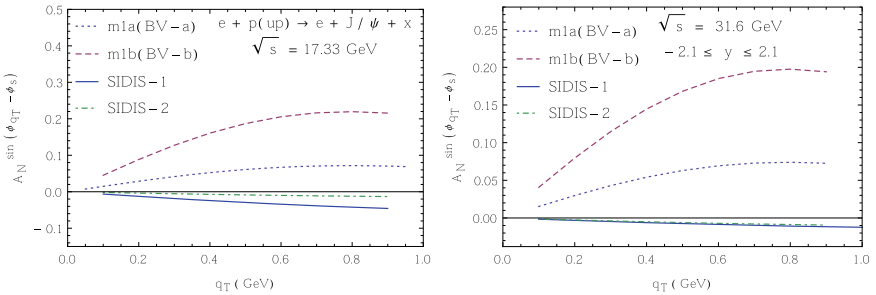

Fig. 47.1 Left panel: prediction of q_T asymmetry at COMPASS energy scale ($\sqrt{s}=17.33\,\text{GeV}$) with rapidity distribution $-1.5\le y\le 1.5$ in the process $e+p^{\uparrow}\to e+J/\psi+X$. Right Panel: prediction of q_T asymmetry at e-RHIC energy scale ($\sqrt{s}=31.6\,\text{GeV}$) with rapidity distribution $-2.1\le y\le 1.5$ in $e+p^{\uparrow}\to e+J/\psi+X$ process. In both the panels, DGLAP evolved densities are used with BV(A), BV(B), SIDIS-1 and SIDIS-2 parametrization

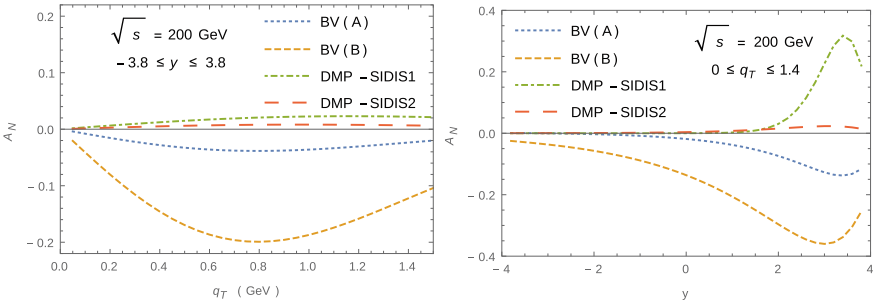

Fig. 47.2 Left panel: prediction of q_T asymmetry at RHIC energy scale ($\sqrt{s}=200\,\text{GeV}$) with rapidity distribution $-3.8\le y\le 3.8$ in the process $p+p^{\uparrow}\to J/\psi+X$. Right Panel: prediction of y asymmetry at RHIC energy scale ($\sqrt{s}=200\,\text{GeV}$) with q_T distribution $0\le q_T\le 1.4$ in $p+p^{\uparrow}\to J/\psi+X$ process. In both the panels, DGLAP evolved densities are used with BV(A), BV(B), SIDIS-1 and SIDIS-2 parametrization

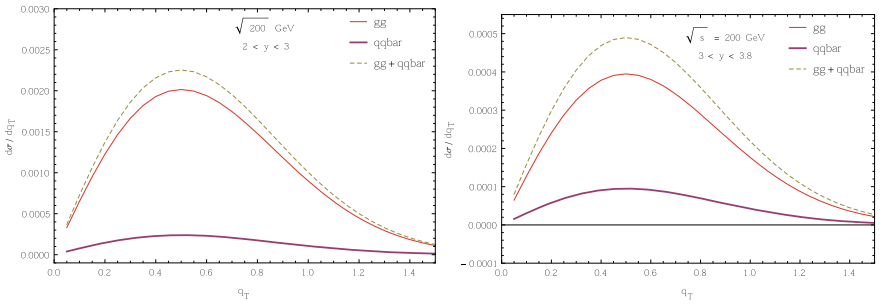

Fig. 47.3 Comparison of gluon-gluon (gg), quark-anti-quark($q\bar{q}$) and total ($gg + q\bar{q}$) contributions in $c\bar{c}$ bound state formation in the process $p + p^{\uparrow} \rightarrow J/\psi + X$ at RHIC energy scale ($\sqrt{s} =$ 200 GeV) using rapidity ranges $2 \leq y \leq 3$ (left panel) and $3 \leq y \leq 3.8$ (right panel)

Table 47.1 SIDIS parameters for GSF and best fit parameters for u and d quarks used in BV parametrization [4, 9]. $\mathcal{N}_g(x) = \frac{\mathcal{N}_u + \mathcal{N}_d}{2} \rightarrow BV(A)$ and $\mathcal{N}_g(x) = \mathcal{N}_d \rightarrow BV(B)$

DMP-SIDIS 1	$N_g = 0.65$	$\alpha_g = 2.8$	$\beta_g = 2.8$	$\rho = 0.687$
DMP-SIDIS 2	$N_g = 0.05$	$\alpha_g = 0.8$	$\beta_g = 1.4$	$\rho = 0.576$
u quark	$N_u = 0.4$	$\alpha_u = 0.35$	$\beta_u = 0.26$	$M_1^2 = 0.19$
d quark	$N_d = -0.97$	$\alpha_d = 0.44$	$\beta_d = 0.90$	

47.4 Conclusion

The q_T distribution and rapidity of TSSA applying DGLAP evolved PDFs show sizable asymmetry in the Electroproduction and Hadroproduction of J/ψ using CEM at COMPASS, e-RHIC, RHIC scales. The signs of estimated TSSA obtained using BV parameters and that of using DMP-SIDIS parameters are opposite. The change in the sign is expected as in BV parametrization as GSF is modeled after quark Sivers function (QSF) and d quark Sivers function has a negative sign. The QSF and GSF contributions to TSSA have been verified by comparing unpolarised cross section by taking account the respective partonic sub-processes. The comparison concludes that QSF is negligible. This study points out that the comparison of asymmetries could be an important tool to understand the production mechanism of heavy quarkonium (Table 47.1).

References

1. D.W. Sivers, Phys. Rev. D **41**, 83 (1990)
2. D.W. Sivers, Phys. Rev. D **43**, 261 (1991)
3. U. D'Alesio, F. Murgia, C. Pisano, P. Taels, Phys. Rev. D **96**(3), 036011 (2017), arXiv:1705.04169 [hep-ph]

4. M. Anselmino, M. Boglione, U. D'Alesio, S. Melis, F. Murgia, A. Prokudin, arXiv:1107.4446 [hep-ph]
5. M.B.G. Ducati, C.B. Mariotto, Phys. Lett. B **464**, 286 (1999), arXiv:hep-ph/9908407
6. R.M. Godbole, A. Misra, A. Mukherjee, V.S. Rawoot, Phys. Rev. D **85**, 094013 (2012). arXiv:1201.1066 [hep-ph]
7. B. Sonawane, R. Godbole, A. Kaushik, A. Misra, V. Rawoot, Springer Proceedings in Physics, vol. 203, pp. 909 (2018)
8. U. D'Alesio, F. Murgia, C. Pisano, JHEP **1509**, 119 (2015). arXiv:1506.03078 [hep-ph]
9. R.M. Godbole, A. Kaushik, A. Misra, V. Rawoot, B. Sonawane, Phys. Rev. D **96**(9), 096025 (2017), arXiv:1703.01991 [hep-ph]
10. R.M. Godbole, A. Kaushik, A. Misra, V. Rawoot, B. Sonawane, Few Body Syst. **58**(2), 96 (2017) arXiv:1612.01167 [hep-ph]
11. B. Sonawane, A. Misra, S. Padval, V. Rawoot, Few Body Syst. **59**(3), 38 (2018), arXiv:1802.02441 [hep-ph]
12. R.M. Godbole, A. Kaushik, A. Misra, Springer Proceedings in Physics, vol. 203, pp. 489 (2018)

Chapter 48
Shear Viscosity and Vorticity Patterns in Relativistic Heavy Ion Collisions

Abhisek Saha and Soma Sanyal

Abstract We study vorticity patterns in Quark-gluon plasma (QGP) in the reaction plane (XZ) of heavy ion collisions with varying collision energies from 20 GeV to 200 GeV. The collision energy is related to the chemical potential of the thermal—statistical models that assume chemical equilibrium after the relativistic collision. We use A Multi-Phase Transport (AMPT) model to get the initial conditions of the collision. We have used different definitions of vorticity and studied the patterns with respect to collision energies and also the change in the global nature of the vorticity. We have also studied shear viscosity to entropy density ratio for various particles. It remains constant in nature over a wide range of energies. The only variation we see is at lower energies.

48.1 Introduction

In heavy ion collisions, two heavy ions collide with each other at relativistic energies such that the temperature and energy density becomes large enough to produce the deconfined state of matter known as the Quark-Gluon Plasma (QGP). There has been a large amount of interest in the rotational aspects of the QGP collective motion. The QGP possesses high angular momentum due to the geometry of the collision [1]. We study the local vorticity patterns at the mid rapidity region in non-central Au+Au collisions as well as the global QGP vorticity with respect to the collision energy. Using different definitions of vorticity, we find that vorticity plays a greater role at lower collision energies than at higher collision energies.

Indications for the existence of quark-gluon plasma comes from the nature of the anisotropic flows observed both in the experiment as well as in simulations [2]. This shows hydrodynamic behavior with extremely small shear viscosity. We also look at other effects of the flow patterns related to the bulk viscosity and the shear viscosity at different collision energies. We discuss the possibilities that these viscous

A. Saha (✉) · S. Sanyal
University of Hyderabad, Hyderabad 500046, India
e-mail: 17phph12@uohyd.ac.in

A. Giri and R. Mohanta (eds.), *Workshop on Frontiers in High Energy Physics 2019*, Springer Proceedings in Physics 248,
https://doi.org/10.1007/978-981-15-6292-1_48

coefficients have on the vorticity patterns that we have obtained from the simulations. We find that the shear viscosity obtained is almost a constant with a small decrease at higher collision energies. Our results indicate that the viscosity plays a greater role at higher chemical potential and lower collision energies.

48.2 Vorticity Simulation

For our study, we use the AMPT code which is a multiphase transport model to generate the initial distribution of the particles [3]. The parameters that we use in our simulations have been used previously in the AMPT model to study vorticity in the $(x - \eta)$ plane [1] and it has reasonably reproduced the yields, transverse momentum spectra, and elliptic flow for low-p_T pions and kaons in central and mid-central $Au + Au$ collisions at collision energies of 200 GeV. The output of the AMPT gives the particles space-time coordinates and three momenta at freeze-out. We take a proper volume and divide it into small cells of length 0.5 fm. The particles are distributed in these cells according to their positions. Now each cell can be considered as a fluid element. We then obtain the average momentum and the energy for each cell and then the velocity is extracted from these two values by taking $\frac{\langle \vec{p} \rangle}{\langle \epsilon \rangle}$. The vorticity captures the rotational motion of the fluid. For a viscous fluid, the rotational motion will also introduce viscous stress between the fluid layers. As there are no boundary conditions in the case of the heavy ion collisions, the local vorticity patterns will be formed due to the viscous stress in the layers of the rotating fluid. In relativistic hydrodynamics, vorticities can be defined in several ways [4]. We study the classical vorticity, the kinematical vorticity and the thermal vorticity with appropriate weights in our simulations. In previous studies, it was shown that the y-component of angular momentum is much larger than the other two components. We have also checked all the components of vorticity distribution but in our study, we only consider the y-component (reaction plane distribution) as it is higher compared to the others.

In the reaction plane, the classical vorticity is given by,

$$\omega_y = \omega_{xz} = \frac{1}{2}(\partial_z v_x - \partial_x v_z) \tag{48.1}$$

Here, v_x, v_y, v_z are the components of the velocity in the three directions. In the relativistic case, the vorticity is given by,

$$\omega_{\mu\nu} = \frac{1}{2}(\partial_\nu u_\mu - \partial_\mu u_\nu) \tag{48.2}$$

where, $\partial_\mu = (\partial_0, \partial_x, \partial_y, \partial_z,)$, $\gamma = 1/\sqrt{1 - v^2}$ and $u_\mu = \gamma(1, -v_x, -v_y, -v_z)$. The vorticity, in this case, has higher fluctuations due to the γ factor. We have also

calculated the thermal vorticity as it is directly related to the particle spin polarization in the plasma which we would study in the future.

The thermal vorticity is defined by,

$$\omega^{T}_{\mu\nu} = \frac{1}{2}(\partial_{\nu}\beta_{\mu} - \partial_{\mu}\beta_{\nu}) \tag{48.3}$$

Here $\beta_{\mu} = \frac{u_{\mu}}{T}$. Here T is the local temperature.

We calculate the weighted vorticity on the XZ plane, both non-relativistic as well as relativistic with respect to the collision energy to deal with the event by event fluctuations. We use energy as a weight factor. The average vorticity for both the classical as well as the relativistic velocities are, $< \omega_{xz} > = \frac{\sum \epsilon_{ij}\omega^{ij}_{xz}}{\sum \epsilon_{ij}}$.

Viscosity plays an important role in anisotropic flows and also in vorticity. We have used a generalized viscosity coefficient from the hadron resonance gas model to include finite chemical potential effects [6]. The shear viscosity is given by,

$$\eta = \frac{5}{64\sqrt{8}r^2}\Sigma_i < |p| > \frac{n_i}{n} \tag{48.4}$$

Here n_i is the number density of the ith particle while r is the radius of the particles concerned.

48.3 Vorticity Results

48.3.1 Vorticity Distribution for the Initial Stages

Figures 48.1 and 48.2 show the vorticity patterns at 200 GeV, 100 GeV and 20 GeV at t = 1 fm/c. We see that the vortex lines indicate distinct contours around the vortices formed. The contours are far more spaced out in the 20 GeV pattern than in the previous two figures.

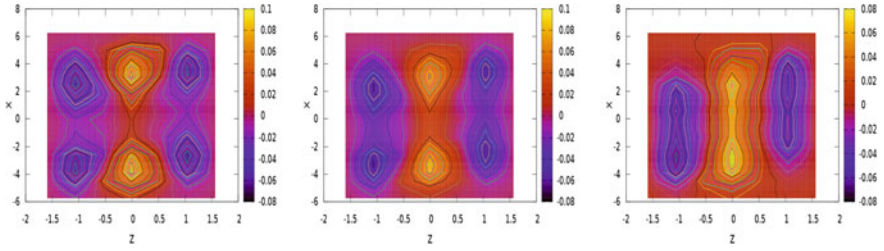

Fig. 48.1 Vorticity distribution at $\sqrt{s_{NN}} = 200$ GeV, 100 GeV and 20 GeV (from left to right) for partons

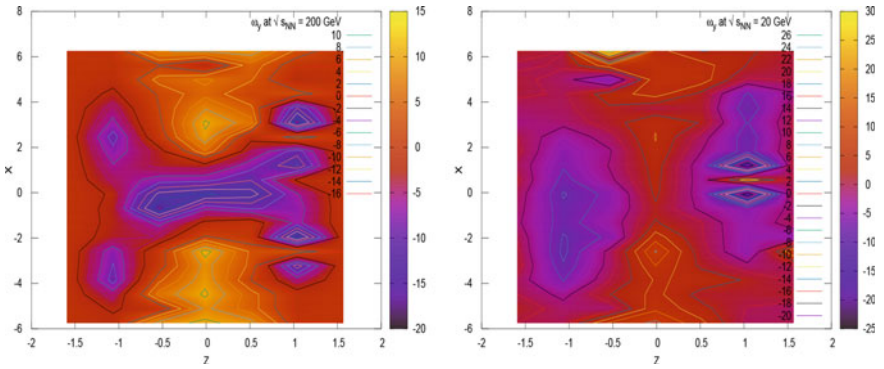

Fig. 48.2 Kinetic vorticity distribution in the reaction (x-z) plane at collision energies of 200 GeV (left panel) and 20 GeV (right panel) for relativistic partons

The vorticity formed tends to be circular if the angular momentum is higher and strain due to the bulk viscous pressure is lower. As the strain due to the bulk viscous pressure around the fluid increases, the vortices tend to spread-out and become more elliptical in nature. The spread-out elliptical vortices are due to the dissipation function which depends on the bulk viscosity. This is reflected in the simulations that we have performed.

We also studied the relativistic vorticity at the same collision energies. As expected, the values of the vorticity are much higher due to the relativistic γ factor. As the particles move with velocities close to that of light, the relativistic γ factor is often of the order of 10^2. Though there is a general similarity between the vorticity patterns, there are also several dissimilarities. The most important difference is noticed at the center of the pattern. Also to be noticed is that the differences are stronger at lower collision energies.

Now we present some patterns for the thermal vorticity. Thermal vorticity is also required for studying the polarization of the particles, so we give the thermal vorticity patterns for the same energies. In all the cases, we observe that the vorticity spreads out as we go to lower and lower collision energies. So it can be concluded that as we go down in collision energies the vorticity pattern is more and more diffuse (Fig. 48.3).

The average vorticity $\langle \omega_{xz} \rangle$ is plotted at different collision energies in Fig. 48.4 and it shows that the average vorticity decreases in all the cases with the increase in collision energy with a small dip below 40 GeV. Our vorticity results seem to be consistent with [5]. We have also studied vorticity pattern for finally produced hadrons at the same energy values. In the hadronic stage, the net vorticity is lower than the partonic stage but the general trend is the same. This is expected as the initial fireball consisting of partons has more angular momentum. So it can be concluded that as we go down in collision energies the vorticity pattern is more and more diffuse.

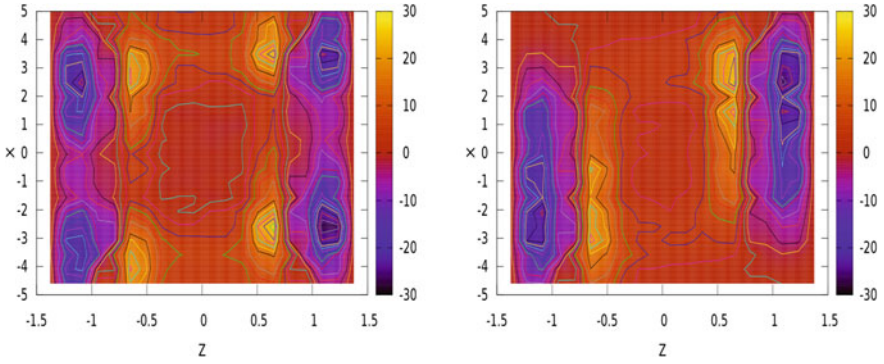

Fig. 48.3 Thermal vorticity distribution in the reaction (x-z) plane at collision energies of 200 GeV (left panel) and 20 GeV (right panel) for partons

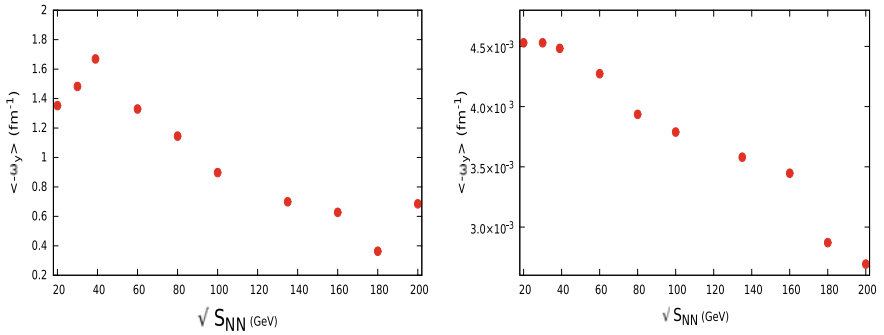

Fig. 48.4 Average thermal and classical vorticity $\langle \omega_{xz} \rangle \equiv \langle \omega_y \rangle$ at different $\sqrt{s_{NN}}$ at an impact parameter $b = 7\ fm$

48.3.2 *Shear Viscosity Dependence on $\sqrt{s_{NN}}$ and Elliptic Flow*

Figure 48.5 shows the specific shear viscosity with increasing collision energy. Instead of taking all the particles, we find the shear viscosity for the neutrons and the protons separately. We also find the shear viscosity of some other particles such as pions and Λ hyperons separately.

As seen from the plot, the specific shear viscosity is highest at lower collision energies which correspond to higher baryon chemical potentials. However, it becomes nearly constant beyond 80 GeV. We know that vorticity diffuses through the fluid through the viscous stresses. So the spreading out of the vorticity patterns indicate that the bulk viscous pressure plays a greater role in the viscous diffusion of the vortices at low collision energies and high baryon chemical potential.

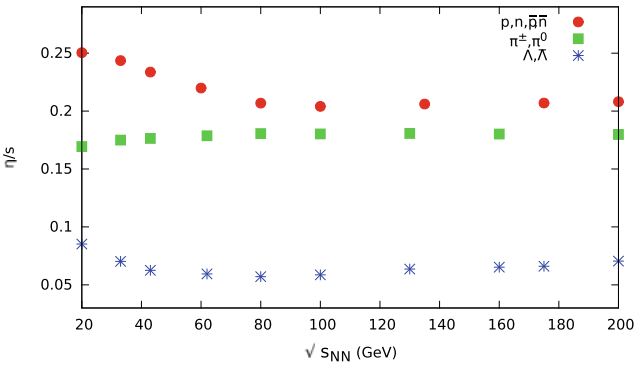

Fig. 48.5 The specific shear viscosity at different $\sqrt{s_{NN}}$ for neutrons and protons, pions, Λ hyperons and their antiparticles

48.4 Conclusions

We study the vorticity patterns and viscous effects at lower collision energies. One of the reasons why lower collision energies are studied experimentally is to include a finite baryon chemical potential. Hadron resonance gas models have been used to model the quark gluon plasma at finite baryon chemical potentials. We are interested to see whether these models can account for the vorticity patterns obtained from the hybrid transport models. Our bridge between these two very different models is the coefficient of shear viscosity. We find that at high collision energies, the local vorticity patterns are circular and well defined. At lower collision energies they appear to be stretched and elliptical in shape. The shape of the local vorticity patterns seem to indicate that viscous stress is higher at lower collision energies where the baryon chemical potential is more. Circular vorticity patterns indicate that the angular momentum dominates over the viscous stress. At higher collision energies, the chemical potential is low, we can infer that the viscous stress will also be low, our local vorticity pattern is circular showing the dominance of the angular momentum. At lower collision energy, the chemical potential is high, so the viscous stress will also be high, this gives rise to the stretched elliptical vortices as we see in the figures.

We also study the specific shear viscosity dependence on collision energy. We found that for higher collision energies, η/s become constant for different particles with a dip at lower collision energy range. The coefficient of shear viscosity depends on the momentum of the particles. We find that the shear viscosity decreases very little when we change the collision energy.

Acknowledgements A.S is supported by INSPIRE Fellowship of the Department of Science and Technology, Govt. of India, (Grant no: IF170627).

References

1. Y. Jiang, Z.-W. Lin, J. Liao, Phys. Rev. C **94**, 044910 (2016)
2. U. Heinz et al., Annu. Rev. Nucl. Part. Sci. **63**, 123–151 (2013)
3. B. Zhang, C.M. Ko, B.A. Li, Z.W. Lin, Phys. Rev. C **61**, 067901 (2000)
4. F. Becattini et al., Eur. Phys. J. C **75**, 406 (2015)
5. W.-T. Deng, X.-G. Huang, Phys. Rev. C **93**, 064907 (2016)
6. G.P. Kadam, H. Mishra, Nucl. Phys. A **934**, 133–147 (2015)

Chapter 49
The 3-D Structure of Kaon in Light-Cone Quark Model

Satvir Kaur and Harleen Dahiya

Abstract The generalized quark distributions (GPDs) describing the 3-D structure of kaon in light-cone quark model are investigated. We use the longitudinal momentum transfer to be zero for the analyses. The dependence of GPDs with respect to the quark longitudinal momentum fraction x and total momentum transfer $-t$ are studied. Further, we study the charge densities of u quark in kaon by using the overlap representation of light-cone wavefunctions. The charge densities are studied in transverse impact-parameter space. Also, the kaon GPDs for non-zero skewedness in the longitudinal impact-parameter space are observed by taking certain Fourier transformations. For all the analyses, we let ourselves focus in DGLAP regions for distributions of u quark.

49.1 Introduction

The multidimensional structure of the hadron to the level of its constituents is the main key to understand under the non-perturbative effects of Quantum Chromodynamics (QCD). To study the hadron structure, different parton distributions are there. In this paper, we focus on the generalized parton distributions (GPDs) [1] and charge densities [2]. The GPDs depend upon three variables, namely, (i) the longitudinal momentum fraction carried by the active parton (x), (ii) the longitudinal momentum transferred to the final state of hadron (ζ) and (iii) the total momentum transferred to the final state of hadron ($t = \Delta^2$). Here, we are dealing with $\zeta = 0$ i.e. when there is no longitudinal momentum transferred from the initial to final state of hadron. Further, for non-zero skewedness $\zeta \neq 0$, the GPDs in the longitudinal impact-parameter space explain the diffraction pattern [3]. One can obtain the longitudinal impact-parameter GPDs by taking the Fourier transform of ζ.

S. Kaur (✉) · H. Dahiya
Department of Physics, Dr. B.R. Ambedkar National Institute of Technology, Jalandhar 144011, India
e-mail: satvirkaur578@gmail.com

A. Giri and R. Mohanta (eds.), *Workshop on Frontiers in High Energy Physics 2019*, Springer Proceedings in Physics 248,
https://doi.org/10.1007/978-981-15-6292-1_49

The charge densities, which are also important to get the probability of charge located at a transverse distance b, also investigated. The transverse impact-parameter $\mathbf{b}_\perp$ defines the distance from the position of struck quark to the center of momentum [4]. The Fourier transform of the electromagnetic form factor provide the charge densities in transverse direction in the absence of any longitudinal momentum transfer.

In this work, we take kaon as a pseudoscalar particle to study the distributions of the quark. The light-cone framework is chosen [5], as it imparts a suitable environment to study the relativistic dynamical effects on hadron structure. We focus on the description of minimal Fock state i.e. quark-antiquark state in light-cone quark model [6].

49.2 Light-Cone Quark Model (LCQM)

Concerning to the constituents of kaon, the two-particle Fock state expansion is indicated as [6]

$$|M(P,S)\rangle = \sum_{\lambda_1,\lambda_2} \int \frac{dx d^2\mathbf{k}_\perp}{\sqrt{x(1-x)}16\pi^3} |x,\mathbf{k}_\perp,\lambda_1,\lambda_2\rangle \psi_{S_z}^{\lambda_1,\lambda_2}(x,\mathbf{k}_\perp). \quad (49.1)$$

where $x = \frac{k^+}{P^+}$ and $\mathbf{k}_\perp$ indicate the light-cone momentum fraction carried by the struck quark and transverse momentum of active quark respectively.

Combining the different helicities of quark (λ_1) and antiquark (λ_2) in the kaon, the possible wavefunctions $\psi_{S_z}^{\lambda_1,\lambda_2}$ are expressed as

$$\begin{aligned}
\psi_0^{\uparrow,\uparrow}(x,\mathbf{k}_\perp) &= -\frac{1}{\sqrt{2}} \frac{k_1 - ik_2}{\sqrt{\mathbf{k}_\perp^2 + (1-x)m_1^2 + xm_2^2 - x(1-x)(m_1-m_2)^2}} \varphi(x,\mathbf{k}_\perp), \\
\psi_0^{\uparrow,\downarrow}(x,\mathbf{k}_\perp) &= \frac{1}{\sqrt{2}} \frac{(1-x)m_1 + xm_2}{\sqrt{\mathbf{k}_\perp^2 + (1-x)m_1^2 + xm_2^2 - x(1-x)(m_1-m_2)^2}} \varphi(x,\mathbf{k}_\perp), \\
\psi_0^{\downarrow,\uparrow}(x,\mathbf{k}_\perp) &= -\psi_0^{\uparrow,\downarrow}(x,\mathbf{k}_\perp), \\
\psi_0^{\downarrow,\downarrow}(x,\mathbf{k}_\perp) &= [\psi_0^{\uparrow,\uparrow}(x,\mathbf{k}_\perp)]^*, \qquad (49.2)
\end{aligned}$$

where the momentum-space wavefunction $\varphi(x,\mathbf{k}_\perp)$ is described as [7]

$$\varphi(x,\mathbf{k}_\perp) = A \exp\left[-\frac{\frac{\mathbf{k}_\perp^2+m_1^2}{x} + \frac{\mathbf{k}_\perp^2+m_2^2}{1-x}}{8\beta^2} - \frac{(m_1^2-m_2^2)^2}{8\beta^2\left(\frac{\mathbf{k}_\perp^2+m_1^2}{x} + \frac{\mathbf{k}_\perp^2+m_2^2}{1-x}\right)} \right]. \quad (49.3)$$

In the wavefunctions defined above, the positive and negative helicities of the quark and the spectator (antiquark in case of kaon), are denoted by $\uparrow$ and $\downarrow$ respectively. Since, for the active quark, the longitudinal momentum fraction and transverse momentum is denoted by x and $\mathbf{k}_\perp$, however, for the spectator antiquark, the parameters are $(1-x)$ and $-\mathbf{k}_\perp$ respectively.

Here, m_1 and m_2 correspond to the masses of u-quark and $\bar{s}$-quark respectively. The parameters β and A define the respective terms, harmonic scale and normalization constant.

49.3 Generalized Parton Distributions (GPDs)

We evaluate GPDs of valence quark in kaon by using the overlap representation of wavefunctions in light-cone quark model. The DGLAP region for quark at $\zeta = 0$ i.e. $0 < x < 1$ is taken into account. The related unpolarized GPD for kaon in the absence of light-cone time and transverse coordinates i.e. at $z^+ = \mathbf{z}_\perp = 0$ is expressed as [1]

$$H^q_{K^+} = \frac{1}{2}\int \frac{dz^-}{2\pi} e^{ixP^+z^-}\Big\langle M(P')\Big|\bar{q}\Big(-\frac{z}{2}\Big)\gamma^+ q\Big(\frac{z}{2}\Big)\Big|M(P'')\Big\rangle, \tag{49.4}$$

where P'' and P' corresponds to the final and initial kaon states.

The explicit relation of GPD can be calculated by putting the meson state from (49.1) and associated quark field operators in above equation. After solving the correlator, the final result for GPD come out to be

$$H^u_{K^+} = \int \frac{d^2\mathbf{k}_\perp}{16\pi^3}\Big[\mathbf{k}^2_\perp - (1-x)^2\frac{\mathbf{\Delta}^2_\perp}{4} + ((1-x)m_1 + xm_2)^2\Big]\phi^\dagger_u(x,\mathbf{k}''_\perp)\phi_u(x,\mathbf{k}'_\perp). \tag{49.5}$$

On using DGLAP domains in symmetric frames, the initial and final state momenta of active quark leads to

$$\mathbf{k}'_\perp = \mathbf{k}_\perp + (1-x)\frac{\mathbf{\Delta}_\perp}{2}; \qquad \mathbf{k}''_\perp = \mathbf{k}_\perp - (1-x)\frac{\mathbf{\Delta}_\perp}{2}, \tag{49.6}$$

We plot the unpolarized GPD $H(x,0,t)$ of the valence quark present in kaon in the absence of longitudinal momentum transfer i.e. at $\zeta = 0$ in Fig. 49.1. We show the three-dimensional image on the basis of longitudinal momentum fraction and total momentum transferred from the initial state to final state of kaon. While increasing the momentum transfer $-t$, we observe the shift in the distribution peak as one approach the higher values of the momentum fraction x. However, magnitude of peak decreases in this case.

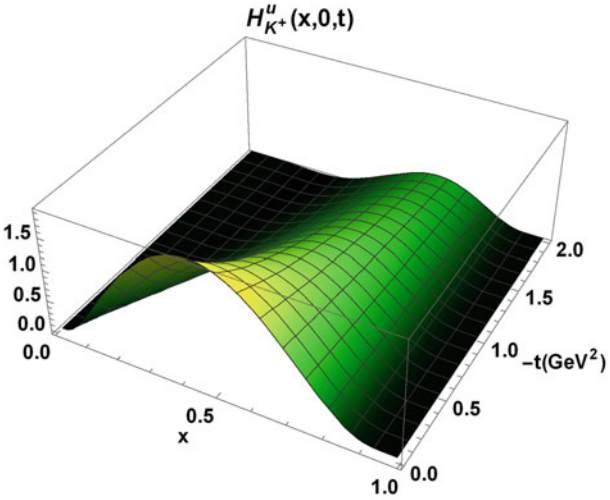

Fig. 49.1 The unpolarized GPD $H(x, 0, t = \boldsymbol{\Delta}_\perp)$ w.r.t. x and $-t$ (in GeV^2) for u-quark in K^+-meson

49.4 Transverse Charge Densities

One can get the transverse charge density by taking the two dimensional Fourier transform of the Dirac form factor ($F_K(Q^2)$) [8], we have

$$\begin{aligned}\rho(b) &= \int \frac{d^2\boldsymbol{\Delta}_\perp}{(2\pi)^2} F_K(Q^2 = \boldsymbol{\Delta}_\perp^2) e^{i\boldsymbol{\Delta}_\perp.\mathbf{b}_\perp} \\ &= \int_0^\infty \frac{dQ}{2\pi} Q J_0(bQ) F_K(Q^2), \end{aligned} \tag{49.7}$$

where

$$F_K(Q^2) = e_u \int dx H^u_{K^+}(x, 0, t, m_1, m_2) + e_{\bar{s}} \int dx H^{\bar{s}}_{K^+}(x, 0, t, m_2, m_1). \tag{49.8}$$

We show the transverse charge densities $\rho_{ch}(\mathbf{b}_\perp)$ of u quark in kaon in Fig. 49.2. We observe the maximum charge density in the center of impact-parameter plane for u-quark case. As the impact-parameter value increases, the density goes on decreasing and eventually become zero at the higher impact-parameter distances.

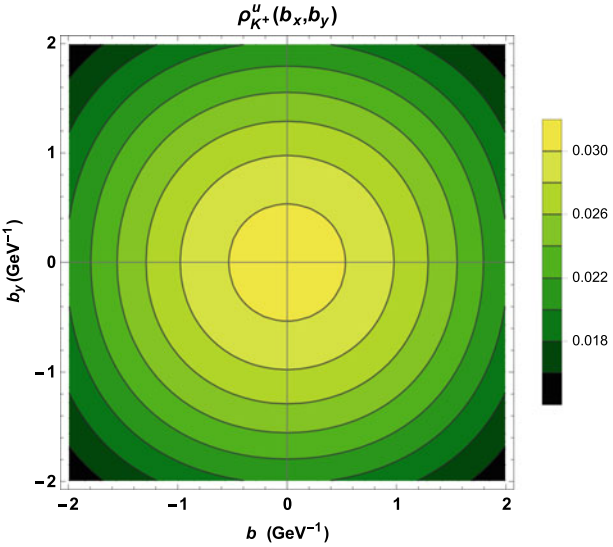

Fig. 49.2 The charge density $\rho^u(\mathbf{b}_\perp)$ of kaon in transverse momentum plane

49.5 Longitudinal Impact-Parameter Dependent GPDs

The three-dimensional structure of kaon in light-front coordinate space is obtained by taking the Fourier transform of ζ, which lead to provide the longitudinal impact-parameter $\sigma = \frac{1}{2}b^- P^+$ [3]. So in longitudinal position space, the unpolarized GPD for kaon is expressed as

$$\begin{aligned} H(x,\sigma,t) &= \frac{1}{2\pi}\int_0^{\zeta_f} d\zeta e^{\frac{i}{2}\zeta P^+ b^-} H(x,\zeta,t); \\ &= \frac{1}{2\pi}\int_0^{\zeta_f} d\zeta e^{i\zeta\sigma} H(x,\zeta,t) \end{aligned} \tag{49.9}$$

Here we are restricted in the DGLAP region $0 < \zeta < 1$ for quark. The upper limit of ζ is given by ζ_F, which depends upon the factor ζ_{max}, we have

$$\zeta_{max} = \sqrt{\frac{-t}{-t+4M^2}}. \tag{49.10}$$

If $x < \zeta_{max}$, the limit ζ_F is given by x, while in reverse case, i.e. $x > \zeta_{max}$, ζ_F depends upon ζ_{max}.

In Fig. 49.3, we plot the Fourier spectrum of unpolarized GPD of kaon for u-quark. We fixed the value of momentum transfer from initial state to final state of kaon as $-t = 0.5$ GeV^2 and show the dependence of σ on longitudinal impact-parameter

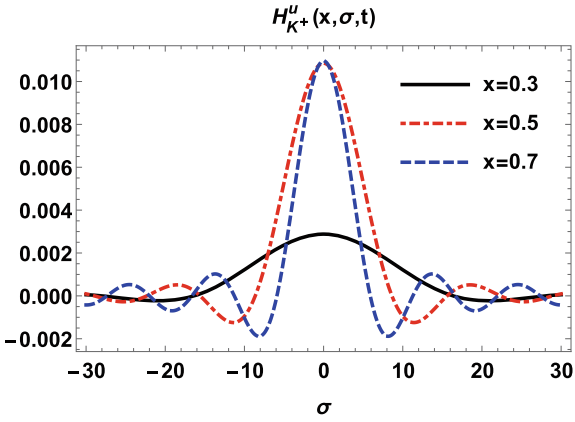

Fig. 49.3 The longitudinal impact-parameter GPD $H(x, \sigma, t)$ w.r.t. σ at different values of x for u-quark in K^+-meson

GPD at different values of longitudinal momentum fractions carried by u-quark i.e. x. It shows the diffraction patterns in the longitudinal impact-parameter space (σ-space). This diffraction pattern is meant to be the analogous to diffraction scattering of a optical wave, where the ζ value is observed as the slit width.

References

1. M. Diehl, Phys. Rep. **388**, 41 (2003)
2. G.A. Miller, Phys. Rev. C **80**, 045210 (2009)
3. S.J. Brodsky, D. Chakrabarti, A. Harindranath, A. Mukherjee, J.P. Vary, Phys. Lett. B **641**, 440 (2006)
4. M. Diehl, Eur. Phys. J. C **25**, 223 (2002). Erratum: Eur. Phys. J. C **31**, 277 (2003)
5. P.A.M. Dirac, Rev. Mod. Phys. **21**, 392 (1949)
6. W. Qian, B.-Q. Ma, Phys. Rev. D **78**, 074002 (2008)
7. B.-W. Xiao, X. Qian, B.-Q. Ma, Eur. Phys. J. A **15**, 523 (2002)
8. G.A. Miller, Phys. Rev. Lett. **99**, 112001 (2007)

Chapter 50
Quark Wigner Distribution and GTMD of Pion Using Soft-Wall AdS/QCD Wavefunctions

Navdeep Kaur and Harleen Dahiya

Abstract We investigate the quark Wigner distribution of the pion by using the soft-wall AdS/QCD light front wavefunctions with total quark orbital angular momentum $L_z = 0$ and $|L_z| = 1$. We calculate the Wigner distribution of an unpolarized quark inside the unpolarized pion. We present the results in impact-parameter space as well as in momentum space. We study the generalized transverse momentum distribution (GTMD) of pion for different values of skewness as well as the case where we take skewness to be zero.

50.1 Introduction

Wigner distributions provide the complete picture of hadrons in terms of quark and gluon degree of freedom. They unify the information about position distribution and momentum distribution of partons inside hadrons. The five-dimensional Wigner distributions are functions of longitudinal momentum fraction, transverse momentum and impact-parameter space [1]. Wigner distributions can not be accessed directly but can be reduced to generalized parton distributions (GPDs) after integration over transverse momentum and to transverse momentum distributions (TMDs) after integration over impact-parameter space which can be measured directly in scattering processes. The light front framework is a suitable framework for the study of hadronic structure due to its simple light front vacuum and the light front wavefunctions (LFWFs) which relate the constituent partons to their hadronic state and provide a very convenient way to study the different distribution functions. In this work, we have used the soft-wall AdS/QCD LFWFs with total quark orbital angular momentum $L_z = 0$ and $|L_z| = 1$ [2]. We study the Wigner distribution of pion. In this model, pion has one Wigner distribution corresponding to the unpolarized quark inside pion at lead-

N. Kaur (✉) · H. Dahiya
Department of Physics, Dr. B.R. Ambedkar National Institute of Technology, Jalandhar 144011, India
e-mail: nkmangat91@gmail.com

A. Giri and R. Mohanta (eds.), *Workshop on Frontiers in High Energy Physics 2019*, Springer Proceedings in Physics 248,
https://doi.org/10.1007/978-981-15-6292-1_50

ing twist. The result is discussed in impact-parameter space as well as in transverse space. We also evaluate the leading twist GTMD of pion for zero skewness as well as for non-zero skewness case.

50.2 Soft-Wall AdS/QCD Wavefunction

The soft-wall AdS/QCD model relates the five dimensional AdS theory to the QCD formulation. In this model, the LFWFs for two-parton bound state are extracted from holographic mapping of AdS/QCD form factor with LF QCD form factor [3]. The extracted wave functions can be further improved to obtain correct scaling behavior of pion PDF and pion form factors. The improved LFWFs of pion $\psi_\pi^{L_z}(x, \mathbf{p}_\perp)$ with total quark orbital angular momentum $L_z = 0, \pm 1$ are [2]

$$\psi_\pi^{(0)}(x, \mathbf{p}_\perp) = \frac{4\pi N_0}{\kappa} \frac{\sqrt{\log(1/x)}}{1-x} \sqrt{f(x)\, \bar{f}(x)}\, \exp\left[-\frac{\mathbf{p}_\perp}{2\kappa^2} \frac{\log(1/x)}{(1-x)^2}\, \bar{f}(x)\right],$$
$$\psi_\pi^{(1)}(x, \mathbf{p}_\perp) = \frac{4\pi N_1}{\kappa^2} \frac{\sqrt{\log^3(1/x)}}{(1-x)^2} \sqrt{f(x)\, \bar{f}^3(x)}\, \exp\left[-\frac{\mathbf{p}_\perp}{2\kappa^2} \frac{\log(1/x)}{(1-x)^2}\, \bar{f}(x)\right]. \tag{50.1}$$

Here κ is the AdS/QCD scale, N_0 and N_1 are the normalization constants. The profile functions $f(x)$ and $\bar{f}(x)$ are

$$f(x) = x^{\alpha-1}(1-x)^\beta(1+\gamma x^\delta), \qquad \bar{f}(x) = x^{\bar{\alpha}}(1-x)^\beta(1+\bar{\gamma} x^{\bar{\delta}}), \tag{50.2}$$

where $\alpha, \bar{\alpha}, \beta, \gamma, \bar{\gamma}, \delta, \bar{\delta}$ are the free parameters. The values of the parameters are fixed by fitting to pion PDF data and electromagnetic form factor data [2]. In the limit $f(x) = \bar{f}(x) = 1$, the improved LFWFs in (50.1) reduce to the original AdS/QCD LFWFs.

50.3 Quark Wigner Distribution

Quark Wigner distribution can be obtained by the two-dimensional Fourier transform of generalized quark-quark correlator as follows [1]

$$\rho^{[\Gamma]}(x,\, \mathbf{p}_\perp, \mathbf{b}_\perp) = \int \frac{\mathrm{d}^2 \Delta_\perp}{(2\pi)^2}\, e^{[-i\Delta_\perp . b_\perp]}\, W^{[\Gamma]}(x, \mathbf{p}_\perp, \Delta_\perp), \tag{50.3}$$

where

$$W^{[\Gamma]}(x,\ \mathbf{p}_\perp,\ \Delta_\perp) = \frac{1}{2}\int \frac{\mathrm{d}z^-\mathrm{d}^2z_\perp}{(2\pi)^3}\, e^{[ip.z]}\, \langle \pi(P^{''})|\bar{\psi}(-Z/2)\Gamma\, \mathscr{W}\, \psi(Z/2)|\pi(P^{'})\rangle. \tag{50.4}$$

Here Γ stands for the Dirac operator. $P = (P^{'} + P^{''})/2$ is the average of initial and final momentum of pion, Δ is the momentum transfer to the pion from initial to final state. x and $\mathbf{p}_\perp$ are the longitudinal momentum fraction and transverse momentum of quark inside pion respectively. For color invariance, the Wilson line $\mathscr{W}$ is introduced in correlator. The initial state and final state momentum of pion of mass M_π are:

$$P^{'} = (P^+, (M_\pi^2 + \mathbf{P}_\perp^{'2})/P^+, \Delta_\perp/2) \qquad P^{''} = (P^+, (M_\pi^2 + \mathbf{P}_\perp^{''2})/P^+, -\Delta_\perp/2), \tag{50.5}$$

respectively. With the minimal Fock state configuration, i.e. $q\bar{q}$, one can define the positively charged pion state with different values of $L_z = 0, \pm 1$ as [4]

$$\begin{aligned}
|\pi^+(P^{'})\rangle &= |\pi^+(P)\rangle_{L_z=0} + |\pi^+(P)\rangle_{|L_z|=1}\,,\\
|\pi^+(P^{'})\rangle_{L_z=0} &= \int \frac{d^2\mathbf{p}_\perp}{16\pi^3}\,\frac{dx}{\sqrt{x(1-x)}}\,\psi_\pi^{(0)}(x,\mathbf{p}_\perp)\,|x,\mathbf{p}_\perp;\,P^+,\mathbf{P}^{'}_\perp,L_z=0\rangle\,,\\
|\pi^+(P^{'})\rangle_{|L_z|=1} &= \int \frac{d^2\mathbf{p}_\perp}{16\pi^3}\,\frac{dx}{\sqrt{x(1-x)}}\,\psi_\pi^{(1)}(x,\mathbf{p}_\perp)\frac{1}{\sqrt{2}}\Big(p_\perp^+\,|x,\mathbf{p}_\perp;\,P^+,\mathbf{P}^{'}_\perp,L_z=1\rangle\\
&\quad + p_\perp^-\,|x,\mathbf{p}_\perp;\,P^+,\mathbf{P}^{'}_\perp,L_z=-1\rangle\Big)\,,
\end{aligned} \tag{50.6}$$

where $p_\perp^\pm = p_1 \pm ip_2$, $\psi_\pi^{(0)}(x,\mathbf{p}_\perp)$ and $\psi_\pi^{(1)}(x,\mathbf{p}_\perp)$ are the pion $L_z = 0$ and $|L_z| = 1$ phenomenological LFWFs respectively. We have obtained the following expression for correlator in terms of LFWFs by using the pion state given in (50.6) in (50.4) with $\Gamma = \gamma^+$:

$$W^{[\gamma^+]}(x,\mathbf{k}_\perp,\Delta_\perp) = \frac{1}{16\pi^3}\Big[\psi_\pi^{(0)\star}(x,\mathbf{k}_\perp^o)\psi_\pi^{(0)}(x,\mathbf{k}_\perp^i) + \mathbf{k}_\perp^o\mathbf{k}_\perp^i\,\psi_\pi^{(1)\star}(x,\mathbf{k}_\perp^o)\psi_\pi^{(1)}(x,\mathbf{k}_\perp^i)\Big], \tag{50.7}$$

where initial and final transverse momentum of active quark are

$$\mathbf{k}_\perp^i = \mathbf{k}_\perp + (1-x)\frac{\Delta_\perp}{2}, \qquad \mathbf{k}_\perp^o = \mathbf{k}_\perp - (1-x)\frac{\Delta_\perp}{2}.$$

The expressions for Wigner distribution of unpolarized quark inside an unpolarized pion for zero skewness ($\zeta = 0$):

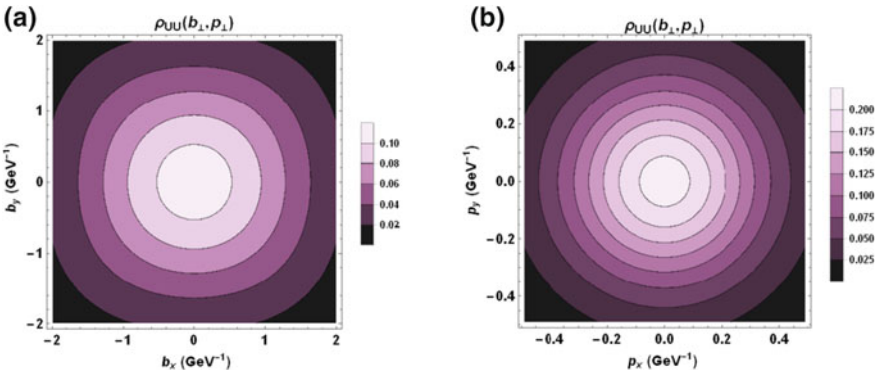

Fig. 50.1 Plot of Wigner distribution of unpolarized quark inside the unpolarized pion $\rho_{UU}(\mathbf{b}_\perp, \mathbf{p}_\perp)$ (**a**) in the impact-parameter space with fixed transverse momentum $\mathbf{p}_\perp = 0.3$ GeV along the y-axis (**b**) in the transverse-momentum space with fixed impact parameter $\mathbf{b}_\perp = 0.3$ fm along the y-axis

$$\rho_{UU}(x, \mathbf{p}_\perp, \mathbf{b}_\perp) = \frac{N_0^2 \log(1/x)\, \bar{f}(x)\, f(x)}{\pi\, \kappa^2\, (1-x)^2} \int \frac{d^2\Delta_\perp\, e^{-i\Delta_\perp \cdot \mathbf{b}_\perp}}{(2\pi)^2} \Big[1 + \Big(\frac{N_1}{N_0}\Big)^2 \frac{\log(1/x)^2\, \bar{f(x)}^2}{\kappa^2\, (1-x)^2} \times \Big(\mathbf{p}_\perp^2 - (1-x)^2\, \frac{\Delta_\perp^2}{4}\Big)\Big] \exp\left[-\Big(\mathbf{p}_\perp^2 + (1-x)^2\, \frac{\Delta_\perp^2}{4}\Big) \frac{\log(1/x)\, \bar{f}(x)}{\kappa^2 (1-x)^2}\right].$$

We plot the obtained result of Wigner distribution of unpolarized quark inside the unpolarized pion $\rho_{UU}(x, \mathbf{p}_\perp, \mathbf{b}_\perp)$ in Fig. 50.1. In Fig. 50.1a, the Wigner distribution $\rho_{UU}(x, \mathbf{p}_\perp, \mathbf{b}_\perp)$ in the impact-parameter space with fixed transverse momentum $\mathbf{p}_\perp = 0.3$ GeV along the y-axis is shown and the Wigner distribution $\rho_{UU}(x, \mathbf{p}_\perp, \mathbf{b}_\perp)$ in the transverse-momentum space with fixed impact parameter $\mathbf{b}_\perp = 0.3$ fm along the y-axis is shown in Fig. 50.1b. $\rho_{UU}(x, \mathbf{p}_\perp, \mathbf{b}_\perp)$ shows circularly symmetric behavior in both impact-parameter space as well as transverse-momentum space. The amplitude of $\rho_{UU}(x, \mathbf{p}_\perp, \mathbf{b}_\perp)$ is maximum at center and start decreasing as move away from center in both spaces. This implicit the maximum probability of finding the quark is with smaller transverse momentum at center.

50.4 Generalized Transverse Momentum Distribution (GTMD)

The quark-quark correlator with non-zero skewness ($\xi \neq 0$) is connected to the leading twist GTMD of pion as

$$W^{[\gamma^+]}(x,\, \xi,\, \mathbf{k}_\perp, \Delta_\perp) = F_1(x,\, \xi, \mathbf{k}_\perp, \Delta_\perp)\,. \tag{50.8}$$

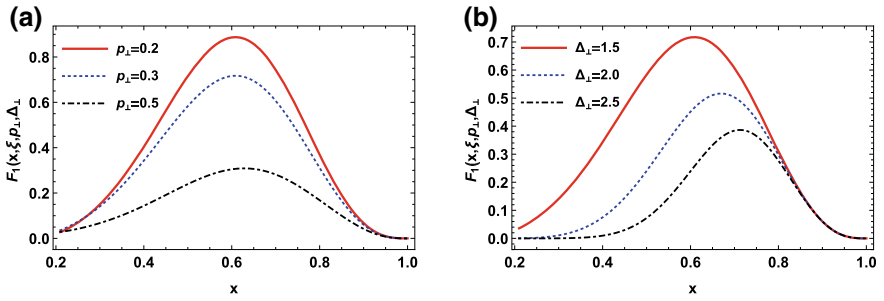

Fig. 50.2 Plot of quark GTMD $F_1(x,\ \xi, \mathbf{k}_\perp,\ \Delta_\perp)$ for $\xi = 0.2$ (**a**) with the fixed value of $\Delta_\perp = 1.5$ GeV for the different values of $\mathbf{k}_\perp$ (**b**) with the fixed value of $\mathbf{p}_\perp = 0.3$ GeV for the different values of $\Delta_\perp$

In this model, the GTMD of pion in overlap representation of LFWFs can be written as

$$F_1(x,\ \xi, \mathbf{k}_\perp,\ \Delta_\perp) = \frac{1}{16\pi^3}\left[\psi_\pi^{(0)\star}(x, \mathbf{k}_\perp^o)\psi_\pi^{(0)}(x, \mathbf{k}_\perp^i) + \mathbf{k}_\perp^o \mathbf{k}_\perp^i \psi_\pi^{(1)\star}(x, \mathbf{k}_\perp^o)\psi_\pi^{(1)}(x, \mathbf{k}_\perp^i)\right], \tag{50.9}$$

where

$$x^i = \frac{x+\xi}{1+\xi}, \qquad \mathbf{k}_\perp^i = \mathbf{k}_\perp + (1-x^i)\frac{\Delta_\perp}{2},$$
$$x^o = \frac{x-\xi}{1-\xi}, \qquad \mathbf{k}_\perp^o = \mathbf{k}_\perp - (1-x^o)\frac{\Delta_\perp}{2}.$$

The explicit expression of the GTMD $F_1(x,\ \xi, \mathbf{k}_\perp,\ \Delta_\perp)$ obtained is given as

$$F_1(x,\ \xi, \mathbf{k}_\perp, \Delta_\perp) = \frac{N_0^2}{\pi}\frac{\sqrt{\log(1/x^o)\ \log(1/x^i)\ \bar{f}(x^o)\ \bar{f}(x^i)\ f(x^o) f(x^i)}}{\kappa^2\ (1-x^o)\ (1-x^i)}$$
$$\times\Big[1 + \Big(\frac{N_1}{N_0}\Big)^2 \frac{\log(1/x^o)\ \log(1/x^i)\ f(\bar{x^o}) f(\bar{x^i})}{\kappa^2\ (1-x^o)(1-x^i)}\Big(\mathbf{k}_\perp^2 + \frac{\mathbf{k}_\perp\ \Delta_\perp (x^o - x^i)}{2} - (1-x^o)\ (1-x^i)\ \frac{\Delta_\perp^2}{4}\Big)\Big]$$
$$\times \exp\Big[-\Big(\mathbf{k}_\perp + (1-x^o)\frac{\Delta_\perp}{4}\Big)^2 \frac{\log(1/x^o)\ \bar{f}(x^o)}{2\kappa^2\ (1-x^o)^2} - \Big(\mathbf{k}_\perp + (1-x^i)\frac{\Delta_\perp}{4}\Big)^2 \frac{\log(1/x^i)\ \bar{f}(x^i)}{2\,\kappa^2\ (1-x^i)^2}\Big]. \tag{50.10}$$

In Fig. 50.2, we have plotted the result of $F_1(x,\ \xi, \mathbf{k}_\perp,\ \Delta_\perp)$ for fixed $\xi = 0.2$. In Fig. 50.2a, the GTMD $F_1(x,\ \xi, \mathbf{k}_\perp,\ \Delta_\perp)$ with the fixed value of $\Delta_\perp = 1.5$ GeV for the different values of $\mathbf{k}_\perp$ is shown. The magnitude of $F_1(x,\ \xi, \mathbf{k}_\perp,\ \Delta_\perp)$ decreases with increase in transverse momentum for fixed longitudinal momentum transfer ξ and transverse momentum transfer $\Delta_\perp$. We have shown the GTMD $F_1(x,\ \xi, \mathbf{k}_\perp,\ \Delta_\perp)$ with the fixed value of $\mathbf{p}_\perp = 0.3$ GeV for the different values of $\Delta_\perp$ in Fig. 50.2b. As

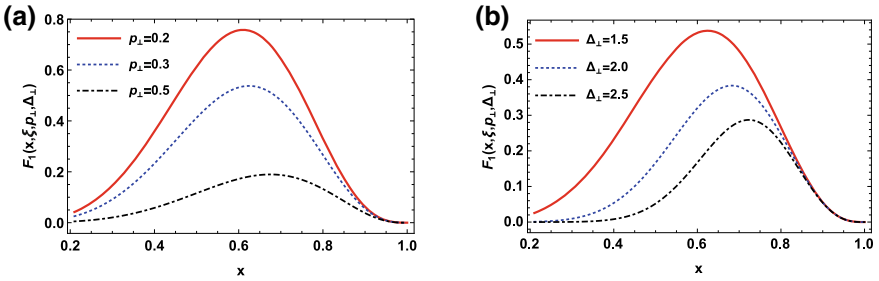

Fig. 50.3 Plot of quark GTMDs F_1 for zero skewness (**a**) with the fixed values of $\Delta_\perp = 1.5$ GeV for the different values of $\mathbf{k}_\perp$ (**b**) with the fixed values of $\mathbf{p}_\perp = 0.3$ GeV for the different values of $\Delta_\perp$

the transverse momentum transfer $\Delta_\perp$ from initial to final state increases for fixed transverse momentum $\mathbf{p}_\perp$ and longitudinal momentum transfer ξ, the amplitude of GTMD $F_1(x, \xi, \mathbf{k}_\perp, \Delta_\perp)$ decreases and the peaks shift towards the higher value of longitudinal momentum fraction. In Fig. 50.3, the GTMD F_1 for zero skewness have shown the similar behavior as non-zero skewness case but have lower amplitude.

50.5 Summary

Quark Wigner distribution of pion has been evaluated by using the AdS/QCD light front wavefunction with total quark orbital angular momentum $L_z = 0$ and $|L_z| = 1$. We have analyzed the Wigner distribution ρ_{UU} in impact-parameter space and also in transverse momentum space. ρ_{UU} distribution is spherically symmetric in both impact-parameter space as well as transverse momentum space. This implies the probability of a quark to spin up equivalent to the probability of quark to spin down. We also study the generalized transverse momentum distribution (GTMD) of pion F_1 in this model with non-zero skewness and for zero skewness.

Acknowledgements N.K. would like to thank the MHRD, Government of India for assistantship at NITJ. This work of H.D. is supported by the funding from Department of Science and Technology, Government of India (Ref No. EMR/2017/001549).

References

1. X. Ji, Phys. Rev. Lett. **91**, 062001 (2003)
2. T. Gutsche, V.E. Lyubovitskij, I. Schmidt, A. Vega, J. Phys. G: Nucl. Part. Phys. **42**, 095005 (2015)
3. S.J. Brodsky, G.F. de Teramond, Phys. Rev. Lett. **78**, 025032 (2008)
4. M. Burkardt, X.D. Ji, F. Yuan, Phys. Lett. B **545**, 345 (2002)

Part V
Heavy Flavour Physics

Chapter 51
Global Fits of B Decay Anomalies

Wolfgang Altmannshofer

Abstract I summarize the current status of the anomalies that are observed in decays of b hadrons based on the charged current $b \to c\ell\nu$ transition and the neutral current $b \to s\ell\ell$ transition. After a quick review of the experimental situation I discuss the results of a recent global fit in the context of the weak effective theory at the b-quark scale, in the Standard Model effective theory above the electroweak scale, and in a simplified Z' model. The experimental data continues to consistently point to new physics in semi-leptonic Wilson coefficients with high significance.

51.1 Introduction

Rare decays of b hadrons are very well recognized as important probes of the Standard Model (SM) flavor sector [1]. If theoretical uncertainties in the SM predictions can be controlled, flavor violating processes can indirectly explore very high mass scales, well beyond the direct reach of collider experiments. Moreover, such processes can be used to learn about the flavor properties of new physics at the TeV-scale.

Interestingly, over the last several years, a significant number of discrepancies have emerged in B meson decays. The discrepancies between the SM predictions and the experimental results can be interpreted as indirect hints for new physics. In the following sections I will review the discrepancies and the possible implications in the context of new physics scenarios. The following is mainly based on [2]. For similar studies see also [3–8].

W. Altmannshofer (✉)
Santa Cruz Institute for Particle Physics, University of California,
Santa Cruz, CA 95064, USA
e-mail: waltmann@ucsc.edu

A. Giri and R. Mohanta (eds.), *Workshop on Frontiers in High Energy Physics 2019*, Springer Proceedings in Physics 248,
https://doi.org/10.1007/978-981-15-6292-1_51

51.2 Anomalies in Rare Flavor Changing Neutral Current Decays

Discrepancies between the SM predictions and the experimental results exist in several observables in rare, loop induced, $b \to s\ell\ell$ decays. Among them is the anomalously low branching ratio of $B_s \to \phi\mu\mu$ [9] (and to a lesser extent also $B \to K^{(*)}\mu\mu$ [10] and $B_s \to \mu\mu$ [11–13]) and the anomaly in the $B \to K^*\mu\mu$ angular observable P_5' [14]. Of particular interest are the anomalies in the theoretically clean lepton flavor universality (LFU) ratios $R_{K^{(*)}} = \text{BR}(B \to K^{(*)}\mu\mu)/\text{BR}(B \to K^{(*)}ee)$. The most precise measurements of R_K and R_{K^*} have been obtained by LHCb [15, 16]

$$R_K = 0.846^{+0.060+0.016}_{-0.054-0.014}\,, \qquad \text{for} \quad 1.1\,\text{GeV}^2 < q^2 < 6\,\text{GeV}^2\,, \tag{51.1}$$

$$R_{K^*} = \begin{cases} 0.66^{+0.11}_{-0.07} \pm 0.03\,, & \text{for } 0.045\,\text{GeV}^2 < q^2 < 1.1\,\text{GeV}^2\,, \\ 0.69^{+0.11}_{-0.07} \pm 0.05\,, & \text{for } 1.1\,\text{GeV}^2 < q^2 < 6\,\text{GeV}^2\,, \end{cases} \tag{51.2}$$

with q^2 the dilepton invariant mass squared. The SM predicts $R^{\text{SM}}_{K^{(*)}} \simeq 1$ with theoretical uncertainties well below the current experimental ones [17]. The above results imply a tension between theory and experiment in three measurements by $\sim 2.5\sigma$, each. Recent measurements of $R_{K^{(*)}}$ by Belle [18, 19] have sizable uncertainties. The Belle results are compatible with both the SM prediction and the LHCb results.

It has been noted early on that a remarkably simple and consistent solution to all the $b \to s\ell\ell$ discrepancies is given by new physics in the form of four fermion contact interactions involving a bottom quark, a strange quark and muons, parameterized by the effective Hamiltonian[1]

$$\mathcal{H}^{\text{NP}}_{\text{eff}} = -\frac{4G_F}{\sqrt{2}} V^*_{ts} V_{tb} \frac{e^2}{16\pi^2} \Big(C_9^{bs\mu\mu} (\bar{s}\gamma_\nu P_L b)(\bar{\mu}\gamma^\nu \mu) + C_{10}^{bs\mu\mu} (\bar{s}\gamma_\nu P_L b)(\bar{\mu}\gamma^\nu \gamma_5 \mu) \Big)\,. \tag{51.3}$$

The left plot in Fig. 51.1 (from [2]) shows the best fit region in the plane of the two new physics Wilson coefficients $C_9^{bs\mu\mu}$ and $C_{10}^{bs\mu\mu}$, taking into account only theoretically clean lepton flavor universality observables (blue), only the absolute branching ratios and angular observables in $b \to s\mu\mu$ transitions (orange) and the result of a full global fit (red). There is strong preference for non-zero values of the new physics Wilson coefficients. Fits with excellent quality can be obtained in 1 parameter new physics scenarios with (a) $C_9^{bs\mu\mu}$ only (muonic vector current), or with (b) $C_9^{bs\mu\mu} = -C_{10}^{bs\mu\mu}$ (left-handed muonic current). The best fit points in these scenarios have pull values with respect to the SM of more than 5σ[2]

[1] The low-q^2 bin of R_{K^*} is hardly affected by a four fermion contact interaction and the corresponding discrepancy can only be partially addressed. Light new degrees of freedom are required to fully resolve the discrepancy in the low-q^2 bin of R_{K^*} [20].

[2] Note that the precise pull values depend on the assumptions about hadronic uncertainties. Taking into account only the theoretically clean LFU ratios one finds pull values of around 4σ.

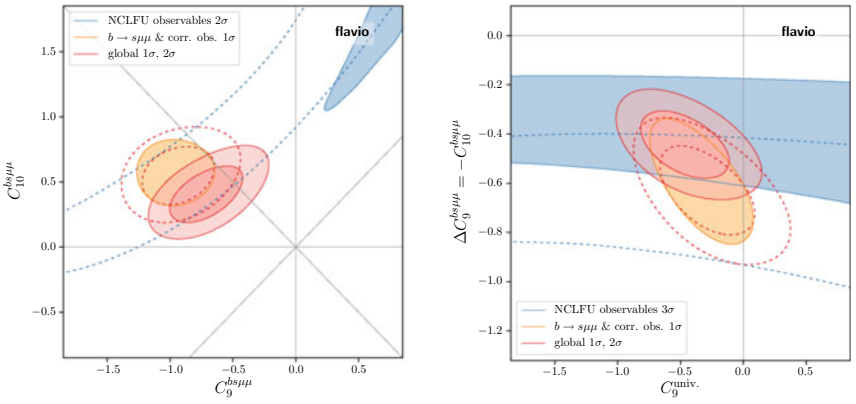

Fig. 51.1 Preferred 1σ and 2σ regions in the plane of the Wilson coefficients $C_9^{bs\mu\mu}$ and $C_{10}^{bs\mu\mu}$ (left), and $C_9^{\text{univ.}}$ and $C_9^{bs\mu\mu} = -C_{10}^{bs\mu\mu}$ (right) at the scale of the b quark mass, m_b. Solid (dashed) contours include (exclude) the Moriond-2019 updates for R_K and R_{K^*}. (From [2].)

$$\text{(a)}\quad C_9^{bs\mu\mu} = -0.97^{+0.16}_{-0.15}\,, \qquad \text{(b)}\quad C_9^{bs\mu\mu} = -C_{10}^{bs\mu\mu} = -0.53 \pm 0.08\,. \tag{51.4}$$

As can be seen from the left plot in Fig. 51.1, with the latest experimental updates a slight tension emerged between the LFU observables and the $b \to s\mu\mu$ observables. The tension can be resolved by introducing in addition also a lepton flavor universal interaction $C_9^{\text{univ.}}(\bar{s}\gamma_\nu P_L b)\sum_\ell(\bar{\ell}\gamma^\nu \ell)$. As shown in the right plot of Fig. 51.1, a fully consistent picture emerges for $C_9^{bs\mu\mu} = -C_{10}^{bs\mu\mu} \simeq C_9^{\text{univ.}} \simeq -0.45$.

The results for the Wilson coefficients can be translated into a new physics scale Λ_{NP}

$$\frac{c_{\text{NP}}}{\Lambda_{\text{NP}}^2} = \frac{4G_F}{\sqrt{2}}\frac{e^2}{16\pi^2}|V_{ts}^* V_{tb}||C_i| \simeq (35\,\text{TeV})^{-2}|C_i|\,. \tag{51.5}$$

Taking for example the best fit value from scenario (a), $C_9^{bs\mu\mu} \simeq -1$, the corresponding new physics scale ranges from $\Lambda_{\text{NP}} \simeq 600$ GeV (assuming a new physics coupling that is CKM and loop suppressed $c_{\text{NP}} \simeq \frac{1}{16\pi^2}|V_{ts}^* V_{tb}|$), to $\Lambda_{\text{NP}} \simeq 35$ TeV (assuming a generic new physics coupling $c_{\text{NP}} \simeq 1$). Based on perturbative unitarity we obtain an upper bound on the new physics scale of

$$\Lambda_{\text{NP}} \lesssim \sqrt{4\pi} \times \frac{v}{\sqrt{2}} \times \frac{4\pi}{e}|V_{ts}^* V_{tb}|^{-1/2}|C_9^{bs\mu\mu}|^{-1/2} \simeq 120\,\text{TeV}\,. \tag{51.6}$$

where $v = 246$ GeV is the Standard Model vacuum expectation value of the Higgs. Below this new physics scale, new degrees of freedom that couple to bottom quarks, strange quarks, and muons have to exist. A more sophisticated analysis finds the slightly stronger bound $\Lambda_{\text{NP}} \lesssim 80$ TeV [21].

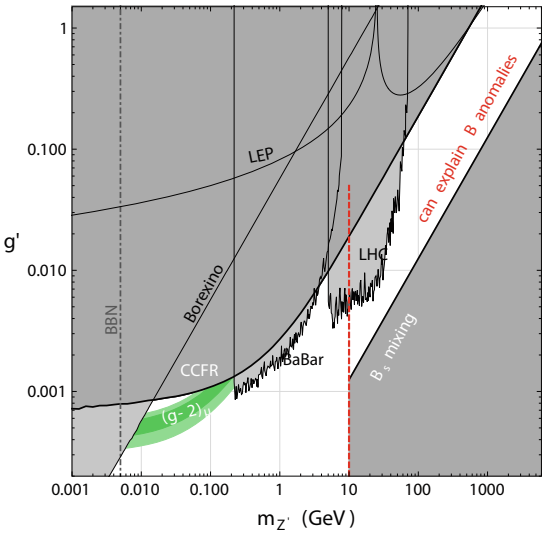

Fig. 51.2 Regions of viable Z' parameter space in the plane of the Z' mass, $m_{Z'}$ and the Z' gauge coupling g'. The gray regions are excluded by the indicated existing constraints. In the green region the long standing discrepancy in the $g-2$ of the muon can be explained. In the white region above $m_{Z'} \sim 10$ GeV, the $b \to s\ell\ell$ anomalies can be explained. (Based on [28].)

Well studied new physics examples that induce at low energies the Wilson coefficient $C_9^{bs\mu\mu}$ are models based on gauged $L_\mu - L_\tau$, the difference of muon number and tau number. The first study of the $L_\mu - L_\tau$ model in the context of the B anomalies [22] aimed at explaining the P_5' anomaly and *predicted* lepton flavor universality violation in $b \to s\ell\ell$ at the level of ∼20%—in excellent agreement with the subsequent R_K and R_{K^*} measurements by LHCb [15, 16, 23]. Given the latest experimental updates, all predictions of the model [24] are still in stunning agreement with the data.

The Z' model can explain the anomalies for a vast range of Z' masses. The viable parameter space is shown in Fig. 51.2 in the plane of the Z' mass, $m_{Z'}$ and the $L_\mu - L_\tau$ gauge coupling g'. The gray regions are excluded by the indicated existing constraints. The most important constraints are from direct searches for the $L_\mu - L_\tau$ gauge boson at the LHC [25], direct searches for the $L_\mu - L_\tau$ gauge boson at BaBar [26], neutrino trident production [27, 28], and B_s mixing. An upper bound on the Z' mass of several TeV can be found by demanding that the $L_\mu - L_\tau$ gauge coupling be perturbative. A lower bound of ∼10 GeV can be derived from the absence of a distortion in the q^2 spectrum of the observed $b \to s\ell\ell$ decay rates.

Note that for very small masses, $m_{Z'} \sim (10\text{–}100)$ MeV the $L_\mu - L_\tau$ gauge boson can address the long standing discrepancy in the anomalous magnetic moment of the muon. The regions of parameter space where the B anomalies and the anomalous magnetic moment of the muon can be explained are, however, mutually exclusive.

51.3 Anomalies in Flavor Changing Charged Current Decays

The charged current $b \to c\ell\nu$ decays are induced at the tree level in the SM. The decays with light leptons (muons and electrons) in the final state are commonly used to extract the magnitude of the CKM matrix element V_{cb}. The LFU ratios involving the decays with taus in the final state, $R_{D^{(*)}} = \text{BR}(B \to D^{(*)}\tau\nu)/\text{BR}(B \to D^{(*)}\ell\nu)$ are considered important probes of new physics. The experimental results on $R_{D^{(*)}}$ from BaBar [29], Belle [30–32], and LHCb [33, 34] are combined by the HFLAV collaboration into he world averages [35]

$$R_D = 0.340 \pm 0.027 \pm 0.013\,, \qquad R_{D^*} = 0.295 \pm 0.011 \pm 0.008\,, \tag{51.7}$$

with an error correlation of $\rho = -38\%$. The SM predicts these LFU ratios with high precision [36–38]. The HFLAV collaboration has adopted the following values [35]

$$R_D^{\text{SM}} = 0.299 \pm 0.003\,, \qquad R_{D^*}^{\text{SM}} = 0.258 \pm 0.005\,. \tag{51.8}$$

The combined discrepancy between the experimental world averages and SM predictions of R_D and R_{D^*} is 3.1σ.

Model independent new physics fits [39–42] find that an enhancement of the SM $b \to c\tau\nu$ amplitude by approximately 10% leads to an excellent description of the data. In the language of four fermion contact interactions, this corresponds to new physics contributions to the effective Hamiltonian

$$\mathcal{H}_{\text{eff}}^{\text{NP}} = \frac{4G_F}{\sqrt{2}} V_{cb}\epsilon_L^\tau (\bar{c}\gamma_\mu P_L b)(\bar{\tau}\gamma^\mu P_L \nu_\tau)\,, \tag{51.9}$$

with a best fit value of the Wilson coefficient of $\epsilon_L^\tau = 0.07 \pm 0.02$ [42].

The related new physics scale is much lower compared to the scale that can be derived from the anomalies in the rare $b \to s\ell\ell$ decays. The upper bound on the new physics scale from perturbative unitarity can be estimated as

$$\Lambda_{\text{NP}} \lesssim \sqrt{4\pi} \times \frac{v}{\sqrt{2}} \times |V_{cb}|^{-1/2} |\epsilon_L^\tau|^{-1/2} \simeq 12\ \text{TeV}\,. \tag{51.10}$$

The more sophisticated analysis in [21] finds $\Lambda_{\text{NP}} \lesssim 9$ TeV.

Weakly coupled models typically need to contain new degrees of freedom at the TeV scale and are therefore subject to a large set of constraints, including constraints from other B decays like $B \to \tau\nu$ or $B \to K\nu\bar{\nu}$ and, in models with new scalars, the $B_c \to \tau\nu$ decay [43, 44]. In many models strong constraints can be derived from measurements of the di-tau invariant mass distribution in $pp \to \tau^+\tau^-$ at the LHC [45], or from mono-tau searches [46, 47]. In many models one finds also strong constraints from Z couplings, W couplings and tau decays that are modified at the loop level [48, 49].

Nevertheless, there are models that can explain the $R_{D^{(*)}}$ anomalies and avoid all known constraints. Among them are lepto-quark models [50] and models with light right-handed neutrinos [51, 52].

51.4 Combined Explanations

There exist new physics scenarios that explain both classes of anomalies (those in $b \to s\ell\ell$ decays, Sect. 51.2, and those in $b \to c\ell\nu$ decays, Sect. 51.3) simultaneously in a consistent way [50, 53]. At the level of effective interactions, the scenarios start with four fermion operators that involve only left-handed quarks and leptons of the third generation. Above the electro-weak scale the corresponding effective Hamiltonian is

$$\mathcal{H}_{\text{eff}}^{\text{NP}} = C_{\ell q}^{(1)}(\bar{\ell}_3\gamma_\mu\ell_3)(\bar{q}_3\gamma^\mu q_3) + C_{\ell q}^{(3)}(\bar{\ell}_3\gamma_\mu\tau_i\ell_3)(\bar{q}_3\gamma^\mu\tau_i q_3)\,, \tag{51.11}$$

where $\ell_3 = (\nu_\tau, \tau_L)$, $q_3 = (t_L, b_L)$ are the left-handed lepton and quark doublets of third generation in the gauge eigenstate basis and τ_i are the Pauli matrices in weak isospin space. Rotating into lepton and quark mass eigenstates one can find $bs\mu\mu$ and $bc\tau\nu$ interactions of the right size to explain the anomalies. Moreover, the $bs\tau\tau$ interaction contained in (51.11) leads at the one loop level to a lepton flavor universal contribution $C_9^{\text{univ.}}$ [54] which is precisely of the size that is preferred by the global fit described in Sect. 51.2.

Overall, one can contemplate an extremely economic scenario which leads to a remarkable good fit to all data. The scenario is characterised by only 2 free new physics parameters, $[C_{\ell q}^{(1)}]_{2223} = [C_{\ell q}^{(3)}]_{2223}$ (which leads to muon specific contributions to $b \to s\mu\mu$ while at the same time avoiding contributions to $b \to s\nu\nu$) and $[C_{\ell q}^{(1)}]_{3323} = [C_{\ell q}^{(3)}]_{3323}$ (which leads to tau specific contributions to $b \to c\tau\nu$ again avoiding contributions to $b \to s\nu\nu$ and, as a bonus, giving the lepton flavor universal contribution to $b \to s\ell\ell$). The corresponding parameter space is shown in Fig. 51.3. The best fit regions corresponding to the lepton universality observables in $b \to c\ell\nu$ (green), the lepton universality observables in $b \to s\ell\ell$ (blue), and the remaining $b \to s\mu\mu$ observables (orange) overlap perfectly.

Such a new physics scenario predicts enhanced rates for the rare decays $B_s \to \tau\tau$, $B \to K^{(*)}\tau\tau$ and generically also lepton flavor changing decays like $B_s \to \tau\mu$, $B \to K^{(*)}\tau\mu$ [55], possibly in reach of LHCb.

The current anomalies in B decays could be the first indirect signs of new physics. It is indeed intriguing that a very simple and consistent new physics explanation of the anomalies exists. Future experimental results from LHCb and Belle II on theoretically clean lepton flavor universality tests are expected to reach a precision which should allow us to conclusively determine whether or not the current anomalies are due to a new physics effect.

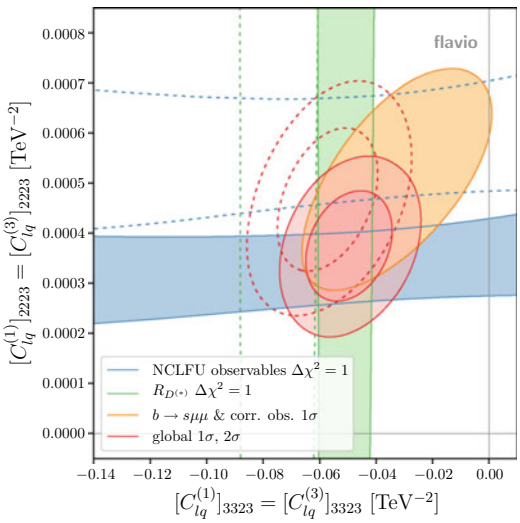

Fig. 51.3 Preferred 1σ and 2σ regions in the plane of the two Wilson coefficients $[C_{lq}^{(1)}]_{3323} = [C_{lq}^{(3)}]_{3323}$ and $[C_{lq}^{(1)}]_{2223} = [C_{lq}^{(3)}]_{2223}$ at a scale of 2 TeV. Solid (dashed) contours include (exclude) the Moriond-2019 results for R_K, R_{K^*}, R_D, and R_{D^*}. (From [2].)

Acknowledgements WA would like to thank the organizers for the invitation to the FHEP 2019 conference. The research of WA is supported by the National Science Foundation under Grant No. PHY-1912719.

References

1. T. Blake, G. Lanfranchi, D.M. Straub, Rare B decays as tests of the standard model. Prog. Part. Nucl. Phys. **92**, 50 (2017). https://doi.org/10.1016/j.ppnp.2016.10.001 [arXiv:1606.00916 [hep-ph]]
2. J. Aebischer, W. Altmannshofer, D. Guadagnoli, M. Reboud, P. Stangl, D.M. Straub, B-decay discrepancies after Moriond 2019, arXiv:1903.10434 [hep-ph]
3. M. Alguero, B. Capdevila, A. Crivellin, S. Descotes-Genon, P. Masjuan, J. Matias, J. Virto, Emerging patterns of new physics with and without lepton flavour universal contributions. Eur. Phys. J. C **79**(8), 714 (2019). https://doi.org/10.1140/epjc/s10052-019-7216-3 [arXiv:1903.09578 [hep-ph]]
4. A.K. Alok, A. Dighe, S. Gangal, D. Kumar, Continuing search for new physics in $b \to s\mu\mu$ decays: two operators at a time. JHEP **1906**, 089 (2019). https://doi.org/10.1007/JHEP06(2019)089 [arXiv:1903.09617 [hep-ph]]
5. M. Ciuchini, A.M. Coutinho, M. Fedele, E. Franco, A. Paul, L. Silvestrini, M. Valli, New physics in $b \to s\ell^+\ell^-$ confronts new data on lepton universality. Eur. Phys. J. C **79**(8), 719 (2019). https://doi.org/10.1140/epjc/s10052-019-7210-9 [arXiv:1903.09632 [hep-ph]]
6. A. Datta, J. Kumar, D. London, The B anomalies and new physics in $b \to se^+e^-$. Phys. Lett. B **797**, 134858 (2019). https://doi.org/10.1016/j.physletb.2019.134858 [arXiv:1903.10086 [hep-ph]]
7. K. Kowalska, D. Kumar, E.M. Sessolo, Implications for new physics in $b \to s\mu\mu$ transitions after recent measurements by Belle and LHCb. Eur. Phys. J. C **79**(10), 840 (2019). https://doi.org/10.1140/epjc/s10052-019-7330-2 [arXiv:1903.10932 [hep-ph]]

8. A. Arbey, T. Hurth, F. Mahmoudi, D.M. Santos, S. Neshatpour, Update on the bs anomalies. Phys. Rev. D **100**(1), 015045 (2019). https://doi.org/10.1103/PhysRevD.100.015045 [arXiv:1904.08399 [hep-ph]]
9. R. Aaij et al., [LHCb Collaboration], Angular analysis and differential branching fraction of the decay $B_s^0 \to \phi\mu^+\mu^-$. JHEP **1509**, 179 (2015). https://doi.org/10.1007/JHEP09(2015)179 [arXiv:1506.08777 [hep-ex]]
10. R. Aaij et al., [LHCb Collaboration], Differential branching fractions and isospin asymmetries of $B \to K^{(*)}\mu^+\mu^-$ decays. JHEP **1406**, 133 (2014). https://doi.org/10.1007/JHEP06(2014)133 [arXiv:1403.8044 [hep-ex]]
11. V. Khachatryan et al., [CMS and LHCb Collaborations], Observation of the rare $B_s^0 \to \mu^+\mu^-$ decay from the combined analysis of CMS and LHCb data. Nature **522**, 68 (2015). https://doi.org/10.1038/nature14474 [arXiv:1411.4413 [hep-ex]]
12. R. Aaij et al., [LHCb Collaboration], Measurement of the $B_s^0 \to \mu^+\mu^-$ branching fraction and effective lifetime and search for $B^0 \to \mu^+\mu^-$ decays. Phys. Rev. Lett. **118**(19), 191801 (2017). https://doi.org/10.1103/PhysRevLett.118.191801 [arXiv:1703.05747 [hep-ex]]
13. M. Aaboud et al., [ATLAS Collaboration], Study of the rare decays of B_s^0 and B^0 mesons into muon pairs using data collected during 2015 and 2016 with the ATLAS detector. JHEP **1904**, 098 (2019). https://doi.org/10.1007/JHEP04(2019)098 [arXiv:1812.03017 [hep-ex]]
14. R. Aaij et al., [LHCb Collaboration], Angular analysis of the $B^0 \to K^{*0}\mu^+\mu^-$ decay using 3 fb^{-1} of integrated luminosity. JHEP **1602**, 104 (2016). https://doi.org/10.1007/JHEP02(2016)104 [arXiv:1512.04442 [hep-ex]]
15. R. Aaij et al., [LHCb Collaboration], Search for lepton-universality violation in $B^+ \to K^+\ell^+\ell^-$ decays. Phys. Rev. Lett. **122**(19), 191801 (2019). https://doi.org/10.1103/PhysRevLett.122.191801 [arXiv:1903.09252 [hep-ex]]
16. R. Aaij et al., [LHCb Collaboration], Test of lepton universality with $B^0 \to K^{*0}\ell^+\ell^-$ decays. JHEP **1708**, 055 (2017). https://doi.org/10.1007/JHEP08(2017)055 [arXiv:1705.05802 [hep-ex]]
17. M. Bordone, G. Isidori, A. Pattori, On the standard model predictions for R_K and R_{K^*}. Eur. Phys. J. C **76**(8), 440 (2016). https://doi.org/10.1140/epjc/s10052-016-4274-7 [arXiv:1605.07633 [hep-ph]]
18. A. Abdesselam et al., [Belle Collaboration], Test of lepton flavor universality in $B \to K^*\ell^+\ell^-$ decays at Belle. arXiv:1904.02440 [hep-ex]
19. A. Abdesselam, et al. [Belle Collaboration], Test of lepton flavor universality in $B \to K\ell^+\ell^-$ decays. arXiv:1908.01848 [hep-ex]
20. W. Altmannshofer, M.J. Baker, S. Gori, R. Harnik, M. Pospelov, E. Stamou, A. Thamm, Light resonances and the low-q^2 bin of R_{K^*}. JHEP **1803**, 188 (2018). https://doi.org/10.1007/JHEP03(2018)188 [arXiv:1711.07494 [hep-ph]]
21. L. Di Luzio, M. Nardecchia, What is the scale of new physics behind the B-flavour anomalies? Eur. Phys. J. C **77**(8), 536 (2017). https://doi.org/10.1140/epjc/s10052-017-5118-9 [arXiv:1706.01868 [hep-ph]]
22. W. Altmannshofer, S. Gori, M. Pospelov, I. Yavin, Quark flavor transitions in $L_\mu - L_\tau$ models. Phys. Rev. D **89**, 095033 (2014). https://doi.org/10.1103/PhysRevD.89.095033 [arXiv:1403.1269 [hep-ph]]
23. R. Aaij et al., [LHCb Collaboration], Test of lepton universality using $B^+ \to K^+\ell^+\ell^-$ decays. Phys. Rev. Lett. **113**, 151601 (2014). https://doi.org/10.1103/PhysRevLett.113.151601 [arXiv:1406.6482 [hep-ex]]
24. W. Altmannshofer, I. Yavin, Predictions for lepton flavor universality violation in rare B decays in models with gauged $L_\mu - L_\tau$. Phys. Rev. D **92**(7), 075022 (2015). https://doi.org/10.1103/PhysRevD.92.075022 [arXiv:1508.07009 [hep-ph]]
25. A.M. Sirunyan et al., [CMS Collaboration], Search for an $L_\mu - L_\tau$ gauge boson using Z$\to 4\mu$ events in proton-proton collisions at $\sqrt{s} = 13$ TeV. Phys. Lett. B **792**, 345 (2019). https://doi.org/10.1016/j.physletb.2019.01.072 [arXiv:1808.03684 [hep-ex]]
26. J.P. Lees et al., [BaBar Collaboration], Search for a muonic dark force at BABAR. Phys. Rev. D **94**(1), 011102 (2016). https://doi.org/10.1103/PhysRevD.94.011102 [arXiv:1606.03501 [hep-ex]]

27. W. Altmannshofer, S. Gori, M. Pospelov, I. Yavin, Neutrino trident production: a powerful probe of new physics with neutrino beams. Phys. Rev. Lett. **113**, 091801 (2014). https://doi.org/10.1103/PhysRevLett.113.091801 [arXiv:1406.2332 [hep-ph]]
28. W. Altmannshofer, S. Gori, J. Martn-Albo, A. Sousa, M. Wallbank, Neutrino tridents at DUNE. arXiv:1902.06765 [hep-ph]
29. J.P. Lees et al., [BaBar Collaboration], Evidence for an excess of $\bar{B} \to D^{(*)}\tau^-\bar{\nu}_\tau$ decays. Phys. Rev. Lett. **109**, 101802 (2012). https://doi.org/10.1103/PhysRevLett.109.101802 [arXiv:1205.5442 [hep-ex]]
30. M. Huschle et al., [Belle Collaboration], Measurement of the branching ratio of $\bar{B} \to D^{(*)}\tau^-\bar{\nu}_\tau$ relative to $\bar{B} \to D^{(*)}\ell^-\bar{\nu}_\ell$ decays with hadronic tagging at Belle. Phys. Rev. D **92**(7), 072014 (2015). https://doi.org/10.1103/PhysRevD.92.072014 [arXiv:1507.03233 [hep-ex]]
31. S. Hirose et al., [Belle Collaboration], Measurement of the τ lepton polarization and $R(D^*)$ in the decay $\bar{B} \to D^*\tau^-\bar{\nu}_\tau$. Phys. Rev. Lett. **118**(21), 211801 (2017). https://doi.org/10.1103/PhysRevLett.118.211801 [arXiv:1612.00529 [hep-ex]]
32. G. Caria et al., [Belle Collaboration], Measurement of $\mathcal{R}(D)$ and $\mathcal{R}(D^*)$ with a semileptonic tagging method, arXiv:1910.05864 [hep-ex]
33. R. Aaij et al., [LHCb Collaboration], Measurement of the ratio of branching fractions $\mathcal{B}(\bar{B}^0 \to D^{*+}\tau^-\bar{\nu}_\tau)/\mathcal{B}(\bar{B}^0 \to D^{*+}\mu^-\bar{\nu}_\mu)$. Phys. Rev. Lett. **115**(11), 111803 (2015). Erratum: [Phys. Rev. Lett. **115**(15), 159901 (2015)]. https://doi.org/10.1103/PhysRevLett.115.159901, https://doi.org/10.1103/PhysRevLett.115.111803 [arXiv:1506.08614 [hep-ex]]
34. R. Aaij et al., [LHCb Collaboration], Measurement of the ratio of the $B^0 \to D^{*-}\tau^+\nu_\tau$ and $B^0 \to D^{*-}\mu^+\nu_\mu$ branching fractions using three-prong τ-lepton decays. Phys. Rev. Lett. **120**(17), 171802 (2018). https://doi.org/10.1103/PhysRevLett.120.171802 [arXiv:1708.08856 [hep-ex]]
35. Y.S. Amhis et al., [HFLAV Collaboration], Averages of b-hadron, c-hadron, and τ-lepton properties as of 2018, arXiv:1909.12524 [hep-ex]
36. F.U. Bernlochner, Z. Ligeti, M. Papucci, D.J. Robinson, Combined analysis of semileptonic B decays to D and D^*: $R(D^{(*)})$, $|V_{cb}|$, and new physics. Phys. Rev. D **95**(11), 115008 (2017). Erratum: [Phys. Rev. D **97**(5), 059902 (2018)]. https://doi.org/10.1103/PhysRevD.95.115008, https://doi.org/10.1103/PhysRevD.97.059902 [arXiv:1703.05330 [hep-ph]]
37. D. Bigi, P. Gambino, S. Schacht, $R(D^*)$, $|V_{cb}|$, and the heavy quark symmetry relations between form factors. JHEP **1711**, 061 (2017). https://doi.org/10.1007/JHEP11(2017)061 [arXiv:1707.09509 [hep-ph]]
38. S. Jaiswal, S. Nandi, S.K. Patra, Extraction of $|V_{cb}|$ from $B \to D^{(*)}\ell\nu_\ell$ and the standard model predictions of $R(D^{(*)})$. JHEP **1712**, 060 (2017). https://doi.org/10.1007/JHEP12(2017)060 [arXiv:1707.09977 [hep-ph]]
39. C. Murgui, A. Penuelas, M. Jung, A. Pich, Global fit to $b \to c\tau\nu$ transitions. JHEP **1909**, 103 (2019). https://doi.org/10.1007/JHEP09(2019)103 [arXiv:1904.09311 [hep-ph]]
40. D. Bardhan, D. Ghosh, B -meson charged current anomalies: the post-Moriond 2019 status. Phys. Rev. D **100**(1), 011701 (2019). https://doi.org/10.1103/PhysRevD.100.011701 [arXiv:1904.10432 [hep-ph]]
41. P. Asadi, D. Shih, Maximizing the impact of new physics in $b \to c\tau\nu$ anomalies. arXiv:1905.03311 [hep-ph]
42. R.X. Shi, L. S. Geng, B. Grinstein, S. Jager, J. Martin Camalich, Revisiting the new-physics interpretation of the $b \to c\tau\nu$ data. arXiv:1905.08498 [hep-ph]
43. X.Q. Li, Y.D. Yang, X. Zhang, Revisiting the one leptoquark solution to the R(D$^{()}$) anomalies and its phenomenological implications. JHEP **1608**, 054 (2016). https://doi.org/10.1007/JHEP08(2016)054 [arXiv:1605.09308 [hep-ph]]
44. R. Alonso, B. Grinstein, J. Martin Camalich, Lifetime of B_c^- constrains explanations for anomalies in $B \to D^{(*)}\tau\nu$. Phys. Rev. Lett. **118**(8), 081802 (2017). https://doi.org/10.1103/PhysRevLett.118.081802 [arXiv:1611.06676 [hep-ph]]
45. D.A. Faroughy, A. Greljo, J.F. Kamenik, Confronting lepton flavor universality violation in B decays with high-p_T tau lepton searches at LHC. Phys. Lett. B **764**, 126 (2017). https://doi.org/10.1016/j.physletb.2016.11.011 [arXiv:1609.07138 [hep-ph]]

46. W. Altmannshofer, P.S. Bhupal Dev, A. Soni, $R_{D^{(*)}}$ anomaly: a possible hint for natural supersymmetry with R-parity violation. Phys. Rev. D **96**(9), 095010 (2017). https://doi.org/10.1103/PhysRevD.96.095010 [arXiv:1704.06659 [hep-ph]]
47. A. Greljo, J. Martin Camalich, J.D. Ruiz-Alvarez, Mono-τ signatures at the LHC constrain explanations of B-decay anomalies. Phys. Rev. Lett. **122**(13), 131803 (2019). https://doi.org/10.1103/PhysRevLett.122.131803 [arXiv:1811.07920 [hep-ph]]
48. F. Feruglio, P. Paradisi, A. Pattori, Revisiting lepton flavor universality in B decays. Phys. Rev. Lett. **118**(1), 011801 (2017). https://doi.org/10.1103/PhysRevLett.118.011801 [arXiv:1606.00524 [hep-ph]]
49. C. Cornella, F. Feruglio, P. Paradisi, Low-energy effects of lepton flavour universality violation. JHEP **1811**, 012 (2018). https://doi.org/10.1007/JHEP11(2018)012 [arXiv:1803.00945 [hep-ph]]
50. D. Buttazzo, A. Greljo, G. Isidori, D. Marzocca, B-physics anomalies: a guide to combined explanations. JHEP **1711**, 044 (2017). https://doi.org/10.1007/JHEP11(2017)044 [arXiv:1706.07808 [hep-ph]]
51. P. Asadi, M.R. Buckley, D. Shih, It's all right(-handed neutrinos): a new W model for the $R_{D^{(*)}}$ anomaly. JHEP **1809**, 010 (2018). https://doi.org/10.1007/JHEP09(2018)010 [arXiv:1804.04135 [hep-ph]]
52. D.J. Robinson, B. Shakya, J. Zupan, Right-handed neutrinos and R(D$^{()}$). JHEP **1902**, 119 (2019). https://doi.org/10.1007/JHEP02(2019)119 [arXiv:1807.04753 [hep-ph]]
53. B. Bhattacharya, A. Datta, D. London, S. Shivashankara, Simultaneous explanation of the R_K and $R(D^{(*)})$ puzzles. Phys. Lett. B **742**, 370 (2015). https://doi.org/10.1016/j.physletb.2015.02.011 [arXiv:1412.7164 [hep-ph]]
54. A. Crivellin, C. Greub, D. Müller, F. Saturnino, Importance of loop effects in explaining the accumulated evidence for new physics in B decays with a vector leptoquark. Phys. Rev. Lett. **122**(1), 011805 (2019). https://doi.org/10.1103/PhysRevLett.122.011805 [arXiv:1807.02068 [hep-ph]]
55. S.L. Glashow, D. Guadagnoli, K. Lane, Lepton flavor violation in B decays? Phys. Rev. Lett. **114**, 091801 (2015). https://doi.org/10.1103/PhysRevLett.114.091801 [arXiv:1411.0565 [hep-ph]]

Chapter 52
Beam-Constrained Vertexing for B Physics at the Belle II Experiment

S. Dey and A. Soffer

Abstract The Belle II experiment, which recently began collecting e^+e^- collision data, will extend the successful physics program of BABAR and Belle with a 30-fold increase in integrated luminosity and an improved detector. In particular, the vertex position resolution of Belle II is better than that of its predecessors by about a factor of two. The high resolution and the very small e^+e^- collision region provide a powerful constraint that can be used in a number of B-physics analyses. This contribution will cover studies performed with this method, as well as the performance of the Belle II experiment.

52.1 Introduction

In time-dependent analyses in B factories, the key ingredient is the difference between the time of decay of two B mesons that come from the decay of the same $\Upsilon(4S)$. To measure this difference, a precise determination of the B decay vertex positions is of utmost importance. In the BABAR and the Belle experiments, the beam spot size was much larger than Belle II. For example, in the BABAR experiment the beam spot size was $(120 \times 5 \times 8000)\ \mu\text{m}^3$, where each value is the width of the Gaussian beam profile in the x, y and z directions, respectively. Here, the x, y and z axes are toward the center of the accelerator, upward out of the plane of the accelerator and along the beam direction, respectively. The average distance travelled by the B meson in the z direction is approximately 260 μm at BABAR (similar to Belle). So, the B mesons decay within the beamspot if we only consider the z direction. Hence, in these cases, to find the decay vertex of the B meson correctly, a fit where the vertex was constrained to be within the beam spot was sufficient.

S. Dey (✉) · A. Soffer
Tel Aviv University, Tel Aviv, Israel
e-mail: souravdey@tauex.tau.ac.il

A. Soffer
e-mail: asoffer@tauex.tau.ac.il

A. Giri and R. Mohanta (eds.), *Workshop on Frontiers in High Energy Physics 2019*, Springer Proceedings in Physics 248,
https://doi.org/10.1007/978-981-15-6292-1_52

In Belle II, the use of the nano-beam scheme reduces the beam spot size drastically. In Belle II, the beam spot size is $(6 \times 0.06 \times 150)\ \mu m^3$. Now, as the B meson would decay at a significant distance from the beam spot, a beam-spot-constrained vertex fit could introduce unnecessary bias and the B decay vertex position could not be measured correctly. Thus, in the remainder of this contribution we describe a new constraint that removes this bias.

52.2 A New Constraint: Btube

The constraint applies to events in which there is a fully reconstructed one B meson, which we refer to as B_{rec}. The other B meson is referred to as B_{other}. The decay chain can be summarised as $\Upsilon(4S) \rightarrow B_{\text{rec}} B_{\text{other}}$. Now, we can propagate the B_{rec} momentum to the beam spot and apply a vertex fit, such as the adaptive vertex fitter from RAVE [1]. The result of this fit is a vertex from which both the B mesons originated. From four-momentum conservation we obtain the direction in which the B_{other} flies. We then stretch the covariance matrix of the fully reconstructed vertex so that it effectively has infinite size in the direction of the flight of the B_{other}. This tube-like object we call "Btube", which we use as a constraint in further B_{other} fits. The construction of the Btube constraint is shown schematically in Fig. 52.1.

52.3 Analysis

To study the Btube constraint, we use a Monte Carlo (MC) sample that is produced using the EVTGEN [2] package to generate the decays and the GEANT4 [3] package to simulate the detector response. The sample contains one million events with the following decay chain: $B^+_{\text{rec}} \rightarrow \bar{D}^0(\rightarrow K^+\pi^-)\pi^+$ and $B^-_{\text{other}} \rightarrow J/\psi(\rightarrow \mu^+\mu^-)K^-\pi^+\pi^-$. We reconstruct the events, then only consider those in which the full decay tree is correctly reconstructed for further analysis. In the selected events, we fit the B_{other} decay vertex with RAVE including the Btube constraint. An example event from our generated samples is shown in Fig. 52.2.

52.4 Results

52.4.1 Quality of BB Production Vertex

In order to check how the Btube constraint performs, first we evaluate the correctness the BB production vertex. In Fig. 52.3 we show the pull distributions and fit them with Gaussian pdfs. The quality of the fits clearly show that the BB production vertex

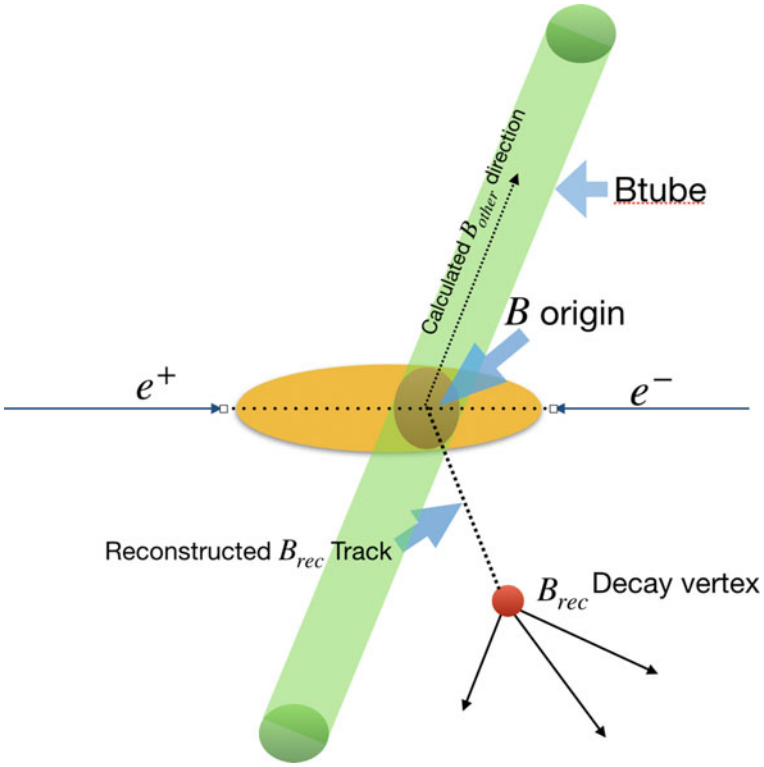

Fig. 52.1 Schematic of the Btube constraint

is reconstructed correctly. In Fig. 52.4 uncertainties of this vertex position is shown. The truncation points at the right hand sides of all the plots are determined by the beam spot size itself.

52.4.2 Comparison of B_{other} Decay Vertex Residuals Obtained with Three Different Constraints

In the Fig. 52.5, we plot the residual distribution of the B_{other} decay vertex fitted using no constraint, using the beamspot constraint and using the Btube constraint. This plot clearly shows an improved fit can be achieved using the Btube constraint.

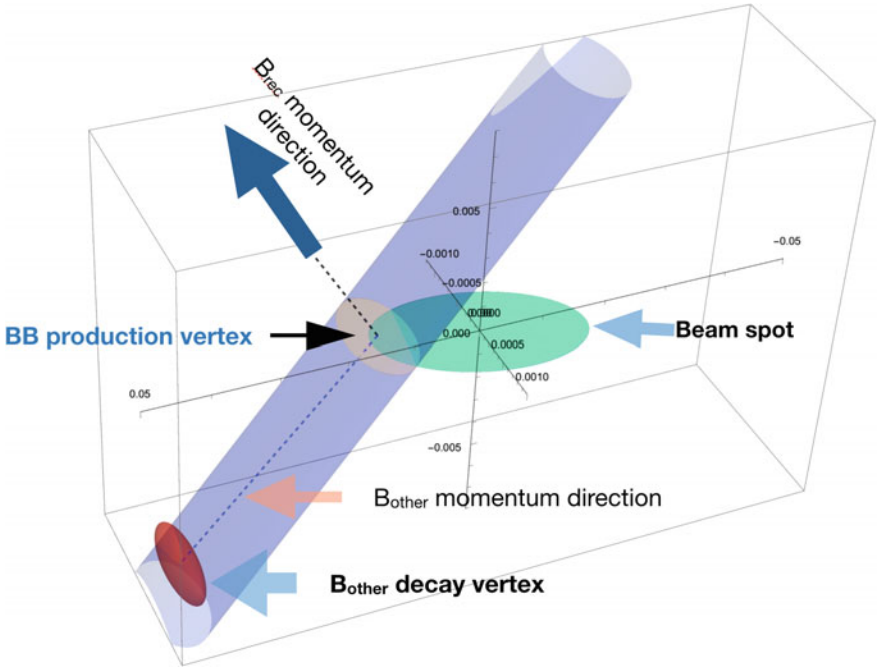

Fig. 52.2 B_{other} decay vertex fitted with Btube constraint. Beam spot, $B\,B$ production vertex and the B_{rec} momentum direction are shown. The figure is generated with Mathematica

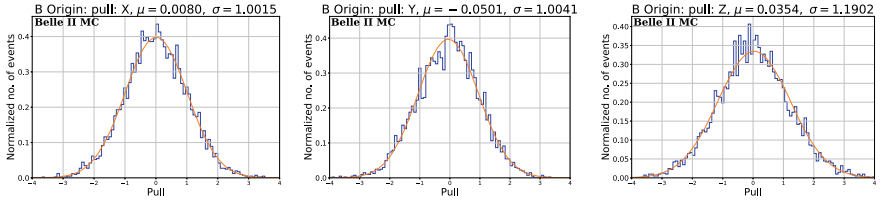

Fig. 52.3 Pull distributions of the $B\bar{B}$ production vertex position in (left) x, (middle) y and (right) z

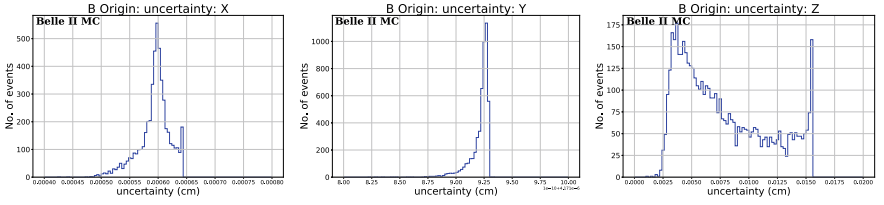

Fig. 52.4 Distributions of the uncertainty on the $B\bar{B}$ production vertex position in (left) x, (middle) y and (right) z

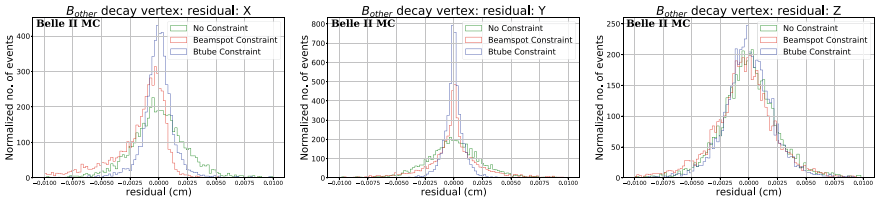

Fig. 52.5 B_{other} vertex position residuals in (left) x, (middle) y and (right) z comparing the use of the Btube constraint, beam-spot constraint and no constraint

52.5 Conclusion

Figure 52.5 shows that using the Btube constraint improves the determination of the B decay position, compared to using either the beam-spot constraint or no constraint. Therefore, using the Btube constraint will reduce bias in Δt measurements and other time-dependent studies. In addition, a Btube constrained fit can be used to improve background rejection in decays like $B \to D\tau\nu$, $B \to K^{(*)}\nu\bar{\nu}$, $B \to \tau\nu$ where $\tau \to 3\pi\nu$ or $\tau \to l\nu$.

References

1. W. Waltenberger et al., IEEE Trans. Nucl. Sci. **58**, 434–444 (2011)
2. D.J. Lange, Nucl. Instrum. Meth. **A462**, 152–155 (2001)
3. T. Abe, Belle II (2010), arXiv:1011.0352

Chapter 53
New Physics Solutions for $b \to c\tau\bar{\nu}$ Anomalies After Moriond 2019

Suman Kumbhakar, Ashutosh Kumar Alok, Dinesh Kumar, and S. Uma Sankar

Abstract At Moriond 2019, Belle collaboration has announced new measurements on the flavour ratios $R_D - R_{D^*}$ which are consistent with their Standard Model predictions within 1.2σ. After inclusion of these measurements, the global tension in $R_D - R_{D^*}$ has reduced from 4.1σ to 3.1σ which is still significant. The measurements of these ratios indicate towards the violation of lepton flavor universality in $b \to cl\bar{\nu}$ decay. Assuming new physics in $b \to c\tau\bar{\nu}$ transition, we have done a global fit to all available data in this sector to identify the allowed new physics solutions. We find that there are seven allowed new physics solutions which can account for all measurements in $b \to c\tau\bar{\nu}$ transition. We show that a simultaneous measurement of the τ polarization fraction and forward-backward asymmetry in $B \to D\tau\bar{\nu}$, the zero crossing point of forward backward asymmetry in $B \to D^*\tau\bar{\nu}$ and the branching ratio of $B_c \to \tau\ \bar{\nu}$ decay can distinguish these seven new physics solutions if they can be measured with a required precision.

S. Kumbhakar (✉) · S. U. Sankar
Indian Institute of Technology Bombay, Mumbai 400076, India
e-mail: suman@phy.iitb.ac.in

S. U. Sankar
e-mail: uma@phy.iitb.ac.in

A. Kumar Alok
Indian Institute of Technology Jodhpur, Jodhpur 342011, India
e-mail: akalok@iitj.ac.in

D. Kumar
University of Rajasthan, Jaipur 302004, India
e-mail: dinesh@uniraj.ac.in

National Centre for Nuclear Research, Warsaw, Poland

A. Giri and R. Mohanta (eds.), *Workshop on Frontiers in High Energy Physics 2019*, Springer Proceedings in Physics 248,
https://doi.org/10.1007/978-981-15-6292-1_53

53.1 Introduction

In recent years, several measurements in B meson decays, reported by LHCb and B-factories, show significant tension with their Standard Model (SM) predictions. One class of such measurements is governed by $b \to cl\bar{\nu}$ transitions. This transition occurs at tree level within the SM. The BaBar, Belle and LHCb experiments made a series of measurements of the flavour ratios

$$R_D = \frac{\mathscr{B}(B \to D\tau\bar{\nu})}{\mathscr{B}(B \to Dl\bar{\nu})}, \; R_{D^*} = \frac{\mathscr{B}(B \to D^*\tau\bar{\nu})}{\mathscr{B}(B \to D^*l\bar{\nu})}, \; l = e \text{ or } \mu. \tag{53.1}$$

The discrepancy between the world average of 2018 and the SM prediction was at a level of $\sim 4\sigma$ [1]. Very recently, Belle collaborations made new measurements of these ratios which are consistent with their SM predictions within $\sim 1.2\sigma$ [2]. These results were announced at Moriond 2019. After inclusion of these new measurements, the present world averges of these ratios are about $\sim 3.1\sigma$ away from the SM predictions [3]. These ratios indicate towards lepton flavour universality violation.

In 2017, LHCb measured another flavour ratio $R_{J/\psi} = \mathscr{B}(B_c \to J/\psi\tau\bar{\nu})/\mathscr{B}(B_c \to J/\psi\mu\bar{\nu})$ and found it to be $\sim 1.7\sigma$ higher than the SM prediction [4]. In addition to these flavour ratios, Belle collaboration has measured two angular observables in $B \to D^*\tau\bar{\nu}$ decay – the τ polarization fraction $P_\tau^{D^*}$ [5] and the longitudinal polarization fraction of D^* meson $f_L^{D^*}$ [6]. The measured value of $P_\tau^{D^*}$ is consistent with the SM prediction because it has a very large statistical error. However, the measured value of $f_L^{D^*}$ is about $\sim 1.6\sigma$ higher than the SM prediction.

The discrepancy in R_D and R_{D^*} could be an indication of presence of new physics (NP) in the $b \to c\tau\bar{\nu}$ transition. The possibility of NP in $b \to c\{e/\mu\}\bar{\nu}$ is excluded by other data [7]. All possible NP four-Fermi operators for $b \to c\tau\bar{\nu}$ transition are listed in [8]. In [7], a fit was performed to all the $b \to c\tau\bar{\nu}$ data available up to summer 2018. It was found that there are six allowed NP solutions. Among those six solutions, four solutions are distinct each with different Lorentz structure. In [9], we have shown that a unique discrimination between the allowed NP solutions can be possible by a simultaneous measurements of four angular observables, $P_\tau^{D^*}$ (τ polarization fraction), $f_L^{D^*}$ (longitudinal D^* polarization fraction), $A_{FB}^{D^*}$ (the forward-backward asymmetry), $A_{LT}^{D^*}$ (longitudinal-transverse asymmetry) in the $B \to D^*\tau\bar{\nu}$ decay [10].

In this work, we study the impact of new Belle measurements of R_D-R_{D^*} and $f_L^{D^*}$ on the NP solutions for $b \to c\tau\bar{\nu}$ anomalies. We redo the global fit by taking all present measurements in this sector and find out the presently allowed NP solutions [11, 12]. We also discuss methods to discriminate between the allowed NP solutions by means of angular observables in $B \to (D, D^*)\tau\bar{\nu}$ decays and the branching ratio of $B_c \to \tau\bar{\nu}$ decay.

53.2 New Physics Solutions After Moriond 2019

The most general effective Hamiltonian for $b \to c\tau\bar{\nu}$ transition can be written as

$$H_{eff} = \frac{4G_F}{\sqrt{2}} V_{cb} \left[O_{V_L} + \frac{\sqrt{2}}{4G_F V_{cb}} \frac{1}{\Lambda^2} \left\{ \sum_i \left(C_i O_i + C_i^{'} O_i^{'} + C_i^{''} O_i^{''} \right) \right\} \right], \quad (53.2)$$

where G_F is the Fermi coupling constant, V_{cb} is the Cabibbo-Kobayashi-Maskawa (CKM) matrix element and the NP scale Λ is assumed to be 1 TeV. We also assume that neutrino is always left chiral. The effective Hamiltonian for the SM contains only the O_{V_L} operator. The explicit forms of the four-fermion operators O_i, $O_i^{'}$ and $O_i^{''}$ are given in [8]. The NP effects are encoded in the NP Wilson coefficients (WCs) C_i, $C_i^{'}$ and $C_i^{''}$. Each primed and double primed operator can be expressed as a linear combination of unprimed operators through Fierz transformation.

First we fit the NP predictions of R_D, R_{D^*}, $R_{J/\psi}$, $P_\tau^{D^*}$ and $f_L^{D^*}$ to the current measured values. The corresponding χ^2 is defined as

$$\chi^2(C_i) = \sum \left(O^{\text{th}}(C_i) - O^{\text{exp}} \right)^T \mathscr{C}^{-1} \left(O^{\text{th}}(C_i) - O^{\text{exp}} \right). \quad (53.3)$$

Here $\mathscr{C}$ is the covariance matrix which includes both theory and experimental correlations. The fit is done by using the CERN minimization code `MINUIT` [13]. We perform three types of fits: (a) taking only one NP operator at a time, (b) taking two similar NP operators at a time, (c) taking two dissimilar NP operators at a time. The branching ratio of $B_c \to \tau\bar{\nu}$ puts a stringent constraint on the scalar/pseudo-scalar NP WCs. In particular, LEP data imposes an upper bound on this quantity which is $\mathscr{B}(B_c \to \tau\bar{\nu}) < 10\%$ [14]. Further we include the renormalization group (RG) effects in the evolution of the WCs from the scale $\Lambda = 1$ TeV to the scale m_b [15].

The $B \to D^{(*)} l\bar{\nu}$ decay distributions depend upon hadronic form-factors. The form factors for $B \to D$ decay are well known in lattice QCD [16] and we use them in our analyses. For $B \to D^*$ decay, the HQET parameters are extracted using data from Belle and BaBar experiments along with lattice inputs. In this work, the numerical values of these parameters are taken from [1, 17].

The best fit solutions are listed in Table 53.1 which satisfy the constraints $\chi^2_{\text{min}} \leq 5$ as well as $\mathscr{B}(B_c \to \tau\bar{\nu}) < 10\%$. Comparing with the previously allowed solutions (Table 4 in [7]), we note that only the $\mathscr{O}_{V_L}$ solution survives among the single operator solutions. However, its coefficient is reduced by a third because of the reduction in discrepancy. Among the two similar operator solutions, only the $(\mathscr{O}''_{S_L}, \mathscr{O}''_{S_R})$ persists in principle, with the WCs $(C''_{S_L}, C''_{S_R}) = (0.05, 0.24)$. The value of C''_{S_L} is quite small, $C''_{S_R} \approx 2C_{V_L}$ and the Fierz transform of $\mathscr{O}''_{S_R}$ is $\mathscr{O}_{V_L}/2$. Therefore, this solution is effectively equivalent to the $\mathscr{O}_{V_L}$ solution. In [18], we have shown that $f_L^{D^*}$ can strongly discriminate against the tensor and scalar NP solutions. The tensor solution $C_T = 0.516$, which was allowed before $f_L^{D^*}$ measurement [7], is now completely ruled out at the level of $\sim 5\sigma$. The O''_{S_L} solution is now ruled out in view of goodness

Table 53.1 Fit values of the coefficients of new physics operators at $\Lambda = 1$ TeV by making use of data of R_D, R_{D^*}, $R_{J/\psi}$, $P_\tau^{D^*}$ and $f_L^{D^*}$. In this fit, we use the HFLAV summer 2019 averages of R_D-R_{D^*}. All new physics solutions satisfy $\chi^2_{\text{min}} \leq 7$ as well as $\mathscr{B}(B_c \to \tau\bar{\nu}) < 10\%$

NP type	Best fit value (s)	χ^2_{min}
SM	$C_i = 0$	21.80
C_{V_L}	0.10 ± 0.02	4.5
(C''_{S_L}, C''_{S_R})	(0.05, 0.24)	4.4
(C_{S_L}, C_T)	(0.06, −0.06)	5.0
(C_{S_R}, C_T)	(0.07, −0.05)	4.6
(C''_{V_R}, C''_T)	(0.21, 0.11)	4.2
C_T	-0.07 ± 0.02	7.1
(C'_{V_R}, C'_{S_L})	(0.38, 0.63)	6.0
(C''_{V_R}, C''_{S_L})	(0.11, −0.58)	6.2

of fit. Table 53.1 also lists three other solutions with $5 \leq \chi^2_{\text{min}} \leq 7$. We consider these solutions because the minimum χ^2 is just a little larger than 5. Hence, they are only mildly disfavoured compare to the five solutions listed above them. One important point to note is that the prediction of R_D (see Table III in [11]) for the tensor NP solution $C_T = -0.07$ is 1.5σ below the present world average. Hence there are seven NP solutions which can account for the present data in $b \to c\tau\bar{\nu}$ transition. After Moriond 2019, several groups have done similar analysis which can be found in [19–22].

53.3 Methods to Distinguish New Physics Solutions

In order to distinguish between these seven NP solutions, we consider the angular observables in $B \to (D, D^*)\tau\bar{\nu}$ decays. We consider the following four observables: (i) The τ polarization P_τ^D in $B \to D\tau\bar{\nu}$, (ii) The forward-backward asymmetry A_{FB}^D in $B \to D\tau\bar{\nu}$, (iii) The zero crossing point (ZCP) of $A_{FB}^{D^*}(q^2)$ in $B \to D^*\tau\bar{\nu}$ and (iii) The branching ratio of $B_c \to \tau\bar{\nu}$. The predictions of each of these quantities for each of the seven solutions are listed in Table 53.2.

From Table 53.2 we find the following discriminating features among the allowed solutions:

- $\mathscr{O}_{V_L}$ and $\mathscr{O}_T$ solutions: The $\mathscr{O}_{V_L}$ and $\mathscr{O}_T$ solutions predict $P_\tau^D \approx 0.35$ whereas all the other solutions predict it to be about 0.45. Therefore a measurement of this observable to a precision of 0.1 can distinguish these two solutions from the other five. A distinction between the $\mathscr{O}_{V_L}$ and $\mathscr{O}_T$ solutions can be obtained by measuring R_D to a precision of 0.01, which can be achieved at Belle II [23].

Table 53.2 The predictions of P_τ^D, A_{FB}^D, $A_{FB}^{D^*}$, $\mathscr{B}(B_c \to \tau\bar{\nu})$ and the zero crossing point (ZCP) of $A_{FB}^{D^*}(q^2)$ for each of the allowed NP solutions

NP type	P_τ^D	A_{FB}^D	$A_{FB}^{D^*}$	$\mathscr{B}(B_c \to \tau\bar{\nu})$ %	ZCP of $A_{FB}^{D^*}(q^2)$ GeV^2
SM	0.324 ± 0.001	0.360 ± 0.001	-0.012 ± 0.007	2.2	5.8
C_{V_L}	0.324 ± 0.002	0.360 ± 0.002	-0.013 ± 0.007	2.5	5.8
(C_{S_L}, C_T)	0.442 ± 0.002	0.331 ± 0.003	-0.069 ± 0.009	0.8	7.0
(C_{S_R}, C_T)	0.450 ± 0.003	0.331 ± 0.002	-0.045 ± 0.007	4.0	6.4
(C''_{V_R}, C''_T)	0.448 ± 0.002	-0.244 ± 0.003	-0.025 ± 0.008	11.0	6.0
C_T	0.366 ± 0.003	0.341 ± 0.002	-0.067 ± 0.011	1.9	7.0
(C'_{V_R}, C'_{S_L})	0.431 ± 0.002	-0.216 ± 0.004	-0.120 ± 0.009	5.7	8.6
(C''_{V_R}, C''_{S_L})	0.447 ± 0.003	0.331 ± 0.003	-0.123 ± 0.010	8.4	8.6

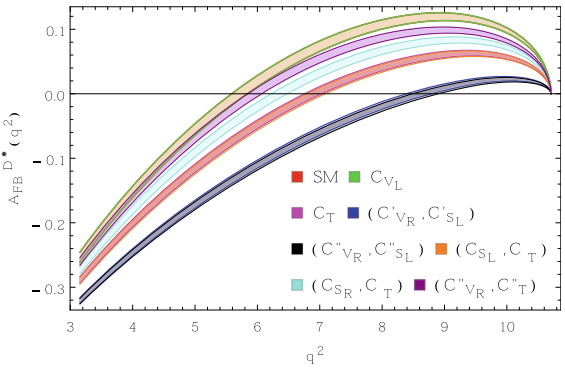

Fig. 53.1 Figure corresponds to $A_{FB}(q^2)$ as a function of q^2 for the $B \to D^*\tau\bar{\nu}$ decay. The band, representing 1σ range, is mainly due to the uncertainties in various hadronic form factors and is obtained by adding these errors in quadrature

- $(\mathscr{O}''_{V_R}, \mathscr{O}''_T)$ and $(\mathscr{O}'_{V_R}, \mathscr{O}'_{S_L})$ solutions: The $(\mathscr{O}''_{V_R}, \mathscr{O}''_T)$ and $(\mathscr{O}'_{V_R}, \mathscr{O}'_{S_L})$ solutions predict A_{FB}^D to be ~ -0.24 whereas other five solutions predict it to be ~ 0.33. Establishing this variable to be negative will distinguish these two solutions from the others. A clear distinction between these two solutions can be made through the measurement of zero crossing point (ZCP) of $A_{FB}^{D^*}(q^2)$. In Fig. 53.1, we have plotted $A_{FB}^{D^*}(q^2)$ as a function of q^2. From this figure, we note that the ZCP for the $(\mathscr{O}''_{V_R}, \mathscr{O}''_T)$ and $(\mathscr{O}'_{V_R}, \mathscr{O}'_{S_L})$ solutions are $\sim 6.0\,\text{GeV}^2$ and $\sim 8.6\,\text{GeV}^2$, respectively. A further discrimination can be made through the branching ratio of $\mathscr{B}(B_c \to \tau\bar{\nu})$,

predicted to be 11% by the ($\mathscr{O}''_{V_R}$, $\mathscr{O}''_T$) solution and 6% by the ($\mathscr{O}'_{V_R}$, $\mathscr{O}'_{S_L}$) solution, provided it is measured to a precision of about 2%.

- The other three solutions: The three solutions, ($\mathscr{O}_{S_L}$, $\mathscr{O}_T$), ($\mathscr{O}_{S_R}$, $\mathscr{O}_T$) and ($\mathscr{O}''_{V_R}$, $\mathscr{O}''_{S_L}$), all predict the same values for P_τ^D and A_{FB}^D. A distinction between these three solution can be done by the measuring the ZCP of $A_{FB}^{D^*}(q^2)$ or by $\mathscr{B}(B_c \to \tau\bar{\nu})$. The ZCP of $A_{FB}^{D^*}(q^2)$ is $\sim$6.8 GeV^2 for the ($\mathscr{O}_{S_L}$, $\mathscr{O}_T$) and ($\mathscr{O}_{S_R}$, $\mathscr{O}_T$) solutions and it is $\sim$8.6 GeV^2 for the ($\mathscr{O}''_{V_R}$, $\mathscr{O}''_{S_L}$) solution. The respective predictions for $\mathscr{B}(B_c \to \tau\bar{\nu})$ of these three solutions are 0.8%, 4.0% and 8.4%. Thus a measurement of $\mathscr{B}(B_c \to \tau\bar{\nu})$ to a precision of 2% can distinguish between these three solutions.

53.4 Conclusions

After Moriond 2019, the discrepancy between the the global average values and the SM predictions of R_D-R_{D^*} reduces to 3.1 σ. The measured value of $f_L^{D^*}$ rules out the previously allowed tensor NP solution at $\sim 5\sigma$ level. We redo the fit with the new global averages and find that there are only **seven** allowed NP solutions. We discuss methods to discriminate between these solutions by angular observables in $B \to (D, D^*)\tau\bar{\nu}$ decays and the branching ratio $\mathscr{B}(B_c \to \tau\bar{\nu})$. We find that each of these seven solutions can be uniquely identified by the combination of the five observables with the following described precision: (i) The τ polarization P_τ^D in $B \to D\tau\bar{\nu}$ to a precision 0.1, (ii) The ratio R_D to a precision of 0.01, (iii) The A_{FB}^D in $B \to D\tau\bar{\nu}$ to be either positive or negative, (iv) The zero crossing point of $A_{FB}^{D^*}(q^2)$ in $B \to D^*\tau\bar{\nu}$ to a precision of 0.5 GeV^2, and (v) The branching ratio of $B_c \to \tau\bar{\nu}$ to a precision of 2%.

Acknowledgements SK thanks to the organizers for financial support to attend the workshop.

References

1. Y. Amhis et al., [HFLAV Collaboration], Eur. Phys. J. C **77**(12), 895 (2017)
2. A. Abdesselam et al., [Belle Collaboration], arXiv:1904.08794 [hep-ex]
3. https://hflav-eos.web.cern.ch/hflav-eos/semi/spring19/html/RDsDsstar/RDRDs.html
4. R. Aaij et al., [LHCb Collaboration], Phys. Rev. Lett. **120**(12), 121801 (2018)
5. S. Hirose et al., [Belle Collaboration], Phys. Rev. Lett. **118**(21), 211801 (2017)
6. K. Adamczyk [Belle and Belle II Collaborations], arXiv:1901.06380 [hep-ex]
7. A.K. Alok, D. Kumar, J. Kumar, S. Kumbhakar, S.U. Sankar, JHEP **1809**, 152 (2018)
8. M. Freytsis, Z. Ligeti, J.T. Ruderman, Phys. Rev. D **92**(5), 054018 (2015)
9. A.K. Alok, D. Kumar, S. Kumbhakar, S. Uma Sankar, Phys. Lett. B **784**, 16 (2018)
10. S. Kumbhakar, A.K. Alok, D. Kumar, S.U. Sankar, Springer Proc. Phys. **234**, 473 (2019)
11. A.K. Alok, D. Kumar, S. Kumbhakar, S. Uma Sankar, arXiv:1903.10486 [hep-ph]
12. S. Kumbhakar, A.K. Alok, D. Kumar, S.U. Sankar, arXiv:1909.02840 [hep-ph]
13. F. James, CERN-D-506, CERN-D506

14. A.G. Akeroyd, C.H. Chen, Phys. Rev. D **96**(7), 075011 (2017)
15. M. Gonzalez-Alonso, J. Martin Camalich, K. Mimouni, Phys. Lett. B **772**, 777 (2017)
16. S. Aoki et al., Eur. Phys. J. C **77**(2), 112 (2017)
17. J.A. Bailey et al., [Fermilab Lattice and MILC Collaborations], Phys. Rev. D **89**(11), 114504 (2014)
18. A.K. Alok, D. Kumar, S. Kumbhakar, S.U. Sankar, Phys. Rev. D **95**(11), 115038 (2017)
19. Q.Y. Hu, X.Q. Li, Y.D. Yang, Eur. Phys. J. C **79**(3), 264 (2019)
20. C. Murgui, A. Penuelas, M. Jung, A. Pich, arXiv:1904.09311 [hep-ph]
21. R.X. Shi, L.S. Geng, B. Grinstein, S. Jager, J. Martin Camalich, arXiv:1905.08498 [hep-ph]
22. M. Blanke, A. Crivellin, T. Kitahara, M. Moscati, U. Nierste, I. Nisandzic, arXiv:1905.08253 [hep-ph]
23. E. Kou et al., [Belle-II Collaboration], arXiv:1808.10567 [hep-ex]

Chapter 54
Analysis of $\bar{B} \to D\tau\bar{\nu}_\tau$ Decay Modes

Suchismita Sahoo and Rukmani Mohanta

Abstract We perform a model-independent analysis of $\bar{B} \to D\tau\bar{\nu}_\tau$ decay modes involving $b \to c\tau\bar{\nu}_\tau$ quark level transitions by considering the most general effective Lagrangian in the presence of new physics. We constrain the new coefficients by using χ^2 fit to $R_{D^{(*)}}$, $R_{J/\psi}$ and $\text{Br}(B_c^+ \to \tau^+\bar{\nu}_\tau)$. Using the constrained new couplings, we then estimate the branching fractions, lepton non-universality ratios and various angular observables of $\bar{B} \to D\tau\bar{\nu}_\tau$ processes in four different bins of q^2.

54.1 Introduction

The study of rare B meson decays involving $b \to sll$ and $b \to c\tau\bar{\nu}_\tau$ transitions play an important role in probing new physics (NP) beyond the Standard Model (SM) due to the presence of discrepancies at the level of $(2-4)\sigma$ in many observables. Specifically, the observation of lepton non-universality (LNU) in $B \to K^{(*)}ll, (R_{K^{(*)}})$ at the level of 2.5σ discrepancy [1], in $\bar{B} \to D^{(*)}\tau\bar{\nu}_\tau$ process at the level of 3.08σ [2]

$$\begin{aligned} R_D^{\text{Expt}} &= 0.340 \pm 0.027 \pm 0.013\,, \quad R_{D^*}^{\text{Expt}} = 0.295 \pm 0.011 \pm 0.008\,, \\ R_D^{\text{SM}} &= 0.299 \pm 0.003\,, \qquad\qquad R_{D^*}^{\text{SM}} = 0.258 \pm 0.005\,, \end{aligned} \tag{54.1}$$

and the LNU parameter in $B_c \to J/\psi\tau\bar{\nu}_\tau$ shows deviation between the experimental measurement and SM predictions by 1.7σ [3]

$$R_{J/\psi}^{\text{Expt}} = 0.71 \pm 0.17 \pm 0.18\,, \qquad R_{J/\psi}^{\text{SM}} = 0.289 \pm 0.01\,. \tag{54.2}$$

S. Sahoo (✉)
Department of Physics, Central University of Karnataka, Kalaburagi 585367, India
e-mail: suchismita8792@gmail.com

R. Mohanta
University of Hyderbad, Hyderabad 500046, Telangana, India
e-mail: rukmani98@gmail.com

A. Giri and R. Mohanta (eds.), *Workshop on Frontiers in High Energy Physics 2019*, Springer Proceedings in Physics 248,
https://doi.org/10.1007/978-981-15-6292-1_54

In this work, we investigate the branching ratio and various angular observables of $\bar{B} \to D^{(*)}\tau\bar{\nu}_\tau$ decay modes in four different q^2 bins: $m_\tau^2 \to 5$, $5 \to 7$, $7 \to 9$ and $9 \to (M_B - M_{D^{(*)}})^2$.

The paper is organized as follows. Section 54.2 discuss the effective Hamiltonian for $b \to c\tau\bar{\nu}_\tau$ transition. The constrained on new couplings from $R_{D^{(*)}}$, $R_{J/\psi}$ and $\text{Br}(B_c^+ \to \tau^+\bar{\nu}_\tau)$ are also discussed in this section. The numerical analysis of $\bar{B} \to D^{(*)}\tau\bar{\nu}_\tau$ are presented in Sect. 54.3 followed by conclusion in Sect. 54.4.

54.2 Effective Lagrangian and Constrained on New Couplings

The most general effective Hamiltonian of $b \to c\tau\bar{\nu}_l$ decay mode is [4]

$$\mathcal{H}_{\text{eff}} = \frac{4G_F}{\sqrt{2}} V_{cb}\Big[(\delta_{l\tau} + V_L)\, \mathcal{O}^l_{V_L} + V_R \mathcal{O}^l_{V_R} + S_L \mathcal{O}^l_{S_L} + S_R \mathcal{O}^l_{S_R} + T\mathcal{O}^l_T \Big], \quad (54.3)$$

where G_F is the Fermi constant, V_{cb} is the CKM matrix element, $\mathcal{O}_{C^{\text{NP}}}$'s are the effective operators with $C^{\text{NP}} = V_{L,R}, S_{L,R}, T$ are the corresponding Wilson coefficients, which vanish in the SM.

We constrain the new coefficients from the χ^2 fit to $R_{D^{(*)}}$, $R_{J/\psi}$ and the upper limit on the $\text{Br}(B_c^+ \to \tau^+\bar{\nu}_\tau)$ process, where χ^2 is defined as

$$\chi^2(C^{\text{NP}}) = \sum_i \frac{(\mathcal{O}_i^{\text{th}}(C^{\text{NP}}) - \mathcal{O}_i^{\text{Expt}})^2}{(\Delta\mathcal{O}_i^{\text{Expt}})^2 + (\Delta\mathcal{O}_i^{\text{SM}})^2}\,. \quad (54.4)$$

Here $\mathcal{O}_i^{\text{th}}(C^{\text{NP}})$ are the total theoretical predictions for the observables, $\mathcal{O}_i^{\text{Expt}}$ represent the respective measured central values, $\Delta\mathcal{O}_i^{\text{Expt}}$ and $\Delta\mathcal{O}_i^{\text{SM}}$ are respectively the experimental and SM uncertainties of the observables. The present measured upper limit [5] and the predicted branching ratio of $B_c^+ \to \tau^+\bar{\nu}_\tau$ by using the decay constant from [6] and the remaining input parameters from [7] are given by

$$\text{BR}(B_c^+ \to \tau^+\nu_\tau)|^{\text{SM}} = (3.6 \pm 0.14) \times 10^{-2}\,, \quad \text{BR}(B_c^+ \to \tau^+\nu_\tau)|^{\text{Expt}} < 30\%\,. \quad (54.5)$$

We consider the presence of two real new coefficients at one time and constrained the coefficients by using the theoretical and experimental values of $R_{D^{(*)}}$, $R_{J/\psi}$ and $\text{Br}(B_c^+ \to \tau^+\bar{\nu}_\tau)$ as shown in Fig. 54.1.

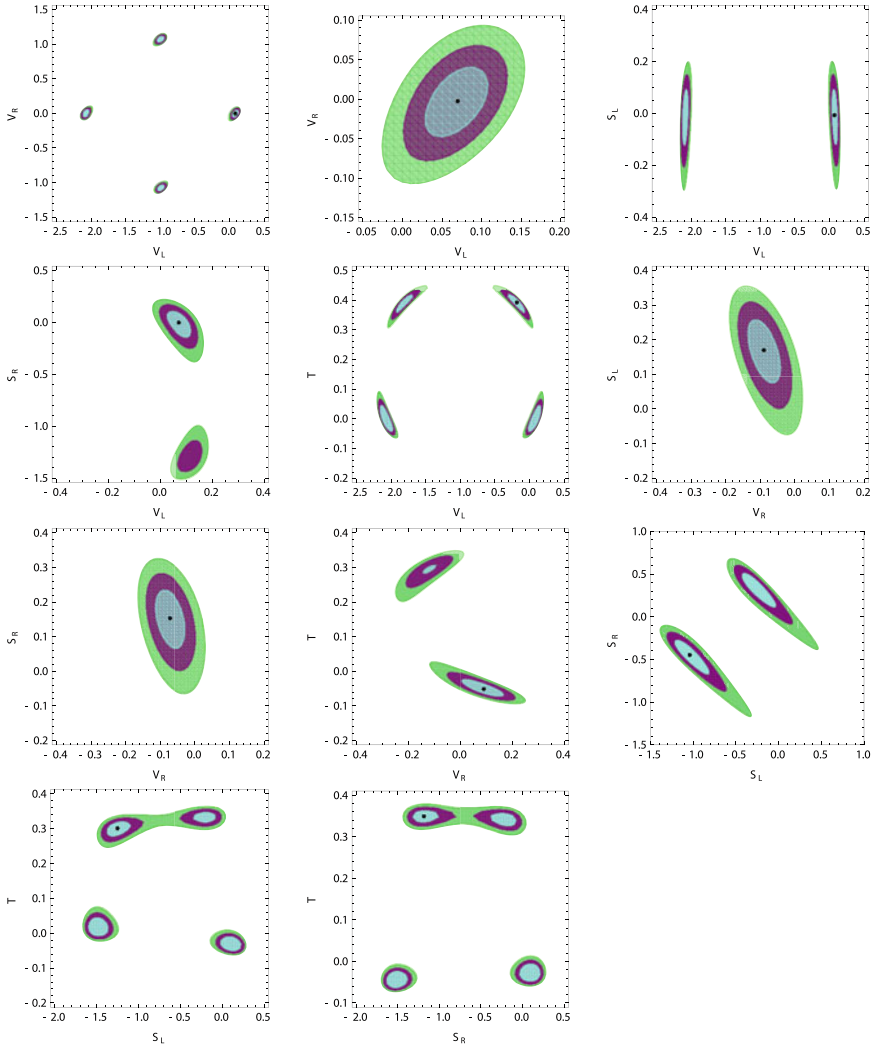

Fig. 54.1 Constraints on all possible combination of two real new coefficients obtained from χ^2 fit to $R_{D^{(*)}}$, $R_{J/\psi}$ and $\text{Br}(B_c^+ \to \tau^+\nu_\tau)$ observables. The zoom plot for $V_L - V_R$ plane is shown in the top-middle panel. The black dot in all the figures represent the best-fit values

54.3 $\bar{B} \to D\tau\bar{\nu}_\tau$

The decay rate of $\bar{B} \to Dl\nu_l$ process with respect to q^2 with the inclusion of all the new physics operators is given by [8]

$$\begin{aligned}\frac{d\Gamma(\bar{B} \to Dl\bar{\nu}_l)}{dq^2} &= \frac{G_F^2|V_{cb}|^2}{192\pi^3 M_B^3} q^2\sqrt{\lambda_P(q^2)}\left(1-\frac{m_l^2}{q^2}\right)^2 \\ &\times\left\{\left|1+V_L+V_R\right|^2\left[\left(1+\frac{m_l^2}{2q^2}\right)H_0^2+\frac{3}{2}\frac{m_l^2}{q^2}H_t^2\right]\right. \\ &+\frac{3}{2}\left|S_L+S_R\right|^2 H_S^2+8\left|T\right|^2\left(1+\frac{2m_l^2}{q^2}\right)H_T^2 \\ &+3\mathrm{Re}\left[(1+V_L+V_R)(S_L^*+S_R^*)\right]\frac{m_l}{\sqrt{q^2}}H_S H_t \\ &\left.-12\mathrm{Re}\left[(1+V_L+V_R)\,T^*\right]\frac{m_l}{\sqrt{q^2}}H_T H_0\right\}, \end{aligned} \tag{54.6}$$

where $\lambda_D = \lambda(M_B^2, M_D^2, q^2)$ with $\lambda(a,b,c) = a^2+b^2+c^2-2(ab+bc+ca)$, $H_{0,t,S,T}$ are the helicity amplitudes which include the form factors ($F_{0,1,T}$) [8]. The differential decay distribution of $\bar{B} \to D^* l\bar{\nu}_l$ decay mode in terms of helicity amplitudes ($H_{i,\pm}$, $H_{i,0}$, H_t, where $i = V, T$) with respect to q^2 is given by [8]

$$\begin{aligned}\frac{d\Gamma(\bar{B} \to D^* l\bar{\nu}_l)}{dq^2} &= \frac{G_F^2|V_{cb}|^2}{192\pi^3 M_B^3} q^2\sqrt{\lambda_V(q^2)}\left(1-\frac{m_l^2}{q^2}\right)^2 \times \\ &\left\{\left(|1+V_L|^2+|V_R|^2\right)\left[\left(1+\frac{m_l^2}{2q^2}\right)\left(H_{V,+}^2+H_{V,-}^2+H_{V,0}^2\right)+\frac{3}{2}\frac{m_l^2}{q^2}H_{V,t}^2\right]\right. \\ &-2\mathrm{Re}\left[(1+V_L)\,V_R^*\right]\left[\left(1+\frac{m_l^2}{2q^2}\right)\left(H_{V,0}^2+2H_{V,+}H_{V,-}\right)+\frac{3}{2}\frac{m_l^2}{q^2}H_{V,t}^2\right] \\ &+\frac{3}{2}|S_L-S_R|^2 H_S^2+8|T|^2\left(1+\frac{2m_l^2}{q^2}\right)\left(H_{T,+}^2+H_{T,-}^2+H_{T,0}^2\right) \\ &+3\mathrm{Re}\left[(1+V_L-V_R)\left(S_L^*-S_R^*\right)\right]\frac{m_l}{\sqrt{q^2}}H_S H_{V,t} \\ &-12\mathrm{Re}\left[\left(1+V_L^*\right)T^*\right]\frac{m_l}{\sqrt{q^2}}\left(H_{T,0}H_{V,0}+H_{T,+}H_{V,+}-H_{T,-}H_{V,-}\right) \\ &\left.+12\mathrm{Re}\left[V_R^* T^*\right]\frac{m_l}{\sqrt{q^2}}\left(H_{T,0}H_{V,0}+H_{T,+}H_{V,-}-H_{T,-}H_{V,+}\right)\right\}, \end{aligned} \tag{54.7}$$

where $\lambda_{D^*} = \lambda(M_B^2, M_{D^*}^2, q^2)$. The forward-backward asymmetry and the Tau polarization parameter are defined as

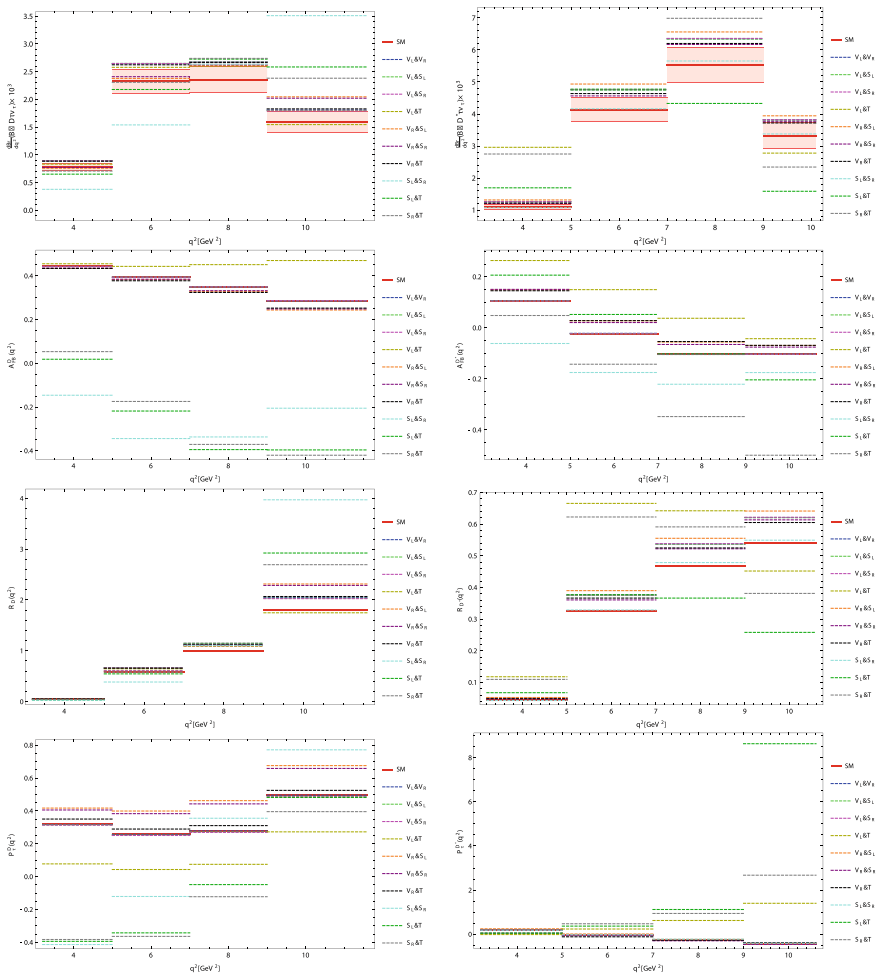

Fig. 54.2 The bin-wise branching ratio (top panel), A_{FB} (first from top panel), $R_D^{(*)}$ (second from top panel) and P_τ (bottom panel) of $\bar{B} \to D\tau\bar{\nu}_\tau$ (left panel) and $\bar{B} \to D^*\tau\bar{\nu}_\tau$ (right panel) mode in four q^2 bins

$$A_{FB}\left(q^2\right) = \left[\int_{-1}^{0} d\cos\theta_l \frac{d^2\Gamma}{dq^2 d\cos\theta_l} - \int_{0}^{1} d\cos\theta_l \frac{d^2\Gamma}{dq^2 d\cos\theta_l}\right], \quad (54.8)$$

$$P_\tau(q^2) = \frac{d\Gamma(\lambda_\tau = 1/2)/dq^2 - d\Gamma(\lambda_\tau = -1/2)/dq^2}{d\Gamma(\lambda_\tau = 1/2)/dq^2 + d\Gamma(\lambda_\tau = -1/2)/dq^2}. \quad (54.9)$$

For numerical estimation, we use all the required particle masses, lifetime of B meson, CKM matrix elements from [7] and the form factor values from [9]. Using the best-fit values from Fig. 54.1 the bin-wise graphical representation of branching ratio (top panel), forward-backward asymmetry (second from top panel), LNU

parameters (third from top panel) and tau-polarization asymmetry (bottom panel) of $\bar{B} \to D^{(*)}\tau\bar{\nu}_\tau$ processes are presented in the left (right) panel of Fig. 54.2. Here, the red solid lines (bands) represent the SM values (1σ uncertainties). We found that the presence of $S_L\&S_R$, $S_L\&T$ and $S_R\&T$ have large effects on all the observables.

54.4 Conclusion

We have presented a bin-wise analysis of rare $\bar{B} \to D^{(*)}\tau\bar{\nu}_\tau$ decays by considering the most general effective Lagrangian in the presence of NP. We have considered the presence of two real coefficients at one time and constrained them from χ^2 fit to $R_{D^{(*)}}$, $R_{J/\psi}$ and $\text{Br}(B_c \to \tau\nu_\tau)$. We then estimate the branching ratio and various angular observables of $\bar{B} \to D^{(*)}\tau\bar{\nu}_\tau$ modes.

References

1. R. Aaij et al., (LHCb) (2019), 1903.09252; A. Abdesselam et al., (Belle) (2019), 1904.02440; C. Bobeth, G. Hiller, G. Piranishvili, JHEP **12**, 040 (2007); B. Capdevila, A. Crivellin, S. Descotes-Genon, J. Matias, J. Virto, JHEP **01**, 093 (2018)
2. Heavy Flavor Averaging Group (2019), https://hflav-eos.web.cern.ch/hflav-eos/semi/spring19/html/RDsDsstar/RDRDs.html; S. Fajfer, J.F. Kamenik, I. Nisandzic, J. Zupan, Phys. Rev. Lett. **109**, 161801 (2012); H. Na, C.M. Bouchard, G.P. Lepage, C. Monahan, J. Shigemitsu (HPQCD), Phys. Rev. D **92**, 054510 (2015), [Erratum: Phys. Rev. D **93**, 119906 (2016)]
3. R. Aaij et al., (LHCb), Phys. Rev. Lett. **120**, 121801 (2018), https://doi.org/10.1103/PhysRevLett.120.121801; W.-F. Wang, Y.-Y. Fan, Z.-J. Xiao, Chin. Phys. C **37**, 093102 (2013), https://doi.org/10.1088/1674-1137/37/9/093102
4. V. Cirigliano, J. Jenkins, M. Gonzalez-Alonso, Nucl. Phys. B **830**, 95 (2010). https://doi.org/10.1016/j.nuclphysb.2009.12.020
5. A.G. Akeroyd, C.-H. Chen, Phys. Rev. D **96**, 075011 (2017)
6. S. Aoki et al., Eur. Phys. J. C **74**, 2890 (2014)
7. M. Tanabashi et al., Particle data group. Phys. Rev. D **98**, 030001 (2018)
8. Y. Sakaki, M. Tanaka, A. Tayduganov, R. Watanabe, Phys. Rev. D **88**, 094012 (2013)
9. J.A. Bailey et al., (MILC), Phys. Rev. D **92**, 034506 (2015); I. Caprini, L. Lellouch, M. Neubert, Nucl. Phys. B **530**, 153 (1998); J.A. Bailey et al., (Fermilab Lattice, MILC), Phys. Rev. D **89**, 114504 (2014); Y. Amhis et al., (HFAG) (2014), 1412.7515; Z.-R. Huang, Y. Li, C.-D. Lu, M.A. Paracha, C. Wang, Phys. Rev. D **98**, 095018 (2018); R. Watanabe, Phys. Lett. B **776**, 5 (2018)

Chapter 55
Effect of New Physics in $\bar{B} \to \rho \ell \bar{\nu}_\ell$ Decay Process

Atasi Ray, Aishwarya Bhatta, and Rukmani Mohanta

Abstract Several anomalies have been observed in various lepton non universality (LNU) observables and other asymmetries associated with semileptonic B-meson decays mediated by $b \to (c, s)$ quark level transitions. In this context we perform a model independent analysis of $\bar{B} \to \rho \ell \bar{\nu}_\ell$ decay process mediated by $b \to u$ quark level transition. In this article, we calculate the branching fraction, lepton spin asymmetry and LNU parameter associated with this decay process and scrutinize whether there will be any deviation in these observables in presence of new Physics (NP).

55.1 Introduction

In B physics several anomalies have been observed in various observables associated with semileptonic decay processes mediated by $b \to (c, s)$ quark level transitions. These days the study of observed (2–4) σ discrepancies of several lepton non universality (LNU) observables are the center of attraction in B-physics. The list of various LNU observables, their theoretical predicted values and experimental values are presented in Table 55.1. As these observables are the ratio of two decay rates, the theoretical uncertainties arising from the form factors and CKM matrix elements cancel out to a great extent, reducing the overall uncertainty in the calculation of these parameters, hence they are considered as sensitive probe for new physics (NP). On the other hand, the decay processes involving τ lepton in the final state are more

A. Ray (✉) · A. Bhatta · R. Mohanta
School of Physics, University of Hyderabad, Hyderabad 500046, India
e-mail: atasiray92@gmail.com

A. Bhatta
e-mail: aish.bhatta@gmail.com

R. Mohanta
e-mail: rukmani98@gmail.com

A. Giri and R. Mohanta (eds.), *Workshop on Frontiers in High Energy Physics 2019*, Springer Proceedings in Physics 248,
https://doi.org/10.1007/978-981-15-6292-1_55

Table 55.1 List of various LNU observables along with their measured values and Standard model predictions and deviations from SM

LNU observable	Measured value	SM value	Deviation
$R_K = \frac{\text{Br}(B^+\to K^+\mu^+\mu^-)}{\text{Br}(B^+\to K^+e^+e^-)}\Big\vert_{q^2\in[1.1,6]\ \text{GeV}^2}$	$0.846^{+0.060+0.016}_{-0.054-0.014}$	1.0003 ± 0.0001	2.5σ
$R_{K^*} = \frac{\text{Br}(\bar{B}\to \bar{K}^*\mu^+\mu^-)}{\text{Br}(\bar{B}\to \bar{K}^*e^+e^-)}\Big\vert_{q^2\in[0.045,1.1]\ \text{GeV}^2}$	$0.660^{+0.110}_{-0.070} \pm 0.024$	0.92 ± 0.02	2.2σ
$R_{K^*}\Big\vert_{q^2\in[1.1,6]\ \text{GeV}^2}$	$0.685^{+0.113}_{-0.007} \pm 0.047$	1.00 ± 0.01	2.4σ
$R_D = \frac{\text{Br}(B\to D\tau\bar{\nu}_\tau)}{\text{Br}(\bar{B}\to \bar{D}l\bar{\nu}_l)}$	$0.340 \pm 0.027 \pm 0.013$	0.299 ± 0.003	1.9σ
$R_{D^*} = \frac{\text{Br}(\bar{B}\to \bar{D}^*\tau\bar{\nu}_\tau)}{\text{Br}(\bar{B}\to \bar{D}^*l\bar{\nu}_l)}$	$0.295 \pm 0.011 \pm 0.008$	0.258 ± 0.005	3.3σ
$R_{J/\psi} = \frac{\text{Br}(\bar{B}\to J/\psi\tau\bar{\nu}_\tau)}{\text{Br}(\bar{B}\to J/\psi\mu\bar{\nu}_\mu)}$	$0.71 \pm 0.17 \pm 0.184$	0.289 ± 0.01	2σ

effective for NP, as the third generation of leptons have comparatively larger mass than the other two generations. In this aspect we scrutinize the possibility of LNU and other asymmetries associated with $\bar{B} \to \rho\ell\bar{\nu}_\ell$ decay process mediated by $b \to u\ell\bar{\nu}_\ell$ transition considering the effective field theory approach.

The outline of our paper is follows. In Sect. 55.2, we present the general effective Lagrangian describing the processes $b \to u\ell\bar{\nu}_\ell$ in presence of new couplings in addition to the SM ones, and the theoretical framework for analysing $\bar{B} \to \rho\ell\bar{\nu}_\ell$ decay process. The constrained parameter space for the new couplings are presented in Sect. 55.3. In Sect. 55.4, we discuss the effect of NP on various parameters. Here we show the q^2 variation of branching fraction, lepton non-universality parameter and lepton spin asymmetry parameter of $\bar{B} \to \rho\ell\bar{\nu}_\ell$ processes in presence of individual new physics coefficients. We summarize our work in Sect. V.

55.2 Theoretical Framework

In the effective field theory approach, the most general effective Lagrangian of $\bar{B} \to \rho\ell\bar{\nu}_\ell$ decay process mediated by $b \to u\ell\bar{\nu}_\ell$ transition can be expressed as [5],

$$L_{eff} = \frac{4G_F}{\sqrt{2}} V_{ub}\Big[(1+V_L)(\bar{u}_L\gamma^\mu b_L)(\bar{\tau}_L\gamma^\mu\nu_L) + V_R(\bar{u}_R\gamma^\mu b_R)(\bar{\tau}_L\gamma^\mu\nu_L) + S_L(\bar{u}_L b_R)(\bar{\tau}_R\nu_L) + S_R(\bar{u}_R b_L)(\bar{\tau}_R\nu_L) + T_L(\bar{b}_R\sigma^{\mu\nu}b_L)(\bar{\tau}_R\sigma_{\mu\nu}\nu_L)\Big], \quad (55.1)$$

where G_F is the Fermi constant, V_{ub} is the CKM matrix element, V_L, V_R, S_L and S_R are new Wilson coefficients. In the SM V_L, V_R, S_L and S_R couplings are zero. Here we have assumed the neutrinos are left handed and the chiral quark and lepton fields are expressed as $(b, u, \ell)_{L,R} = P_{L,R}(b, u, \ell)$ with $P_{L,R} = (1 \mp \gamma^5)/2$.

The differential decay rate of $\bar{B} \to \rho \ell \bar{\nu}_\ell$ decay process mediated by $b \to u \ell \bar{\nu}_\ell$ transition in presence of additional Wilson coefficients can be written as,

$$\begin{aligned}
\frac{d\Gamma}{dq^2} = & \frac{G_F^2 |V_{ub}|^2}{192\pi^3 m_{\bar{B}}^3} q^2 \sqrt{\lambda(q^2)} \left(1 - \frac{m_\ell^2}{q^2}\right) \times \\
& \left[(|1 + V_L|^2 + |V_R|^2) \left\{ \left(1 + \frac{m_\ell^2}{q^2}\right) (H_{V_+}^2 + H_{V_-}^2 + H_{V_0}^2) + \frac{3}{2} \frac{m_\ell^2}{q^2} H_{V_t}^2 \right\} \right. \\
& -2Re\{(1 + V_L) V_R^*\} \{ \left(1 + \frac{m_l^2}{q^2}\right) (H_{V_0}^2 + 2H_{V_+} H_{V_-}) + \frac{3}{2} \frac{m_\ell^2}{q^2} H_{V_t}^2 \} \\
& + \frac{3}{2} |S_L - S_R|^2 H_S^2 + 8|T_L^2| \left(1 + \frac{2m_\ell^2}{q^2}\right) (H_{T_+}^2 + H_{T_-}^2 + H_{T_0}^2) \\
& + 3Re[(1 + V_L - V_R)(S_L - S_R)] \frac{m_\ell^2}{\sqrt{q^2}} H_S H_{V_t} \\
& - 12Re[(1 + V_L) T_L^*] \frac{m_\ell^2}{\sqrt{q^2}} (H_{T_0} H_{V_0} + H_{T_+} H_{V_+} - H_{T_-} H_{V_-}) \\
& \left. + 12Re[V_R T_L^*] \frac{m_\ell^2}{\sqrt{q^2}} (H_{T_0} H_{V_0} + H_{T_+} H_{T_-} - H_{T_-} H_{V_+}) \right],
\end{aligned} \tag{55.2}$$

where $H_{V_{+,-,0,t}}$, H_S, $H_{T_{+,-,0}}$ are the helicity amplitudes which are the function of form factors, $\lambda = ((m_B - m_\rho)^2 - q^2)((m_B + m_\rho)^2 - q^2)$, q^2 is the momentum transferred square.

The parameters sensitive to NP are,

- Lepton non-universality parameter:

$$R_\rho(q^2) = \frac{d\Gamma(\bar{B} \to \rho^+ \tau^- \bar{\nu}_\tau)/dq^2}{d\Gamma(\bar{B} \to \rho^+ l^- \bar{\nu}_l)/dq^2} \ .$$

- Lepton-spin asymmetry:

$$A_\lambda^P(q^2) = \frac{d\Gamma(\lambda_l = -1/2)/dq^2 - d\Gamma(\lambda_l = 1/2)/dq^2}{d\Gamma(\lambda_l = -1/2)/dq^2 + d\Gamma(\lambda_l = 1/2)/dq^2}.$$

55.3 Constraints on New Couplings

In our analysis, the new Wilson coefficients are considered as complex. we consider the contribution of one additional coefficient at a time while all other coefficients are considered to be zero. The constraints on new parameter space associated with $b \to u \ell \bar{\nu}_\ell$ transitions are computed by performing a χ^2 fit on experimentally measured

Table 55.2 Best-fit values and corresponding 1σ ranges of new complex coefficients associated with $b \to u\tau\bar{\nu}_\tau$ transition

New coefficients	Best-fit	1σ range	χ^2/d.o.f
(Re[V_L], Im[V_L])	$(-0.8318, 1.098)$	$([-1.43, -0.43], [1.0, 1.2])$	0.265
(Re[V_R], Im[V_R])	$(-0.115, 0)$	$([-0.2, -0.025], [-0.45, 0.45])$	0.1363
(Re[S_L], Im[S_L])	$(-0.0236, 0)$	$([-0.042, -0.006], [-0.09, 0.09])$	0.1906
(Re[S_R], Im[S_R])	$(-0.439, 0)$	$([-0.46, -0.42], [-0.09, 0.09])$	0.1906

values of R_π^ℓ, Br($B_u \to \tau\bar{\nu}_\tau$) and Br($B^0 \to \pi^+\tau^-\bar{\nu}_\tau$) observables [2]. The allowed range of new couplings we used in our analysis are presented in Table 55.2.

55.4 Effect of New Physics

We consider the effect of left-handed vector like new coupling (V_L) in addition to the SM and the contribution due to all other coefficients are taken to be zero. In presence of only V_L coefficient we calculate the branching ratio, LNU parameter and lepton spin asymmetry parameter of $\bar{B} \to \rho\ell\bar{\nu}_\ell$ decay process. Similarly we calculate all these parameters in presence of individual couplings V_R, S_L and S_R. The numerical values of branching fraction and LNU parameters in presence of various couplings are shown in Table. The q^2 deviation of all these parameters in presence individual couplings for their 1σ allowed range and best-fit values are shown in Fig. 55.1. The blue dashed line represents the SM variation whereas the orange, cyan, magenta and green bands represent the variation in presence of V_L, V_R, S_L, S_R coefficients respectively. The black line stands for the variation for the best-fit value of the corresponding Wilson coefficients. We also present the plots containing the variation of differential decay rate, LNU parameter and lepton spin asymmetry for the best-fit value of all the new coefficients in Fig. 55.2.

Numerical values	$\mathcal{B}(B \to \rho^+\tau^-\bar{\nu}_\tau)$	R_ρ
SM Value	2.58933×10^{-4}	1.00718
$S_L(Best-fit)$	2.57162×10^{-4}	1.00067
$S_L(1\sigma)$	$(2.53062 \to 2.55831) \times 10^{-4}$	0.85616→ 0.995773
$S_R(Best-fit)$	2.71036×10^{-4}	1.05222
$S_R(1\sigma)$	$(2.5996 \to 2.83176) \times 10^{-4}$	1.01114→1.09739
$V_L(Best-fit)$	4.01063×10^{-4}	1.54296
$V_L(1\sigma)$	$(1.56969 \to 16.7189) \times 10^{-4}$	0.597757→ 6.44812
$V_R(Best-fit)$	3.02434×10^{-4}	1.1804
$V_R(1\sigma)$	$(3.3915 \to 5.20621) \times 10^{-4}$	1.1804

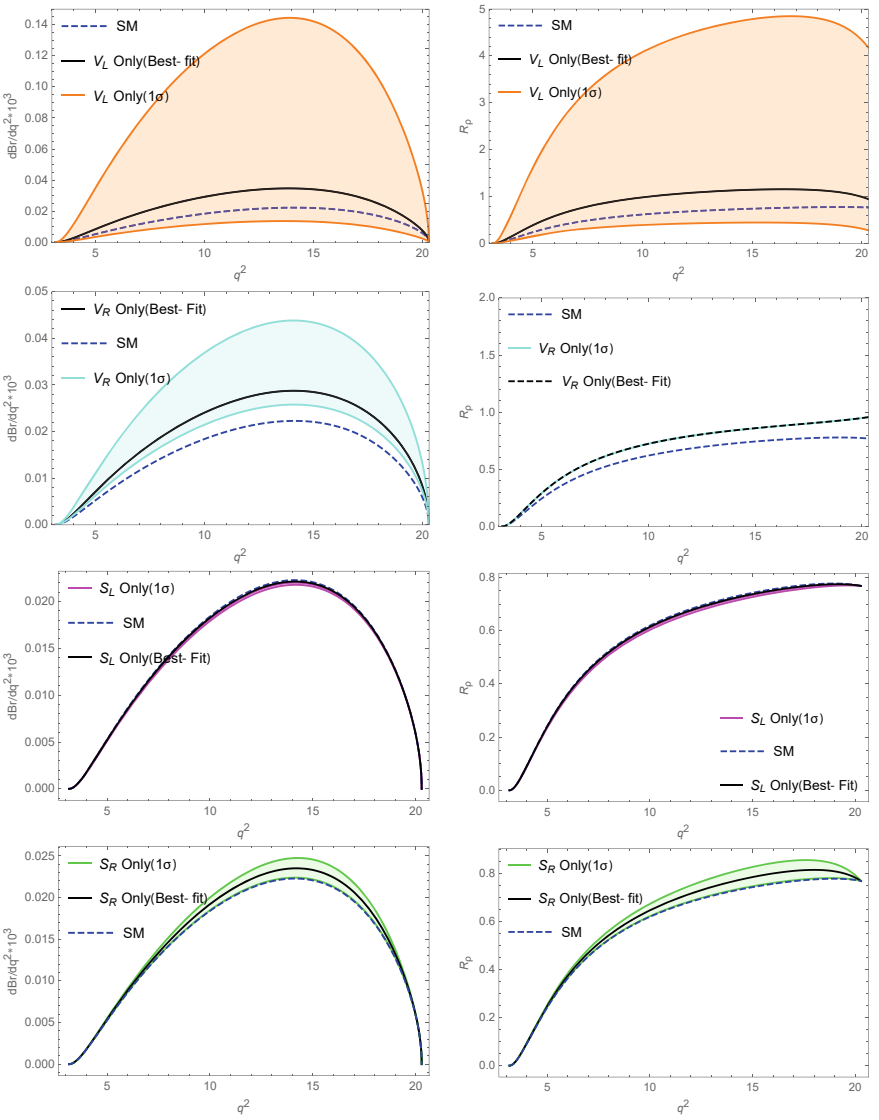

Fig. 55.1 The q^2 variation of the differential Branching ratio (left panel), LNU parameter (right panel) of $\bar{B} \to \rho \tau \bar{\nu}_\tau$ decay process in presence of individual NP coefficients

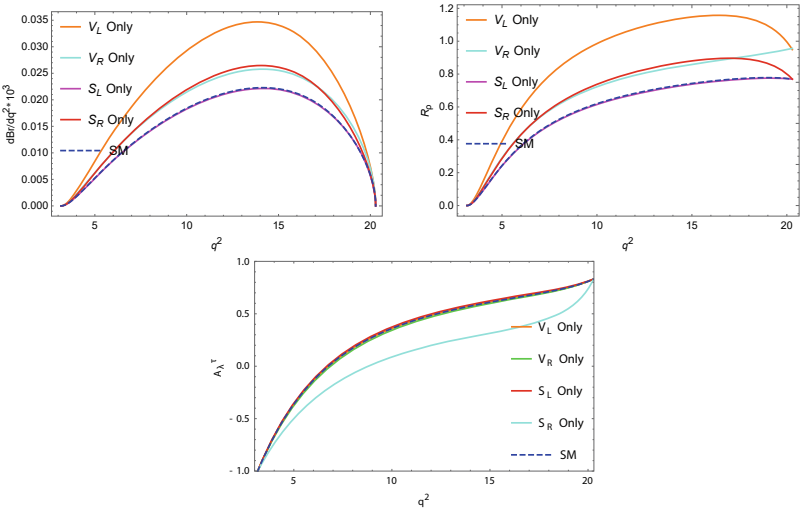

Fig. 55.2 The q^2 variation of differential branching ratio (top-left panel), Lepton non universality Parameter (top-right panel) and lepton spin asymmetry (bottom panel) for the best-fit values of NP coefficients. Blue dashed line represents the variation in SM whereas the orange, cyan, magenta and red lines represent the variation for the best-fit value of V_L, V_R, S_L and S_R coefficients respectively

55.5 Conclusion

In this analysis we have performed a model independent study of $\bar{B} \to \rho \ell \bar{\nu}_\ell$ decay process. We consider the new Wilson coefficients as complex quantities and calculated the branching ratio, LNU parameter and lepton spin asymmetry parameter in presence of individual couplings. We also show the q^2 variation of all these parameters in presence of all these new coefficients.

Acknowledgements AR and RM would like to thank SERB, Govt. of India for financial support through grant No. EMR/2017/001448. AB would like to acknowledge DST for the INSPIRE fellowship.

References

1. R. Aaji et al., Measurement of the ratio of branching fractions $\mathcal{B}(\bar{B}^0 \to D^{*+}\tau^-\bar{\nu_\tau})/\mathcal{B}(\bar{B}^0 \to D^{*+}\mu^-\bar{\nu_\mu})$. Phys. Rev. Lett. **115**, 111803 (2015). https://doi.org/10.1103/PhysRevLett.115.159901
2. A. Ray, S. Sahoo, R. Mohanta, Model independent analysis of $B^* \to P \ell \bar{\nu}_\ell$ decay processes. Eur. Phys. J. C **79**, 670 (2015). https://doi.org/10.1140/epjc/s10052-019-7183-8

3. R. Aaij et al., Measurement of the ratio of branching fractions $\mathcal{B}(B_c{}^+ \to J/\psi\tau^+\nu_\tau)/\mathcal{B}(B_c{}^+ \to J/\psi\mu^+\nu_\mu)$. Phys. Rev. Lett. **120**, 121801 (2018). https://doi.org/10.1103/PhysRevLett.120.121801
4. R. Watanabe, New physics effect on $B_c \to J/\psi\tau\bar{\nu}$ in relation to the $R_{D^{(*)}}$ anomaly. Phys. Lett. B **776**, 5 (2018). https://doi.org/10.1016/j.physletb.2017.11.016
5. T. Bhattacharya, V. Cirigliano, S. D. Cohen, A. Filipuzzi, M. Gonzalez-Alonso, Graesser, R. Gupta, H.-W. Lin, Probing novel scalar and tensor interactions from (ultra) cold neutrons to the LHC . Phys. Rev. D **85**, 054512 (2012). https://doi.org/10.1103/PhysRevD.85.054512

Chapter 56
Exploring Lepton Flavor Universality Violation in $B_s \to D_s^* l \nu$ Decay

Nilakshi Das and Rupak Dutta

Abstract The current world average of the ratio of branching ratios R_D and R_{D^*} in $B \to (D, D^*) l\nu$ $(l \in e, \tau)$ decay modes stand 3.1σ away from the standard model expectations. Motivated by these anomalies, we study the corresponding $B_s \to D_s{}^* l\nu$ $(l \in e, \tau)$ decay mode mediated via same underlying quark level transition in a model independent effective field theory formalism. To understand the underlying physics of the lepton flavour universality violation in this decay mode, we study various physical observable within the standard model and beyond.

56.1 Introduction

There has been an intense survey to understand the lepton flavor universality violation (LFUV) in both charged current $b \to c\, l\, \nu$ and neutral current $b \to s l^+ l^-$ quark level transition. The flavor ratios such as, R_D and R_{D^*}, the lepton polarization fraction $P_\tau^{D^*}$ and the longitudinal polarization fraction of the D^* meson in $B \to D^{(*)}\, \tau\, \nu$ decay mode and $R_{J/\psi}$ in $B_c \to J/\psi\, l\, \nu$ decay mode show a significant deviation from the standard model (SM) prediction. At present, the combined deviation by including R_D, R_{D^*}, $P_\tau^{D^*}$, and $F_L^{D^*}$ is found to be 3.3σ away from the SM expectations [1].

We follow a model independent effective field theory formalism and study the implications of R_D, R_{D^*},$R_{J/\psi}$,$P_\tau^{D^*}$ and $F_L^{D^*}$ anomalies on $B_s \to D_s^* \tau \nu$ decay mode. For our analysis we have considered the form factors obtained from the relativistic quark model [2].

N. Das (✉) · R. Dutta
National Institute of Technology Silchar, Silchar 788010, India
e-mail: nilakshi_rs@phy.nits.ac.in

R. Dutta
e-mail: rupak@phy.nits.ac.in

A. Giri and R. Mohanta (eds.), *Workshop on Frontiers in High Energy Physics 2019*, Springer Proceedings in Physics 248,
https://doi.org/10.1007/978-981-15-6292-1_56

56.2 Theory

The most general effective lagrangian for $b \to c l \nu$ quark level transition can be written as [3, 4]

$$\begin{aligned}\mathcal{L}_{eff} = -\frac{4G_F V_{cb}}{\sqrt{2}}\Big\{&(1+V_L)\bar{l}_L\gamma_\mu\nu_L\bar{c}_L\gamma^\mu b_L + V_R\bar{l}_L\gamma_\mu\nu_L\bar{c}_R\gamma^\mu b_R + \widetilde{V}_L\bar{l}_R\gamma_\mu\nu_R\bar{c}_L\gamma^\mu b_L \\ &+\widetilde{V}_R\bar{l}_R\gamma_\mu\nu_R\bar{c}_R\gamma^\mu b_R + S_L\bar{l}_R\nu_l\bar{c}_R b_L + S_R\bar{l}_R\nu_L\bar{c}_L b_R + \widetilde{S}_L\bar{l}_L\nu_R\bar{c}_R b_L \\ &+\widetilde{S}_R\bar{l}_L\nu_R\bar{c}_L b_R\Big\} + h.c \end{aligned} \tag{56.1}$$

The differential decay distribution for $b \to c l \nu$ can be written as [5]

$$\begin{aligned}\frac{d\Gamma}{dq^2 dcos\theta} = NP_{D_s^*}\Big\{&2\mathcal{A}_0^2\sin^2\theta_l(G_A^2+\widetilde{G}_A^2) + (1+\cos^2\theta)[\mathcal{A}_{||}^2(G_A^2+\widetilde{G}_A^2) + \\ &\mathcal{A}_\perp^2(G_V^2+\widetilde{G}_V^2)] - 4\mathcal{A}_{||}\mathcal{A}_\perp\cos\theta_l(G_A G_V - \widetilde{G}_A\widetilde{G}_V) + \frac{m_l^2}{q^2}\sin^2\theta \\ &[\mathcal{A}_{||}^2(G_A^2+\widetilde{G}_A^2) + \mathcal{A}_\perp^2(G_V^2+\widetilde{G}_V^2)] + \frac{2m_l^2}{q^2}[\Big\{\mathcal{A}_0 G_A\cos\theta_l - (\mathcal{A}_t G_A \\ &+\frac{\sqrt{q^2}}{m_l}\mathcal{A}_P G_P)\Big\}^2 + \Big\{\mathcal{A}_0\widetilde{G}_A\cos\theta_l - (\mathcal{A}_t\widetilde{G}_A + \frac{\sqrt{q^2}}{m_l}\mathcal{A}_P\widetilde{G}_P)\Big\}^2\Big\} \end{aligned} \tag{56.2}$$

Using (56.2), we define various physical observable such as the differential branching ratio DBR, the ratio of branching ratio R, the polarization fraction P_l, the forward-backward asymmetry A_{FB}^l, the convexity parameter C_F^l. Similarly, we also define the forward backward asymmetry of transversely polarized D_s^* meson A_{FB}^T and the longitudinal polarization fraction of the D_s^* meson $F_L^{D^*}$ [6].

56.3 Results and Discussions

56.3.1 SM Prediction

In Table 56.1, we give the SM predictions for the central values as well as the corresponding 1σ ranges of various physical observables for both e and τ mode. Here, we observe that the branching ratio in $B_s \to D_s^* l \nu$ decay for both e and τ mode is in the order of 10^{-2}.

From the q^2 dependent observable we can discussed as follows.

The differential decay distribution is zero at minimum and maximum value of q^2. The peak of the DBR is found to be at $q^2 \approx 8.3$ GeV^2 and $q^2 \approx 6.35$ GeV^2 for the e mode and the τ mode respectively. The A_{FB}^e is negative in the whole q^2 region whereas a zero crossing has been observed has at $q^2 \approx 6$ GeV^2 for the e-mode. The

Table 56.1 The central values and 1σ ranges for both e mode and τ mode within SM

Observable	e mode		τ mode	
	Central value	1σ range	Central value	1σ range
$DBR \times 10^{-2}$	5.92	(5.37, 6.49)	1.42	(1.29, 1.56)
A_{FB}^l	−0.256	(−0.269, −0.244)	−0.087	(−0.097, −0.078)
P^l	−1.000	−1.000	−0.523	(−0.532, −0.514)
C_F^l	−0.362	(−0.385, −0.339)	−0.042	(−0.048, −0.036)
A_{FB}^T	−0.507	(−0.521, −0.490)	−0.356	(−0.369, −0.343)
$F_L^{D^*}$	0.494	(0.484, 0.504)	0.431	(0.425, 0.437)
$R_{D_s^*}$	0.241		(0.238, 0.244)	

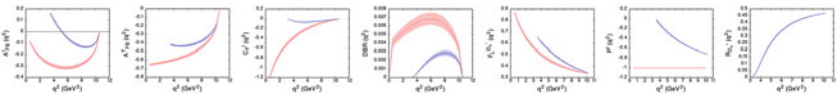

Fig. 56.1 Standard Model plots of q^2 dependence $B_s \to D_s^* l \nu$ decay observables

convexity parameter C_F^e is found to have the negative values for the whole q^2 range. Similarly,the $P^e(q^2)$ is constant for the whole q^2 region and $P^\tau(q^2)$ decreases as q^2 increases. It has been observed that the A_{FB}^T is negative for the whole q^2 region for both e and τ mode and it becomes zero at maximum q^2. Similarly, the $F_L^{D_s^*}$ is observed to have maximum value at low q^2 for both τ mode and e mode and gradually decreases as q^2 increases (Fig. 56.1).

56.3.2 New Physics Prediction

To obtain the best fit values we perform a χ^2 test which is defined as

$$\chi^2 = \sum_i \frac{(\mathcal{O}_i^{th} - \mathcal{O}_i^{exp})^2}{(\Delta\mathcal{O}_i^{exp})^2}; \tag{56.3}$$

where, $\mathcal{O}_i^{th}$ represents the theoretical prediction and $\mathcal{O}_i^{exp}$ refers to the experimental prediction of R_D, R_{D^*}, $R_{J/\psi}$, $P_\tau^{D^*}$ and $F_L^{D^*}$. The SM χ^2_{min} is obtained by performing random scan over the form factor input parameters and the CKM matrix element within 1σ. Similarly, in Table 56.2 the χ^2_{min} for each NP scenario is also calculated by considering each left handed and right handed neutrino couplings (WC coefficient) one at a time. We observe that the χ^2_{min} corresponding to the scalar NP coupling is almost similar to the SM χ^2_{min}. Hence we can say that the vector NP coupling V_L, V_R, $\widetilde{V}_L$, $\widetilde{V}_R$ can provide better explanation than the scalar NP coupling S_L, S_R, $\widetilde{S}_L$, $\widetilde{S}_R$.

Table 56.2 Best fit values of various observables for $B_s \to D_s^* \tau \nu$ decay mode within the SM and within various NP scenarios

Coefficient	Best fit value	$R_{D_s^*}$	$DBR\%$	$P_\tau^{D_s^*}$	$F_L^{D_s^*}$	A_{FB}^τ	A_{FB}^T	C_F^τ	χ^2_{min}
SM		0.240	1.374	−0.520	0.433	−0.084	−0.355	−0.043	14.267
V_L	0.087	0.284	1.618	−0.521	0.431	−0.089	−0.360	−0.041	4.762
V_R	−0.063	0.269	1.483	−0.521	0.436	−0.066	−0.326	−0.046	8.580
S_L	0.001	0.241	1.403	−0.519	0.428	−0.093	−0.366	−0.038	14.614
S_R	0.211	0.247	1.497	−0.484	0.443	−0.104	−0.360	−0.039	11.353
$\widetilde{V}_L$	0.418	0.282	1.660	−0.368	0.435	−0.022	−0.244	−0.046	4.750
$\widetilde{V}_R$	0.418	0.282	1.660	−0.368	0.435	−0.080	−0.347	−0.046	4.750
$\widetilde{S}_L$	0.576	0.242	1.374	−0.529	0.441	−0.084	−0.354	−0.044	12.625
$\widetilde{S}_R$	0.576	0.242	1.374	−0.529	0.441	−0.084	−0.354	−0.044	12.625

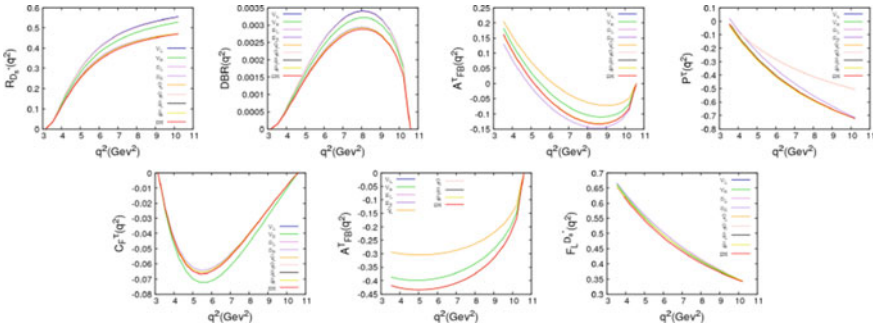

Fig. 56.2 The q^2 dependency of various observable in the SM (red) and the corresponding best fits for V_L (blue), V_R (green), S_L (violet), S_R (purple), $\widetilde{V}_L$ (orange), $\widetilde{V}_R$ (pink), $\widetilde{S}_L$ (black), $\widetilde{S}_R$ (yellow) for each physical observable of $B_s \to D_s^* \tau \nu$ decay mode

We report in Fig. 56.2, the q^2 dependent best fits of each observable in SM and in the presence of each NP couplings for $B_s \to D_s^* \tau \nu$ decay mode. We observe that in $R_{D_s^*}(q^2)$ and $DBR(q^2)$, the V_L NP coupling deviates more compared to the other NP couplings. The zero crossing for $A_{FB}^\tau(q^2)$ is at $q^2 \approx 5.2\,\text{GeV}^2$ in SM whereas in the presence of V_R and S_R NP couplings they are found to be at 5.5 GeV^2 and 4.8 GeV^2. In $P^\tau(q^2)$ the deviation observed from the SM is more in case of $\widetilde{V}_L$, $\widetilde{V}_R$ NP couplings. In case of $C_F^l(q^2)$, the scalar NP couplings $\widetilde{S}_L$, $\widetilde{S}_R$ show slight deviation from the SM. In $A_{FB}^T(q^2)$, the vector NP coupling $\widetilde{V}_L$ show maximum deviation from the SM prediction. In case of $F_L^{D_s^*}(q^2)$, the V_R, S_R and $\widetilde{S}_L$, $\widetilde{S}_R$ show slight deviation from the SM.

56.4 Conclusion

We study the $B_s \to D_s^* l \nu$ decay mode in a model independent effective field theory approach using the relativistic quark model form factors. We give the predictions of various physical observable within the SM and also in the presence of vector and scalar NP couplings. The future experimental study of $B_s \to D_s^* l \nu$ decay mode will clearly help us in understanding LFUV and allow us to determine the precise value of the CKM matrix element $|V_{cb}|$.

References

1. M. Blanke, A. Crivellin, T. Kitahara, M. Moscati, U. Nierste, I. Niandi, Phys. Rev. D **100**(3), 035035 (2019)
2. R.N. Faustov, V.O. Galkin, Phys. Rev. D **87**(3), 034033 (2013)
3. T. Bhattacharya, V. Cirigliano, S.D. Cohen, A. Filipuzzi, M. Gonzalez-Alonso, M.L. Graesser, R. Gupta, H.W. Lin, Phys. Rev. D **85**, 054512 (2012)
4. V. Cirigliano, J. Jenkins, M. Gonzalez-Alonso, Nucl. Phys. B **830**, 95 (2010)
5. R. Dutta, A. Bhol, A.K. Giri, Phys. Rev. D **88**(11), 114023 (2013). https://doi.org/10.1103/PhysRevD.88.114023
6. R. Dutta, J. Phys. G **46**(3), 035008 (2019). https://doi.org/10.1088/1361-6471/ab0059

Chapter 57
Model Independent Study of LFUV in $\Sigma_b \to \Sigma_c \tau \nu$ and $\Omega_b \to \Omega_c \tau \nu$ Baryonic Decays

N. Rajeev, Rupak Dutta, and Suman Kumbhakar

Abstract Unlike B meson decays which are rigorously studied both theoretically and experimentally over the decade, the baryonic decay modes which undergo similar quark level transitions are less explored. In this context, we study the implication of $R_{D^{(*)}}$ anomalies in the corresponding $\Sigma_b \to \Sigma_c \tau \nu$ and $\Omega_b \to \Omega_c \tau \nu$ semileptonic decays using a model independent effective field theory formalism. We give predictions of various physical observables such as the ratio of branching ratios, total differential decay rate, forward-backward asymmetry, lepton side polarization fraction and convexity parameter within the standard model and within various new physics scenarios. These results can be tested in the ongoing or in future experiments and can provide complementary information regarding the observed anomalies in the meson sector.

57.1 Introduction

The two classes of particles called the mesons and baryons are distinguished mainly by their quark combinations. The quark flavor changing processes in the associated hadrons via electroweak interactions is of great interest for several reasons. In fact, these flavor changing process serve as the indirect ingredients to test the SM. In SM, the electroweak decays of hadrons mediating both charged and neutral gauge bosons inherit a condition called the lepton flavor universality (LFU). The indication of LFU violation in the b flavored meson decays have been witnessed at the experiments in the flavor observables such as $R_{D^{(*)}}$, $P^{\tau}_{D^*}$ and $F_L^{D^*}$ in $B \to D^{(*)} l \nu$ decay modes. At

N. Rajeev (✉) · R. Dutta
National Institute of Technology Silchar, Silchar 788010, India
e-mail: rajeev_rs@phy.nits.ac.in

S. Kumbhakar
Indian Institute of Technology, Bombay, India

A. Giri and R. Mohanta (eds.), *Workshop on Frontiers in High Energy Physics 2019*, Springer Proceedings in Physics 248,
https://doi.org/10.1007/978-981-15-6292-1_57

present the combined deviation in $R_{D^{(*)}}$ is reported to be 3.08σ from the SM expectations [1]. In this regard, we discuss the opportunities to look for new physics (NP) in the flavor observables in the baryon sectors. The heavy quark symmetry assumes the treatment of semileptonic decays of baryons can be considered to be very much analogous to that of mesons. Hence, we study the implications of $R_{D^{(*)}}$ on $\Sigma_b \to \Sigma_c \tau \nu$ and $\Omega_b \to \Omega_c \tau \nu$ decay modes and give predictions of various observables in SM and in the presence of various NP couplings.

57.2 Theory

Effective field theory parameterizes the effects of new interactions with the NP coefficients. The relevant effective Lagrangian for $b \to c\, l\, \nu$ transition decays represented at the scale of bottom quark, containing both the SM and the possible NP operators is defined as [2–4],

$$\mathcal{H}_{eff} = \frac{4G_F}{\sqrt{2}} V_{cb} \Big[(1 + V_L)\, \mathcal{O}_{V_L} + V_R \mathcal{O}_{V_R} + S_L \mathcal{O}_{S_L} + S_R \mathcal{O}_{S_R} + T\, \mathcal{O}_T \Big] + \text{h.c.}\,,$$

$$\mathcal{O}_{V_L} = (\bar{c}\gamma^\mu b_L)\left(\bar{l}_L \gamma_\mu \nu_{l\,L}\right); \quad \mathcal{O}_{V_R} = \left(\bar{c}\gamma_\mu b_R\right)\left(\bar{l}_L \gamma_\mu \nu_{l\,L}\right); \quad \mathcal{O}_{S_L} = (\bar{c} b_L)\left(\bar{l}_R \nu_{l\,L}\right);$$

$$\mathcal{O}_{S_R} = (\bar{c} b_R)\left(\bar{l}_R \nu_{l\,L}\right); \quad \mathcal{O}_T = (\bar{c}\sigma^{\mu\nu} b_L)\left(\bar{l}_R \sigma_{\mu\nu} \nu_{l\,L}\right).$$

We follow [5] and write the expression for differential decay distribution for $B_1 \to B_2\, l\, \nu$ decays in terms of the helicity amplitudes $H^{V/A}_{\lambda_2 \lambda_W}$ which are expressed in terms of $\mathcal{A}_1, \mathcal{A}_2, \mathcal{A}_3, \mathcal{A}_4$ as follows:

$$\frac{d^2\Gamma}{dq^2\, d\cos\theta} = N \left(1 - \frac{m_l^2}{q^2}\right)^2 \left[\mathcal{A}_1 + \frac{m_l^2}{q^2}\mathcal{A}_2 + 2\mathcal{A}_3 + \frac{4m_l}{\sqrt{q^2}}\mathcal{A}_4\right] \tag{57.1}$$

All the relevant expressions for the helicity amplitudes can be referred from [5]. Meanwhile, the relevant form factors obtained in the relativistic quark model are taken from [6]. We define various q^2 dependent observables such as $R_{B_2}(q^2)$, $A^l_{FB}(q^2)$, $P^l(q^2)$, $C^l_F(q^2)$ as:

$$R_{B_2}(q^2) = \frac{\Gamma(B_1 \to B_2 \tau\nu)}{\Gamma(B_1 \to B_2\, l\, \nu)}, \quad C^l_F(q^2) = \frac{1}{\left(d\Gamma/dq^2\right)} \frac{d^2}{d(\cos\theta)^2}\left[\frac{d^2\Gamma}{dq^2\, d\cos\theta}\right]$$

$$P^l(q^2) = \frac{d\Gamma(+)/dq^2 - d\Gamma(-)/dq^2}{d\Gamma(+)/dq^2 + d\Gamma(-)/dq^2}, \quad A^l_{FB}(q^2) = \frac{\left(\int_{-1}^{0} - \int_{0}^{1}\right) d\cos\theta \frac{d^2\Gamma}{dq^2\, d\cos\theta}}{\frac{d\Gamma}{dq^2}} \tag{57.2}$$

All omitted details can be found in [7].

Table 57.1 The SM central values and 1σ ranges for Σ_b and Ω_b decay modes

		$\Sigma_b \to \Sigma_c l\nu$		$\Omega_b \to \Omega_c l\nu$	
		e mode	τ mode	e mode	τ mode
$\Gamma \times 10^{10}$ s^{-1}	Central value	1.401	0.473	1.235	0.447
	1σ range	[1.325, 1.474]	[0.447, 0.506]	[1.162, 1.284]	[0.422, 0.480]
$\langle P^l \rangle$	Central values	−1.000	0.131	−1.000	0.135
$\langle A^l_{FB} \rangle$	Central value	0.050	−0.253	0.050	−0.251
$\langle C^l_F \rangle$	Central value	−1.172	−0.200	−1.148	−0.196
$\langle R \rangle$	Central value	0.338		0.362	

57.3 Results and Discussions

57.3.1 Standard Model Predictions

In Table 57.1, we report the average values of various observables for both electron mode and tau mode of $\Sigma_b \to \Sigma_c l\nu$ and $\Omega_b \to \Omega_c l\nu$ decay modes. We see that except for the total decay rate, the form factor uncertainties exactly cancel in all the observables. The q^2 dependence of all the observable are distinct for both e and τ modes. In Fig. 57.1, we show each observable as a function of q^2 for $\Sigma_b \to \Sigma_c \tau\nu$ and $\Omega_b \to \Omega_c \tau\nu$ where the red line represents the SM. For more discussions one can refer to [7].

57.3.2 New Physics Analysis

We investigate the NP effects in four different scenarios. To obtain the allowed NP parameter space, we impose the 3σ constraint coming from the measured values of R_D and R_{D^*}. The corresponding best fit values of each observable is obtained from the χ^2 test. The best fit average values of each observable associated with V_L, V_R, S_L and S_R NP couplings are reported in Table 57.2 for the $\Sigma_b \to \Sigma_c \tau\nu$ and $\Omega_b \to \Omega_c \tau\nu$ decay modes. Similarly, in Fig. 57.1 we depict the best fits corresponding to each NP coupling as a function of q^2 only for $\Sigma_b \to \Sigma_c \tau\nu$ and $\Omega_b \to \Omega_c \tau\nu$ decay modes.

In the presence of V_L NP coupling, no deviation from SM is observed in $P^\tau(q^2)$, $A^\tau_{FB}(q^2)$ and $C^\tau_F(q^2)$. Deviations are observed only in $R(q^2)$ and $d\Gamma/dq^2$. In the presence of V_R NP coupling, there is no cancellation of NP effects in $P^\tau(q^2)$, $A^\tau_{FB}(q^2)$ and $C^\tau_F(q^2)$. Very less deviations are observed in $d\Gamma/dq^2$, $R(q^2)$, $A^\tau_{FB}(q^2)$ and $C^\tau_F(q^2)$. The effect of scalar NP coupling S_L comes into the decay amplitude through the scalar and pseudoscalar helicity amplitudes. Compared to V_L and V_R NP couplings, more pronounced deviations are found in all the observables. Moreover, at $q^2 \approx 7.5$ GeV^2 and $q^2 \approx 3.5$ GeV^2 we find a zero crossing for $P^\tau(q^2)$ and $A^\tau_{FB}(q^2)$

Table 57.2 Best fit values in each NP couplings for Σ_b and Ω_b decay modes

	$\Sigma_b \to \Sigma_c \tau \nu$				$\Omega_b \to \Omega_c \tau \nu$			
	V_L	V_R	S_L	S_R	V_L	V_R	S_L	S_R
$\Gamma \times 10^{10}$ s^{-1}	0.548	0.450	0.489	0.538	0.518	0.426	0.466	0.509
$\langle P^\tau \rangle$	0.131	0.092	0.159	0.236	0.135	0.095	0.170	0.241
$\langle A_{FB}^\tau \rangle$	−0.253	−0.241	0.242	−0.250	−0.251	−0.239	0.240	−0.248
$\langle C_F^\tau \rangle$	−0.200	−0.192	−0.193	−0.176	−0.196	−0.189	−0.188	−0.172
$\langle R \rangle$	0.391	0.321	0.349	0.384	0.419	0.345	0.377	0.421

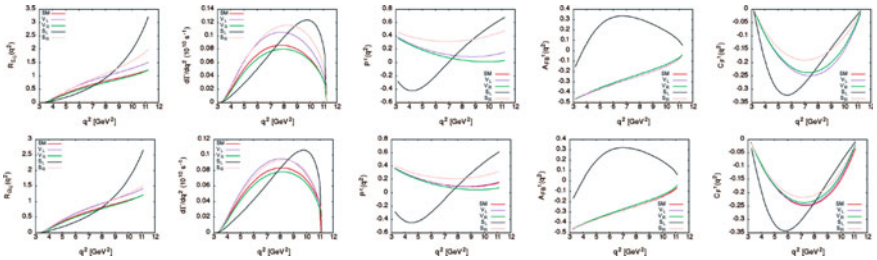

Fig. 57.1 SM (red) curve and various best fits in the presence of V_L (purple), V_R (green), S_L (black), S_R (pink) NP couplings for $\Sigma_b \to \Sigma_c \tau \nu$ (upper row) and $\Omega_b \to \Omega_c \tau \nu$ (lower row) decays

respectively. This is a clear distinction from SM where there is no zero crossing at all. Again a significant deviation from the SM prediction is observed in the presence of S_R NP coupling, in particular for $R(q^2)$, $d\Gamma/dq^2$, $P^\tau(q^2)$ and $C_F^\tau(q^2)$. It is interesting fact that the NP effect in $A_{FB}(q^2)$ is quite negligible in the presence of S_R NP coupling. Similar conclusions can be made for the $\Omega_b \to \Omega_c \tau \nu$ decay mode as well. All omitted details can be found in [7].

57.4 Conclusion

Inconsistency between the SM and various experimental measurements of the flavor observables which indicates LFU violation in $B \to D^{(*)}\, l\, \nu$ decay modes motivate us to study the similar $b \to c$ quark level transition in the baryon sector. We follow a model independent effective field theory formalism to study the $\Sigma_b \to \Sigma_c \tau \nu$ and $\Omega_b \to \Omega_c \tau \nu$ decay modes and give predictions of various physical observables in SM and in the presence of new vector and scalar type NP couplings. These studies provide us complementary information regarding NP in various B meson decays.

References

1. https://hflav-eos.web.cern.ch/hflav-eos/semi/spring19/html/RDsDsstar/RDRDs.html
2. V. Cirigliano, J. Jenkins, M. Gonzalez-Alonso, Nucl. Phys. B **830**, 95 (2010)
3. T. Bhattacharya, V. Cirigliano, S.D. Cohen, A. Filipuzzi, M. Gonzalez-Alonso, M.L. Graesser, R. Gupta, H.W. Lin, Phys. Rev. D **85**, 054512 (2012)
4. R. Dutta, A. Bhol, A.K. Giri, Phys. Rev. D **88**(11), 114023 (2013)
5. R. Dutta, Phys. Rev. D **97**(7), 073004 (2018)
6. D. Ebert, R.N. Faustov, V.O. Galkin, Phys. Rev. D **73**, 094002 (2006)
7. N. Rajeev, R. Dutta, S. Kumbhakar, Phys. Rev. D **100**(3), 035015 (2019)

Chapter 58
Test of LFU in $B \to K\ell\ell$ Decays at Belle

S. Choudhury

Abstract The observable R_K which is the ratio of branching fractions for $B \to K\mu\mu$ to $B \to Kee$, tests lepton flavor universality (LFU) in the standard model (SM), and hence constitutes an important probe for new physics (NP). Another strong observable A_I, CP-averaged isospin asymmetry, can also be used to verify the SM. We report herein the measurement of R_K and A_I for different bins of q^2, invariant mass square of two leptons.

58.1 Introduction

The $B \to K\ell\ell$, $\ell = e, \mu$ mediated by $b \to s$ quark level transition are flavor-changing-neutral-currents. These decays are forbidden at tree level in the SM and propagate throught loop-level diagrams. The SM can be verified by calculating ratio,

$$R_H = \frac{\int \frac{d\Gamma}{dq^2}[B \to H\mu^+\mu^-]dq^2}{\int \frac{d\Gamma}{dq^2}[B \to He^+e^-]dq^2}, \tag{58.1}$$

where, H is a K or K^* meson and these are measured in terms of $q^2 = M^2_{\ell\ell}$, invariant mass square of two leptons. LHCb [2] has recently measured R_K with 5 fb^{-1} data sample and the result shows 2.5 standard deviation (σ) from SM expectation for a bin of $q^2 \in (1.1, 6.0)$ GeV$^2/c^4$. The Belle [3] result of R_K with 657×10^6 $B\bar{B}$ events published in 2009 was consistent with SM prediction for the whole q^2 bin. Another theoretically robust observable which can test SM is CP-averaged isospin asymmetry,

$$A_I = \frac{(\tau_{B^+}/\tau_{B^0})\mathscr{B}(B^0 \to K^0\ell^+\ell^-) - \mathscr{B}(B^+ \to K^+\ell^+\ell^-)}{(\tau_{B^+}/\tau_{B^0})\mathscr{B}(B^0 \to K^0\ell^+\ell^-) + \mathscr{B}(B^+ \to K^+\ell^+\ell^-)}, \tag{58.2}$$

S. Choudhury (✉)
Indian Institute of Technology Hyderabad, Telangana 502285, India
e-mail: ph16resch11007@iith.ac.in

A. Giri and R. Mohanta (eds.), *Workshop on Frontiers in High Energy Physics 2019*, Springer Proceedings in Physics 248,
https://doi.org/10.1007/978-981-15-6292-1_58

where, $\tau_{B^+}/\tau_{B^0} = 1.076$ is the lifetime ratio of B^+ to B^0. The A_I results for $B \to K\mu\mu$ show negative deviation from null asymmetry for LHCb [4, 5], BaBar [6] and Belle [3], below the J/ψ resonance.

Here, we present the recent R_K and A_I results [1] obtained from multi-dimensional fit with Belle full data sample of 772×10^6 $B\bar{B}$ events for relevant q^2 bins, including the higher bin, which is not available in LHCb analysis.

58.2 Reconstruction of $B \to K\ell\ell$

The decay mode reconstructed for the study are $B^+ \to K^+\ell\ell$ and $B^0 \to K^0_S\ell\ell$, $\ell = e, \mu$. The charged particles like $K^\pm$, $e^\pm$ and $\mu^\pm$ are selected near interaction point (IP), which satisfied the PID criteria. K^0_S are reconstructed from two oppositely charged tracks treated as pion and within $\pm 3\sigma$ about K^0_S nominal mass. The kinematic variables which distinguish the signal from the background are beam energy constraint mass, $M_{bc} = \sqrt{(E_{beam}/c^2)^2 - (p_B/c)^2}$, and the energy difference, $\Delta E = E_B - E_{beam}$. The p_B and E_B are the momentum and energy of B candidate, and E_{beam} is the beam energy. The B candidate is selected with $5.2 < M_{bc} < 5.29\ \text{GeV}/c^2$ and $-0.1 < \Delta E < 0.25$ GeV.

58.3 Background Suppression

The irreducible source of background coming from charmonium resonances like $B \to KJ/\psi(\to \ell\ell)$ and $B \to K\psi(2S)(\to \ell\ell)$ are removed by applying a set of vetoes, $8.75 < q^2 < 10.2\ \text{GeV}^2/c^4$ and $13.0 < q^2 < 14.0\ \text{GeV}^2/c^4$ with the dimuon; $8.5 < q^2 < 10.2\,\text{GeV}^2/c^4$ and $12.8 < q^2 < 14.0\,\text{GeV}^2/c^4$ with the dielectron final states for J/ψ and $\psi(2S)$, respectively. The background from $B^+ \to \bar{D}^0(K^+\pi^-)\pi^+$ for $B^+ \to K^+\mu^+\mu^-$, coming from misidentification of pion as muon, is removed by $1.85 < M_{K\pi} < 1.87\ \text{GeV}/c^2$. The background coming from continuum ($q\bar{q} = u\bar{u}, d\bar{d}, c\bar{c}, s\bar{s}$) and generic B are suppressed by multivariate analysis technique, neutral network (NN). The NN output obtained is translated to $\mathscr{O}'$ using a log function,

$$\mathscr{O}' = \log\left(\frac{\mathscr{O} - \mathscr{O}_{\text{min}}}{\mathscr{O}_{\text{max}} - \mathscr{O}}\right)$$

where, $\mathscr{O}_{\text{min}} = -0.6$ is the minimum NN cut applied and $\mathscr{O}_{\text{max}}$ is the maximum value of it and obtained from signal MC. The minimun NN cut reduced more than 75% of background with 5–6% of signal efficiency loss.

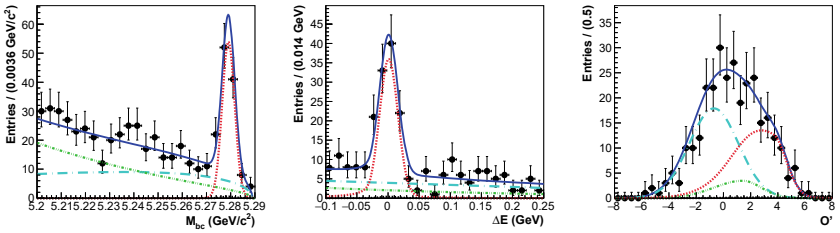

Fig. 58.1 The signal enhanced projection plots for $B^+ \to K^+\mu\mu$ mode in M_{bc} (left), ΔE (middle) and $\mathscr{O}'$ (right). The red marker is for signal, cyan and green markers are continuum and generic B backgrounds, respectively

58.4 Results

The signal is extracted by performing three-dimensional fit in M_{bc}, ΔE and $\mathscr{O}'$. The $B \to KJ/\psi(\to \ell\ell)$ sample is used to calibrate the signal PDF of $B \to K\ell\ell$. The off-resonance sample is used to calibarte the continuum background and the scaled, according to luminosity and cross-section, off-resonance yield is fixed in the final fit. The signal region is defined as $M_{bc} > 5.27\ \text{GeV}/c^2$, $|\Delta E| < 0.05$ GeV and $\mathscr{O}' > 1$. The signal enhanced projection plots for $B^+ \to K^+\mu\mu$ is shown in Fig. 58.1 for demonstration.

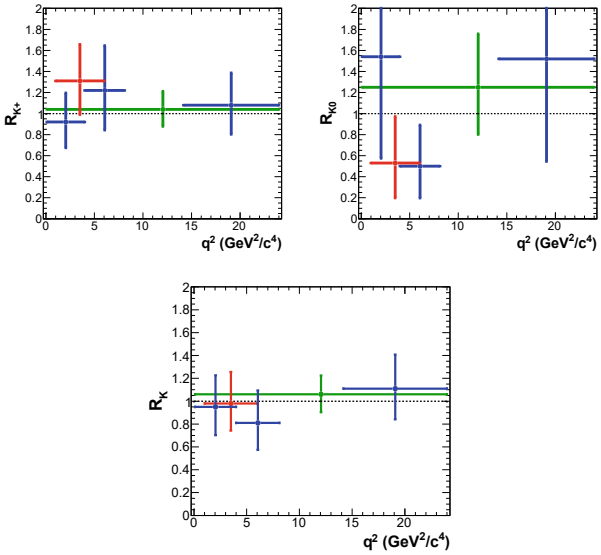

Fig. 58.2 R_K in bins of q^2, for $B^+ \to K^+\ell\ell$ (top-left), $B^0 \to K^0_S\ell\ell$ (top-right), and combining both modes (bottom). The red marker represents the bin of $1 < q^2 < 6\ \text{GeV}^2/c^4$, and the blue markers are for $0.1 < q^2 < 4$, $4 < q^2 < 8.12$ and $q^2 > 14.18\ \text{GeV}^2/c^4$ bins. The green marker denotes the whole q^2 region excluding the charmonium resonances

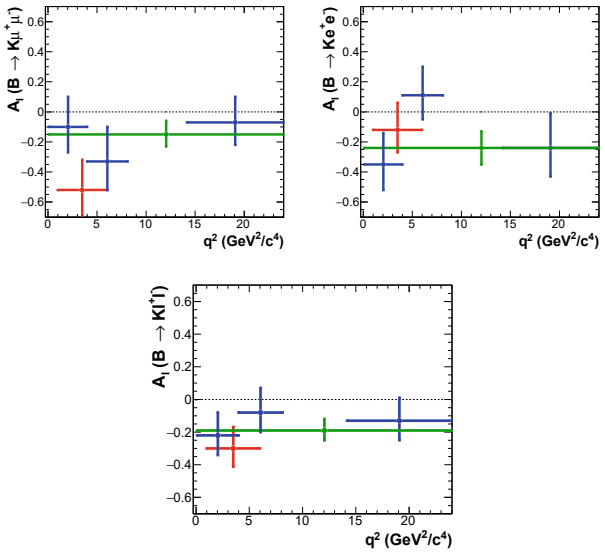

Fig. 58.3 A_I measurements in bins of q^2, for decays $B \to K\mu\mu$ (top-left), $B \to Kee$ (top-right), and combining both modes (bottom). The legends are the same as that of Fig. 58.2

The R_K is calculated using (58.1) and the results are shown in Fig. 58.2 for charged, neutral and combined case. The combined case or R_K is the weighted average of R_{K^+} and R_{K^0}. All the results are found to be consistent with SM prediction within the uncertainty limit. The A_I values are calculated using (58.2). The $A_I(B \to K\ell\ell)$ is evaluated as weighted average of $A_I(B \to K\mu\mu)$ and $A_I(B \to Kee)$. These plots are shown in Fig. 58.3. The A_I shows negative deviation from null asymmetry for almost all the bins. The maximum deviation observed is for $B \to K\mu\mu$ for $1 < q^2 < 6\ \text{GeV}^2/c^4$ bin and is 2.7σ.

Acknowledgements We thank the KEKB group for excellent operation of the accelerator; the KEK cryogenics group for efficient solenoid operations; and the KEK computer group the NII, and PNNL/EMSL for valuable computing and SINET5 network support. We acknowledge support from MEXT,JSPS and Nagoya's TLPRC(Japan); ARC (Australia); FWF (Austria); NSFC and CCEPP(China), MSMT (Czechia); CZF, DFG, EXC153, and VS (Germany); DST (India); INFN (Italy); MOE, MSIP, NRF, RSRI, FLRFAS project and GSDC of KISTI (Korea); MNiSW and NCN (Poland); MES and RFAAE (Russia); ARRS (Slovenia); IKERBASQUE and MINECO (Spain); SNSF (Switzerland); MOE and MOST (Taiwan); and DOE and NSF (USA).

References

1. A. Abdesselam et al. (Belle Collaboration). arXiv: 1908.01848
2. R. Aaij et al. (LHCb Collaboration). arXiv: 1903.09252
3. J.-T. Wei et al. (Belle Collaboration). arXIv: 0904.0770

4. R. Aaji et al. (LHCb Collaboration). arXiv: 1205.4322
5. R. Aaji et al. (LHCb Collaboration). arXiv: 1403.8044
6. B. Aubert et al. (BaBar Collaboration). arXiv: 0807.4119

Chapter 59
Search for the Decay $B_s^0 \longrightarrow \pi^0\pi^0$ at $\Upsilon(5S)$ Resonance Using Belle Detector

Jyotirmoi Borah and Bipul Bhuyan

Abstract The decay $B_s^0 \to \pi^0\pi^0$ is a neutral, charmless, non-leptonic, charged current mediated and strangeness non-conserving decay whose theoretical branching fraction(BF) within the Standard Model(SM) is predicted to be 0.40×10^{-6} [1], calculated in the framework of flavor SU(3) symmetry . The analysis reported in this paper is based on full data sample available at Belle with an integrated luminosity of $121.4\, fb^{-1}$. This will be the first attempt to search for this rare decay using the Belle dataset. The decay process was first studied in the year 1995, by the L3 experiment [2] using three million hadronic Z decays with an efficiency of approximately 8%. In the absence of any signal, an upper limit on the BF was set at 2.4×10^{-4} at 90% confidence level. We expect to achieve the SM sensitivity for this decay using higher statistics available at Belle which is close to 14 million $B_s^0\bar{B}_s^0$ pairs and adoption of newer background suppression techniques such as Neural Networks and better statistical tools for PDF modelling.

59.1 Introduction

In the recent years, there have been a tremendous impetus towards the study of rare B meson decays. These studies are important to test the Standard Model (SM) at the precision level allowed by the present generation of experiments such as Babar, Belle, Belle II and LHCb. There are several approaches for understanding these rare decays such as the QCD factorization method (QCDF) [3], perturbative QCD (pQCD) [4] and the Soft Collinear Effective Field Theory (SCET) [5]. An important limitation in these approaches is that in the power expansion only the leading order terms are considered. But theoretical studies on these rare decays [1, 6, 7] show the presence of suppressed interactions which are difficult to accommodate in these generic QCD approaches.

J. Borah (✉) · B. Bhuyan
Indian Institute of Technology Guwahati, Assam 781039, India
e-mail: borah176121103@iitg.ac.in

B. Bhuyan
e-mail: bhuyan@iitg.ac.in

A. Giri and R. Mohanta (eds.), *Workshop on Frontiers in High Energy Physics 2019*, Springer Proceedings in Physics 248,
https://doi.org/10.1007/978-981-15-6292-1_59

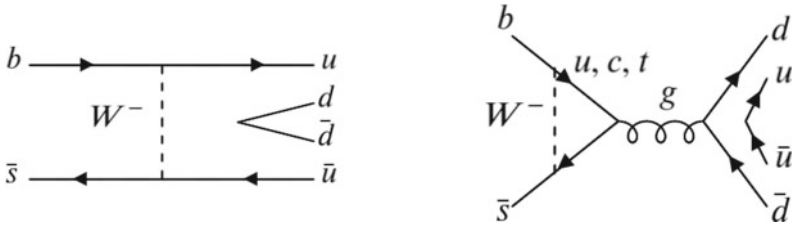

Fig. 59.1 W-exchange(E) and Annihilation Penguin(PA) topological diagrams (from left to right)

However, the flavor diagram approach (FDA) [8] which is based on the flavor SU(3) symmetry has gained prominence owing to its inclusive strong interaction effects upto all orders of magnitute. In contrast to other approaches, this is strictly non-perturbative in nature and deals with topological diagrams. Figure 59.1 shows the topological diagrams for this analysis. The decay $B_s^0 \longrightarrow \pi^0\pi^0$ is charmless and non-leptonic in nature and hence can be an important test to understand the interactions among strong and weak processes.

In this analysis, we shall search for the decay with the Belle data corresponding to an integrated luminosity of 121.4 $(fb)^{-1}$ produced by e^+e^- collision tuned to operate at $\Upsilon(5S)$ resonance. However, this analysis is in preliminary stage and as such all the results so far are based on Monte-Carlo (MC) data. These MC data are generated through `EvtGen` [9] based on the decay probabilities of particles involved in a decay chain and simulated using `GEANT3` [10]. We have generated 500, 000 MC signal events for this analysis.

The Belle detector [11] is a composite detector placed inside a solenoidal magnetic field of strength 1.5 T. The innermost detector is the silicon vertex detector (SVD) followed by the central drift chamber (CDC), aerogel Cherenkov counter (ACC) and the time-of-flight counters (TOF). The electromagnetic calorimeter (ECL) composed of CsI crystals measures the energy deposition of charged and neutral particles. The outermost KLM detector detects the K_L^0 and helps in the identification of muons.

59.2 Analysis

A candidate B_s^0 in an event is reconstructed from two neutral π^0's, each of which in turn are reconstructed from two photons. The photons which take part in this reconstruction should not originate from any charged tracks in the CDC. Beam background photons are suppressed using particle identity available for MC data [12]. This criterion will be replaced by the timing information of the ECL crystals in real data. Moreover, we require the selected photons to have a minimum energy deposition of 30 MeV in the ECL. The π^0's reconstructed from these photons need to have an invariant mass lying in the range, $114 - 155\ MeV/c^2$ on which a mass constraint fit has been performed. This invariant mass range corresponds to 3σ about the

nominal π^0 mass [13], where the standard deviation, σ is obtained after a fit on the reconstructed π^0's mass. The π^0's which pass these selection criteria are then used to reconstruct B_s^0 candidates. The reconstruction of its conjugate decay is being implied henceforth. At this stage, two kinematic variables are defined which have strong discrimination between the signal and the background. They are the beam constrained mass, M_{bc} and the energy difference, ΔE. They are defined as $M_{bc} = \sqrt{E_{beam}^{*2} - P_{B_s^0}^{*2}}$ and $\Delta E = E_{B_s^0}^* - E_{beam}^*$, where $P_{B_s^0}^{*2}$, $E_{B_s^0}^*$ are the momentum and the energy of the reconstructed B_s^0 in the center of mass (CM) frame, respectively and E_{beam} is beam energy in the CM frame. Loose selection criterion on $M_{bc} > 5.30\ GeV/c^2$ and $-0.8 < \Delta E < 0.2\ GeV$ are being applied on the reconstructed B_s^0. As these reconstructions are based on combinatorics, misreconstruction is a common feature. We find 33% of multiple B_s^0 candidates out of total reconstructed B_s^0. As we require a single B_s^0 candidate per event, a best candidate selection criterion has been applied. It is based on the minimum deviation of the invariant mass of the reconstructed B_s^0 from the actual mass of the B_s^0 [13]. We find this selection criterion 96.1% efficient in selecting a correct B_s^0 candidate.

For background MC study, the contribution from $e^+e^- \longrightarrow q\bar{q}$, where $q = u$, d, s and c continuum backgrounds are studied separately. In addition, $e^+e^- \longrightarrow \Upsilon(5S) \longrightarrow B_s^0\bar{B}_s^0$ and $e^+e^- \longrightarrow \Upsilon(5S) \longrightarrow B^*\bar{B}^*\pi$, $\Upsilon(4S)\gamma$ type backgrounds are also analysed. The same set of selection criteria used for signal MC are applied. The dominant background is found to be the `uds` continuum background. For further suppression of the background, topologically discriminating variables [14] such as the event shapes of the continuum background and the signal, also known as the Fox-Wolfram (FW) moments [15] , the cosine of the thrust angle between the reconstructed B_s^0 and the rest-of-event (ROE) in the CM frame and the cosine of the polar angle between the momentum of the reconstructed B_s^0 and the electron beam axis are considered. We have used the modified FW moments combined with the transverse momentum of the final state particles to form a Fisher discriminant [16] known as the Kakuno-Super-Fox-Wolfram (KSFW) moments. The modified moments used in this paper are described in [17]. The 16 KSFW moments along with the thrust angle and the polar angle are then used as input variables to the neural network (NN) for classification of the signal and the background. Belle uses the NeuroBayes (NB) [18] package to implement NN algorithm in its analyses. It consists of two stages, namely, NB teacher (training) and NB expert (validation). The NB teacher is used with a $2/3^{rd}$ of a random MC data sample for signal and the background to learn the topologies of the input variables. The NB expert is then used to validate the rest $1/3^{rd}$ of the MC events to check for any significant overtraining. We found no such significant overtaining during our analysis. The output of the NN, $\mathcal{C}_{NB}$ for signal and background MC peaks at $+1$ and -1, respectively. We apply a selection criteria on $\mathcal{C}_{NB} > 0.90$ which rejects 99% of the total background and retaining 44% of signal MC events. The variable $\mathcal{C}_{NB}$ is often difficult to parametrize. Instead, a modified variable defined as $\mathcal{C}_{NB'} = log[\frac{\mathcal{C}_{NB} - \mathcal{C}_{NB_{cut}}}{\mathcal{C}_{NB_{max}} - \mathcal{C}_{NB}}]$ is used. Here, $\mathcal{C}_{NB}$ is the neural network

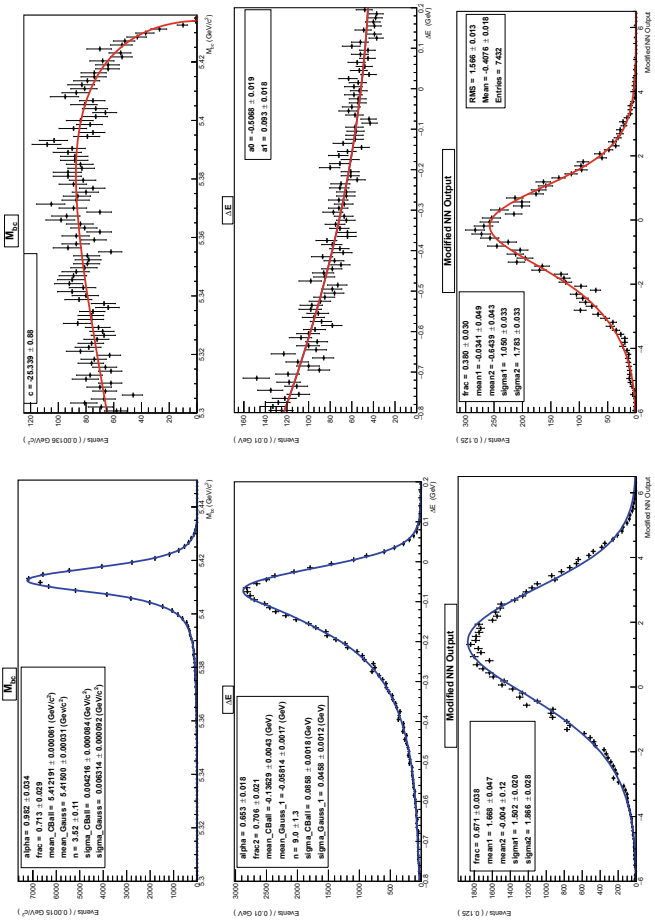

Fig. 59.2 Fitted distributions of M_{bc}, ΔE and $\mathcal{C}_{N\,B'}$ (left hand side top to bottom) for signal MC while the right hand side are the corresponding background MC distributions. The modified neural network outplot signifies, $\mathcal{C}_{N\,B'}$

output, $\mathcal{C}_{NB_{cut}}$ (0.90) is the selection criteria applied on the $\mathcal{C}_{NB}$ output and $\mathcal{C}_{NB_{max}}$ (0.998) is the maximum value of the $\mathcal{C}_{NB}$ output.

For parametrizing the signal and background MC, we have used a $3D$ unbinned maximum likelihood fit [19] on the variables, namely, M_{bc}, ΔE and $\mathcal{C}_{NB'}$. There are no significant correlations among these variables for signal and background MC. The probability distribution functions (PDF)'s selected for parametrizing the signal MC for the variables M_{bc} and ΔE is a combined PDF of a Crystal Ball function [20] and a Gaussian distribution while for $\mathcal{C}_{NB'}$ it is a double Gaussian distribution. For parametrizing the background MC for the variables M_{bc}, ΔE and $\mathcal{C}_{NB'}$ the PDF's Argus function [21], second order Chebychev polynomial and a double Gaussian distribution have been selected, respectively. The fitted distributions for the signal and background MC are shown in Fig. 59.2.

59.3 Preliminary Results and Outlook

The reconstruction efficiency from the signal MC study is found to be 18.86%. We expect, approximately 160 background events in the signal region defined by $5.39 < M_{bc} < 5.44\ GeV/c^2$ and $-0.4 < \Delta E < 0.2\ GeV$. The signal expectancy is about 1 or 2 with the aforementioned efficiency. The signal MC misconstruction in the candidate and the signal region are 3.9% and 2.5%, respectively.

We plan to parametrize the misreconstructed signal MC events and combined them with the background MC PDF's. We also plan to check the fitter stability of the PDF's and perform control sample study to understand the differences between the MC and real data.

Acknowledgements We are thankful to all the collaborators working in Belle and Belle II for their help and support towards this analysis. We are also grateful to MHRD, Govt. of India for the financial support provided.

References

1. H.Y. Cheng, C.W. Chiang, A.L. Kuo, Phys. Rev. D **91**, 014011 (2015)
2. M. Acciarri et al., Phys. Lett. B **363**, 127 (1995)
3. M. Beneke, G. Buchalla, M. Neubert, C.T. Sachrajda, Nucl. Phys. B **591**, 313 (2000)
4. C.D. Lu, K. Ukai, M.Z. Yang, Phys. Rev. D **63**, 074009 (2001)
5. C.W. Bauer, S. Fleming, D. Pirjol, I.W. Stewart, Phys. Rev. D **63**, 114020 (2001)
6. M. Gronau, D. London, J.L. Rosner, Phys. Rev. D **87**, 036008 (2013)
7. M. Kaur, R. Dhir, A. Sharma, R.C. Verma, Phys. Part. Nucl. Lett. **12**, 230 (2015)
8. D. Zeppenfeld, Z. Phys. C **8**, 77 (1981); L.L. Chau, H.Y. Cheng, Phys. Rev. Lett. **56**, 655 (1986); L.L. Chau, H.Y. Cheng, Phys. Rev. D **36**, 137 (1987); M.J. Savage, M.B. Wise, Phys. Rev. D **39**, 3346 (1989) [Erratum: Phys. Rev. D **40**, 3127 (1989)]; L.L. Chau, H.Y. Cheng, W.K. Sze, H. Yao, B. Tseng, Phys. Rev. D **43**, 2176 (1991) [Erratum: Phys. Rev.D **58**, 019902 (1998)]
9. D.J. Lange, Nucl. Instrum. Methods Phys. Res. Sect. A **462**, 152 (2001)

10. R. Brun et al., GEANT 3.21, CERN Report DD/EE/84-1 (1984)
11. A. Abashian et al., Belle Collaboration. Nucl. Instrum. Methods Phys. Res. Sect. A **479**, 117 (2002); J. Brodzicka et al., Prog. Theor. Exp. Phys. **2012**, 04D001 (2012)
12. S. Villa (Belle Collaboration), Belle Internal Note, BN **811** (2005)
13. M. Tanibashi et al., Particle data group. Phys. Rev. D **98**, 030001 (2018)
14. A.J. Bevan, B. Golob, T. Mannel, S. Prell, B.D. Yabsley, Eur. Phys. J. C **74**, 3026 (2014), SLAC-PUB-15968, KEK Preprint 2014-3
15. G.C. Fox, S. Wolfram, Phys. Rev. Lett. **41**, 1581 (1978)
16. R.A. Fisher, Ann. Hum. Genet. **7**, 179 (1936)
17. S.H. Lee et al., Belle Collaboration. Phys. Rev. Lett. **91**, 261801 (2003)
18. U. Kerzel, M. Feindt, Nucl. Instrum. Meth. A **559**, (2006)
19. W. Verkerke, D. Kirkby, arXiv: physics/0306116v1 (2003)
20. T. Skwarnicki, Ph.D. Thesis, Institute for Nuclear Physics, Krakow 1986, DESY Internal Report, DESY F31-86-02 (1986)
21. H. Albrecht et al., ARGUS Collaboration. Phys. Lett. B **241**, 278 (1990)

Chapter 60
New Physics Effects on $B_s \to K^+K^-$ Decay Mode

Manas K. Mohapatra

Abstract We inspect the decay mode $B_s \to K^+K^-$ in Z' model. The measured values of branching ratio ($\mathcal{BR}$), and observables such as direct (C_{KK}) as well as mixing induced (S_{KK}) CP asymmetry have discrepancies from SM. We constrain the new parameter space by using leptonic $B_s \to \ell\ell(\ell = e, \mu, \tau)$ decays with their experimental results. Then we study the impact of new physics on the observables of $B_s \to K^+K^-$ decay mode.

60.1 Introduction

The Standard model (SM) could not explain matter-antimatter asymmetry, dark matter and dark energy thus motivates towards new physics (NP) beyond the SM. In this regard, B meson decays grasp the deep understanding of CP violation. We consider $B_s \to K^+K^-$ that have mismatches in the SM result of $\mathcal{BR}$, C_{KK} and S_{KK} [1] with their corresponding world averages [2] which scrutinize in NP scenario. On the other side, in leptonic B_s sector, the $\mathcal{BR}$ has upper limit of 2.8×10^{-7} [3](6.8×10^{-3} [4]) reported by LHCb(CDF) for $e(\tau)$ case where as the μ mode has precise result of $(2.7^{+0.6}_{-0.5}) \times 10^{-9}$ from [2]. The SM values of all leptonic modes are of the order of $10^{-14}(10^{-9})$ and $\mathcal{O}(10^{-7})$ for $e(\mu)$ and τ modes respectively. Motivated by these discrepancies, we study the impact of NP on the observables of $B_s \to KK$ in Z' model.

The paper is assembled as follows. In Sect. 60.2, we study the observables of $B_s \to KK$ in SM. In Sect. 60.3, we constrain the new parameter space arising due to branching ratios of all leptonic B_s decays and scrutinize the impact of the new coupling on the $B_s \to KK$ decay mode in Sect. 60.4. We deliver our conclusion in Sect. 60.5.

M. K. Mohapatra (✉)
Indian Institute of Technology, Kandi, Hyderabad 502285, India
e-mail: manasmohapatra12@gmail.com

A. Giri and R. Mohanta (eds.), *Workshop on Frontiers in High Energy Physics 2019*, Springer Proceedings in Physics 248,
https://doi.org/10.1007/978-981-15-6292-1_60

60.2 $B_s \to K^+K^-$ Process in the Standard Model

The effective Hamiltonian of $B_s \to KK$ decay mode describing the quark level transition $b \to sq\bar{q}(q = u, d)$ is given as [5]

$$\mathcal{H}_{\text{eff}} = \frac{G_F}{\sqrt{2}}\left\{V_{ub}V_{us}^*\left[C_1(\mu)O_1^u(\mu) + C_2(\mu)O_2^u(\mu)\right] - V_{tb}V_{ts}^*\left[\sum_{i=3}^{10} C_i(\mu)O_i(\mu)\right]\right\} + h.c \quad (60.1)$$

where $G_F = 1.166 \times 10^{-5}$ GeV^{-2}, $V_{\rho\sigma}(\rho, \sigma = u, t, b, s)$ are the CKM elements. $O_i's(i = 1, ..., 10)$ are the effective operators and $C_i(\mu)$ are the Wilson coefficients evaluated at renormalization scale $\mu = m_b$[5].

The amplitude of the decay mode in QCDF can be symbolically written as

$$\mathcal{A}_{B_s^0 \to K^+K^-} = \zeta_u\mathcal{A}_u + \zeta_c\mathcal{A}_c = \zeta_c\mathcal{A}_c\left[1 + \wp a e^{i(\delta_1 - \gamma)}\right], \quad (60.2)$$

where $\zeta_q = V_{qb}V_{qs}^*(q = u, c)$, $a = |\frac{\zeta_u}{\zeta_c}|$, $\wp = |\frac{\mathcal{A}_u}{\mathcal{A}_c}|$, γ is the phase of V_{ub}, and δ_1 is the relative strong phase between $\mathcal{A}_u$ and $\mathcal{A}_c$. From the time dependent amplitude in terms of CP-violating observables, we have $C_{KK} = \frac{|\lambda|^2-1}{1+|\lambda|^2}$ and $S_{KK} = 2\frac{\text{Im}(\lambda)}{1+|\lambda|^2}$ where $\lambda = \frac{q}{p}\frac{\bar{\mathcal{A}}}{\mathcal{A}}$ including q, p as mixing parameters.

The expressions of CP-averaged $\mathcal{BR}$, C_{KK} and S_{KK} are given in [6]. Using the weak(mixing) angle $\gamma(\beta_s)$, all particle masses and life time of B_s meson are taken from [2], form factor $F_0^{B_s \to KK}(0)$, decay constants f_{B_s} and f_K from [7, 8], the predicted observables in SM are given as

$$\mathcal{BR} = (34.37^{+7.90}_{-5.61}) \times 10^{-6}, \quad C_{KK} = -0.11^{+0.0168}_{-0.0151}, \quad S_{KK} = 0.32^{+0.042}_{-0.035}.$$

The errors are taken from form factor, decay constants and CKM elements.

60.3 Constraints on New Couplings

In the SM, the effective Hamiltonian for $b \to s\ell^+\ell^-$ is given by

$$\mathcal{H}_{\text{eff}} = -\frac{G_F}{\sqrt{2}}\left[\lambda_t^{(q)}\mathcal{H}_{\text{eff}}^{(t)} + \lambda_u^{(q)}\mathcal{H}_{\text{eff}}^{(u)}\right] + h.c., \quad (60.3)$$

where $\mathcal{H}_{\text{eff}}^{(u)}$ and $\mathcal{H}_{\text{eff}}^{(t)}$ are composed of Wilson coefficients and effective operators. $\lambda_k^{(q)} = V_{kb}V_{ks}^*$. The effective Hamiltonian in Z' is given as [9]

$$\mathcal{H}_{\text{eff}}^{Z'} = -\frac{2G_F}{\sqrt{2}}\left(\frac{g'M_Z}{g_1M_{Z'}}\right)^2 U_{bs}^L(\bar{s}b)_{V-A}\left[U_{\ell\ell}^L(\bar{\ell}\ell)_{V-A} - U_{\ell\ell}^R(\bar{\ell}\ell)_{V+A}\right] + \text{h.c}, \quad (60.4)$$

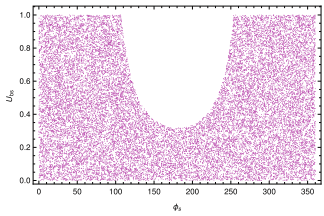

Fig. 60.1 Constraints on new coupling from the branching ratios of leptonic $B_s \to \ell\ell(\ell = e, \mu, \tau)$ processes

Comparing the effective Hamiltonian with SM, the couplings are given as

$$C^{Z'}_{9(10)} = \mp 2\left(\frac{g' M_Z}{g_1 M_{Z'}}\right)^2 \frac{|U^L_{bs}|e^{i\phi_s}}{V_{tb}V^*_{ts}}(U^L_{\ell\ell} \pm U^R_{\ell\ell}), \tag{60.5}$$

where $g_1(g')$ is the coupling constant of $Z^{(\prime)}$. ϕ_s is the weak phase associated with U_{bs}. Assuming the groups of both couplings have origin from some GUT, we consider $g'/g_1 \sim 1$ and the new Z' boson of order TeV-scale, $\frac{M_Z}{M_{Z'}} \sim 10^{-1}$. We consider $U^{L(R)}_{\ell\ell}$ to be SM like. Using the theoretical $\mathcal{BR}$ with 1σ deviation of experimental results, we constrain U_{bs} with ϕ_s shown in the Fig. 60.1.

60.4 Impact on Non-leptonic $B_s \to KK$ Decay Mode

The effective Hamiltonian in presence of Z' having quark level transition $b \to sq\bar{q}$ is given by

$$\mathcal{H}^{Z'}_{\text{eff}} = \frac{2G_F}{\sqrt{2}}\left(\frac{g' M_Z}{g_1 M_{Z'}}\right)^2 U^L_{bs}(\bar{s}b)_{V-A} \sum_q \left[U^L_{qq}(\bar{q}q)_{V-A} + U^R_{qq}(\bar{q}q)_{V+A}\right] + h.c.. \tag{60.6}$$

Now comparing the effective Hamiltonian of Z' contribution with the general effective Hamiltonian given in (60.1), we get the new coupling constants as

$$C'_{9(7)} = 4\left(\frac{g' M_Z}{g_1 M_{Z'}}\right)^2 U^L_{bs} = 4\left(\frac{g' M_Z}{g_1 M_{Z'}}\right)^2 \frac{|U^L_{bs}|e^{i\phi_s}}{V_{tb}V^*_{ts}}, \tag{60.7}$$

where we have assumed $U^{L(R)}_{uu} \simeq -2U^{L(R)}_{dd}$ [10] and $U^{L(R)}_{qq} \sim 1$ has been taken from experimental data of B_s meson [11].

Similar to SM, the observables $\mathcal{BR}, C_{KK}, S_{KK}$ in the presence of new physics can be found in [6]. Now using the constraint having some benchmark points we study the effect on the observables of $B_s \to KK$ and are shown in Fig. 60.2.

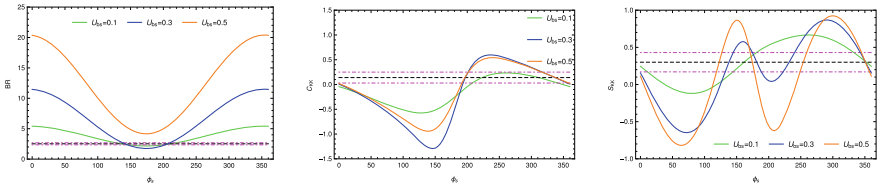

Fig. 60.2 Variation of CP-averaged $\mathcal{BR}$ ($O(10^{-5})$) (left panel), C_{KK} (middle) and S_{KK} (right panel) (in %) with the phase ϕ_s for different $|U_{bs}|$ entries. The black (magenta) dotted line represents the experimental values (1σ limit)

60.5 Conclusion

We studied $B_s \to KK$ in Z' model. Using the observed experimental values of leptonic B_s decays, we constrained the new parameter space. In the end, the new constraint have significant impact on the branching ratio and CP violating observables and can accommodate the observed data.

Acknowledgements MM would like to thank DST, Govt of India for the financial support through Inspire Fellowship.

References

1. H.-Y. Cheng, C.-K. Chua, QCD factorization for charmless hadronic B_s decays revisited. Phys. Rev. D **80**, 114026 (2009)
2. M. Tanabashi et al., Review of particle physics. Phys. Rev. D **98**(3), 030001 (2018)
3. R. Aaij et al., Search for the decays $B_s^0 \to \tau^+\tau^-$ and $B^0 \to \tau^+\tau^-$. Phys. Rev. Lett. **118**(25), 251802 (2017)
4. T. Aaltonen et al., Search for the decays $B_s^0 \to e^+\mu^-$ and $B_s^0 \to e^+e^-$ in CDF run II. Phys. Rev. Lett. **102**, 201801 (2009)
5. G. Buchalla, A.J. Buras, M.E. Lautenbacher, Weak decays beyond leading logarithms. Rev. Mod. Phys. **68**, 1125–1144 (1996)
6. M.K. Mohapatra, Inspection of new physics in $B_s^0 \to K^+K^-$ decay mode (2019)
7. A. Khodjamirian, A.V. Rusov, $B_s \to K\ell\nu_\ell$ and $B_{(s)} \to \pi(K)\ell^+\ell^-$ decays at large recoil and CKM matrix elements. JHEP **08**, 112 (2017)
8. C.-D. Lü, Y.-L. Shen, Y.-M. Wang, and Y.-B. Wei, QCD calculations of $B \to \pi$, K form factors with higher-twist corrections. JHEP **01**, 024 (2019)
9. V. Barger, L.L. Everett, J. Jiang, P. Langacker, T. Liu, C.E.M. Wagner, b –> s transitions in family-dependent U(1)-prime models. JHEP **12**, 048 (2009)
10. S. Baek, J.H. Jeon, C.S. Kim, B_s 0 - $\bar{B}_s$ 0 mixing and $B \to \pi K$ decays in stringy leptophobic Z'. Phys. Lett. B **664**, 84–91 (2008)
11. Y. Li, W.-L. Wang, D.-S. Du, Z.-H. Li, H.-X. Xu, Impact of family-non-universal Z' boson on pure annihilation $B_s \to \pi^+\pi^-$ and $B_d \to K^+K^-$ decays. Eur. Phys. J. C **75**(7), 328 (2015)

Chapter 61
Analysis of $b \to s\gamma$ Transition in VQM Model

Aishwarya Bhatta and Swayamshree Senapati

Abstract We study the extra benefaction due to an extra generation of vector-like quarks to the isospin asymmetry observable associated with the radiative b→ sγ transition which is perceptive to the nonunitary parameter U_{sb}. We endeavour at constraining both the magnitude and phase of new Wilson coefficient C_7, which control the weak radiative decays of B meson, using a systematic approach.

61.1 Introduction

The effective Hamiltonian for the rare decays of B mesons involving $b \to s\gamma$ transition at low energy is given by [1, 2],

$$\mathcal{H}_{eff} = \frac{G_F}{\sqrt{2}} V_{CKM} \sum_i C_i(\mu)\mathcal{O}_i(\mu), \tag{61.1}$$

where V_{CKM} is the combination of CKM matrix elements, $\mathcal{O}_i(\mu)$'s are the dimension-six effective operators and C_i's are the coupling constants which characterize the strength of the operators in the Hamiltonian and are known as Wilson Coefficients (WC). The constraint on a particular WC depends very much on the assumptions made on the type of New Physics (NP) present and its impact on different WCs. We propose to focus on the two WCs associated with the electromagnetic operator $\mathcal{O}_7$ and its chirally-flipped counterpart $\mathcal{O}'_7$ as tools to search for NP. The radiative inclusive decay $B \to X_s\gamma$, which is due to the underlying flavor changing neutral current (FCNC) quark transition $b \to s\gamma$, and its exclusive mode $B \to K^*\gamma$ have proven to be quite important processes for examining the SM and NP. The isospin asymmetry and a better understanding of the SM prediction should provide a sensitive testing

A. Bhatta (✉) · S. Senapati
University of Hyderabad, Hyderabad 500 046, India
e-mail: aish.bhatta@gmail.com

S. Senapati
e-mail: swayam231196@gmail.com

A. Giri and R. Mohanta (eds.), *Workshop on Frontiers in High Energy Physics 2019*, Springer Proceedings in Physics 248,
https://doi.org/10.1007/978-981-15-6292-1_61

avenue for possible models of NP, one such model is the extension of the SM with an extra generation of iso-singlet quarks [3, 4] known as Vector-like Quark Model (VQM). The heavy fields, like W and top-quark fields, are integrated out of the electroweak Lagrangian and the effective Hamiltonian is written in terms of a series of operators with increasing mass dimensions, only the lowest and next-to-lowest mass dimension operators contribute to the transitions. These operators are QCD penguin operators(O_3, O_4, O_5, O_6), Electroweak penguin operators(O_7, O_8, O_9, O_{10}) [11] and electro, chromo-magnetic operators(O_γ, O_g). O_γ has the main contribution to the $b \to s\gamma$ transition in the leading order. This leads to the SM prediction of $Br(B \to X_s\gamma) = (3.6 \pm 0.30) \times 10^{-4}$ and consequently provides constraints on the new physics beyond the SM [5–8].

61.2 Vector-Like Quark Model

The gauge structure of the SM remains intact except for an additional pair of iso-singlet quarks, which we denote them by U and D. The difference between these new quarks and ordinary quarks of the SM three generations is that, unlike the latter ones, both left- and right-handed components of the former quarks are $SU(2)_L$ singlets. The mass terms of vector-like quarks in Dirac notation

$$m_U(\bar{U}_L U_R + \bar{U}_R U_L) + m_D(\bar{D}_L D_R + \bar{D}_R D_L), \tag{61.2}$$

are invariant under electroweak gauge symmetry. The masses of the ordinary quarks arise from their gauge invariant Yukawa couplings to an iso-doublet scalar Higgs field ϕ as follows:

$$-\, f_d^{ij}\bar{\psi}_L^i d_R^j \phi - f_u^{ij}\bar{\psi}_L^i u_R^j \tilde{\phi} \;+\; \text{H.c.} \tag{61.3}$$

Because of the mixing between the SM quarks with the vector-like quarks the CKM mixing matrix is no longer unitary and thus, the transformations of O_γ lead to inter-generational mixing among quarks not only in the charged current sector but also in the neutral current interactions. This is only due to the extra iso-singlet quarks carry zero weak isospin and thus, are not involved in $SU(2)_L$ interactions as weak eigenstates. The mixing parameter is expressed as

$$\begin{aligned} U_{\alpha\beta} &= \sum_{i=1}^{3} (A_L^q)^*_{i\alpha}(A_L^q)_{i\beta} = \delta^{\alpha\beta} - (A_L^q)^*_{4\alpha}(A_L^q)_{4\beta} \\ U_{\alpha\beta} &= \begin{pmatrix} (V^\dagger V)_{\alpha\beta}\ ,\ q \equiv \text{down} - \text{type} \\ (VV^\dagger)_{\alpha\beta}\ ,\ q \equiv \text{up} - \text{type} \end{pmatrix} \end{aligned} \tag{61.4}$$

The non-unitarity of the mixing matrix V [9] in the VQM leads to the tree level FCNC in the Z sector. This in turn results in additional contributions to the isospin symmetry breaking.

61.2.1 Constraints on C_7 and C_7'

Using the recent experimental data from Particle Data Group [10] for the branching ratio of $B \to K^*\gamma$ we find the allowed region for r, which is nothing but related to the non unitary parameter U_{sb} for $b \to s\gamma$ transition, i.e. $C_7^{NP}/C_7 = re^{i\theta}$ (Fig. 61.1). The decay width for $B \to K^*\gamma$ is given as

$$\Gamma(B \to K^*\gamma) = \frac{\alpha\, G_F^2\, m_b^2}{128\pi^4 M_B^5} |V_{ts}V_{tb}|^2 |C_7(\mu)|^2 (M_B^2 - M_{K^*}^2)^3 \left[(M_B + M_{K^*})A_1(0) + (M_B - M_{K^*})V(0)\right]^2. \tag{61.5}$$

- We now proceed to study the exclusive rare radiative decay rate $\Lambda_b \to \Lambda\gamma$ for the emission of a real photon ($k^2 = 0$), where the decay width is given by

$$\Gamma(\Lambda_b \to \Lambda\gamma) = \frac{\alpha}{64\pi^4} G_F^2 m_b^2 M_{\Lambda_b}^3 |V_{tb}V_{ts}|^2 |C_7|^2 \left(1 - \frac{M_\Lambda^2}{M_{\Lambda_b}^2}\right)^3 \left(\left|f_2^{TV}\right|^2 + \left|f_2^{TA}\right|^2\right). \tag{61.6}$$

  Substituting the values of the form factors $f_2^{TV,TA}(0)$ we get the prediction for the branching fraction plot as shown in Fig. 61.2

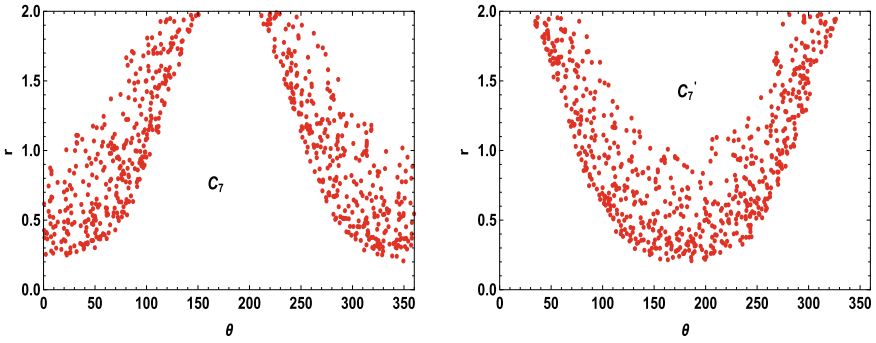

Fig. 61.1 Bound on C_7 and C_7' for $b \to s\gamma$ transition in $r - \theta$ plane

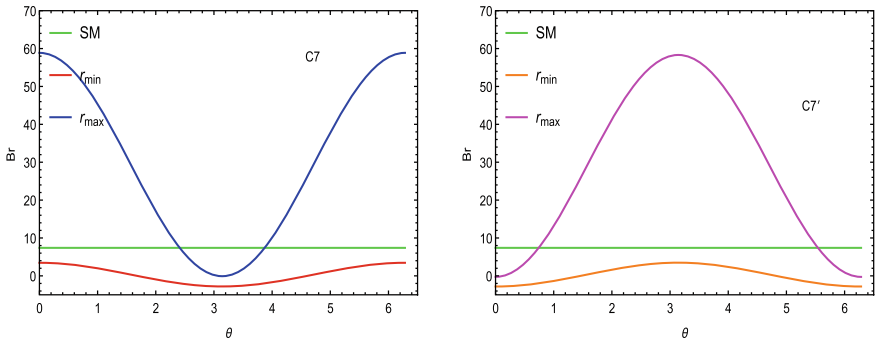

Fig. 61.2 Constraint imposed by C_7 and $C_7{}'$ to the values of $\mathcal{B}(\Lambda_b \to \Lambda\gamma) \times 10^5$, versus θ (in degree)

61.2.2 Isospin Asymmetry in VQM

Isospin symmetry breaking in $B \to K^*\gamma$ is defined as

$$\Delta_{0-} = \frac{\Gamma(\bar{B}^0 \to \bar{K}^{*0}\gamma) - \Gamma(B^- \to K^{*-}\gamma)}{\Gamma(\bar{B}^0 \to \bar{K}^{*0}\gamma) + \Gamma(B^- \to K^{*-}\gamma)}. \tag{61.7}$$

The amplitude for $b\bar{q} \to s\bar{q}$ via Z^0 exchange in VQM can be written

$$A^{VQM} = \frac{ig}{2\cos(\theta)}\left(-\frac{1}{2}U^{sb}\right)\bar{s}\gamma^{\mu}(1-\gamma_5)b \times \frac{1}{M_Z^2}\frac{ig}{2\cos(\theta)} \left[(I_W^q - Q_q \sin^2\theta)\bar{q}\gamma_{\mu}(1-\gamma_5)q - Q_q \sin^2\theta\,\bar{q}\gamma_{\mu}(1+\gamma_5)q\right], \tag{61.8}$$

where $U^{sb} = (V^{\dagger}V)^{sb}$ is a measure of the non-unitarity of the extended quark mixing matrix.

- Thus, we obtain the value of isospin asymmetry:
  $B \to K^*\gamma$: Δ_{0-}^{VQM}=-0.0699$\mathcal{R}(\frac{U^{sb}}{V_{tb}V_{ts}^*}) = -0.362$

61.2.3 Summary

We calculated the additional contribution to the isospin asymmetry due to an extra generation of vector quarks. NP can not only change the value of the SM WC, but also introduce new operators with a Dirac structure that is different from the SM ones. We have also shown that this type of new physics has also significant impact on the branching fraction of $\Lambda_b \to \Lambda\gamma$ process.

References

1. G. Hiller, E.O. Iltan, Phys. Lett. B **409**, 425-434 (1997). https://doi.org/10.1016/S0370-2693(97)00861-7, arXiv:hep-ph/9704385
2. B. Grinstein, Y. Grossman, Z. Ligeti. D. Pirjol, Phys. Rev. D **71**, 011504 (2005). https://doi.org/10.1103/PhysRevD.71.011504, arXiv:hep-ph/0412019
3. M. Ahmady, M. Nagashima, A. Sugamoto, Phys. Rev. D **64**, 054011 (2001)
4. M. Ahmady, F. Chishtie, arXiv:hep-ph/0507114
5. BELLE Collab. (M. Nakao, et al.), Phys. Rev. D **69**, 112001 (2004)
6. BABAR Collab. (E. Paoloni), Talk at the Rencontres de Moriond, Electroweak Session, La Thuile, Italy, March (2004), arXiv:hep-ex/0406083
7. CLEO Collab. (T.E. Coan, et al.), Phys. Rev. Lett. **84**, 5283 (2000)
8. P. Gambino, M. Misiak, Nucl. Phys. B **611**, 338 (2001)
9. M. Kobayashi, T. Maskawa, Prog. Theor. Phys. **49**, 652 (1973); N. Cabibbo, Phys. Rev. Lett. **10**, 531 (1963)
10. M. Tanabashi et al., Particle data group. Phys. Rev. D **98**, 030001 (2018)
11. D. Atwood, G. Hiller, arXiv:hep-ph/0307251

Correction to: UV Origin of Discrete Symmetries

Michael Ratz

Correction to:
Chapter 18 in: A. Giri and R. Mohanta (eds.),
***Workshop on Frontiers in High Energy Physics 2019*,**
Springer Proceedings in Physics 248,
https://doi.org/10.1007/978-981-15-6292-1_18

In the original version of this book, chapter 18 was published with incorrect equations. The chapter and book have been updated with the changes.

The updated version of this chapter can be found at
https://doi.org/10.1007/978-981-15-6292-1_18

A. Giri and R. Mohanta (eds.), *Workshop on Frontiers in High Energy Physics 2019*, Springer Proceedings in Physics 248,
https://doi.org/10.1007/978-981-15-6292-1_62